

The Pennsylvania State University
The Graduate School
College of Earth and Mineral Sciences

**BIOGEOCHEMISTRY OF MANGANESE CONTAMINATION
IN A TEMPERATE FORESTED WATERSHED**

A Dissertation in
Geosciences and Biogeochemistry

by

Elizabeth Maureen Herndon

© 2012 Elizabeth Herndon

Submitted in Partial Fulfillment
of the Requirements
for the Degree of

Doctor of Philosophy

December 2012

The dissertation of Elizabeth Herndon was reviewed and approved* by the following:

Susan Brantley
Distinguished Professor of Geosciences
Dissertation Advisor
Chair of Committee

Carmen Enid Martínez
Associate Professor of Environmental Soil Chemistry
Co-chair of Committee

Peter Heaney
Professor of Geosciences

Jennifer Macalady
Associate Professor of Geosciences

David Eissenstat
Professor of Woody Plant Physiology

Chris Marone
Professor of Geosciences
Associate Head for Graduate Programs and Research

*Signatures are on file in the Graduate School

ABSTRACT

Many ecosystems throughout the world are experiencing significant biogeochemical perturbation from anthropogenic activities. As one example, manganese (Mn) is enriched in surface soils at the Susquehanna Shale Hills Critical Zone Observatory (SSHCZO), a small watershed in Huntingdon County, PA. Soils at the SSHCZO record the legacy of industrial Mn inputs from the numerous iron furnaces operating in Huntingdon County during the mid-19th century and the widespread industrialization of PA into the 20th century. Atmospheric inputs of manganese to soils from disperse industrial sources have led to widespread but patchy contamination of soils with Mn in previously or currently industrialized regions throughout Pennsylvania and the United States. The enrichment of Mn in a soil profile relative to the parent lithology can be quantified to derive estimates of past atmospheric inputs. We establish that although atmospheric deposition rates of Mn have fallen with the decline of the iron and steel industries, soils, vegetation, and water systems in Pennsylvania exhibit high concentrations of Mn, and impacted ecosystems slowly release accumulated Mn from soils and vegetation into rivers.

The rate of transfer of Mn contamination from soils into rivers is strongly impacted by vegetation in SSHCZO. Specifically, trees take up dissolved Mn from the soil and store it in biomass for years to decades. Additionally, the soluble Mn that is stored in biomass is oxidized and immobilized as Mn-oxides in the soil during biomass decomposition. The continuing process of uptake, storage, and oxidation of Mn in vegetation leads to long-term retention of Mn within impacted ecosystems, and Mn is only slowly leaked from soils and vegetation into rivers. Conversely, high concentrations of soil organic matter in parts of the catchment lead to high concentrations of dissolved organic carbon that facilitate Mn mobilization from soils. Thus, the Shale Hills catchment is characterized by spatial and temporal heterogeneities in the rates that Mn is leached from soils into pore fluids and streams. Specifically, Mn is input to the SSHCZO stream dominantly from organic-rich swales during periods of low stream discharge, and Mn concentrations in the stream are diluted by inputs from organic-poor hillslopes during periods of high stream discharge. Overall, biological cycling increases Mn retention in ecosystems impacted by industrial inputs and concentrates the Mn into soils with high soil organic matter before the Mn is lost from the catchment. Vegetation therefore acts as a capacitor that concentrates Mn inputs in this temperate catchment.

TABLE OF CONTENTS

LIST OF FIGURES	vi
LIST OF TABLES	xv
ACKNOWLEDGEMENTS	xvi
Chapter 1 Manganese contamination in the Critical Zone	1
Introduction	1
Summary of chapters	4
Conclusions	7
Acknowledgements	8
References cited	9
Chapter 2 Soils reveal widespread manganese enrichment from industrial inputs	17
Abstract	17
Introduction	17
Methods	19
Results	20
Discussion	21
Acknowledgements	28
References cited	28
Chapter 3 Using mesocosm experiments to estimate the influence of vegetation on manganese in soils	35
Abstract	35
Introduction	36
Methods	39
Results	42
Discussion	45
Conclusions	53
Acknowledgements	54
References cited	55
Chapter 4 Spectroscopic characterization of Mn in the soil-plant system	65
Abstract	65
Introduction	65
Methods	69
Results	72
Discussion	77
Conclusions	80
Acknowledgements	80
References cited	81

Chapter 5 Quantifying spatial variability in Mn transport from soils to rivers using data from the Shale Hills CZO	100
Abstract	100
Introduction	101
Methods	103
Results	109
Discussion	115
Conclusions	130
Acknowledgements	132
References cited	133
Appendix A Supplementary material for Chapter 2	158
Appendix B Supplementary material for Chapter 3	174
Appendix C Supplementary material for Chapter 4	203
Appendix D Supplementary material for Chapter 5	221
Appendix E Sequential extractions	270
Appendix F Weathering lyrics	278

LIST OF FIGURES

- Figure 1-1.** Atmospheric deposition rates ($\text{kg ha}^{-1} \text{y}^{-1}$) of nitrate (NO_3^-), sulfate (SO_4^{2-}), and hydrogen ions (H^+) are plotted versus year of deposition as measured at a National Atmospheric Deposition Program site within 4 miles of SSHCZO in Huntingdon County, PA (PA-42; NADP, 2012). The best-fit slopes of linear regression lines indicate that atmospheric deposition rates have decreased significantly ($p < 0.0001$) over the past few decades for nitrate ($-0.32 \pm 0.06 \text{ kg ha}^{-1} \text{y}^{-1}$), sulfate ($-0.67 \pm 0.08 \text{ kg ha}^{-1} \text{y}^{-1}$), and hydrogen ($-0.015 \pm 0.002 \text{ kg ha}^{-1} \text{y}^{-1}$). Here, the uncertainty of the best-fit slope is reported as standard error.....12
- Figure 1-2.** Atmospheric deposition rates of manganese ($\mu\text{g cm}^{-2} \text{y}^{-1}$) are plotted as log values versus year of measurement and have declined significantly ($-0.033 \pm 0.007 \mu\text{g cm}^{-2} \text{y}^{-1}$; $p < 0.0001$) in urban and industrialized areas (orange circles) since monitoring began in the 1950s. In contrast, deposition rates recorded in rural and remote areas (blue diamonds) did not change significantly during the same time period ($p > 0.05$). The sources and calculation of the data presented here are discussed in more detail in Appendix A.13
- Figure 1-3.** Concentrations of dissolved manganese ($\mu\text{g L}^{-1}$) in the Susquehanna River, plotted here on a log scale, have decreased since the mid-20th century when the earliest data are available. The negative correlation between dissolved Mn and year is highly significant ($p < 0.0001$) and is demonstrated on the plot by a best-fit regression line ($R^2 = 0.11$). The different symbols denote water samples collected at different USGS monitoring stations located along the Susquehanna River as reported by the National Water Information System and discussed in Chapter 5 (U.S. Geological Survey, 2012).14
- Figure 1-4.** Annual raw steel production in the United States (red circles) increased steadily throughout the early 1900s and peaked around 1970 before experiencing significant decline (Jones, 1994; World Steel Association, 2010). Manganese has been used by industry in the United States primarily in steel production, and trends in manganese consumption in the United States (open squares) closely follow trends in steel production. Apparent manganese consumption is calculated by Jones (1994) as the sum of annual production and import of manganese minus annual export...15

Figure 1-5. A simplified diagram is shown here to summarize the catchment-averaged pools (in units of mmol m^{-2} as labelled) and fluxes of Mn estimated for the Susquehanna Shale Hills CZO. Fluxes of Mn between reservoirs are indicated by arrows, and values or ranges of values for each flux are displayed in white boxes in units of $\text{mmol m}^{-2} \text{y}^{-1}$. Ranges of values are given in cases where large spatial heterogeneities in fluxes were estimated. Today, the SSHCZO watershed is a net exporter of Mn.16

Figure 2-1. Normalized Mn concentrations ($\tau_{Zr,Mn}$, Eqn. 1) are plotted as different symbols versus depth for 21 ridge top soil cores at the Susquehanna Shale Hills Observatory (SSHO). Here, depth in the soil is normalized so that 1 = depth of the bedrock-soil interface. Soils document Mn enrichment ($\tau_{Zr,Mn} > 0$) near the surface that approaches underlying parent rock composition ($\tau_{Zr,Mn} = 0$) at depth. Surface soils are up to 13 times more enriched in Mn than parent. Error bars represent the propagated uncertainty in chemical analyses ($\pm 3\%$). Where no errors are shown, the bars are the size of symbols or smaller.....31

Figure 2-2. A) Model outputs for the integrated mass flux of Mn ($m_{Mn,w}$, Eqn.2) calculated for 21 SSHO ridge soils as a function of varying atmospheric deposition rates of Mn, A , over time. Each soil profile begins at a steady state mass of Mn consistent with $m_{Mn,w} = 0$ and is perturbed by atmospheric input of either anthropogenic ($A = 5 - 500 \mu\text{g cm}^{-2} \text{y}^{-1}$) or natural ($A < 5 \mu\text{g cm}^{-2} \text{y}^{-1}$) dust and solute Mn inputs at $t > 0$. The dashed horizontal line indicates the average $m_{Mn,w}$ of SSHO soils ($\sim 47 \text{mg cm}^{-2}$). B) Rates of Mn deposition reported in the literature show decreasing deposition levels between 1950 - 2010, with the highest levels associated with industrial point-sources and urban areas, and the lowest values associated with sites impacted only by natural processes (Table A-4).32

Figure 2-3. The total area-normalized Mn mass ($M_{Mn,w}$, \circ) and integrated mass flux of Mn ($m_{Mn,w}$, \blacksquare) are shown for 12 soil cores augered at distances between 1 to 24 km from the steel plant source at Burnham, PA. Soils near the plant are elevated in Mn relative to soils further away. Error bars for $m_{Mn,w}$ represent the standard deviations in calculated mass flux values for each core as described in the text. Error bars for $M_{Mn,w}$ represent analytical error in $C_{Mn,w}$ ($\pm 3\%$) and are smaller than symbols. Large standard deviations result mostly from variability in measured compositions of samples used to infer parent composition.33

Figure 2-4. Distributions of calculated $m_{Mn,w}$ (Eqn.2) for reported soil chemistry in Pennsylvania (a), the United States (b), and Europe (c) and $m_{Fe,w}$ for soils in the United States (d) (see text for dataset attributions). Values of $m_{j,w}$ for each dataset were fit to a normal distribution to determine the fraction (ϕ) of measurements falling above or below each given value of $m_{j,w}$. Values of ϕ are plotted for the absolute values of $m_{j,w}$ where net enrichment ($m_{j,w} > 0$) is plotted as a solid line and net depletion ($m_{j,w} < 0$) as a dashed line. The mean of each dataset (the value at the peak where $\phi = 0.5$) documents that net enrichment of Mn is more common than depletion in soils in Pennsylvania, the United States, and Europe, but depletion is more common for Fe in the United States.....34

Figure 3-1. The ranges of Mn concentrations in effluent ($C_{Mn,eff}$, μM) are shown on a log-scale for vegetated and non-vegetated pots containing mineral soil only, or containing soil and receiving aqueous, oxide, or organic amendments. For all pots, we excluded data for effluent collected prior to Mn addition. Each box gives the mean $C_{Mn,eff}$ for each treatment, with black diamonds indicating the 95% confidence intervals about the mean, and dashed lines designating the range of measured $C_{Mn,eff}$ values. Letters designate treatments with statistically equivalent ($p > 0.05$ for same letter) or different ($p < 0.05$ for different letters) mean $C_{Mn,eff}$ values.....58

Figure 3-2. Foliar Mn concentration ($C_{Mn,fol}$) and foliar Mn mass ($m_{Mn,fol}$) plotted versus leaf area for seedlings grown in soil-only pots (green symbols) or pots with aqueous (blue symbols), oxide (red symbols), or organic (orange symbols) additions. No significant correlation between $C_{Mn,fol}$ and leaf size is observed in the aqueous, oxide, and soil-only pots (**A**), resulting in a linear increase in total Mn with increasing leaf area (best-fit slope = $0.66 \pm 0.06 \mu\text{mol cm}^{-2}$, $p < 0.001$) (**C**). However, in organic pots, foliar Mn concentrations decrease with increasing leaf area ($p < 0.05$) (**B**), resulting in only minor increases in $m_{Mn,fol}$ with increasing leaf size (best-fit slope = $0.20 \pm 0.06 \mu\text{mol cm}^{-2}$; $p < 0.01$) (**D**). Confidence intervals (95%) for each regression are plotted as dashed lines.....59

Figure 3-3. Fractional vegetative uptake ($U_{i,s}$) plotted versus fractional leaching ($L_{i,s}$) shown on a log-log plot for eight elements (Al, Ca, Fe, K, Mg, Mn, Na, P) as measured in soil-only pots, i.e.,

pots without Mn additions. $U_{i,s} > L_{i,s}$ for Mn, Ca, Fe, K, Mg and P, while $U_{i,s} < L_{i,s}$ for Na and $U_{i,s} = L_{i,s}$ for Al ($p < 0.05$). Fractional uptake of Mn is higher than all other nutrient elements. Individual replicates (pots) are shown by each point within colored circles that group each element. Average $L_{i,s}$ values for non-vegetated pots, plotted on the x-axis in corresponding colors, exceed $L_{i,s}$ averages for vegetated pots for all elements.....60

Figure 3-4. The cumulative fraction of Mn loss ($L_{Mn,j}$) from each soil component (j = mineral soil (s), Mn-oxide (ox), Mn-rich organic matter (org), or aqueous Mn (aq)) plotted versus time for vegetated (green triangles) and non-vegetated (blue circles) pots. Note that the axes differ for the treatments because of the range of values observed: the range decreases in the order aqueous > Mn-oxide > soil-only > organic. In the aqueous treatments, non-vegetated pots released much more Mn ($L_{Mn,aq} \leq 0.20$) than vegetated pots (≤ 0.010): note that non-vegetated values are plotted on a second axis for the panel for aqueous Mn pots. In one soil-only pot that is not plotted, a step increase in cumulative Mn loss resulted from a single sample of effluent collection that exhibited an anomalously high Mn concentration.61

Figure 4-1. Left panels: Values for the absorption coefficient μ are normalized and plotted versus energy E (eV) for the manganese mineral standards MnO, Mn₂O₃, and MnO₂. **Right panels:** The derivative of each normalized $\mu(E)$ spectrum is plotted versus energy. The absorption edge energy (E_0) for each Mn-oxide standard was defined as the peak of the first derivative of $\mu(E)$, and the average and range of E_0 are indicated in each plot. An alignment of E_0 values for the MnO₂ standards was used to calibrate energies for all standard and sample spectra.....85

Figure 4-2. Spectra for Mn compounds used in the linear combination fits include four oxides (MnO, Mn₂O₃, Mn₂O₄, and MnO₂), two organic complexes (Mn²⁺-formate and Mn³⁺-acetate), and the divalent Mn cation dissolved in water (Mn²⁺ aqueous).....86

Figure 4-3. Mn K-edge XANES spectra for four bulk soil samples collected from a ridge soil core and one bulk soil sample collected from the soil-bedrock interface in a valley floor soil core.....87

Figure 4-4. The XANES spectrum for a ground bulk soil sample collected from 11 – 16 cm depth in a SSHCZO ridge top soil profile (black line, core RT08) is plotted with model spectra from linear combination fits (red lines) and the difference between the sample and model fits (dotted

line). **A)** Soil is adequately fit as 74% MnO_2 and 26% Mn_2O_3 ($R = 0.0021$), giving an average oxidation state of $\text{Mn}^{3.7+}$ in this sample. **B)** The addition of birnessite (Mn_2O_4) as a standard in the linear combination fit improves the model only slightly ($R = 0.0016$); however, the shape of the XANES spectra for all soil samples is visually more similar to birnessite than any other oxide in the model fits (Figure 4-2).....88

Figure 4-5. The XANES spectrum for a ground bulk leaf-litter sample (black line) is plotted with model spectra from linear combination fits (red lines) and the difference between the sample and model fits (dotted line). **A)** Leaf litter is adequately fit as 70% Mn^{+2} -formate and 30% aqueous Mn^{+2} (R -factor = 0.10%). **B)** Leaf litter is poorly fit by MnO , Mn_2O_3 , and MnO_2 and returns 100% similarity to Mn_2O_3 (R -factor = 11.6%).....89

Figure 4-6. Upper: Diagram of the Susquehanna Shale Hills CZO plant-soil system with reservoirs that were analyzed in this study. We infer the dominant Mn components found in each reservoir using XANES spectra: A) Green leaves, B) Leaf litter, C) Tree roots, D) Organic horizon soil and decomposing vegetation; E) Mineral soil from the ridge top and valley floor, F) Tree stems, G) Dark spots on leaves. **Lower:** Spectra of normalized $\mu(E)$ for bulk soil and vegetation samples are stacked from top to bottom as fresh vegetation (green), decomposing vegetation (brown), and soil samples (blue) and exhibit the transition from samples dominated by organic and aqueous Mn^{2+} to samples with $\text{Mn}^{3+/4+}$ -oxides.....90

Figure 4-7. Top) Optical and corresponding XRF images of a leaf collected from a mature red oak at SSHCZO. In the XRF image, pixels with warm colors correspond to high Mn fluorescence values and indicate regions of high Mn concentration. Three spots (ROIs #1, 2 and 3) were chosen for μ XANES spectral analysis. **Bottom)** Spectra from two Mn-rich dark spots on foliage (ROI #1 and #2) are distinct from bulk vegetation samples (Figure 5) and a spectrum taken from the green leaf tissue (ROI #3). The model output of a linear combination fit (red) on ROI #1 (black) are most consistent with 16% Mn^{+2} -formate and 84% Mn^{+3} -acetate (R -factor = 0.09%). The difference spectrum is shown with the dotted black line.91

Figure 4-8. Cross-section of a stem (diameter = 4 mm) from a mature chestnut oak growing at SSHCZO. Mn is distributed heterogeneously across the map and is concentrated in the outer portion of the stem tissue, likely either phloem or cambium tissue. The inner xylem tissue, in comparison,

contains low levels of Mn. The map is 4.5 x 4.5 mm with a 10 x 30 μm spot size. A) Optical image; B) XRF map of Mn; C) μXANES on ROI1; D) XRF map of K; E) XRF map of Ca.....92

Figure 4-9A: Root A: cross-section of a fine root from a red oak seedling cut through right at resin surface. Map is 0.3 x 0.3 mm with 5 μm spot size. Mn is localized to a hot spot that correlates fairly well with K, indicating Mn is present in the inner portion of the root, whereas Ca is located in the outer portion of the root.....93

Figure 4-9B: Root B: Cross-section of a fine root embedded in LR White resin. The map is 0.45 x 0.40 mm with 5 μm step sizes. Mn is distributed heterogeneously across the sample. Maps of K and Ca clearly show the boundaries of the root cross-section. The Mn-rich region in the interior of the root is most consistent with 100% Mn-formate (R-factor = 0.22%). A Mn-rich region that does not correlate with other elements (ROI 2) is most consistent with 73% Mn-formate and 27% Mn_2O_4 (R-factor = 0.36%), although Mn-formate + MnO_2 yielded a similar fit (R-factor = 0.37%).....94

Figure 4-10. A. Edge of a cross-section of a large woody root (~8 mm diameter). Map is 1.6 x 1.2 mm with 5 μm spot size. B. Mn has a broad range ($\text{Mn}/\text{I}_0 = 0 - 1.69$) across the sample, although bright specks contain the highest levels of Mn (e.g. ROI #6) while most of the root tissue contains $\text{Mn}/\text{I}_0 < 0.8$. Mn is localized to the outer part of the root. C. Mn XANES spectra are similar in all measured parts of the roots. D. K is enriched in a band slightly more interior to the root than Mn and Ca. E. Ca is distributed similarly to Mn but more diffuse.....95

Figure 4-11A. A mineral soil grain embedded with LR white resin and cut with a slow saw. The map was collected over 1.5 mm x 1 mm with a 25 μm step size. Mn/I_0 ranges from 0.0 – 0.83 with a Mn-rich region correlating to black staining on a grain. The Mn-rich zone at the top of the grain is depleted in K and only slightly enriched in Fe and Si relative to the rest of the mineral grain.....96

Figure 4-11B. A μXANES spectrum (solid black line) obtained from a Mn-rich region on a mineral soil grain (Figure 11-A) is most consistent with a combination of $\text{Mn}^{3+}/\text{Mn}^{4+}$ -oxides (linear fit shown as solid red line), similar to the bulk soil. The difference between the sample and model spectra is shown as a dotted black line.....97

Figure 5-1. Map view of the Susquehanna Shale Hills CZO showing water and soil sampling sites. Soil cores were augered to point of refusal at 23 ridge (yellow symbols), 6 slope (orange symbols), and 7 valley floor (red symbols) positions, including transects along planar (SPRT, SPMS, and SPVF) and swale (SSRT, SPMS, and SPVF) hillslopes. Pore fluid samples were collected from lysimeters installed along the planar and swale transects on the south slope and north slope (planar sites NPRT, NPMS, and NPVF and swale sites NSRT, NSMS, NSVF). Additional water samples were collected at the stream weir (SW) and from groundwater (GW). The underlying figure is adapted from Lin *et al.* (2006) and shows soil depth (color gradient) and elevation (contour lines).....138

Figure 5-2. $\tau_{Zr,Mn}$ is plotted versus depth for ridge (closed symbols), midslope (half-filled symbols), and valley floor (open symbols) for soil cores augered on planar and swale transects on the south slope of SSHCZO as shown in Figure 1 (data from Jin *et al.*, 2010; Jin and Brantley, 2011).139

Figure 5-3. $\tau_{Zr,Mn}$ (black squares), $\tau_{Zr,Mg}$ (red squares), and $\tau_{Zr,Fe}$ (blue square) values are plotted versus depth for ridge, midslope, and valley soil cores augered on planar and swale hillslopes (Figure 5-1)140

Figure 5-4. Manganese concentrations in soil pore fluids ($C_{Mn,pf}$, μM) are plotted on a log-scale versus depth in the soil profile. Pore fluids were collected from lysimeters installed at ridge, slope and valley floor positions along planar and swale transects on the south slope of SSHCZO (see Figure 5-1). The gray bars on the graphs for the south planar hillslope indicate zones of advective water transport at horizon interfaces as identified by Jin *et al.* (2011).....141

Figure 5-5. Top) Dissolved Mn concentrations in the stream ($C_{Mn,stream}$, μM) are plotted versus concurrent discharge values recorded at the stream outlet (Q_{stream} , $\text{m}^3 \text{d}^{-1}$) in log space. $C_{Mn,stream}$ values measured for $Q_{stream} < \text{DL}$ are plotted as open circles at $Q_{stream} = 0.05 \text{ m}^3 \text{d}^{-1}$. **Bottom)** Dissolved Mn loads ($L_{Mn,stream}$, mmol d^{-1} ; Eqn. 2) are plotted versus concurrent Q_{stream} values in log space. For both graphs, $C_{Mn,stream}$ values below the instrument detection limit (DL = $0.09 \mu\text{M}$) have been replaced with one-half DL (= $0.045 \mu\text{M}$) and are shown as open triangles.

Eight values measured over a one week period in November 2009 were identified as outliers and are plotted as half-filled circles..... 142

Figure 5-6. top: $\text{Log}(C_{j,stream})$ (μM) plotted versus $\text{log}(Q_{stream})$ ($\text{m}^3 \text{d}^{-1}$) for a suite of elements ($j = \text{Ca, K, Mg, Na, Si, Fe, Mn}$) measured in the SSHCZO stream. $C_{Mn,stream}$ values show similar trends compared to $C_{Fe,stream}$ but distinct trends from the major weathering elements. **bottom:** $\text{Log}(L_{j,stream})$ (mmol d^{-1}) plotted versus $\text{log}(Q_{stream})$ ($\text{m}^3 \text{d}^{-1}$) for a suite of elements ($j = \text{Ca, K, Mg, Na, Si, Fe, Mn}$) measured in the SSHCZO stream. $C_{j,stream}$ values below the detection limit are plotted as open symbols at one-half DL ($= 0.045 \mu\text{M}$). Slopes of best fit lines to each group are given in Table 5-3..... 143

Figure 5-7. Concentrations of dissolved elements in pore fluids ($C_{j,pf}$) of swale soils are plotted versus concentrations of dissolved elements in pore fluids of planar soils. The symbols represent the slope position: ridge (square), midslope (circles), or valley floor (triangle). Symbols are grouped by color for each element. $C_{j,pf}$ values for $j = \text{Al, K, Na, Mg, and Si}$ are similar in planar and swale soils and fall along the 1:1 line. For $j = \text{Mn and Fe}$, $C_{Mn,pf}$ values are higher in the swale than on the planar transect at all slope positions, and $C_{Fe,pf}$ are high in the swale ridge than the planar ridge soil. In contrast, $C_{Ca,pf}$ values are higher in the planar valley than the swale valley soils..... 144

Figure 5-8. Average Mn concentrations measured in green leaves and leaf litter ($C_{Mn,veg}$, mmol kg^{-1}) sorted by species for green leaves and by collection date for leaf litter. All green leaf samples were collected in August and September. Tree species are shown along the x-axis and identified in the main text. Error bars indicate the standard error about the mean (solid lines) and the minima and maxima (dashed lines) for $C_{Mn,veg}$ in each group..... 145

Figure 5-9. Annual water budget calculated for a box model of the planar and swale hillslopes. The model hillslope is segmented into ridge, slope, and valley boxes with equal surface area ($A = 25 \text{ m}^2$). The flux of water into pore fluids in each box ($V_{pf,s}$, $\text{m}^3 \text{m}^{-2} \text{y}^{-1}$) and the flux of water that exits each box to flow downslope ($V_{out,s}$, $\text{m}^3 \text{m}^{-2} \text{y}^{-1}$) are calculated with mass balance using

average measured annual values for precipitation ($V_{ppt} = 1.0 \text{ m}^3 \text{ m}^{-2} \text{ y}^{-1}$) and evapotranspiration ($V_{ET} = 0.5 \text{ m}^3 \text{ m}^{-2} \text{ y}^{-1}$).....146

Figure 5-10. Diagram of the average, standard error (\pm), and range (xx – xx) of Mn concentrations measured in water at the SSHCZO, including precipitation ($C_{Mn,ppt}$), groundwater ($C_{Mn,GW}$), stream water ($C_{Mn,stream}$) and pore fluids in high-flow ($C_{Mn,high}$) and low-flow ($C_{Mn,low}$) zones of ridge (SPRT), midslope (SPMS), and valley floor (SPVF) soils on the south planar transect.....147

Figure 5-11. A) Box model of Mn fluxes ($\text{mmol m}^{-2} \text{ y}^{-1}$) to and from soils on the south planar transect at SSHCZO, including inputs from precipitation (F_{ppt}), outputs from downslope transport ($F_{out,s}$), fluxes into pore fluids ($F_{pf,s}$), and recycling in vegetation (F_{veg}). **B)** Similar box model of Mn fluxes on the south swale transect.....148

Figure 5-12. Log $C_{Mn,stream}$ values measured at 14 USGS stations along the Susquehanna River between 1957 – 2010 are plotted by year with different symbols for each station. Three sites, Danville, PA (pink circles), Harrisburg, PA (blue down triangles), and Conowingo, MD (green left triangles) were targeted to further investigate changes in $C_{Mn,stream}$ over these five decades. $C_{Mn,stream}$ values measured at the other 11 USGS sites are plotted as open symbols. A best-fit linear regression line ($R^2 = 0.11$) is fit to all data points and indicates significant decline in dissolved Mn concentrations in the Susquehanna River since the 1950s ($p < 0.001$).....149

Figure 5-13. First-order rate constants (k_w , y^{-1} , Eqn.. 21) for Mn losses from soils to rivers in the Susquehanna River Basin are plotted by decade for the Danville (pink circle), Harrisburg (blue down triangle), and Conowingo (green left triangle) sites. For comparison, k_w values for SSHCZO soils (dotted line) and Mn-oxide particles (dashed line) are shown.....150

LIST OF TABLES

Table 3-1. Summary of variables used in the mass balance model for mesocosm experiments.....	62
Table 3-2. Soil-only pots: Fractional uptake ($U_{i,s}$) and leaching ($L_{i,s}$) x 10^{-5}	63
Table 3-3. Average concentrations, fluxes, rate constants, and half-lives (\pm standard error).....	64
Table 4-1. Linear combination fits on soil and vegetation samples.....	98
Table 4-2. LCF of environmental samples using vegetation and soil end-members.....	90
Table 5-1. Soil chemistry for planar and swale hillslopes and O horizon.....	151
Table 5-2. Summary of Mn concentrations in water collected from the SSHCZO.....	153
Table 5-3. Slopes of regression lines fit to elemental data in Figure 5-6.....	154
Table 5-4. Litter collected from SSHCZO in 2011.....	155
Table 5-5. Concentrations of elements in pore fluids in planar and swale soils.....	156
Table 5-6. Fluxes (F_w and F_{veg}) and rate constants (k_w and k_{veg}) \pm Standard Error.....	157

ACKNOWLEDGEMENTS

This research was made possible by funding from the National Science Foundation through the Center for Environmental Kinetics Analysis (CEKA, NSF CHE 0431328 to S. Brantley), the Susquehanna Shale Hills Critical Zone Observatory (SSHCZO, NSF EAR 0725019 to C. Duffy), and NSF grant EAR 1052614 to S. Brantley (and E. Herndon), “Soils and vegetation as a record of anthropogenic pollutants: Mn in the Shale Hills CZO”. Additional support was provided by a University Graduate Fellowship, Muan Graduate Fellowship, Biogeochemistry Research Fellowship, and grants from the Tait Scholarship, Krynine Memorial Fund, and the Geochemical Society. Synchrotron work was conducted at beamlines 13-BM, 13-ID, and 20-BM at the Advanced Photon Source, Argonne National Laboratory. GeoSoilEnviroCARS (13-BM and 13-ID) is supported by the NSF - Earth Sciences (EAR-1128799) and DOE - Geosciences (DE-FG02-94ER14466). PNC/XSD facilities at the APS (20-BM), and research at these facilities, are supported by the US DOE - Basic Energy Sciences, a Major Resources Support grant from NSERC, the University of Washington, Simon Fraser University and the Advanced Photon Source.

I am fortunate to have had the help and support of countless people during my tenure at Penn State. In particular, I could not have succeeded without the technical support team of Laura Liermann, Henry Gong, Waleska Castro, and Melanie Saffer, who always provided quality instruction and copious amounts of timely data. Beamline scientists Matt Newville (13-BM/13-ID) and Dale Brewe (20-BM) provided essential assistance with collecting data at APS, while Tim Fischer and Enid Martinez helped me unravel the mysteries of the XAS data I collected. Members of the Eissenstat lab group, specifically Dave Eissenstat, Luke McCormack, Katie Gaines, and Jane Wubbels, made my foray into the plant world possible by introducing me to the intricacies of greenhouse experiments and leaf collection. Furthermore, I thank all members of the Shale Hills CZO for providing a collaborative and energizing community to work with.

The love and support of family and friends helped me to grow personally and professionally during my years in graduate school. I thank the members of the Brantley group for all their kindness, and especially Lixin Jin for being a wonderful mentor to a new graduate student. I thank Carla Rosenfeld for being my social and scientific sounding board, Lauren Philbrook for the ~4,000 miles and counting that we've run together, and Greg Larsen for his unfailing belief in me. I thank my parents for their support and the freedom they gave me to pursue my own path. Finally, I thank my advisor, Susan Brantley, for shaping a naïve student into a scientist and for showing me all that was possible to achieve.

Chapter 1

Manganese contamination in the Critical Zone

I. Introduction

1.1. Anthropogenic impacts on the Critical Zone

Humans have transferred large quantities of material from the lithosphere to the atmosphere and Critical Zone, drastically altering the natural flow of elements (Nriagu and Pacyna, 1988; Pacyna and Pacyna, 2001; Klee and Graedel, 2004; Sen and Peucker-Ehrenbrink, 2012). One such element, carbon, has been extensively studied due to its pronounced impact on global climate (IPCC, 2007), while others, such as mercury (Hg) and lead (Pb), have been investigated due to their toxic effects and wide dispersal through the atmosphere and into soils (Galloway et al., 1982; Driscoll et al., 2007; Johnson et al., 2010). However, C, Hg, and Pb are only a few of the elements that have been perturbed by anthropogenic activities. Like Pb and Hg, other trace metals (e.g. Mn, Zn, Cu, Cr) are also emitted to the atmosphere and subsequently deposited to the land surface, and as such, can have dramatic influence on biotic systems (Nriagu and Pacyna, 1988; Pacyna and Pacyna, 2001; Kabata-Pendias and Pendias, 2001; Rauch and Pacyna, 2009). The “anthropogenic” flow of many of these trace metals now matches or exceeds their “natural” flow (Klee and Graedel, 2004; Rauch and Pacyna, 2009; Sen and Peucker-Ehrenbrink, 2012). Although a large fraction of metals used by humans are temporarily stored in the products of industry, ultimately, they are all dispersed to the environment in the form of wastes or contamination in air, soil, or water. Direct effects of trace metal deposition and secondary effects from impacted biota can lead to complex changes in soil chemistry and water quality in impacted areas (Driscoll et al., 2007; Johnson et al., 2010).

Many areas of the world are currently experiencing an increase in environmental perturbation due to the expansion of industry in these regions; however, other areas, including much of the United States, are left with the legacy of significant environmental change from past anthropogenic activity. In these regions, inputs of contaminants to soils have declined, but the soils and vegetation retain contaminants that accumulated over the period of anthropogenic influence (Landre et al., 2010). Thus, ecosystems that were once net sinks for atmospheric deposition may now act as sources of atmospherically-deposited contaminants to water systems. As an example of changing inputs, we can observe declines in the rates of atmospheric deposition of both major ions H^+ , sulfate and nitrate (Figure 1-1) and the trace metal manganese (Figure 1-2) in the northeastern United

States since the mid-20th century. We observe a similar decline in manganese concentrations in the Susquehanna River over the same time period (Figure 1-3). These trends are influenced both by increased environmental regulation of industrial emissions and a decline in industrial productivity in the region (e.g. steel production in Figure 1-4). Quantifying the effects of trace metal deposition from the air to soils is critical for predicting disturbance to ecosystem function, the residence time of trace metals in soils, and potential consequences of these environmental pollutants on human health.

As described further throughout this dissertation, we developed an approach to read the record of trace metal deposition from industrial sources in soils. In this approach described in Chapter 2 herein (Herndon et al., 2011), we identified, perhaps for the first time, widespread albeit patchy Mn contamination in surface soils throughout the United States and Europe. While researchers had previously identified sites of Mn contamination in specific localities (e.g. Boudissa et al., 2006), little has been written in the literature about widespread contamination as documented in top soils regionally. In this dissertation, I further developed this approach by tackling the following questions with respect to a small forested catchment in Pennsylvania: At what rates do trees accumulate Mn from the soil? What environmental factors contribute to retention of Mn in soils, and what effects will such contamination have on ecosystem function? What biotic processes are important in controlling rates of Mn cycling, and what Mn-compounds are formed from these biotic processes? In this first chapter, I provide background for the dissertation, review each component of my study, and provide a summary of its major findings.

1.2. Manganese in the environment

Manganese (Mn) constitutes ~0.1% of the Earth's crust where it is predominantly found in soils as finely-crystalline oxides (Post, 1999; Schaetzl and Anderson, 2002; Tebo et al., 2004). An extremely small fraction of global Mn is present in the atmosphere (Garrels et al., 1975). This Mn has been attributed to both anthropogenic emissions and natural erosion of soils; however, Mn pollution may overshadow Mn in natural mineral dusts in industrialized regions and can disseminate widely as particulates or solutes in rain (Rahn & Lowenthal, 1984; U.S. Environmental Protection Agency, 1984; Nriagu & Pacyna, 1988; Parekh, 1990; Lytle et al., 1995; Pacyna & Pacyna, 2001; Boudissa et al., 2006; Buck et al., 2010). Steel and ferroalloy manufacturing processes have historically been the primary sources of anthropogenic Mn emissions to the atmosphere (U.S. Environmental Protection Agency, 1984). Mn in the form of tricarbonylmethylcyclopentadienylmanganese (MMT) was developed as an anti-knock agent in 1957 and used as an additive in American and Canadian gasoline to replace lead compounds; however, the use of MMT

has been controversial and was banned in the U.S. during the 1980s (U.S. Environmental Protection Agency, 1984). More recently, coal combustion has become a dominant industrial source of atmospheric Mn (Nriagu and Pacyna, 1988). In fact, while steel and ferroalloy industries produced about 90% of the United States's Mn emissions in the 1960s, coal combustion became the leading Mn emitter by the 1990s (Pacyna and Pacyna, 2001).

Mn-compounds that are deposited or that form at the Earth's surface become highly-reactive soil constituents that influence the mobility of heavy metals (e.g. Co, Ni, Cu, Zn, Mo) and participate in both abiotic and microbial redox reactions (Suarez and Langmuir, 1976; Kabata-Pendias and Pendias, 2001; Tebo et al., 2004). Mn is an essential element for all life forms and is used to catalyze enzymatic reactions and facilitate photosynthesis in plants (Mukhopadhyay & Sharma, 1991; Kabata-Pendias & Pendias, 2001; Broadley et al., 2012). However, excess levels of Mn in leaves can lead to photooxidative stress and decline in tree vitality (Gonzalez & Lynch, 1999; St. Clair et al., 2005). The effects of Mn toxicity have been seen throughout the northeastern United States where sugar maples, a Mn-sensitive species, have experienced extensive dieback due to the combined effects of high Mn and low base cation saturation in soils (Horsley et al., 2000; Juice et al., 2006; Kogelmann & Sharpe, 2006). Additionally, where present in the air at very high concentrations, Mn is regulated as a human health hazard by the United States Environmental Protection Agency (EPA) due to well-established links between respirable Mn and neurological disorders (U.S. Environmental Protection Agency, 1984; Merger et al., 1994; Dobson et al., 2004).

Mn concentrations in the air have declined since monitoring began (National Research Council, 1973; U.S. Environmental Protection Agency, 1984; references in Herndon et al., 2011). However, no data is available in the U.S.A. prior to the 1950s that can be used to assess total deposition over the entire time scale of industrial impact. Nonetheless, as shown in this dissertation, the geographic distribution and environmental fate of atmospheric Mn can be deciphered from regolith profiles. These profiles record the time-integrated net effects of inputs, outputs, and internal redistribution processes and can be used to quantify influences on soil development, including past inputs from the air (Brimhall & Dietrich, 1987; Chadwick et al., 1990; Chadwick et al., 1999; Kurtz et al., 2001; Brantley and White, 2009; Brantley and Lebedeva, 2011). For example, elemental profiles of regolith that include analysis of deep protolith samples can document net enrichment of certain elements relative to the parent material and are interpreted as addition profiles. In contrast, other profiles that document net leaching due to natural weathering processes are interpreted as depletion profiles (Brantley & White, 2009; Brantley & Lebedeva, 2011).

1.3. Susquehanna Shale Hills Critical Zone Observatory

While such mass balance arguments document net addition or depletion, integrated soil, geological, ecological, and hydrological observations are necessary to infer long-term rates of deposition or other chemical processes in the soil. In this dissertation, I utilized such observations that are available for the Susquehanna Shale Hills Observatory (SSHCZO), one of six Critical Zone Observatories (CZO) in the United States. The Critical Zone is defined as the region of the Earth's surface extending from groundwater to the top of vegetation that includes complex interactions amongst water, air, rock, soil and biota. The SSHCZO is a small, forested watershed developed on Rose Hill shale and is the focus of extensive multidisciplinary characterization (Lin, 2006; Lin et al., 2006; Qu and Duffy, 2007; Jin et al., 2010; Ma et al., 2010; Andrews et al., 2011; Jin et al., 2011). Our detailed soil characterization at SSHO reveals that Mn is commonly observed as an addition profile while the geochemically similar element Fe is consistently present as a depletion profile (Jin et al., 2010; Herndon et al., 2011). Such inferences can be explained by loss of Fe to weathering but gain of Mn due to atmospheric inputs.

The SSHCZO is located in Huntingdon County, Pennsylvania, USA. Central PA was the epicenter for iron production in the early 19th century United States and contained approximately 87 operational furnaces and forges at its peak in 1840. Forty-seven of these furnaces, including Monroe Furnace at 4 km from SSHO, were located in Huntingdon County (Stine, 1964). Our observations of excess soil Mn at SSHO led us to analyze soils near a modern steel factory in Burnham, PA and to analyze databases of Pennsylvania (Ciolkosz & Amistadi, 1993; Ciolkosz et al., 1998; Ciolkosz, 2000), the United States (Muhs et al., 1998; Teutsch et al., 1999; NRCS, 2010), and European soils (FOREGS, 2010). These databases, along with our specific observations for SSHCZO and Burnham soils, lead to the conclusion that the topsoils of industrialized regions are commonly contaminated with excess Mn and that such contamination is widely, albeit heterogeneously, distributed. The best explanation for this widespread Mn addition is atmospheric contamination from industrial activity. The patchy distribution is due to both the point nature of many Mn emission sources and the variable capabilities of soils to retain as opposed to leach Mn.

II. Summary of chapters

The second chapter in this dissertation, *Soils reveal widespread manganese enrichment from industrial inputs*, identifies Mn contamination in soils in central Pennsylvania and throughout the United States and Europe (Herndon et al., 2011). In a detailed geochemical study at the Susquehanna Shale Hills Critical Zone Observatory, ridge top soils were found to be enriched in

Mn relative to the shale bedrock. High Mn concentrations were observed near the soil surface, and Mn concentrations decreased with depth in the profile until reaching parent composition, consistent with an addition profile for atmospherically input elements (Brantley & Lebedeva, 2011). Soil chemistry, water chemistry, and regolith production rates were integrated to create a mass balance model that was used to derive the timeframe and magnitude of Mn inputs to the soil. Mn enrichment in the soil was found to be consistent with short-term, high-magnitude atmospheric inputs from industrial deposition. To corroborate the hypothesis that Mn could be input to soils from industrial processes, soils near a steel production plant in Burnham, PA were analyzed and also observed to exhibit Mn enrichment near the plant. By compiling soil geochemistry data from various databases, it was discovered that over half of the soils in the dataset for the United States and Europe, particularly those in industrialized regions, contain excess Mn relative to their parent material. This study provided a model for assessing atmospheric inputs to soils and was the first to identify widespread, patchy Mn contamination from anthropogenic sources. The chapter is reproduced here as published (Herndon et al., 2011).

The third chapter describes a mesocosm system developed to investigate vegetative cycling of Mn in SSHCZO and to quantify rates of Mn leaching from soil. Each mesocosm was built as a tree pot containing soil from SSHCZO. Pots received one of four treatments: aqueous Mn addition, Mn-oxide particle addition, addition of Mn-rich organic matter, or no extra Mn. In addition, some mesocosms were vegetated by red oak seedlings while other tree pots were left non-vegetated. First-order rate constants describing the rate of Mn leaching from each Mn-bearing source were derived by using effluent from each mesocosm to quantify mass outputs of Mn over time. Mn from soil “contaminants” (e.g. Mn-oxides, aqueous Mn) was leached more quickly than Mn from the background soil (i.e. shale-derived minerals), while organic matter slowed Mn leaching from the mesocosms. Furthermore, the vegetated mesocosm systems exhibited less Mn loss than the non-vegetated systems, indicating that vegetation may slow the removal of Mn contamination from soils into rivers by concentrating it in living biomass and decomposing organic matter. Rate constants derived at the mesocosm-scale were successfully used to predict rates of Mn leaching and uptake into vegetation at the field-scale. The results of this study allow better predictions of the timescales that Mn contamination persists in soils and how quickly Mn moves into river systems.

The fourth chapter details the results of a spectroscopic investigation into Mn speciation in soils and vegetation at the SSHCZO. Synchrotron-source techniques, such as X-Ray Fluorescence (XRF) and X-ray Absorption Near Edge Structure (XANES) spectroscopy, are particularly suited to probe the chemical speciation and microscale distribution of Mn in environmental samples. This

study was used to explore biogeochemical processes that may increase or decrease rates of Mn removal from soils. Plant tissues (e.g. leaves, roots, stems) were found to store aqueous and organic Mn(II). In contrast, decomposing leaves, organic matter, and mineral soils contain predominantly Mn(III/IV)-oxides. In short, vegetation slowed the removal of Mn from the soil by accumulating soluble Mn(II) which was rapidly immobilized as Mn(III/IV)-oxides during decomposition of organic matter. This process may contribute to the retention of Mn in soils relative to other contaminant elements. Furthermore, differences in Mn chemistry were seen with depth in the soil profile and may represent a mixing of Mn from the parent shale and addition sources.

The purpose of the last chapter was to evaluate how rates of Mn mobilization vary across landscapes. In particular, the mass balance models developed in Chapters 2 and 3 were expanded in Chapter 5 to model Mn transport in pore fluids on planar and swale hillslopes at SSHCZO. Swales were found to be dominant sources of dissolved Mn transport into the stream relative to planar hillslopes, most likely due to the low pH and high organic content of swale soils in comparison to soils on planar hillslopes. This observation is of interest in comparison to the results of Chapter 3 where we observed that organic matter accumulated Mn in the mesocosms. The best way to explain this apparent discrepancy is to note that organic matter can both accumulate and release Mn and that the net output of Mn from organic matter can change with time. Over a short timescale in the mesocosms, organic matter accumulated Mn that leached from the mineral soil, whereas in the catchment, the decomposition of organic matter that had accumulated high amounts of Mn led to the release of Mn from soils into the stream. The role of vegetation and soil organic matter as “capacitors” also can explain a long-standing puzzle in the literature of catchment hydrogeochemistry. Namely, it is well known that in many streams, the concentrations of major elements derived from rock weathering vary little over a wide range of stream discharge rates while concentrations of trace elements can vary considerably (Kirchner, 2002; Gaillardet et al., 2004; Godsey et al., 2009). At Shale Hills, concentrations of Mn were observed to vary significantly with discharge such that dissolved Mn fluxes did not respond strongly to hydrologic forcing by precipitation events. This behavior is best explained by noting that vegetation in the catchment has accumulated Mn and concentrated it into organic matter that is disproportionately stored in swales whose continuously wet soils release Mn to the stream throughout all weather conditions. Thus, Mn fluxes into the stream were highly affected by both soil/sediment properties and hydrological conditions. Finally, these short timescale patterns of release of Mn were overprinted by longer term trends: the historical records of Mn concentrations in the Susquehanna River document significant

decreases since the 1950s, a trend that is here attributed to a shift from the weathering predominantly of Mn-oxide contaminants to the weathering of bedrock minerals.

III. Conclusions

The environmental impacts of Mn addition to soils and its effect on nutrient cycling are poorly understood. It is important to elucidate the chemical behavior of Mn given that Mn is a highly-reactive soil component affecting organic matter breakdown, contaminant transport, and forest health (Suarez & Langmuir, 1976; Hofrichter, 2002; Horsley et al., 2000; Kogelmann & Sharpe, 2006; Berg et al., 2007). In summary, I present a first quantification of Mn biogeochemistry in one temperate watershed impacted by atmospheric Mn deposition, estimated using soil, water, and vegetation data from the Shale Hills CZO (Figure 1-5).

In this diagram, pools and fluxes of Mn represent catchment-averaged values and are compiled from estimates detailed in various chapters of this dissertation. Briefly, values for the mineral soil and foliage pools and for uptake and litterfall fluxes are described in Chapter 5. Atmospheric deposition rates, past and present, are presented in Chapter 2. The organic horizon pool was calculated as the product of the average Mn concentration in the organic horizon (Chapter 5) and the area-normalized mass of the organic horizon (Chapter 3). Reported ranges of soil production and erosion fluxes (see Chapter 2 for equations) encompass ranges of values derived for ridgetop, midslope, and valley floor positions using average soil chemistry (Chapter 5) and regolith production rates (Lin et al., 2010) at each slope position. Ranges that represent values obtained from a variety of estimation methods are also reported for the flux of dissolved Mn from soils to the stream and for the flux of dissolved Mn exiting the catchment in streamwater (Chapter 5). The pool of Mn in shale bedrock summarized in the figure was estimated for a volume of shale protolith equivalent to the volume of soil in the catchment (see Chapter 5 for estimates of soil volume). This estimate assumed that the rock weathers isovolumetrically (zero strain); however, soils at SSHCZO are observed to have positive strain, i.e. the soil has expanded to a larger volume than the protolith (Jin et al., 2010). Therefore, the pool of Mn in the shale is an upper-level estimate. Finally, the pool of Mn stored in woody biomass was calculated as the product of Mn concentration in xylem wood reported for an analogous Pennsylvania forest (Kogelmann and Sharpe, 2006) and total aboveground biomass, minus foliar biomass (see Chapter 5), calculated using an allometric equation (Jenkins et al., 2004) and tree metrics reported for the SSHCZO (Wubbels, 2010).

This compilation of the pools and fluxes of Mn at SSHCZO highlights the dominant role that vegetation plays in moving Mn within the watershed. Specifically, the annual mass of Mn taken up

from the soil into tree biomass and returned from trees to soil as litterfall far exceeds other mass fluxes. This dissertation presents one of the first efforts to both quantify inputs of Mn to soils and to understand the long-term biogeochemistry of Mn contamination. Vegetation was found to act as a capacitor for atmospherically-deposited Mn, sequestering Mn in biomass and slowly releasing it to the environment over time. Specifically, we determined that certain types of vegetation, such as the temperate forest studied here, have the ability to slow the rate of transfer of Mn contaminants from soils into water systems by an order of magnitude or more.

IV. Acknowledgements

This dissertation has been completed under the auspices of two NSF-funded interdisciplinary programs. The first, the Center for Environmental Kinetics Analysis (CEKA, NSF CHE-0431328), brought together scientists from a variety of disciplines to measure rates of environmental reactions and model the temporal evolution of natural and anthropogenically-perturbed systems. One important goal of this program was to examine how rates of environmental reactions change across spatial scales. This dissertation tackles both the objective to derive rates for environmental processes and the mandate to cross spatial scales. In particular, this research scales across microscale spectroscopy (Chapter 4), mesocosm experiments (Chapter 3), a first-order watershed (Chapters 2 and 5), the Susquehanna River Basin (Chapter 5), and soils of the United States and Europe (Chapter 2).

The second program, the Susquehanna Shale Hills Critical Zone Observatory (NSF EAR-#0725019), aims to “quantitatively predict the creation, evolution, and structure of regolith as a function of the geochemical, hydrologic, biologic, and geomorphologic processes operating in a temperate, forested landscape” (www.czo.psu.edu). This dissertation benefited immensely from the interdisciplinary collaboration at SSHCZO, particularly group efforts to obtain soil, water, and vegetation samples, and discussions garnered from research presentations. I generated the field data presented in this study in collaboration with other members of the SSHCZO. In particular, Lixin Jin, Jennifer Williams, Blake Ketchum, Zoe Ruge, Danielle Andrews, Katya Bazilevskaya, Molly Holleran, and Tiffany Yesavage contributed greatly to augering soil cores and sampling lysimeters and stream water. Additionally, the water chemistry data and much of the soil chemistry data from SSHCZO were provided by Lixin Jin. Additional soil cores from both the SSHCZO and from sites near Burnham, PA were collected and analyzed by members of the Geosc 413W Techniques in Environmental Geochemistry course in 2009 under my mentorship.

V. References

- Andrews D. M., Lin H., Zhu Q., Jin L. and Brantley S. L. (2011) Hot Spots and Hot Moments of Dissolved Organic Carbon Export and Soil Organic Carbon Storage in the Shale Hills Catchment. *Vadose Zone Journal* **10**, 943.
- NRCS (2010) National Cooperative Soil Characterization Data. Available at: <http://soils.usda.gov/survey/geochemistry/>.
- Berg B., Steffen K. T. and McClaugherty C. (2007) Litter decomposition rate is dependent on litter Mn concentrations. *Biogeochemistry* **82**, 29–39.
- Boudissa S. M., Lambert J., Müller C., Kennedy G., Gareau L. and Zayed J. (2006) Manganese concentrations in the soil and air in the vicinity of a closed manganese alloy production plant. *The Science of the total environment* **361**, 67–72.
- Brantley S.L. and White A. (2009) Approaches to modeling weathered regolith. In *Thermodynamics and Kinetics of Water-Rock Interaction* (eds. E. H. Oelkers and J. Schott). The Mineralogical Society of America, Chantilly, VA. pp. 435–484.
- Brantley S. L. and Lebedeva M. (2011) Learning to Read the Chemistry of Regolith to Understand the Critical Zone. *Annual Review of Earth and Planetary Sciences* **39**, 387–416.
- Brimhall G. H. and Dietrich W. E. (1987) Constitutive mass balance relations between chemical composition, volume, density, porosity, and strain in metasomatic hydrochemical systems: Results on weathering and pedogenesis. *Geochimica et Cosmochimica Acta* **51**, 567–587.
- Broadley M., Brown P., Cakmak I., Rengel Z. and Zhao F. (2012) Function of Nutrients: Micronutrients. In *Marschner's Mineral Nutrition of Higher Plants* pp. 191–248.
- Buck C. S., Landing W. M., Resing J. a. and Measures C. I. (2010) The solubility and deposition of aerosol Fe and other trace elements in the North Atlantic Ocean: Observations from the A16N CLIVAR/CO2 repeat hydrography section. *Marine Chemistry* **120**, 57–70.
- Chadwick O A, Derry L A, Vitousek P. M., Huebert B. J. and Hedin L. O. (1999) Changing sources of nutrients during four million years of ecosystem development. *Nature* **397**, 491–497.
- Chadwick O. A., Brimhall G. H. and Hendricks D. M. (1990) From a black to a gray box — a mass balance interpretation of pedogenesis. *Geomorphology* **3**, 369–390.
- Ciolkosz E. J. (2000) Major and Trace Elements in Southwestern Pennsylvania Soils. *Agronomy Series Number 148*, The Pennsylvania State University.
- Ciolkosz E. J. and Amistadi M. K. (1993) Metals in Pennsylvania Soils. *Agronomy Series Number 128*, The Pennsylvania State University.
- Ciolkosz E. J., Stehouwer R. C. and Amistadi M. K. (1998) Metals Data for Pennsylvania Soils. *Agronomy Series Number 140*, The Pennsylvania State University.
- Dobson A. W., Erikson K. M. and Aschner M. (2004) Manganese Neurotoxicity. *Ann. N.Y. Acad. Sci.* **1012**, 115–128.
- Driscoll C. T., Han Y.-J., Chen C. Y., Evers D. C., Lambert K. F., Holsen T. M., Kamman N. C. and Munson R. K. (2007) Mercury Contamination in Forest and Freshwater Ecosystems in the Northeastern United States. *BioScience* **57**, 17.
- FOREGS (2010) Geochemical Atlas of Europe. Available at: <http://www.gtk.fi/publ/foregsatlas/>.
- Galloway J. N., Thornton J. D., Norton S. a., Volchok H. L. and McLean R. A. N. (1982) Trace metals in atmospheric deposition: A review and assessment. *Atmospheric Environment* **16**, 1677–1700.
- Garrels R. M., Mackenzie F. T. and Hunt C. (1975) *Chemical cycles and the global environment - assessing human influences.*, W. Kaufman, Inc., Los Altos, CA.
- Gonzalez A. and Lynch J P (1999) Subcellular and tissue Mn compartmentation in bean leaves under Mn toxicity stress. *Australian Journal of Plant Physiology* **26**, 811–822.

- Herndon E. M., Jin Lixin and Brantley Susan L (2011) Soils reveal widespread manganese enrichment from industrial inputs. *Environmental science & technology* **45**, 241–7.
- Hofrichter M. (2002) Review: lignin conversion by manganese peroxidase (MnP). *Enzyme and Microbial Technology* **30**, 454–466.
- Horsley S. B., Long R. P., Bailey S. W., Hallett R. A. and Hall T. J. (2000) Factors associated with the decline disease of sugar maple on the Allegheny Plateau. *Canadian Journal of Forest Research* **30**, 1365–1378.
- Jenkins J.C., Chojnacky D.C., Heath L.S., Birdsey R.A. (2004) Comprehensive database of diameter-based biomass regressions for North American tree species. USDA Forest Service General Technical Report NE-319.
- Jin Lixin, Andrews D. M., Holmes G. H., Lin Henry and Brantley Susan L. (2011) Opening the “Black Box”: Water Chemistry Reveals Hydrological Controls on Weathering in the Susquehanna Shale Hills Critical Zone Observatory. *Vadose Zone Journal* **10**, 928.
- Jin L., Ravella R., Ketchum B., Bierman P. R., Heaney P., White T. and Brantley S. L. (2010) Mineral weathering and elemental transport during hillslope evolution at the Susquehanna/Shale Hills CZO. *Geochimica et Cosmochimica Acta* **74**, 3669–3691.
- Johnson C. E., Siccama T. G., Driscoll C. T., Likens G. E. and Robert E. (2010) Changes in Lead Biogeochemistry in Response to Decreasing Atmospheric Inputs. *Ecological Applications* **5**, 813–822.
- Jones T. S. (1994) *Manganese Material Flow Patterns*. Bureau of Mines Information Circular 9399.
- Juice S. M., Fahey T. J., Siccama T. G., Driscoll C. T., Denny E. G., Eagar C., Cleavitt N. L., Minocha R. and Richardson A. D. (2006) Response of sugar maple to calcium addition to northern hardwood forest. *Ecology* **87**, 1267–80.
- Kabata-Pendias A. (2004) Soil–plant transfer of trace elements—an environmental issue. *Geoderma* **122**, 143–149.
- Kabata-Pendias A. and Pendias H. (2001) *Trace elements in soils and plants*. 3rd ed., CRC Press LLC, Boca Raton.
- Kirchner, J.W. (2002) A double paradox in catchment hydrology and geochemistry. *Hydrol. Process.* **17**, 871–874.
- Klee R. J. and Graedel T. E. (2004) Elemental Cycles: A Status Report on Human or Natural Dominance. *Annual Review of Environment and Resources* **29**, 69–107.
- Kogelmann W. J. and Sharpe W. E. (2006) Soil acidity and manganese in declining and nondeclining sugar maple stands in Pennsylvania. *Journal of environmental quality* **35**, 433–41.
- Kurtz A. C., Derry L.A. and Chadwick O.A. (2001) Accretion of Asian dust to Hawaiian soils: Isotopic, elemental, and mineral mass balances. *Geochimica et Cosmochimica Acta* **65**, 1971–1983.
- Landre A. L., Watmough S. A. and Dillon P. J. (2010) Metal Pools, Fluxes, and Budgets in an Acidified Forested Catchment on the Precambrian Shield, Central Ontario, Canada. *Water, Air, & Soil Pollution* **209**, 209–228.
- Lin H. S., Kogelmann W., Walker C. and Bruns M. A. (2006) Soil moisture patterns in a forested catchment: A hydrogeological perspective. *Geoderma* **131**, 345–368.
- Lin H. and Zhou X. (2008) Evidence of subsurface preferential flow using soil hydrologic monitoring in the Shale Hills catchment. *European Journal of Soil Science* **59**, 34–49.
- Lin Henry (2006) Temporal stability of soil moisture spatial pattern and subsurface preferential flow pathways in the Shale Hills catchment. *Vadose Zone Journal* **5**, 317–340.
- Lytle C., Smith B. and Mckinnon C. (1995) Manganese accumulation along Utah roadways: a possible indication of motor vehicle exhaust pollution. *Science of The Total Environment* **162**, 105–109.

- Ma L., Chabaux F., Pelt E., Blaes E., Jin L and Brantley Susan L (2010) Regolith production rates calculated with uranium-series isotopes at Susquehanna/Shale Hills Critical Zone Observatory. *Earth and Planetary ...* **297**, 211–225.
- Mergler D., Huel G. and Bowler R. (1994) Nervous system dysfunction among workers with long-term exposure to manganese. *Environmental Research* **64**, 151–180.
- Muhs D. R., Bettis E. A., Been J. and Mcgeehin J. P. (1998) Impact of Climate and Parent Material on Chemical Weathering in Loess-derived Soils of the Mississippi River Valley., 1761–1777.
- Mukhopadhyay M. J. and Sharma A. (1991) Manganese in Cell Metabolism of Higher Plants. *The Botanical Review* **57**, 117–149.
- NADP (2012) National Atmospheric Deposition Program. Available at: nadp.sws.uiuc.edu/.
- National Research Council ed. (1973) *Medical and biological effects of environmental pollutants: manganese*. National Academy of Sciences, Washington, D.C.
- Nriagu J. and Pacyna J. (1988) Quantitative assessment of worldwide contamination of air, water and soils by trace metals. *Nature* **333**, 134–139.
- Pacyna J.M. and Pacyna E. G. (2001) An assessment of global and regional emissions of trace metals to the atmosphere from anthropogenic sources worldwide. *Environmental Reviews* **9**, 269–298.
- Parekh P. P. (1990) A study of manganese from anthropogenic emissions at a rural site in the eastern United States. *Atmospheric Environment* **24A**, 415–421.
- Post J. E. (1999) Manganese oxide minerals: Crystal structures and economic and environmental significance. *Proceedings of the National Academy of Sciences* **96**, 3447–3454.
- Qu Y. and Duffy C. J. (2007) A semidiscrete finite volume formulation for multiprocess watershed simulation. *Water Resources Research* **43**, W08419.
- Rahn K. and Lowenthal D. (1984) Elemental tracers of distant regional pollution aerosols. *Science* **223**, 132–139.
- Rauch J. N. and Pacyna Jozef M. (2009) Earth's global Ag, Al, Cr, Cu, Fe, Ni, Pb, and Zn cycles. *Global Biogeochemical Cycles* **23**, GB2001.
- Schaetzl R. and Anderson S. (2002) *Soils genesis and geomorphology.*, University Press, Cambridge, UK.
- Sen I. S. and Peucker-Ehrenbrink B. (2012) Anthropogenic Disturbance of Element Cycles at the Earth's Surface. *Environmental science & technology* **46**, 8601–9.
- St. Clair S. B., Carlson J. E. and Lynch Jonathan P (2005) Evidence for oxidative stress in sugar maple stands growing on acidic, nutrient imbalanced forest soils. *Oecologia* **145**, 258–69.
- Stine H. E. (1964) The story of Juniata iron. Master's Thesis, The American University.
- Suarez D. and Langmuir D. (1976) Heavy metal relationships in a Pennsylvania soil. *Geochimica et Cosmochimica Acta* **40**, 589–598.
- Tebo B. M., Bargar J. R., Clement B. G., Dick G. J., Murray K. J., Parker D., Verity R. and Webb S. M. (2004) Biogenic manganese oxides: Properties and mechanisms of formation. *Annual Review of Earth and Planetary Sciences* **32**, 287–328.
- Teutsch N., Erel Y., Halicz L. and Chadwick O. (1999) The influence of rainfall on metal concentration and behavior in the soil. *Geochimica et Cosmochimica Acta* **63**, 3499–3511.
- U.S. Environmental Protection Agency (1984) *Health Assessment Document for Manganese.*, Cincinnati, Ohio.
- U.S. Geological Survey (2012) USGS Water Data for the Nation. Available at: <http://waterdata.usgs.gov/nwis>.
- World Steel Association (2010) *Steel Statistical Yearbook 2009*, Brussels.
- Wubbels J. K. (2010) Tree species distribution in relation to stem hydraulic traits and soil moisture in a mixed hardwood forest in central Pennsylvania. Master's Thesis, The Pennsylvania State University.

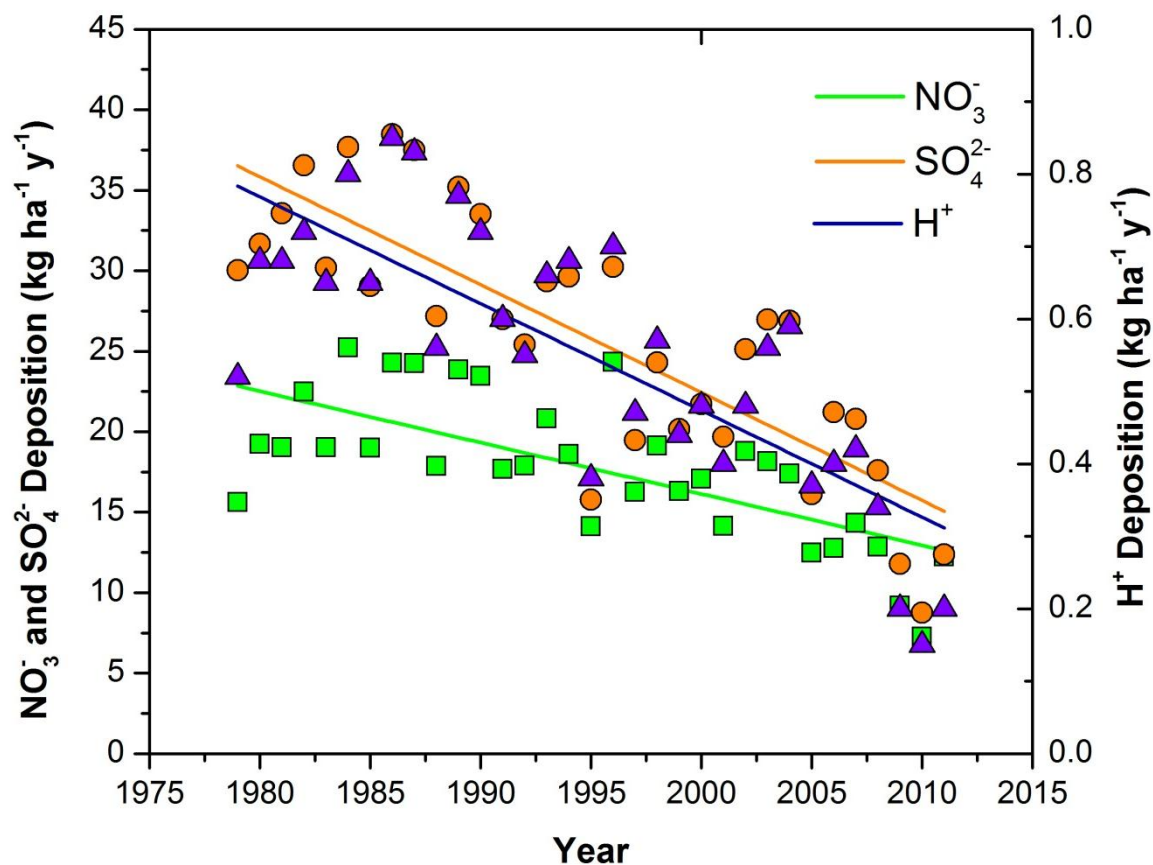


Figure 1-1. Atmospheric deposition rates ($\text{kg ha}^{-1} \text{y}^{-1}$) of nitrate (NO_3^-), sulfate (SO_4^{2-}), and hydrogen ions (H^+) are plotted versus year of deposition as measured at a National Atmospheric Deposition Program site within 4 miles of SSHCZO in Huntingdon County, PA (PA-42; NADP, 2012). The best-fit slopes of linear regression lines indicate that atmospheric deposition rates have decreased significantly ($p < 0.0001$) over the past few decades for nitrate ($-0.32 \pm 0.06 \text{ kg ha}^{-1} \text{y}^{-1}$), sulfate ($-0.67 \pm 0.08 \text{ kg ha}^{-1} \text{y}^{-1}$), and hydrogen ($-0.015 \pm 0.002 \text{ kg ha}^{-1} \text{y}^{-1}$). Here, the uncertainty of the best-fit slope is reported as standard error.

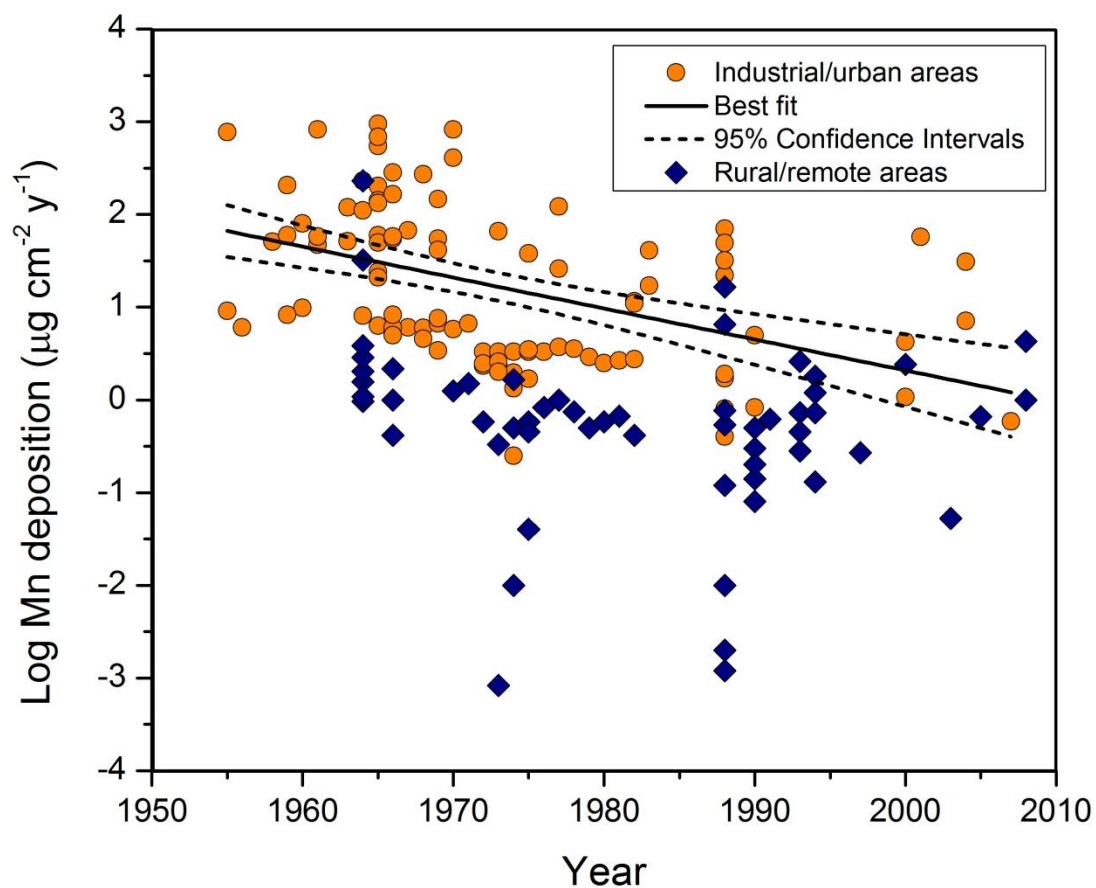


Figure 1-2. Atmospheric deposition rates of manganese ($\mu\text{g cm}^{-2} \text{y}^{-1}$) are plotted as log values versus year of measurement and have declined significantly ($-0.033 \pm 0.007 \mu\text{g cm}^{-2} \text{y}^{-1}$; $p < 0.0001$) in urban and industrialized areas (orange circles) since monitoring began in the 1950s. In contrast, deposition rates recorded in rural and remote areas (blue diamonds) did not change significantly during the same time period ($p > 0.05$). The sources and calculation of the data presented here are discussed in more detail in Appendix A.

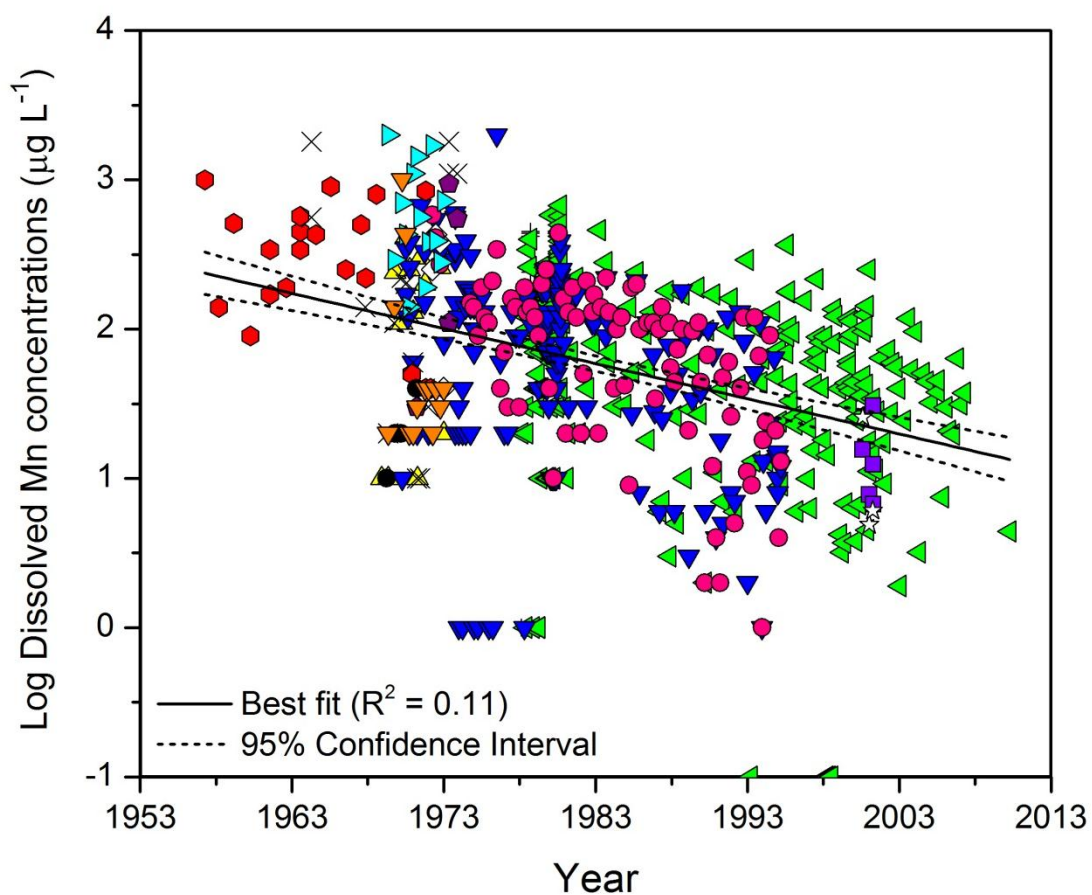


Figure 1-3. Concentrations of dissolved manganese ($\mu\text{g L}^{-1}$) in the Susquehanna River, plotted here on a log scale, have decreased since the mid-20th century when the earliest data are available. The negative correlation between dissolved Mn and year is highly significant ($p < 0.0001$) and is demonstrated on the plot by a best-fit regression line ($R^2 = 0.11$). The different symbols denote water samples collected at different USGS monitoring stations located along the Susquehanna River as reported by the National Water Information System and discussed in Chapter 5 (U.S. Geological Survey, 2012).

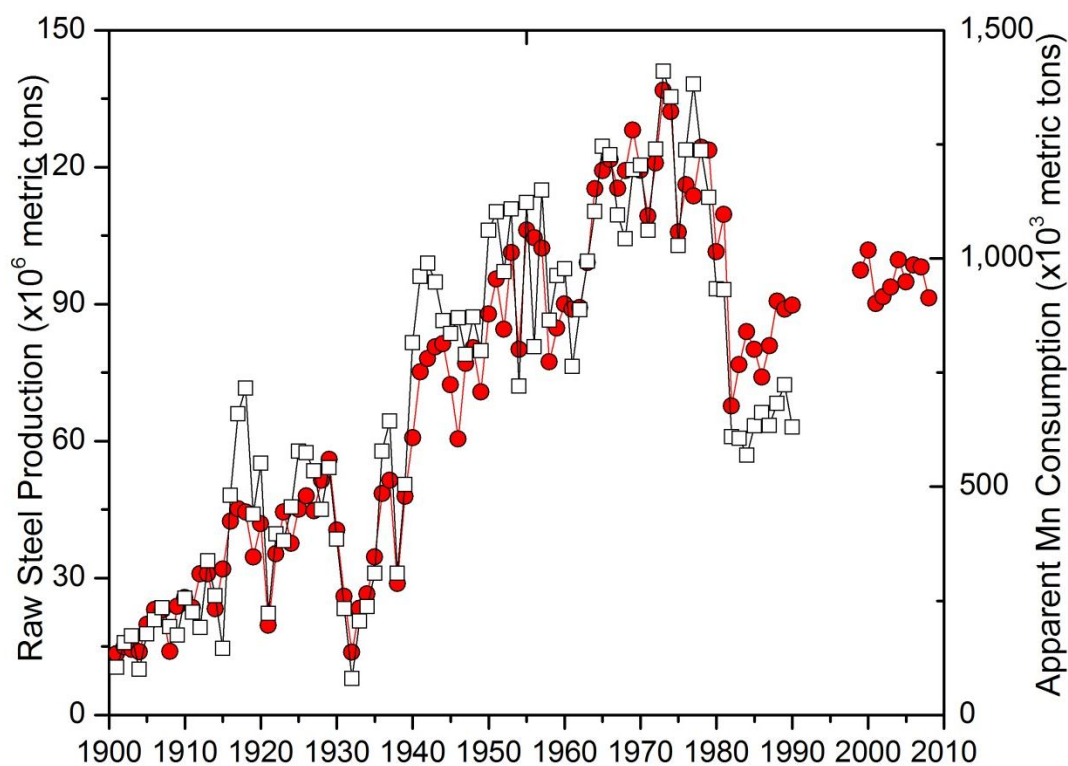


Figure 1-4. Annual raw steel production in the United States (red circles) increased steadily throughout the early 1900s and peaked around 1970 before experiencing significant decline (Jones, 1994; World Steel Association, 2010). Manganese has been used by industry in the United States primarily in steel production, and trends in manganese consumption in the United States (open squares) closely follow trends in steel production. Apparent manganese consumption is calculated by Jones (1994) as the sum of annual production and import of manganese minus annual export.

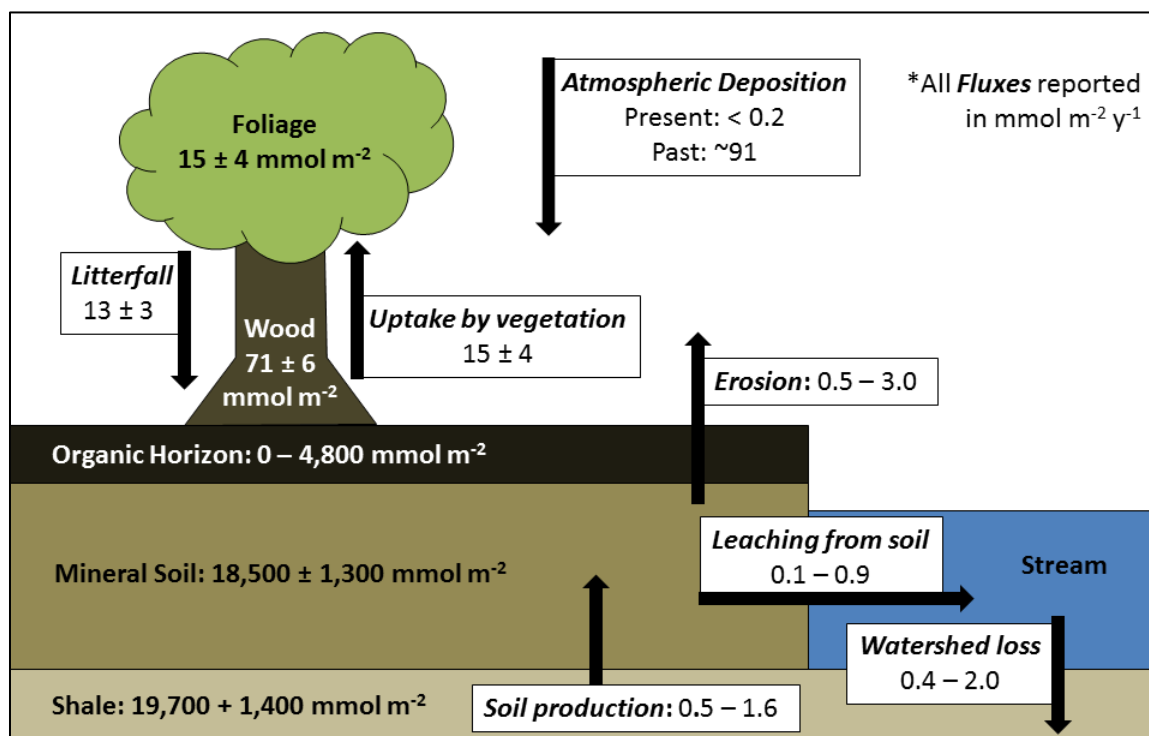


Figure 1-5. A simplified diagram is shown here to summarize the catchment-averaged pools (in units of mmol m^{-2} as labelled) and fluxes of Mn estimated for the Susquehanna Shale Hills CZO. Fluxes of Mn between reservoirs are indicated by arrows, and values or ranges of values for each flux are displayed in white boxes in units of $\text{mmol m}^{-2} \text{y}^{-1}$. Ranges of values are given in cases where large spatial heterogeneities in fluxes were estimated. Today, the SSHCZO watershed is a net exporter of Mn.

Chapter 2

Soils reveal widespread manganese enrichment from industrial inputs

Abstract

It is well known that metals are emitted to the air by human activities and subsequently deposited to the land surface; however, we have not adequately evaluated the geographic extent and ecosystem impacts of industrial metal loading to soils. Here, we demonstrate that atmospheric inputs have widely contaminated soils with Mn in industrialized regions. Soils record elemental fluxes impacting the Earth's surface and can be analyzed to quantify inputs and outputs during pedogenesis. We use a mass balance model to interpret details of Mn enrichment by examining soil, bedrock, precipitation, and porefluid chemistry in a first-order watershed in central Pennsylvania, USA. This reveals that ~53% of Mn in ridge soils can be attributed to atmospheric deposition from anthropogenic sources. An analysis of published datasets indicates that over half of the soils surveyed in Pennsylvania (70%), North America (60%), and Europe (51%) are similarly enriched in Mn. We conclude that soil Mn enrichment due to industrial inputs is extensive, yet patchy in distribution due to source location, heterogeneity of lithology, vegetation, and other attributes of the land surface. These results indicate that atmospheric transport must be considered a potentially critical component of the global Mn cycle during the Anthropocene.

I. Introduction

Manganese (Mn), the 12th most abundant element in the Earth's crust, is predominantly found in soils as fine-grained, poorly-crystalline oxides (Manceau et al., 1992; Post, 1999). A small fraction of global Mn is present in the atmosphere. This Mn has been attributed to both anthropogenic emissions and wind erosion of soils; however, Mn pollution may overshadow mineral dust in industrialized regions and can disseminate widely as dust particulates or solutes in rain (National Research Council, 1973; Garrels et al., 1976; Rahn and Lowenthal, 1984; U.S. Environmental Protection Agency, 1984; Nriagu and Pacyna, 1988; Parekh, 1990; Lytle et al., 1995; Pacyna and Pacyna, 2001; Brewer and Belzer, 2001; Boudissa et al., 2006; Buck et al., 2010). Steel and ferroalloy manufacturing have historically been the primary sources of anthropogenic Mn emissions (U.S. Environmental Protection Agency, 1984); however, Mn has also been used as an

additive in gasoline, and coal combustion has recently become a dominant industrial source of atmospheric Mn (U.S. Environmental Protection Agency, 1984; Pacyna and Pacyna, 2001).

Most Mn-compounds in soils comprise highly-reactive constituents that influence the mobility of heavy metals (Co, Ni, Cu, Zn, Mo) and participate in abiotic and microbial redox reactions that can affect soil fertility (Suarez and Langmuir, 1976). For example, high Mn bioavailability in soils has led to tree toxicity and forest decline in the northeastern United States (Horsley et al., 2000; Kogelmann and Sharpe, 2006). Additionally, Mn is regulated as a human health hazard by the United States Environmental Protection Agency (EPA) due to well-established links between respirable Mn and neurological disorders (U.S. Environmental Protection Agency, 1984; Boudissa et al., 2006).

Although Mn levels in the air have declined since monitoring began (National Research Council, 1973; U.S. Environmental Protection Agency, 1984), there is no data available prior to the 1950s that can be used to assess total deposition over industrial time scales. However, past deposition of atmospheric Mn can be deciphered from soil profiles. These depth profiles record inputs, outputs, and internal redistribution processes and can be used to quantify influences on soil development, including past inputs from the air (Brimhall and Dietrich, 1987; Chadwick et al., 1990; Chadwick et al., 1999; Kurtz et al., 2001; Porder et al., 2007). For example, soil profiles that exhibit net enrichment of certain elements relative to parent material are interpreted as addition profiles, while other profiles that document net depletion due to natural weathering processes are interpreted as depletion profiles (Brantley and White, 2009).

Integrated soil, geologic, ecologic, and hydrologic observations are necessary to decipher long-term records of chemical processes in the soil. Such observations are now available for the Susquehanna Shale Hills Observatory (SSHO; Figure A-1), one of six Critical Zone Observatories (CZOs) in the United States and the focus of multidisciplinary characterization (Lin et al., 2006; Ma et al., 2010; Jin et al., 2010). The Critical Zone is defined as the region of the Earth's surface extending from groundwater to the top of vegetation that includes complex interactions amongst water, air, rock, soil and biota. Our detailed soil characterization at SSHO reveals that Mn is commonly observed as an addition profile while the geochemically similar element Fe is consistently present as a depletion profile. Like iron, manganese is mobilized under acidic soil conditions such as those present at Shale Hills; however, Mn-oxide solubilization occurs at higher pH values than is observed for Fe, potentially leading to greater Mn losses (Schaetzl and Anderson, 2002). The concurrent Fe depletion and Mn enrichment observed at SSHO can be explained by loss of Fe to weathering but gain of Mn due to atmospheric inputs.

We hypothesized that atmospheric contamination from industrial activity caused the observed Mn enrichment in SSHO soils. The SSHO is located in Huntingdon County, Pennsylvania, USA, an epicenter for iron production in the early 19th century that contained approximately 87 operational furnaces and forges at its peak in 1840. Forty-seven of these furnaces, including Monroe Furnace (4 km from SSHO), were located in Huntingdon County (Stine, 1964). In this study, we quantify excess soil Mn at SSHO and develop a mass balance model to estimate rates of atmospheric input over industrial and geologic time scales. Additionally, we analyze soils near a modern steel factory in Burnham, PA to demonstrate Mn enrichment near a point source. Our observations of local Mn enrichment led us to analyze databases of Pennsylvania, U.S., and European soils in order to ascertain broader geographic patterns of Mn enrichment in soils. These databases, along with our specific observations for SSHO and Burnham soils, lead to the conclusion that the top soils of industrialized regions are widely contaminated with patchy occurrences of excess Mn.

II. Methods

2.1. Sampling Locations

SSHO is a 7.9-hectare first-order catchment located within the Juniata watershed and larger Susquehanna River Basin. SSHO contains residual and colluvial soils derived from the Silurian-aged Rose Hill shale formation, an oxidized, organic-poor shale that extends throughout the Appalachian region. Here, soils are thin, well-drained Inceptisols on the ridges (thicknesses < 0.5 m) which transition downslope towards thicker Ultisols in the valley and swales (< 3 m) (Lin, 2006; Lin et al., 2006). Annual precipitation in the Shale Hills region is ~105 cm y⁻¹, and rainwater is currently acidic (average pH 4.35) and enriched in nitrate and sulfate (NADP, 2010). The vegetation is dominated by oak species with smaller populations of hickory, maple, hemlock and pines.

Soil cores were excavated with a stainless steel auger to point of refusal, the depth to which we could manually auger and our closest approximation for the soil-bedrock interface (Jin et al., 2010), at 21 locations along the SSHO ridge. Each core was sampled in 2-12 cm depth intervals starting at the top of mineral soil and ending at the soil-bedrock interface. Given this sampling methodology, our definition here for “soil” is all material that could be sampled with a hand auger and had an average thickness (L) of 32 cm.

Pore water samples were collected between 2006-2009 from four tension lysimeters installed at the soil-bedrock interface (30-40 cm depth) at two ridgetop locations on the north and south slopes.

Samples were collected approximately biweekly during wet periods when sufficient soil moisture was available. The porous ceramic cups of the lysimeters have a maximum pore size of $1.3\mu\text{m}$, so pore water samples were not further filtered after collection. Representative precipitation samples ($n = 61$) collected in 2002 by the National Atmospheric Deposition Program (NADP) were obtained from sites PA-42 and PA-15 located 2.5 km and 14.5 km from SSHO. Precipitation samples were collected in plastic buckets, and we analyzed samples of the distilled water used to rinse the buckets to determine potential trace metal contamination.

Our second field location, Burnham, PA, is located approximately 28 km southeast of SSHO and has supported steel manufacturing since 1795. Burnham is bordered to the north by Jack's Mountain, a Tuscarora sandstone ridge with soil-mantled slopes developed on the Silurian Clinton group (S_c) containing Rose Hill shale and Keefer sandstone, undifferentiated Bloomsburg claystone and Mifflintown shale (S_{bm}), and Wills Creek shale (S_{wc}) (Hoskins, 1981; PA Geological Survey, 2007). Twelve soil cores were augered to point of refusal at 10 locations between 1.1 and 23.8 km from the steel plant. The closest two sampling sites were located in Burnham on S_{wc} and S_{bm} . The other eight sampling sites were located along the slope of Jack's Mountain on the Rose Hill and Wills Creek shales.

2.2. Chemical analyses.

To determine the total concentration of major elements (e.g. Mn, Ti, Zr) in soils, representative air-dried bulk samples that included all rock fragments, sand, silt, and clay particles at each depth were ground to pass a 100-mesh sieve ($<149\mu\text{m}$), fused with lithium metaborate at 950°C , and dissolved in 5% HNO_3 for analysis on a Leeman Labs PS3000UV inductively coupled plasma atomic emission spectrophotometer (ICP-AES) at the Penn State Materials Characterization Laboratory. Pore water and precipitation samples were acidified with ultrapure concentrated HNO_3 and analyzed for cation concentrations on ICP-AES (pore water) or quadrupole ICP-mass spectrometry (precipitation). Anion concentrations in the water samples were measured using a Dionex ion chromatograph.

III. Results

3.1. SSHO Soils

For mineral soils sampled at SSHO ridges, the depth-weighted average Mn concentration ($C_{Mn,w} = 2,200 \pm 2,100\mu\text{g g}^{-1}$; $n = 111$ samples) is elevated relative to the average concentration of the Rose Hill shale ($C_{Mn,p} = 800 \pm 300\mu\text{g g}^{-1}$; $n = 24$ samples). This "parent rock" was drilled at

the ridgetop and analyzed previously (Jin et al., 2010). The highest concentrations of Mn occur near the soil surface, with concentrations ranging up from 900 to 14,400 $\mu\text{g g}^{-1}$ in the uppermost soil sample from each core (Table A-1).

3.2. SSHO Pore Waters and Precipitation

Pore fluids sampled at the soil-bedrock interface contain higher concentrations of Mn ($C_{Mn,pf} = 0.082 \pm 0.137 \mu\text{g mL}^{-1}$; $n = 66$) than influent precipitation ($C_{Mn,ppt} = 0.0025 \pm 0.0024 \mu\text{g mL}^{-1}$; $n = 61$). Mn concentrations in the control samples of distilled water used to rinse the precipitation collectors showed no Mn contamination ($C_{Mn,ppt} < 0.00004 \mu\text{g mL}^{-1}$; $n = 7$). Chloride concentrations in the pore fluids ($C_{Cl,pf} = 1.35 \pm 1.02 \mu\text{g mL}^{-1}$; $n = 70$) are also high relative to influent precipitation as reported by the NADP ($C_{Cl,ppt} = 0.20 \pm 0.20 \mu\text{g mL}^{-1}$) and will be used to constrain the effects of evapotranspiration.

3.3. Burnham Soils

At Burnham, depth-averaged Mn concentrations in soils (340 - 1,300 $\mu\text{g g}^{-1}$) are elevated relative to the deepest soil sampled from each core (100 - 600 $\mu\text{g g}^{-1}$) for 6 out of 7 soil cores augered within ~6 km of the Standard Steel facility (Table A-2). In these cores, Mn concentrations are highest near the surface and decrease with depth. For the soil core augered closest to the facility (1.1 km), Mn concentrations are consistently high with depth (400 - 700 $\mu\text{g g}^{-1}$). Furthermore, the deepest sample remains high in Mn concentration (650 $\mu\text{g g}^{-1}$) and its Mn content may not be representative of parent material. In contrast, for soil cores sampled 6.6 to 15.8 km from the source, Mn concentrations are consistently low through the profiles ($< 400 \mu\text{g g}^{-1}$). However, for the two soil cores augered ~24 km from the steel facility that lie within 50 m of a road, depth-averaged soil Mn concentrations are elevated (700 and 960 $\mu\text{g g}^{-1}$) relative to the deepest samples (310 and 390 $\mu\text{g g}^{-1}$).

IV. Discussion

4.1. SSHO Soils

We use the mass transfer coefficient, $\tau_{i,j}$, to further investigate Mn concentrations in SSHO soils (Eqn. 1). $\tau_{i,j}$ values indicate enrichment ($\tau_{i,j} > 0$) or depletion ($\tau_{i,j} < 0$) of a soluble element j in weathered material or soil (subscript w) relative to parent material (subscript p). The mass transfer coefficient accounts for variations in bulk density and concentration changes due to depletions or additions of other elements by ratioing concentrations of j to an insoluble element i such as Zr or Ti (Brimhall and Dietrich; 1987; Egli and Fitze, 2000):

$$\tau_{i,j} = \frac{C_{j,w}C_{i,p}}{C_{j,p}C_{i,w}} - 1 \quad (1)$$

Titanium (Ti) was measured in all samples and was observed to be relatively immobile. However, Zr shows less depletion than Ti in SSHO because its host mineral, zircon, is less soluble than Ti oxide (Jin et al., 2010). Depletion of Ti relative to Zr yielded average $\tau_{Zr,Ti} = -0.21$ in the 88 samples where Ti and Zr were both measured. Using $i = \text{Ti}$ may overestimate element addition and underestimate element depletion; therefore, Zr was used as the immobile element in equation 1. For the remaining 23 of 111 soil samples where Zr was not measured, Zr concentrations were estimated from measured Ti concentrations by using $\tau_{Zr,Ti} = -0.21$.

With Zr as the immobile element, all sampled ridge cores ($n = 21$) exhibit Mn in excess of parent material ($\tau_{Zr,Mn} > 0$). The enrichment, highest at the soil surface and decreasing to parent concentration at depth, is characteristic of an addition profile (Brantley and White, 2009) (Figure 2-1). Specifically, mass balance requires that $\tau > 0$ documents external additions from natural sediments, direct anthropogenic inputs, or the atmosphere (Brantley and White, 2009). In ridge soils such as those investigated here, sediment inputs are insignificant because the soils are situated at local topographic highs. Direct anthropogenic inputs are unlikely for SSHO given that the catchment has never been intensively farmed nor have the soils been moved or manipulated to any great extent. Atmospheric inputs are left as the likely source of excess Mn.

Vegetation can recycle nutrients, enriching elements in the surface soil via litterfall while concurrently depleting the subsurface in that element through root uptake (Jobbagy and Jackson, 2004). However, vegetation alone cannot explain Mn enrichment of SSHO ridge top soils because there is insufficient Mn depletion in the subsurface. Therefore, the chemical data document net addition to the soil.

The mass of element j in soils per unit land surface area ($M_{j,w}$, mg cm^{-2}) can be estimated for one depth interval Δz (cm) as $M_{j,w} = \rho_w C_{j,w} \Delta z$. The total value for soil is calculated as a summation over all depths in the soil core. Here, ρ_w (g cm^{-3}) is the bulk density of the soil sample. Bulk density measurements previously obtained at SSHO were used to estimate bulk densities for each soil sample as a function of depth (Table A-3). For this calculation, the sum of all sampling intervals must equal the total soil depth. $M_{Mn,w}$ averages $88.7 \pm 63.4 \text{ mg Mn cm}^{-2}$ in SSHO ridge soils (Table A-1).

The *integrated mass outflux* or *influx*, $m_{j,w}$ (mg cm^{-2}), is the net loss ($m_{j,w} < 0$) or gain ($m_{j,w} > 0$) of j in the mineral soil relative to the Rose Hill shale parent (Chadwick et al., 1990). The shale

bulk density (ρ_p) has been measured at 2.42 g cm^{-3} (Jin et al., 2010). Values of $m_{j,w}$ are calculated by integration of $\tau_{i,j}$ over depth, z , from the mineral soil surface ($z = 0$) to the depth of auger refusal (L). This integration is corrected for volume strain (ε) following previous authors (Brimhall and Dietrich, 1987; Egli and Fitze, 2000):

$$m_{j,w} = C_{j,p} \rho_p \sum_{z=0}^{z=L} \frac{\tau_{i,j}(z) \Delta z}{\varepsilon(z)+1} \quad (2)$$

Strain is a measure of soil volume change ($\varepsilon > 0$ for expansion or $\varepsilon < 0$ collapse) and is calculated as $\varepsilon(z) + 1 = (C_{i,p} \rho_p) / (C_{i,w}(z) \rho_w(z))$ (Brimhall and Dietrich, 1987).

For the ridge cores sampled at SSHO, the average core $m_{Mn,w}$ is equal to $47.2 \text{ mg Mn cm}^{-2}$, indicating net enrichment of Mn in the soil relative to the parent shale. Only one core was slightly depleted in Mn (Table A-1, Site N; $m_{Mn,w} = -1.8 \text{ mg cm}^{-2}$). Since erosion and chemical weathering remove Mn from the soil, external inputs must equal or exceed these outputs to result in positive values of $m_{Mn,w}$ for 20 of 21 cores. The ratio of average $m_{Mn,w}$ to $M_{Mn,w}$ ($= 47.2/89.2 = 0.53$) is consistent with the conclusion that at least half of the Mn in ridge soils is derived from external Mn additions.

4.2. Mass balance model

To estimate rates of atmospheric Mn addition to SSHO, we model inputs and outputs to each sampled ridge soil using the chemical data reported here. In this model, Mn enrichment in soils changes over time as a function of varying atmospheric input rates, A ($\mu\text{g cm}^{-2} \text{ y}^{-1}$), representing dust or solutes of either natural or anthropogenic origin. Regardless of whether the excess Mn is due to natural or anthropogenic influxes, the soil thickness of each profile is presumed to be constant with time, i.e., at steady state. If the rates of erosion differed significantly from the soil production rate, ω (m My^{-1}), the soil would eventually disappear or thicken over geological timeframes. Ma et al. (2010) have estimated the soil production rate ω for the ridge top soils in the SSHO to equal 45 m My^{-1} based on U series isotopes. This soil production rate is consistent with a residence time of $\sim 7100 \text{ y}$ ($= 0.32 \text{ m} / 45 \text{ m My}^{-1}$) for particles in the observed average soil thickness, L ($= 0.32 \text{ m}$), at SSHO ridges.

For our model calculations, the time zero point is a hypothetical steady state where the mass of Mn present in the ridge soil is identical to that derived from its protolith (i.e. $\tau_{Zr,Mn} = 0$; $C_{Mn,w} = 997 \mu\text{g g}^{-1}$) and is based on the assumption of no significant net additions or removals of Mn during pedogenesis. The assumption that $m_{Mn,w} = 0$ at time zero is conservative in that soils in temperate climates typically experience depletion of mobile elements, characterized by $\tau_{Zr,Mn} < 0$ (Brantley

and White, 2009). Thus, our estimates for the atmospheric deposition rates (A) required to explain SSHO observations will constitute a lower limit.

Under the assumption of steady state, the input and output fluxes of Mn to the soil can be calculated. At the ridge, one Mn input to the soil column is soil production (B):

$$B = C_{Mn,p}\rho_p\omega \quad (3)$$

This rate of Mn input to the soil due to soil production from bedrock, B , is assumed constant for all profiles and is calculated to equal $8.7 \mu\text{g cm}^{-2} \text{y}^{-1}$ from the average values of the three terms in (3) reported earlier.

One outflux of Mn from ridgetop soil is physical erosion (E):

$$E = C_{Mn,w}\rho_w\omega \quad (4)$$

The loss of Mn due to physical erosion at time zero, E ($= 5.9 \pm 0.8 \mu\text{g cm}^{-2} \text{y}^{-1}$), is calculated as the background soil Mn concentration ($C_{Mn,w} = 997 \mu\text{g g}^{-1}$ when $\tau_{Zr,Mn} = 0$) multiplied by depth-averaged soil bulk density (ρ_w) and denudation rate. For this calculation, we assume uniform Mn concentration with depth in the soil profile consistent with neither loss nor gain of Mn from the hypothetical starting point soil. With this assumption, E varies for each ridge top profile only due to different total depths that create differences in depth-averaged bulk density for each profile.

Assuming that the values for A due to atmospheric inputs are initially negligible, as dictated current observations of natural dust (Table A-4), the output solute flux due to chemical weathering, W ($= 2.8 \pm 0.8 \mu\text{g cm}^{-2} \text{y}^{-1}$), must be equal to the difference between B and E under the condition of steady state Mn mass. This value for W is compared to the modern chemical weathering flux, calculated as the difference in the Mn concentrations between influent precipitation ($C_{Mn,ppt} = 0.0025 \mu\text{g mL}^{-1}$) and effluent pore fluid ($C_{Mn,pf} = 0.082 \mu\text{g mL}^{-1}$):

$$W = MAP * \left(\frac{C_{Cl,ppt}}{C_{Cl,pf}} C_{Mn,pf} - C_{Mn,ppt} \right) \quad (5)$$

These concentrations are corrected for evapotranspiration using the standard correction based on Cl concentrations in pore fluid ($C_{Cl,pf} = 1.3 \mu\text{g mL}^{-1}$) and influent precipitation ($C_{Cl,ppt} = 0.20 \mu\text{g mL}^{-1}$, (NADP, 2010), with mean annual precipitation, $MAP = 104.9 \text{ g cm}^{-2} \text{y}^{-1}$. The modern value for W ($= 1.0 \mu\text{g cm}^{-2} \text{y}^{-1}$) is slightly less than the calculated initial steady state estimate; therefore, the steady state values for W ($= 2.8 \pm 0.8 \mu\text{g cm}^{-2} \text{y}^{-1}$) will be used in the model as an upper limit estimate of chemical weathering.

In the model calculation after time zero, Mn is input to the soil through atmospheric deposition, A , perturbing the soil profile away from steady state with respect to Mn mass. B and W are held constant, but E is allowed to change over time as the Mn concentrations in the soil profile change

with time (see equation 4). In Figure 2-2a, we show values of $m_{Mn,w}$ for SSHO soils calculated over time for different values of A representing short-term “anthropogenic” and long-term “natural mineral dust” fluxes. The values for anthropogenic ($5 - 500 \mu\text{g cm}^{-2} \text{y}^{-1}$) and natural ($0.5 - 5 \mu\text{g cm}^{-2} \text{y}^{-1}$) Mn deposition are order of magnitude estimates representing measurements compiled from the literature (Figure 2-2b; Table A-4). Soil profiles receiving Mn as natural mineral dust or solutes ($A = 0.5 \mu\text{g cm}^{-2} \text{y}^{-1}$) reach a new steady state level for $m_{Mn,w}$ well below the average calculated value for SSHO soil profile data. Only 4 out of 21 soil profiles reach SSHO enrichment of Mn with inputs of $A = 5 \mu\text{g cm}^{-2} \text{y}^{-1}$, the upper level “natural” and lower level “anthropogenic” rate, and even this does not occur within the soil residence time ($<7,100 \text{ y}$). Therefore, inputs of mineral dust, even over timescales much longer than the residence time of the soils, are generally insufficient to explain the Mn enrichment. In contrast, the Mn concentrations observed in the soils are consistent with anthropogenic levels of A over industrial timescales. For example, at $A = 500 \mu\text{g cm}^{-2} \text{y}^{-1}$, $m_{Mn,w}$ reaches the SSHO average value of 47.1 mg cm^{-2} within 100 years. Mn enrichment in SSHO soils is therefore best explained as the result of industrial deposition.

4.3. Burnham soils

To understand the implications of this interpretation, we investigated soils around the Standard Steel, LLC steel manufacturing plant located $\sim 28 \text{ km}$ southeast of SSHO in Burnham, PA. Within $\sim 6 \text{ km}$ of the facility, Mn concentrations are high in surface soils ($1,600 \pm 700 \mu\text{g g}^{-1}$) relative to deep soils ($300 \pm 100 \mu\text{g g}^{-1}$) with $m_{Mn,w}$ values ($\sim 35 \text{ mg cm}^{-2}$) comparable to SSHO (Figure 2-3; Figure A-2; Table A-2). In contrast, soils sampled far from roads at points 15-16 km away from the plant contain relatively low Mn ($200 \pm 100 \mu\text{g g}^{-1}$) at all depths and $m_{Mn,w} < 10 \text{ mg cm}^{-2}$. Soils collected $\sim 24 \text{ km}$ away and within 50 m of a state road have slightly elevated Mn concentrations and $m_{Mn,w} \approx 17 \text{ mg cm}^{-2}$, consistent with contamination due to vehicular exhaust (U.S. Environmental Protection Agency, 1984; Lytle et al., 1995).

For the Burnham sites, we compare values for $\tau_{Ti,Mn}$ and $m_{Mn,w}$ using two different assumptions for parent: 1) parent composition assumed equal to the deepest augered sample from each core, 2) parent composition equal to the average composition of all the deepest augered samples from all cores. Ti was used as the immobile element and strain values were calculated using SSHO bulk density measurements. Although the total mass of soil Mn ($M_{Mn,w}$) is highest near the source, estimates of $m_{Mn,w}$ have large standard deviations due to variability in inferred parent compositions. Even with these considerations, soils nearest to Burnham are enriched in Mn relative to those further away.

4.4. Soil Chemistry Compilations

To assess whether the inferred Mn contamination in these central Pennsylvania soils was unusual, we collated available geochemical data for United States and European soils. For the U.S., we combined 385 chemical profiles for U.S. soils from the Natural Resources Conservation Service's Spatial Geochemical Database ($n = 290$) with as many published studies as we were able to find with the requisite data ($n = 95$) (Ciolkosz and Amistadi, 1993; Ciolkosz et al., 1998; Muhs et al., 1998; Teutsch et al., 1999; Ciolkosz, 2000; NRCS, 2010). For the U.S. soils, we used every dataset we found that provided: i) chemical composition of C horizon soil or parent, ii) concentrations for at least 3 depth intervals covering 2/3 of total pedon depth to parent, iii) concentrations of both Mn and an insoluble element. For the European soils, enrichment of Mn in topsoil (0-25 cm depth) was calculated relative to the C horizon from data reported in the Geochemical Baseline Mapping Programme (FOREGS, 2010). The FOREGS database has been previously used to predict heavy metal distribution in topsoils based on various factors (e.g. parent lithology, topography, population density) (Lado et al., 2008), and MnO distribution had been found to potentially correlate with anthropogenic influence (Imrie et al., 2008). Similar to the approach we used in the Burnham calculations, total Mn influx or outflux to each pedon ($m_{Mn,w}$; Eqn.2) was evaluated using Ti as the immobile element since Ti concentrations were reported more often than Zr and Ti is relatively immobile in many soils (Brimhall and Dietrich, 1987; Neaman et al., 2006). Since no bulk density data were available for bedrock or soils in the compilations, parent bulk density was set equal to that of the Rose Hill Shale (2.4 g cm^{-3}) and soils were assumed to weather isovolumetrically ($\varepsilon = 0$). Differences amongst common lithological bulk densities introduces only small variability to the calculated $m_{Mn,w}$ value.

All of these datasets define positively skewed distributions consistent with the majority of soils demonstrating Mn addition rather than depletion (Figure 4). For Pennsylvania soils ($n = 64$), $m_{Mn,w}$ averages 20 mg cm^{-2} and $\sim 70\%$ of the soils show $m_{Mn,w} > 0$. For the U.S. dataset ($n = 385$), $m_{Mn,w}$ averages 16 mg cm^{-2} with $> 60\%$ of profiles showing Mn enrichment. A map of $m_{Mn,w}$ in the United States reveals the sparseness of the available soils data for trace metals (Figure A-3). In Europe, the mean topsoil Mn concentrations ($620 \pm 510 \text{ } \mu\text{g g}^{-1}$) are only slightly higher than C horizon concentrations ($570 \pm 460 \text{ } \mu\text{g g}^{-1}$), and average values of $m_{Mn,w} = 2.4 \text{ mg cm}^{-2}$ document that 51% of the soils show enrichment. However, a map of the data shows large spatial variance and a concentration of enriched sites near industrialized regions (Figure A-4). The data

therefore document that the spatial heterogeneity in values of $m_{Mn,w}$ is large but that a significant number of soils sampled in PA, the U.S., and Europe are consistent with Mn contamination. Patchiness of the Mn contamination in soils is attributed partly to the existence of point sources of Mn emission to the atmosphere, including steel plants and coal-burning power plants, as well as more diffuse contributions from gasoline (National Research Council, 1973; U.S. Environmental Protection Agency, 1984; Lytle et al., 1995; Pacyna and Pacyna, 2001). However, widespread dissemination of anthropogenic Mn to the atmosphere has been documented as deposition to the ocean over thousands of kilometers in the North Atlantic (Buck et al., 2010). The patchiness of soil Mn is therefore presumably not just due to the localized nature of the source, but is also due to the variability of soils themselves. For example, in the Pennsylvania dataset, Mn is enriched in soils developed on basic crystalline rock, limestone, and shale, while soils derived from sandstones exhibit net Mn depletion (Ciolkosz and Amistadi, 1993; Ciolkosz et al., 1998; Ciolkosz, 2000). Thus, patchiness in the soil Mn enrichment may also be related to patchiness of lithologies that outcrop at Earth's surface. Finally, vegetation acts as a capacitor in that it biolifts, stores, and recycles the Mn (Jobbagy and Jackson, 2004), and different vegetation types presumably cause or exacerbate the patchiness.

The evidence for common but spatially heterogeneous Mn contamination in industrialized areas is amplified by observations of Pb and Cd concentrations, two other trace metals that are known to be heavily impacted by human activity (Pacyna and Pacyna, 2001; Rauch and Pacyna, 2009). The data from the European topsoils also show positively-skewed distributions for Pb and Cd similar to Mn (Fig. A-5). In contrast, the distribution of $m_{Fe,w}$ in U.S. soils is negatively skewed towards Fe depletion (Figure 2-4d) even though Mn and Fe are leached from soils at comparable redox conditions (Schaetzl and Anderson, 2002). Mn enrichment concurrent with Fe depletion is consistent with Mn additions. In these soils, Fe fluxes have been dominated by depletion while Mn fluxes have been dominated by atmospheric inputs.

Additional research is needed to assess the global impacts of atmospheric deposition on soil geochemistry and ecological processes. Numerous trace metals are discharged to the air by anthropogenic activities, yet there remains a distinct lack of knowledge on where these elements are deposited, in which environmental pools they accumulate, and the rates of transfer amongst these pools. The increased availability of global soil data through compilation efforts would facilitate the documentation of long-term anthropogenic metal inputs to ecosystems worldwide.

V. Acknowledgements

This material is based upon work supported by the National Science Foundation under Grant No. CHE-0431328 for the Center for Environmental Kinetics Analysis and under Grant No. EAR-0725019 to Chris Duffy (Penn State) for the Susquehanna Shale Hills Critical Zone Observatory. The authors would like to acknowledge Danielle Andrews, Jennifer Williams, and other members of the Susquehanna Shale Hill Observatory for help with soil and water sample collection.

VI. References

- Boudissa S. M., Lambert J., Müller C., Kennedy G., Gareau L. and Zayed J. (2006) Manganese concentrations in the soil and air in the vicinity of a closed manganese alloy production plant. *The Science of the total environment* **361**, 67–72.
- Brantley S.L. and White A. (2009) Approaches to modeling weathered regolith. In *Thermodynamics and Kinetics of Water-Rock Interaction* (eds. E. H. Oelkers and J. Schott). The Mineralogical Society of America, Chantilly, VA. pp. 435–484.
- Brewer R. and Belzer W. (2001) Assessment of metal concentrations in atmospheric particles from Burnaby Lake, British Columbia, Canada. *Atmospheric Environment* **35**, 5223–5233.
- Brimhall G. H. and Dietrich W. E. (1987) Constitutive mass balance relations between chemical composition, volume, density, porosity, and strain in metasomatic hydrochemical systems: Results on weathering and pedogenesis. *Geochimica et Cosmochimica Acta* **51**, 567–587.
- Buck C. S., Landing W. M., Resing J. a. and Measures C. I. (2010) The solubility and deposition of aerosol Fe and other trace elements in the North Atlantic Ocean: Observations from the A16N CLIVAR/CO2 repeat hydrography section. *Marine Chemistry* **120**, 57–70.
- Chadwick O A, Derry L A, Vitousek P. M., Huebert B. J. and Hedin L. O. (1999) Changing sources of nutrients during four million years of ecosystem development. *Nature* **397**, 491–497.
- Chadwick O., Brimhall G. H. and Hendricks D. M. (1990) From a black to a gray box — a mass balance interpretation of pedogenesis. *Geomorphology* **3**, 369–390.
- Ciolkosz E. J. (2000) Major and Trace Elements in Southwestern Pennsylvania Soils. *Agronomy Series No. 148*, The Pennsylvania State University.
- Ciolkosz E. J. and Amistadi M. K. (1993) Metals in Pennsylvania Soils. *Agronomy Series Number 128*, The Pennsylvania State University.
- Ciolkosz E. J., Stehouwer R. C. and Amistadi M. K. (1998) Metals Data for Pennsylvania Soils. *Agronomy Series No. 140*, The Pennsylvania State University.
- Egli M. and Fitze P. (2000) Formulation of pedologic mass balance based on immobile elements: a revision. *Soil Science* **165**, 437–443.
- FOREGS (2010) Geochemical Atlas of Europe. Available at: <http://www.gtk.fi/publ/foregsatlas/>.
- Garrels R. M., Lerman A. and Mackenzie F. T. (1976) Controls of Atmospheric O₂ and CO₂ Past, Present, and Future. *American Scientist* **64**, 306–315.
- Horsley S. B., Long R. P., Bailey S. W., Hallett R. A. and Hall T. J. (2000) Factors associated with the decline disease of sugar maple on the Allegheny Plateau. *Canadian Journal of Forest Research* **30**, 1365–1378.
- Hoskins D. M. (1981) Burnham Quadrangle. In *Atlas of Preliminary Geologic Quadrangle Maps of Pennsylvania* PA Geological Survey.

- Imrie C. E., Korre A., Munoz-Melendez G., Thornton I. and Durucan S. (2008) Application of factorial kriging analysis to the FOREGS European topsoil geochemistry database. *The Science of the total environment* **393**, 96–110.
- Jin L., Ravella R., Ketchum B., Bierman P. R., Heaney P., White T. and Brantley Susan L. (2010) Mineral weathering and elemental transport during hillslope evolution at the Susquehanna/Shale Hills Critical Zone Observatory. *Geochimica et Cosmochimica Acta* **74**, 3669–3691.
- Jobbagy E. G. and Jackson R. B. (2004) The uplift of soil nutrients by plants: biogeochemical consequences across scales. *Ecology* **85**, 2380–2389.
- Kogelmann W. J. and Sharpe W. E. (2006) Soil acidity and manganese in declining and nondeclining sugar maple stands in Pennsylvania. *Journal of environmental quality* **35**, 433–41.
- Kurtz A. C., Derry L.A. and Chadwick O.A. (2001) Accretion of Asian dust to Hawaiian soils: Isotopic, elemental, and mineral mass balances. *Geochimica et Cosmochimica Acta* **65**, 1971–1983.
- Lado L. R., Hengl T. and Reuter H. I. (2008) Heavy metals in European soils: A geostatistical analysis of the FOREGS Geochemical database. *Geoderma* **148**, 189–199.
- Lin H. (2006) Temporal stability of soil moisture spatial pattern and subsurface preferential flow pathways in the Shale Hills catchment. *Vadose Zone Journal* **5**, 317–340.
- Lin H. S., Kogelmann W., Walker C. and Bruns M. A. (2006) Soil moisture patterns in a forested catchment: A hydrogeological perspective. *Geoderma* **131**, 345–368.
- Lytle C., Smith B. and Mckinnon C. (1995) Manganese accumulation along Utah roadways: a possible indication of motor vehicle exhaust pollution. *Science of The Total Environment* **162**, 105–109.
- Ma L., Chabaux F., Pelt E., Blaes E., Jin L and Brantley Susan L (2010) Regolith production rates calculated with uranium-series isotopes at Susquehanna/Shale Hills Critical Zone Observatory. *Earth and Planetary Science Letters* **297**, 211–225.
- Manceau A., Gorshkov A. and Drits V. (1992) Structural chemistry of Mn, Fe, Co, and Ni in manganese hydrous oxides: Part I. Information from XANES spectroscopy. *American Mineralogist* **77**, 1133–1143.
- Muhs D. R., Bettis E. A., Been J. and Mcgeehin J. P. (1998) Impact of Climate and Parent Material on Chemical Weathering in Loess-derived Soils of the Mississippi River Valley. , 1761–1777.
- NADP (2010) National Atmospheric Deposition Program. Available at: <http://nadp.sws.uiuc.edu/>.
- National Research Council (1973) *Medical and biological effects of environmental pollutants: manganese.*, National Academy of Sciences, Washington, D.C.
- Neaman A., Chorover J. and Brantley S. L. (2006) Effects of organic ligands on granite dissolution in batch experiments at pH 6. *American Journal of Science* **306**, 451–473.
- NRCS (2010) National Cooperative Soil Characterization Data. Available at: <http://soils.usda.gov/survey/geochemistry/>.
- Nriagu J. and Pacyna J. (1988) Quantitative assessment of worldwide contamination of air, water and soils by trace metals. *Nature* **333**, 134–139.
- PA Geological Survey (2007) *Bedrock geologic map of the Allensville Quadrangle, Huntingdon and Mifflin Counties, Pennsylvania.*,
- Pacyna J.M. and Pacyna E. G. (2001) An assessment of global and regional emissions of trace metals to the atmosphere from anthropogenic sources worldwide. *Environmental Reviews* **9**, 269–298.
- Parekh P. P. (1990) A study of manganese from anthropogenic emissions at a rural site in the eastern United States. *Atmospheric Environment* **24A**, 415–421.

- Porder S., Hilley G. E. and Chadwick O. (2007) Chemical weathering, mass loss, and dust inputs across a climate by time matrix in the Hawaiian Islands. *Earth and Planetary Science Letters* **258**, 414–427.
- Post J. E. (1999) Manganese oxide minerals: Crystal structures and economic and environmental significance. *Proceedings of the National Academy of Sciences* **96**, 3447–3454.
- Rahn K. and Lowenthal D. (1984) Elemental tracers of distant regional pollution aerosols. *Science* **223**, 132–139.
- Rauch J. N. and Pacyna Jozef M. (2009) Earth's global Ag, Al, Cr, Cu, Fe, Ni, Pb, and Zn cycles. *Global Biogeochemical Cycles* **23**, GB2001.
- Schaetzl R. and Anderson S. (2002) *Soils genesis and geomorphology.*, University Press, Cambridge, UK.
- Stine H. E. (1964) The story of Juniata iron. Master's Thesis, The American University.
- Suarez D. and Langmuir D. (1976) Heavy metal relationships in a Pennsylvania soil. *Geochimica et Cosmochimica Acta* **40**, 589–598.
- Teutsch N., Erel Y., Halicz L. and Chadwick O. (1999) The influence of rainfall on metal concentration and behavior in the soil. *Geochimica et Cosmochimica Acta* **63**, 3499–3511.
- U.S. Environmental Protection Agency (1984) *Health Assessment Document for Manganese.*, Cincinnati, Ohio.

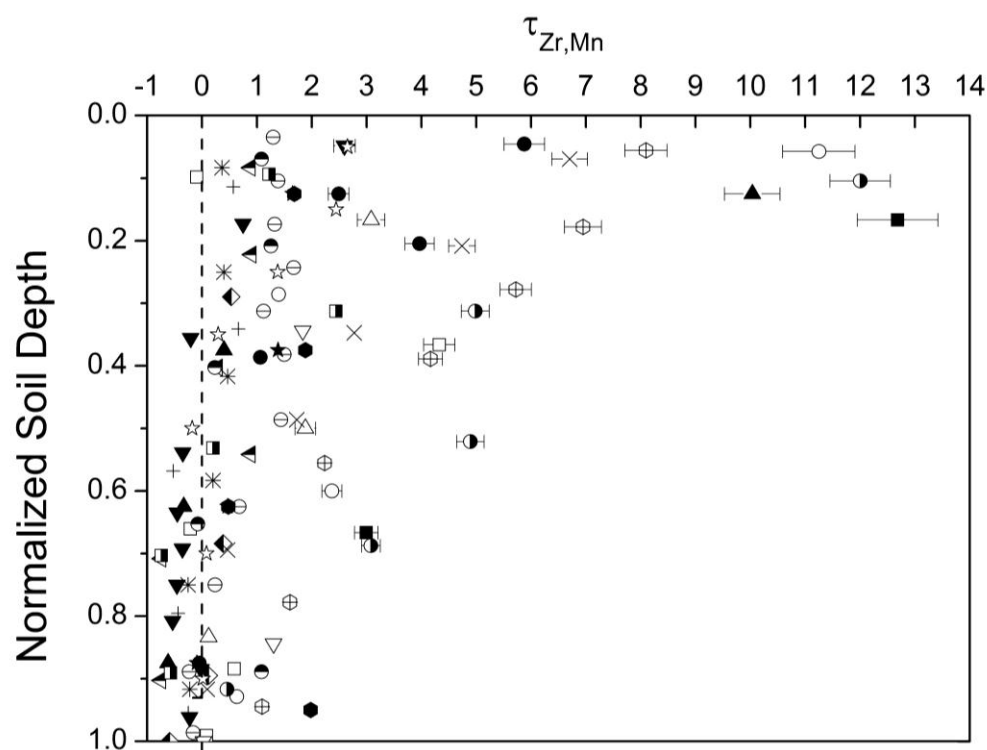


Figure 2-1. Normalized Mn concentrations ($\tau_{Zr,Mn}$, Eqn. 1) are plotted as different symbols versus depth for 21 ridge top soil cores at the Susquehanna Shale Hills Observatory (SSHO). Here, depth in the soil is normalized so that 1 = depth of the bedrock-soil interface. Soils document Mn enrichment ($\tau_{Zr,Mn} > 0$) near the surface that approaches underlying parent rock composition ($\tau_{Zr,Mn} = 0$) at depth. Surface soils are up to 13 times more enriched in Mn than parent. Error bars represent the propagated uncertainty in chemical analyses ($\pm 3\%$). Where no errors are shown, the bars are the size of symbols or smaller.

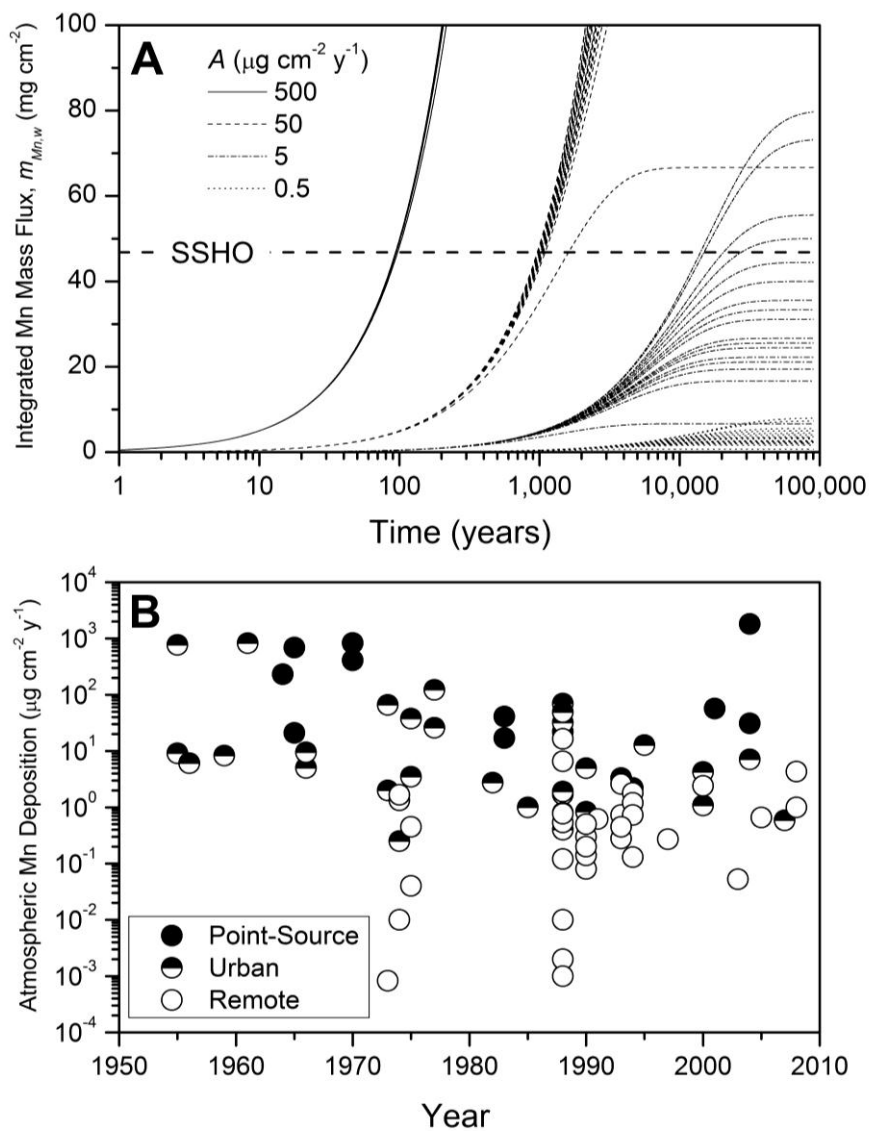


Figure 2-2. A) Model outputs for the integrated mass flux of Mn ($m_{Mn,w}$, Eqn.2) calculated for 21 SSHO ridge soils as a function of varying atmospheric deposition rates of Mn, A , over time. Each soil profile begins at a steady state mass of Mn consistent with $m_{Mn,w} = 0$ and is perturbed by atmospheric input of either anthropogenic ($A = 5 - 500 \mu\text{g cm}^{-2} \text{y}^{-1}$) or natural ($A < 5 \mu\text{g cm}^{-2} \text{y}^{-1}$) dust and solute Mn inputs at $t > 0$. The dashed horizontal line indicates the average $m_{Mn,w}$ of SSHO soils ($\sim 47 \text{ mg cm}^{-2}$). B) Rates of Mn deposition reported in the literature show decreasing deposition levels between 1950 - 2010, with the highest levels associated with industrial point-sources and urban areas, and the lowest values associated with sites impacted only by natural processes (Table A-4).

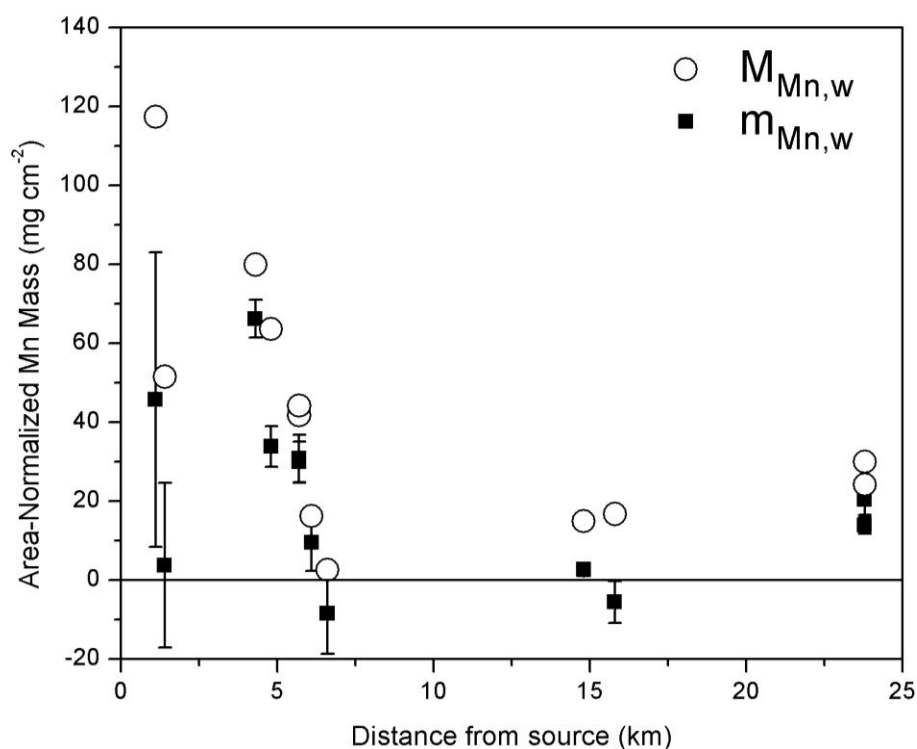


Figure 2-3. The total area-normalized Mn mass ($M_{Mn,w}$, \circ) and integrated mass flux of Mn ($m_{Mn,w}$, \blacksquare) are shown for 12 soil cores augered at distances between 1 to 24 km from the steel plant source at Burnham, PA. Soils near the plant are elevated in Mn relative to soils further away. Error bars for $m_{Mn,w}$ represent the standard deviations in calculated mass flux values for each core as described in the text. Error bars for $M_{Mn,w}$ represent analytical error in $C_{Mn,w}$ ($\pm 3\%$) and are smaller than symbols. Large standard deviations result mostly from variability in measured compositions of samples used to infer parent composition.

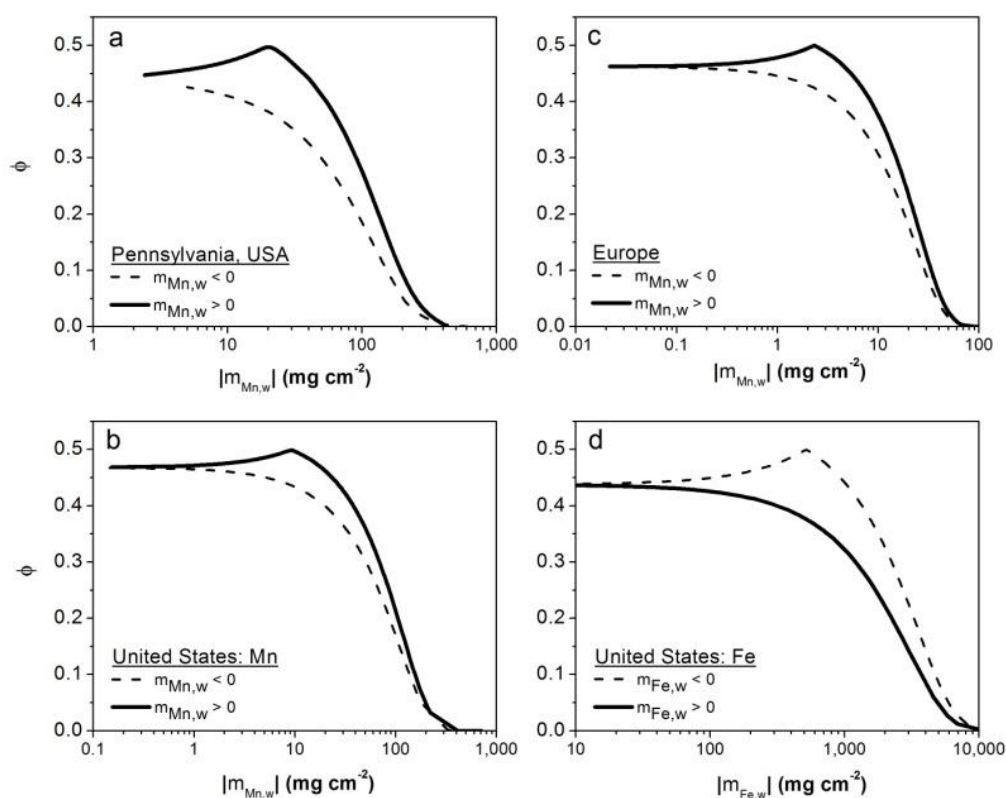


Figure 2-4. Distributions of calculated $m_{Mn,w}$ (Eqn.2) for reported soil chemistry in Pennsylvania (a), the United States (b), and Europe (c) and $m_{Fe,w}$ for soils in the United States (d) (see text for dataset attributions). Values of $m_{j,w}$ for each dataset were fit to a normal distribution to determine the fraction (ϕ) of measurements falling above or below each given value of $m_{j,w}$. Values of ϕ are plotted for the absolute values of $m_{j,w}$ where net enrichment ($m_{j,w} > 0$) is plotted as a solid line and net depletion ($m_{j,w} < 0$) as a dashed line. The mean of each dataset (the value at the peak where $\phi = 0.5$) documents that net enrichment of Mn is more common than depletion in soils in Pennsylvania, the United States, and Europe, but depletion is more common for Fe in the United States.

Chapter 3

Using mesocosm experiments to estimate the influence of vegetation on manganese in soils

Abstract

Soils in industrialized regions can be enriched in trace metals due to inputs from atmospheric deposition. To predict the residence time of these metals in soils after deposition requires better understanding of the factors that impact the rates of their removal into water systems. At the Susquehanna Shale Hills Critical Zone Observatory (CZO) in central Pennsylvania, USA, a temperate watershed vegetated by an oak-hickory forest, soils are enriched in manganese as the result of past industrial inputs. Today, Mn concentrations are also high in the tree foliage and leaf litter at Shale Hills relative to typical concentrations, and the annual fluxes from soil into vegetation and from vegetation to soil are large compared to other fluxes into and out of the soil. We grew oak tree seedlings in mineral soil collected from the Shale Hills catchment in mesocosm experiments in order to examine field observations under controlled greenhouse conditions. In this study, we explored how vegetation stores Mn in the soil system and mobilizes Mn from sources found in the Shale Hills watershed, including shale-derived mineral grains, aqueous inputs, Mn-oxides, and Mn-rich organic matter. The mesocosms were used to measure leached Mn, defined as the mass of Mn lost in water effluent, and Mn uptake, defined as the mass of Mn transferred into foliage.

In the mesocosm system, the ratio of uptake to leaching for Mn (> 100) exceeded that for similar measurements of the plant macronutrients Mg, P, K, and Ca (< 10). Vegetation increased total chemical weathering (uptake + leaching) of Mn from shale-derived soil, but substantially decreased chemical denudation (leaching) relative to that observed from non-vegetated soils. Furthermore, rates of Mn loss into effluent depended on the Mn source, decreasing in the following order: aqueous Mn $>$ Mn-oxide $>$ shale-derived mineral grains $>$ Mn-containing organic matter. We observed that vegetated pots receiving aqueous Mn had a lag time in the peak in effluent Mn concentrations relative to non-vegetated pots, consistent with the idea that vegetation slows the removal of Mn from soils into rivers. In fact, vegetation increased the estimated half-life of Mn from years to decades in pots receiving aqueous additions compared to non-vegetated mesocosm pots. Likewise, the calculated half-lives of Mn added as Mn-oxide increased in the presence of vegetation from centuries to millennia, or for Mn in the shale-derived soil from millennia to tens of millennia. Thus, “contaminant Mn” sources such as aqueous and oxide Mn are predicted to persist

for shorter timescales than Mn derived from the parent bedrock because the latter is likely hosted by both clay and oxide minerals. In contrast, additions of Mn-rich organic matter resulted in net decreases in the cumulative Mn mass released in effluent, consistent with adsorption of soluble Mn onto the solid-phase organic matter.

Rate constants derived at the mesocosm-scale were useful predictors of rates of Mn uptake and leaching observed at the CZO and should be relevant toward understanding the response of landscapes to the historical metal loading in the U.S.A. and Europe and ongoing contamination in Asia and Latin America. Results from the mesoscale experiments are consistent with the conclusion that Mn contaminants that are input to soils will be temporarily stored in vegetation. As a result, contaminant Mn will persist in soils and be slowly leached into river systems for centuries to millennia.

I. Introduction

1.1. Background

Over the geologically brief time-scale of industrialization (~200 years), humans have transferred large quantities of material from the lithosphere to the atmosphere. Currently, human activity dominates the global fluxes of many trace metals, leading to the redistribution of elements across the Earth's surface and the enrichment of many metals (e.g. Mn, Cu, Cr, Cd) in soils, water, and biota (Nriagu and Pacyna, 1988; Rauch and Pacyna, 2009). Environmental regulation has curbed industrial emissions in many countries; however, soils act as a sink for atmospheric deposition and provide a long-term record of pollution. The residence times of contaminants in soils and the biogeochemical processes impacting their retention or removal remain unclear. To understand long-term impacts of soil contamination, it is necessary to identify the factors affecting contaminant mobility and quantify rates of contaminant transfer between different ecosystem reservoirs. By predicting rates of contaminant transfer, we can also evaluate human exposure to contaminants in soils, vegetation, and water.

The impact of vegetation on mineral weathering and the mobility of rock-derived elements has been noted by many researchers (Bormann *et al.*, 1998; Drever, 1994; Berner *et al.*, 2003; Taylor *et al.*, 2009). Additionally, many studies investigate the use of plants as a tool to remediate soils through enhanced biological uptake of contaminants (phytoremediation), filtration of contaminated water through the rooting zone (rhizofiltration), or immobilization of mobile contaminants (phytostabilization) (Chaney *et al.*, 1997). Certainly, vegetation impacts the mobility of elements in

the soil and may play a dominant role in modulating the residence time of contaminants. However, more studies are needed to examine the complex interactions of vegetation with trace metals.

Plants can enhance mineral weathering through the exudation of protons, organic acids, and chelating compounds that promote reductive and ligand-promoted dissolution (Drever, 1994; Drever & Stillings, 1997; Neaman *et al.*, 2005). While these factors can increase dissolution rates of minerals and solute fluxes from watersheds (Moulton *et al.*, 2000), plants can also inhibit the removal of elements from soils into rivers, at least over short intervals, due to elemental uptake into biomass (Johnson *et al.*, 1969; Balogh-Brunstad *et al.*, 2008). Disturbance of vegetation (e.g. clear cutting) can increase both physical erosion (Bormann *et al.*, 1974) and the release of elements from soils into rivers (Likens *et al.*, 1970; Balogh-Brunstad *et al.*, 2008). Thus, the timescale of observation is important: vegetation may increase metal leaching over long time-scales while decreasing leaching over short time-scales.

Manganese is delivered as atmospheric deposition to many soils in industrialized areas, resulting in net enrichment of Mn in the top of soil profiles (Herndon *et al.*, 2011). The widespread but patchy contamination of soils by Mn was first discovered in the Susquehanna Shale Hills Critical Zone Observatory (SSHCZO) in central Pennsylvania. The patchy nature of Mn contamination presumably derives both from the point-source nature of most Mn emitters and the variability in soils' capacity to sequester Mn due to lithology and biotic factors. Mn is a redox sensitive trace element that both impacts redox reactions in soils and serves as a biologically essential micronutrient. At 0.1 wt% of the Earth's crust, Mn is one of the most abundant trace elements in rocks. Although anthropogenic activity is estimated to input large quantities of Mn to soils, enrichment is often masked by its high natural abundance (Nriagu and Pacyna, 1988). Due to the effects of acid rain, Mn mobility has increased in many soils throughout the northeastern United States, facilitating the uptake of Mn into vegetation and leading to widespread Mn toxicity in sensitive species such as sugar maples (Horsley *et al.*, 2000; Kogelmann & Sharpe, 2006). Thus, both inputs of Mn to soils and effects of acid rain impact Mn biogeochemistry in industrialized areas.

Mn is also being released into rivers near the Mn-impacted soils of central PA (Herndon and Brantley, 2011). If release of Mn from the soil occurred immediately after atmospheric deposition, riverine Mn concentrations would more or less track the peak in Mn concentrations in the atmosphere. We observed that Mn concentrations in the atmosphere sharply declined after 1970, roughly consistent with the peak and decline in U.S. steel production. In contrast, we have observed a lag of approximately 5-10 years between the peak and decline in atmospheric and

riverine concentrations in the Susquehanna River (Herndon and Brantley, 2011). Various field studies note the large flux of Mn through vegetation in forested watersheds (Shanley, 1986; Jobbagy & Jackson, 2001; Navrátil *et al.*, 2007; Li *et al.*, 2008; Landre *et al.*, 2010). This paper tests the hypothesis that Mn has not only been sequestered in Pennsylvania watersheds due to sorption-desorption reactions, but also due to tight cycling in vegetation.

1.2. Mn in the SSHCZO

A mesocosm system was used to quantify the influence of vegetation on rates of Mn leaching from soil constituents. Mesocosm systems have been used previously to investigate plant- and mycorrhiza-driven silicate weathering (Andrews *et al.*, 2011). Here, mesocosms were designed to represent field conditions at the SSHCZO. We investigated Mn leaching from the four main sources of Mn in SSHCZO soils: shale-derived mineral grains in the soil, Mn-oxides delivered by atmospheric deposition, dissolved Mn from rain- or throughfall, and Mn-rich organic matter from the decomposition of vegetation.

Soils at SSHCZO are derived from the Rose Hill formation, an organic-poor marine shale, and are composed primarily of clay (illite/chlorite/vermiculite/minor kaolinite) and quartz with Fe-oxides (Jin *et al.*, 2010). Shale is an important lithology of continental surfaces, comprising ~25% of the exposed surface (Amiotte-Suchet *et al.*, 2003). Mn concentrations in the Rose Hill shale ($800 \mu\text{g g}^{-1}$) are similar to world averages for shale ($= 850 \mu\text{g g}^{-1}$, Turekian and Wedepohl, 1961). X-ray diffraction analysis of the Rose Hill shale documents no specific Mn mineral present at levels greater than a few vol. % (Jin *et al.*, 2010; Liermann *et al.*, 2011). Thus, Mn is most likely incorporated in protolith and soil material as clays or Fe-oxides. The catchment is vegetated by a dominantly oak-hickory forest, and the Mn concentrations reported here for foliage ($20 - 90 \mu\text{mol g}^{-1}$) far exceed the typical “nutritionally sufficient” range for vegetation ($0.55 - 5.5 \mu\text{mol g}^{-1}$; Kabata-Pendias and Pendias, 2001). Mn dissolved in soil pore waters can be taken up by vegetation, incorporated in biotic matter, and eventually returned to the soil in throughfall or as Mn-enriched organic material (Shanley, 1986; Bergkvist and Folkesson, 1995; Navrátil *et al.*, 2007; Watmough *et al.*, 2007; Landre *et al.*, 2010). High concentrations of Mn in throughfall ($\sim 2 \mu\text{M}$) relative to incoming precipitation have been observed for areas with foliar Mn levels similar to SSHCZO (Shanley, 1986; Navrátil *et al.*, 2007; Landre *et al.*, 2010). At the Shale Hills CZO, measurements of foliar Mn concentrations have been used to calculate that annual uptake of Mn into foliage far exceeds losses due to chemical weathering (Herndon and Brantley, 2011). A thin ($< 5 \text{ cm}$) organic horizon formed from decomposing vegetation is also found everywhere in the CZO

(Lin, 2006) and has been measured to contain significant Mn as reported below ($230 \pm 220 \mu\text{mol g}^{-1}$).

In addition to shale-derived Mn, soils at SSHCZO contain ~50% excess Mn due to atmospheric deposition from industrial sources (Herndon *et al.*, 2011). Although no monitoring was in place to document Mn deposition over the course of industrialization in central PA (1800-present), it is likely that Mn in this deposition occurred as either Mn-oxide particles or dissolved in rain. Specifically, anthropogenic Mn-oxide particles generally enter the atmosphere as the result of crushing of Mn-bearing ores and erosion from ore stockpiles as well as fossil fuel combustion and ore smelting (U.S. Environmental Protection Agency, 1984; U.S. Environmental Protection Agency, 1985; Nriagu and Pacyna, 1988; Pacyna and Pacyna, 2001). While precipitation generally contains low levels of Mn solutes, areas near industrial sources may receive high dissolved Mn in precipitation due to dissolution of Mn from anthropogenic aerosols and the acid nature of rain in many industrialized areas (Lindberg and Harriss, 1983; Williams *et al.*, 1988). Dissolved Mn in soil pore waters can precipitate as Mn-oxides either abiotically in the presence of natural catalysts (Diem and Stumm, 1984; Junta and Hochella, 1994; Learman *et al.*, 2011a) or as the result of bacterial and fungal oxidation processes (Tebo *et al.*, 2004; Learman *et al.*, 2011, Santelli *et al.*, 2011).

Here, we investigated mobilization of Mn from Mn-bearing soil constituents (shale-derived mineral soil, organic matter, Mn-oxides, and aqueous Mn) in the presence or absence of red oak seedlings. Although the mesocosms were designed to replicate SSHCZO soils, these soil constituents are common in many forested watersheds. This study was designed to quantify the dominant source of Mn that leaches from the soils and to estimate the residence time of Mn derived from soil constituents in the presence or absence of vegetation.

II. Methods

Small mesocosm experiments were designed to examine Mn uptake into trees and loss in effluent. For the experiments, bulk mineral soil was collected from the SSHCZO in March 2011, air dried, and sieved to < 4 mm. The collected soil was obtained from all depths from a pit dug on the north slope of the catchment, an area mapped as the Weikert soil series (loamy-skeletal, mixed, active, mesic, Lithic Dystrudepts) by Lin (2006). The surface of the mineral soil (~5 cm) and the organic horizon were discarded due to likely contamination from industrial inputs. The sieved fraction was mixed thoroughly with medium-coarse sand in a 1:1 by volume ratio to prevent compaction and allow good aeration. Prior to the experiment, a sample of the soil medium was

fused with Li-metaborate and analyzed with inductively coupled plasma atomic emission spectroscopy (ICP-AES) at Penn State's Material Characterization Laboratory. The soil medium was determined to contain $980 \mu\text{g g}^{-1}$ Mn (Table B-1). Other compositional attributes of soils from the SSHCZO have been reported elsewhere (Jin *et al.*, 2010; Liermann *et al.*, 2011).

The experiments were conducted in 2.8 L plastic tree pots (10 x 10 x 36 cm; Stuewe and Sons, Inc., Corvallis, OR) which were filled with a bottom layer of polyester-fiber fill and approximately 3.2 kg of the air-dried soil medium. Plastic sheets were wrapped around the bottom of each tree pot to funnel the effluent water into plastic tubing which dripped into 250 mL acid-washed amber-colored glass bottles. Twelve small plastic pots (~1.0 L) were prepared in the same manner as the large pots but with approximately 1.3 kg soil medium, were left non-vegetated. The pots contained either ~57 mmol (large pots) or ~13 mmol (small pots) total Mn in the mineral soil.

Fifty-six red oak seedlings (6-12" height, Cold Stream Farm, Freesoil, MI) were rinsed thoroughly to remove root-adhering soil and planted one-per-pot in moistened soil in May 2011 and kept in a greenhouse under ambient temperature and light. The seedlings had buds upon delivery and leaves emerged within one week.

Drip lines delivered deionized (DI) water to each pot twice weekly (150-350 mL/pot/week). The average concentrations in the input were below detection limits by ICP-AES for Al, Ca, Fe, Mg, Mn, Si, and Zn (DL = $0.05 \mu\text{g mL}^{-1}$) and K, Na, and P (DL = $0.10 \mu\text{g mL}^{-1}$). After 4 weeks, pots were treated with 10 mL nutrient solution (10 mM KH_2PO_4 , 10 mM $\text{Ca}(\text{NO}_3)_2 \cdot 4\text{H}_2\text{O}$, 1 mM $\text{MgCl}_2 \cdot 6\text{H}_2\text{O}$; pH 3.4) and 5 mL 1mM K_2CO_3 (pH 9.6) once per week. At six weeks, 10 seedlings were removed from their pots after failing to produce leaves and these pots were used as additional non-vegetated replicates. Thus, the experiment consisted of 46 vegetated pots and 20 non-vegetated pots. All seedlings were planted in large pots, while non-vegetated mesocosms consisted of both large and small pots. Due to poor drainage, 7 out of 66 pots were eventually excluded from calculations of leaching rates (Figure B-1); however, all 46 seedlings were included in measurements of foliar mass and chemical composition.

When trees were well established 46 days after planting, additional manganese was added to the soil medium in a subset of the pots. The three types of amendments included: organic (n = 16), Mn-oxide (n = 16), or aqueous (n = 17) (Tables B-24 and B-25). In contrast, 17 soil pots received no Mn additions (referred to here as "soil-only"). Five soil pots in each treatment set were non-vegetated. Organic and oxide Mn were added only once while aqueous Mn was added in small increments weekly for 10 total weeks. The amendments were prepared as described below.

Organic: Organic matter was collected from the organic horizon at SSHCZO, dried, and sieved to < 4 mm. A subsample of the sieved fraction was ashed, digested by Li-metaborate fusion, and determined to contain 102 $\mu\text{mol Mn g}^{-1}$ dry weight as analyzed by ICP-AES at the Penn State Materials Characterization Laboratory (Table B-1). In the greenhouse, approximately 20 g of this material were mixed into the top 5 cm of each soil pot, i.e., 2.08 ± 0.03 mmol Mn were added to each pot in the organic Mn treatment.

Mn-oxide: Sodium birnessite ($\text{Na}_{0.5}(\text{Mn}^{+3}, \text{Mn}^{+4})_2\text{O}_4 \cdot 1.5\text{H}_2\text{O}$) is a common natural form of Mn in oxygenated soils and sediments (Post, 1999). We use birnessite to represent all Mn-oxides that are input from industrial processes or precipitate in soils. This mineral was prepared using a published procedure (Golden *et al.*, 1986). Briefly, oxygen gas was bubbled through a 400 mL solution of 0.5M $\text{MnCl}_2 \cdot 4\text{H}_2\text{O}$. Then, 500 mL of 5.50M NaOH solution was slowly added, stirring continuously. Oxygenation and stirring of the solution continued for five hours. The resulting suspension was poured into 50 mL centrifuge tubes and centrifuged at 8,000 g for 10 min. Next, the supernatant was removed and replaced with ultrapure deionized water. Rinsing and centrifugation at 8,000 g for 5 min was repeated 3 times. The resulting precipitates were recombined and suspended in ultrapure deionized water. The birnessite was added to the soils as an aqueous suspension (~ 0.055 g mL^{-1}) in 15 mL aliquots. The mass of each aliquot was measured and the birnessite added per pot in the Mn-oxide treatment was determined to be 0.78 ± 0.13 g birnessite (7.4 ± 1.2 mmol Mn).

Aqueous: An aqueous solution was made up from $\text{MnCl}_2 \cdot 4\text{H}_2\text{O}$ and ultrapure deionized water to contain 0.16 M $\text{Mn}_{\text{aq}}^{2+}$. In the absence of catalysts, Mn^{2+} is stable in oxygenated aqueous solution for years (Diem and Stumm, 1984; Chiswell and Mokhtar, 1986). Using a graduated pipette, 5 mL of the solution was dispersed across the top of the soil once per week for 10 weeks for a total addition of 8.0 mmol Mn to all pots in the aqueous Mn treatments.

All the effluent water draining from the bottom of each pot was collected and sampled once per week over 16 weeks. The total volume of effluent was recorded (Tables B-2 and B-3) and a subsample of the solution was transferred to a 15 mL metal-free centrifuge tube. No effluent was collected at week 14, when the collection bottles were removed and acid-washed to remove algal growth. Each effluent sample was measured for pH (Tables B-4 and B-5), then acidified with 2-3 drops ultrapure concentrated nitric acid. Sometimes effluent was cloudy and had to be filtered (0.45 μm) before acidification. However, for the 509 (out of 567) analyzed samples that were filtered, no systematic differences were observed with respect to concentrations in unfiltered versus filtered samples. Solutions from 11 of the weekly sample sets were analyzed with ICP-AES. In

addition, a subset of samples with Mn concentrations below the ICP-AES detection limit was reanalyzed with inductively coupled plasma mass spectrometry (ICP-MS). For weeks where volume was recorded but effluent chemistry was not determined (5 out of 16), we estimated the concentration of elements in the effluent as the average of concentrations from the bracketing collection dates (Tables B-6 through B-21).

Experiments were terminated and oak seedlings were harvested after 19 weeks of growth. Leaves were separated from the woody shoots, rinsed with DI water, and measured for leaf area prior to drying. Leaf area was measured with a LI-COR LI-3000A to within 0.1cm^2 accuracy. Dried leaves were weighed for total mass. Dried and ground leaf samples were chemically analyzed on ICP-AES following dry ash and acid dissolution (Miller, 1998) at Penn State's Agricultural Analytical Services Laboratory. Physical and chemical foliar data are reported in Tables B-22 and B-23.

Statistical analyses were performed in Origin®. Two-sample t-tests were used to assess whether mean parameters recorded for pots receiving Mn treatments were significantly different from mean parameters recorded for the controls (soil-only pots) to a maximum significance level of $\alpha = 0.05$. The mean, standard error of the mean, and p-value are reported for each parameter. Paired-sample t-tests were used to assess differences between different parameters measured for the same set of samples (e.g. uptake versus leaching of elements within one treatment). Additionally, t-tests were used to determine whether slopes of best-fit regression lines were significantly different from zero ($\alpha = 0.05$). Upper and lower 95% confidence intervals, adjusted R^2 values, and p-values are reported for regression lines.

III. Results

3.1. Effluent

For all treatments, Mn concentrations in effluent ($C_{Mn,eff}$; μM) were on average higher for non-vegetated than vegetated pots (Figure 3-1). Although there was high variability amongst individual replicates in each group, average Mn concentrations decreased for both vegetated and non-vegetated pots in the order, aqueous > oxide > soil-only \approx organic. Specifically, Mn concentrations in effluent from vegetated pots decreased in the order, aqueous ($C_{Mn,eff} = 16 \pm 5 \mu\text{M}$) > oxide ($C_{Mn,eff} = 1.8 \pm 0.3 \mu\text{M}$) > soil-only ($C_{Mn,eff} = 0.76 \pm 0.27 \mu\text{M}$) \approx organic ($C_{Mn,eff} = 0.63 \pm 0.16 \mu\text{M}$), and in non-vegetated pots, aqueous ($C_{Mn,eff} = 290 \pm 83 \mu\text{M}$) > oxide ($C_{Mn,eff} = 7.8 \pm 1.3 \mu\text{M}$) > soil-only ($C_{Mn,eff} = 2.7 \pm 0.8 \mu\text{M}$) \approx organic ($C_{Mn,eff} = 1.9 \pm 0.3 \mu\text{M}$).

Variability in effluent Mn concentrations was likely due to variability in sizes of seedlings and differences in Mn mass between the mineral soil in small and large pots. The mass of Mn contained in the mineral soil in large versus small pots is accounted for in calculations below.

No significant trends in effluent Mn concentrations with time were detected over the course of the experiment; however, in the aqueous-added pots, effluent from non-vegetated pots immediately increased in Mn concentration and continued increasing over the 10 week course of aqueous addition (Figure B-2). In contrast, in the vegetated aqueous pots, effluent Mn did not begin to increase until one month after the start of additions. After that lag, Mn concentrations increased until Mn additions stopped. These temporal changes in effluent Mn in the aqueous treatments likely contributed to the high variability in Mn concentrations averaged over all effluent collections.

Due to transpiration, the average weekly effluent volume from vegetated pots ($= 78 \pm 43$ mL, $n = 656$) was approximately half of the volume draining from non-vegetated pots ($= 146 \pm 34$ mL, $n = 288$), and average effluent volume for each pot was negatively correlated with leaf area (Figure B-1). No differences in weekly effluent volume were observed between treatments, or between the small and large pots used for non-vegetated systems.

3.2. Foliage

The majority of seedlings in all pots, regardless of whether excess Mn was added, exhibited black spots on their leaves, a prime indicator of Mn toxicity (Wissemeier and Horst, 1987; Horiguchi, 1987). For example, after ~18 weeks of growth, black spots were observed on leaves in 7 out of 12 aqueous-added, 7 out of 11 oxide-added, 8 out of 11 organic-added, and 6 out of 12 soil-only pots. The physical manifestation of the black spots varied amongst the seedlings. While for some seedlings the black spots were distributed uniformly across the leaf blade, in other seedlings black spots were observed to concentrate around the veins or leaf margins. Furthermore, the spots were observed as large splotches, tiny dustings, and/or in ring structures (Figure B-3).

Mn concentrations in the foliage ($C_{Mn,fol}$) were high and similar to concentrations reported for red oak seedlings grown on acidic soils in Pennsylvania (St. Clair and Lynch, 2005). Average $C_{Mn,fol}$ did not differ significantly among the treatments: i.e., soil-only pots (79.9 ± 5.1 $\mu\text{mol g}^{-1}$), aqueous-added (84.7 ± 14.7 $\mu\text{mol g}^{-1}$), oxide-added (73.6 ± 10.4 $\mu\text{mol g}^{-1}$), organic-added ($= 70.2 \pm 7.4$ $\mu\text{mol g}^{-1}$). A significant difference in $C_{Mn,fol}$ was observed between seedlings exhibiting signs of Mn toxicity ($C_{Mn,fol} = 87.4 \pm 6.2$ $\mu\text{mol g}^{-1}$, $n = 28$) versus those without ($C_{Mn,fol} = 61.6 \pm 7.2$ $\mu\text{mol g}^{-1}$, $n = 18$) ($p < 0.05$). However, even 16 out of 18 seedlings with no toxicity signs had values of $C_{Mn,fol}$ deemed to be excessive (i.e., > 7 $\mu\text{mol g}^{-1}$, (Kabata-Pendias and Pendias, 2001).

To account for effects of tree size, we also measured leaf area, which is a proxy for leaf mass. Given that other factors (e.g. radiation, plant-available water) were held constant for all replicates in this experiment, observed increases in leaf area serve as a proxy for increases in transpiration (Zhang *et al.*, 2001). The result of an increase in leaf area is increased water flux through the foliar tissue but decreased drainage through the soil. Furthermore, Mn is delivered to foliar tissue primarily via aqueous solute transport through xylem tissue as driven by the transpiration stream (White, 2012). As such, leaf area for different seedlings may impact both the extent of Mn uptake into foliage and Mn loss into effluent. For aqueous-added, oxide-added, and soil-only pots, the lowest $C_{Mn,fol}$ values occurred in seedlings with the smallest leaf area; however, no statistically significant correlation with leaf area was observed (Figure 3-2A). As a result, Mn mass in foliage ($m_{Mn,fol}$, μmol), i.e., the product of leaf mass (m_{fol} , g) and foliar Mn concentration ($C_{Mn,fol}$, $\mu\text{mol g}^{-1}$), increased linearly with leaf area for aqueous-added, oxide-added, and soil-only pots (Figure 3-2C). In contrast, $C_{Mn,fol}$ decreased with increasing leaf area for the organic treatments (Figure 3-2B), leading to less total uptake at high leaf area relative to the other treatments (Figure 3-2D).

3.3. Effects of pH

The average pH of all effluent samples from vegetated pots (4.52 ± 0.04 ; $n = 243$) was significantly higher ($p < 0.001$) than the average pH of all effluent samples from non-vegetated pots ($\text{pH} = 4.23 \pm 0.07$; $n = 126$) (Tables B-4 and B4). For effluent collected after the start of Mn additions, pH values were higher for vegetated pots than non-vegetated pots in the soil-only, aqueous-added, and organic-added treatments, but higher for the non-vegetated pots in the oxide-added treatment ($p < 0.05$; Table B-26). Comparing treatments, only the aqueous-added treatment differed significantly (lower effluent pH) from the soil-only treatment in the vegetated pots, while both the aqueous-added (lower pH) and oxide-added (higher pH) treatments differed from the soil-only treatment in non-vegetated pots ($p < 0.05$). The organic-added treatment was not significantly different from the soil-only treatment in either vegetated or non-vegetated pots.

Soil pH is known to influence Mn mobility in soils, with Mn becoming increasingly more bioavailable at $\text{pH} < 4$ (Kogelmann and Sharpe, 2006; Houle *et al.*, 2007). Across all effluent samples, Mn concentrations increased with decreasing pH (Figure B-4A). However, when we examined averages for individual pots, this trend only occurred consistently in the soil-only treatments (Figure B-4B): no significant trends between pH and effluent Mn concentrations were observed in the aqueous, oxide, and organic treatments.

IV. Discussion

An element that is mobilized in a tree pot can subsequently be immobilized, taken up into vegetation, or lost as leached Mn in the effluent. Here, we only assessed net mobilization, also referred to as chemical denudation (Balogh-Brunstad *et al.*, 2008), and ignored internal Mn cycles where Mn is mobilized but re-precipitated in the soil. We quantified rates of uptake and leaching and derived rate constants which were used to predict rates of Mn mobilization and residence times of Mn components in the field. A summary of variables used in the model is presented in Table 3-1.

4.1. Mn uptake exceeds leaching

In experiments discussed here, an element i that was mobilized from a reservoir j was either taken up into foliar tissue ($U_{i,j}$) or lost as solute in effluent ($L_{i,j}$). First, we assessed pots containing only mineral soil without Mn amendments ($j = s$) to evaluate differences in uptake ($U_{i,s}$) and leaching losses ($L_{i,s}$) for a suite of elements ($i = \text{Mn, Fe, Al, K, Mg, Na, Ca, P}$). The mobilized mass of each element was normalized to the mass of that element in the soil ($M_{i,s}$) in order to account for differences in soil mass and element concentration in the starting soil. $M_{i,s}$ also included the mass of elements added in the nutrient solution (K, P, Ca, and Mg), although this mass was minor compared to mass of elements in the soil. The fraction of i taken from the soil and accumulated into foliage ($U_{i,s}$) equals:

$$U_{i,s} = \frac{m_{fol} C_{i,fol}}{M_{i,s}} \quad (1)$$

Here, $M_{i,s}$ was calculated as the product of soil mass (m_s , g) and concentration of i in soil ($C_{i,s}$; mol g⁻¹). Concentration of i in foliage, $C_{i,fol}$, is reported in mol g⁻¹. No attempt was made to include the Mn in woody tissue or roots in $U_{i,s}$ because woody tissue grew little over the course of the experiment and research has documented that little Mn accumulates in this tissue compared to leaves (Kogelmann and Sharpe, 2006; Houle *et al.*, 2007).

The mass transfer of i from soil into effluent ($b_{i,s}$, mol) was calculated as:

$$b_{i,s}(t) = \sum_{t=0}^{t_{final}} C_{i,eff}(t)V(t) \quad (2)$$

Here, cumulative mass loss to effluent equals the summation of the products of effluent volume ($V(t)$, liters) and element concentration in the effluent ($C_{i,eff}(t)$, mol L⁻¹) collected at each time t and summed over the time period $t = 0$ to t_{final} .

The fraction of i in soil that is transferred and lost in effluent, $L_{i,s}$, equals $b_{i,s}$ normalized to $M_{i,s}$:

$$L_{i,s} = \frac{b_{i,s}(t_{final})}{M_{i,s}} \quad (3)$$

Here, to compare $U_{i,s}$ to $L_{i,s}$ over an equal amount of time, $L_{i,s}$ was calculated for the total time that effluent was collected. Thus, these values include all effluent samples collected between planting and harvest.

For vegetated pots containing only soil, the mass of Mn that was taken up into foliage ($U_{Mn,s}$) far exceeded the mass leached into effluent ($L_{Mn,s}$, Figure 3-3). Furthermore, we found that $U_{Mn,s}/L_{Mn,s} > 100$, higher than for the major plant nutrients, K, Mg, Ca, and P, for which $U_{i,s}/L_{i,s} < 10$ (Table 3-2). Micronutrient Fe was also preferentially taken up, while the non-essential element Na was lost to leaching ($U_{i,s}/L_{i,s} \leq 1$) because it was taken up in relatively small quantities. For Al, $U_{i,s}/L_{i,s} \approx 1$.

For all elements, leaching from non-vegetated pots exceeded leaching from vegetated pots (Figure 3-3; Table 3-2). This was due in part to transpiration, which reduced average effluent volume by ~50% in vegetated pots. However, $L_{i,s}$ for elements in non-vegetated pots exceeded $L_{i,s}$ in vegetated pots by factors of 28 (Mn), 18 (P), 8 (K), and 4 (Ca and Mg). The transpiration effect can only explain differences in $L_{Na,s}$, which was reduced by 50% in the vegetated pots, similar to the reduction in effluent volume.

Although Mn leaching from soil-only pots decreased in the presence of vegetation, total mobilization ($L_{Mn,s} + U_{Mn,s}$) increased by a factor of four for vegetated compared to non-vegetated systems (Table 3-2). Ca showed a trend of increased mobilization but decreased leaching in vegetated pots, similar to Mn. In contrast, total mobilization in vegetated systems was less than or approximately equal to that in non-vegetated systems for Al, Fe, K, Mg, P, and Na.

4.2. Rates of Mn loss to effluent

We now use an equation analogous to Eqn. (2) to examine cumulative Mn loss to effluent for $b_{Mn,j}$, i.e., we evaluate rates of Mn solubilization and loss from each source reservoir j ($= org, ox,$ or aq) separately from losses from the mineral soil ($j = s$). For pots receiving no Mn addition ($j = s$), $b_{Mn,s}$ equals the mass of Mn leached from the shale-derived soil and released in effluent (Eqn. 2). However, for pots receiving Mn addition ($j = org, ox, aq$), effluent contained Mn derived from both the shale-derived soil and the Mn addition. To calculate Mn loss from the Mn-addition alone, the mineral soil contribution, i.e. the product of $M_{Mn,s}$ and φ (L^{-1}), is subtracted from Eqn. (2):

$$b_{Mn,j}(t) = \sum_{t=0}^{t_{final}} (C_{Mn,eff}(t) - \varphi M_{Mn,s})V(t) \quad (4)$$

For consistency amongst all treatments, $b_{Mn,j}$ is calculated over the same time period for all pots. For the following calculations, we do not include effluent collected prior to the date of Mn additions, even for the mineral soil pots which experienced no amendments. Therefore, $t = 0$ represents the date of Mn additions and t_{final} is the last date of effluent collection.

The mineral soil contribution to pots with amendments is determined separately for each pot because of differences in $M_{Mn,s}$ per pot. Here, φ (L^{-1}) is the fraction of Mn in the mineral soil that was leached per unit volume of effluent in the soil-only pots:

$$\varphi = \frac{\hat{C}_{Mn,eff}}{M_{Mn,s}} \quad (5)$$

$\hat{C}_{Mn,eff}$ (mol L^{-1}) is the average concentration of Mn in effluent for soil-only pots. While φ differed between vegetated and non-vegetated pots, in our calculation it did not vary with time or effluent volume; therefore, φ is used as a constant to determine the mineral soil contribution to effluent in vegetated ($= 2.0 \pm 0.3 \times 10^{-5} L^{-1}$) and non-vegetated ($= 6.8 \pm 1.8 \times 10^{-5} L^{-1}$) pots.

The rate of Mn loss to effluent from each Mn reservoir, $F_{j,k}$ (mol y^{-1}), is equal to the change in $b_{Mn,j}$ (moles) over time (years). While some pots showed variable rates versus time, for simplicity these temporal rate variations were not modeled but instead were treated by assuming that $F_{j,k}$ is first-order with respect to $M_{Mn,j}$:

$$F_{j,k} = \frac{d(b_{Mn,j})}{dt} = k_{j,k} M_{Mn,j} \quad (6)$$

Subscripts indicate the source ($j = s, aq, ox, org$) and sink (here, $k = eff$) reservoirs. Given that $b_{i,j}$ normalized to $M_{i,j}$ equals the fractional loss $L_{i,j}$, as used previously to calculate total leaching of multiple elements from the soil medium (Eqn.3), Eqn. (6) is rearranged to yield the definition of the first-order rate constant ($k_{j,eff}$; y^{-1}):

$$k_{j,eff} = \frac{d(L_{Mn,j})}{dt} \quad (7)$$

Here, $k_{j,eff}$ was calculated as the slope of a plot of $L_{Mn,j}$ versus time for all pots in each treatment (Figure 3-4; Table 3-3). Note that here $M_{Mn,j}$ is the mass of Mn in the soil ($j = s$, i.e., for the soil-only pots) or added as an amendment ($j = aq, ox, org$), and time is in years. For soil-only pots, $k_{s,eff} = 2.7 \pm 0.4 \times 10^{-5} y^{-1}$ (vegetated) and $26 \pm 3 \times 10^{-5} y^{-1}$ (non-vegetated) ($p < 0.001$). In

the oxide treatments, $k_{ox,eff} = 22 \pm 12 \times 10^{-5} \text{ y}^{-1}$ (vegetated) and $620 \pm 110 \times 10^{-5} \text{ y}^{-1}$ (non-vegetated); however, the slope of the linear regression used to calculate $k_{ox,eff}$ (vegetated) was not statistically significant ($p = 0.06$).

In the organic treatments, Mn loss in effluent was inhibited relative to the soil-only pots: $k_{org,eff} = -93 \pm 21 \times 10^{-5} \text{ y}^{-1}$ (vegetated) and $-640 \pm 96 \times 10^{-5} \text{ y}^{-1}$ (non-vegetated) ($p < 0.001$). Note that a negative rate constant in this context means that Mn is retained in the soil with organic amendments compared to soil-only pots. However, in analyzing the data, we realized that the first-order rate equation with respect to $M_{Mn,org}$ was not appropriate since Mn sorption is expected to be first order with respect to mass of organic matter rather than mass of Mn in the organic matter. Therefore, Mn release from these pots into effluent was modeled as first-order with respect to the mass of organic matter itself:

$$F_{org,k} = k_{org,k} m_{org} \quad (8)$$

The m_{org} -dependent first-order rate constant for Mn release from the organic-addition pots was calculated for vegetated pots as $k_{org,eff} (= -0.010 \pm 0.002 \times 10^{-5} \text{ mol Mn (gram organic matter)}^{-1} \text{ y}^{-1})$ and non-vegetated as $k_{org,eff} (= -0.064 \pm 0.010 \times 10^{-5} \text{ mol g}^{-1} \text{ y}^{-1})$ (Table 3-3). These negative rate constants again reflect the mass retention of Mn per gram of organic matter addition.

For $j = s, ox,$ and org , $M_{Mn,j}$ did not change appreciably during the course of the experiment. However, in the aqueous treatments, $M_{Mn,aq}(t)$ was considered the cumulative addition of Mn solute to each pot by time t . This value was corrected for the Mn in outflow with equation (9):

$$M_{Mn,aq}(t) = m_{aq}n - b_{Mn,aq}(t - 1) \quad (9)$$

Here, m_{aq} is the moles of Mn in one aqueous addition ($= 8.0 \times 10^{-4}$ moles), n is the number of aqueous Mn additions prior to t , and $b_{Mn,aq}$ (Eqn. 4) is the cumulative moles of aqueous Mn leached prior to t (beginning at the point of Mn additions). Using these values and equations 6 and 7, we calculated $k_{aq,eff} = 796 \pm 164 \times 10^{-5} \text{ y}^{-1}$ (vegetated) and $25,400 \pm 7,000 \times 10^{-5} \text{ y}^{-1}$ (non-vegetated) ($p < 0.001$). Additionally, breakthrough behavior was observed in the aqueous treatments. While $b_{Mn,aq}$ values began to increase in non-vegetated pots anywhere from 7 to 30 days following the start of aqueous Mn additions, they did not substantially increase in vegetated pots until ~60 days. Thus, vegetation caused a lag time of about 1- 2 months in the release of soluble Mn. Nonetheless, although the aqueous Mn was leached more quickly than Mn from the pots with oxides, organic matter, or soil-only, the majority of added aqueous Mn was retained in

both vegetated ($99.8 \pm 0.3\%$) and non-vegetated pots ($95.8 \pm 6\%$) over the course of the experiment.

In summary, first-order rate constants for Mn release were significantly higher for non-vegetated pots than vegetated pots in all treatments (Table 3-3). Furthermore, $k_{j,eff}$ values for Mn losses from aqueous and oxide additions were larger than for the shale-derived soil, indicating that the Mn additions were being removed from the system more quickly than from the background soil. In contrast, pots containing soil + organic matter showed less Mn loss than the soil-only pots, suggesting that organic matter inhibited Mn loss from the soil.

4.3. Mn uptake into foliage

We used the mass of Mn measured in foliage at harvest ($m_{Mn,fol}$) to calculate the rate that Mn was mobilized from the soil and taken up into vegetation ($F_{j,fol}$, mol y^{-1}):

$$F_{j,fol} = \frac{m_{Mn,fol}}{T} \quad (10)$$

For simplicity, we assumed constant uptake rates over the course of the experiment. Thus, $m_{Mn,fol}$ was divided by the total growth period T and expressed in units of mol y^{-1} . Here, the growth period is defined for each seedling as the time between leaf out and harvest ($T = 107 - 132$ days). For soil-only pots, $F_{s,fol} = 34.3 \pm 4.0 \times 10^{-5}$ mol y^{-1} . To determine uptake from Mn addition alone ($j = ox, org, aq$), we subtract the mass of Mn in foliage that is derived from the mineral soil:

$$F_{j,fol} = \frac{m_{fol}(C_{Mn,fol} - \hat{C}_{Mn,fol})}{T} \quad (11)$$

Here, $\hat{C}_{Mn,fol}$ ($= 79.9 \pm 5.1 \mu\text{mol g}^{-1}$) is the average foliar concentration of Mn in soil-only pots, and $F_{j,fol}$ is converted to units of mol y^{-1} . For aqueous additions, $F_{aq,fol}$ ($= 5.8 \pm 4.2 \times 10^{-5}$ mol y^{-1}) differed from zero and was significantly lower than $F_{s,fol}$ but within error of the average leaching rate ($F_{aq,eff}$) in vegetated systems. In contrast, uptake from the oxide addition ($F_{ox,fol} = 0.37 \pm 2.7 \times 10^{-5}$ mol y^{-1}) was not significantly different from zero. In pots with soil + organic matter, uptake of Mn into foliage was inhibited relative to the soil-only pots ($F_{org,fol} = -8.0 \pm 4.9 \times 10^{-5}$ mol y^{-1}). In summary, for all treatments, the mass of Mn in foliage attributed to uptake or inhibited uptake from $j = aq, ox, \text{ or } org$ was small relative to the total mass of Mn in foliage.

For soil-only, oxide-added, and aqueous-added pots, rate constants for the uptake of Mn into foliage ($k_{j,fol}$, y^{-1}) were calculated using Eqn. (6) and $F_{j,fol}$ values. For organic-added pots, $k_{org,fol}$ values were calculated using Eqn. (8) and $F_{org,fol}$ values. For soil-only pots, the rate constant for uptake $k_{s,fol}$ ($= 602 \pm 530 \times 10^{-5} y^{-1}$) was greater than the rate constant for leaching

$k_{s,eff}$ by $\sim 10x$ for non-vegetated pots and $\sim 100x$ for vegetated pots (Table 3-3). This is consistent with the data presented in Figure 3-3 that shows large uptake of Mn into vegetation. For pots receiving Mn additions, the average rate constant for uptake was within error of the rate constant for leaching for aqueous ($k_{aq,fol} = 720 \pm 530 \times 10^{-5} \text{ y}^{-1}$) and oxide ($k_{ox,fol} = 26 \pm 340 \times 10^{-5} \text{ y}^{-1}$) treatments, while the addition of organic matter inhibited Mn uptake relative to the soil-only pots (Eqn. 8: $k_{org,fol} = -0.40 \pm 0.24 \text{ mol g}^{-1} \text{ y}^{-1}$). However, $k_{j,fol}$ values for $j = aq, ox,$ and org were small relative to $k_{s,fol}$ and not significant ($p > 0.05$). As such, we concluded that foliar chemistry showed no response to Mn additions in the mesocosm experiments.

Given that foliar Mn concentrations are relatively constant with or without Mn additions, we could infer that Mn dissolved from the mineral soil is the main source of Mn taken up by vegetation. However, most of the Mn in the effluent derives from the aqueous and oxide amendments where present, indicating that the mass of Mn dissolved from these added sources equals or exceeds the mass of Mn dissolved from the soil and should be available for uptake by vegetation. Since we can only measure Mn concentration in the bulk foliage, we can make no conclusions about where the Mn comes from that is taken into the trees (e.g. from soil or from amendments). However, the fact that Mn concentrations in foliage are the same, regardless of treatment, is also consistent with trees regulating Mn uptake and maintaining foliar concentrations below a certain level. If the latter scenario that is true, it is likely that seedlings receiving a Mn addition would contain less foliar Mn derived from the mineral soil than seedlings receiving no Mn addition.

Given these observations, the trees growing in the Mn-contaminated soils in our pots are likely taking up Mn from Mn additions; however, Mn toxicity symptoms in the seedlings were observed in the absence of additions, likely as a response to naturally-abundant Mn that is mobilized under acidic soil conditions. The correlation of Mn toxicity with acid rain and acid soils has been documented by several previous researchers (Horsley *et al.*, 2000; Kogelmann and Sharpe, 2006; Houle *et al.*, 2007). We also note that the uptake from the soil-only pots was higher than from the organic-amended pots. As mentioned previously, we infer that organic matter sorbs Mn, retaining it in the soil and perhaps sequestering it from being taken up by trees.

4.4. Mn half-life in soil components

The rate constants for Mn leaching derived above can be extrapolated to assess the duration of Mn retention in soils. Assuming first-order kinetics, a half-life ($t_{Mn,j}^{1/2}$, years) can be determined by the equation:

$$t_{Mn,j}^{1/2}(y) = \frac{\ln(2)}{k_{j,eff}} \quad (12)$$

The half-life of Mn in each reservoir j was calculated for vegetated and non-vegetated systems (Table 3-3). Here, we calculate that the half-life of Mn in shale-derived soil with no Mn additions, $t_{Mn,s}^{1/2}$, equals $2,700 \pm 870$ years for non-vegetated systems and $25,700 \pm 9,960$ years for vegetated systems, i.e., a difference of $\sim 10x$. Similarly, the presence of vegetation increases $t_{Mn,aq}^{1/2}$ from 2.7 ± 1.4 to 87 ± 39 years ($\sim 32x$) and $t_{Mn,ox}^{1/2}$ from 110 ± 47 to $3,120 \pm 2,290$ years ($\sim 28x$). Thus, Mn added to the soil as solute or as oxide particulates is expected to be removed from the soil more quickly than Mn derived from the parent shale. This makes sense in that Mn in the parent shale is likely substituted in clay minerals (e.g. illite/chlorite/kaolinite) or Fe-oxides in the parent shale, which have slower weathering rates than Mn-oxides (Brantley *et al.*, 2008; Saal and Duckworth, 2010). Likewise, mineral oxides have longer residence times in soils than soil pore fluids that contain aqueous Mn.

Meanwhile, organic matter inhibits Mn leaching by $0.064 \times 10^{-5} \text{ mol g}^{-1} \text{ y}^{-1}$ in the absence of vegetation and $0.010 \times 10^{-5} \text{ mol g}^{-1} \text{ y}^{-1}$ in the presence of vegetation. However, the inhibition of Mn leaching by organic matter is a short-term rather than long-term effect, as neither the mass of Mn in organic matter nor the mass of the organic matter itself increases indefinitely in a soil. The decomposition of organic matter will ultimately re-release adsorbed Mn to the soil where it can be precipitated, leached, or taken up into vegetation.

4.5. Comparison to SSHCZO

Rates measured on the mesocosm scale can be compared to rates derived from a field study at the Susquehanna Shale Hills CZO. To do this, we use $k_{j,eff}$ values calculated from the vegetated mesocosms. Although we analyzed seedlings in our mesocosms and mature trees at SSHCZO, we observed no dependence of $k_{j,eff}$ on seedling size and thus use the mesocosm-derived values as a first approximation (Figure B-5). The $k_{j,eff}$ values for $j = s, aq, ox$, and org are combined with $\bar{M}_{Mn,j}$ and \bar{m}_{org} values estimated for SSHCZO ridge soils to extrapolate net Mn losses in effluent from SSHCZO soils on an area-normalized basis ($\bar{F}_{Mn,eff}$):

$$\bar{F}_{Mn,eff} = k_{s,eff}\bar{M}_{Mn,s} + k_{aq,eff}\bar{M}_{Mn,aq} + k_{ox,eff}\bar{M}_{Mn,ox} + k_{org,eff}\bar{m}_{org} \quad (13)$$

We extrapolate to the CZO using a new variable, $\bar{F}_{Mn,eff}$, i.e., the Mn in effluent per unit time normalized by the unit ground surface area ($\text{mol m}^{-2} \text{ y}^{-1}$). Additionally, we define $\bar{M}_{Mn,j}$ as the mass of Mn in each reservoir j per unit ground surface area of the CZO (mol m^{-2}) and \bar{m}_{org} as the

mass of organic matter per unit ground surface area (g m^{-2}). Elemental concentrations have been previously reported for ridgetop mineral soils at SSHCZO (Herndon *et al.*, 2011). Soils that were sampled from the land surface to point of refusal for hand augering (≈ 0.32 m depth in soil) roughly average 16 mol Mn m^{-2} . We have calculated previously that on average, 47% of Mn in the soils is derived from the parent shale ($\bar{M}_{Mn,s} = 7.7 \text{ mol m}^{-2}$) and 53% is derived from inputs of industrial deposition (Herndon *et al.*, 2011).

Here, we assume the industrial inputs consist primarily of particulate Mn-oxides, which is consistent with reported characterization of Mn contamination from combustion sources (U.S. Environmental Protection Agency, 1984). Thus, we calculate that $\bar{M}_{Mn,ox}$ ($= 8.5 \text{ mol m}^{-2}$) equals 53% of the total mass of Mn in the soil profile. While this input may not have been as birnessite as modeled in this study, we nonetheless assume we can use birnessite to assess the solubility of deposited Mn oxides. A value for aqueous Mn input to the soil ($\bar{M}_{Mn,aq}$) is derived from both precipitation and throughfall data. Although current inputs in precipitation are small ($4.5 \times 10^{-5} \text{ mol m}^{-2} \text{ y}^{-1}$), Mn concentrations in foliage are high ($20\text{-}90 \text{ }\mu\text{mol g}^{-1}$), similar to foliar concentrations reported for the mesocosm experiments (Table 3-3). Studies in other regions with similar enrichments in foliar Mn have documented high inputs of aqueous Mn to soil as throughfall, and an average value for throughfall reported in the literature is therefore used here to estimate $\bar{M}_{Mn,aq} = 1.7 \times 10^{-3} \text{ mol m}^{-2}$ (Shanley, 1986; Navrátil *et al.*, 2007; Landre *et al.*, 2010). Finally, the organic horizon at the ridges varies in thickness (< 0.005 m), and using a reported value for the bulk density of the organic horizon ($= 425 \text{ kg m}^{-3}$; (Lin, 2006), we calculated a range for \bar{m}_{org} ($= 0 - 21 \text{ kg m}^{-2}$).

Using these $\bar{M}_{Mn,j}$ values, the previously derived values of the rate constants from the mesocosms, and Equation 13, we predict a range of $\bar{F}_{Mn,eff}$ values for the range of organic horizon thicknesses, i.e. $\bar{m}_{org} = 0.0 - 21 \text{ kg m}^{-2}$. When $\bar{m}_{org} = 0 \text{ kg m}^{-2}$, $\bar{F}_{Mn,eff} = 2.1 \times 10^{-3} \text{ mol m}^{-2} \text{ y}^{-1}$, with losses of $2.1 \times 10^{-4} \text{ mol m}^{-2} \text{ y}^{-1}$ (10%) from the shale-derived soil, $1.9 \times 10^{-3} \text{ mol m}^{-2} \text{ y}^{-1}$ (90%) from the Mn-oxide additions to the soil, and $1.4 \times 10^{-5} \text{ mol m}^{-2} \text{ y}^{-1}$ ($< 0.01\%$) from the aqueous throughfall inputs. Using an upper estimated value for \bar{m}_{org} ($= 21 \text{ kg m}^{-2}$) yields $\bar{F}_{Mn,eff} = 1.0 \times 10^{-5} \text{ mol m}^{-2} \text{ y}^{-1}$, indicating that the presence of an organic horizon impedes Mn losses from the soil. The calculated range for $\bar{F}_{Mn,eff}$ is consistent with field-measured values for both average ($= 1.8 \times 10^{-4} \text{ mol m}^{-2} \text{ y}^{-1}$) and maximum ($1.9 \times 10^{-3} \text{ mol m}^{-2} \text{ y}^{-1}$) recorded leaching of Mn from ridge soils at SSHCZO (Herndon *et al.*, 2011). In comparison, we calculate Mn leaching in the absence of vegetation using $k_{j,eff}$ values derived from non-vegetated mesocosms and find that $\bar{F}_{Mn,eff} = 4.2 - 5.5 \times 10^{-2} \text{ mol m}^{-2} \text{ y}^{-1}$ – i.e., fluxes would be much higher than the measured values at SSHCZO.

Furthermore, we can estimate uptake rates into foliage for ridgetop soils ($\bar{F}_{Mn,fol}$, mol m⁻² y⁻¹) using $\bar{M}_{Mn,j}$ and derived rate constants for uptake ($k_{j,fol}$):

$$\bar{F}_{Mn,fol} = k_{s,fol}\bar{M}_{Mn,s} + k_{aq,fol}\bar{M}_{Mn,aq} + k_{ox,fol}\bar{M}_{Mn,ox} + k_{org,fol}\bar{m}_{org} \quad (14)$$

We estimate $\bar{F}_{Mn,fol} = -3.7 - 4.8 \times 10^{-2}$ mol m⁻² y⁻¹, with 4.6×10^{-2} mol m⁻² y⁻¹ (95%) from the shale-derived soil, 2.2×10^{-3} mol m⁻² y⁻¹ from the Mn-oxides (4.5%), 1.2×10^{-5} mol m⁻² y⁻¹ (< 0.001%) from aqueous inputs, and inhibition between 0 - 8.4×10^{-2} mol m⁻² y⁻¹ from the organic matter. An estimate of uptake based on field measurements (= 1.5×10^{-2} mol m⁻² y⁻¹; Herndon and Brantley, 2011) is again within the predicted range for $\bar{F}_{Mn,fol}$; however, inclusion of the organic horizon in $\bar{F}_{Mn,fol}$ calculations results in unrealistic implications, i.e. that there is negative uptake of Mn into vegetation when organic horizon thickness > 2.8 cm. Furthermore, as discussed previously, adsorption of Mn to organic matter is a short-term effect that was likely amplified in the mesocosm experiments, and organic matter can become a Mn source with organic matter degradation.

While it is interesting to compare meso- and field-scale systems, this comparison does not take into account three potentially large factors: species variation, seasonality, and tree size (i.e. seedlings versus mature trees). Nonetheless, our approach has yielded first-order rate constants that are useful in quantifying the Mn cycling in the CZO.

V. Conclusions

In our mesocosm experiments, the ratio of Mn uptake into vegetation to leaching as effluent was observed to exceed that of other major nutrients. The weathering and transport of rock-derived elements such as Ca, Mg, K, and P are extensively studied due to their importance in biological systems and role in climate regulation; however, as the role of trace metals in major element cycling is increasingly studied, the importance of these metals is starting to be understood. Here, we highlight the dominant role of vegetation in the environmental behavior of Mn, a geochemical and biologically important trace metal.

In mesocosms and in a field study, we have presented evidence that vegetation increases the mobilization of Mn out of soil components. Mn was taken up into vegetation (here, into leaves), and this effect decreased the mass fluxes of Mn in the leaching effluent. Thus, in industrialized areas such as the Ohio-Pennsylvania-West Virginia corridor in the U.S.A. where Mn has been emitted to the atmosphere since the late 1700s and deposited into watersheds, we infer that Mn has been stored in soil + organic matter + vegetation, slowing the release of Mn into soil pore waters

and into rivers. In previous work, we noted a 5-10 year lag time between the peak in atmospheric Mn concentrations and the peak of riverine Mn concentrations in Pennsylvania (Herndon and Brantley, 2011). We proposed that this lag time was due to uptake and storage of Mn by vegetation. In this study, we observed a lag time in Mn release from vegetated soils relative to non-vegetated soils. Specifically, in pots receiving aqueous Mn additions, no time lag was observed between the start of Mn inputs and an increase in Mn outputs for non-vegetated soils, but a lag of about ~30-60 days was observed for vegetated soils.

In these experiments, both the presence of vegetation and the Mn source strongly influenced the half-life of Mn. In the vegetated systems, both oxide Mn and aqueous Mn were leached more rapidly than the Mn from the shale-derived soil. Since industrial inputs into soils have been observed or inferred to be in the form of Mn-oxide particles or Mn solutes (Lindberg and Harriss, 1983; U.S. Environmental Protection Agency, 1984; U.S. Environmental Protection Agency, 1985; Williams *et al.*, 1988), we conclude that Mn contamination persists in the soils for much shorter time durations than the Mn in the primary minerals is retained in the native soil. Over the month-long timescales of our mesocosm experiments, organic matter was found to inhibit leaching of Mn from the soil, most likely because of adsorption of soluble Mn onto the solid-phase organics. Alternatively, the hydrophobic effect of organic matter may change water infiltration to become less homogeneous through a soil (Lin & Zhou, 2008). Although degradation of organic matter will ultimately release sorbed Mn; organic matter may serve to buffer Mn releases from the soil.

VI. Acknowledgements

This study was supported by an NSF grant to SLB (EAR #1052614) and by NSF grant EAR #0725019 for the Susquehanna Shale Hills CZO, and by the NSF Center for Environmental Kinetics Analysis grant (NSF CHE #0431328). We especially thank associates at the University of Sheffield (Jonathan Leake, Steve Banwart, and Megan Andrews) and Penn State (David Eissenstat) for helpful discussion and implementation of the mesocosm system. Assistance in greenhouse setup and maintenance from M. Luke McCormack, Scott DiLoreto, Nina Bingham, and Maggie Davis is gratefully acknowledged. We thank Henry Gong for ICP-AES analysis and Melanie Saffer for use of laboratory facilities in Penn State's Laboratory for Isotopes and Metals in the Environment.

VII. References

- Amiotte-Suchet P., Probst J. and Ludwig W. (2003) Worldwide distribution of continental rock lithology: Implications for the atmospheric/soil CO₂ uptake by continental weathering and alkalinity river transport to the. *Global Biogeochem. Cycles* **17**, 13 PP.
- Andrews M. Y., Leake J. R., Palmer B. G., Banwart S. A. and Beerling D. J. (2011) Plant and mycorrhizal driven silicate weathering: Quantifying carbon flux and mineral weathering processes at the laboratory mesocosm scale. *Applied Geochemistry* **26**, S314–316.
- Balogh-Brunstad Z., Keller C. K., Bormann B. T., O'Brien R., Wang D. and Hawley G. (2008) Chemical weathering and chemical denudation dynamics through ecosystem development and disturbance. *Global Biogeochemical Cycles* **22**, 1–11.
- Bergkvist B. and Folkesson L. (1995) The Influence of Tree Species on Acid Deposition , Proton Budgets and Element Fluxes in South Swedish Forest. *Ecological Bulletins* **44**, 90–99.
- Berner E., Berner R. and Moulton K. (2003) Plants and mineral weathering: present and past. *Treatise on geochemistry* **5**, 169–188.
- Bormann B. T., Wang D., Bormann F. H., Benoit G., Snyder M. C., April R. and Michael C. (1998) Rapid , plant-induced weathering in an aggrading experimental ecosystem. *Biogeochemistry* **43**, 129–155.
- Brantley S. L., Kubicki J. and White A. (2008) *Kinetics of Water-Rock Interaction*. First. ed. Springer, New York.
- Chaney R. L., Malik M., Li Y. M., Brown S. L., Brewer E. P., Angle J. S. and Baker a J. (1997) Phytoremediation of soil metals. *Current opinion in biotechnology* **8**, 279–84.
- Chiswell B. and Mokhtar M. B. (1986) The speciation of manganese in freshwaters. *Talanta* **33**, 669–677.
- Diem D. and Stumm W. (1984) Is dissolved Mn(II) being oxidized by O₂ in absence of Mn-bacteria or surface catalysts? *Geochimica et Cosmochimica Acta* **48**, 1571–1573.
- Drever J.I. and Stillings L. L. (1997) The role of organic acids in mineral weathering. *Colloids and Surfaces A: Physicochemical and Engineering Aspects* **120**, 167–181.
- Drever James I. (1994) The effect of land plants on weathering rates of silicate minerals. *Geochimica et Cosmochimica Acta* **58**, 2325–2332.
- Golden D. C., Chen C. C. and Dixon J. B. (1986) Synthesis of todorokite. *Science* **231**, 717–9.
- Herndon E. M. and Brantley S. L. (2011) Movement of manganese contamination through the Critical Zone. *Applied Geochemistry* **26**, S40–S43.
- Herndon E. M., Jin L. and Brantley S. L. (2011) Soils reveal widespread manganese enrichment from industrial inputs. *Environmental science & technology* **45**, 241–7.
- Horiguchi T. (1987) Mechanism of manganese toxicity and tolerance of plants. *Soil Science and Plant Nutrition* **33**, 595–606.
- Horsley S. B., Long R. P., Bailey S. W., Hallett R. A. and Hall T. J. (2000) Factors associated with the decline disease of sugar maple on the Allegheny Plateau. *Canadian Journal of Forest Research* **30**, 1365–1378.
- Houle D., Tremblay S. and Ouimet R. (2007) Foliar and wood chemistry of sugar maple along a gradient of soil acidity and stand health. *Plant and Soil* **300**, 173–183.
- Jin L., Ravella R., Ketchum B., Bierman P. R., Heaney P., White T. and Brantley S. L. (2010) Mineral weathering and elemental transport during hillslope evolution at the Susquehanna/Shale Hills Critical Zone Observatory. *Geochimica et Cosmochimica Acta* **74**, 3669–3691.
- Jobbagy E. G. and Jackson R. B. (2001) The distribution of soil nutrients with depth : Global patterns and the imprint of plants. *Biogeochemistry* **53**, 51–77.

- Johnson N. M., Likens G. E., Bormann F. H., Fisher D. W. and Pierce R. S. (1969) A Working Model the Variation in Stream Water Chemistry at the Hubbard Brook Experimental Forest, New Hampshire. *Water Resources Research* **5**, 1353–1363.
- Junta J. L. and Hochella M. F. (1994) Manganese (II) oxidation at mineral surfaces: A microscopic and spectroscopic study. *Geochimica et Cosmochimica Acta* **58**, 4985–4999.
- Kabata-Pendias A. and Pendias H. (2001) *Trace elements in soils and plants*. 3rd ed., CRC Press LLC, Boca Raton.
- Kogelmann W. J. and Sharpe W. E. (2006) Soil acidity and manganese in declining and nondeclining sugar maple stands in Pennsylvania. *Journal of environmental quality* **35**, 433–41.
- Landre A. L., Watmough S. A. and Dillon P. J. (2010) Metal Pools, Fluxes, and Budgets in an Acidified Forested Catchment on the Precambrian Shield, Central Ontario, Canada. *Water, Air, & Soil Pollution* **209**, 209–228.
- Learman D. R., Voelker B. M., Vazquez-Rodriguez a. I. and Hansel C. M. (2011) Formation of manganese oxides by bacterially generated superoxide. *Nature Geoscience* **4**, 95–98.
- Learman D. R., Wankel S. D., Webb S.M., Martinez N., Madden a. S. and Hansel C.M. (2011) Coupled biotic–abiotic Mn(II) oxidation pathway mediates the formation and structural evolution of biogenic Mn oxides. *Geochimica et Cosmochimica Acta* **75**, 6048–6063.
- Li J., Richter D., Mendoza A. and Heine P. (2008) Four-decade responses of soil trace elements to an aggrading old-field forest: B, Mn, Zn, Cu, and Fe. *Ecology* **89**, 2911–2923.
- Liermann L. J., Mathur R., Wasylenki L. E., Nuester J., Anbar A. D. and Brantley S. L. (2011) Extent and isotopic composition of Fe and Mo release from two Pennsylvania shales in the presence of organic ligands and bacteria. *Chemical Geology* **281**, 167–180.
- Likens G. E., Bormann F. H., Johnson N. M., Fisher D. W. and Pierce R. S. (1970) Effects of Forest Cutting and Herbicide Treatment on Nutrient Budgets in the Hubbard Brook Watershed-Ecosystem. *Ecological Monographs* **40**, 23–47.
- Lin H. (2006) Temporal stability of soil moisture spatial pattern and subsurface preferential flow pathways in the Shale Hills catchment. *Vadose Zone Journal* **5**, 317–340.
- Lindberg S. E. and Harriss R. C. (1983) Water and acid soluble trace metals in atmospheric particles. *Journal of Geophysical Research* **88**, 5091–5100.
- Miller O. (1998) High-Temperature Oxidation: Dry Ashing. In *Handbook and Reference Methods for Plant Analysis* (ed. Y. P. Kalra). CRC Press LLC, New York.
- Moulton K., West J. and Berner R. (2000) Solute flux and mineral mass balance approaches to the quantification of plant effects on silicate weathering. *American Journal of Science* **300**, 539–570.
- Navrátil T., Shanley J. B., Skřivan P., Krám P., Mihaljevič M. and Drahota P. (2007) Manganese Biogeochemistry in a Central Czech Republic Catchment. *Water, Air, and Soil Pollution* **186**, 149–165.
- Neaman A., Chorover J. O. N. and Brantley S. L. (2005) Implications of the evolution of organic acid moieties for basalt weathering over geologic time. *American Journal of Science* **305**, 147–185.
- Nriagu J. and Pacyna J. (1988) Quantitative assessment of worldwide contamination of air, water and soils by trace metals. *Nature* **333**, 134–139.
- Pacyna J.M. and Pacyna E. G. (2001) An assessment of global and regional emissions of trace metals to the atmosphere from anthropogenic sources worldwide. *Environmental Reviews* **9**, 269–298.
- Post J. E. (1999) Manganese oxide minerals: Crystal structures and economic and environmental significance. *Proceedings of the National Academy of Sciences* **96**, 3447–3454.
- Rauch J. N. and Pacyna Jozef M. (2009) Earth's global Ag, Al, Cr, Cu, Fe, Ni, Pb, and Zn cycles. *Global Biogeochemical Cycles* **23**, GB2001.

- Saal L. B. and Duckworth O. W. (2010) Synergistic Dissolution of Manganese Oxides as Promoted by Siderophores and Small Organic Acids. *Soil Science Society of America Journal* **74**, 2021.
- Santelli C. M., Webb Samuel M., Dohnalkova A. C. and Hansel Colleen M. (2011) Diversity of Mn oxides produced by Mn(II)-oxidizing fungi. *Geochimica et Cosmochimica Acta* **75**, 2762–2776.
- Shanley J. B. (1986) Manganese biogeochemistry in a small Adirondack forested lake watershed. *Water Resources Research* **22**, 1647.
- St Clair S. B. and Lynch J. P. (2005) Element accumulation patterns of deciduous and evergreen tree seedlings on acid soils: implications for sensitivity to manganese toxicity. *Tree physiology* **25**, 85–92.
- Taylor L. L., Leake J. R., Quirk J., Hardy K., Banwart S. and Beerling D. (2009) Biological weathering and the long-term carbon cycle: integrating mycorrhizal evolution and function into the current paradigm. *Geobiology* **7**, 171–91.
- Tebo B. M., Bargar J. R., Clement B. G., Dick G. J., Murray K. J., Parker D., Verity R. and Webb Samuel M. (2004) Biogenic manganese oxides: Properties and mechanisms of formation. *Annual Review of Earth and Planetary Sciences* **32**, 287–328.
- Turekian K. K. and Wedepohl K. H. (1961) Distribution of the Elements in Some Major Units of the Earth's Crust. *Geological Society of America Bulletin* **72**, 175–192.
- U.S. Environmental Protection Agency (1984) *Health Assessment Document for Manganese.*, Cincinnati, Ohio. EPA 600/8-83-013F.
- U.S. Environmental Protection Agency (1985) *Locating And Estimating Air Emissions From Sources Of Manganese.* EPA-450/4-84-007h.
- Watmough S. A., Eimers M. C. and Dillon P. J. (2007) Manganese cycling in central Ontario forests: Response to soil acidification. *Applied Geochemistry* **22**, 1241–1247.
- White P. J. (2012) Long-distance Transport in the Xylem and Phloem. In *Marschner's Mineral Nutrition of Higher Plants* Elsevier Ltd. pp. 49–70.
- Williams P. T., Radojevic M. and Clarke A. G. (1988) Dissolution of trace metals from particles of industrial origin and its influence on the composition of rainwater. *Atmospheric Environment* **22**, 1433–1442.
- Wissemeier A. H. and Horst W. J. (1987) Callose deposition in leaves of cowpea (*Vigna unguiculata* [L.] Walp .) as a sensitive reponse to high Mn supply. *Plant and Soil* **102**, 283–286.
- Zhang L., Dawes W. R. and Walker G. R. (2001) Response of mean annual evapotranspiration to vegetation changes at catchment scale. *Water Resources Research* **37**, 701–708.

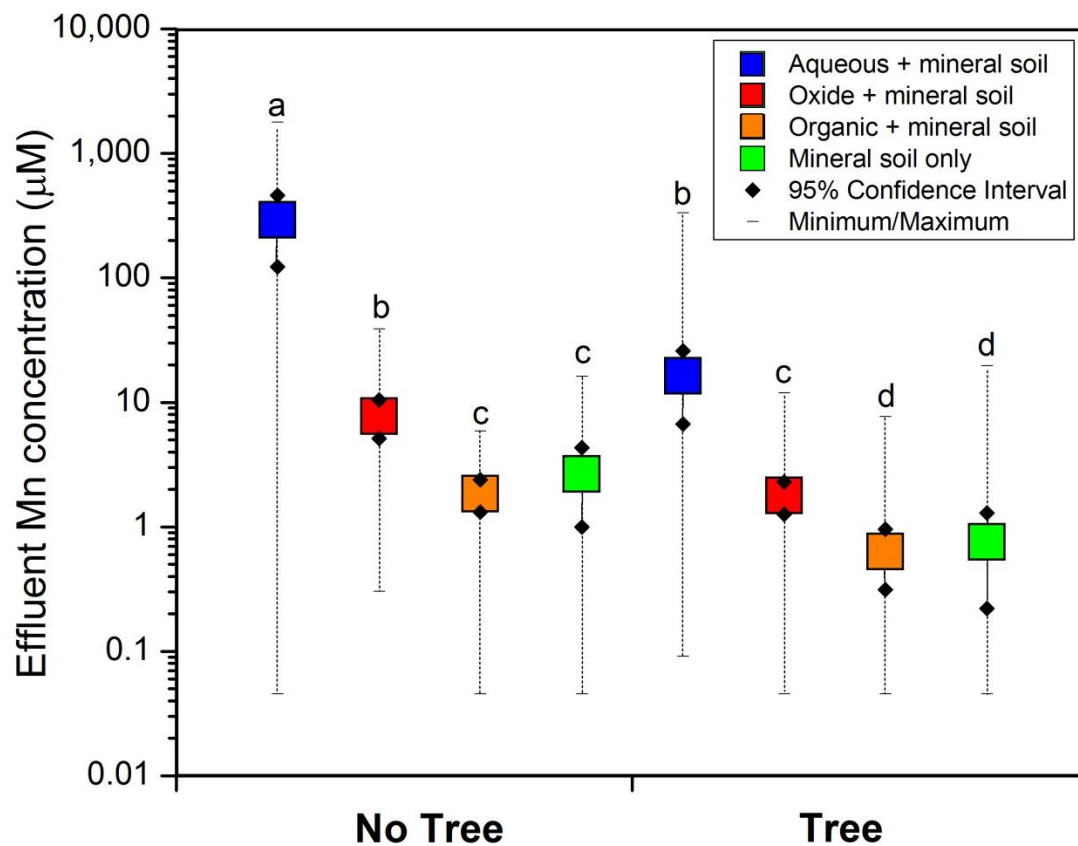


Figure 3-1. The ranges of Mn concentrations in effluent ($C_{Mn,eff}$, μM) are shown on a log-scale for vegetated and non-vegetated pots containing mineral soil only, or containing soil and receiving aqueous, oxide, or organic amendments. For all pots, we excluded data for effluent collected prior to Mn addition. Each box gives the mean $C_{Mn,eff}$ for each treatment, with black diamonds indicating the 95% confidence intervals about the mean, and dashed lines designating the range of measured $C_{Mn,eff}$ values. Letters designate treatments with statistically equivalent ($p > 0.05$ for same letter) or different ($p < 0.05$ for different letters) mean $C_{Mn,eff}$ values.

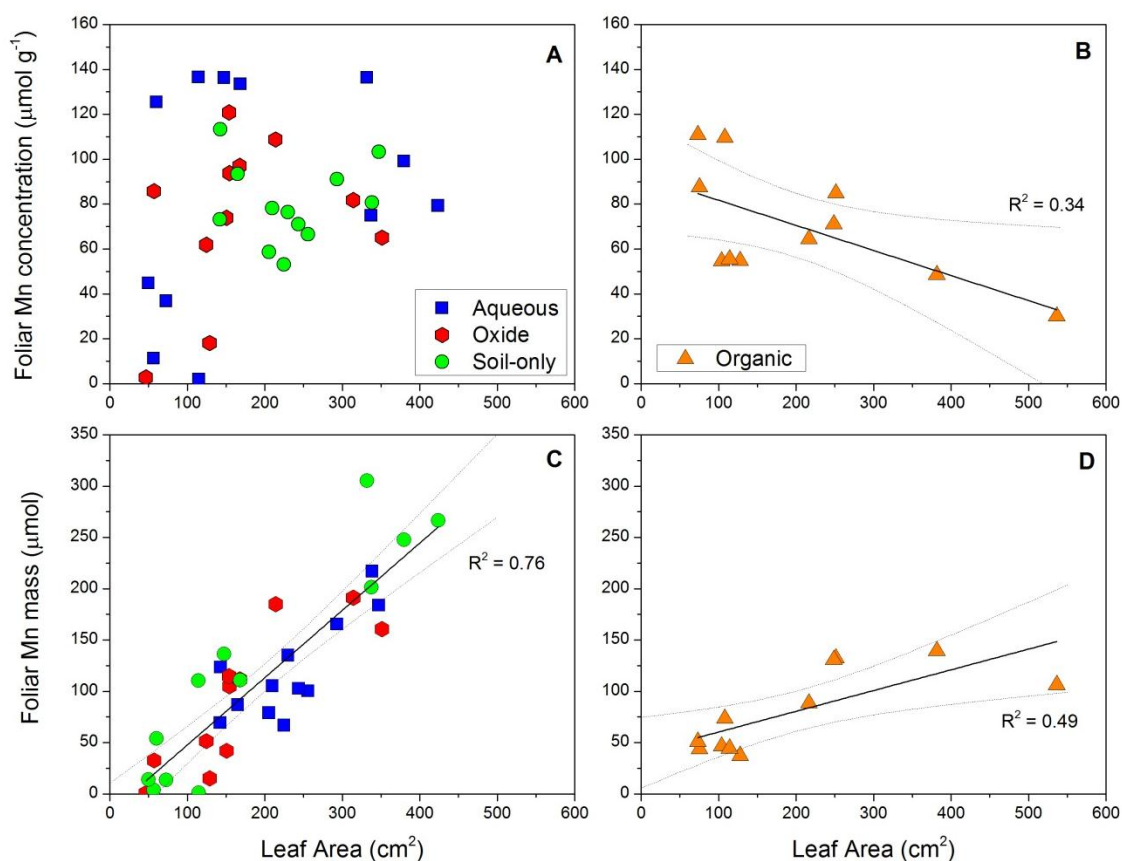


Figure 3-2. Foliar Mn concentration ($C_{Mn,fol}$) and foliar Mn mass ($m_{Mn,fol}$) plotted versus leaf area for seedlings grown in soil-only pots (green symbols) or pots with aqueous (blue symbols), oxide (red symbols), or organic (orange symbols) additions. No significant correlation between $C_{Mn,fol}$ and leaf size is observed in the aqueous, oxide, and soil-only pots (A), resulting in a linear increase in total Mn with increasing leaf area (best-fit slope = $0.66 \pm 0.06 \mu\text{mol cm}^{-2}$, $p < 0.001$) (C). However, in organic pots, foliar Mn concentrations decrease with increasing leaf area ($p < 0.05$) (B), resulting in only minor increases in $m_{Mn,fol}$ with increasing leaf size (best-fit slope = $0.20 \pm 0.06 \mu\text{mol cm}^{-2}$; $p < 0.01$) (D). Confidence intervals (95%) for each regression are plotted as dashed lines.

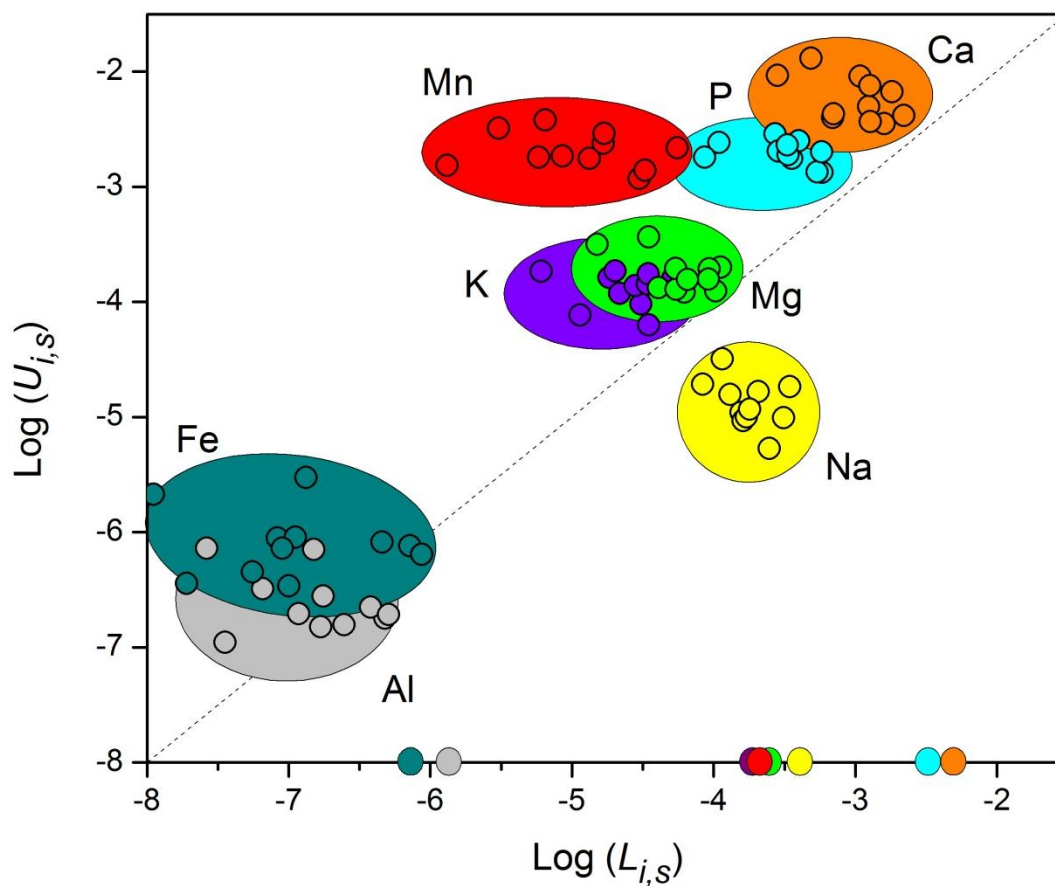


Figure 3-3. Fractional vegetative uptake ($U_{i,s}$) plotted versus fractional leaching ($L_{i,s}$) shown on a log-log plot for eight elements (Al, Ca, Fe, K, Mg, Mn, Na, P) as measured in soil-only pots, i.e., pots without Mn additions. $U_{i,s} > L_{i,s}$ for Mn, Ca, Fe, K, Mg and P, while $U_{i,s} < L_{i,s}$ for Na and $U_{i,s} = L_{i,s}$ for Al ($p < 0.05$). Fractional uptake of Mn is higher than all other nutrient elements. Individual replicates (pots) are shown by each point within colored circles that group each element. Average $L_{i,s}$ values for non-vegetated pots, plotted on the x-axis in corresponding colors, exceed $L_{i,s}$ averages for vegetated pots for all elements.

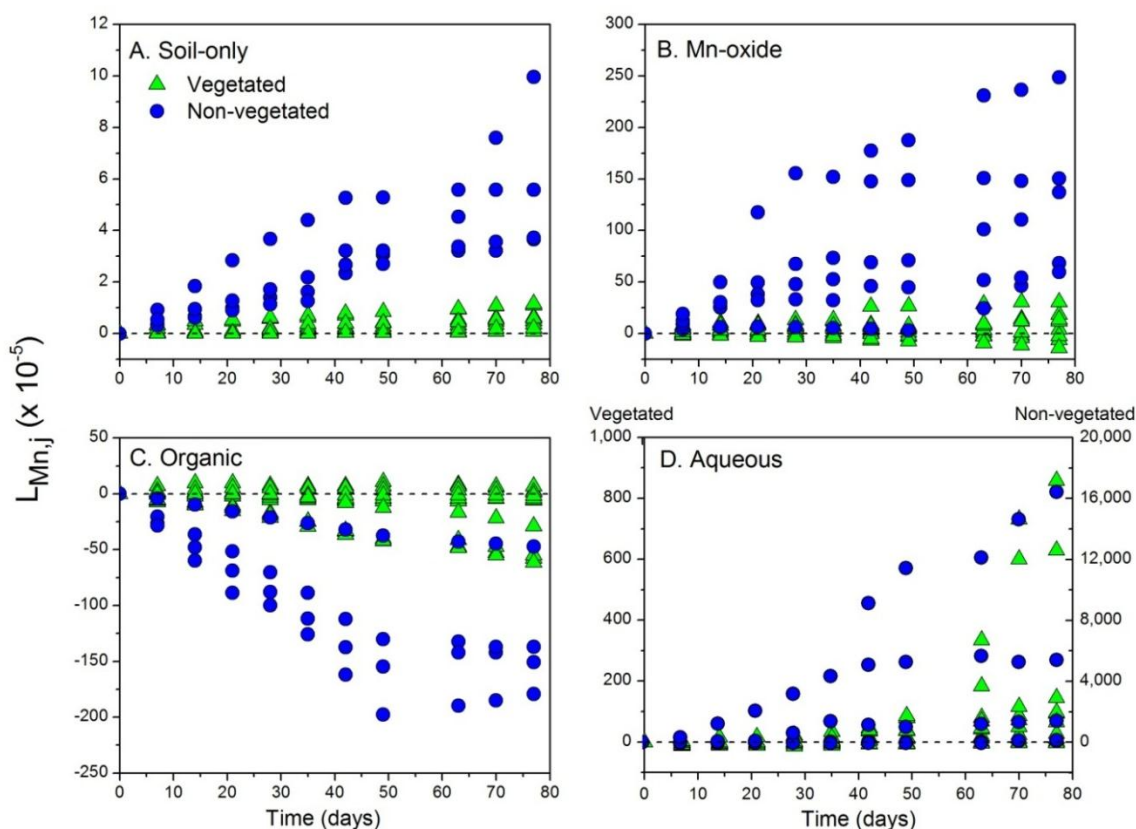


Figure 3-4. The cumulative fraction of Mn loss ($L_{Mn,j}$) from each soil component (j = mineral soil (s), Mn-oxide (ox), Mn-rich organic matter (org), or aqueous Mn (aq)) plotted versus time for vegetated (green triangles) and non-vegetated (blue circles) pots. Note that the axes differ for the treatments because of the range of values observed: the range decreases in the order aqueous > Mn-oxide > soil-only > organic. In the aqueous treatments, non-vegetated pots released much more Mn ($L_{Mn,aq} \leq 0.20$) than vegetated pots (≤ 0.010): note that non-vegetated values are plotted on a second axis for the panel for aqueous Mn pots. In one soil-only pot that is not plotted, a step increase in cumulative Mn loss resulted from a single sample of effluent collection that exhibited an anomalously high Mn concentration.

Table 3-1. Summary of variables used in the mass balance model for mesocosm experiments

Variable	Units	Description
$C_{i,j}$	$\mu\text{mol g}^{-1}$	Concentration of i in reservoir j
$C_{i,fol}$	$\mu\text{mol g}^{-1}$	Concentration of i in foliage
$C_{i,eff}$	$\mu\text{mol mL}^{-1}$	Concentration of i in effluent
$\hat{C}_{i,eff}$	$\mu\text{mol mL}^{-1}$	Average concentration of i in effluent for $j = s$
$\hat{C}_{i,fol}$	$\mu\text{mol mL}^{-1}$	Average concentration of i in foliage for $j = s$
m_j	grams	Mass of reservoir j
m_{fol}	grams	Mass of foliage at harvest
$m_{i,fol}$	moles	Mass of i in foliage
m_{aq}	moles	Mass of Mn in one aqueous addition
V	liter	Volume of effluent collected for one week
$M_{i,j}$	moles	Mass of i in reservoir j
$b_{i,j}$	moles	Cumulative mass of i leached from j over time period t
$L_{i,j}$	unitless	Fraction of i transferred from j into effluent
$U_{i,j}$	unitless	Fraction of i transferred from j into foliage
$F_{j,k}$	mol y^{-1}	Rate of mass transfer from reservoir j to k
$k_{j,k}$	y^{-1}	Rate constant for mass transfer from reservoir j to k
$t_{i,j}^{1/2}$	years	Half-life of constituent i in reservoir j
φ	liter^{-1}	Fraction of Mn leached from $j = s$ per volume effluent
$\bar{F}_{j,k}$	$\text{mol m}^{-2} \text{y}^{-1}$	Area-normalized rate of mass transfer from j to k
$\bar{M}_{i,j}$	mol m^{-2}	Area-normalized mass of i in reservoir j
\bar{m}_j	kg m^{-2}	Area-normalized mass of reservoir j
<i>subscript i</i>		Element of interest
<i>subscript j</i>		Source reservoir: $j = s, aq, ox, \text{ or } org$
<i>subscript k</i>		Sink reservoir: $k = eff \text{ or } fol$

Reservoirs are noted with subscripts $s = \text{soil}$, $aq = \text{aqueous}$, $ox = \text{oxide}$, $org = \text{organic}$, $eff = \text{effluent}$, and $fol = \text{foliage}$.

Table 3-2. Soil-only pots: Fractional uptake ($U_{i,s}$) and leaching ($L_{i,s}$) x 10^{-5}

	Ca	K	Mg	P
$L_{i,s}$, veg.	120	2.6	6.6	35
<i>Standard Error</i>	± 18	± 0.4	± 0.9	± 5.1
$U_{i,s}$, veg.	620	13	19	200
<i>Standard Error</i>	± 87	± 1.2	± 2.3	± 13
$L_{i,s} + U_{i,s}$, veg.	760	16	26	240
<i>Standard Error</i>	± 85	± 1.3	± 2.2	± 13
$L_{i,s}$, non-veg.	520	20	24	630
<i>Standard Error</i>	± 130	± 4.0	± 6.4	± 330
	Mn	Al	Fe	Na
$L_{i,s}$, veg.	1.7	0.021	0.024	19
<i>Standard Error</i>	± 0.5	± 0.005	± 0.009	± 2.4
$U_{i,s}$, veg.	210	0.028	0.096	1.5
<i>Standard Error</i>	± 24	± 0.006	± 0.023	± 0.2
$L_{i,s} + U_{i,s}$, veg.	220	0.051	0.12	21
<i>Standard Error</i>	± 25	± 0.007	± 0.03	± 2.4
$L_{i,s}$, non-veg.	49	0.17	0.16	45
<i>Standard Error</i>	± 38	± 0.08	± 0.11	± 12

Table 3-3. Average concentrations, fluxes, rate constants, and half-lives (\pm standard error)

	Soil-only	Aqueous	Mn-Oxide	Organic
Vegetated Pots				
Average $C_{Mn,eff}$ (μM)	0.76 ± 0.27	16 ± 5	1.8 ± 0.3	0.63 ± 0.16
$F_{j,eff}$ ($\times 10^{-5}$ mol y^{-1})	0.14 ± 0.02	6.1 ± 1.3	0.18 ± 0.09	-0.19 ± 0.04
$k_{j,eff}$ ($\times 10^{-5}$ y^{-1})	2.7 ± 0.4	796 ± 164	22 ± 12	-0.010 ± 0.002^a
$t_{Mn,j}^{1/2}$ (years)	$25,700 \pm 9,960$	87 ± 39	$3,120 \pm 2,290$	
<hr/>				
$C_{Mn,fol}$ ($\mu\text{mol g}^{-1}$)	79.9 ± 5.1	84.7 ± 14.7	73.6 ± 10.4	70.2 ± 7.4
$F_{j,fol}$ ($\times 10^{-5}$ mol y^{-1})	34.3 ± 4.0	5.8 ± 4.2	0.37 ± 2.7	-8.0 ± 4.9
$k_{j,fol}$ ($\times 10^{-5}$ y^{-1})	602 ± 69	720 ± 530	26 ± 340	-0.40 ± 0.24^a
<hr/>				
Non-vegetated Pots				
$C_{Mn,eff}$ (μM)	2.7 ± 0.8	290 ± 83	7.8 ± 1.3	1.9 ± 0.3
$F_{j,eff}$ (mol y^{-1})	0.94 ± 0.19	180 ± 45	4.0 ± 0.6	-1.3 ± 0.2
$k_{j,eff}$ ($\times 10^{-5}$ y^{-1})	26 ± 3	$25,400 \pm 7,010$	620 ± 110	-0.064 ± 0.010^a
$t_{Mn,j}^{1/2}$ (years)	$2,700 \pm 870$	2.7 ± 1.4	110 ± 47	

^a $k_{org,k}$ values reported in mol g^{-1} y^{-1} (Eqn.8)

Chapter 4

Spectroscopic characterization of Mn in the soil-plant system

Abstract

Soils at the Susquehanna Shale Hills Critical Zone Observatory (SSHCZO) in central Pennsylvania, USA are enriched in manganese due to past atmospheric deposition from industrial sources. Vegetation takes up and stores large quantities of Mn from the soil, slowing the removal of Mn from soils into river systems. Here, we use synchrotron source spectroscopy techniques – X-ray absorption near edge structure (XANES) and X-ray fluorescence (XRF) – to investigate the spatial distribution and chemical speciation of Mn in soil and vegetation within the Shale Hills system. We find that roots, stems, and foliar tissue are dominated by organic and aqueous Mn^{2+} complexes. In contrast, dark spots on leaves, an indicator of Mn toxicity, are Mn-rich relative to the surrounding leaf tissue and are dominated by a compound that is most consistent with a Mn^{3+} -organic complex. Soils at all depths contain predominantly $\text{Mn}^{3+/4+}$ -oxides similar to birnessite, and we observe discrete Mn-rich regions on soil grains that we infer to be Mn-oxide coatings or particles. The Mn that is stored in vegetation is oxidized and immobilized as mixed-valence Mn-oxides in the soil during decomposition. We propose that significant uptake of Mn by certain tree species as well as Mn oxidation in the soil to form relatively immobile species both contribute to long-term retention in ecosystems impacted by Mn contamination.

I. Introduction

1.1. Manganese

Manganese is an essential element to terrestrial ecosystems. Although considered a trace element, it is generally present at concentrations of 350 to 2,000 ppm in soils and in a nutritionally sufficient range of 30 – 300 ppm in leaf tissue (Kabata-Pendias and Pendias, 2001), making it one of the most abundant trace metals in soils and plants. Mn is a highly reactive component of soils and plays a central role in contaminant transport, redox reactions, and the breakdown of soil organic matter (Suarez & Langmuir, 1976; Hofrichter, 2002; Berg *et al.*, 2007). Anthropogenic endeavors such as steel production and coal combustion have led to the enrichment of Mn in soils, water, and biota throughout the globe (Nriagu & Pacyna, 1988; Pacyna & Pacyna, 2001; Herndon *et al.*, 2011). Here, we shed light on the biogeochemical processes that impact Mn contamination in a terrestrial ecosystem in order to understand potential environmental impacts.

In the environment, Mn occurs in three oxidation states (+2, +3, and +4) as either the aqueous ion Mn^{2+} , as organic chelates of Mn^{2+} or Mn^{3+} , or in the solid-phase as Mn^{2+} , Mn^{3+} , and Mn^{4+} . In soils and sediments, Mn minerals are dominated by phylломanganate (e.g. birnessite, lithiophorite, buserite) and tectomanganate (e.g. todorokite, ramsdellite, pyrolusite) oxides (Manceau *et al.*, 1992a; Post, 1999). Phylломanganates are characterized by sheets of edge-sharing Mn(III/IV)O_6 octahedra, while tectomanganates have edge- or corner-sharing MnO_6 octahedra arranged in tunnel structures. Characterization of Mn minerals is often complicated by the nature of the reactive, poorly-crystalline Mn minerals; however, significant advances in synchrotron-source techniques, including X-ray Absorption Near Edge Structure (XANES), Extended X-ray Absorption Fine Structure (EXAFS), and X-Ray Diffraction (XRD) have been used to provide significant insight into Mn-oxide formation, structures, and interactions with heavy metal contaminants (Manceau *et al.*, 1992a; Manceau *et al.*, 1992b; Post, 1999; McKeown & Post, 2001; Stueben *et al.*, 2004; Saratovsky *et al.*, 2006).

1.2. Biogenic manganese oxides

Mn oxidation and reduction processes are well known to occur via microbial reactions. At low pH, the kinetics of Mn^{2+} oxidation are slow, and bacteria catalyze the process in a one-electron step oxidation that leads to the formation of Mn^{3+} -ligand complexes and a δMnO_2 -like phylломanganate (Bargar *et al.*, 2005; Webb *et al.*, 2005). Two mechanisms have been proposed for this reaction. In the first, a multicopper oxidase-like enzyme directly catalyzes both oxidation steps (Webb *et al.*, 2005). XANES investigation of *in situ* bio-oxidation was able to detect the presence of the Mn^{+2} substrate, the birnessite product, and the organically-complexed Mn^{+3} intermediate (Webb *et al.*, 2005). In the second proposed mechanism, bacterial proteins produce extracellular superoxides that initiate oxidation of aqueous Mn^{2+} , a process that proceeds more quickly in the presence of light and organic matter (Learman *et al.*, 2011a). The initial product of the reaction, hexagonal birnessite, acts as a catalyst for abiotic Mn oxidation until transitioning to a less reactive, triclinic birnessite phase.

Mn oxidation by fungi is also prevalent in terrestrial systems (Schulze *et al.*, 1995; Miyata *et al.*, 2006; Santelli *et al.*, 2011). Many fungal species produce a manganese peroxidase enzyme that oxidizes Mn^{2+} to form a highly-reactive, chelated Mn^{3+} compound that mediates redox reactions to break down phenolic lignin structures (Hofrichter, 2002). However, this process is catalytic and results in regeneration of aqueous Mn^{2+} . A variety of fungal species are able to oxidize Mn^{2+} to a nanoparticulate, hexagonal birnessite phase (Santelli *et al.*, 2011), similar to that previously characterized as a product of bacterial Mn oxidation (Bargar *et al.*, 2005; Webb *et al.*, 2005;

Learman et al., 2011a). The conversion of hexagonal birnessite to more ordered structures (e.g. todorokite, triclinic birnessite) also depends on fungal species, and significant variability in both the spatial distribution of Mn-oxides relative to fungal hyphae and in Mn-oxide morphology suggests natural variability in Mn-oxidation pathways (Santelli et al., 2011), including direct enzymatic oxidation (Webb et al., 2005; Miyata et al., 2006) or indirect oxidation by superoxide (Learman et al., 2011b).

1.3. Mn in vegetation

Mn is a plant micronutrient that is primarily used to split water in the oxygen-evolving complex (OEC) in Photosystem II and to serve as a cofactor in superoxide dismutase (SOD) (Broadley et al., 2012). The OEC functions to produce oxygen while SOD protects plant tissue from oxygen radical byproducts. While only a few enzymes require Mn as a cofactor, Mn can substitute for other cations and act as a cofactor for ~35 enzymes, facilitating redox reactions, decarboxylation, and lignin biosynthesis.

Plants take up Mn from soil pore waters as dissolved Mn^{2+} . The Mn^{+2} ion is stable in solution at low pH; thus, Mn is highly bioavailable in acid soils (pH < 5.5) (Kabata-Pendias and Pendias, 2001). Mn^{+2} can enter root cells through carrier proteins that also facilitate the uptake of other divalent cations (e.g. Fe, Zn, Cu). In the root, Mn^{+2} competes with Mg^{+2} and Ca^{+2} for active transport into the xylem (Dou et al., 2009; White, 2012a). Mn is transported through the xylem and then enters leaf cells as Mn^{+2} or a Mn^{2+} -organic complex (e.g. citrate) (White, 2012b). In the supernatant fraction (which constitutes ~80% of the total Mn) of the bulk foliar tissue of a Mn-hyperaccumulator (*Phytolacca acinosa*), Mn was found to associate with oxalate in gel filtration, and Mn XANES spectra were 90% similar to Mn-oxalate with contributions (< 5%) from Mn-malate and aqueous Mn (Xu et al., 2009).

Due to the high mobility of Mn in the xylem but low mobility in the phloem, Mn is readily transported to leaf tissue via the transpiration stream and is not redistributed from leaves to other plant tissues. Despite a recognized immobility of Mn in the phloem, Mn concentration in phloem solution has been measured to exceed Mn concentration in xylem solution, potentially due to the build-up of immobile compounds (Hocking, 1980). Mn accumulates preferentially in sun relative to shade leaves and reaches maximum foliar concentration between mid-summer and just prior to senescence (McCain and Markley, 1989).

Mn toxicity typically occurs in soils with high levels of bioavailable Mn, particularly in soils with low pH and base cation depletion (Horsley et al., 2000; Kogelmann & Sharpe, 2006). Excess Mn can induce deficiency of Ca, Mg, Fe and Zn and lead to interveinal necrosis on leaves

(Broadley et al., 2012). The range of Mn concentrations deemed toxic in plant tissue varies widely among species, which suggests that Mn uptake is not well buffered at the roots, and leaves must possess mechanisms to combat excess Mn (Römheld, 2012). Plants have developed varied strategies to deal with excess Mn, including exclusion or oxidation at the roots, increased uptake of Si, deposition of oxidized Mn in leaves, and sequestration in vacuoles or cell walls throughout the plant (Horst & Marschner, 1978; Horiguchi, 1987; McCain & Markley, 1989; Peiter et al., 2007). Excess Mn in the leaf tissue is thought to result in oxidative stress, and studies on bean plants have shown increased expression of antioxidant enzymes such as superoxide dismutase (SOD) and peroxidase (POD) in response to increasing Mn levels (Gonzalez & Lynch, 1999; St. Clair et al., 2005). Peroxidase can oxidize Mn^{+2} in the presence of H_2O_2 and may contribute to the formation of black spots on foliage, which are in turn primary indicators of Mn toxicity that contain oxidized Mn and polyphenols (Horiguchi, 1987).

The distribution of excess Mn in plant tissue depends on the mechanisms of Mn tolerance in different plants. In many plant species, Mn accumulates at the bases of trichomes (Blamey et al., 1986; Broadhurst et al., 2009; Horiguchi, 1987; McNear et al., 2005). A XANES spectrum from a trichome base was identified as being most consistent with Mn(II) rather than the oxidized Mn(IV) (Broadhurst et al., 2009). In both Norway spruce and sugar maple, Mn localizes in vacuoles and the thylakoid membrane of chloroplasts (McCain and Markley, 1989; McQuattie and Schier, 2000). Additionally, elevated Mn exposure in sugar maples results in the accumulation of phenolic compounds in roots and in palisade and epidermal cells in leaves (McQuattie and Schier, 2000). Oxidized Mn deposits have also been observed on root surfaces, either in the presence or absence of mycorrhizal fungi (Horiguchi, 1987; Schulze et al., 1995).

Gonzalez and Lynch (1999) also observed significant enrichment of Mn in leaf vacuoles of Mn-sensitive and Mn-tolerant bean plants, with Mn-tolerant plants also showing Mn enrichment in the epidermis. In the vacuolar fraction, Mn was enriched in oxalate-like crystals. Distinct Ca-oxalate and Mn-oxalate crystals have also been observed in the leaves of the Mn-hyperaccumulator pokeweed (Dou et al., 2009). Mn crystals were morphologically distinct from the Ca-oxalate crystals, appearing as clusters on the surface of vacuolar membranes. These crystals also contained high levels of C, O, and P, suggesting a role for phosphate in Mn deposition.

Fernando et al. (2006a, 2006b, 2007, 2008a, 2008b) conducted numerous studies to establish the subcellular distribution of Mn in Mn accumulators and hyperaccumulators. Depending on species, Mn was found to accumulate in both photosynthetic and non-photosynthetic cells, and in vacuoles or dermal tissue. XANES spectroscopy was used to identify Mn^{2+} bound to carboxylate

moieties (e.g. malate, citrate) as the dominant form of Mn in bulk foliar tissue from all examined species (Fernando et al., 2010). Fernando et al. made no attempt to examine subcellular differences in Mn speciation in the various tissues exhibiting Mn enrichment.

In this study, we use XRF and XANES spectroscopy to investigate the distribution and chemical speciation of Mn in vegetation and soils. We integrate spectroscopic data with bulk chemistry observations in order to evaluate the biogeochemical processes impacting Mn transport through the SSHCZO watershed.

II. Methods

2.1. Sample collection and preparation

2.1.1. Soils

Soil samples were obtained from the Susquehanna Shale Hills CZO (Critical Zone Observatory) in fall 2008. One soil core (RT08) was augered from the ridge top of the south slope of the SSHCZO (RT08). The core was collected from 0-11 cm, 11-16 cm, and 16-22 cm depth in the soil, where 0 was defined as the top of the mineral soil. Point of refusal, defined as the depth in the soil at which we could no longer physically auger, was reached at 22 cm and is the best approximation for the soil-bedrock interface. Additionally, the organic horizon was collected by hand from the surface of the soil and included a mat of organic material that was pulled away from the mineral soil surface but excluded leaf litter. An additional mineral soil sample was collected from a core augered in the valley floor directly downslope from the ridge core (VF08). This sample was collected at the soil-bedrock interface (62-66 cm). Soil samples were kept at field moisture conditions at 4°C until analysis.

2.1.2. Vegetation

Upper-canopy leaves and stems were sampled in June 2011 from two mature *Quercus prinus* trees and one mature *Acer saccharum* tree growing at the Shale Hills CZO. *Quercus* species represent >50% of all canopy tree species at SSHCZO while *Acer* species are less abundant (~7%) (Wubbels, 2010). Leaves and stems were obtained by climbing the trees and using a pole cutter to remove a section of the tree branch. Leaf samples from undergrowth seedlings and roots from the organic horizon were collected by hand from SSHCZO in early fall 2008. Additionally, leaf and root samples were obtained from red oak seedlings grown in two separate pot experiments in a greenhouse in 2010 and 2011 (see Chapter 3).

For bulk vegetation analysis, fresh leaves were ground in liquid nitrogen and stored as a powder. Foliage and root samples that were collected from SSHCZO in fall 2008 were also

allowed to decompose in closed vessels in the laboratory for six months before reanalysis with XANES spectroscopy. For XRF maps and μ XANES analysis, intact fresh leaves were vacuum-sealed using a FoodSaverTM vacuum-sealing system and frozen until transport to the beamline. Fresh roots and stems were sectioned with a box cutter, vacuum-sealed, and frozen.

Fine roots that were collected from red oak seedlings in the greenhouse experiment could not be sectioned fresh due to their size; therefore, we embedded these roots in LR White Hard Grade acrylic resin embedding medium (#14383; Electron Microscopy Sciences). Methods for embedding the roots were adapted from Tippkötter & Ritz (1996), Nunan et al., (2001), and Eickhorst & Tippkötter (2008). The fine roots were cut into small segments, placed in microcentrifuge tubes, and fixed with 3% paraformaldehyde in a pH 7.2 Na-phosphate buffer for 2 hours. Using a transfer pipet to exchange the solution in the microcentrifuge tubes, the roots were rinsed three times with the Na-phosphate buffer and dehydrated with cold ethanol in a series of 50% ethanol:water (15 min), 70% ethanol (15 min), 90% ethanol (10 min), and 100% ethanol (10 min). The roots were then incubated overnight in a mixture of 50% ethanol and 50% LR White embedding medium, then in 100% LR White for 2 hours. Finally, the roots were transferred into cavities filled with LR White in a flat embedding mold (#70905; Electron Microscopy Sciences). The embedding mold was filled with resin and wrapped in parafilm to exclude oxygen and cured in an oven at 65°C until the resin was fully polymerized (3-5 days). Once the resin cured, a box cutter was used to slice 1 mm thick sections of each sample to expose cross-sections of embedded roots.

2.2. Spectroscopy

XRF maps and Mn K-edge XANES were obtained at the Advanced Photon Source on beamline 20-BM in October 2008, March 2009, and August 2009 (XANES), 13-BM-D GSECARS in November 2010 and July 2011 (XRF/XANES) and 13-ID-C GSECARS in October 2011 (XRF/XANES). Beamline 20-BM operates with a bending magnet source, Si(111) monochromator, and unfocused beam (30 x 1 mm) with a flux of 1×10^{11} photons/s at 10 keV. Beamline 13-BM-D utilizes a bending magnet source with a 1×10^9 flux (photons/sec) at 10 keV, a Si(111) monochromator, and a Vortex ME-4 Silicon Drift Detector. An unfocused beam (50 x 4 mm) was used for ground bulk samples and a focused beam (10 x 30 μ m) was used for mapping and obtaining μ XANES spectra on regions of interest. Beamline 13-ID-C utilizes an undulator source with a flux of 1×10^{13} photons/sec for the unfocused beam (3 x 1 mm) and 1×10^{11} photons/sec for the focused beam (5 x 5 μ m) at 10 keV. Additional hardware included a Si(111) monochromator, a Vortex ME-4 Silicon Drift Detector, and Kirkpatrick-Baez mirrors for focusing.

Mineral standards were prepared by spreading thin layers of the powdered material on X-ray transparent Kapton tape and stacking squares of the tape to achieve transmissive samples with adequately high Mn counts. Ground soil and vegetation samples were packed into plastic sample holders and sealed with Kapton tape. Aqueous standards were pipetted into plastic sample holders and sealed with x-ray transparent tape. All samples were secured with tape to a sample mount in the beamline hatch.

Bulk minerals were run in transmission mode. A fluorescence detector was used for bulk samples with low Mn concentrations (e.g. bulk vegetation, bulk soil), samples that were not transmissive (e.g. leaves, buried wells, roots and stems), and for mapping. In the XRF maps, fluorescence counts for each element are averaged over the area of the pixel, and pixels with warm colors correspond to high fluorescence counts while pixels with cool colors correspond to low fluorescence counts. Here, we present only qualitative differences in fluorescence counts within each map due to differences in beam energies during collection of the maps.

For XANES spectra, data were collected between -100 and +200-500 eV around the zero-valent Mn K-edge ($E_0 = 6539$ eV). Multiple scans were collected for each sample, and no beam damage was observed during subsequent scans. At 13-ID-C, due to the risk for beam damage under the high intensity photon flux, vegetation samples were kept in a cold stage during data collection. XRF maps were collected at 10 keV with a focused beam and a step size of 5 μm (13-ID-C) or 25-40 μm (13-BM-D).

2.3. Data processing

Athena software was used to process XANES spectra (merging of replicate scans, energy calibration, background-removal, and normalization) and perform linear combination fits (Newville, 2001; Ravel and Newville, 2005). XRF maps were visualized using DataViewer (Newville, 2006).

For energy calibration, spectra were collected from a set of divalent (MnO), trivalent (Mn_2O_3), and tetravalent (MnO_2) Mn-oxides at 20-BM and 13-BM-D and from an Fe foil at 13-BM-D (July 2011) and 13-ID-C (October 2011). Edge energies were used to calibrate spectra and determine Mn oxidation states and are defined as the first peak after the pre-edge peak in the $\mu(E)$ derivative spectrum (McKeown & Post, 2001; Bunker, 2010) (Figure 4-1). Of these oxides, MnO_2 was chosen as the best candidate to calibrate spectra taken on different collection dates due to its fully oxidized state. E_0 for spectra obtained for the Fe foils were consistent with reported values and indicated no energy shift was required for July 2011 or October 2011 spectra. Therefore, all MnO_2 spectra were calibrated to the MnO_2 spectrum collected July 2011 by aligning peaks in the

$\mu(E)$ derivative spectrum. The energy shifts calculated from the alignment of the MnO_2 spectra ($E_0 = 6552.0 \pm 0.6$ eV) were sufficient to align both the Mn_2O_3 ($E_0 = 6547.5 \pm 0.2$ eV) and MnO ($E_0 = 6543.9 \pm 0.4$ eV) standards across all dates.

Linear combination fits were performed between -20 eV and +30 eV around the Mn K-edge ($E_0 = 6539$ eV). Standards used in the fits include powders of mineral oxides containing Mn in divalent (MnO), trivalent (Mn_2O_3), or tetravalent (MnO_2) states, a mixed-valence Mn-oxide, birnessite ($\text{Mn}(3+/4+)_2\text{O}_4$), organic compounds containing divalent (Mn-formate, $\text{MnC}_2\text{H}_2\text{O}_4$) or trivalent (Mn acetate hydrate, $\text{MnC}_6\text{H}_9\text{O}_6 \cdot x\text{H}_2\text{O}$) manganese, and aqueous Mn^{+2} (Figure 4-2). Powdered standards were purchased from Alfa Aesar at > 99% (oxides) or > 96% (organics) purity. Birnessite was acquired from a library of Mn minerals available at beamline 20. An aqueous Mn standard was prepared by dissolving $\text{MnCl}_2 \cdot 4\text{H}_2\text{O}$ (Sigma, >99% purity) in deionized water to obtain a 12.5 mM solution. In the absence of catalysts, the Mn^{2+} ion is stable in oxygenated aqueous solution for years (Diem & Stumm, 1984; Chiswell & Mokhtar, 1986). Shifts of the edge energies of each standard relative to MnO are consistent with theoretical predictions (Appendix Section C1).

The relative qualities of linear combination fits were assessed using statistical output from the Athena software, including the R-factor, chi-square value, and reduced chi-square value. In this paper, we report the R-factor (%), which is equal to the sum of the squared differences between the data points and the model fit, divided by the sum of the squared data points. Thus, lower R values indicate better model fits to the data.

III. Results

3.1. XANES

3.1.1 Soil

Small changes with depth were observed in four bulk soil samples collected from the ridge soil profile and a soil sample collected at the soil-bedrock interface in the valley floor soil profile (Figure 4- 3). In particular, we observed a peak on the absorption edge ($E = 6558.0$ eV) that increases relative to the maximum absorption peak ($E = 6562.0$ eV) with increasing depth in the soil profile.

For all these samples, the edge energies ($E_0 = 6550.7 \pm 0.3$ eV) are intermediate between Mn_2O_3 (6547.7 eV) and MnO_2 (6552.3 eV), consistent with the presence of $\text{Mn}^{3+/4+}$ -oxides. Linear combination fits (LCF) were performed using MnO , Mn_2O_3 , and MnO_2 standards to calculate an average oxidation state for Mn in each sample. In the ridge soils, LCF yielded fits of $7 \pm 7\%$ Mn^{+2} ,

$19 \pm 7\%$ Mn^{3+} , and $74 \pm 1\%$ Mn^{+4} (R-factor = $0.31 \pm 0.10\%$) for an average oxidation state of $+3.7 \pm 0.1$. The errors equal the standard deviation of the percent contribution of each component amongst the four soil samples. In the valley floor soil, LCF yielded a fit of 12% Mn^{2+} , 57% Mn^{3+} , and 30% Mn^{+4} (R-factor = 0.29%) for an average oxidation state of $+3.2$.

Another way to fit the soil spectra is to create a LCF using the birnessite standard ($\text{Mn}^{3+/4+}_2\text{O}_4$; Figure 4-2). Thus, we reexamined the soil samples by evaluating all combinations of birnessite, MnO , Mn_2O_3 , and MnO_2 in a linear combination fit. We averaged the best three fits for each sample and found that birnessite is a major component of soils at all depths, while the relative contribution of the other oxides is variable. Near the top of the ridge profile, mineral soils contain approximately equal amounts of MnO_2 and Mn_2O_4 ($\sim 45\%$) (Figure 4-4), while soils collected from the O horizon and the soil-bedrock interface contain little MnO_2 ($< 15\%$) and higher proportions of oxides containing Mn^{2+} and Mn^{3+} (Table 4-1).

3.1.2. Vegetation

The Mn K-edge energy varied little amongst vegetation samples ($E_0 = 6547.9 \pm 0.6$ eV), including leaf litter, fresh foliage, and roots. The E_0 values in the vegetation samples are consistent with Mn_2O_3 ; however, linear combination fits using the Mn-oxide standards yielded poor fits (R-factor $> 5\%$). Fits were drastically improved for all vegetation samples by using organic and aqueous Mn^{+2} standards (R-factor = $0.29 \pm 0.21\%$), and fits to leaf litter are shown as an example (Figure 4-5). Forty-one spectra obtained from green leaf, leaf litter, stem, and root tissues, including both bulk XANES and μXANES described below, yielded, on average, a relative contribution of $26 \pm 31\%$ aqueous Mn^{+2} and $74 \pm 31\%$ organic Mn^{+2} . Overall, no significant differences were observed amongst spectra obtained from the different parts of vegetation (Table 4-1).

3.1.3. Decomposition of vegetation

We evaluated Mn XANES from fresh and decomposing foliage and root tissue, including leaves from undergrowth and roots from the soil that were analyzed while fresh, and then reanalyzed after 6 months of open-air decomposition in the laboratory. We compare these spectra to other samples included leaf litter and soil as previously characterized (Figs. 4-4 and 4-5) and find that spectra from the decomposing samples are intermediate between fresh vegetation and the mineral soil (Figure 4-6).

Spectra from two samples, fresh foliar tissue and mineral soil, were used as end members in a linear combination fit to characterize decomposing vegetation. The fresh vegetation end-member spectrum was generated by averaging spectra from ground red oak leaves collected from seedlings grown in a greenhouse (Mn concentrations = $3,450 - 11,000 \mu\text{g g}^{-1}$; $n = 3$). The mineral soil end-

member spectrum was obtained from a ground soil sample (Mn concentration = 2,600 $\mu\text{g g}^{-1}$) that was collected from 11 – 16 cm depth in a ridge soil at SSHCZO and kept at field moisture conditions until analysis. A deeper soil sample (16 – 22 cm) was not used because it contained little Mn (< 1,200 $\mu\text{g g}^{-1}$) and yielded a noisy spectrum.

Fresh foliar tissue was 100% similar and fresh roots were 96% similar to the vegetation end-member; however, spectra for four out of seven of the decomposing vegetation samples were not well-fit unless a large contribution (11-50%, R-factor < 0.05%) from the mineral soil end-member was included (Table 4-2). Leaf litter, however, was 100% similar to the vegetation end-member (R-factor = 0.08%), indicating that decomposition does not commence until after litter fall. The organic horizon, which contains highly decomposed leaf material, had a large mineral Mn component (90% \pm 1%, R-factor = 0.26 \pm 0.18%). Thus, we infer that XANES spectra for decomposing vegetation are intermediate between vegetation and mineral soil and contain a mixture of aqueous and organic Mn^{2+} complexes and $\text{Mn}^{3+/4+}$ -oxides. Similar results were observed for leaf litter samples that were analyzed after burial in soils for 7-9 weeks (Appendix Section C2).

3.2. XRF and μXANES

We used the XRF maps to analyze the spatial distribution of Mn and other elements in soil, roots, stems, and leaves. Additionally, we identified regions of interest on the XRF maps to collect Mn μXANES spectra.

3.2.1. Leaves

Dark spots on sampled leaves, a symptom of Mn toxicity, contain much higher levels of Mn than surrounding foliar tissue (Figure 4-7). This feature was observed in leaves from both greenhouse cultivated *Q. rubra* seedlings and mature *Q. prinus* and *A. saccharum* trees growing at SSHCZO. The correlation between dark spots and high Mn was observed in both small concentrated spots (~0.1 mm diameter), more diffuse spots (~1 mm diameter), and in ring structures (Figure C-4).

Two spectra obtained from Mn-rich dark spots on a red oak leaf showed poor fits when using organic and aqueous Mn^{+2} standards (R-factor > 10%). In contrast, a spectrum obtained from the Mn-poor green area was consistent with 20% aqueous Mn^{+2} and 80% Mn-formate (R-factor = 0.40%) (Figure 4-7). To characterize the speciation of Mn in the dark spots, linear combination fits were calculated using aqueous Mn^{+2} , Mn-formate, and one additional Mn compound, either MnO, Mn_2O_3 , Mn_2O_4 , MnO_2 , or organic Mn^{3+} (Mn^{3+} -acetate).

We found that spectra from the Mn-rich black spots were most consistent with a combination of Mn^{2+} -formate (10 \pm 6%) and Mn^{3+} -acetate (90 \pm 6%) (R-factor = 0.10%). In contrast, fits

including MnO, Mn₂O₃, or Mn₂O₄ were less robust and not statistically different from each other (R-factor = $0.26 \pm 0.03\%$), and models including MnO₂ had the poorest fit (R-factor = $0.32 \pm 0.02\%$).

In one additional leaf sample from a red oak seedling, μ XANES spectra were taken on two Mn-rich dark spots of differing Mn intensity (Figure C-5). The less Mn-rich spot was consistent with 72% Mn-formate and 28% aqueous Mn²⁺ (R-factor = 0.08%) while the more Mn-rich spot was not (R-factor = 0.60%). Model fits to the more Mn-rich spot were not significantly improved by the addition of Mn³⁺-acetate nor any Mn-oxide to the linear combination; however, the maximum absorbance peak in the spectrum ($E = 6551$ eV) is most consistent with aqueous and organic Mn²⁺ ($E = 6552$ eV) while a second prominent peak ($E = 6561$ eV) is consistent with the maximum absorbance peaks of Mn³⁺-acetate and Mn₂O₄.

In total, we analyzed μ XANES spectra from nine dark spots and six green areas on leaves. We compared model results from linear combination fits that included Mn³⁺-acetate, Mn-formate, and aqueous Mn²⁺ to model results from fits without Mn³⁺-acetate. Model fits to six out of nine spectra taken on dark spots improved by $67 \pm 30\%$ with Mn³⁺-acetate and yielded fits containing 7-96% Mn³⁺-acetate (e.g. Figure C-6B). In contrast, model fits to five out of six spectra taken on green areas of leaves did not improve with the addition of Mn³⁺-acetate.

Like the fits for μ XANES spectra for dark spots, model fits to two bulk oak leaf samples exhibiting dark spots were also improved with the addition of Mn³⁺-acetate (R-factor = $0.13 \pm 0.05\%$) relative to fits with only Mn²⁺-formate and Mn²⁺ aqueous (R-factor = $1.04 \pm 0.05\%$). From these fits, organic-Mn³⁺ was estimated to contribute ~20% to the bulk leaf tissue. For these bulk samples, however, fits with each Mn-oxide were not statistically distinct from fits with Mn³⁺-acetate (R-factor = $0.15 \pm 0.06\%$). The similar fits amongst the Mn-oxides and Mn³⁺-acetate are likely due to the high abundance of Mn²⁺ in the bulk tissue, which dominates the signal of the bulk leaf samples.

Overall, we conclude that Mn is concentrated in the spots in a form distinct from the surrounding tissue: the best fits to spectra are consistent with organically-complexed Mn³⁺ as the dominant form of Mn in these black spots. However, given the differences in visual and spectral observations for spots from different leaves, we infer that the dark spots are not uniform in composition in that they may differ in their relative proportions of Mn-compounds as toxicity progresses. Dark coloration that is visible by eye in the leaf may furthermore develop prior to the accumulation of oxidized Mn-compounds in the leaf at concentration levels that can be measured by XANES.

3.2.2 Stems

A map made of a *Q. prinus* stem cross-section revealed that Mn is concentrated in the phloem tissue of the stem, while the xylem tissue contains relatively little Mn (Figure 4-8). Spectra taken from the Mn-rich phloem, Mn-poor xylem, and the outer rim of the stem are indistinguishable and consistent with a mixture of organic and aqueous Mn^{2+} .

3.2.3. Roots

The spatial distribution of Mn was compared between coarse and fine roots. In fine roots with no woody tissue, Mn is concentrated in the inner portion of the root, similar to K, and opposite to Ca (Figure 4-9). A network of fine roots shows a fairly homogenous distribution of Mn throughout the branching structures, with some patches of high Mn that correlate to other rock-derived elements (Figure C-7). This latter observation is consistent with soil particles attached to the roots. In larger roots with woody tissue, Mn is concentrated in the outer portion of the root, exhibiting a Mn-rich band in what is likely phloem tissue (Figure 4-10). Resolution of the image makes determination of the exact tissue difficult. Analysis of the edge of a woody chestnut oak root (8 mm diameter) reveals that Mn distribution does not correlate with other elements but forms a distinct band around a K-rich region.

Spectra from 12 μXANES spots and 1 bulk root sample are consistent with $86 \pm 24\%$ organic Mn^{2+} and $14 \pm 24\%$ aqueous Mn^{2+} , similar to spectra from leaf and stem samples (Table 1). In the three fine root samples, spectra were taken from spots on or near fine roots that contain high levels of Mn relative to the surrounding sample. In one sample, we examined a large patch ($\sim 400 \mu\text{m}$ diameter) that is enriched in various elements, but shows a heterogeneous distribution (Figure C-7). A μXANES spectrum from this patch is most consistent with 58% aqueous Mn^{2+} and 42% Mn_2O_3 (R-factor = 0.37%). In another fine root sample, a small particle on the root ($\sim 50 \mu\text{m}$ diameter) contains Mn that is consistent with $\sim 50\%$ Mn^{2+} -formate and 50% of either Mn_2O_4 or MnO_2 (R-factor = $0.65 \pm 0.01\%$), i.e., consistent with the presence of a small soil particle (Figure C-8). In the third sample, we observe a Mn-rich region on the exterior of the root that does not correlate with other elements (Figure 4-9). With the exception of these small soil particles, the abundance of organic and aqueous Mn^{+2} in all portions of the root tissue indicate that Mn-oxidation is not occurring in or near the roots in these red oak seedlings.

3.2.4. Soil components

In XRF images of soil grains, we observed discrete Mn-rich regions (Figure 4-11; Figure C-9). In regions of low Mn concentration, Mn, Si, Ca, K, and Fe were observed to be strongly

positively correlated. In Mn-rich regions, Mn did not correlate with any other element. In one sample, high Si concentrations showed poor correlation with other elements (Figure C9-A). These observations are consistent with mineral soil that contains dominantly clay particles containing Si, K, and Fe with some quartz particles (containing Si and O alone) and discrete particles with high Mn concentration.

IV. Discussion

Our analysis of decomposing leaves and roots reveals that Mn in these tissues consists largely of organic Mn^{2+} that transforms to $\text{Mn}^{3/+4+}$ -oxides in the soil upon decomposition (Figure 4-6). XANES spectra for Mn in green leaves and leaf litter were similar; thus, we infer that oxidation of the Mn in plant tissues does not commence until after litterfall. Significant alteration of Mn in leaf tissue occurred within 2-6 months of the initiation of decomposition, as measured in our laboratory decomposition experiments (Figure 4-6). Mn oxidation was more pronounced in leaves decomposed in fungi-rich field soil relative to fungi-poor potting soil which may point to fungi as the dominant Mn oxidizers in this soil system (Appendix section C2). Spontaneous abiotic precipitation of Mn-oxides is not expected in aqueous solution at the low pH conditions present in these soils (Tebo et al., 2004). Indeed, many other researchers have observed that bacteria and fungi are largely responsible for Mn-oxide formation in the environment, but fungi may be more important than bacteria in many terrestrial systems (Santelli et al., 2010; Thompson et al., 2005). Both bacteria and fungi catalyze the production of Mn-oxide minerals that yield XANES spectra similar to those obtained for the organic horizon and surface soil in this study (Barger et al., 2005; Miyata et al., 2006; Santelli et al., 2011).

We observed changes in Mn XANES with depth in the soil profile that are consistent with formation of different pools of Mn. In particular, the proportion of Mn^{2+} and Mn^{3+} present in the soil increased relative to Mn^{4+} with increasing depth. This trend is indicated by the increasing intensity of an absorption peak in spectra taken from the mineral soil samples from the soil surface down to bedrock (Figure 4-3). This trend is consistent with an increasing contribution from a reduced form of Mn lower in the soil. In previous research, Jin et al., (2010) documented that the ridge soils at SSHCZO are 50-56 wt.% quartz, 30 wt.% illite, 2-3 wt.% Fe oxides, < 3 wt.% kaolinite, and 5-8% “chlorite”, where the “chlorite” term was used to represent chlorite, vermiculite, and hydroxyl-interlayered vermiculite phases. In comparison, the deepest soils collected from the valley floor were found to contain 36 wt.% quartz, 54 wt.% illite, and 9% “chlorite” with no detectable Fe-oxides or kaolinite. The protolith shale was similar in composition

to the deepest soil sample, but contained trace Fe-oxides and feldspar minerals. Using that information, we suggest that Mn in soils near the bedrock interface is principally contained in protolith minerals such as illite and “chlorite” while Mn in the organic horizon and surface soils is present in Mn³⁺/Mn⁴⁺-oxides. In fact, the Mn XANES spectrum for the deepest soil sample exhibited the same double peak and prominent shoulder previously observed for Mn in illite (Huggins et al., 1997). No Mn-oxide minerals were documented by XRD in the soils, likely due to their relatively low abundance (< 1.5 wt.%) and poorly-crystalline structure (Jin et al., 2010).

At SSHCZO, the mass balance on Mn calculated for ridge top soil profiles is consistent with significant Mn atmospheric inputs over the last 200 y (Herndon et al., 2011). Ridgetop soils in the catchment vary from 0 to 70 cm in thickness, but are generally close to 20 or 30 cm thick. Ma et al. (2010) documented that the residence time for particles in these ridgetop soils, as they move out of the underlying unweathered bedrock upward and out of the ridge due to erosion, averages ~7 ky. During that time, the protolith particles that contain Mn in clay or Fe-oxide minerals likely lose aqueous Mn as meteoric fluids leach the soils. Some of the mobilized Mn likely also oxidizes to precipitate Mn-oxide minerals *in situ*. For such ridgetop soils, depletion and re-precipitation would generally produce Mn depletion profiles (i.e. soils that are increasingly Mn-depleted upward in each soil profile) or Mn enrichment-depletion profiles (i.e. soils that are Mn-depleted at the surface and Mn-enriched at depth).

As shown by Herndon et al. (2011), however, Mn concentrations in the ridgetop soils at SSHCZO increase upwards toward the soil surface, consistent with an addition profile. Net enrichment of Mn in the soil profiles was attributed to atmospheric inputs from industrial sources. Atmospheric inputs were inferred to have consisted of both aqueous Mn and particulate Mn-oxide species. Although the full suite of industrially-sourced Mn compounds has not been well-characterized, previous researchers report emissions of soluble Mn sulfates and phosphates and insoluble Mn₃O₄ and MnO₂ from anthropogenic sources (U.S. Environmental Protection Agency, 1984; Zayed et al., 1999; Ressler et al., 2000). In addition to atmospheric inputs, however, Mn uptake into vegetation and deposition to the land surface through litter decomposition comprises another Mn source at the top of each profile. As shown in Figure 4-6, this Mn may be released as an aqueous species but likely quickly transforms to particulate Mn^{3+/4+}-oxides.

Due to similarities in mineralogy, we cannot distinguish between Mn-oxide particles input through industrial deposition and Mn-oxides formed during decomposition of plant biomass near the soil surface. However, net enrichment of Mn in the soils is consistent with external inputs from atmospheric deposition. Vegetation rapidly accumulates soluble Mn²⁺ from soil pore fluids which

is then oxidized to insoluble Mn-oxides in the soil during biomass decomposition. Mn that is leached from the atmospherically-deposited Mn particles may be accumulated by vegetation and reprecipitated as biogenic Mn-oxides. Thus, industrial inputs are still the ultimate source of Mn at the soil surface. The uptake and storage of aqueous Mn^{2+} by vegetation and eventual immobilization as Mn-oxides in the soil likely slows the removal of Mn contamination from soils into rivers.

Similar to previous studies, we find that Mn in the plant biomass is predominantly aqueous or organic-bound Mn^{2+} (Xu et al., 2009; Fernando et al., 2010). Despite the demonstrated immobility of Mn in phloem sap (Hocking, 1980; Riesen and Feller, 2005), we observed high levels of Mn in phloem tissues relative to the xylem. This observation also does not contradict previous studies, but rather suggests that Mn is utilized for biochemical processes in the living phloem cells and merely transported through dead xylem cells without storage. Although many plant species are able to oxidize Mn in the root zone (Horiguchi, 1987), we observed no evidence of Mn oxidation in these root samples. Furthermore, there were no significant differences between Mn-compounds contained in root, stem, or green foliar tissue. While the particular organic moiety binding Mn may differ amongst these compartments, Mn K-edge XANES could not satisfactorily distinguish among them.

The leaves analyzed in this study often exhibited dark spots, a symptom of Mn toxicity in plants. These spots were found to be Mn-rich relative to the surrounding leaf tissue and to contain varying degrees of Mn^{2+} and Mn^{3+} -organic complexes. Previous studies have attributed the dark spots to the accumulation of phenolic compounds and/or oxidized Mn deposits, but no previous researchers identified the presence of a Mn^{3+} compound (Horiguchi, 1987; Broadhurst et al., 2009). The Mn^{3+} ion is unstable in aqueous solution and has only recently been found to persist in the environment when bound to strong organic ligands (Duckworth & Sposito, 2005; Trouwborst et al., 2006; Madison et al., 2011). Mn^{3+} compounds have been implicated as an intermediate in the formation of biogenic Mn-oxides, either via direct enzymatic oxidation or biologically-produced, extracellular superoxides (Tebo et al., 2004; Learman et al., 2011). Superoxides are also produced in leaves as a byproduct of photosynthesis, and superoxide production is enhanced in leaves containing elevated Mn (Gonzalez et al., 1998; St. Clair et al., 2005). We conjecture the Mn^{3+} -organic complexes detected in the dark spots on the leaves are produced via the oxidation of Mn^{2+} by excess superoxide and subsequent stabilization by organic compounds. From this study, it is unclear whether the Mn^{3+} -compounds eventually transform into Mn-oxides.

V. Conclusions

The fate and transport of industrial contaminants through the environment depend on their interactions with soil minerals and biota. In previous studies, we suggested that vegetation can act as a capacitor for Mn contamination, taking up large quantities of Mn from the soil, storing it, and slowly releasing it into rivers over time. Here, we demonstrated that Mn that is taken up by vegetation is taken up as Mn^{2+} species that are then rapidly oxidized as vegetation is decomposed in the soil. Most of the Mn in plant tissue is present in the leaves, with only minor Mn in woody tissues. Upon senescence and leaf fall in autumn, the Mn is released but rapidly immobilized during litter decomposition. We propose that Mn can be preferentially retained in soils relative to other elements due to this process of uptake and immobilization. Namely, vegetation takes up the majority of Mn that is solubilized in the soil within the rooting zone and drastically reduces the quantity that can be leached from the soil profile. The Mn that is taken up into plant biomass exists in aqueous and organic Mn^{2+} compounds that are immobilized as $\text{Mn}^{3+/4+}$ -oxides during decomposition. The recurring cycle of solubilization from the solid-phase followed by uptake into vegetation and subsequent immobilization effectively retains Mn within the soil-plant system.

VI. Acknowledgements

This study was supported by NSF grant EAR #1052614 to SLB, the NSF Susquehanna Shale Hills Critical Zone Observatory grant EAR #0725019 to C. Duffy (Penn State), and NSF grant CHE #0431328 to SLB. The authors particularly acknowledge the invaluable help of Matthew Newville (GSECARS) and Dale Brewe (PNC/XSD) at APS and Timothy Fischer for scientific support at the beamlines, and Katie Gaines, Jim Savage, and Jane Wubbels for leaf collection at SSHCZO.

Portions of this work (μXRF and μXANES) were performed at GeoSoilEnviroCARS (Sector 13), Advanced Photon Source (APS), Argonne National Laboratory. GeoSoilEnviroCARS is supported by the NSF - Earth Sciences (EAR-1128799) and DOE - Geosciences (DE-FG02-94ER14466). Use of the APS was supported by the U. S. DOE, Office of Science, Office of Basic Energy Sciences, under Contract No. DE-AC02-06CH11357. Other portions of this work (bulk XANES) were performed at PNC/XSD facilities. PNC/XSD facilities at the APS, and research at these facilities, are supported by the US DOE - Basic Energy Sciences, a Major Resources Support grant from NSERC, the University of Washington, Simon Fraser University and the Advanced Photon Source. Use of the Advanced Photon Source, an Office of Science User Facility operated

for the U.S. DOE Office of Science by Argonne National Laboratory, was supported by the U.S. DOE under Contract No. DE-AC02-06CH11357.

VII. References

- Bargar J.R., Webb S.M. and Tebo B.M. (2005) EXAFS , XANES and In-Situ SR-XRD Characterization of Biogenic Manganese Oxides Produced in Sea Water. *Physica Scripta* **T115**, 888–890.
- Berg B., Steffen K.T. and McLaugherty C. (2007) Litter decomposition rate is dependent on litter Mn concentrations. *Biogeochemistry* **82**, 29–39.
- Blamey F. P. C., Joyce D. C., Edwards D. G. and Asher C. J. (1986) Role of trichomes in sunflower tolerance to manganese toxicity. *Plant and Soil* **91**, 171–180.
- Broadhurst C.L., Tappero R.V., Mangel T.K., Erbe E.F., Sparks D.L. and Chaney R.L. (2009) Interaction of nickel and manganese in accumulation and localization in leaves of the Ni hyperaccumulators *Alyssum murale* and *Alyssum corsicum*. *Plant and Soil* **314**, 35–48.
- Broadley M., Brown P., Cakmak I., Rengel Z. and Zhao F. (2012) Function of Nutrients: Micronutrients. In *Marschner's Mineral Nutrition of Higher Plants* pp. 191–248.
- Bunker G. (2010) *Introduction to XAFS: A practical guide to X-ray Absorption Fine Structure Spectroscopy*. First Edit., Cambridge University Press.
- Chiswell B. and Mokhtar M. B. (1986) The speciation of manganese in freshwaters. *Talanta* **33**, 669–677.
- Diem D. and Stumm W. (1984) Is dissolved Mn(II) being oxidized by O₂ in absence of Mn-bacteria or surface catalysts? *Geochimica et Cosmochimica Acta* **48**, 1571–1573.
- Dou C., Fu X., Chen X., Shi J. and Chen Y. (2009) Accumulation and interaction of calcium and manganese in *Phytolacca americana*. *Plant Science* **177**, 601–606.
- Duckworth O.W. and Sposito G. (2005) Siderophore-Manganese(III) Interactions II . Manganite Dissolution Promoted by Desferrioxamine B. *Environmental Science and Technology* **39**, 6045–6051.
- Eickhorst T. and Tippkötter R. (2008) Detection of microorganisms in undisturbed soil by combining fluorescence in situ hybridization (FISH) and micropedological methods. *Soil Biology and Biochemistry* **40**, 1284–1293.
- Fernando D.R., Bakkaus E.J., Perrier N., Baker A.J.M., Woodrow I.E., Batianoff G.N. and Collins R.N. (2006) Manganese accumulation in the leaf mesophyll of four tree species: a PIXE/EDAX localization study. *New Phytologist* **171**, 751–7.
- Fernando D.R., Mizuno T., Woodrow I.E., Baker A.J.M. and Collins R.N. (2010) Characterization of foliar manganese (Mn) in Mn (hyper)accumulators using X-ray absorption spectroscopy. *New Phytologist* **188**, 1014–27.
- Fernando D.R., Woodrow I.E., Jaffré T., Dumontet V., Marshall A.T. and Baker A.J.M. (2008) Foliar manganese accumulation by *Maytenus founieri* (Celastraceae) in its native New Caledonian habitats: populational variation and localization by X-ray microanalysis. *New Phytologist* **177**, 178–85.
- Fernando D. R., Woodrow I. E., Bakkaus E. J., Collins R. N., Baker A.J.M. and Batianoff G. N. (2007) Variability of Mn hyperaccumulation in the Australian rainforest tree *Gossia bidwillii* (Myrtaceae). *Plant and Soil* **293**, 145–152.
- Fernando Denise R, Marshall Alan T, Gouget B., Carrie M., Collins Richard N, Woodrow Ian E and Baker A. J. (2008) Novel pattern of foliar metal distribution in a manganese hyperaccumulator. *Functional Plant Biology* **35**, 193–200.

- Fernando D.R., Batianoff G.N., Baker A.J. and Woodrow I.E. (2006) In vivo localization of manganese in the hyperaccumulator *Gossia bidwillii* (Benth.) N. Snow & Guymmer (Myrtaceae) by cryo-SEM/EDAX. *Plant, Cell and Environment* **29**, 1012–1020.
- Gonzalez A. and Lynch J.P. (1999) Subcellular and tissue Mn compartmentation in bean leaves under Mn toxicity stress. *Australian Journal of Plant Physiology* **26**, 811–822.
- Gonzalez A., Steffen K. and Lynch J. (1998) Light and excess manganese . Implications for oxidative stress in common bean. *Plant physiology* **118**, 493–504.
- Herndon E. M., Jin L. and Brantley S. L. (2011) Soils reveal widespread manganese enrichment from industrial inputs. *Environmental Science & Technology* **45**, 241–7.
- Hocking P. J. (1980) The Composition of Phloem Exudate and Xylem Sap from Tree Tobacco (*Nicotiana glauca* Grah.). *Annals of Botany* **45**, 633–643.
- Hofrichter M. (2002) Review: lignin conversion by manganese peroxidase (MnP). *Enzyme and Microbial Technology* **30**, 454–466.
- Horiguchi T. (1987) Mechanism of manganese toxicity and tolerance of plants. *Soil Science and Plant Nutrition* **33**, 595–606.
- Horsley S. B., Long R. P., Bailey S. W., Hallett R. A. and Hall T. J. (2000) Factors associated with the decline disease of sugar maple on the Allegheny Plateau. *Canadian Journal of Forest Research* **30**, 1365–1378.
- Horst W. J. and Marschner H. (1978) Effect of silicon on manganese tolerance of bean plants (*Phaseolus vulgaris* L.). *Plant and Soil* **50**, 287–303.
- Huggins F. E., Srikantapura S., Parekh B. K., Blanchard L. and Robertson J. D. (1997) XANES Spectroscopic Characterization of Selected Elements in Deep-Cleaned Fractions of Kentucky No. 9 Coal. *Energy & Fuels* **11**, 691–701.
- Jin L., Ravella R., Ketchum B., Bierman P. R., Heaney P., White T. and Brantley S. L. (2010) Mineral weathering and elemental transport during hillslope evolution at the Susquehanna/Shale Hills Critical Zone Observatory. *Geochimica et Cosmochimica Acta* **74**, 3669–3691.
- Kabata-Pendias A. and Pendias H. (2001) *Trace elements in soils and plants*. 3rd ed., CRC Press LLC, Boca Raton.
- Kogelmann W. J. and Sharpe W. E. (2006) Soil acidity and manganese in declining and nondeclining sugar maple stands in Pennsylvania. *Journal of environmental quality* **35**, 433–41.
- Learman D. R., Voelker B. M., Vazquez-Rodriguez a. I. and Hansel C. M. (2011) Formation of manganese oxides by bacterially generated superoxide. *Nature Geoscience* **4**, 95–98.
- Learman D. R., Wankel S. D., Webb S.M., Martinez N., Madden A.S. and Hansel C.M. (2011) Coupled biotic–abiotic Mn(II) oxidation pathway mediates the formation and structural evolution of biogenic Mn oxides. *Geochimica et Cosmochimica Acta* **75**, 6048–6063.
- Ma L., Chabaux F., Pelt E., Blaes E., Jin L. and Brantley S. L. (2010) Regolith production rates calculated with uranium-series isotopes at Susquehanna/Shale Hills Critical Zone Observatory. *Earth and Planetary ...* **297**, 211–225.
- Madison A. S., Tebo Bradley M and Luther G. W. (2011) Simultaneous determination of soluble manganese(III), manganese(II) and total manganese in natural (pore)waters. *Talanta* **84**, 374–81.
- Manceau A., Gorshkov A. and Drits V. (1992a) Structural chemistry of Mn, Fe, Co, and Ni in manganese hydrous oxides: Part I. Information from XANES spectroscopy. *American Mineralogist* **77**, 1133–1143.
- Manceau A., Gorshkov A. and Drits V. (1992b) Structural chemistry of Mn, Fe, Co, and Ni in manganese hydrous oxides: Part II. Information from EXAFS spectroscopy and electron and X-ray diffraction. *American Mineralogist* **77**, 1144–1157.

- McCain D. C. and Markley J. L. (1989) More Manganese Accumulates in Maple Sun Leaves than in Shade Leaves. *Plant physiology* **90**, 1417–1421.
- McKeown D. and Post J. (2001) Characterization of manganese oxide mineralogy in rock varnish and dendrites using X-ray absorption spectroscopy. *American Mineralogist* **86**, 701–713.
- McNear D. H., Peltier E., Everhart J., Chaney R. L., Sutton S., Newville M., Rivers M. and Sparks D. L. (2005) Application of quantitative fluorescence and absorption-edge computed microtomography to image metal compartmentalization in *Alyssum murale*. *Environmental Science & Technology* **39**, 2210–8.
- McQuattie C. J. and Schier G. a. (2000) Response of sugar maple (*Acer saccharum*) seedlings to manganese. *Canadian Journal of Forest Research* **30**, 456–467.
- Miyata N., Tani Y., Maruo K., Tsuno H., Sakata M. and Iwahori K. (2006) Manganese(IV) oxide production by *Acremonium* sp. strain KR21-2 and extracellular Mn(II) oxidase activity. *Applied and environmental microbiology* **72**, 6467–73.
- Newville M. (2006) DataViewer. Available at: <http://cars.uchicago.edu/~newville/dataviewer>.
- Newville M. (2001) EXAFS analysis using FEFF and FEFFIT. *Journal of synchrotron radiation* **8**, 96–100.
- Nriagu J. and Pacyna J. (1988) Quantitative assessment of worldwide contamination of air, water and soils by trace metals. *Nature* **333**, 134–139.
- Nunan N., Ritz K., Crabb D., Harris K., Wu K., Crawford J. W. and Young I. M. (2001) Quantification of the in situ distribution of soil bacteria by large-scale imaging of thin sections of undisturbed soil. *FEMS Microbiology Ecology* **36**, 67–77.
- Pacyna J. M. and Pacyna E. G. (2001) An assessment of global and regional emissions of trace metals to the atmosphere from anthropogenic sources worldwide. *Environmental Reviews* **9**, 269–298.
- Peiter E., Montanini B., Gobert A., Pedas P., Husted S., Maathuis F. J. M., Blaudez D., Chalot M. and Sanders D. (2007) A secretory pathway-localized cation diffusion facilitator confers plant manganese tolerance. *Proceedings of the National Academy of Sciences* **104**, 8532–7.
- Post J. E. (1999) Manganese oxide minerals: Crystal structures and economic and environmental significance. *Proceedings of the National Academy of Sciences* **96**, 3447–3454.
- Ravel B. and Newville M. (2005) Athena, Artemis, and Hephaestus: Data analysis for x-ray absorption spectroscopy using IFEFFIT. *Journal of synchrotron radiation* **12**, 537–541.
- Ressler T., Wong J., Roos J. and Smith I. L. (2000) Quantitative Speciation of Mn-Bearing Particulates Emitted from Autos Burning (Methylcyclopentadienyl)manganese Tricarbonyl-Added Gasolines Using XANES Spectroscopy. *Environmental Science & Technology* **34**, 950–958.
- Riesen O. and Feller U. (2005) Redistribution of Nickel, Cobalt, Manganese, Zinc, and Cadmium via the Phloem in Young and Maturing Wheat. *Journal of Plant Nutrition* **28**, 421–430.
- Römheld V. (2012) Diagnosis of Deficiency and Toxicity of Nutrients. In *Marschner's Mineral Nutrition of Higher Plants* Elsevier Ltd. pp. 299–312.
- Santelli C. M., Pfister D. H., Lazarus D., Sun L., Burgos W. D. and Hansel C.M. (2010) Promotion of Mn(II) oxidation and remediation of coal mine drainage in passive treatment systems by diverse fungal and bacterial communities. *Applied and environmental microbiology* **76**, 4871–5.
- Santelli C.M., Webb S.M., Dohnalkova A.C. and Hansel C.M. (2011) Diversity of Mn oxides produced by Mn(II)-oxidizing fungi. *Geochimica et Cosmochimica Acta* **75**, 2762–2776.
- Saratovsky I., Wightman P. G., Pastén P. a, Gaillard J.-F. and Poepfelmeier K. R. (2006) Manganese oxides: parallels between abiotic and biotic structures. *Journal of the American Chemical Society* **128**, 11188–98.

- Schulze D., McCay-Buis T., Sutton SR and Huber D. (1995) Manganese oxidation states in Gaeumannomyces-infested wheat rhizospheres probed by micro-XANES spectroscopy. *Phytopathology* **85**, 990–994.
- St. Clair S. B., Carlson J. E. and Lynch Jonathan P (2005) Evidence for oxidative stress in sugar maple stands growing on acidic, nutrient imbalanced forest soils. *Oecologia* **145**, 258–69.
- Stueben B. L., Cantrelle B., Sneddon J. and Beck J. N. (2004) Manganese K-edge XANES studies of Mn speciation in Lac des Allemands as a function of depth. *Microchemical Journal* **76**, 113–120.
- Suarez D. and Langmuir D. (1976) Heavy metal relationships in a Pennsylvania soil. *Geochimica et Cosmochimica Acta* **40**, 589–598.
- Tebo B.M., Bargar J.R., Clement B.G., Dick G.J., Murray K. J., Parker D., Verity R. and Webb S.M. (2004) Biogenic manganese oxides: Properties and mechanisms of formation. *Annual Review of Earth and Planetary Sciences* **32**, 287–328.
- Thompson I., Huber D.M., Guest C. and Schulze D.G. (2005) Fungal manganese oxidation in a reduced soil. *Environmental microbiology* **7**, 1480–7.
- Tippkötter R. and Ritz K. (1996) Evaluation of polyester, epoxy and acrylic resins for suitability in preparation of soil thin sections for in situ biological studies. *Geoderma* **69**, 31–57.
- Trouwborst R. E., Clement B. G., Tebo B.M, Glazer B. T. and Luther G.W. (2006) Soluble Mn(III) in suboxic zones. *Science (New York, N.Y.)* **313**, 1955–7.
- U.S. Environmental Protection Agency (1984) *Health Assessment Document for Manganese.*, Cincinnati, Ohio.
- Webb S.M., Dick G.J., Bargar J.R. and Tebo B.M. (2005) Evidence for the presence of Mn(III) intermediates in the bacterial oxidation of Mn(II). *Proceedings of the National Academy of Sciences* **102**, 5558–63.
- White P. J. (2012a) Ion Uptake Mechanisms of Individual Cells and Roots: Short-distance Transport. In *Marschner's Mineral Nutrition of Higher Plants* Elsevier Ltd. pp. 7–47.
- White P. J. (2012b) Long-distance Transport in the Xylem and Phloem. In *Marschner's Mineral Nutrition of Higher Plants* Elsevier Ltd. pp. 49–70.
- Wubbels J. K. (2010) Tree species distribution in relation to stem hydraulic traits and soil moisture in a mixed hardwood forest in central Pennsylvania. Master's Thesis, The Pennsylvania State University.
- Xu X., Shi J., Chen X., Chen Y. and Hu T. (2009) Chemical forms of manganese in the leaves of manganese hyperaccumulator *Phytolacca acinosa* Roxb. (Phytolaccaceae). *Plant and Soil* **318**, 197–204.
- Zayed J., Hong B. and L'esperance G. (1999) Characterization of Manganese-Containing Particles Collected from the Exhaust Emissions of Automobiles Running with MMT Additive. *Environmental Science and Technology* **33**, 3341–3346.

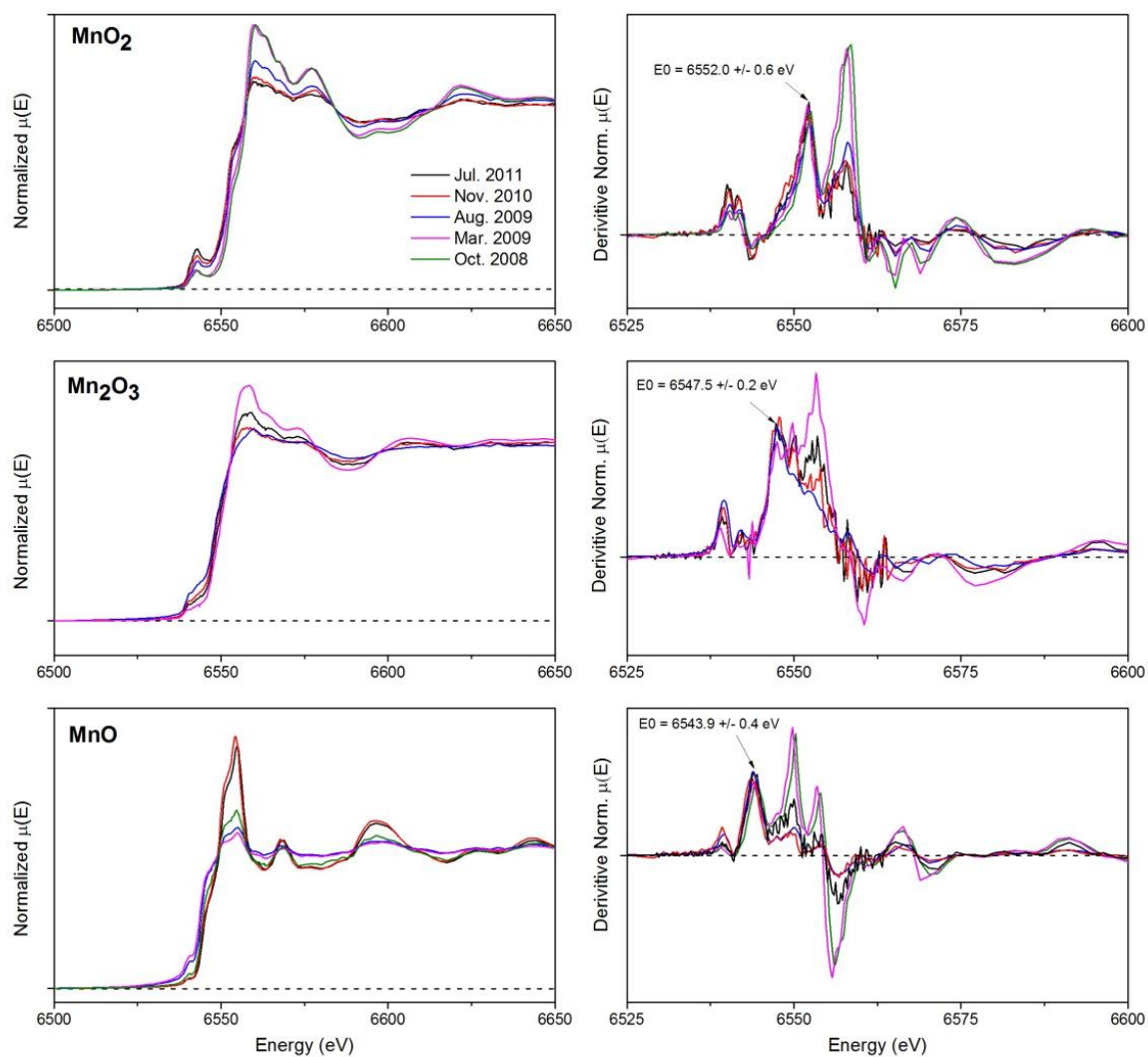


Figure 4-1. Left panels: Values for the absorption coefficient μ are normalized and plotted versus energy E (eV) for the manganese mineral standards MnO, Mn₂O₃, and MnO₂. **Right panels:** The derivative of each normalized $\mu(E)$ spectrum is plotted versus energy. The absorption edge energy (E_0) for each Mn-oxide standard was defined as the peak of the first derivative of $\mu(E)$, and the average and range of E_0 are indicated in each plot. An alignment of E_0 values for the MnO₂ standards was used to calibrate energies for all standard and sample spectra.

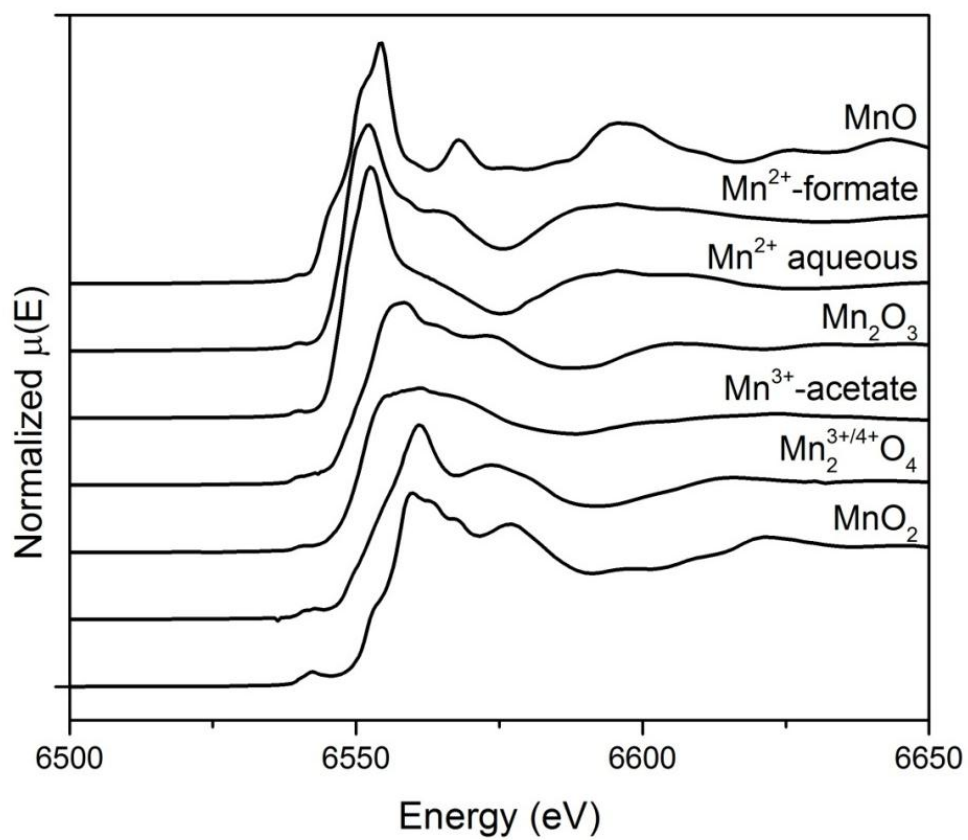


Figure 4-2. Spectra for Mn compounds used in the linear combination fits include four oxides (MnO , Mn_2O_3 , Mn_2O_4 , and MnO_2), two organic complexes (Mn^{2+} -formate and Mn^{3+} -acetate), and the divalent Mn cation dissolved in water (Mn^{2+} aqueous).

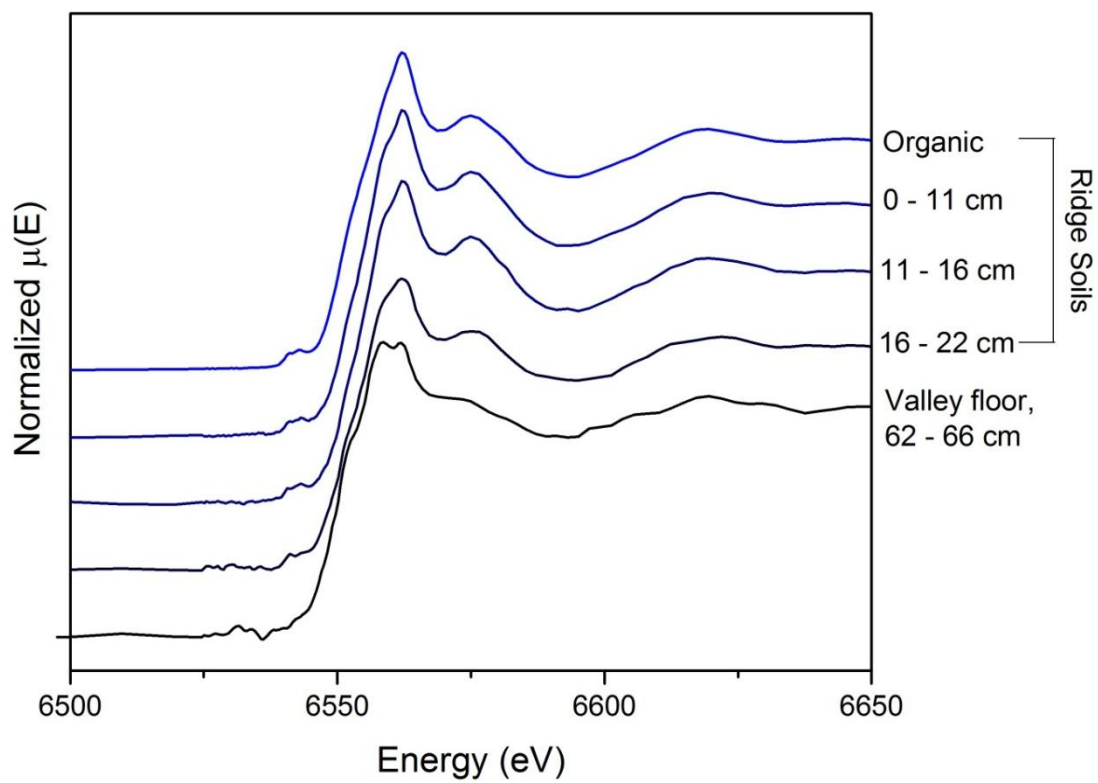


Figure 4-3. Mn K-edge XANES spectra for four bulk soil samples collected from a ridge soil core and one bulk soil sample collected from the soil-bedrock interface in a valley floor soil core.

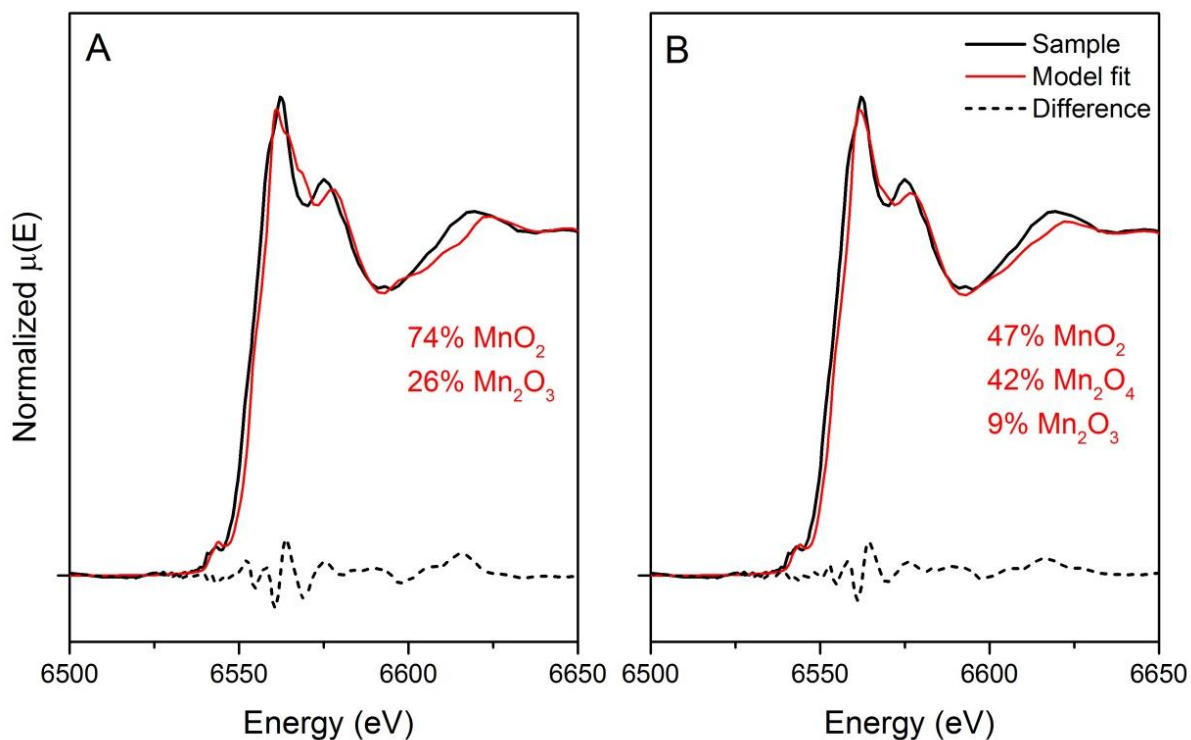


Figure 4-4. The XANES spectrum for a ground bulk soil sample collected from 11 – 16 cm depth in a SSHCZO ridge top soil profile (black line, core RT08) is plotted with model spectra from linear combination fits (red lines) and the difference between the sample and model fits (dotted line). **A)** Soil is adequately fit as 74% MnO_2 and 26% Mn_2O_3 ($R = 0.0021$), giving an average oxidation state of $\text{Mn}^{3.7+}$ in this sample. **B)** The addition of birnessite (Mn_2O_4) as a standard in the linear combination fit improves the model only slightly ($R = 0.0016$); however, the shape of the XANES spectra for all soil samples is visually more similar to birnessite than any other oxide in the model fits (Figure 4-2).

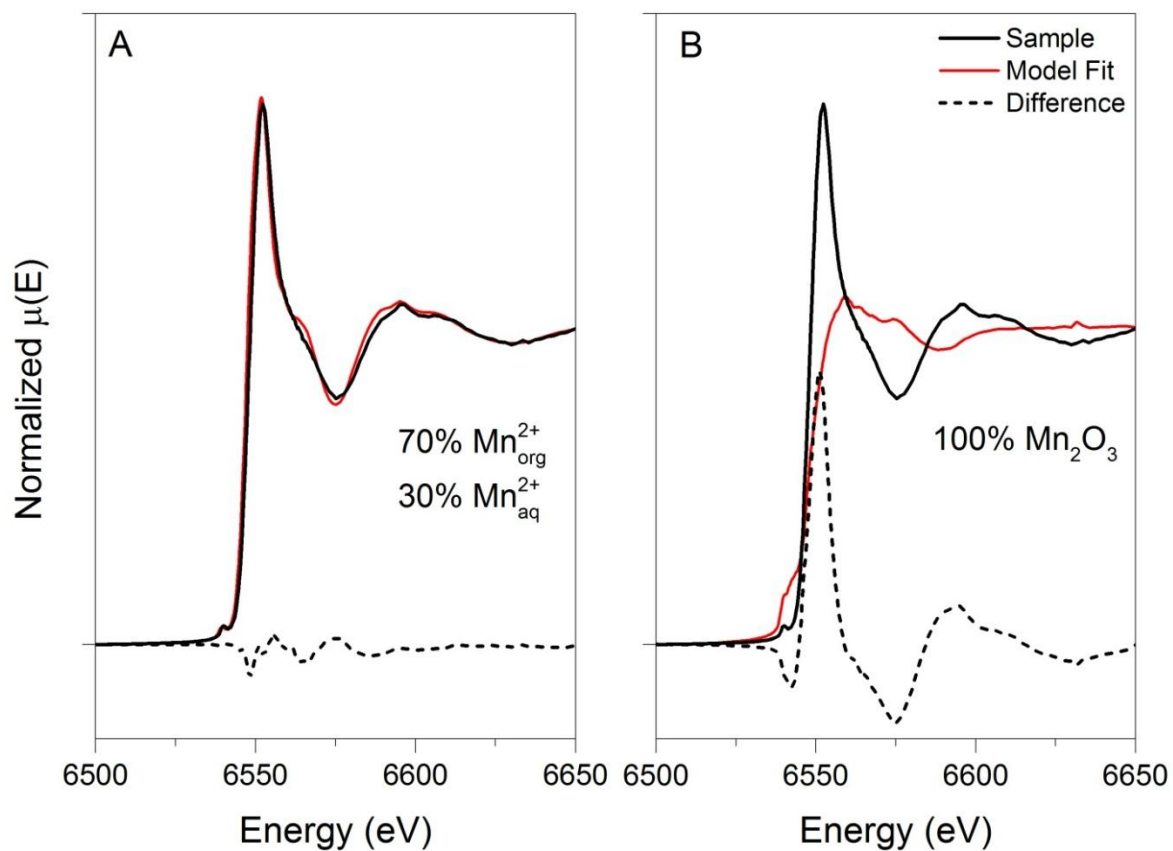


Figure 4-5. The XANES spectrum for a ground bulk leaf-litter sample (black line) is plotted with model spectra from linear combination fits (red lines) and the difference between the sample and model fits (dotted line). **A)** Leaf litter is adequately fit as 70% Mn^{+2} -formate and 30% aqueous Mn^{+2} (R-factor = 0.10%). **B)** Leaf litter is poorly fit by MnO , Mn_2O_3 , and MnO_2 and returns 100% similarity to Mn_2O_3 (R-factor = 11.6%).

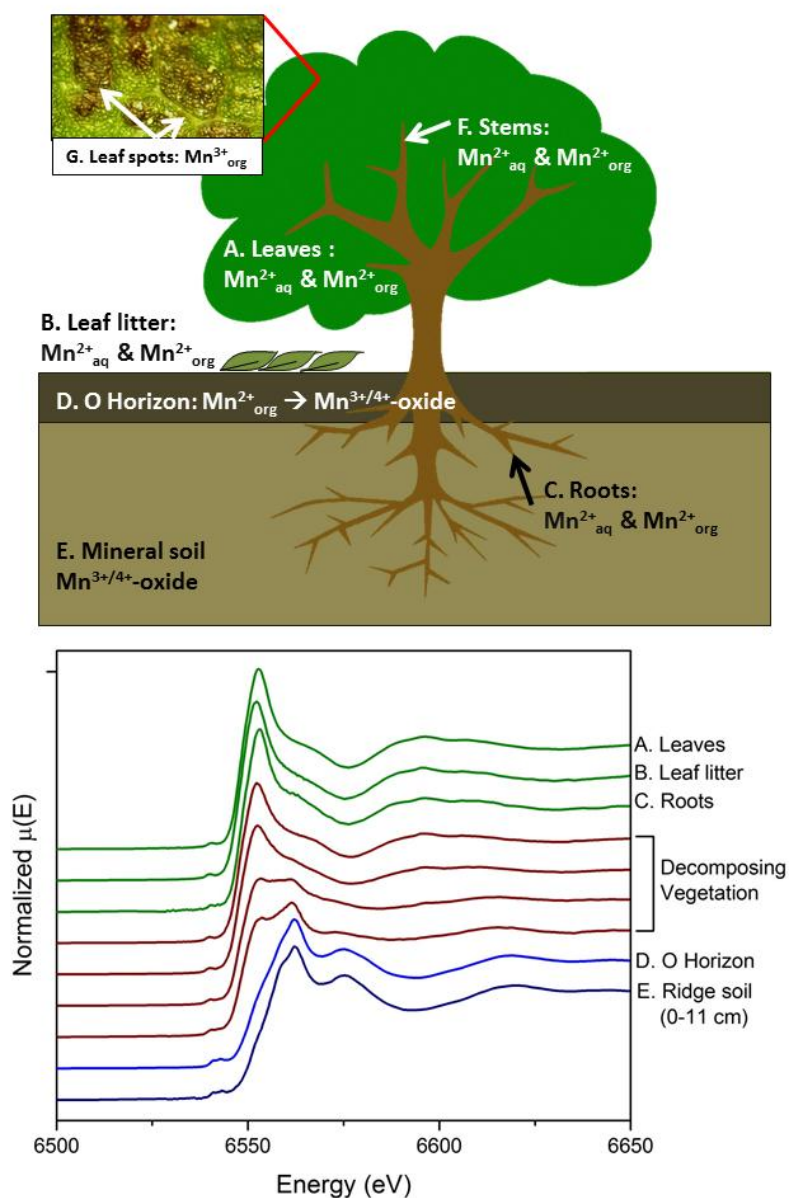


Figure 4-6. Upper: Diagram of the Susquehanna Shale Hills CZO plant-soil system with reservoirs that were analyzed in this study. We infer the dominant Mn components found in each reservoir using XANES spectra: A) Green leaves, B) Leaf litter, C) Tree roots, D) Organic horizon soil and decomposing vegetation; E) Mineral soil from the ridge top and valley floor, F) Tree stems, G) Dark spots on leaves. **Lower:** Spectra of normalized $\mu(E)$ for bulk soil and vegetation samples are stacked from top to bottom as fresh vegetation (green), decomposing vegetation (brown), and soil samples (blue) and exhibit the transition from samples dominated by organic and aqueous Mn^{2+} to samples with $Mn^{3+/4+}$ -oxides.

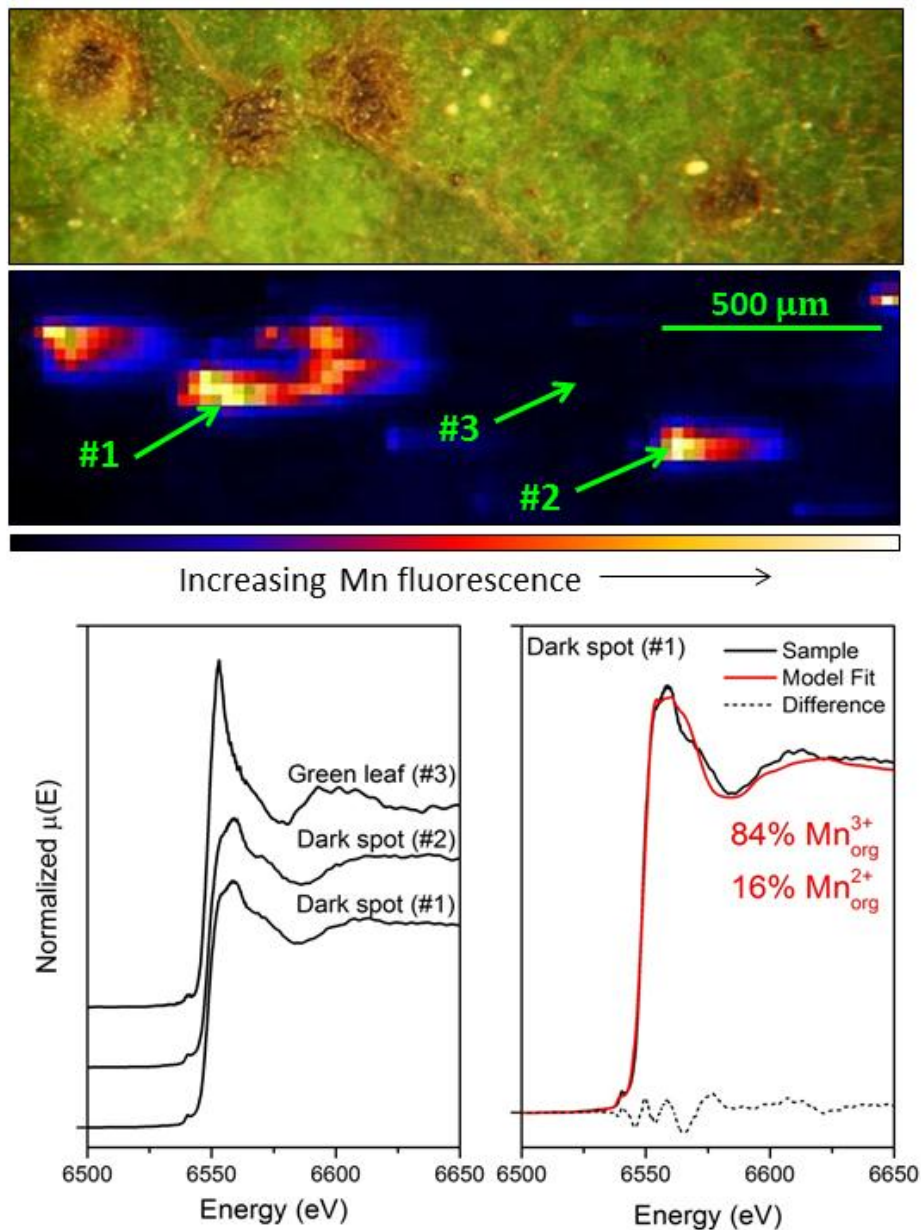


Figure 4-7. Top) Optical and corresponding XRF images of a leaf collected from a mature red oak at SSHCZO. In the XRF image, pixels with warm colors correspond to high Mn fluorescence values and indicate regions of high Mn concentration. Three spots (ROIs #1, 2 and 3) were chosen for μ XANES spectral analysis. **Bottom)** Spectra from two Mn-rich dark spots on foliage (ROI #1 and #2) are distinct from bulk vegetation samples (Figure 5) and a spectrum taken from the green leaf tissue (ROI #3). The model output of a linear combination fit (red) on ROI #1 (black) are most consistent with 16% Mn^{2+} -formate and 84% Mn^{3+} -acetate (R -factor = 0.09%). The difference spectrum is shown with the dotted black line.

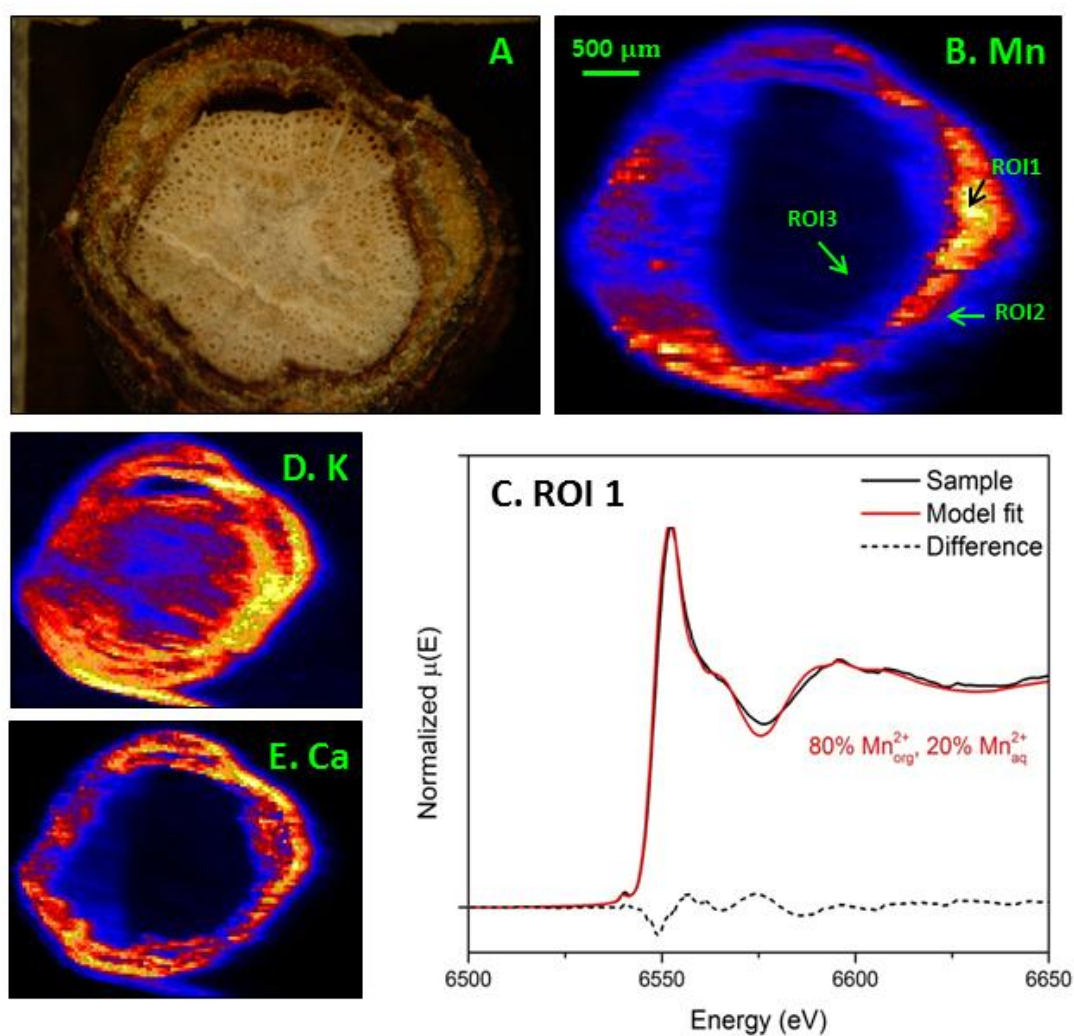


Figure 4-8. Cross-section of a stem (diameter = 4 mm) from a mature chestnut oak growing at SSHCZO. Mn is distributed heterogeneously across the map and is concentrated in the outer portion of the stem tissue, likely either phloem or cambium tissue. The inner xylem tissue, in comparison, contains low levels of Mn. The map is 4.5 x 4.5 mm with a 10 x 30 μm spot size. A) Optical image; B) XRF map of Mn; C) μXANES on ROI1; D) XRF map of K; E) XRF map of Ca.

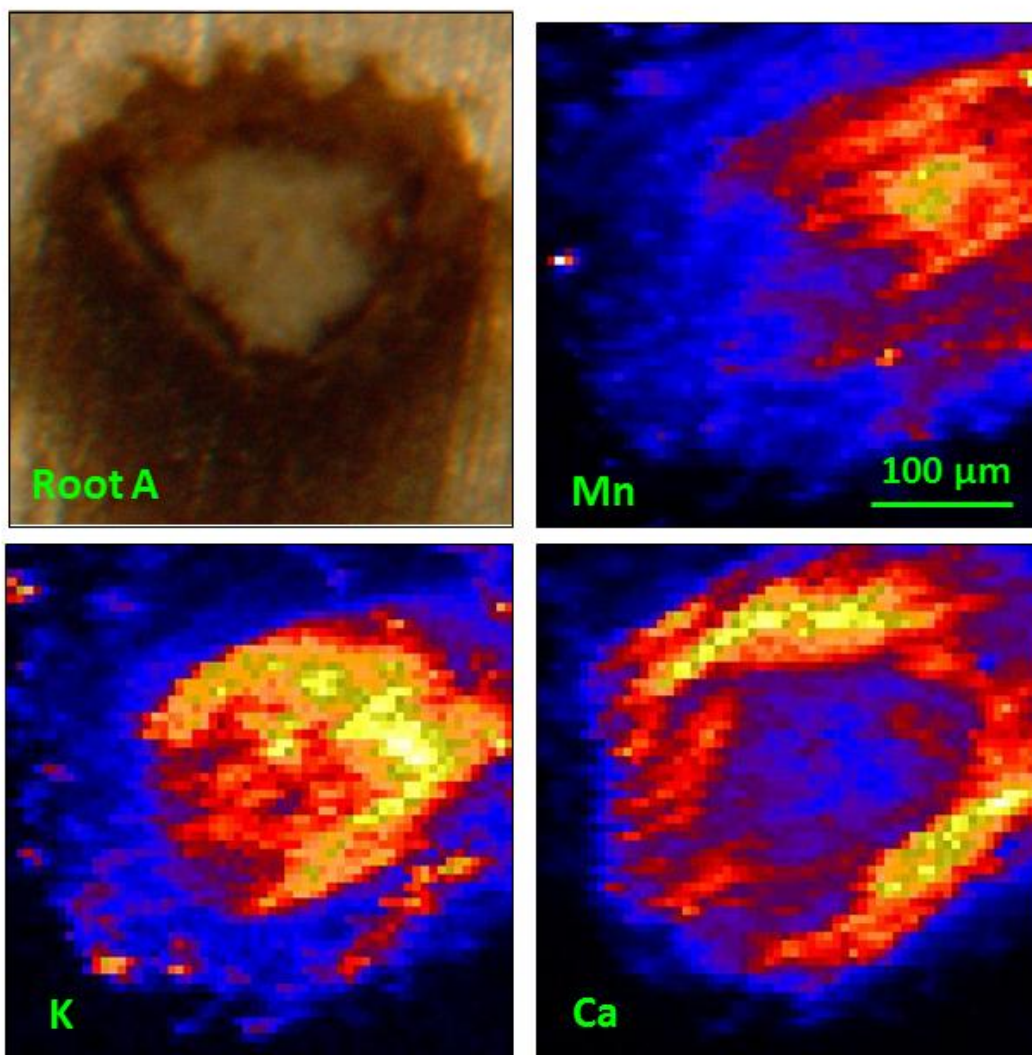


Figure 4-9A: Root A: cross-section of a fine root from a red oak seedling cut through right at resin surface. Map is 0.3 x 0.3 mm with 5 μm spot size. Mn is localized to a hot spot that correlates fairly well with K, indicating Mn is present in the inner portion of the root, whereas Ca is located in the outer portion of the root.

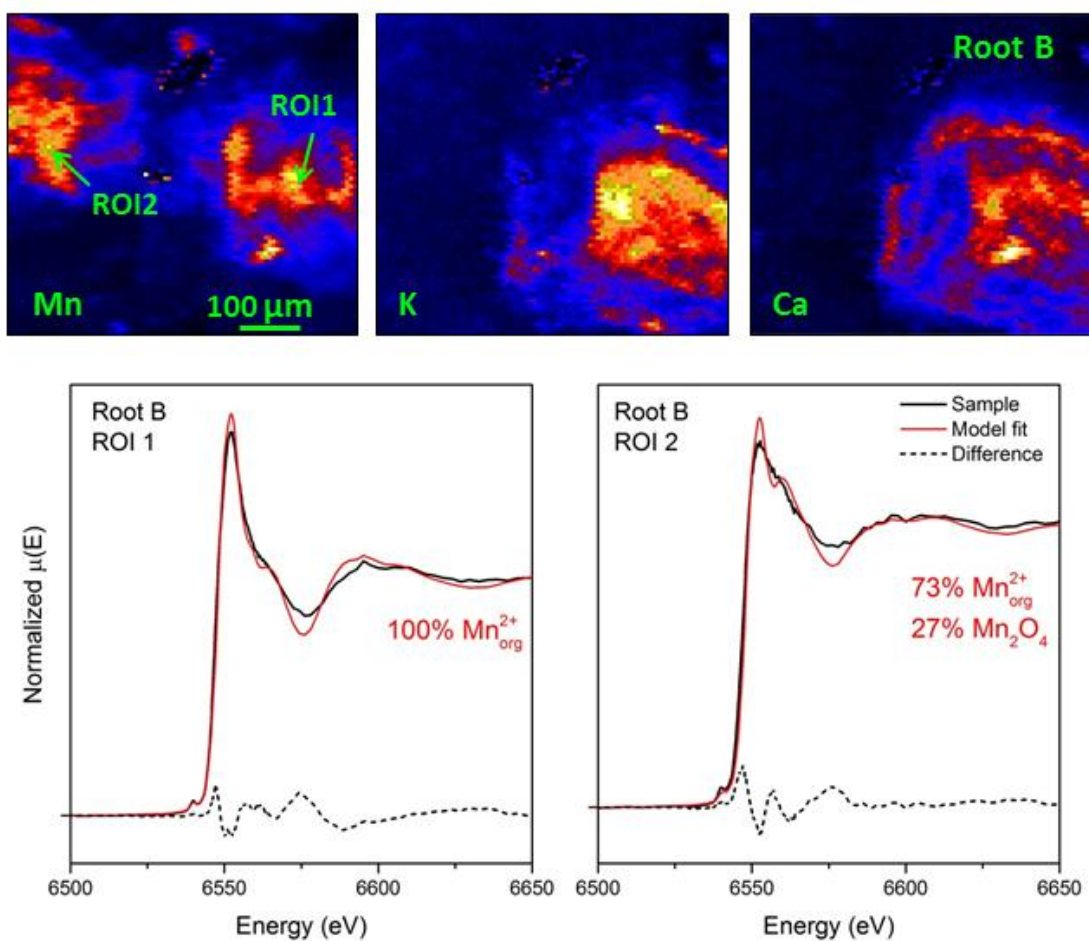


Figure 4-9B: Root B: Cross-section of a fine root embedded in LR White resin. The map is 0.45 x 0.40 mm with 5 μm step sizes. Mn is distributed heterogeneously across the sample. Maps of K and Ca clearly show the boundaries of the root cross-section. The Mn-rich region in the interior of the root is most consistent with 100% Mn-formate (R-factor = 0.22%). A Mn-rich region that does not correlate with other elements (ROI 2) is most consistent with 73% Mn-formate and 27% Mn_2O_4 (R-factor = 0.36%), although Mn-formate + MnO_2 yielded a similar fit (R-factor = 0.37%).

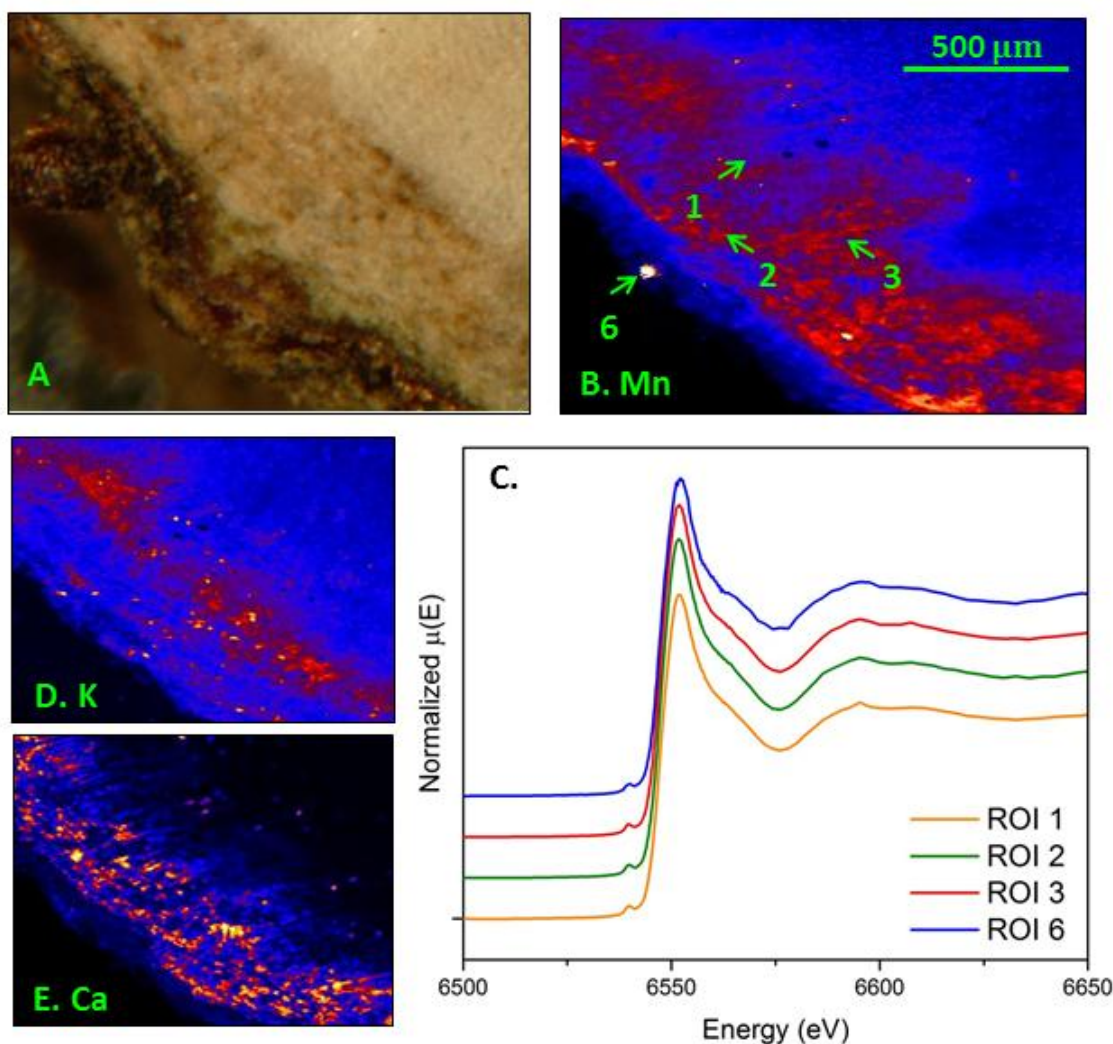


Figure 4-10. A. Edge of a cross-section of a large woody root (~8 mm diameter). Map is 1.6 x 1.2 mm with 5 μm spot size. B. Mn has a broad range ($\text{Mn}/I_0 = 0 - 1.69$) across the sample, although bright specks contain the highest levels of Mn (e.g. ROI #6) while most of the root tissue contains $\text{Mn}/I_0 < 0.8$. Mn is localized to the outer part of the root. C. Mn XANES spectra are similar in all measured parts of the roots. D. K is enriched in a band slightly more interior to the root than Mn and Ca. E. Ca is distributed similarly to Mn but more diffuse.

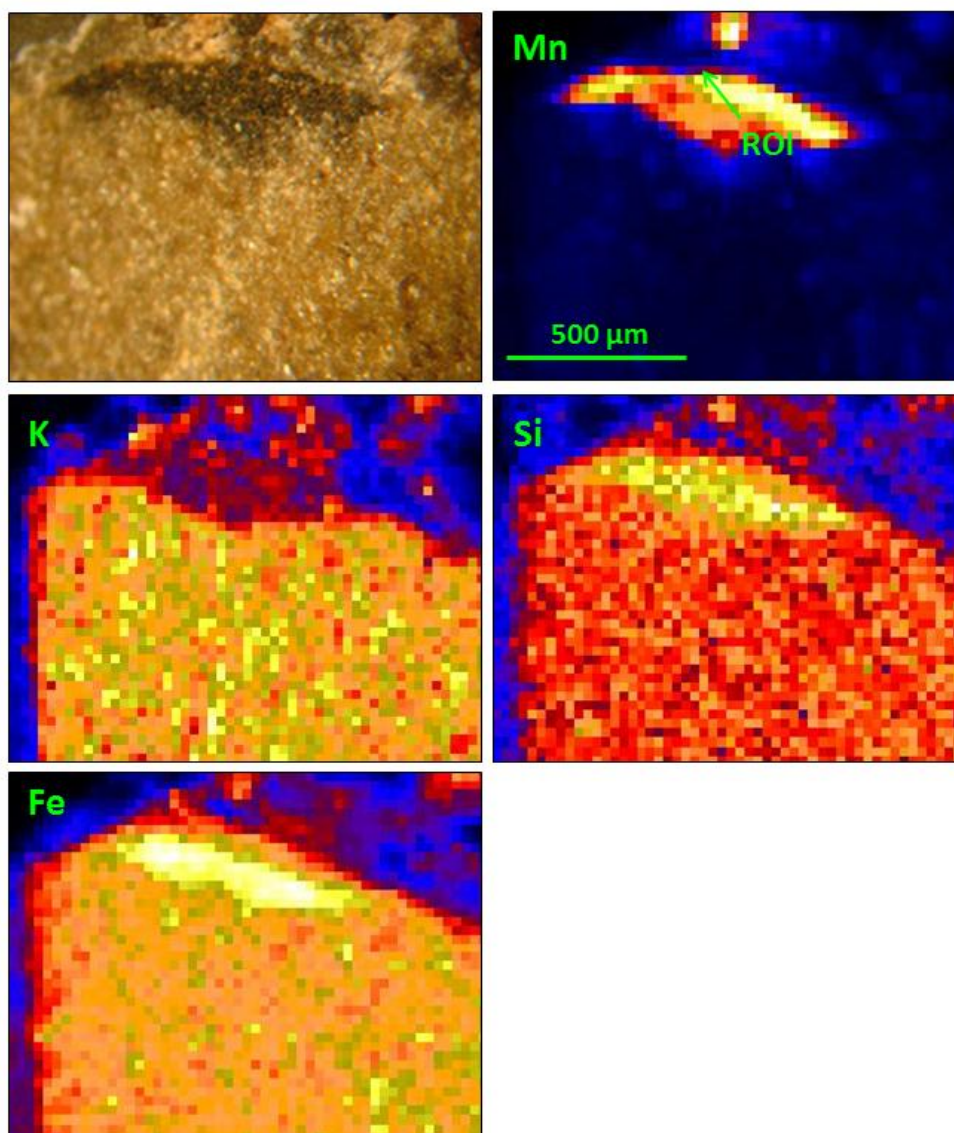


Figure 4-11A. A mineral soil grain embedded with LR white resin and cut with a slow saw. The map was collected over 1.5 mm x 1 mm with a 25 μm step size. Mn/I_0 ranges from 0.0 – 0.83 with a Mn-rich region correlating to black staining on a grain. The Mn-rich zone at the top of the grain is depleted in K and only slightly enriched in Fe and Si relative to the rest of the mineral grain.

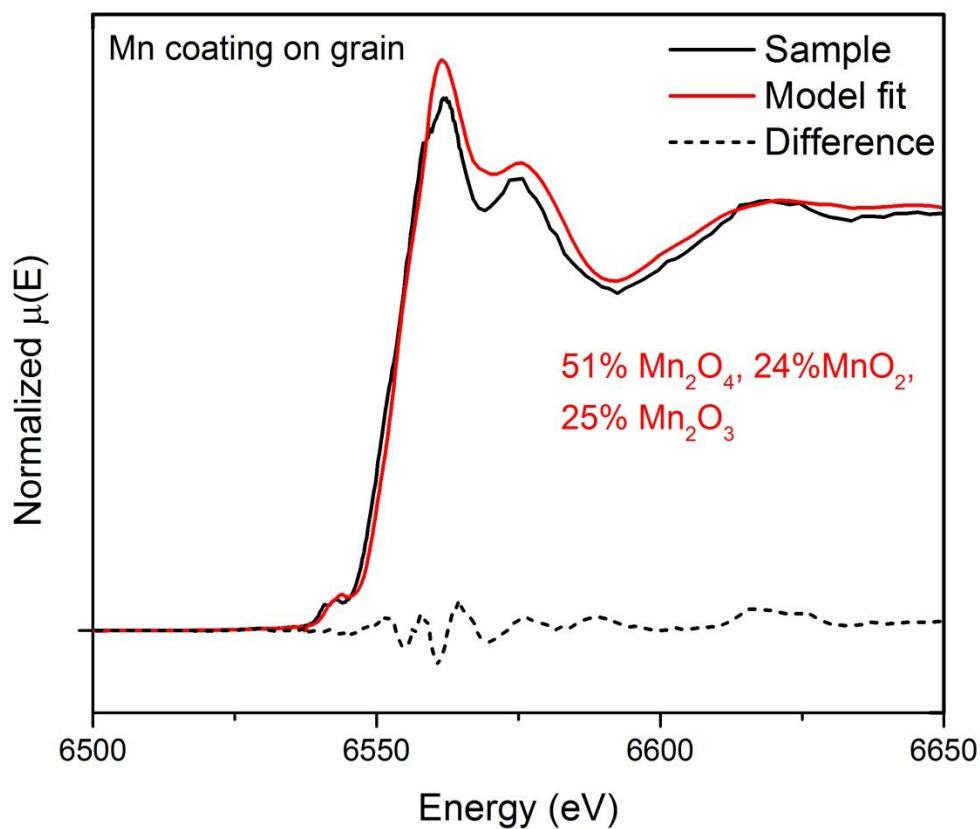


Figure 4-11B. A μ XANES spectrum (solid black line) obtained from a Mn-rich region on a mineral soil grain (Figure 11-A) is most consistent with a combination of $\text{Mn}^{3+}/\text{Mn}^{4+}$ -oxides (linear fit shown as solid red line), similar to the bulk soil. The difference between the sample and model spectra is shown as a dotted black line.

Table 4-1. Linear combination fits on soil and vegetation samples

^a Soil Samples	MnO (%)	Mn ₂ O ₃ (%)	Mn ₂ O ₄ (%)	MnO ₂ (%)	^c R-factor (%)
RT08, O Horizon	6 ± 2	3 ± 2	78 ± 12	14 ± 12	0.17 ± 0.01
RT08, 0-11 cm	1 ± 1	7 ± 6	49 ± 9	43 ± 4	0.18 ± 0.02
RT08, 11-16 cm	1 ± 2	9 ± 8	42 ± 9	47 ± 2	0.17 ± 0.02
RT08, 16-22 cm	9 ± 2	0 ± 0	77 ± 15	15 ± 13	0.27 ± 0.02
VF08, 62-66 cm	10 ± 2	53 ± 4	27 ± 23	10 ± 18	0.26 ± 0.03
^b Vegetation Samples	Mn(aq) (%)	MnC ₂ H ₂ O ₄ (%)			^c R-factor (%)
Root tissue (± 24%)	14	84	-	-	0.30 ± 0.25
Stem tissue (± 11%)	28	72	-	-	0.21 ± 0.02
Green leaves (± 35%)	29	71	-	-	0.37 ± 0.14
Leaf litter	31	70	-	-	0.11

^aPercentages for the soil samples are calculated as the standard deviation of each Mn-oxide's contribution in the best three fits of all combinations of fits

^bPercentages for the vegetation samples are calculated as the standard deviation in fits in samples within each category

^cR-factor (%) = $100 * \frac{\sum_i (\text{experimental} - \text{fit})^2}{\sum_i (\text{experimental})^2}$ where i = all data points in the fitting region.

Table 4-2. LCF of environmental samples using vegetation and soil end-members

Sample type (# samples)	%Vegetation	%Mineral Soil	R-factor (%)
Fresh foliage (3)	100 ± 0	0 ± 0	0.57 ± 0.40
Fresh roots (1)	96	4	0.18
Leaf litter (1)	100	0	0.08
Decomposing vegetation (7)	83 ± 21	17 ± 21	0.09 ± 0.09
Organic horizon soil (4)	10 ± 1	90 ± 1	0.26 ± 0.18
Mineral soil, 0-11 cm (1)	0	100	0.01

Chapter 5

Quantifying spatial variability in Mn transport from soils to rivers using data from the Shale Hills CZO

Abstract

Many soils are enriched in trace elements due to atmospheric inputs from industrial sources; however, little is known about how long these contaminants persist in soils or the rates that they are transferred into rivers. Modeling the movement of contaminants through the environment is complicated by the heterogeneity of soils and the variability of contaminant mobility across spatial scales. In this study, we use soil, water, and vegetation chemistry to examine the rates that Mn is mobilized from contaminated soils at ridge top, planar hillslope, swale hillslope, and watershed-scales in the Susquehanna Shale Hills Critical Zone Observatory (SSHCZO). Studies from the SSHCZO are compared to trends in long-term water quality measurements for the Susquehanna River Basin.

We find that Mn is leached more quickly from soils in hillslopes with convergent flow (swales) than soils on planar or broadly convex hillslopes; thus, swales are a large source of dissolved Mn to the stream. Area-normalized release rates of Mn from all soils are dwarfed by rates of uptake into vegetation, consistent with the hypothesis that trees temporarily slow the removal of atmospherically-deposited Mn from the soil by accumulating it in plant biomass. However, concentrations of dissolved organic carbon in pore waters correlate with Mn concentrations, documenting that organic matter enhances Mn release in the swales. As a result, vegetation decreases rates of Mn removal from soils but soil organic matter increases loss rates. Unlike the major rock-derived elements, high Mn fluxes in the stream occur in short pulses that only weakly respond to precipitation events. Thus, dissolved Mn loads in rivers are not solely driven by the hydrology but are strongly impacted by processes in the soil and stream bed. On an area-normalized basis, current release rates of Mn from the Shale Hills watershed are consistent with rates estimated for the Susquehanna River Basin (SRB). Although we have no data for decadal variations in Mn fluxes from SSHCZO, the SRB shows a decline in riverine Mn fluxes from the 1950s to the present. Current Mn fluxes in the SRB are consistent with weathering losses from residual soil as exemplified by SSHCZO today, but Mn fluxes documented in the SRB in the past are more consistent with weathering losses from atmospherically-derived Mn-oxide contaminants. We propose that rates of Mn weathering in the past reflect rapid leaching of Mn

contaminants that declined as inputs of Mn decreased, leaving more recalcitrant Mn species in the soil.

I. Introduction

Many soils in industrialized regions are contaminated with manganese due to inputs from atmospheric deposition (Herndon et al., 2011). Mn can be emitted to the atmosphere as a byproduct of industrial processes including steel manufacturing, fossil fuel combustion, and refuse incineration (National Research Council, 1973; Nriagu and Pacyna, 1988; Pacyna and Pacyna, 2001). Mn enrichment in air and soils has been observed in the near vicinity of ferroalloy plants and roadways (Lytle et al., 1995; Boudissa et al., 2006; Lucchini et al., 2007), but only recently established to be widespread in soils over broad but patchy regions (Herndon et al., 2011). Consistent with broad geographic distribution of Mn, it has been documented that, although coarse Mn-bearing particles fall out of the atmosphere near their source, fine Mn-rich particles or Mn dissolved in rain can disperse across great distances (Rahn and Lowenthal, 1984; Parekh, 1990; Buck et al., 2010).

Excess Mn in the air, soils, and water can have negative impacts on humans and ecosystem quality. Manganism is a well-documented neurological disorder that can develop from chronic exposure to respirable Mn. The majority of reported manganism cases and manganism precursor symptoms involve workplace exposure, e.g. in welding, mining, and alloy production (U.S. Environmental Protection Agency, 1984; Mergler et al., 1994; Dobson et al., 2004); however, similar symptoms of nervous system dysfunction have been detected in communities living near Mn point sources (Lucchini et al., 2007; Solís-Vivanco et al., 2009; Kim et al., 2011). Additionally, Mn exposure through air and water has been implicated in intellectual impairment and manganism symptoms in children (Riojas-Rodríguez et al., 2010; Wasserman et al., 2011; Khan et al., 2012).

In plants, Mn toxicity initially presents as black spots on cellular tissue that contain oxidized Mn and progresses to leaf chlorosis and cell deformity (Horiguchi, 1987; McQuattie and Schier, 2000). Excess Mn may induce toxicity by increasing production of superoxides in leaf tissue, leading to oxidative stress (Gonzalez et al., 1998; St. Clair et al., 2005). High levels of foliar Mn have been reported in tree species throughout the northeastern United States, leading to the decline of Mn-sensitive sugar maple populations (Horsley et al., 2000; St. Clair and Lynch, 2005; Kogelmann and Sharpe, 2006). In addition to potential toxicity effects, high foliar Mn may increase rates of late-stage litter decomposition, impacting carbon storage in soils (Berg et al., 2007).

Various researchers have noted the important role vegetation plays in the biogeochemical cycling of Mn (Shanley, 1986; Jobbagy and Jackson, 2001; Heal et al., 2002, Scudlark et al., 2005; Navrátil et al., 2007, Li et al., 2008; Landre et al., 2010). In particular, vegetation can significantly redistribute Mn in the soil within a few decades. A primary example of this is demonstrated by the ability of eucalyptus trees to rapidly mobilize and accumulate Mn, leading to enrichment of Mn near the soil surface and depletion of Mn in the subsurface (Jobbagy and Jackson, 2004). In another study, the transition from cultivated cotton fields to a mature pine forest resulted in significant transfer of Mn from the mineral soil to the standing biomass and organic horizon (Li et al., 2008). Mineral weathering could not replace the transferred Mn, and the soil became Mn depleted.

Changes in elemental and mineralogical composition with depth in soils can be used to decipher chemical and physical processes that have occurred during soil formation. Depth profiles of normalized element concentrations can be sorted into five end-member profiles: depletion, addition, depletion-enrichment, biogenic, and immobile (Brantley and Lebedeva, 2011). Depletion profiles are characterized by net loss and addition profiles are characterized by net addition of a constituent in the soil relative to its parent. Mass translocation can be represented by an enrichment-depletion profile, in which an element is mobilized from surface horizons and reprecipitated at depth, or a biogenic profile, in which an element is depleted at depth due to biological uptake and enriched at the surface due to inputs from vegetation. An immobile constituent experiences neither mass loss nor gain during soil formation. Numerous researchers provide models that use depletion profiles to quantify regolith weathering (Brimhall and Dietrich, 1987; Chadwick et al., 1990; Anderson et al., 2002; Riebe et al., 2003; Jin et al., 2010, Brantley and Lebedeva, 2011), while fewer studies model addition profiles to quantify atmospheric inputs to soils (Chadwick et al., 1999; Kurtz et al., 2001; Porder et al., 2007; Herndon et al., 2011). At the Shale Hills CZO, Mn exhibits a strong addition profile due to past inputs from atmospheric deposition (Herndon et al., 2011); however, nutrient uplift by trees may aid in Mn retention in the soils (Jobbagy and Jackson, 2004).

Annual fluxes of Mn through plant biomass, estimated by measuring litterfall and throughfall inputs to soils, often exceed inputs to and outputs from watersheds when compared on an area-normalized basis (Scudlark et al., 2005; Watmough et al., 2007; Navrátil et al., 2007; Landre et al., 2010). Throughfall is enriched in Mn relative to precipitation due to leaching of Mn from foliar tissue during rain events (Shanley, 1986; Scudlark et al., 2005; Navrátil et al., 2007; Landre et al., 2010). In some environments, storage of Mn in the organic horizon may provide a pool of

bioavailable Mn that can be used by vegetation to compensate for a lack of readily weatherable Mn-bearing minerals in the subsurface (Shanley, 1986). In such environments where fluxes of Mn through vegetation exceed inputs from weathering, leakage of Mn from the biotic cycle rather than directly from mineral weathering may contribute heavily to outputs in rivers (Navrátil et al., 2007; Landre et al., 2010).

The organic horizon can act as a sponge for aqueous Mn that is input to soils as throughfall or precipitation, and Mn mobility can be reduced by adsorption to solid phase organic matter (Shanley, 1986; Navrátil et al., 2007). In one study, adsorption of Mn to organic matter was thought to buffer Mn concentrations in a stream, and Mn concentrations were observed to vary little over a wide range of discharge values (Shanley, 1986). In contrast, disturbance of the organic horizon can send pulses of Mn into stream waters. For example, accumulation of atmospherically-derived sulfate during the dry season can enhance mobilization of Mn from the organic horizon during the wet season (Watmough et al., 2007). Increased rainfall and decomposition of organic matter in the fall can lead to flushing of aqueous Mn or organic Mn-complexes (Heal et al., 2002; Andrews, 2011).

High concentrations of dissolved Mn in soil pore fluids are often attributed to extremely low soil pH, particularly related to mineral rather than organic acidity (Shanley, 1986; Watmough et al., 2007; Navrátil et al., 2007); however, high concentrations of dissolved organic carbon may also contribute to Mn mobilization (Andrews, 2011). Regardless of whether Mn is directly complexed by dissolved organic carbon, organic-rich soils can act as a prominent source of Mn to rivers (Heal et al., 2002; Watmough et al., 2007, Landre et al., 2010).

Here, in comparison to previous studies, we examine biogeochemical Mn processes at multiple spatial scales and quantify rates of Mn losses from soils and uptake into vegetation in one small, well-studied catchment. It is our objective to predict the timescales over which Mn contamination is retained in soils and transported into rivers. We furthermore quantify the impact of environmental factors, including vegetation, soil chemistry, and landscape position, on the long-term mobility of Mn contaminants in soils.

II. Methods

2.1. Susquehanna Shale Hills Critical Zone Observatory

The Susquehanna Shale Hills Critical Zone Observatory (SSHCZO) is a 7.9-ha first-order catchment located in central Pennsylvania nested within the Juniata and larger Susquehanna River watersheds. The SSHCZO watershed is underlain almost exclusively by the Silurian-age Rose Hill

Formation, an oxidized, organic-poor marine shale that extends throughout the Appalachian region. A drill core of Rose Hill shale was obtained from the north ridge of the catchment and determined to contain dominantly illite, “chlorite” (a mixture of chlorite, vermiculite, and hydroxyl-interlayered vermiculite phases), and quartz minerals with trace amounts of feldspar and Fe-oxides (Jin et al., 2010). In this study, we use the average chemical composition of the Rose Hill Shale reported in Jin et al. (2010) as the composition of the parent material for all soils.

SSHCZO is V-shaped and oriented in an east-west direction with north- and south-facing slopes. Elevation ranges from 256 m at the stream outlet to 310 m on the ridge. Annual precipitation in the Shale Hills region is $\sim 100 \text{ cm y}^{-1}$, and rainwater is acidic (2000 – 2010 average pH = 4.4) and enriched in nitrate and sulfate (NADP, 2011). Soils in the catchment are thin and well-drained at the ridges ($< 0.5 \text{ m}$) and thicken downslope towards the stream ($< 3 \text{ m}$). The catchment is characterized by planar hillslopes with seven distinct depressions (swales) experiencing convergent flow and containing deep soils (Lin et al., 2006). While soils on the convex-upward hillslopes are well-drained and oxic, soils in the valley and river channel experience seasonal water saturation and exhibit redoximorphic features that suggest periodic reducing conditions (Lin and Zhou, 2008). A depth-averaged value for soil bulk density ($= 1,520 \text{ kg m}^{-3}$) was previously calculated for SSHCZO soils (Herndon et al., 2011) using reported data (Lin, 2006; Jin et al., 2010).

Soil production rates are high at the ridges ($\sim 45 \text{ m My}^{-1}$) and decrease exponentially downslope ($\sim 15 \text{ m My}^{-1}$), yielding soil residence times (6 – 45 kyr) that are consistent with stripping of regolith material from the ridges during the periglacial climate during the last glacial maximum (ca. 15 kya) and storage of some of this regolith in the swales and valley floor (Ma et al., 2010). In the soils, illite and “chlorite” weather to form vermiculite and kaolinite minerals, resulting in the loss of soluble cations (e.g. Mg and K) and fine particles containing Al and Fe (Jin et al., 2010). Additionally, carbonate and feldspar weathering fronts are observed $> 20 \text{ m}$ and $0 - 6 \text{ m}$ below the soil-bedrock interface respectively. On the planar hillslopes, chemical weathering rates decrease from the ridges to the valley and some elements (e.g. Al, Si) show net accumulation in the valley floor (Jin et al., 2010). Elemental depth profiles are complex in the midslope and valley positions in swales relative to the planar hillslope and are consistent with the accumulation of colluvial sediments (Jin and Brantley, 2011).

Stream response to precipitation forcing is rapid, and stream flow peaks within one day of a major precipitation event (Lin et al., 2006). Water flows preferentially through macropores and is transported downslope at the interface of the A-B horizons and the soil-bedrock layers (Lin et al.,

2006; Jin et al., 2011). In dry periods, precipitation may penetrate to the fractured bedrock through macropores before it infiltrates the soil column itself due to hydrophobicity of the organic horizon (Lin and Zhou, 2008). Pore water chemistry is consistent with relatively long residence times for water in the A and B horizons where clay dissolution occurs (Jin et al., 2011). Solutes that are dissolved from the clays in those horizons diffuse or percolate into water that is advecting through the horizon interfaces, and the advecting water is transported quickly downslope and into the stream. Pore fluids in swales exhibit low pH and high concentrations of both dissolved organic carbon (DOC) and metals (Fe, Al, Mn) relative to fluids collected from lysimeters along planar hillslopes. Indeed, Mn concentrations are correlated with DOC concentrations in soil pore fluids, and the formation of metal-organic complexes has been suggested as a mechanism for metal mobilization from the soils (Andrews, 2011).

The Shale Hills watershed has experienced several natural and anthropogenic perturbations during soil formation. First, the area shows evidence of disturbance (e.g. freeze-thaw, stratified slope deposits) consistent with a periglacial climate that was present in the region ~15 kya (Gardner et al., 1991). Central Pennsylvania was also extensively cut for timber during colonial times and SSHCZO was most recently harvested in the 1930s (Wubbels, 2010). Finally, numerous ruins of iron furnaces are located within 20 miles of the field site. Soils at SSHCZO retain metals deposited from the atmospheric deposition of particulates released to the atmosphere during iron smelting at these sites, as well as other industrial byproducts (Herndon et al., 2011).

2.2. Field methods

2.2.1. Soil

Soil cores were obtained from ridge top, midslope, and valley floor positions along planar and swale catenas on the south slope (Figure 5-1): these six sites are identified as SPRT (south planar ridge top), SPMS (south planar midslope), SPVF (south planar valley floor), SSRT (south swale ridge top), SSMS (south swale midslope), and SSVF (south swale valley floor). In previous work, these soil cores were used to characterize physical and chemical weathering processes at SSHCZO (Ma et al., 2010; Jin et al., 2010; Jin and Brantley, 2011). Additional cores (n = 21) were sampled at multiple locations along the catchment ridge (Herndon et al., 2011) and at midslope (n = 4) and valley (n = 5) locations. Soil chemistry for soil cores are reported in the literature (Jin et al., 2010; Jin and Brantley, 2011; Herndon et al., 2011) and in an online database (Niu et al., 2011). At some sites, organic horizon samples (n = 9) were collected by hand from the soil surface prior to augering. Soil cores were excavated with a stainless steel auger (2 inch diameter) to point of refusal, the depth at which it was impossible to manually auger further and a good approximation of

the soil-bedrock interface. Each core was sampled in ~5-10 cm depth intervals with the top of mineral soil = 0 depth, and ending at the soil-bedrock interface. Given this sampling methodology, our definition here for “soil” is all material that could be sampled with a hand auger.

2.2.2. Water

Soil pore fluid samples ($n = 879$) were collected between 2006-2009 from suction lysimeters (48 mm diameter, SoilMoisture 1900 series, Soil Moisture, Inc.) installed at the ridge, midslope, and valley floor locations from which soil cores were augered (Figure 5-1). Additional water samples ($n = 389$) were collected in 2008 and 2009 from ridge, midslope, and valley floor locations in swale and planar transects on the north slope. Methods of lysimeter installation and water collection and results of chemical characterization for these samples have been previously described (Andrews et al., 2011; Jin et al., 2011). Briefly, the lysimeters were installed at 10 or 20 cm depth intervals from the soil surface down to the point of auger refusal. Samples were collected approximately biweekly during wet periods when sufficient soil moisture was available. Samples were obtained by pulling vacuum (-0.5 bar) to draw water into the lysimeters, and subsequently collecting the water with a syringe and plastic tubing. The syringe apparatus was rinsed with approximately 5 mL of water from the lysimeter being sampled before collecting additional samples for chemical analyses. The porous ceramic cups of the lysimeters have a maximum pore size of 1.3 μm , so pore fluid samples were not further filtered after collection. Test filtration (0.45 μm) on a subset of water samples yielded no significant difference in water chemistry (Jin et al., 2011). Water samples were transferred into pre-cleaned plastic bottles. Samples for cation analysis were acidified with 2-3 drops of concentrated nitric acid.

Stream water samples ($n = 345$) were collected into acid-washed plastic bottles by a Teledyne ISCO 3700C auto-sampler at the catchment weir during 2008-2010. These samples were subsequently filtered (0.45 μm) into secondary sample bottles in the field. Fifteen additional samples were collected by hand over the same time period by using a syringe to pull water from the stream and filtering the water into sample bottles. Samples for cation analysis were acidified with 2-3 drops of concentrated nitric acid. Stream water sampled in 2010 ($n = 45$) was not included in models of annual dissolved loads because data were only available for April – June.

Discharge data at the stream weir has been reported at 10 min intervals for each day in this period ($n = 144$ per day; (Duffy, 2012)). Daily discharge rates were calculated as the average of 144 instantaneous discharge measurements for each day. Over 2008-2009, daily discharge at the outlet weir averaged $113 \pm 10 \text{ m}^3 \text{ d}^{-1}$ and ranged from 0 to $4,160 \text{ m}^3 \text{ d}^{-1}$, with zero flow occurring primarily in summer months and high flow following precipitation events in early spring and late

fall. Stream samples were collected on days with discharge $< 484 \text{ m}^3 \text{ d}^{-1}$, a range which is observed ~96% of the year but does not capture 38% of the annual flow volume. Specifically, high flow events in December – March were not sampled due to the potential for the ISCO sampler to freeze during these time periods.

Precipitation samples ($n = 61$) were obtained from the National Atmospheric Deposition Program (NADP) which collected the samples in 2002 at sites PA-42 and PA-15 located 2.5 km and 14.5 km from SSHO. Precipitation samples were collected in plastic buckets, and samples of the distilled water used to rinse the buckets were analyzed to determine potential trace metal contamination.

2.2.3. Vegetation

A survey of dominant vegetation has been completed in the catchment for the coordinates, elevation, height, diameter at breast height (DBH, measured at 1.3 m height from ground), and species of each tree in the watershed with $\text{DBH} > 20 \text{ cm}$ ($n = 2,058$) (Figure D-1). Details of the survey are provided in Wubbels (2010). Oak species, the dominate catchment vegetation, comprise 63% of the total basal area of the forest (Wubbels, 2010). Additional important genera include hemlock (16%), hickory (13%), pine (8%), and maple (5%).

Upper canopy leaves were sampled from six tree species (*Quercus prinus*, QUPR – chestnut oak; *Q. alba*, QUAL – white oak; *Carya tormentosa*, CATO – mockernut hickory; *C. glabra*, CAGL – pignut hickory, *Pinus strobus*, PIST – eastern white pine; and *P. virginiana*, PIVI – Virginia pine) multiple times from June – September 2009 and two tree species (*Q. prinus* and *Acer saccharum*, ACSA – sugar maple) from June – September 2011 (Figure D-2; Table D-5). These species represent 82% of all surveyed trees. Leaves were obtained by rope climbing the trees and using a pole cutter to remove a section of the tree branch. The leaves were placed in plastic sample bags, transported to the laboratory, then immediately air-dried to prevent decomposition. No systematic differences in foliar chemistry were observed between leaves that were rinsed with deionized water relative to leaves that were not rinsed (Table D-6).

Litter traps were placed at 35 locations throughout the catchment in August 2011 (Figure D-3; Table D-7). The traps consisted of plastic trays (0.172 m^2) that were lined with hardware cloth to capture litter while allowing water to drain through four holes drilled in the bottom of the tray. The traps were installed at a height of 15 to 30 cm off the ground surface by leveling the tray on PVC pipe that was hammered into the ground. Litter was collected once per week between August 31 and November 28, 2011 and weighed for total and species-specific mass by L. Smith. Subsets of

bulk litter samples were retained for chemical analysis from litter collected August 31 (9 sites), October 3 (17 sites), and October 31 (9 sites) (Table D-8).

2.3. Laboratory methods

2.3.1. Soils

To determine the total concentration of major elements in soils, representative air-dried bulk samples that included all rock fragments, sand, silt, and clay particles at each depth were ground to pass a 100-mesh sieve ($< 149 \mu\text{m}$), fused with lithium metaborate at 950°C , and dissolved in 5% nitric acid for analysis on a Leeman Laboratories PS3000UV inductively coupled plasma atomic emission spectrophotometer (ICP-AES) at Penn State's Materials Characterization Laboratory. To determine the total concentration of trace elements in soils, ~ 100 mg of each ground soil sample underwent complete hot acid digestion in ultrapure concentrated HF and HNO_3 . The acid digest solutions were analyzed for trace elements on a Thermo X-Series II Quadrupole inductively coupled plasma mass spectrometer (ICP-MS) at Penn State. Complete chemical characterization of soils from the planar and swale transects is reported elsewhere (Jin et al., 2010; Jin and Brantley, 2011).

2.3.2. Water

Water samples were acidified with ultrapure concentrated nitric acid in the field and analyzed for cation concentrations on ICP-AES (pore fluid and stream samples) or quadrupole ICP-mass spectrometry (precipitation). Anion concentrations were measured in non-acidified water samples with a Dionex ion chromatograph at Penn State University. Four out of 664 soil pore fluid samples from the south slopes were identified as outliers for Mn and removed from the dataset. Out of the 360 days where stream water chemistry is available, 97 days have zero discharge and are excluded from the dataset (Table D-4). Of the 263 remaining samples, 131 have Mn concentrations below the detection limit for ICP-AES ($\text{DL} = 0.09 \mu\text{mol L}^{-1}$), leaving 49% of the dataset censored (Table D-3). A value of one half the DL ($= 0.045 \mu\text{mol Mn L}^{-1}$) is used in place of censored values for calculations.

2.3.3. Vegetation

The digestion procedure for plant material (green leaves and leaf litter) was adapted from Hokura et al. (2000). First, dried leaf samples were ground in liquid nitrogen with a ceramic mortar and pestle. Approximately ~ 150 mg of ground sample was precisely weighed and transferred to acid pre-cleaned Teflon vessels. Additionally, three replicates of a peach leaf standard (NIST 1547) and three empty Teflon vessels were included in each digestion set. All subsequent steps were performed in a metal-free clean laboratory.

First, 2.5 mL of 70% ultrapure HNO_3 were pipetted into each vessel and the solutions were allowed to react at room temperature overnight. After adding an additional 2.5 mL HNO_3 , the vessels were heated at 130°C for 1 hour, then at 200°C for 2 hours. The vessels were allowed to cool, then 1 mL ultrapure H_2O_2 (30%) and 0.1 mL ultrapure HF (60%) were added to each solution, and the vessels were heated for 2 hours at 180°C. Then, if particles were visible in solution, the vessels were heated and additional acid was added until all particles were dissolved.

Once the solutions were fully digested and allowed to cool, 2 mL of HNO_3 were added to each vessel. The contents of each vessel were then transferred into pre-weighed, pre-cleaned 250 mL Nalgene bottles. The vessels were rinsed 3 times with ultrapure deionized water into the bottle to ensure full transfer of all contents. The acid digests were diluted with ~200 mL ultrapure deionized water to dilute the HNO_3 to ~2%. The mass of added water was precisely weighed. Due to variability in the surface temperature of the hot plate, all reported temperatures are approximate. For samples collected in 2011, HF was eliminated from the procedure for safety precaution and due to potential damage to instrument parts.

Digest solutions were run by ICP-MS at Penn State using appropriate calibration curves. Method standards and blanks were included in each sample set to assess potential contamination, bias, and efficiency of the acid digestion procedure.

III. Results

3.1. Soil chemistry

Average Mn concentrations in weathered soil material ($C_{Mn,w}$; mmol kg^{-1}) collected from all depths in all sampled soils at SSHCZO are high in ridge ($= 44 \pm 4 \text{ mmol kg}^{-1}$, $n = 120$), slope ($= 23 \pm 3 \text{ mmol kg}^{-1}$, $n = 46$), and valley soils ($= 21 \pm 2 \text{ mmol kg}^{-1}$, $n = 91$) relative to the parent shale ($C_{Mn,p} = 15 \pm 2 \text{ mmol kg}^{-1}$) (Table 5-1; (Jin et al., 2010; Niu et al., 2011)). Additionally, high Mn concentrations were measured for the organic horizon in nine soils ($C_{Mn,org} = 229 \pm 75 \text{ mmol kg}^{-1}$). The highest $C_{Mn,w}$ values are observed near the soil surface and decrease with depth (Figure D-4). While ridge soils are high in Mn throughout the soil profile, $C_{Mn,w}$ in soils on hillslopes and in the valley decrease to $< 15 \text{ mmol kg}^{-1}$ in soils below ~ 0.30 m.

We investigate element mobility in the soil relative to the shale bedrock using the mass transfer coefficient $\tau_{i,j}$ (Brimhall and Dietrich, 1987; Anderson et al., 2002). $\tau_{i,j}$ values indicate enrichment ($\tau_{i,j} > 0$) or depletion ($\tau_{i,j} < 0$) of a soluble element j in weathered soil (subscript w) relative to its parent material (subscript p):

$$\tau_{i,j} = \frac{(C_{j,w}C_{i,p})}{(C_{j,p}C_{i,w})} - 1 \quad (1)$$

$\tau_{i,j}$ accounts for variation in bulk density and element concentration due to depletion or addition of other elements by normalizing mobile element concentrations to an immobile element i (e.g. Ti, Zr). Zr, present in these soils in the mineral zircon, was shown to be immobile relative to Ti, and $i = \text{Zr}$ is used in this study (Jin et al., 2010; Herndon et al., 2011). Previously, we demonstrated that the depth-averaged values of $\tau_{Zr,Mn}$ are positive for ridge soils at Shale Hills, consistent with addition from an external source (Herndon et al., 2011). In contrast to a biogenic profile, in which an element is redistributed from the subsurface to the surface soils by vegetation (Jobbagy and Jackson; 2004; Brantley and Lebedeva, 2011), ridge soils at SSHCZO did not exhibit subsurface depletion of Mn. Mn enrichment was attributed to atmospheric deposition from industrial sources and similar enrichment was observed in soils throughout industrialized areas in the northeastern U.S.A and in Europe. Here, we examine $\tau_{Zr,Mn}$ for ridge, slope, and valley soils along convex-upward, planar slopes and concave-upward, convergent-flow swales to assess transport of Mn contamination through contaminated soils (Table 5-1).

First, we examine depth profiles of Mn in soils from a planar hillslope to compare to previously studied ridge soils (Herndon et al., 2011). At the ridge (SPRT), $\tau_{Zr,Mn} > 0$ throughout the soil profile. In contrast, $\tau_{Zr,Mn} > 0$ only near the surface in the midslope soil core (SPMS), and $\tau_{Zr,Mn} < 0$ at all depths in the valley (SPVF) (Figure 5-2). Integrations of the $\tau_{Zr,Mn}$ profiles over depth at the midslope and valley sites are most consistent with net depletion. In other words, we could infer that Mn has only been input to soils at the ridge. However, we compare $\tau_{Zr,Mn}$ to $\tau_{Zr,j}$ for elements with no external inputs ($j = \text{Mg}$ and Fe) for these sites and find that Mn is enriched relative to Mg and Fe in the top 30-40 cm of SPRT, SPMS, and SPVF (Figure 5-3). Therefore, the observed $\tau_{Zr,Mn}$ trends at mid-slope and valley are best interpreted as addition profiles overprinting depletion profiles.

We also evaluate soils from a swale transect adjacent to the planar hillslope on the south slope of the catchment (SSRT, SSMS, and SSVF in Figure 5-1). Swales are small valleys or gullies that experience convergent water flows. Swales receive inputs from both upslope and from lateral sites along the swale, making soil profiles more difficult to interpret than ridge and planar hillslope soils. Like the planar catena, in the swale soils, $\tau_{Zr,Mn} > 0$ near the soil surface in the ridge (SSRT), midslope (SSMS), and valley soil cores (SSVF) (Figure 5-2). In contrast with the planar catena, Mn is depleted at depth relative to Mg and Fe in all swale soils (Figure 5-3). The zones of

depletion extend from just below the zones of enrichment down to the soil-bedrock interface. Mg and Fe exhibit highly similar depth profiles, although Fe is slightly less depleted than Mg in all soils and significantly less depleted in the colluvial layer at the midslope.

While SSRT and SSVF exhibit Mn depletion at depths > 0.1 m, SSMS is enriched in Mn throughout the upper 0.6 m depth and is only depleted in Mn in deeper samples. The zone of Mn enrichment in SSMS is also constant in $\tau_{Zr,Fe}$ and $\tau_{Zr,Mg}$, a feature previously attributed to the presence of a colluvial soil layer that homogenized the soil column over that depth zone (Jin and Brantley, 2011). The sharp contrast between $\tau_{Zr,Mn}$ values above and below 0.6 m and the thickness of the soil at the midslope (1.6 m) relative to the ridgetop and valley (< 1.0 m) are consistent with the presence of a Mn-rich colluvial layer at SSMS.

Addition profiles are also observed for a suite of other trace elements (e.g. Pb, Cd, Zn, Mo, Co, Ba) in the ridge soil profiles (Figure D-5). The highest enrichment relative to bedrock is observed for Pb (average $\tau_{Zr,Pb} = 1.1 \pm 0.2$) followed by Cd (average $\tau_{Zr,Cd} = 0.54 \pm 0.12$) and Mo (average $\tau_{Zr,Mo} = 0.29 \pm 0.06$). We calculate the integrated mass influx or outflux ($m_{j,w}$, mmol m^{-2}) to determine the net loss ($m_{j,w} < 0$) or net gain ($m_{j,w} > 0$) of j in the soil relative to the parent shale (Appendix Section D3). Net addition to the soil for each element is estimated as $m_{Pb,w} = 850 \pm 150 \mu\text{g cm}^{-2}$, $m_{Cd,w} = 7.6 \pm 2.6 \mu\text{g cm}^{-2}$, $m_{Mo,w} = 20.0 \pm 6.3 \mu\text{g cm}^{-2}$, $m_{Zn,w} = 1,510 \pm 470 \mu\text{g cm}^{-2}$, $m_{Ba,w} = 4,800 \pm 2,200 \mu\text{g cm}^{-2}$, and $m_{Co,w} = 89 \pm 61 \mu\text{g cm}^{-2}$ (Co).

3.2. Water chemistry

3.2.1. Precipitation

In precipitation samples collected in 2002 at two NADP sites near the SSHCZO, Mn concentrations were low ($C_{Mn,ppt} = 2.46 \pm 0.32 \mu\text{M}$, $n = 60$) relative to base cations Mg ($30.8 \pm 4.6 \mu\text{M}$), Ca ($192 \pm 26 \mu\text{M}$), and K ($31.3 \pm 13.2 \mu\text{M}$), and metals Al ($8.98 \pm 1.19 \mu\text{M}$), Fe ($13.4 \pm 7.70 \mu\text{M}$), Cu ($17.2 \pm 1.86 \mu\text{M}$), Zn ($10.5 \pm 1.30 \mu\text{M}$), and Pb ($3.92 \pm 0.43 \mu\text{M}$) (Table D-1). In contrast, Cd concentrations were lower than Mn ($0.028 \pm 0.004 \mu\text{M}$). Mn concentrations in rain were higher during summer months (May – August) than winter months (September – April) (Figure D-6). $C_{Mn,ppt}$ values were strongly positively correlated ($R^2 > 0.6$) with Mg, Al, and Ca concentrations and moderately correlated ($R^2 > 0.2$) with Cu, Zn, Cd, and Pb. Additionally, $C_{Mn,ppt}$ were negatively correlated with pH ($R^2 = 0.26$).

3.2.2. Pore fluids

Mn concentrations in pore fluids ($C_{Mn,pf}$; μM) were higher in soils on the swale transect ($< 25 \mu\text{M}$) than on the planar transect ($< 5 \mu\text{M}$) on the south slope (Table 5-2; Table D-2). In

particular, the average $C_{Mn,pf}$ in the planar ridge ($= 0.74 \pm 0.11 \mu\text{M}$), midslope ($= 0.64 \pm 0.05 \mu\text{M}$), and valley soils ($= 0.49 \pm 0.05 \mu\text{M}$) were significantly lower than in the swale ridge ($= 7.70 \pm 0.63 \mu\text{M}$), midslope ($= 1.01 \pm 0.07 \mu\text{M}$) and valley soils ($1.81 \pm 0.22 \mu\text{M}$). For the planar transect on the north slope, $C_{Mn,pf}$ values measured for the ridge ($= 1.25 \pm 0.23 \mu\text{M}$), midslope ($= 1.29 \pm 0.12 \mu\text{M}$), and valley ($0.98 \pm 0.09 \mu\text{M}$) soils are significantly higher than for the planar transect on the south slope. On the north swale, $C_{Mn,pf}$ values were only available for a two-month period in fall 2009 and may not be representative of annual averages. However, $C_{Mn,pf}$ values for the midslope ($= 2.74 \pm 0.45 \mu\text{M}$) and valley ($= 1.35 \pm 0.21 \mu\text{M}$) soils in the north swale are higher than $C_{Mn,pf}$ values measured for the south swale midslope ($= 1.20 \pm 0.25 \mu\text{M}$) and valley ($= 1.09 \pm 0.15 \mu\text{M}$) soils over the same two-month period. Due to the current limited scope of data for the north slope, we only include $C_{Mn,pf}$ data from the south slope in further calculations.

At all landscape positions in soils from both planar and swale transects, $C_{Mn,pf}$ values are highest near the soil surface, except at the south planar valley floor (Figure 5-4). Mn concentrations in pore fluids at the midslope were less variable with depth than in ridge or valley soils. $C_{Mn,pf}$ values were most variable in the valley soils and were consistently high at specific depths, including the 30 cm depth in the planar hillslope soil and 10 and 40 cm in the swale soil. In all soils, $C_{Mn,pf}$ values were low at the soil-bedrock interface regardless of total soil depth.

Using Mg concentrations and δD values, Jin et al. (2011) identified zones of “high-flow” and “low-flow” water transport through the ridge, midslope, and valley soils of the south planar transect. In high-flow zones located at the A-B and B-C soil horizon interfaces, water was inferred to advect quickly downslope in perched saturated layers and Mg concentrations were consistently low. Likewise, in the low-flow zones located within each of the A and B horizons, Mg concentrations were also consistently high, and, water was therefore inferred to be retained for longer residence times, moving primarily via diffusion until reaching the high-flow zones. Average concentrations of pore fluid Mn in the high-flow ($C_{Mn,high}$) and low-flow ($C_{Mn,low}$) zones document that $C_{Mn,low} > C_{Mn,high}$ for all south planar soils, consistent with Mg (Figure 5-4). Jin et al. (2011) contend that the flux of Mg out of the soil from the planar hillslope into the stream is equivalent to the Mg flux from the high flow zones. Based on that study, we also infer that Mn concentrations in the high-flow zones are most representative of pore fluids being transported out of the hillslopes into the stream and groundwater at the valley.

In contrast to dissolved Mg, however, $C_{Mn,pf}$ values were highest near the soil surface, and in general, Mn concentrations at each depth did not increase downslope (Figure 5-4). These

differences in pore waters are attributed to differences in the concentrations of Mg and Mn on cation exchange sites in the soil (Jin et al., 2010). Mg concentrations on cation exchange sites increase from the ridge to the valley and with depth in the soil; in contrast, Mn concentrations on cation exchange sites do not increase or decrease from the ridge to the valley and decrease with depth in the soil. Cations held in the exchange sites can rapidly replace the cations in pore fluids that are flushed out of the soil; thus, spatial differences in pore fluid Mg and Mn reflect differences in the pools of exchangeable cations. In turn, the differences are consistent with a largely natural source for Mg and an atmospheric deposition source for Mn.

3.2.3. Stream water

Mn concentrations in the stream at the watershed outlet ($C_{Mn,stream}$; mmol m^{-3}) were negatively correlated with stream discharge (Q_{stream} , $\text{m}^3 \text{d}^{-1}$), consistent with a dilution effect (Figure 5-5; Table D-3). Thus, Mn concentrations were generally high during summer months when stream flow was minimal and lower during spring and fall when stream flow was high (Figure D-7). One exception was seen in early November, when exceptionally high $C_{Mn,stream}$ and $C_{Fe,stream}$ were observed to peak two weeks following a heavy storm event (Figure D-8). However, Mn concentrations showed no steady trends within seasons, instead sharply increasing and decreasing in individual pulses lasting < 1 week (Figure D-7).

The dissolved load of a mobile element j in the stream ($L_{j,stream}$, mmol d^{-1}) is a function of both $C_{j,stream}$ and stream discharge:

$$L_{j,stream} = Q_{stream} C_{j,stream} \quad (2)$$

Here, we first calculated daily $L_{Mn,stream}$ values as the product of the daily average stream discharge (Q_{stream}) and $C_{Mn,stream}$ from stream samples. Despite the overall inverse correlation between discharge and concentration, $L_{Mn,stream}$ generally increased with increasing stream flow (Figure 5-5). Daily changes in $L_{Mn,stream}$ reflected mostly the changes in Q_{stream} at high discharge but were more closely aligned with $C_{Mn,stream}$ at low discharge (Figure D-7).

An estimate for the mass of dissolved Mn leaving the catchment at the weir, $\hat{L}_{Mn,stream}$ (mmol y^{-1}), was first calculated as the product of the average $C_{Mn,stream}$ measured at the catchment weir ($= 3.94 \pm 0.86 \mu\text{M}$) and the annual average discharge ($Q_{stream} = 39,500 \pm 4,400 \text{ m}^3 \text{ y}^{-1}$) to yield $\hat{L}_{Mn,stream} = 156 \pm 38 \text{ mol y}^{-1}$. For all further discussion, we distinguish daily dissolved loads ($L_{j,stream}$, mmol d^{-1}) from annual dissolved loads ($\hat{L}_{j,stream}$, mol y^{-1}). A more refined estimate for $\hat{L}_{Mn,stream}$ was calculated by using the USGS program LOADEST (Runkel et al., 2004). The

program derives estimates of $L_{j,stream}$ and $\hat{L}_{Mn,stream}$ by fitting a model to concurrent measurements of concentration-discharge data and extrapolating the fit across all discharge values. The LOADEST model yielded a low value for $\hat{L}_{Mn,stream} = 30.0 \pm 1.6 \text{ mol y}^{-1}$ relative to the initial estimate ($= 156 \pm 38 \text{ mol y}^{-1}$), likely due to the elimination of outlier $C_{Mn,stream}$ values from the LOADEST model (Appendix section D2). The removal of these outliers was required for the model to converge. Thus, we use the LOADEST estimate as a more accurate representation of $\hat{L}_{Mn,stream}$, but consider the initial estimate as an upper limit.

The flux of an element j out of the watershed ($F_{j,stream}$, $\text{mmol m}^{-2} \text{ y}^{-1}$) can be calculated to normalize $\hat{L}_{j,stream}$ to the surface area of the drainage basin:

$$F_{j,stream} = \frac{\hat{L}_{j,stream}}{A_{SH}} \quad (3)$$

Normalizing to the surface area of the catchment ($A_{SH} = 79,000 \text{ m}^2$), we calculated $F_{Mn,stream} = 0.38 \pm 0.02 \text{ mmol m}^{-2} \text{ y}^{-1}$.

Out of the 131 samples with Mn concentrations $< \text{DL}$, 93 (71%) occurred at stream discharge $> 20 \text{ m}^3 \text{ d}^{-1}$, which is consistent with dilution behavior (Figure 5-5). The remaining 38 samples occurred at discharge rates $< 20 \text{ m}^3 \text{ d}^{-1}$, which is not consistent with dilution. Samples with $C_{Mn,stream} < \text{DL}$ at $Q_{stream} < 20 \text{ m}^3 \text{ d}^{-1}$ occurred periodically between May and October following peaks of high Mn concentration (Figure D-7). These variations in concentration thus caused a “pulsing” in $L_{Mn,stream}$.

We compare the relationship between concentration and discharge for a suite of elements and find that Mn concentrations in the stream varied by a factor of $\sim 10^3 \times$ ($< 0.09 - 89 \mu\text{M}$) over all measured discharge rates while Fe varied by $\sim 10^2 \times$, and major weathering products (i.e. Ca, K, Mg, Na, Si) varied by $< 10 \times$. The concentration-discharge trends observed for the major elements are consistent with a “chemostatic” response to variable water fluxes (Godsey et al., 2009). In other words, the concentrations of these elements are not significantly diluted by precipitation but rather remain constant despite changes in discharge (Figure 5-6). In contrast to the base cations and Si, Mn, Fe, and Al are not consistent with a chemostatic response (Table 5-3). $C_{j,stream}$ values for $j = \text{Fe}$ and Mn decrease rapidly with increasing discharge (Figure 5-6) while $C_{Al,stream}$ values increase at high discharge (Figure D-9). Furthermore, while $L_{j,stream}$ values for major elements increase with discharge with a nearly 1:1 relationship in log space, dissolved Mn loads show a slope on Figure 5-6 of 0.59 (Table 5-3).

3.2. Vegetation chemistry

Mn concentrations in foliage ($C_{Mn,fol}$; mmol kg^{-1}) varied by species, collection date, and slope position (Table D-6). For example, *QUPR* leaves collected in late summer (August/September 2011) had higher $C_{Mn,fol}$ ($= 30.7 \pm 3.3 \text{ mmol kg}^{-1}$) than *QUPR* leaves collected in June 2011 ($= 24.8 \pm 2.4 \text{ mmol kg}^{-1}$). A similar trend was observed for *ACSA* leaves collected in June ($C_{Mn,fol} = 34.1 \pm 3.5 \text{ mmol kg}^{-1}$) and late summer ($= 48.6 \pm 4.0 \text{ mmol kg}^{-1}$). Similar to previous studies, we used $C_{Mn,fol}$ values from late summer as a best approximation of the maximum foliar Mn concentration (McCain and Markley, 1989). Out of the examined tree species, hickories exhibited the highest late-summer concentrations of foliar Mn (*CAGL* = $73 \pm 1.3 \text{ mmol kg}^{-1}$ and *CATO* = $61 \pm 3.4 \text{ mmol kg}^{-1}$), followed by oaks (*QUAL* = $55 \pm 1.9 \text{ mmol kg}^{-1}$ and *QUPR* = $36 \pm 4.0 \text{ mmol kg}^{-1}$) and maples (*ACSA* = $49 \pm 4.0 \text{ mmol kg}^{-1}$) (Figure 5-8). Pine species contained low levels of Mn in their needles relative to the deciduous species (*PIST* = $18.5 \pm 0.4 \text{ mmol kg}^{-1}$ and *PIVI* = $15.7 \pm 1.0 \text{ mmol kg}^{-1}$).

Additionally, foliar Mn generally increased with increasing elevation (Figure D-10). In order to minimize errors introduced by variations in digestion efficiency, we normalized Mn concentrations (mmol kg^{-1}) to P concentrations (mmol kg^{-1}). We observed a 3-4% increase in Mn/P ratios per meter of elevation change in both pignut ($R^2 = 0.85$) and mockernut ($R^2 = 0.68$) hickory species and sugar maple ($R^2 = 0.15$). White oak exhibited a 1.6% increase ($R^2 = 0.63$), while pine and chestnut oak showed no trend. Although $C_{Mn,fol}$ varied with elevation, the relative variability was small compared to the magnitude of uptake and interspecies differences, and we assumed that $C_{Mn,fol}$ was independent of elevation for future calculations.

Mn concentrations in leaf litter increased from late August ($= 33.0 \pm 3.1 \text{ mmol kg}^{-1}$) to early October ($= 52.2 \pm 3.8 \text{ mmol kg}^{-1}$) to late October ($59.0 \pm 4.6 \text{ mmol kg}^{-1}$) (Figure 5-8; Table D-8). Although K concentrations decreased in litter over the same time period, concentrations of Ca, Mg, Al and P showed no trend with collection date. The rate of litterfall ($\text{g m}^{-2} \text{ week}^{-1}$) peaked in late October, concurrent with maximum concentrations of Mn in litter; thus, inputs of Mn to the soil from leaf litter were highest in late October (Figure D-11).

IV. Discussion

In the following sections, we first outline a mass balance model used to quantify fluxes through pore fluids and vegetation in swale and planar hillslopes at the Shale Hills CZO (Section 4.1). We then discuss results derived from the model, including an analysis of chemical fluxes in pore fluids and in the stream (Section 4.2), estimates of short-term and time-integrated weathering

rates at the pedon and catchment scales (Section 4.3), and an examination of fluxes of Mn through vegetation (Section 4.4). Finally in Section 4.5, we scale up from the SSHCZO and assess trends in Mn weathering from the Susquehanna River Basin over a period of six decades.

4.1. Hillslope Model

We incorporate physical and chemical analyses of soil, water, and vegetation into a mass balance model in order to quantify fluxes of Mn from hillslope soils into the stream. First, we evaluate Mn transport along the planar catena. A hillslope model is defined here to consist of three adjacent boxes that represent the ridge top, slope, and valley soils (Jin et al., 2010). Each box is 25 m in length (downslope) and 1 m in width (perpendicular to slope) to give a surface area of 25 m². Soil depth for each box is assumed everywhere equal to the point of refusal measured for soil cores augered at either the ridge (0.30 m), midslope (0.59 m), or valley floor (0.67 m) positions. Jin et al. (2010) previously showed that such a “reactor on a slope” stepped-flow box model could be used to interpret weathering fluxes for major elements.

The area-normalized mass of Mn in the soil in each box ($\bar{M}_{Mn,w,s}$; mmol m⁻²) is calculated as:

$$\bar{M}_{Mn,w,s} = d_s \rho_s C_{Mn,w,s} \quad (4)$$

Here, d_s is the soil depth (m), ρ_w is the average bulk density of soil (= 1,520 kg m⁻³), and $C_{Mn,w,s}$ (mmol kg⁻¹) is the depth-averaged concentration of Mn in the soil for each location. Subscript s indicates the slope position, such that $s = rt$ (ridgetop), ms (midslope), or vf (valley floor).

Fluxes of dissolved Mn to and from each box are calculated using precipitation and evapotranspiration rates (Figure 5-9) and precipitation and pore fluid chemistry (Figure 5-10). Mn concentrations in pore fluids are averaged for each depth in each soil over all collected samples (Table 5-2). The annual water budget for each box is calculated from water fluxes (e.g. precipitation, evapotranspiration) averaged over one year. We divide the annual average discharge at the stream weir (= 39,500 ± 4,400 m³ y⁻¹) by the annual precipitation delivered to the entire catchment (= 79,000 m³ y⁻¹) and calculate that one half of annual precipitation is returned to the atmosphere through evapotranspiration (NADP, 2011; Duffy, 2012). Mn concentrations in precipitation are averaged over all samples collected January – December 2002 ($C_{Mn,ppt} = 0.045 \pm 0.006 \mu\text{M}$). The flux of precipitation delivered to each box ($V_{ppt} = 1.0 \text{ m}^3 \text{ m}^{-2} \text{ y}^{-1}$) equals the precipitation rate (= 1.0 m y⁻¹) multiplied by one square meter of ground surface area. Mn input as precipitation ($F_{ppt} = 0.045 \text{ mmol m}^{-2} \text{ y}^{-1}$) is calculated as the product of V_{ppt} and $C_{Mn,ppt}$.

For each box, $V_{ET} = 0.5 \text{ m}^3 \text{ m}^{-2} \text{ y}^{-1}$, and V_{ppt} and V_{ET} are assumed to be the same regardless of slope position (Figure 5-9). The water that is not removed through evapotranspiration is assumed to move downslope to the next box or to the stream through preferential flow paths at horizon interfaces (Lin and Zhou, 2008; Jin et al., 2011). The flux of pore fluid through each box each year is the sum of V_{ppt} and the water contribution from upslope soils ($V_{in,s}$, $\text{m}^3 \text{ m}^{-2} \text{ y}^{-1}$). Subtracting V_{ET} yields the volume flux of water that exits each soil box and flows downslope ($V_{out,s}$, $\text{m}^3 \text{ m}^{-2} \text{ y}^{-1}$):

$$V_{out,s} = V_{in,s} + V_{ppt} - V_{ET} \quad (5)$$

We assume that $V_{in,s}$ for each downslope box equals $V_{out,s}$ of the upslope box. Here, the subscript s can refer to ridgetop ($s = rt$), midslope ($s = ms$), or valley floor ($s = vf$). In the ridge soil box, $V_{in,rt} = 0$ and $V_{out,rt} = 0.5 \text{ m}^3 \text{ m}^{-2} \text{ y}^{-1}$. In the midslope soil box, $V_{out,ms} = 1.0 \text{ m}^3 \text{ m}^{-2} \text{ y}^{-1}$ in the midslope soil box and $V_{out,vf} = 1.5 \text{ m}^3 \text{ m}^{-2} \text{ y}^{-1}$ in the valley soil box.

Jin et al. (2011) identified that water moves quickly through high-flow zones located at soil horizon interfaces and slowly through low-flow zones located within horizons. Average Mn concentrations in pore fluids were therefore calculated for the high-flow zones ($C_{Mn,high}$) identified by Jin et al. and used to calculate the downslope flux of dissolved Mn from each slope position ($F_{out,s}$):

$$F_{out,s} = C_{Mn,high} V_{out,s} \quad (6)$$

In addition to input and output fluxes of advected water for each hillslope box, Mn is taken up into vegetation (F_{veg}). Each year, dissolved Mn is transferred from soil into vegetation during the growing season (approximately April – August) and subsequently returned to the soil as litterfall (September – November). To estimate vegetative uptake for each soil box, we calculate an average annual uptake rate for the catchment, F_{veg} ($\text{mmol m}^{-2} \text{ y}^{-1}$) from the mass of Mn in foliage in the catchment ($M_{Mn,fol}$):

$$F_{veg} = \frac{M_{Mn,fol}}{A_{SH} T} \quad (7)$$

Here, $M_{Mn,fol}$ (mmol) is the total mass of Mn in foliage in the catchment, A_{SH} ($= 79,000 \text{ m}^2$) is the total surface area of the CZO, and T is one annual cycle for foliage ($= 1 \text{ year}$). This calculation is a lower estimate of Mn uptake in that it is based on the assumption that the mass of Mn stored in woody tissue is small relative to the Mn that is present in the leaves as documented by previous researchers (Kogelmann and Sharpe, 2006; Houle et al., 2007). $M_{Mn,fol}$ is calculated as the sum of foliar Mn in each tree over all surveyed trees in the catchment:

$$M_{Mn,fol} = \sum m_{fol} C_{Mn,fol} \quad (8)$$

We use an average $C_{Mn,fol}$ for each species from leaves collected in August and September, prior to senescence (Table D-6). For species for which no foliar chemistry was available, $C_{Mn,fol}$ was set equal to the average of either deciduous or evergreen species that were measured. An allometric equation was used to estimate the mass of foliage (m_{fol} , kg) for each surveyed tree in the catchment (Harris et al., 1973):

$$\ln(m_{fol}) = -3.498 + 1.695 \ln(DBH) \quad (9)$$

Here, DBH values (cm) were obtained for each tree from the tree survey. The area-normalized mass of foliage in the catchment ($\bar{m}_{fol} = 0.31 \text{ kg m}^{-2}$) is similar to the area-normalized mass of leaf litter deposited to the land surface as averaged from measurements in 2011 ($\bar{m}_{litter} = 0.34 \text{ kg litter m}^{-2}$) (Table 5-4).

We calculate the rate of Mn return from vegetation to the soil, i.e., the flux of Mn in litterfall (F_{litter} , $\text{mmol m}^{-2} \text{ y}^{-1}$), from the Mn concentration in leaf litter ($C_{Mn,litter}$; mmol kg^{-1}) and \bar{m}_{litter} :

$$F_{litter} = \frac{\sum_{t=0}^{t=T} \bar{m}_{litter}(t) C_{Mn,litter}(t)}{T} \quad (10)$$

Here, $C_{Mn,litter}$ and \bar{m}_{litter} are calculated for each time interval t ($= 1 \text{ week}$) over a total time T ($= 1 \text{ year}$) (Table 5-4).

4.2. Mn fluxes in water

4.2.1. Hillslope inputs to stream

In Figure 5-10, we show a schematic diagram, based on Jin et al. (2011), summarizing concentrations of Mn in water reservoirs for the south planar hillslope. Although not as obvious as the observations for Mg (Jin et al., 2011), average Mn concentrations are significantly higher in the low-flow ($C_{Mn,low}$) than the high-flow ($C_{Mn,high}$) zones for each slope position on the planar transect (Figure 5-10). Unlike Mg however, $C_{Mn,high}$ and $C_{Mn,low}$ values decrease from the ridge to the valley. Nonetheless, using Eqn. 6, we find that the calculated downslope flux of Mn for the box model increases from the ridge ($F_{out,rt} = 0.21 \pm 0.06 \text{ mmol m}^{-2} \text{ y}^{-1}$) to the midslope ($F_{out,ms} = 0.42 \pm 0.05 \text{ mmol m}^{-2} \text{ y}^{-1}$) (Figure 5-11A). In contrast, the mid-slope and valley outfluxes ($F_{out,vf} = 0.39 \pm 0.06 \text{ mmol m}^{-2} \text{ y}^{-1}$) are identical within error.

The flux of Mn out of the valley box is equated here to the Mn input from the hillslope to the stream. If the south planar hillslope is a good representation of hillslopes throughout Shale Hills,

then we should be able to extrapolate $F_{out,vf}$ across the entire watershed to compare losses of Mn from the planar soil ($L_{soil,stream}$, mmol y^{-1}) to losses of Mn at the watershed outlet:

$$L_{soil,stream} = F_{out,vf} \left(\frac{A_{vf}}{A_{hill}} \right) A_{SH} \quad (11)$$

First, $F_{out,vf}$, previously normalized to the area of the valley floor ($A_{vf} = 25 \text{ m}^2$), is corrected for the area of the hillslope ($A_{hill} = 75 \text{ m}^2$). According to Eqn. (11), if all areas of the watershed deliver Mn to the stream at the same rate as the planar transect, then $L_{soil,stream} = 10.3 \pm 1.6 \text{ mol y}^{-1}$.

Previously, we estimated $\hat{L}_{Mn,stream} = 30.0 \pm 1.6 \text{ mol y}^{-1}$; thus, the value of $L_{soil,stream}$ extrapolated from the planar hillslope data does not account for the dissolved Mn load in the stream.

We investigate Mn outputs from soils in the swale transect to the stream using the same box model developed for the planar transect (Figure 5-11B). Here, we assume that the area-normalized swale water fluxes are the same as the planar fluxes (Figure 5-9). Although swales experience convergent water transport, the total area of a swale receives the same input of precipitation as an equivalent area on the planar hillslope; thus, the water flux out of the swale when normalized by its total area should equal the water flux out of a planar hillslope. In addition, we also assume no preferential flow paths. Thus, Mn concentrations for pore fluids exiting the swale box are averaged over all depths of the soil profile ($C_{Mn,pf}$). Presumably, this calculation will yield a maximum output from the swale since we are implicitly assuming that the porewater concentrations in the swale are everywhere equal to those measured by the swale lysimeters which are located at the center line of convergent flow. Under these assumptions, the $F_{out,s}$ values, equal to the product of $C_{Mn,pf}$ and $V_{out,s}$, are higher ($1.0 - 3.8 \text{ mmol m}^{-2} \text{ y}^{-1}$) for all slope positions in the swale relative to those for the planar transect ($0.21 - 0.42 \text{ mmol m}^{-2} \text{ y}^{-1}$) (Figure 5-11). From this, we infer that swales could act as the dominant source of dissolved Mn to the stream as compared to planar hillslopes.

Given these arguments, the value of $L_{soil,stream}$ (Eqn. 11) extrapolated from the planar transect is a lower limit and $F_{out,vf}$ from the swale transect can be used to calculate an upper estimate of Mn fluxes to the river. To do this, we assume that all areas of the watershed deliver Mn to the stream at the same rate as the swale transect. This upper estimate for total Mn flux out of an entire catchment consisting of swale hillslopes ($L_{soil,stream} = 71.6 \pm 8.4 \text{ mol y}^{-1}$) is sufficient to account for the mass of dissolved Mn leaving the watershed in the stream ($\hat{L}_{Mn,stream} = 30.0 \pm 1.6 \text{ mol y}^{-1}$).

A more refined extrapolation can also be made, rather than just lower and upper estimates, by combining values for inputs to the stream from planar ($L_{soil,stream,planar}$) and swale ($L_{soil,stream,swale}$) hillslopes. For example, soils on planar hillslopes encompass ~79% of the land surface area at SSHCZO while soils in swales cover ~16% (Lin et al., 2006). As pointed out above, although swales experience convergent water transport, planar and swale hillslopes receive equal inputs from precipitation per unit surface area. By normalizing $L_{soil,stream,swale}$ to the total area of the swale, we account for redistribution of water within the swale. We calculate combined inputs from planar and swale hillslopes to the stream by multiplying $L_{soil,stream}$ for planar and swale hillslopes by the fraction of land surface area each hillslope covers ($X_{planar} = 0.79$ and $X_{swale} = 0.16$):

$$L_{soil,stream} = L_{soil,stream,planar}X_{planar} + L_{soil,stream,swale}X_{swale} \quad (12)$$

Here, the remaining 5% of A_{SH} is in the stream bed and is disregarded. We find that swales contribute 58% of total Mn input to the stream despite covering only 16% of the total catchment area. However, the combined estimate for $L_{soil,stream}$ ($= 19.6 \pm 8.6 \text{ mmol y}^{-1}$) accounts for only $65 \pm 28\%$ of the lower estimate that we reported earlier based on stream chemistry and discharge, i.e. $\hat{L}_{Mn,stream}$ ($= 30.0 \pm 1.6 \text{ mmol y}^{-1}$).

We consider whether it is possible that an additional important source of Mn to the stream has been neglected. For example, a non-soil source of Mn could input Mn to the stream or the stream channel could be a significant source. The most likely such source is ground water, and Jin et al. (2011) proposed that dissolution of ankerite, a Mn-rich mineral observed in a deep core from the CZO, occurs in groundwater and contributes to stream chemistry. However, although periodically high concentrations of Mn in groundwater ($C_{Mn,GW}$) were observed in samples taken from wells near the valley floor, $C_{Mn,GW}$ was generally low ($< 9 \mu\text{M}$) relative to $C_{Mn,stream}$ values ($< 90 \mu\text{M}$) (Table D-9). It is more likely that periodically high Mn in groundwater is due to inputs from the surface than vice versa. Alternatively, the stream sediments may contain high concentrations of Mn-oxides. It is known that sunlight can promote Mn reduction and mobilization from Mn-oxides in the presence of organic matter or bacteria (Sunda and Huntsman, 1988; Sunda and Huntsman, 1994; Matsunaga et al., 1995). However, the forest canopy reduces light inputs to the forest floor, and this process is largely observed in marine environments. Furthermore, weekly to biweekly sampling schedule of porewaters is less frequent than the daily stream water sampling during the wet season. As such, short pulses of high Mn concentrations may have been recorded in

the stream but missed in the pore fluids. For example, a pulse of high $C_{Mn,stream}$ was observed for one week in November 2009 (Figure D-8), but no pore fluids were collected over that time period.

Perhaps the most likely explanation for why the estimate of $L_{soil,stream}$ does not equal $\hat{L}_{Mn,stream}$ is related to spatial and temporal constraints on the $C_{Mn,pf}$ values used in the model. We considered only $C_{Mn,pf}$ data from the south slope; however, although collected over a more limited range of dates, average $C_{Mn,pf}$ values on the north slope were observed to be higher than $C_{Mn,pf}$ values on the south slope (Table D-2). Thus, the $C_{Mn,pf}$ values used in the model may have underestimated the flux of dissolved Mn transported to the stream. For example, we can calculate a very coarse, catchment-wide estimate for the Mn flux from the hillslopes to the stream as the product of an average Mn concentration for all pore fluids collected from valley soils on planar and swale transects on the north and south slopes ($C_{Mn,pf} = 1.18 \pm 0.09 \mu\text{M}$; $n = 434$) and annual discharge ($Q_{stream} = 39,500 \pm 4,400 \text{ m}^3 \text{ y}^{-1}$) to yield $L_{soil,stream} = 71.5 \pm 8.6 \text{ mol y}^{-1}$. This value is within the estimated $\hat{L}_{Mn,stream}$ range (30.0 – 156 mol y^{-1}). From this, we infer that soils on the north slope deliver more Mn to the stream than soils on the south slope.

4.2.2. Stream chemistry

$C_{j,stream}$ values for major weathering elements ($j = \text{K, Na, Mg, Si, Ca}$) vary little over a wide range of discharge values (Figure 5-6): by this definition, the major elements are “chemostatic”. Note that in this discussion we use the standard descriptor, “major elements”, to include Na and Ca although both are low in abundance in the CZO (< 0.5 wt% in soils; (Jin et al., 2010)). Such behavior could be expected for elements derived from minerals that are equilibrated with pore waters at all times. The only such fast-dissolving minerals known to be present in the CZO, albeit at depth (Jin et al., 2010), are carbonates. Therefore, such an explanation cannot explain chemostasis for elements not present in carbonates (K, Na, Si), nor, given that carbonates are only present at depth, is it likely to explain Mg and Ca. Godsey et al. (2009) suggest that changes in mineral-water interfacial area during periods of high and low discharge explain chemostasis; however, this model is untenable if the source of the elements during rain events is clay dissolution since dissolution rates are so slow.

Another possible explanation is that the source of the chemostatic elements during rain events is the exchangeable cation pool. The cation exchange capacity of soils along the planar hillslope ranges from 35 to 71 meq kg^{-1} and is dominated by Al cations at the ridge and midslope and Ca and Mg cations in the valley (Jin et al., 2010). The slope of a log-log concentration-discharge plot indicates the degree of chemostasis exhibited by each element. Slopes vary from zero (full

chemostatis) to -1 (complete dilution with rainwater) (Godsey et al., 2009). For chemostatic elements in the Shale Hills stream, the degree of chemostasis observed decreased from $\text{Na} > \text{K} > \text{Mg} > \text{Ca}$ (Table 5-3), the order of which is directly inverse of the elements' relative strengths of adsorption to cation exchange sites (Evangelou and Phillips, 2005). All these elements are displaced from cation exchange sites into solution by H^+ (i.e. protonation of the exchange sites), and we observe that easily displaced cations (e.g. K, Na) exhibited a higher degree of chemostasis than less easily displaced cations (e.g. Mg, Ca). Furthermore, this explanation can even account for the highly chemostatic, non-cationic solute Si, which is present in the exchangeable pool (Jin et al., 2010) but likely weakly associated to exchange sites as $\text{Si}(\text{OH})_4^0$. The similar $C_{j,pf}$ values observed for major weathering elements in the planar and swale soils are attributed to the quick exchange of protons in rain for cations in the exchange pool throughout the catchment (Figure 5-7 and Table 5-5). As a result, $L_{j,stream}$ increased with increasing discharge.

In contrast to the major elements, Mn, Fe, and Al did not exhibit chemostatic behavior (Figs. 5-6 and D-9). Al, present at very low concentrations in the stream, exhibited a positive log-log slope ($= 0.06$); thus, $C_{Al,stream}$ values increased at high discharge. Al cations that are held on cation exchange sites in the soil are not displaced by H^+ in the rain and may be dominantly bound to exchange sites on organic matter rather than clays (Bloom et al., 2005). Therefore, Al mobilization into the stream is not expected to be governed by exchange reactions with the clays, and high $C_{Al,stream}$ values observed at high discharge are best explained by release of Al from the organic matter at high soil saturation levels.

Similar to Al, Mn and Fe are not displaced from exchange sites by H^+ and do not follow chemostatic behavior (Bloom et al., 2005; Evangelou and Phillips, 2005). In contrast to Al, concentrations of Mn and Fe decrease at high discharge and are more consistent with dilution behavior. In the previous section, we demonstrated that swales are a dominant source of dissolved Mn input to the stream. While $C_{Mn,pf}$ values were much higher in the swales than in the planar soils, average $C_{j,pf}$ values for the major weathering elements and for Al were similar at all slope positions on planar and swale hillslopes (Figure 5-7 and Table 5-5). In addition to not being governed by exchange reactions, the non-chemostatic behavior for Mn is thus attributed to differential inputs from the swale and planar hillslopes. During a rain event, the water that initially enters the unsaturated soils infiltrates vertically into pores. The nature of unsaturated flow is such that little to no water flows down the hillslopes to the stream as long as the entire slope is unsaturated (Lin and Zhou, 2008). At some point during a larger rain event, water begins saturating

some of the horizon interfaces to create limited perched water tables, allowing water to flow downslope. Because soils in the swales are generally wetter and therefore saturate more quickly than the planar hillslope soils (Lin et al., 2006; Qu and Duffy, 2007), the initial increases in stream flow following a precipitation event consist of water contributed from the swales.

High $C_{Mn,pf}$ values in the swales therefore likely lead to a rapid increase in stream Mn concentrations (and $L_{Mn,stream}$) as Q_{stream} increases. As rainfall intensifies, water eventually begins to form small perched saturated layers within the planar soils (Lin et al., 2006; Jin et al., 2011). This water flows into the streams, carrying the lower concentrations of dissolved Mn that are characteristic of the planar hillslopes (due to lower soil organic matter and DOC) and diluting the inputs from the swales. Thus, $C_{Mn,stream}$ decreases and $L_{Mn,stream}$ shows a dilution effect at high Q_{stream} . Consistent with this conceptual model, $C_{Mn,stream}$ values are generally highest during drier periods when water fluxes to the stream are presumed to come dominantly from the swales (Figure D-7). In addition, small precipitation events are associated with pulses of Mn to the stream, as if accumulated Mn is being flushed from the swales.

Dissolved organic carbon (DOC) may enhance mobilization of Mn and Fe from the swales relative to the planar soils. Previously, Andrews et al. (2011) identified the swales in Shale Hills as “hot-spots” of DOC transport to the stream and observed that flushing of DOC from soils into the stream occurred after dry seasons. Furthermore, as pointed out by Andrews (2011), dissolved concentrations of Mn and Fe correlate with DOC in planar and swale pore fluids and in the stream. As shown in Figure D-12, Mn concentrations in the stream increase exponentially with linear increases in DOC. Swales exhibit elevated levels of both Mn and DOC in pore fluids relative to the planar soils (Figure D-13).

In summary, to explain the behavior of all solutes, we invoke i) rapid proton exchange for major element cations and Si on the exchangeable pool; and ii) saturated flow down hillslopes during rain events that delivers water to the stream first from swales and then later from both swales and planar hillslopes. Due to rapid exchange with protons, K, Na, Mg, Ca, and Si are equally concentrated in pore fluids for planar and swale hillslopes, and concentrations of these elements in stream water remain relatively constant. Al is also equally concentrated in pore fluids on planar and swale hillslopes, but is only mobilized to the stream at high discharge when water saturation conditions are reached. Fe and Mn are more highly concentrated in pore fluids in swales compared to planar slopes; thus, concentrations do not remain constant at high discharge. As long as swales dominate stream flow, minimal dilution effects are observed for Fe and Mn; however, once a rain

event saturates the planar hillslopes, Mn and Fe concentrations in the stream decrease because a more dilute pool is accessed on the planar hillslopes.

4.3. Weathering Rates

4.3.1. Modern soil weathering rates

The net weathering rate that Mn is removed from the soil ($F_{w,s}$; $\text{mmol m}^{-2} \text{y}^{-1}$) is equivalent to the difference between outputs and inputs of dissolved Mn for each soil box:

$$F_{w,s} = F_{out,s} - F_{in,s} - F_{ppt} \quad (13)$$

In the planar transect, rates of Mn weathering are approximately equal for the ridge ($F_{w,rt} = 0.17 \pm 0.04 \text{ mmol m}^{-2} \text{y}^{-1}$) and midslope ($F_{w,ms} = 0.16 \pm 0.08 \text{ mmol m}^{-2} \text{y}^{-1}$) soils; however, although Mn is net depleted in valley soils, current inputs of Mn to the valley soil exceed outputs, leading to accumulation of Mn in that box ($F_{w,vf} = -0.072 \pm 0.080 \text{ mmol m}^{-2} \text{y}^{-1}$). In the swale transect, Mn is lost from ridge ($F_{w,rt} = 3.8 \pm 0.3 \text{ mmol m}^{-2} \text{y}^{-1}$) and valley ($F_{w,vf} = 1.7 \pm 0.3 \text{ mmol m}^{-2} \text{y}^{-1}$) and accumulates at the midslope ($F_{w,ms} = -2.9 \pm 0.3 \text{ mmol m}^{-2} \text{y}^{-1}$).

To understand this Mn loss, we treat the rate as first-order with respect to the mass of Mn in the soil:

$$F_{w,s} = k_{w,s} \bar{M}_{Mn,w,s} \quad (14)$$

Eqn. (14) is a first-order rate equation that describes the weathering-derived release of Mn from soil particles. We use Eqn. (14) to derive a first-order rate constant for each slope position ($k_{w,s}$, y^{-1}).

For the planar transect, $k_{w,s}$ is similar for the ridge ($k_{w,rt} = 6.5 \pm 2.6 \times 10^{-6} \text{ y}^{-1}$) and midslope ($k_{w,ms} = 8.8 \pm 4.7 \times 10^{-6} \text{ y}^{-1}$) soils. In contrast, Mn accumulates in the valley ($k_{w,vf} = -5.2 \pm 5.8 \times 10^{-6} \text{ y}^{-1}$). In this case, the negative rate constant documents that there is current net Mn precipitation rather than dissolution in the valley floor. Rate constants calculated for the swale, using the minimum water estimates as described above, are ~ 100 x greater than rate constants for the planar transect and decrease from the ridge ($k_{w,rt} = 73 \pm 12 \times 10^{-5} \text{ y}^{-1}$) to the valley ($k_{w,vf} = 12 \pm 3.0 \times 10^{-5} \text{ y}^{-1}$) with net accumulation in the midslope ($k_{w,ms} = -7.3 \pm 1.3 \times 10^{-5} \text{ y}^{-1}$).

4.4.2. Time-integrated soil weathering rates

We can also use soil chemistry to compare average weathering rates integrated over the entire period of soil formation to the modern weathering rates measured with pore fluids as calculated above in section 4.4.1 (Appendix section D3). Briefly, the integrated mass influx or outflux ($m_{j,w}$, mmol m^{-2}) is the net loss ($m_{j,w} < 0$) or net gain ($m_{j,w} > 0$) of j in the soil relative to the parent shale. For each soil profile, $m_{j,w}$ is divided by the amount of time it took that soil profile to develop (T_{soil} ,

years) to obtain an integrated weathering rate W_j ($\text{mmol m}^{-2} \text{y}^{-1}$). To obtain a value for W_j that is not impacted by atmospheric inputs, the total thickness of soil in each soil profile exhibiting $\tau_{Zr,Mn} > 0$ is excluded from this calculation. In other words, the addition profiles are excluded from the calculations. Positive values of W_j indicate net removal of an element from the soil. The calculations of $m_{j,w}$ and T_{soil} were described previously (Ma et al. 2010; Herndon et al., 2011) and are described in more detail in section D3 in Appendix D. We calculate that W_{Mn} decreases from the midslope ($= 0.32 \pm 0.06 \text{ mmol m}^{-2} \text{y}^{-1}$) to the valley floor ($= 0.11 \pm 0.02 \text{ mmol m}^{-2} \text{y}^{-1}$) in the planar transect and from the ridge ($= 0.49 \pm 0.12 \text{ mmol m}^{-2} \text{y}^{-1}$) to the midslope ($= 0.36 \pm 0.05 \text{ mmol m}^{-2} \text{y}^{-1}$) to the valley floor ($= 0.26 \pm 0.04 \text{ mmol m}^{-2} \text{y}^{-1}$) in the swale transect.

Rate constants for the loss of Mn integrated over the full time period of soil formation (k_w, y^{-1}) can also be calculated by dividing W_{Mn} by the mass of Mn present in the protolith prior to weathering (i.e. $\tau_{Zr,Mn} = 0$). These rate constants decrease downslope and are higher for the swale slope relative to the planar slope (Table 5-6). When we compare the time-integrated k_w values to current k_w values calculated from water chemistry in section 4.4.1., we find that the time-integrated values are higher than current values for planar hillslopes but lower than current values for swale hillslopes. Thus, the short-term rates observed with water fluxes differ from long-term weathering rates. The current decrease in the rate of Mn loss from the planar hillslope is attributed to short-term enhanced uptake in vegetation, and the current increase in the rate of Mn loss from the swale hillslope is attributed to increased mobilization from organic matter inputs.

4.4.3. Watershed-scale weathering

A similar approach to the approach used for weathering on the pedon-scale (Eqns 13 & 14) can be used to estimate a rate constant for weathering losses of Mn on the watershed scale:

$$\hat{L}_{stream} = k_{w,SH} M_{Mn,w,SH} \quad (15)$$

$\hat{L}_{Mn,stream}$ ($= 30.0 \pm 1.5 \text{ mol y}^{-1}$) is the rate that dissolved Mn is removed from the watershed at the stream outlet (Eqn. 2). $M_{Mn,w,SH}$ (moles) is the total estimated mass of Mn in soil in the watershed:

$$M_{Mn,w,SH} = \sum_s A_s \bar{M}_{Mn,w,s} \quad (16)$$

$\bar{M}_{Mn,w,s}$ (mmol m^{-2} ; Eqn. 4) is calculated for each slope position s (ridge, midslope, and valley floor) for the planar and swale transects. The total area covered by each type of landscape position s ($A_s; \text{m}^2$) is estimated as the fraction (X_s) of the total surface area of Shale Hills ($A_{SH} = 79,000 \text{ m}^2$):

$$A_s = X_s A_{SH} \quad (17)$$

X_s is calculated assuming that the ridge, midslope and valley soils each cover one-third of the hillslope as indicated in Fig. 5-11. Again planar soils are set to ~79% of A_{SH} and swale soils ~16% (Lin et al., 2006). Thus, for planar soils, $X_{s,planar} = 0.26$ (i.e. 0.33×0.79) and $A_{s,planar} = 20,700 \text{ m}^2$, and for swale soils, $X_{s,swale} = 0.054$ (i.e. 0.33×0.16) and $A_{s,swale} = 4,250 \text{ m}^2$ at all slope positions. From Eqn. (16), we estimate $M_{Mn,w,SH} = 1,460,000 \pm 101,000$ moles, i.e. total Mn in mineral soils in the catchment. Thus, from Eqn. (15), the rate constant for Mn weathering on the watershed scale is calculated to be $k_{w,SH} = 2.1 \pm 0.1 \times 10^{-5} \text{ y}^{-1}$. As expected, this value is intermediate between the range of rate constants estimated for soils on the planar hillslope ($k_{w,s} = 0.52 - 0.88 \text{ y}^{-1}$) and soils on the swale hillslope ($k_{w,s} = -7.3 - 73 \text{ y}^{-1}$).

4.4. Vegetation

From equations 8 and 9, we calculate that the area-normalized mass of Mn in foliage in the watershed is $\bar{M}_{Mn,fol} = 14.7 \pm 3.7 \text{ mmol Mn m}^{-2}$. As discussed previously, we can use $\bar{M}_{Mn,fol}$ as a lower estimate of the mass of Mn that is taken up from the soil into vegetation and returned to the soil as litterfall in a one year cycle. Using equations 7 and 10 to determine the flux of Mn into and out of vegetation for each box in the hillslope reactor model, we find that F_{veg} ($= 14.8 \text{ mmol m}^{-2} \text{ y}^{-1}$) and F_{litter} ($= 13.2 \text{ mmol m}^{-2} \text{ y}^{-1}$) are much larger than both F_{ppt} ($= 0.045 \text{ mmol m}^{-2} \text{ y}^{-1}$) and $F_{out,s}$ ($= 0.21 - 3.8 \text{ mmol m}^{-2} \text{ y}^{-1}$) for the planar and swale hillslopes. This indicates that fluxes of Mn into and out of vegetation are approximately equal and greater than inputs and outputs from the hillslope reactor. An estimate for the flux of dissolved Mn that is available in the soil for uptake by vegetation is calculated as the product of $C_{Mn,pf}$ and V_{ET} :

$$F_{pf,s} = C_{Mn,pf} V_{ET} \quad (18)$$

Here, $C_{Mn,pf}$ is averaged over all pore fluid samples from all depths at each slope position. This calculation is based on the assumption that soil evaporation is negligible and that all water taken up by vegetation has a concentration of Mn equal to $C_{Mn,pf}$. $F_{pf,s}$ values calculated using Eqn. (18) for the planar ($0.25 - 0.37 \text{ mmol m}^{-2} \text{ y}^{-1}$) and swale ($0.51 - 3.9 \text{ mmol m}^{-2} \text{ y}^{-1}$) soils are not sufficient to account for the flux of Mn into vegetation, F_{veg} ($= 15 \text{ mmol m}^{-2} \text{ y}^{-1}$). In fact, the average $C_{Mn,pf}$ needed to explain F_{veg} (calculated by setting $F_{pf,s} = F_{veg}$ in Eqn. (18), $C_{Mn,pf} = 29.6 \pm 6.0 \text{ } \mu\text{M}$) is equivalent only to the highest measured $C_{Mn,pf}$ value ($24.3 \text{ } \mu\text{M}$). Therefore, it is likely the pore fluids sampled by the lysimeters generally do not represent the chemical composition of the pore fluids taken up by vegetation.

Pore fluid chemistry in the rhizosphere often differs from bulk soil solution due to root-induced concentration gradients, inputs of protons and organic matter, and a localized proliferation of microorganisms (Neumann and Römheld, 2012). Researchers have shown that diffusion-limited elements such as Mn, Fe, Zn, and K often exhibit low concentrations in soil solution near roots relative to in the bulk soil, defining a diffusion gradient that enhances the release of those cations from mineral structures near the root (Hinsinger and Jaillard, 1993; Neumann and Römheld, 2012). In other words, when the rate of Mn uptake into the root exceeds the rate of water uptake, a depletion zone is created that enhances diffusion of Mn towards the root. Diffusion may thus account for the high mass of Mn in foliage despite generally lower concentrations of Mn in pore fluids.

On the other hand, high concentrations of microorganisms and organic ligands can substantially increase concentrations of soluble Mn in the rhizosphere (Godo and Reisenauer, 1980; Posta et al., 1994). For example, water-extractable Mn can increase by a factor of seven in the rhizosphere relative to the bulk soil (Séguin et al., 2004). If the water that is transpired contains a higher concentration of Mn than is measured in the bulk pore fluids, it may be sufficient to account for the mass of Mn observed in foliage. Thus, rhizosphere processes may regulate Mn uptake into vegetation.

We investigate the total mass of exchangeable Mn in soils on the planar transect ($\bar{M}_{Mn,CEC}$; mmol m^{-2}) as a source of bioavailable Mn:

$$\bar{M}_{Mn,CEC} = \sum_{z=0}^{z=d_s} \rho_w C_{Mn,CEC}(z) \Delta z \quad (19)$$

The mass of exchangeable Mn is summed over all sampled depth intervals (Δz , m) from $z = 0$ to $z = d_s$. Here, $C_{Mn,CEC}$ (mmol kg^{-1}) is the previously reported concentration of Mn held on the exchangeable sites in the soil measured by washing soils with $\text{BaCl}_2/\text{NH}_4\text{Cl}$ solution (Jin et al., 2010). Similar to bulk $C_{Mn,w}$, exchangeable Mn is highest at the surface and decreases with depth in the soil profile, reaching a relatively constant concentration ($C_{Mn,CEC} = 0.36 \pm 0.04 \text{ mmol kg}^{-1}$) below 20 cm (Figure D-14). We calculate that $\bar{M}_{Mn,CEC}$ for the ridge ($= 740 \text{ mmol m}^{-2}$), midslope ($= 840 \text{ mmol m}^{-2}$), and valley soils ($= 580 \text{ mmol m}^{-2}$) provides a large pool of bioavailable Mn for plant uptake. In fact, the calculated F_{veg} value would deplete $< 3\%$ of $\bar{M}_{Mn,CEC}$ each year. Therefore, it is likely that plants derive their Mn by mobilizing cations bound to the exchange sites into pore fluids within the rhizosphere. Given that 40-60% of exchangeable Mn is present in the top 10 cm of the soil profile, vegetation may acquire Mn largely from the surface soils.

Furthermore, even though the Mn content of soils varies significantly, Jin et al. (2010) observed little variation in exchangeable Mn along the planar hillslope, and this may explain the relatively constant uptake at all slope positions.

4.4.4. Rate constants for uptake by vegetation

Similar to chemical weathering, we model uptake of Mn into vegetation as first-order with respect to $M_{Mn,w}$ to derive a first-order rate constant k_{veg} (y^{-1}) at ridge, hillslope, and catchment scales:

$$F_{veg} = k_{veg}M_{Mn,w} \quad (20)$$

F_{veg} ($= 15 \pm 4 \text{ mmol m}^{-2} \text{ y}^{-1}$) is assumed the same for all locations in the catchment; thus, k_{veg} changes as a function of $M_{Mn,w}$ for ridge, hillslope, and catchment-scales. The range of k_{veg} values for the planar ($5.7 - 10.6 \times 10^{-4} \text{ y}^{-1}$) and swale ($3.8 - 28.2 \times 10^{-4}$) soils are consistent with estimates for ridge soils ($k_{veg} = 9.3 \pm 2.5 \times 10^{-4} \text{ y}^{-1}$; $\bar{M}_{Mn,w} = 16.1 \text{ mol m}^{-2}$ as reported in Herndon et al. (2011) and the whole watershed ($k_{veg} = 7.9 \pm 2.1 \times 10^{-4} \text{ y}^{-1}$; $\bar{M}_{Mn,w} = 18.5 \text{ mol m}^{-2}$) (Table 5-6).

In contrast to the relative homogeneity of Mn vegetative uptake across the landscape (k_{veg} varies by a factor of 7), the rate constants describing Mn losses from soil, k_w , vary by greater than a factor of 100. Thus, while uptake into vegetation – which is balanced by Mn flux back to the soil in litter – exceeds chemical weathering in all vegetated soils, the relative importance of biotic versus weathering fluxes changes as a function of landscape position. For example, the magnitude by which k_{veg} is greater than k_w ranges from 85 to 210x on the planar hillslope but only 4 – 9x on the swale hillslope. Spatial differences in k_w are most likely controlled by factors such as the pH and organic matter in the bulk soil, which differ between the planar and swale hillslopes and have been proposed to influence Mn mobilization (Andrews, 2011). In comparison, uptake of Mn into vegetation may be regulated by processes in the rhizosphere, as discussed previously.

4.5. Susquehanna River Basin

To study the transport of Mn contamination from soils into rivers on a larger scale, we examine records of water chemistry along the Susquehanna River. Water quality data and discharge rates were obtained from the National Water Information System provided by the U.S. Geological Survey (U.S. Geological Survey, 2012). From this database, we collated concentrations of dissolved Mn ($\mu\text{g/L}$) for all sites along the main branch of the Susquehanna River for which more than three water quality samples are reported ($n = 14$ sites). Averaged values of these $C_{Mn,stream}$ measurements along the Susquehanna River have decreased by a factor of 10 from the

first measurements in 1957 to the most recently reported data in 2010 (Figure 5-12). Specifically, decadal averages for $C_{Mn,stream}$ declined from $380 \pm 66 \mu\text{g L}^{-1}$ (1957 – 1970, $n = 43$) to $168 \pm 15 \mu\text{g L}^{-1}$ (1971 – 1980, $n = 295$) to $140 \pm 9.5 \mu\text{g L}^{-1}$ (1981 – 1990, $n = 172$) to $54 \pm 5.4 \mu\text{g L}^{-1}$ (1991 – 2000, $n = 122$) to $43 \pm 6.4 \mu\text{g L}^{-1}$ (2001 – 2010, $n = 50$). The slope of a linear equation fit to all data points from the 14 sites yields an average decrease in riverine Mn concentration of $8.1 \pm 0.7 \mu\text{g L}^{-1} \text{y}^{-1}$.

We further examined three sites (USGS sites 01540500, 01570500, and 01578310) for which there were both adequate Q_{stream} and $C_{Mn,stream}$ data across a wide span of dates. Specifically, Danville, PA (site 01540500, 40.95814218, -76.6191222) reports $Q_{stream} = 15,500 \pm 350 \text{ft}^3 \text{s}^{-1}$ (1906 – 2011) and 85 $C_{Mn,stream}$ values (1972 – 1995), Harrisburg, PA (site 01570500, 40.25481164, -76.8860846) reports $Q_{stream} = 35,200 \pm 680 \text{ft}^3 \text{s}^{-1}$ (1891 – 2011) and 186 $C_{Mn,stream}$ values (1970 – 1995), and Conowingo, MD (site 01578310, 39.6579133, -76.1741754) reports $Q_{stream} = 41,400 \pm 1,670 \text{ft}^3 \text{s}^{-1}$ (1968 – 2011) and 283 $C_{Mn,stream}$ values (1978 – 2010). The linear decrease in $C_{Mn,stream}$ with respect to time for Danville ($= 9.0 \pm 1.4 \mu\text{g L}^{-1} \text{y}^{-1}$), Harrisburg ($= 6.1 \pm 1.8 \mu\text{g L}^{-1} \text{y}^{-1}$), and Conowingo ($= 4.9 \pm 0.7 \mu\text{g L}^{-1} \text{y}^{-1}$) bracket the overall trend observed for the Susquehanna River. To estimate the rate of Mn removal from soils in the Susquehanna River Basin, we calculate k_w for the catchment above each Susquehanna river site for each decade by rearranging Eqns. (2), (15), and (16):

$$k_w = \frac{Q_{stream} C_{Mn,stream}}{A_{SRB} d \rho_w C_{Mn,w}} \quad (21)$$

The drainage area (A_{SRB} ; m^2) is reported for the sites at Danville ($= 2.91 \times 10^{10} \text{m}^2$), Harrisburg ($= 6.24 \times 10^{10} \text{m}^2$), and Conowingo ($= 7.02 \times 10^{10} \text{m}^2$) (U.S. Geological Survey, 2012). For simplicity, we set $\rho_w = 1,520 \text{kg m}^{-3}$ and the average depth of the soil $d = 1 \text{m}$ for the entire drainage area. We use an average $C_{Mn,w}$ ($= 810 \pm 60 \text{mg kg}^{-1}$) measured in 360 soil samples from 65 soil cores developed on various lithologies throughout Pennsylvania (Ciolkosz and Amistadi, 1993; Ciolkosz et al., 1998; Ciolkosz, 2000). Based on these values, we estimate that the total dissolved mass of Mn in the river over the 53 year period comprises $< 1\%$ of total soil Mn in the drainage basin. In other words, the total loss of Mn from the basin is small compared to the total Mn mass in the soil. Thus, we can use Equation 21 and assume $C_{Mn,w}$ remains constant.

Based on these considerations, the release rate of Mn in the Susquehanna River Basin is approximately equal at all sites and decreases from the 1960s ($k_w = 16 \pm 8.6 \times 10^{-5} \text{y}^{-1}$) to the 2000s ($k_w = 1.8 \pm 0.95 \times 10^{-5} \text{y}^{-1}$) (Figure 5-13 and Table 5-6). Furthermore, current k_w values for the

SRB are within error of current k_w values calculated for the Shale Hills CZO, while SRB k_w values prior to 1990 are nine times greater. We consider a few possibilities to explain decreasing rates of Mn loss in the SRB.

First, many streams in Pennsylvania are strongly impacted by acid mine drainage which causes high levels of dissolved Mn (Cravotta, 2008). Water chemistry at Danville on the Susquehanna River was previously shown to be impacted by inputs from heavily mined watersheds such as the Lackawanna basin (Raymond and Oh, 2009). However, Mn concentrations in the Lackawanna River peak before 1950 and decline rapidly while Mn concentrations in the Susquehanna River at Danville do not peak until ~1970 (Figs. 5-12 and D-15). Additionally, sulfate concentrations, which are used by Raymond and Oh as a chemical indicator of AMD and which correlate to Mn concentrations in the Lackawanna River, begin to decline prior to the decline in Mn concentrations in the Susquehanna River. From this, we infer that Mn inputs from acid mine drainage did not substantially contribute to peak Mn concentrations in the Susquehanna River, especially after 1970.

Second, as shown previously (Chapter 3), vegetation may slow the loss of Mn from soils into rivers. Forests throughout the northeastern United States, including in the SRB, have experienced significant regrowth over the past century (Turner et al., 1995; Goodale et al., 2002). However, forest aggradation has occurred gradually since 1900 while riverine Mn concentrations decreased rapidly after 1970 (Houghton and Hackler, 2000; Goodale et al., 2002). Thus, while increased storage of Mn in forest biomass may contribute to a decrease in Mn losses from the SRB, it cannot explain the overall trend.

Finally, weathering of Mn from atmospherically-deposited contaminants in the soil (e.g. Mn-oxides), significant contributors to $C_{Mn,stream}$ in the past, may be decreasing today. For example, we observe that k_w values for the SRB prior to 1990 are intermediate between k_w values for the modern SSHCZO and k_w values measured in the laboratory for Mn-oxide contaminants (Figure 5-13; Chapter 4). Decreases in riverine Mn concentrations in the Susquehanna River since 1957 are therefore attributed to a decadal-long decrease in weathering fluxes from Mn-oxide contaminants following decreases in atmospheric Mn inputs.

V. Conclusions

Manganese contamination in soils has been identified at the regional scale and in soils throughout the United States and Europe (Herndon et al., 2011). The long-term impacts of Mn contamination are unknown, but may have implications for soil redox reactions, organic matter

storage, forest health, and water quality. Predicting the impacts of soil contamination on environmental processes requires a better understanding of the rates that contamination moves from air, through soils, and into rivers. In this study, our goal was to quantify how the fluxes of Mn vary across one small catchment and then to extrapolate these rates across scales. Identifying spatial differences in Mn mobilization will enable more accurate predictions of how long Mn contaminants persist in soils and how quickly they are transferred into water systems.

Mn in soils and pore fluids exhibit spatial variability in the Shale Hills watershed. Mn is heavily enriched in soils at the ridge relative to the shale bedrock, but depleted in deeper soils on the slope and in the valley. By comparing Mn to depth profiles for Mg and Fe, we find that the soils with net Mn depletion actually exhibit a Mn addition signal near the soil surface. Therefore, the Mn addition signal is younger and is imprinted on top of the natural depletion profile.

Although all soils have generally experienced similar rates of Mn loss over geologic time, there is significant spatial variation in current rates of Mn leaching. For example, the flux of Mn from the swale transect into the stream exceeds the flux from the planar transect. On an area-normalized basis, more Mn is found in swales than on planar hillslopes, and swales release more Mn at least partly because more Mn is present. However, we also calculated that swales lose a higher fraction of the total mass of Mn in the soil per unit time relative to the planar soils. The enhanced rate of removal of Mn from swale soils is likely a function of differing soil chemistry. For example, Andrews (2011) observed that concentrations of Mn in pore fluids at Shale Hills are strongly correlated with dissolved organic matter and pH and concluded that swales act as “hot-spots” of Mn mobilization to the stream. Therefore, the low soil pH and high organic matter content of swale soils may facilitate Mn leaching, leading to more rapid depletion of Mn from these soils. Some of the midslope and valley-floor soils at SSHCZO are currently accumulating Mn from upslope. Although the mechanisms driving accumulation are unknown, these soils are also observed to act as accumulation sites for other elements (Jin et al., 2010; Jin and Brantley, 2011). Overall, however, each hillslope is losing, rather than accumulating, Mn.

Similar to other studies conducted at Shale Hills and in mesocosms (Chapter 3, Herndon and Brantley, 2011), we find that rates of Mn uptake from the soil into vegetation and return to soil in litterfall exceed net input (precipitation) and output (downslope transport) fluxes to the soil. We have suggested previously that the uptake of Mn into vegetation has led to accumulation of Mn in living and dead organic matter in Shale Hills and elsewhere in the northeast, effectively slowing the removal of Mn contamination from soils into rivers (Herndon and Brantley, 2011). However, the rate of Mn release from watersheds also depends on the balance between uptake by vegetation and

decomposition of organic matter. As shown here, uptake of Mn into vegetation may slow leaching of Mn from the soil, but organic-rich soils can act as dominant sources for Mn inputs to streams, and the breakdown of Mn-rich organic matter ultimately releases stored Mn. In this manner, vegetation acts as a capacitor, storing Mn in biomass and releasing it slowly to soils and rivers over time.

Non-chemostatic behavior of Mn in the stream is attributed to the differential inputs of Mn from the planar and swale hillslopes. The concentrations of major rock-derived elements are similar in planar and swale soil waters and exhibit minimal variation in the stream over a wide range of discharge values. The chemostatic behavior exhibited by the major elements (Si, Na, K, Mg, Ca) is attributed to rapid displacement of these elements from exchange sites by protons during rainfall events. In contrast, high Mn fluxes from the swales are diluted by low Mn fluxes from the planar hillslopes, and pulses of high Mn are observed in the stream following precipitation events in the dry season.

Many of the observations concerning Mn in the small CZO catchment can be used to understand Mn concentrations in the Susquehanna River. These concentrations have steadily declined between the start of water quality monitoring in the 1950s until the present. This observed decline is attributed to decreased inputs of Mn from air to land as the result of environmental regulation and decreases in industrial productivity. While Mn from the air can be directly input into the river, inputs from land to the rivers are much larger, and the change in river Mn concentrations are attributed to a change in the release rate of Mn from the soil. Indeed, current release rates of Mn in the Susquehanna River Basin are consistent with release rates estimated for the Shale Hills CZO. In contrast, rates of Mn release from the SRB in the 1960s are intermediate between rates estimated for SSHCZO and for Mn-oxide contaminants in laboratory experiments. We therefore infer that the record of Mn chemistry in the Susquehanna River reflects a rapid weathering of Mn contaminants that continues to decline as atmospheric inputs of Mn have decreased and the remaining contaminants have become less reactive.

VI. Acknowledgements

Logistical support and/or data were provided by the NSF-supported Susquehanna Shale Hills Critical Zone Observatory. We acknowledge all members of the SSHCZO who assisted sample collection and analyses, especially Lixin Jin, Danielle Andrews, and Jennifer Williams for soil and water collection and analyses, Katie Gaines for vegetation collection, and Lauren Smith for providing the leaf litter biomass data used in this study.

VII. References

- Anderson S. P., Dietrich W. E. and Brimhall G.H. (2002) Weathering profiles, mass-balance analysis, and rates of solute loss: Linkages between weathering and erosion in a small, steep catchment. *GSA Bulletin* **114**, 1143–1158.
- Andrews D. M. (2011) Control of DOC and pH on Spatio-temporal Concentrations of Al, Fe, and Mn in Soil Pore Water and Stream Water in the Shale Hills Critical Zone Observatory. PhD Thesis, The Pennsylvania State University.
- Andrews D. M., Lin H., Zhu Q., Jin L. and Brantley S. L. (2011) Hot Spots and Hot Moments of Dissolved Organic Carbon Export and Soil Organic Carbon Storage in the Shale Hills Catchment. *Vadose Zone Journal* **10**, 943.
- Berg B., Steffen K. T. and McLaugherty C. (2007) Litter decomposition rate is dependent on litter Mn concentrations. *Biogeochemistry* **82**, 29–39.
- Bloom P. R., Skyllberg U. L. and Sumner M. E. (2005) Soil Acidity. In *Chemical processes in soils* (eds. M. A. Tabatabai and D. L. Sparks). Soil Science Society of America, Madison, WI. pp. 411–459.
- Boudissa S. M., Lambert J., Müller C., Kennedy G., Gareau L. and Zayed J. (2006) Manganese concentrations in the soil and air in the vicinity of a closed manganese alloy production plant. *The Science of the total environment* **361**, 67–72.
- Brantley S. L. and Lebedeva M. (2011) Learning to Read the Chemistry of Regolith to Understand the Critical Zone. *Annual Review of Earth and Planetary Sciences* **39**, 387–416.
- Brimhall G. H. and Dietrich W. E. (1987) Constitutive mass balance relations between chemical composition, volume, density, porosity, and strain in metasomatic hydrochemical systems: Results on weathering and pedogenesis. *Geochimica et Cosmochimica Acta* **51**, 567–587.
- Buck C. S., Landing W. M., Resing J. A. and Measures C. I. (2010) The solubility and deposition of aerosol Fe and other trace elements in the North Atlantic Ocean: Observations from the A16N CLIVAR/CO₂ repeat hydrography section. *Marine Chemistry* **120**, 57–70.
- Chadwick O A, Derry L A, Vitousek P. M., Huebert B. J. and Hedin L. O. (1999) Changing sources of nutrients during four million years of ecosystem development. *Nature* **397**, 491–497.
- Chadwick O. A., Brimhall G. H. and Hendricks D. M. (1990) From a black to a gray box — a mass balance interpretation of pedogenesis. *Geomorphology* **3**, 369–390.
- Ciolkosz E. J. (2000) Major and Trace Elements in Southwestern Pennsylvania Soils. *Agronomy Series No. 148*, The Pennsylvania State University.
- Ciolkosz E. J. and Amistadi M. K. (1993) Metals in Pennsylvania Soils. *Agronomy Series No. 128*, The Pennsylvania State University.
- Ciolkosz E. J., Stehouwer R. C. and Amistadi M. K. (1998) Metals Data for Pennsylvania Soils. *Agronomy Series No. 140*, The Pennsylvania State University.
- Cravotta C. A. (2008) Dissolved metals and associated constituents in abandoned coal-mine discharges, Pennsylvania, USA. Part 1: Constituent quantities and correlations. *Applied Geochemistry* **23**, 166–202.
- Dobson A. W., Erikson K. M. and Aschner M. (2004) Manganese Neurotoxicity. *Ann. N.Y. Acad. Sci.* **1012**, 115–128.
- Duffy C. (2012) Stream Flow Data. Available at: <http://www.czo.psu.edu>.
- Evangelou V. P. and R.E. Phillips (2005) Cation exchange in soils. In *Chemical processes in soils* (eds. M. A. Tabatabai and D. L. Sparks). Soil Science Society of America, Madison, WI. pp. 343–410.
- Gardner T. W., Ritter J. B., Shuman C. A., Bell J. C., Sasowsky K. C. and Pinter N. (1991) A Periglacial Stratified Slope Deposit in the Valley and Ridge Province of Central Pennsylvania,

- USA: Sedimentology, Stratigraphy, and Geomorphic Evolution. *Permafrost and Periglacial Processes* **2**, 141–162.
- Godsey S. E., Kirchner J. W. and Clow D. W. (2009) Concentration – discharge relationships reflect chemostatic characteristics of US catchments. *Hydrological Processes* **23**, 1844–1864.
- Gonzalez A., Steffen K. and Lynch J. (1998) Light and excess manganese . Implications for oxidative stress in common bean. *Plant physiology* **118**, 493–504.
- Goodale C. L., Lajtha K., Nadelhoffer K. J., Boyer E. W. and Jaworski N. A. (2002) Forest nitrogen sinks in large eastern U.S. watersheds: estimates from forest inventory and an ecosystem. *Biogeochemistry* **57/58**, 239–266.
- Harris W. F., Goldstein R. A. and Henderson G. S. (1973) Analysis of forest biomass pools, annual primary production and turnover of biomass for a mixed deciduous forest watershed. In *Proceedings of working party on forest biomass of IUFRO* (ed. H. Young). University of Maine Press, Orono, Maine. pp. 41–64.
- Heal K. V., Kneale P. E. and McDonald A. T. (2002) Manganese in runoff from upland catchments: temporal patterns and controls on mobilization. *Hydrological Sciences Journal* **47**, 769–780.
- Herndon E. M. and Brantley S. L. (2011) Movement of manganese contamination through the Critical Zone. *Applied Geochemistry* **26**, S40–S43.
- Herndon E. M., Jin Lixin and Brantley S. L. (2011) Soils reveal widespread manganese enrichment from industrial inputs. *Environmental science & technology* **45**, 241–7.
- Hinsinger P. and Jaillard B. (1993) Root-induced release of interlayer potassium and vermiculitization of phlogopite as related to potassium depletion in the rhizosphere of ryegrass. *Journal of Soil Science* **44**, 525–534.
- Hokura A., Matsuura H., Katsuki F. and Haraguchi H. (2000) Multielement Determination of Major-to-Ultratrace Elements in Plant Reference Materials by ICP-AES / ICP-MS and Evaluation of Their Enrichment Factors. *Analytical Sciences* **16**, 1161–1168.
- Horiguchi T. (1987) Mechanism of manganese toxicity and tolerance of plants. *Soil Science and Plant Nutrition* **33**, 595–606.
- Horsley S. B., Long R. P., Bailey S. W., Hallett R. A. and Hall T. J. (2000) Factors associated with the decline disease of sugar maple on the Allegheny Plateau. *Canadian Journal of Forest Research* **30**, 1365–1378.
- Houghton R. A. and Hackler J. A. (2000) Changes in terrestrial carbon storage in the United States. I: the roles of agriculture and forestry. *Global Ecology and Biogeography* **9**, 125–144.
- Houle D., Tremblay S. and Ouimet R. (2007) Foliar and wood chemistry of sugar maple along a gradient of soil acidity and stand health. *Plant and Soil* **300**, 173–183.
- Jin L., Andrews D. M., Holmes G. H., Lin H. and Brantley S. L. (2011) Opening the “Black Box”: Water Chemistry Reveals Hydrological Controls on Weathering in the Susquehanna Shale Hills Critical Zone Observatory. *Vadose Zone Journal* **10**, 928.
- Jin L. and Brantley S. L. (2011) Soil chemistry and shale weathering on a hillslope influenced by convergent hydrologic flow regime at the Susquehanna/Shale Hills Critical Zone Observatory. *Applied Geochemistry* **26**, S51–56.
- Jin L., Ravella R., Ketchum B., Bierman P. R., Heaney P., White T. and Brantley S. L. (2010) Mineral weathering and elemental transport during hillslope evolution at the Susquehanna/Shale Hills Critical Zone Observatory. *Geochimica et Cosmochimica Acta* **74**, 3669–3691.
- Jobbagy E.G. and Jackson R.B. (2004) The uplift of soil nutrients by plants: biogeochemical consequences across scales. *Ecology* **85**, 2380–2389.
- Khan K., Wasserman G. A., Liu X., Ahmed E., Parvez F., Slavkovich V., Levy D., Mey J., van Geen A., Graziano J. H. and Factor-Litvak P. (2012) Manganese exposure from drinking water and children’s academic achievement. *Neurotoxicology* **33**, 91–7.

- Kim Y., Bowler R. M., Abdelouahab N., Harris M., Gocheva V. and Roels H. a (2011) Motor function in adults of an Ohio community with environmental manganese exposure. *Neurotoxicology* **32**, 606–14.
- Kogelmann W. J. and Sharpe W. E. (2006) Soil acidity and manganese in declining and nondeclining sugar maple stands in Pennsylvania. *Journal of environmental quality* **35**, 433–41.
- Kurtz A. C., Derry L.A. and Chadwick O.A. (2001) Accretion of Asian dust to Hawaiian soils: Isotopic, elemental, and mineral mass balances. *Geochimica et Cosmochimica Acta* **65**, 1971–1983.
- Landre A. L., Watmough S. A. and Dillon P. J. (2010) Metal Pools, Fluxes, and Budgets in an Acidified Forested Catchment on the Precambrian Shield, Central Ontario, Canada. *Water, Air, & Soil Pollution* **209**, 209–228.
- Li J., Richter D., Mendoza A. and Heine P. (2008) Four-decade responses of soil trace elements to an agrading old-field forest: B, Mn, Zn, Cu, and Fe. *Ecology* **89**, 2911–2923.
- Lin H. S., Kogelmann W., Walker C. and Bruns M. A. (2006) Soil moisture patterns in a forested catchment: A hydrogeological perspective. *Geoderma* **131**, 345–368.
- Lin H. and Zhou X. (2008) Evidence of subsurface preferential flow using soil hydrologic monitoring in the Shale Hills catchment. *European Journal of Soil Science* **59**, 34–49.
- Lin H. (2006) Temporal stability of soil moisture spatial pattern and subsurface preferential flow pathways in the Shale Hills catchment. *Vadose Zone Journal* **5**, 317–340.
- Lucchini R. G., Albini E., Benedetti L., Borghesi S., Coccaglio R., Malara E. C., Parrinello G., Garattini S., Resola S. and Alessio L. (2007) High Prevalence of Parkinsonian Disorders Associated to Manganese Exposure in the Vicinities of Ferroalloy Industries. *American Journal of Industrial Medicine* **50**, 788–800.
- Lytle C., Smith B. and Mckinnon C. (1995) Manganese accumulation along Utah roadways: a possible indication of motor vehicle exhaust pollution. *Science of The Total Environment* **162**, 105–109.
- Ma L., Chabaux F., Pelt E., Blaes E., Jin L and Brantley S. L. (2010) Regolith production rates calculated with uranium-series isotopes at Susquehanna/Shale Hills Critical Zone Observatory. *Earth and Planetary Science Letters* **297**, 211–225.
- Matsunaga K., Ohyama T., Kuma K., Kudo I. and Suzuki Y. (1995) Photoreduction of manganese dioxide in seawater by organic substances under ultraviolet or sunlight. *Water Research* **29**, 757–759.
- McCain D. C. and Markley J. L. (1989) More Manganese Accumulates in Maple Sun Leaves than in Shade Leaves. *Plant physiology* **90**, 1417–1421.
- McQuattie C. J. and Schier G. (2000) Response of sugar maple (*Acer saccharum*) seedlings to manganese. *Canadian Journal of Forest Research* **30**, 456–467.
- Mergler D., Huel G. and Bowler R. (1994) Nervous system dysfunction among workers with long-term exposure to manganese. *Environmental Research* **64**, 151–180.
- NADP (2011) National Atmospheric Deposition Program. Available at: <http://nadp.sws.uiuc.edu/>.
- National Research Council (1973) *Medical and biological effects of environmental pollutants: manganese.*, National Academy of Sciences, Washington, D.C.
- Navrátil T., Shanley J. B., Skřivan P., Krám P., Mihaljevič M. and Drahotka P. (2007) Manganese Biogeochemistry in a Central Czech Republic Catchment. *Water, Air, and Soil Pollution* **186**, 149–165.
- Neumann G. and Römheld V. (2012) Rhizosphere Chemistry in Relation to Plant Nutrition. In *Marschner's Mineral Nutrition of Higher Plants* Elsevier Ltd. pp. 347–368.
- Niu X., Lenhart K. A., Williams J. and Brantley S. (2011) CZChemDB and EarthChem: Advancing management and access of critical zone geochemical data. *Applied Geochemistry* **26**, S108–S110.

- Nriagu J. and Pacyna J. (1988) Quantitative assessment of worldwide contamination of air, water and soils by trace metals. *Nature* **333**, 134–139.
- Pacyna J. M. and Pacyna E. G. (2001) An assessment of global and regional emissions of trace metals to the atmosphere from anthropogenic sources worldwide. *Environmental Reviews* **9**, 269–298.
- Parekh P. P. (1990) A study of manganese from anthropogenic emissions at a rural site in the eastern United States. *Atmospheric Environment* **24A**, 415–421.
- Porder S., Hilley G. E. and Chadwick O. (2007) Chemical weathering, mass loss, and dust inputs across a climate by time matrix in the Hawaiian Islands. *Earth and Planetary Science Letters* **258**, 414–427.
- Posta K., Marschner H. and Römheld V. (1994) Manganese reduction in the rhizosphere of mycorrhizal and nonmycorrhizal maize. *Mycorrhiza* **5**, 119–124.
- Qu Y. and Duffy C. J. (2007) A semidiscrete finite volume formulation for multiprocess watershed simulation. *Water Resources Research* **43**, W08419.
- Rahn K. and Lowenthal D. (1984) Elemental tracers of distant regional pollution aerosols. *Science* **223**, 132–139.
- Raymond P. and Oh N.-H. (2009) Long term changes of chemical weathering products in rivers heavily impacted from acid mine drainage: Insights on the impact of coal mining on regional and global carbon and sulfur budgets. *Earth and Planetary Science Letters* **284**, 50–56.
- Godo G. and Reisenauer H. (1980) Plant Effects on Soil Manganese Availability. *Soil Sci. Soc. Am. J.* **44**, 993–995.
- Riebe C. S., Kirchner J. W. and Finkel R. C. (2003) Long-term rates of chemical weathering and physical erosion from cosmogenic nuclides and geochemical mass balance. *Geochimica et Cosmochimica Acta* **67**, 4411–4427.
- Riojas-Rodríguez H., Solís-Vivanco R., Schilman A., Montes S., Rodríguez S., Ríos C. and Rodríguez-Agudelo Y. (2010) Intellectual Function in Mexican Children Living in a Mining Area and Environmentally Exposed to Manganese. *Environmental Health Perspectives* **118**, 1465–1470.
- Runkel R., Crawford C. G. and Cohn T. A. (2004) Load estimator (LOADEST): A FORTRAN program for estimating constituent loads in streams and rivers. In *Techniques and Methods Book 4* (ed. U.S. Geological Survey). Reston, Virginia.
- Scudlark J. R., Rice K. C., Conko K. M., Bricker O. P. and Church T. M. (2005) Transmission of atmospherically derived trace elements through an undeveloped, forested Maryland watershed. *Water, Air, & Soil Pollution* **163**, 53–79.
- Shanley J. B. (1986) Manganese biogeochemistry in a small Adirondack forested lake watershed. *Water Resources Research* **22**, 1647.
- Solís-Vivanco R., Rodríguez-Agudelo Y., Riojas-Rodríguez H., Ríos C., Rosas I. and Montes S. (2009) Cognitive impairment in an adult Mexican population non-occupationally exposed to manganese. *Environmental toxicology and pharmacology* **28**, 172–8.
- St. Clair S. B., Carlson J. E. and Lynch J. P. (2005) Evidence for oxidative stress in sugar maple stands growing on acidic, nutrient imbalanced forest soils. *Oecologia* **145**, 258–69.
- St. Clair S. B. and Lynch J. P. (2005) Element accumulation patterns of deciduous and evergreen tree seedlings on acid soils: implications for sensitivity to manganese toxicity. *Tree physiology* **25**, 85–92.
- Sunda W. G. and Huntsman S. (1988) Effect of sunlight on redox cycles of manganese in the southwestern Sargasso Sea. *Deep Sea Research* **35**, 1297–1317.
- Sunda W. G. and Huntsman S. (1994) Photoreduction of manganese oxides in seawater. *Marine Chemistry* **46**, 133–152.

- Séguin V., Gagnon C. and Courchesne F. (2004) Changes in water extractable metals, pH and organic carbon concentrations at the soil-root interface of forested soils. *Plant and Soil* **260**, 1–17.
- Turner D. P., Koerper G. J., Harmon M. E. and Lee J. J. (1995) A Carbon Budget for Forests of the Conterminous United States. *Ecological Applications* **5**, 421–436.
- U.S. Environmental Protection Agency (1984) *Health Assessment Document for Manganese.*, Cincinnati, Ohio.
- U.S. Geological Survey (2012) USGS Water Data for the Nation. <http://waterdata.usgs.gov/nwis>.
- Wasserman G., Liu X., Parvez F., Factor-Litvak P., Ahsan H., Levy D., Kline J., van Geen A., Mey J., Slavkovich V., Siddique A. B., Islam T. and Graziano J. H. (2011) Arsenic and manganese exposure and children's intellectual function. *Neurotoxicology* **32**, 450–7.
- Watmough S. A., Eimers M. C. and Dillon P. J. (2007) Manganese cycling in central Ontario forests: Response to soil acidification. *Applied Geochemistry* **22**, 1241–1247.
- Wubbels J. K. (2010) Tree species distribution in relation to stem hydraulic traits and soil moisture in a mixed hardwood forest in central Pennsylvania. Master's Thesis, The Pennsylvania State University.

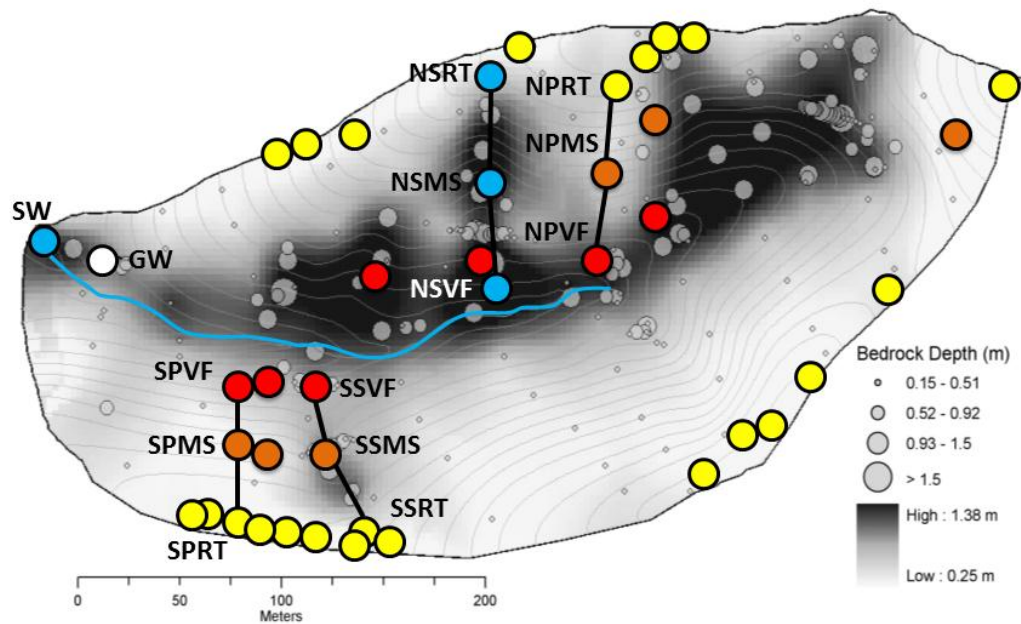


Figure 5-1. Map view of the Susquehanna Shale Hills CZO showing water and soil sampling sites. Soil cores were augered to point of refusal at 23 ridge (yellow symbols), 6 slope (orange symbols), and 7 valley floor (red symbols) positions, including transects along planar (SPRT, SPMS, and SPVF) and swale (SSRT, SPMS, and SPVF) hillslopes. Pore fluid samples were collected from lysimeters installed along the planar and swale transects on the south slope and north slope (planar sites NPRT, NPMS, and NPVF and swale sites NSRT, NSMS, NSVF). Additional water samples were collected at the stream weir (SW) and from groundwater (GW). The underlying figure is adapted from Lin *et al.* (2006) and shows soil depth (color gradient) and elevation (contour lines).

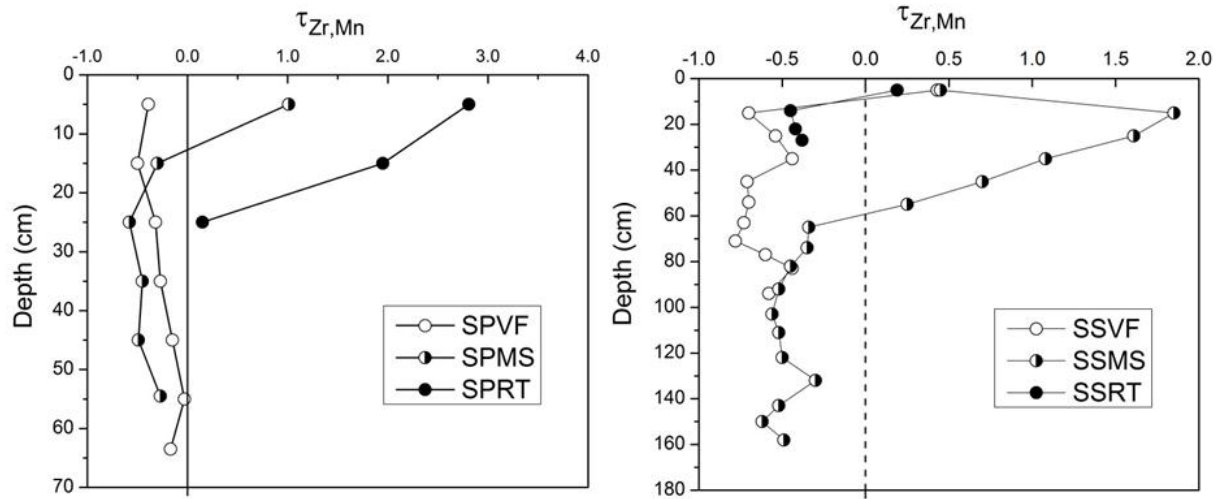


Figure 5-2. $\tau_{Zr,Mn}$ is plotted versus depth for ridge (closed symbols), midslope (half-filled symbols), and valley floor (open symbols) for soil cores augered on planar and swale transects on the south slope of SSHCZO as shown in Figure 1 (data from Jin et al., 2010; Jin and Brantley, 2011).

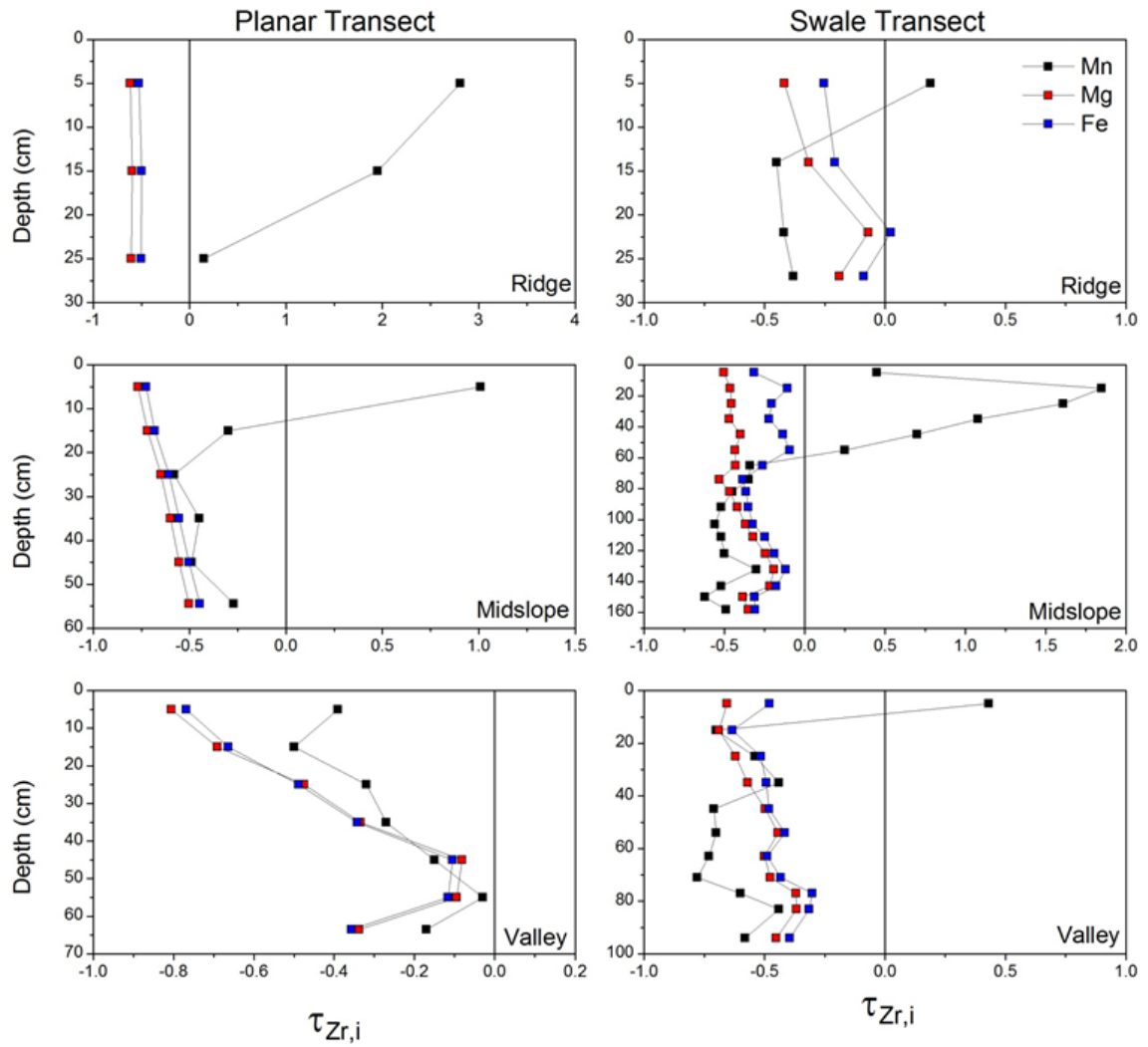


Figure 5-3. $\tau_{Zr,Mn}$ (black squares), $\tau_{Zr,Mg}$ (red squares), and $\tau_{Zr,Fe}$ (blue square) values are plotted versus depth for ridge, midslope, and valley soil cores augered on planar and swale hillslopes (Figure 5-1).

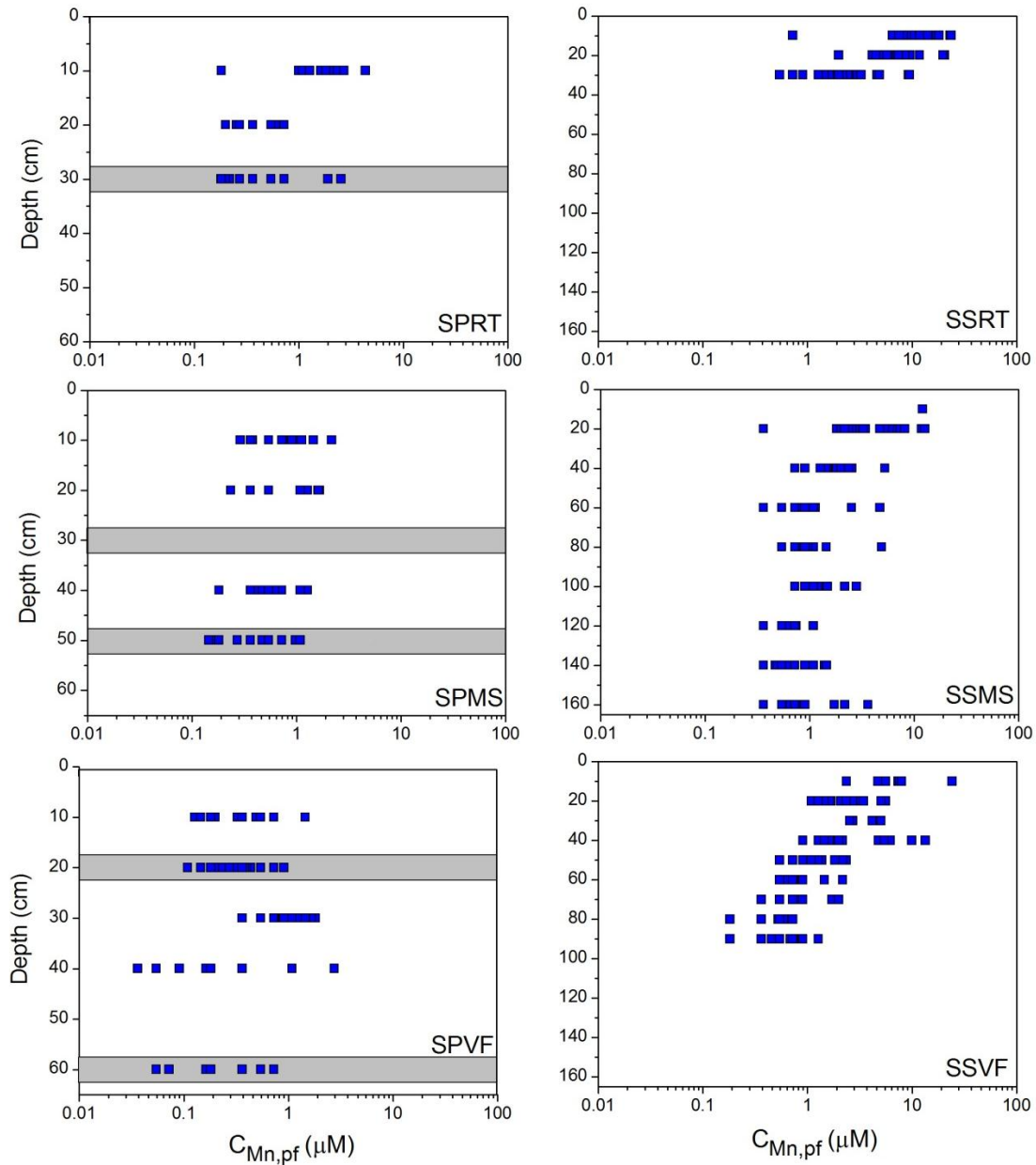


Figure 5-4. Manganese concentrations in soil pore fluids ($C_{Mn,pf}$, μM) are plotted on a log-scale versus depth in the soil profile. Pore fluids were collected from lysimeters installed at ridge, slope and valley floor positions along planar and swale transects on the south slope of SSHCZO (see Figure 5-1). The gray bars on the graphs for the south planar hillslope indicate zones of advective water transport at horizon interfaces as identified by Jin et al. (2011).

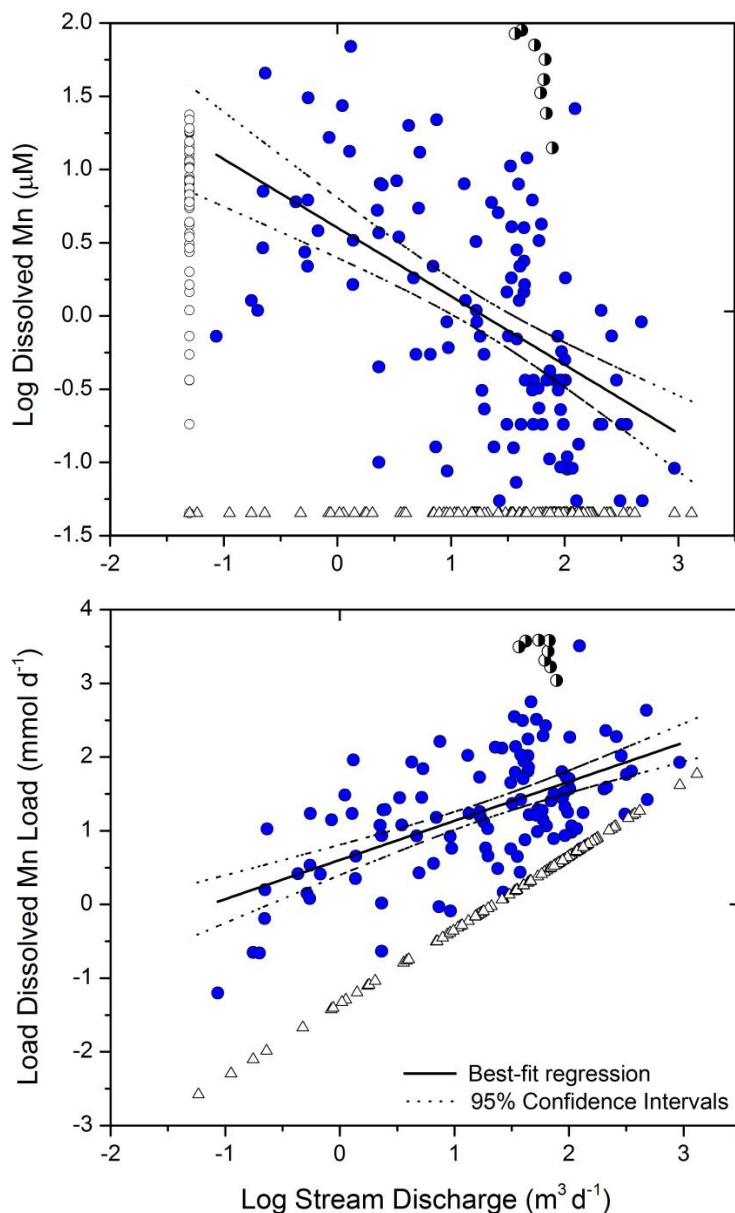


Figure 5-5. Top) Dissolved Mn concentrations in the stream ($C_{Mn,stream}$, μM) are plotted versus concurrent discharge values recorded at the stream outlet (Q_{stream} , $\text{m}^3 \text{d}^{-1}$) in log space. $C_{Mn,stream}$ values measured for $Q_{stream} < \text{DL}$ are plotted as open circles at $Q_{stream} = 0.05 \text{ m}^3 \text{d}^{-1}$. **Bottom)** Dissolved Mn loads ($L_{Mn,stream}$, mmol d^{-1} ; Eqn. 2) are plotted versus concurrent Q_{stream} values in log space. For both graphs, $C_{Mn,stream}$ values below the instrument detection limit (DL = $0.09 \mu\text{M}$) have been replaced with one-half DL (= $0.045 \mu\text{M}$) and are shown as open triangles. Eight values measured over a one week period in November 2009 were identified as outliers and are plotted as half-filled circles.

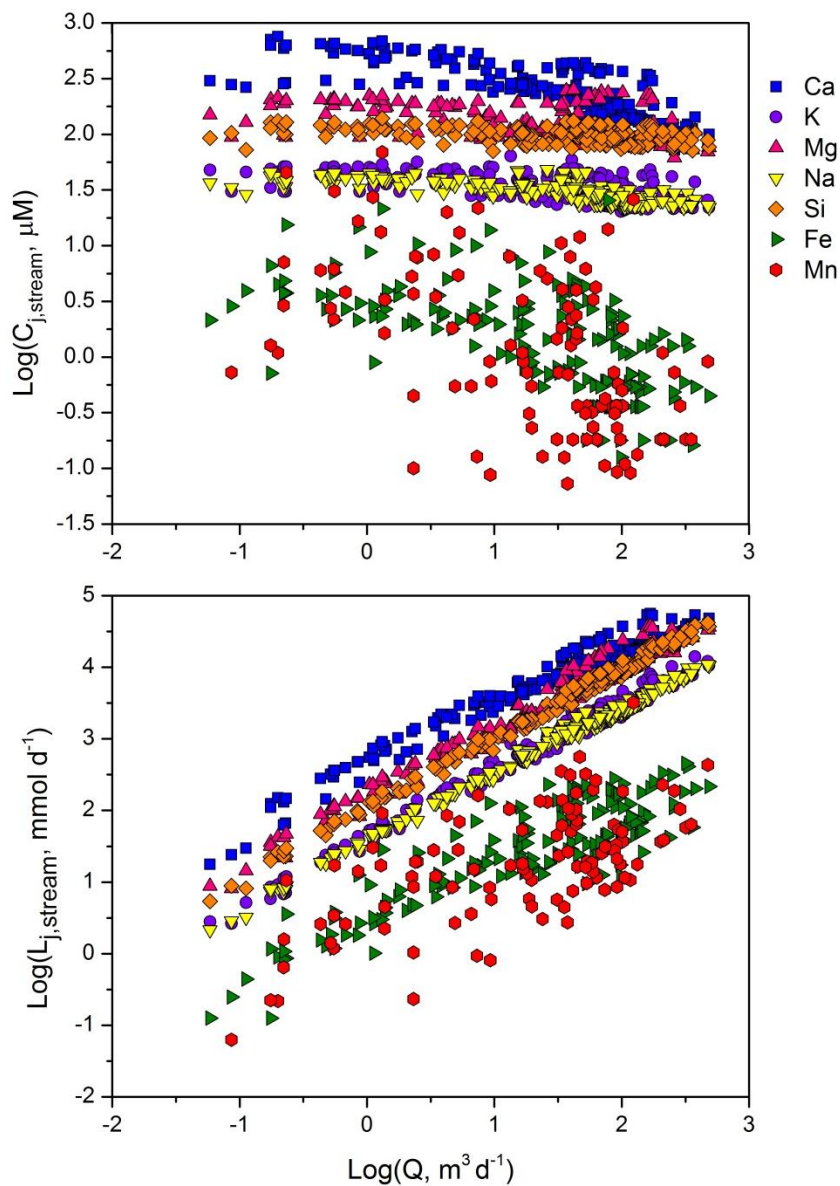


Figure 5-6. top: $\text{Log}(C_{j,stream})$ (μM) plotted versus $\text{log}(Q_{stream})$ ($\text{m}^3 \text{d}^{-1}$) for a suite of elements ($j = \text{Ca, K, Mg, Na, Si, Fe, Mn}$) measured in the SSHCZO stream. $C_{Mn,stream}$ values show similar trends compared to $C_{Fe,stream}$ but distinct trends from the major weathering elements. **bottom:** $\text{Log}(L_{j,stream})$ (mmol d^{-1}) plotted versus $\text{log}(Q_{stream})$ ($\text{m}^3 \text{d}^{-1}$) for a suite of elements ($j = \text{Ca, K, Mg, Na, Si, Fe, Mn}$) measured in the SSHCZO stream. $C_{j,stream}$ values below the detection limit are plotted as open symbols at one-half DL (= 0.045 μM). Slopes of best fit lines to each group are given in Table 5-3.

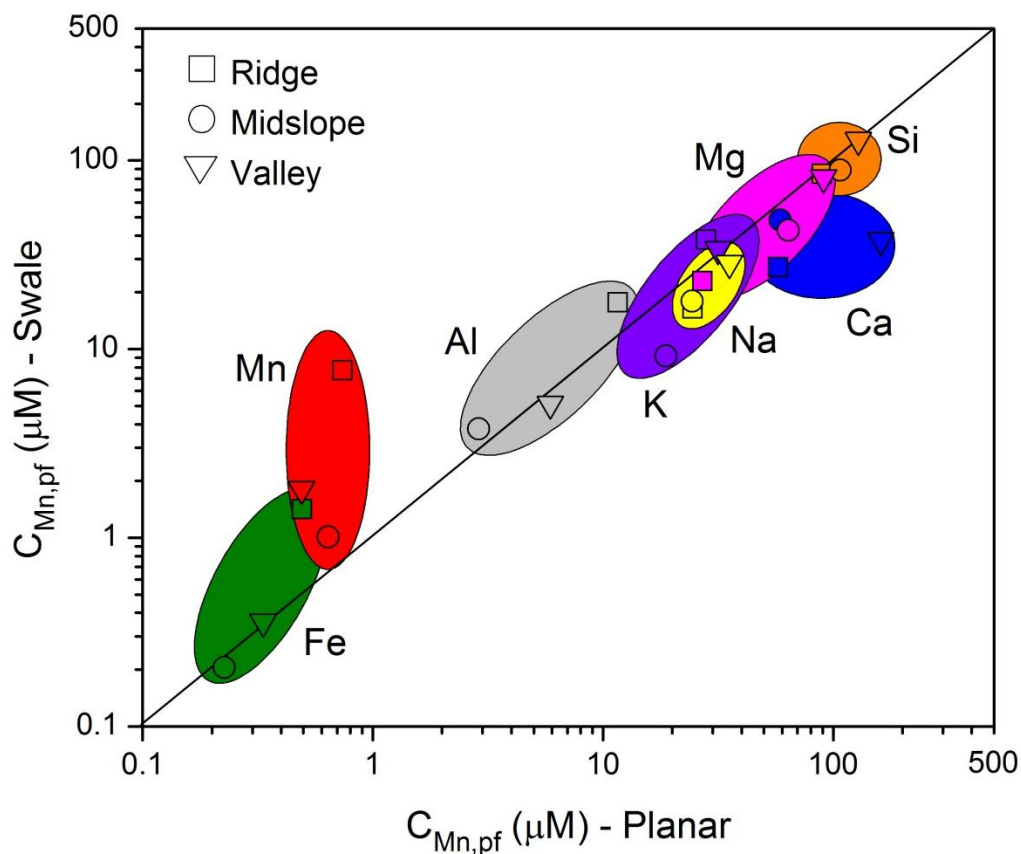


Figure 5-7. Concentrations of dissolved elements in pore fluids ($C_{j,pf}$) of swale soils are plotted versus concentrations of dissolved elements in pore fluids of planar soils. The symbols represent the slope position: ridge (square), midslope (circles), or valley floor (triangle). Symbols are grouped by color for each element. $C_{j,pf}$ values for $j = \text{Al, K, Na, Mg, and Si}$ are similar in planar and swale soils and fall along the 1:1 line. For $j = \text{Mn and Fe}$, $C_{Mn,pf}$ values are higher in the swale than on the planar transect at all slope positions, and $C_{Fe,pf}$ are high in the swale ridge than the planar ridge soil. In contrast, $C_{Ca,pf}$ values are higher in the planar valley than the swale valley soils.

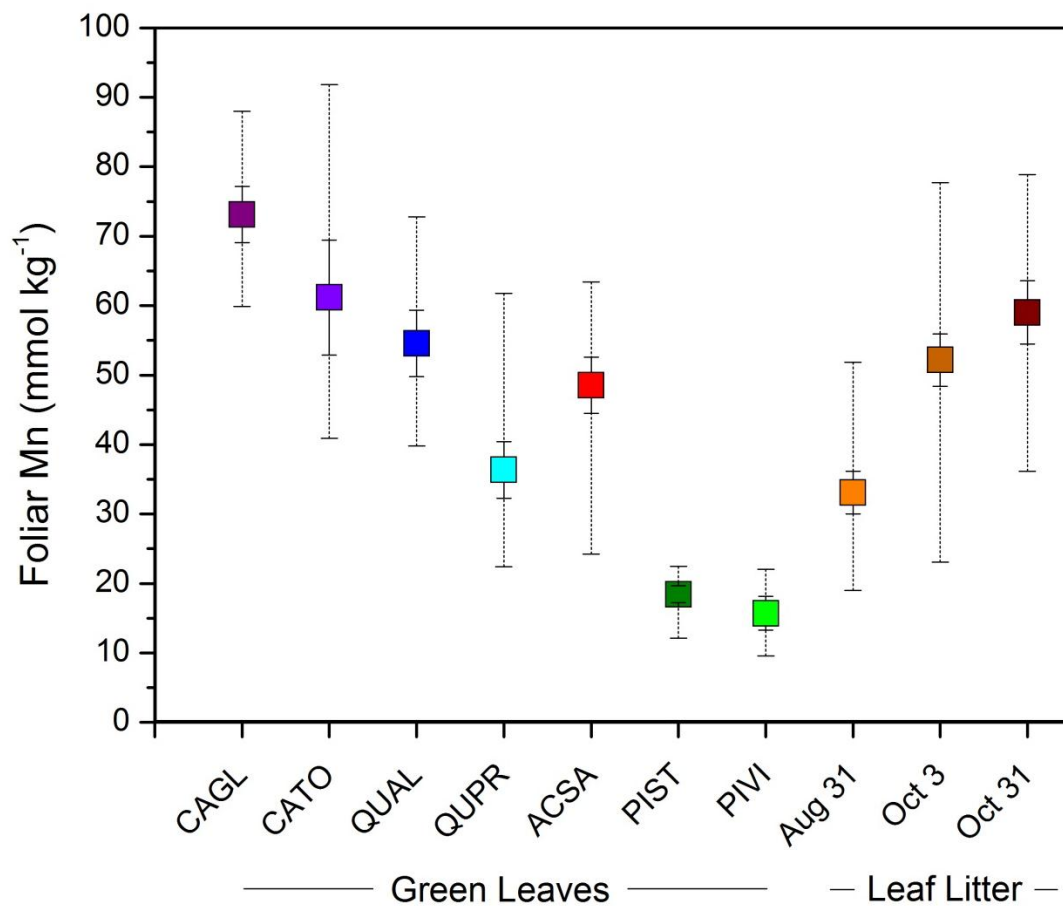


Figure 5-8. Average Mn concentrations measured in green leaves and leaf litter ($C_{Mn,veg}$, mmol kg⁻¹) sorted by species for green leaves and by collection date for leaf litter. All green leaf samples were collected in August and September. Tree species are shown along the x-axis and identified in the main text. Error bars indicate the standard error about the mean (solid lines) and the minima and maxima (dashed lines) for $C_{Mn,veg}$ in each group.

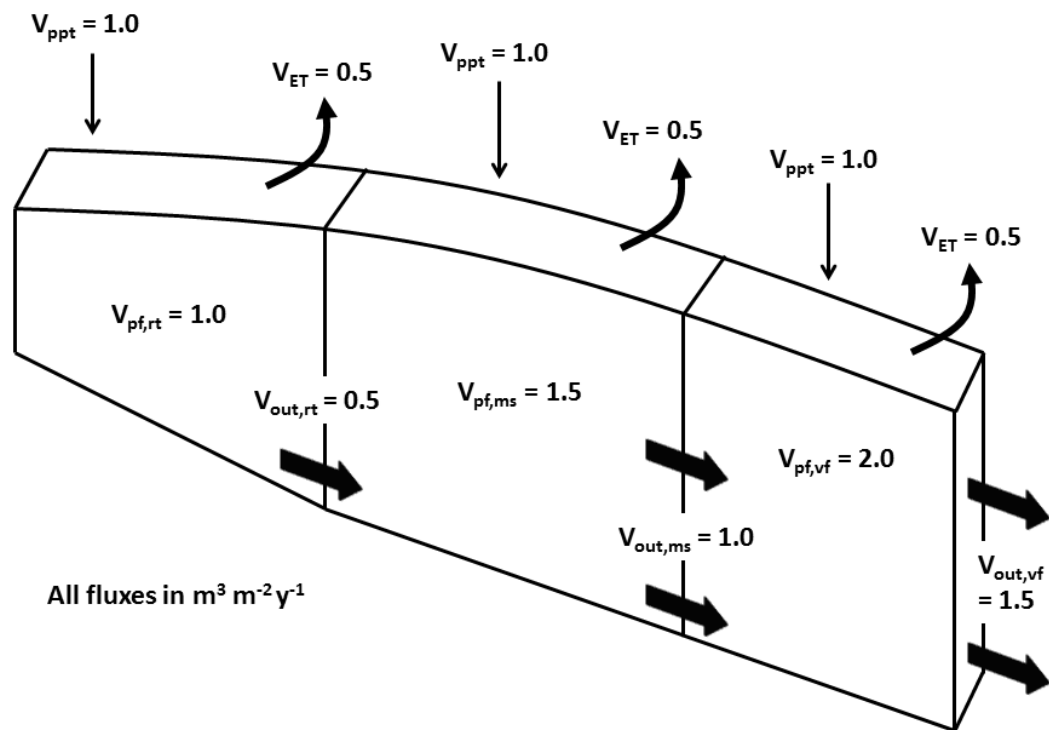


Figure 5-9. Annual water budget calculated for a box model of the planar and swale hillslopes. The model hillslope is segmented into ridge, slope, and valley boxes with equal surface area ($A = 25 \text{ m}^2$). The flux of water into pore fluids in each box ($V_{pf,s}$, $\text{m}^3 \text{m}^{-2} \text{y}^{-1}$) and the flux of water that exits each box to flow downslope ($V_{out,s}$, $\text{m}^3 \text{m}^{-2} \text{y}^{-1}$) are calculated with mass balance using average measured annual values for precipitation ($V_{ppt} = 1.0 \text{ m}^3 \text{m}^{-2} \text{y}^{-1}$) and evapotranspiration ($V_{ET} = 0.5 \text{ m}^3 \text{m}^{-2} \text{y}^{-1}$).

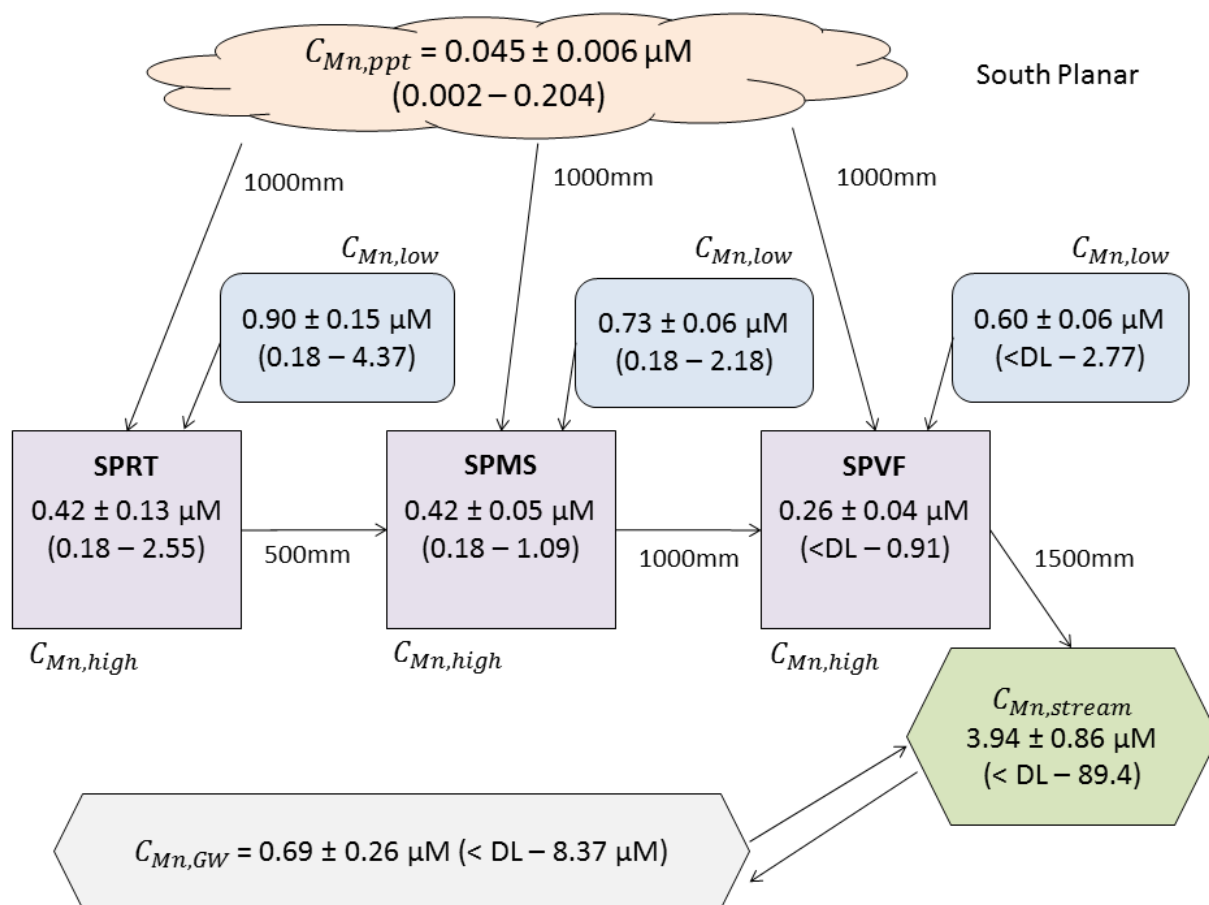


Figure 5-10. Diagram of the average, standard error (\pm), and range (xx – xx) of Mn concentrations measured in water at the SSHCZO, including precipitation ($C_{Mn,ppt}$), groundwater ($C_{Mn,GW}$), stream water ($C_{Mn,stream}$) and pore fluids in high-flow ($C_{Mn,high}$) and low-flow ($C_{Mn,low}$) zones of ridge (SPRT), midslope (SPMS), and valley floor (SPVF) soils on the south planar transect.

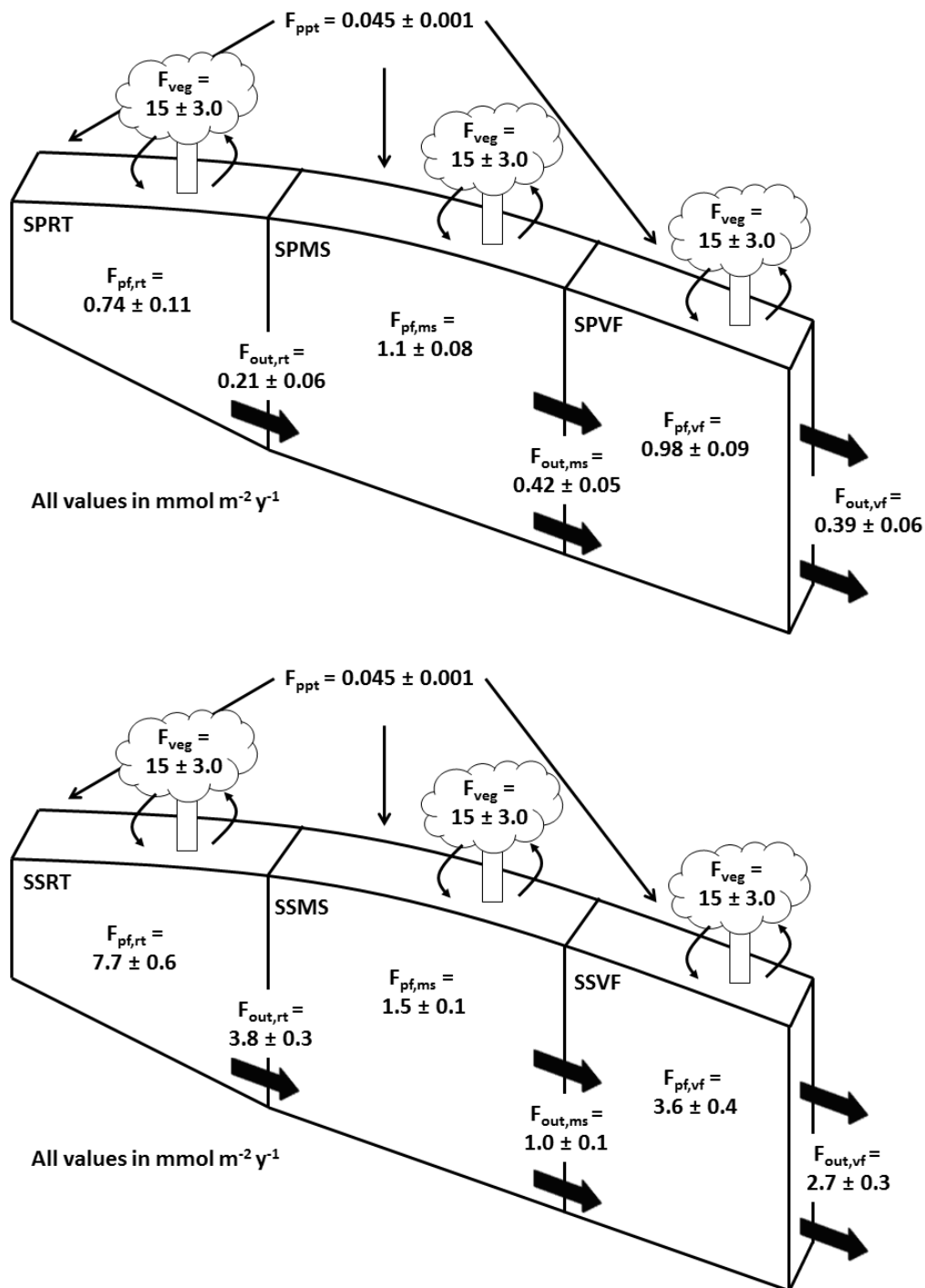


Figure 5-11. A) Box model of Mn fluxes (mmol m⁻² y⁻¹) to and from soils on the south planar transect at SSHCZO, including inputs from precipitation (F_{ppt}), outputs from downslope transport ($F_{out,s}$), fluxes into pore fluids ($F_{pf,s}$), and recycling in vegetation (F_{veg}). B) Similar box model of Mn fluxes on the south swale transect.

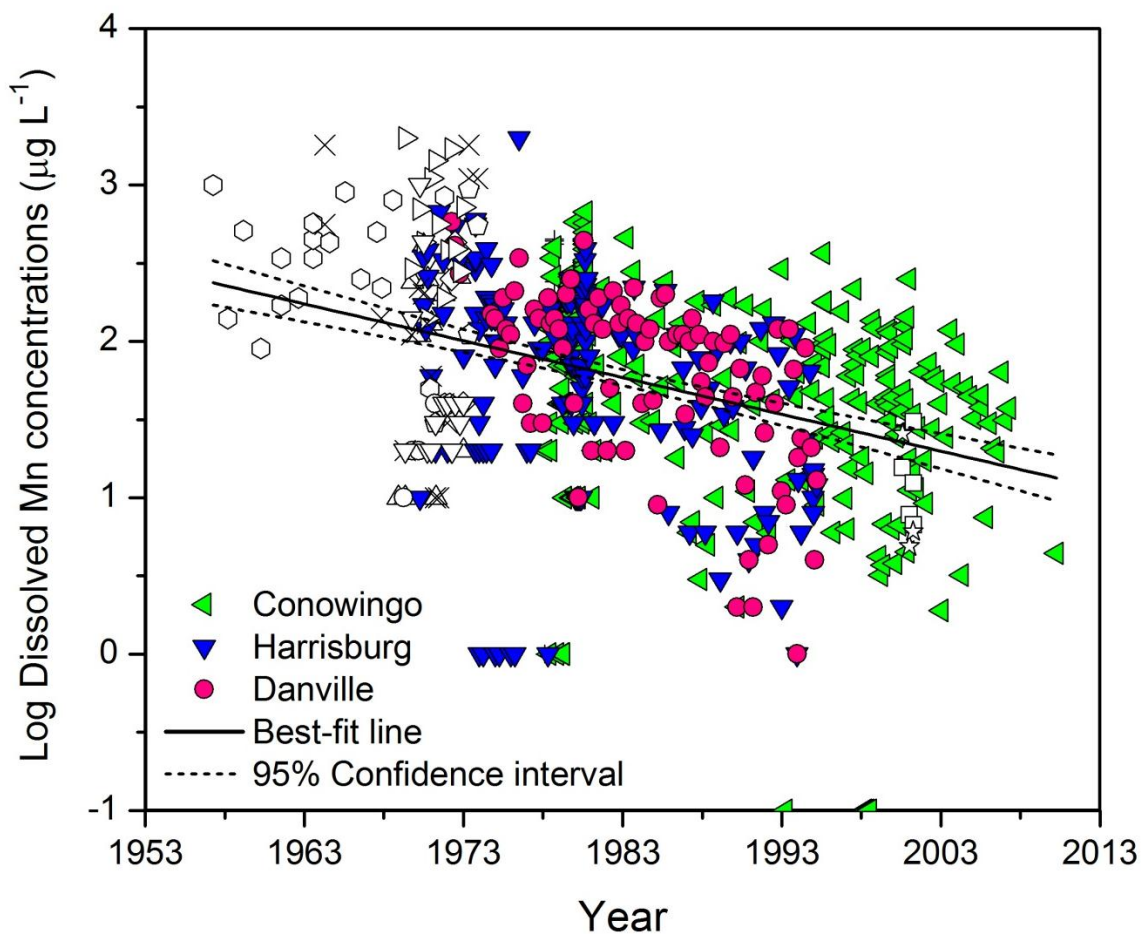


Figure 5-12. Log $C_{Mn,stream}$ values measured at 14 USGS stations along the Susquehanna River between 1957 – 2010 are plotted by year with different symbols for each station. Three sites, Danville, PA (pink circles), Harrisburg, PA (blue down triangles), and Conowingo, MD (green left triangles) were targeted to further investigate changes in $C_{Mn,stream}$ over these five decades. $C_{Mn,stream}$ values measured at the other 11 USGS sites are plotted as open symbols. A best-fit linear regression line ($R^2 = 0.11$) is fit to all data points and indicates significant decline in dissolved Mn concentrations in the Susquehanna River since the 1950s ($p < 0.001$).

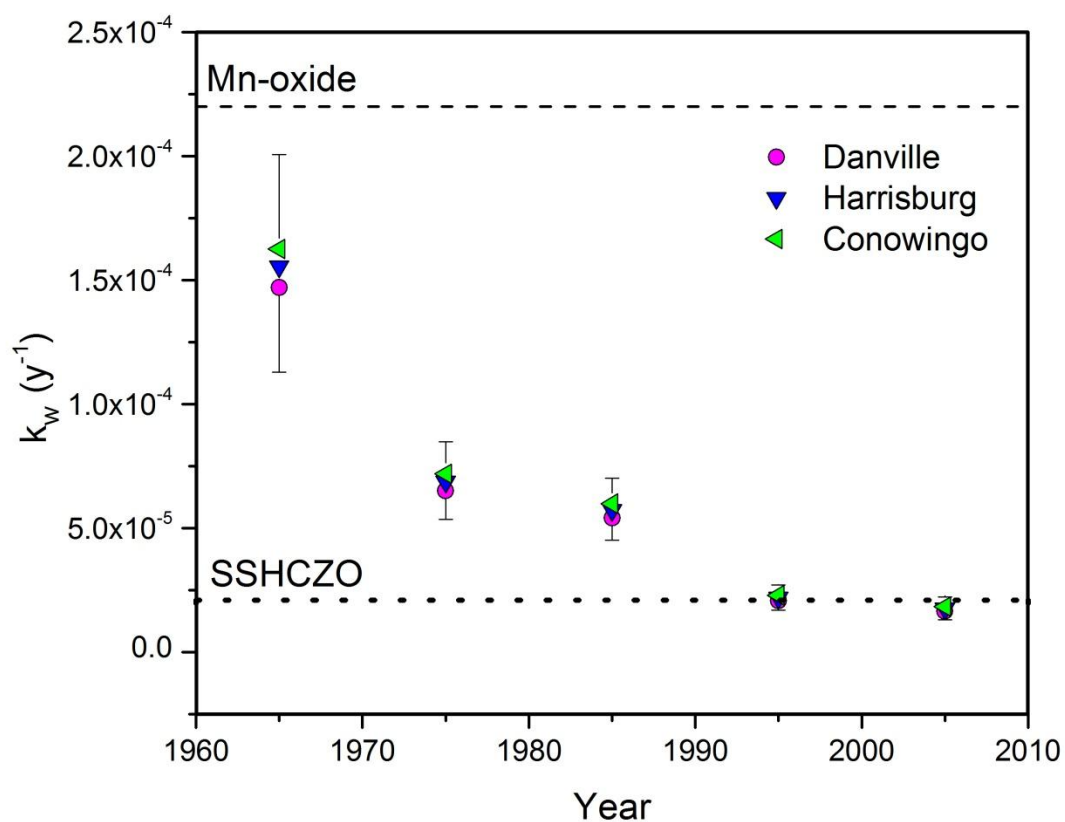


Figure 5-13. First-order rate constants (k_w , y^{-1} , Eqn. 21) for Mn losses from soils to rivers in the Susquehanna River Basin are plotted by decade for the Danville (pink circle), Harrisburg (blue down triangle), and Conowingo (green left triangle) sites. For comparison, k_w values for SSHCZO soils (dotted line) and Mn-oxide particles (dashed line) are shown.

Table 5-1. Soil chemistry for planar and swale hillslopes and O horizon

Depth Range		$C_{Mn,w}$	$C_{Zr,w}$	$C_{Mg,w}$	$C_{Fe,w}$	$\tau_{Zr,Mn}$	$\tau_{Zr,Mg}$	$\tau_{Zr,Fe}$
m		mmol kg ⁻¹	mmol kg ⁻¹	mmol kg ⁻¹	mmol kg ⁻¹			
<i>South planar ridge top (SPRT)</i>								
0.00	0.10	59.2	2.80	261	789	2.75	-0.62	-0.53
0.10	0.20	46.5	2.71	270	890	1.88	-0.60	-0.50
0.20	0.30	21.1	2.75	261	807	0.12	-0.61	-0.50
<i>South planar midslope (SPMS)</i>								
0.00	0.10	56.4	3.85	179	534	0.96	-0.77	-0.73
0.10	0.20	18.3	3.61	203	582	-0.32	-0.72	-0.68
0.20	0.30	9.9	3.23	228	645	-0.59	-0.65	-0.60
0.30	0.40	12.7	3.16	253	711	-0.46	-0.60	-0.55
0.40	0.50	11.3	3.04	270	763	-0.50	-0.56	-0.50
0.50	0.59	15.5	2.92	290	814	-0.29	-0.50	-0.45
<i>South planar valley floor (SPVF)</i>								
0.00	0.10	16.9	3.83	149	447	-0.41	-0.81	-0.77
0.10	0.20	12.7	3.49	216	592	-0.51	-0.69	-0.66
0.20	0.30	14.1	2.83	298	730	-0.33	-0.47	-0.49
0.30	0.40	12.7	2.40	320	797	-0.29	-0.33	-0.34
0.40	0.50	14.1	2.00	367	902	-0.05	-0.08	-0.10
0.50	0.60	12.7	2.09	380	934	-0.19	-0.09	-0.12
0.60	0.67	12.7	2.47	327	800	-0.31	-0.34	-0.36
<i>South swale ridge top (SSRT)</i>								
0.00	0.10	18.2	2.12	247	799	0.15	-0.42	-0.25
0.10	0.18	9.1	2.10	288	842	-0.42	-0.32	-0.21
0.18	0.25	7.3	1.66	309	856	-0.41	-0.07	0.02
0.25	0.29	9.1	1.87	304	863	-0.35	-0.19	-0.09
<i>South swale midslope (SSMS)</i>								
0.00	0.10	25.5	2.40	239	829	0.42	-0.50	-0.32
0.10	0.20	43.7	2.10	226	949	1.78	-0.46	-0.11
0.20	0.30	41.9	2.23	243	894	1.52	-0.46	-0.20
0.30	0.40	34.6	2.32	247	911	0.99	-0.47	-0.22
0.40	0.50	25.5	2.05	247	894	0.67	-0.40	-0.14
0.50	0.60	20.0	2.17	247	994	0.24	-0.43	-0.09
0.60	0.70	9.1	2.05	235	765	-0.41	-0.43	-0.26
0.70	0.77	9.1	2.46	230	761	-0.50	-0.53	-0.39
0.77	0.86	9.1	2.47	263	790	-0.51	-0.47	-0.37
0.86	0.99	9.1	2.43	284	795	-0.50	-0.42	-0.35
0.99	1.07	7.3	2.21	280	756	-0.56	-0.37	-0.32
1.07	1.16	7.3	2.00	272	757	-0.51	-0.32	-0.25
1.16	1.27	7.3	1.93	292	790	-0.49	-0.24	-0.19
1.27	1.38	9.1	1.93	313	860	-0.37	-0.19	-0.12

Depth Range		C_{Mn,w}	C_{Zr,w}	C_{Mg,w}	C_{Fe,w}	τ_{Zr,Mn}	τ_{Zr,Mg}	τ_{Zr,Fe}
m		mmol kg⁻¹	mmol kg⁻¹	mmol kg⁻¹	mmol kg⁻¹			
1.38	1.47	7.3	2.02	317	838	-0.52	-0.22	-0.18
1.47	1.53	7.3	2.54	313	883	-0.62	-0.39	-0.31
1.53	1.63	9.1	2.28	296	793	-0.47	-0.35	-0.31
<i>South swale valley floor (SSVF)</i>								
0.00	0.10	27.3	2.57	177	673	0.43	-0.66	-0.48
0.10	0.20	7.3	3.23	202	600	-0.70	-0.69	-0.63
0.20	0.30	9.1	2.92	222	714	-0.58	-0.62	-0.51
0.30	0.40	10.9	2.77	239	711	-0.47	-0.57	-0.49
0.40	0.50	5.5	2.65	267	695	-0.72	-0.50	-0.48
0.50	0.58	5.5	2.59	288	763	-0.72	-0.44	-0.42
0.58	0.68	5.5	2.92	292	752	-0.75	-0.50	-0.49
0.68	0.74	3.6	2.59	272	740	-0.81	-0.48	-0.43
0.74	0.80	7.3	2.44	309	861	-0.60	-0.37	-0.30
0.80	0.86	9.1	2.43	309	842	-0.50	-0.37	-0.31
0.86	0.95	9.1	2.77	304	845	-0.56	-0.45	-0.40

Table 5-2. Water Chemistry

	Depth cm	Min. Value	Max. Value	Average	n =
		C _{Mn,pf} (µM)			
Precipitation (2002)		0.002	0.203	0.046	61
Soil Water (SPRT)	10	0.18	4.37	1.59	14
	20	0.20	0.73	0.42	20
	30	0.18	2.55	0.42	18
Soil Water (SPMS)	10	0.29	2.18	0.79	28
	20	0.24	1.67	1.06	8
	40	0.18	1.27	0.57	25
	50	0.18	1.09	0.42	25
Soil Water (SPVF)	10	0.00	1.46	0.37	27
	20	0.00	0.91	0.32	24
	30	0.36	1.82	0.93	32
	40	< DL	2.77	0.35	18
	60	< DL	0.73	0.16	14
Soil Water (SSRT)	10	0.73	23.95	12.53	30
	20	2.00	20.66	7.70	23
	30	0.55	9.48	2.34	27
Soil Water (SSMS)	10	-	-	12.10	1
	20	0.36	12.73	4.30	26
	40	0.73	5.28	1.62	23
	60	0.36	4.73	0.93	26
	80	0.55	4.91	0.94	21
	100	0.73	2.82	1.10	20
	120	0.36	1.09	0.57	17
	140	0.36	1.46	0.69	21
Soil Water (SSVF)	160	0.36	3.64	0.97	19
	10	2.37	24.28	8.59	7
	20	1.09	5.61	2.20	23
	30	2.55	5.09	3.64	4
	40	0.91	13.46	3.66	20
	50	0.55	2.36	1.12	22
	60	0.55	2.18	0.78	19
	70	0.36	2.00	0.87	22
	80	0.18	0.73	0.53	16
90	0.18	1.27	0.58	20	
Stream (SW)		< DL/0.0	89.37	3.94	218
Groundwater		< DL/0.0	8.37	0.69	41

Table 5-3. Slopes of regression lines fit to elemental data in Figure 5-6.

$\log(C_{j,stream}) = A + b * \log(Q_{stream})$								
	Mn^a	Ca	K	Mg	Na	Si	Fe^a	Al^a
Slope (<i>b</i>) ^c	-0.42	-0.21	-0.09	-0.10	-0.07	-0.03	-0.32	0.055*
Standard Error	0.07	0.01	0.01	0.01	0.01	0.01	0.03	0.028
R ²	0.25	0.60	0.36	0.31	0.50	0.16	0.36	0.02
R.S.S. ^b	42.7	4.7	2.1	3.5	0.84	0.76	25.6	14.4
$\log(L_{j,stream}) = A + b * \log(Q_{stream})$								
	Mn^a	Ca	K	Mg	Na	Si	Fe^a	Al^a
Slope (<i>b</i>) ^c	0.57	0.79	0.91	0.90	0.93	0.97	0.68	1.05
Standard Error	0.07	0.01	0.01	0.01	0.01	0.01	0.03	0.03
R ²	0.40	0.95	0.98	0.97	0.99	0.99	0.74	0.91
R.S.S. ^b	40.9	4.7	2.1	3.5	0.84	0.76	23.5	14.4

^aExcludes values falling below the detection limit and outliers

^bR.S.S. = residual sum of squares

^cAll slopes are significant to $p < 0.001$ with the exception of Al* ($p = 0.05$)

Table 5-4. Litter collected from SSHCZO in 2011

Collection Date	8/31	9/12	9/19	9/26	10/3	10/10
\bar{m}_{litter} (g m ⁻² week ⁻¹)	8.59	5.88	7.97	15.02	32.21	8.36
$C_{Mn,litter}$ (μmol g ⁻¹)	33.09	33.09	33.09	33.09	52.17	52.17
F_{litter} (μmol m ⁻² week ⁻¹)	284	195	264	497	1,680	436
Collection Date	10/24	10/31	11/7	11/13	11/18	11/28
\bar{m}_{litter} (g m ⁻² week ⁻¹)	39.87	62.51	26.50	31.61	6.28	3.82
$C_{Mn,litter}$ (μmol g ⁻¹)	52.17	59.03	59.03	59.03	59.03	59.03
F_{litter} (μmol m ⁻² week ⁻¹)	2,080	3,690	1,564	1,866	371	226

Table 5-5. Concentrations of elements in pore fluids in planar and swale soils on the south hillslope

Site		Al	Ca	K	Mg	Na	Si	Fe	Mn
		μM	μM						
SPRT	Average	12	58	28	27	25	90	0.49	0.74
	Std. Error	1.3	1.8	1.8	0.8	1.7	2.9	0.05	0.11
SPMS	Average	2.9	59	19	64	24	107	0.23	0.64
	Std. Error	0.2	2.6	0.8	3.5	1.3	2.7	0.03	0.05
SPVF	Average	5.9	161	32	91	35	129	0.33	0.49
	Std. Error	0.5	15	1.3	7.7	1.7	2.8	0.03	0.05
Planar	Average	6.3	107	27	68	30	113	0.34	0.60
	Std. Error	0.4	7.8	0.8	4.0	1.0	1.9	0.02	0.03
SSRT	Average	18	27	38	23	16	85	1.41	7.70
	Std. Error	1.1	0.7	2.0	1.6	1.2	3.0	0.12	0.62
SSMS	Average	3.8	48	9	43	18	89	0.20	1.01
	Std. Error	0.1	1.2	0.5	0.9	0.5	1.6	0.04	0.07
SPVF	Average	5.1	38	34	81	28	128	0.36	1.81
	Std. Error	0.5	1.7	2.3	2.1	0.7	2.1	0.05	0.22
Swale	Average	7.0	40	24	53	21	102	0.56	2.85
	Std. Error	0.4	0.8	1.0	1.3	0.4	1.4	0.04	0.18

Table 5-6. Fluxes (F_w and F_{veg}) and rate constants (k_w and k_{veg}) \pm Standard Error

	F_w (mmol m ⁻² y ⁻¹)	F_{veg} (mmol m ⁻² y ⁻¹)	k_w (x 10 ⁻⁵ y ⁻¹)	k_{veg} (x 10 ⁻⁵ y ⁻¹)
Mesocosm ^a (veg)	0.14 \pm 0.02	34 \pm 4	2.7 \pm 0.4	602 \pm 69
Mesocosm ^a (no veg)	0.94 \pm 0.19	0	26 \pm 3	0
Ridge soils ^b	0.35 \pm 0.17	15 \pm 4	2.1 \pm 1.0	92 \pm 25
Planar Hillslope				
Ridge	0.17 \pm 0.04	15 \pm 4	0.65 \pm 0.26	57 \pm 15
Midslope	0.16 \pm 0.08	15 \pm 4	0.88 \pm 0.47	79 \pm 22
Valley floor	-0.072 \pm 0.080	15 \pm 4	-0.52 \pm 0.58	110 \pm 29
Swale Hillslope				
Ridge	3.8 \pm 0.3	15 \pm 4	73 \pm 12	280 \pm 77
Midslope	-2.9 \pm 0.3	15 \pm 4	-7.3 \pm 1.3	38 \pm 10
Valley floor	1.7 \pm 0.3	15 \pm 4	12 \pm 3	110 \pm 29
Watershed	0.38 \pm 0.02	15 \pm 4	2.1 \pm 0.1	79 \pm 21
Susquehanna RB				
1957 – 1970	3.5 \pm 0.2	n/a	16 \pm 3.6	n/a
1970 – 1980	1.5 \pm 0.08		6.9 \pm 1.2	
1980 – 1990	1.3 \pm 0.06		5.7 \pm 1.0	
1990 – 2000	0.49 \pm 0.02		2.2 \pm 0.4	
2000 – 2010	0.39 \pm 0.01		1.8 \pm 0.4	
Planar, long-term				
Ridge	n/a		n/a	
Midslope	0.32 \pm 0.06		2.4 \pm 1.2	
Valley	0.11 \pm 0.02		0.74 \pm 0.36	
Swale, long-term				
Ridge	0.49 \pm 0.12		9.4 \pm 4.8	
Midslope	0.36 \pm 0.05		1.3 \pm 0.6	
Valley	0.26 \pm 0.04		1.1 \pm 0.5	

^a F_w and F_{veg} for the mesocosms are normalized to the surface area of each tree pot (= 0.01 m²) for values reported in Table 4-3.

^bValues from Herndon *et al.* (2011)

Appendix A

This appendix was originally published as Supplementary Material by Herndon et al. (2011). The material is reproduced here exactly as published.

Section A1. Description of Mass Balance Model

A1.1. Mass Balance System

A mass balance model is applied to a soil profile having set properties that are averaged from SSHO ridge soil data. The profile is treated as a black box with no depth-dependence for box properties or mass fluxes. In the model, the ridge soil is at steady state with constant soil thickness ($L = 32$ cm). Thus, the erosion rate equals the soil production rate (ω , 45 m/My), both of which do not vary over time in the model (Ma et al., in review). A depth-averaged value for bulk density is obtained from field measurements (Table 3). For a soil profile of 32 cm thickness, average $\rho_w = 1.37$ g cm⁻³. Soil bulk density is assumed to remain constant over time. The average soil Zr concentration ($C_{Zr,w} = 222$ ppm) is also held constant over time. Properties of the parent shale, including bulk density ($\rho_p = 2.42$ g cm⁻³), Zr concentration ($C_{Zr,p} = 178$ $\mu\text{g g}^{-1}$), and Mn concentration ($C_{Mn,p} = 800$ $\mu\text{g g}^{-1}$), also remain constant.

The area-normalized total mass of Mn in the soil profile ($M_{Mn,w}$, mg Mn cm⁻²) is calculated as the product of soil thickness (L), average soil bulk density (ρ_w), and depth-averaged soil Mn concentrations ($C_{Mn,w}$). $M_{Mn,w}$ changes as a function of time due to changes in input fluxes from atmospheric deposition (A , $\mu\text{g Mn cm}^{-2} \text{y}^{-1}$) and bedrock weathering (B , $\mu\text{g Mn cm}^{-2} \text{y}^{-1}$) and output fluxes from chemical weathering (W , $\mu\text{g Mn cm}^{-2} \text{y}^{-1}$) and physical erosion (E , $\mu\text{g Mn cm}^{-2} \text{y}^{-1}$). A is a model input for which we used different values representing geogenic (0.5 and 5 $\mu\text{g Mn cm}^{-2} \text{y}^{-1}$) and anthropogenic (50 and 500 $\mu\text{g Mn cm}^{-2} \text{y}^{-1}$) sources (Table A-4) to assess their impact on $M_{Mn,w}$. $B (= 8.7 \mu\text{g cm}^{-2} \text{y}^{-1})$ is the product of the soil production rate (ω), Mn concentration in the parent shale ($C_{Mn,p}$), and parent shale bulk density (ρ_p) and so remains constant over time. W is the product of discharge and average dissolved Mn concentrations when water exits the soil profile and is held constant. E is the product of the soil production rate (ω), soil bulk density (ρ_w), and time-variable Mn concentration in the soil ($C_{Mn,w}$).

A1.2. Initial Conditions

At time zero, assuming no net Mn mass has been added to or removed from the soil profile as it weathers from bedrock, then $\tau = 0$, $C_{j,w} = C_{j,p}(C_{i,w}/C_{i,p}) = 998$ $\mu\text{g g}^{-1}$, and $M_{Mn,w} = 44$ mg cm⁻². To maintain steady-state Mn concentrations in this system, $A + B = E + W$. In this steady-state

system, $E = 6.2 \mu\text{g cm}^{-2} \text{y}^{-1}$. Assuming that atmospheric inputs are negligible in this system, $W = B - E = 2.6 \mu\text{g cm}^{-2} \text{y}^{-1}$.

For comparison, the modern chemical weathering flux, $W (=1.5 \mu\text{g cm}^{-2} \text{y}^{-1})$, is measured from the difference between pore fluid Mn concentrations at the ridge soil-bedrock interface ($C_{Mn,pf} = 0.025 \mu\text{g mL}^{-1}$) and influent precipitation ($C_{Mn,ppt} = 0.004 \mu\text{g mL}^{-1}$) normalized for evapotranspiration using the standard correction based on Cl concentrations for pore fluid ($C_{Cl,pf} = 0.25 \mu\text{g mL}^{-1}$) and influent precipitation ($C_{Cl,ppt} = 0.18 \mu\text{g mL}^{-1}$), with mean annual precipitation, $m_{ppt} = 104.9 \text{ g cm}^{-2} \text{y}^{-1}$ (NADP 2010):

$$W = m_{ppt} \left(\frac{C_{Cl,ppt}}{C_{Cl,pf}} C_{Mn,pf} - C_{Mn,ppt} \right)$$

Based on these two calculations, the initial conditions value ($W = 2.6 \mu\text{g cm}^{-2} \text{y}^{-1}$) will be used in the model as an upper limit estimate of chemical weathering.

A1.3. Modeling approach

This model aims to evaluate changes in Mn mass in the ridge soils in response to various amounts of dust input. The integrated mass flux of Mn, $m_{Mn,w}$, is the difference between the total Mn mass at time t , and the initial condition, $M_{Mn,w} = 44 \text{ mg cm}^{-2}$, and changes as a function of input and output fluxes:

$$m_{Mn,w} = M_{Mn,w}(t) - M_{Mn,w}^0 = \int_0^t (A + B - W - E) dt$$

Assuming that A (variable input), $B (= 8.7 \mu\text{g cm}^{-2} \text{y}^{-1})$ and $W (= 2.6 \mu\text{g cm}^{-2} \text{y}^{-1})$ are constant, then the only flux that changes over time is E . Since $M_{Mn,w} = \rho_w C_{Mn,w} L$, we evaluate E as a function of the time-dependant total Mn mass ($M_{Mn,w}(t)$) rather than concentration ($C_{Mn,w}(t)$):

$$E(t) = \omega \rho_w C_{Mn,w}(t) = \omega M_{Mn,w}(t) / L$$

With an increase in A , $M_{Mn,w}$ will be elevated, which leads to higher erosion fluxes assuming a first order dependence. Thus, a positive feedback is expected between A and E , so that a new steady state can be reached with each new A value.

Our model results from varying A ($0.5, 5, 50, \text{ or } 500 \mu\text{g Mn cm}^{-2} \text{y}^{-1}$) suggest that geogenic input of Mn can never reach the current Mn levels observed at Shale Hills (Fig. 2-2). A flux of $\sim 240 \mu\text{g Mn cm}^{-2} \text{y}^{-1}$ is required for 200 years, arguing for industrial sources.

Section A2. Burnham Soil Samples

The integrated mass flux for Mn ($m_{Mn,w}$, Eqn.2) reported in Table 2-2 is the average \pm standard deviation of four values calculated for the Burnham cores that vary the following conditions:

- 1) Parent composition for each core is the bottommost sample obtained from that core.
- 2) Parent composition for all cores is the average composition of the bottommost samples from all cores (n=21).
- 3) Strain is applied to each core as a depth-averaged single value:

$$m_{j,w} = \rho_p C_{j,p} \sum_{z=0}^{z=L} \frac{\tau_{i,j}(z) \Delta z}{\varepsilon_{avg} + 1}$$

- 4) Strain values vary as a function of depth in the core:

$$m_{j,w} = \rho_p C_{j,p} \sum_{z=0}^{z=L} \frac{\tau_{i,j}(z) \Delta z}{\varepsilon(z) + 1}$$

Soils augured near Burnham, PA share similar chemistry and mineralogy to those at SSHO, and strain values are calculated using SSHO bulk density measurements (Table 2-3).

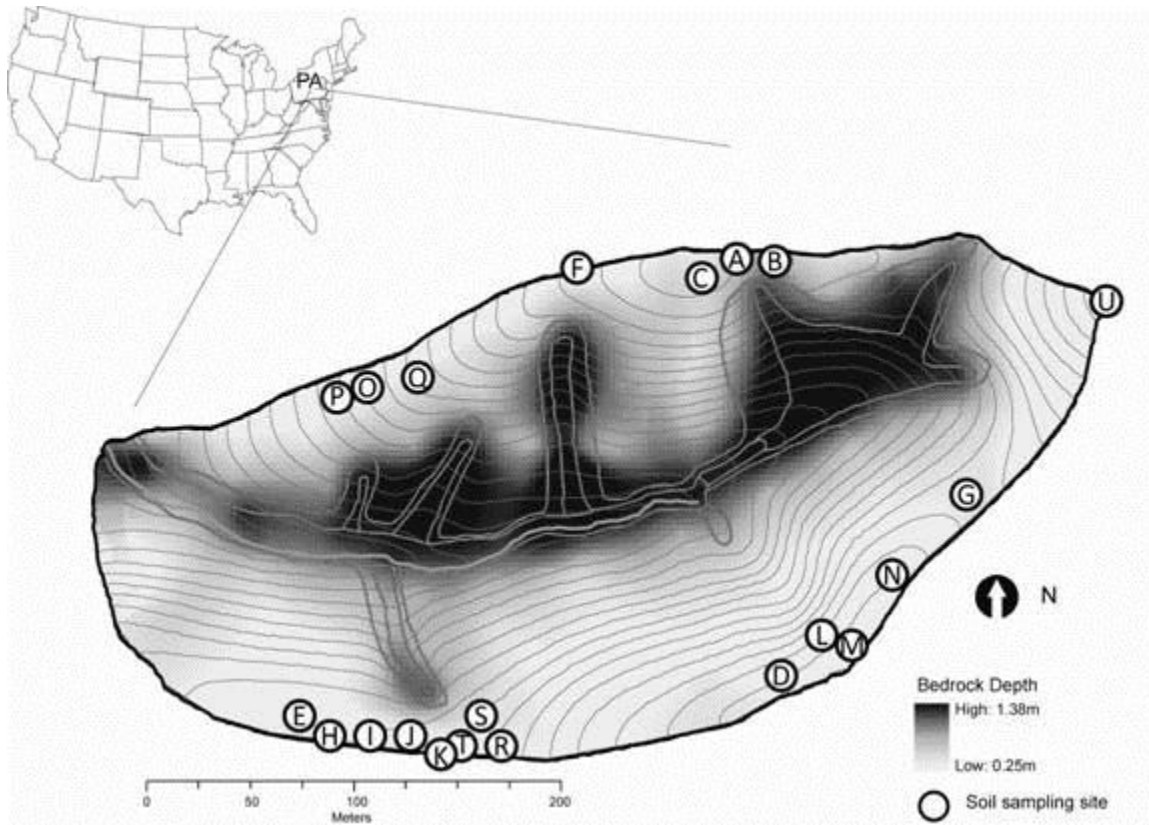


Figure A-1. Sampling locations at the Susquehanna Shale Hills Critical Zone Observatory. This study uses data from twenty-one soil cores (location indicated by lettered circles) augered along the SSHCO catchment ridge during 2006 - 2009. Letters correspond to the cores listed in Table A-1. This map view of SSHCO (adapted from Lin et al., 2006) shows depth to bedrock throughout the catchment with darker colors indicating deeper soils and grey lines indicating elevation change.

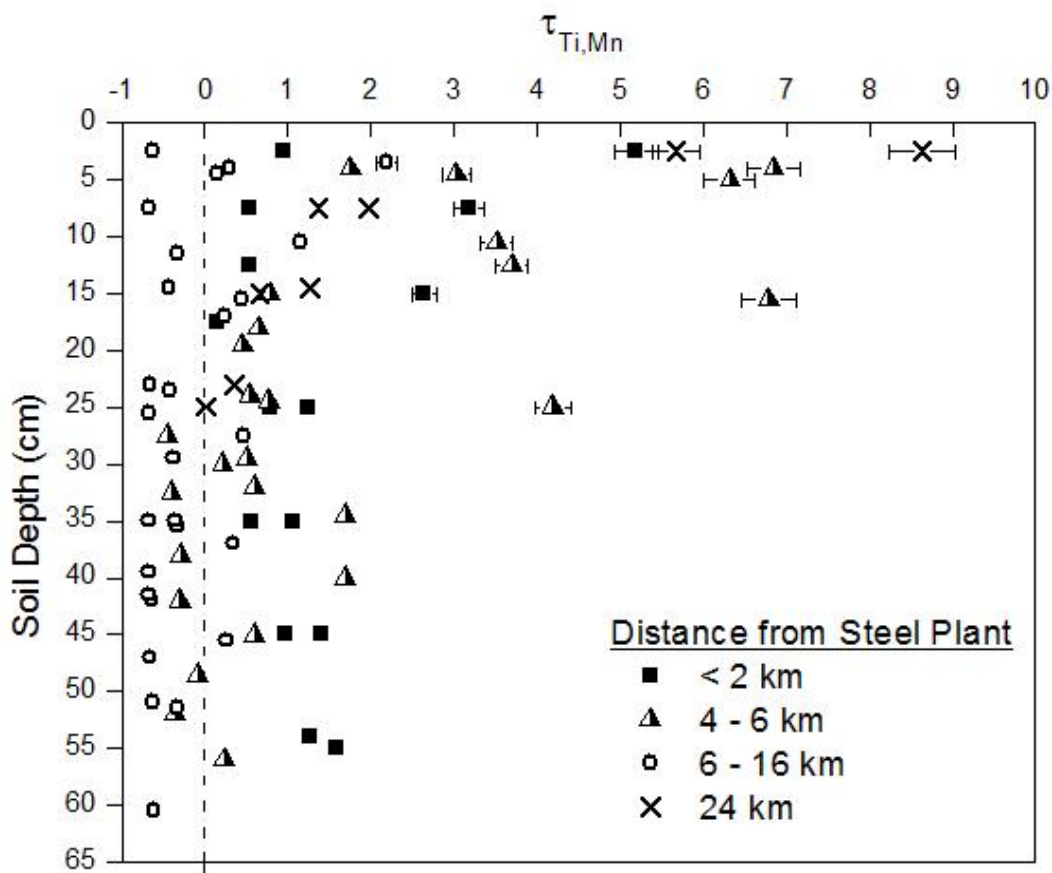


Figure A-2. $\tau_{Ti,Mn}$ profiles for soils in Burnham, PA (U.S.A). $\tau_{Ti,Mn}$ values are plotted versus depth for 12 soil cores augered within 25 km of a steel processing plant in Burnham, PA. Different symbols denote soil cores grouped by distance from the plant (see Fig.3 in text), and $m_{Mn,w}$ and $M_{Mn,w}$ are shown to decrease with increasing distance. Most profiles show surface addition such as that observed at SSHO; however, substantial depletion is calculated for soils 6 - 16 km from the plant. The parent composition is taken as the average of the twelve bottommost samples from each core. Error bars represent the propagated uncertainty in the chemical measurement of each sample (3%) and are smaller than the symbol for $\tau_{Ti,Mn} < 2$.

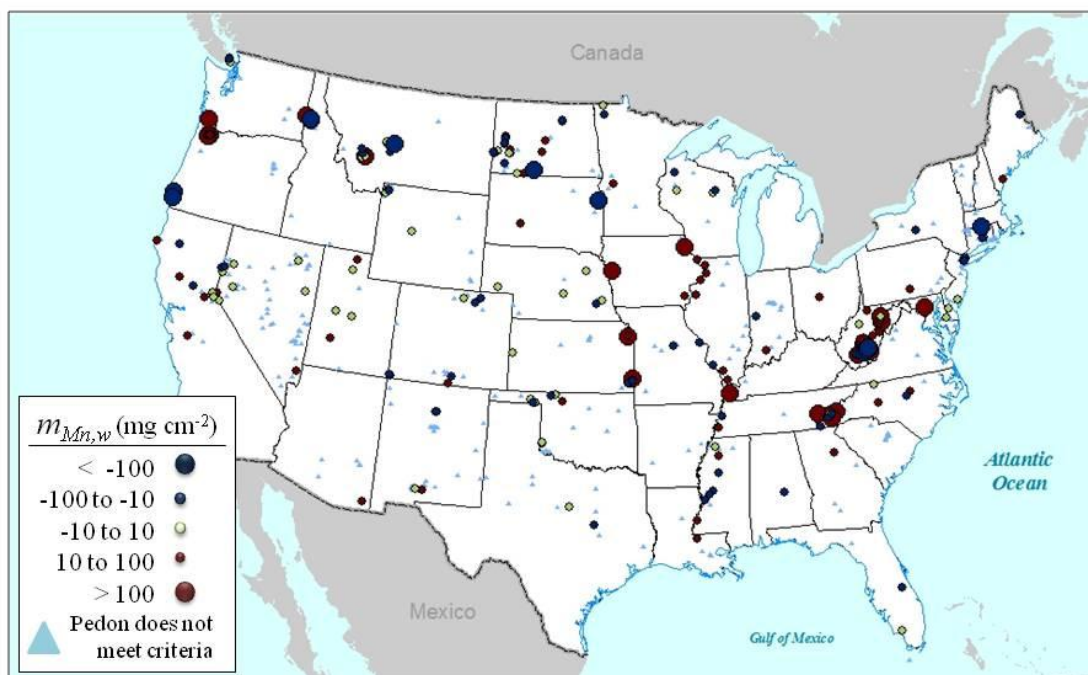


Figure A-3. Mn in- or outflux in U.S. soils. Integrated mass flux values of Mn ($m_{Mn,w}$) are plotted for each soil profile in the continental United States dataset for which the requisite data were reported as described in text and where latitude and longitude were provided⁴⁰⁻⁴¹. Red symbols are proportional to large ($m_{Mn,w} > 100 \text{ mg cm}^{-2}$) or moderate ($10 < m_{Mn,w} < 100 \text{ mg cm}^{-2}$) Mn enrichment while blue symbols are proportional to large or moderate depletion. Locations of soil data for which sufficient chemical data were not provided for $m_{Mn,w}$ calculation (see text) are marked as blue triangles.

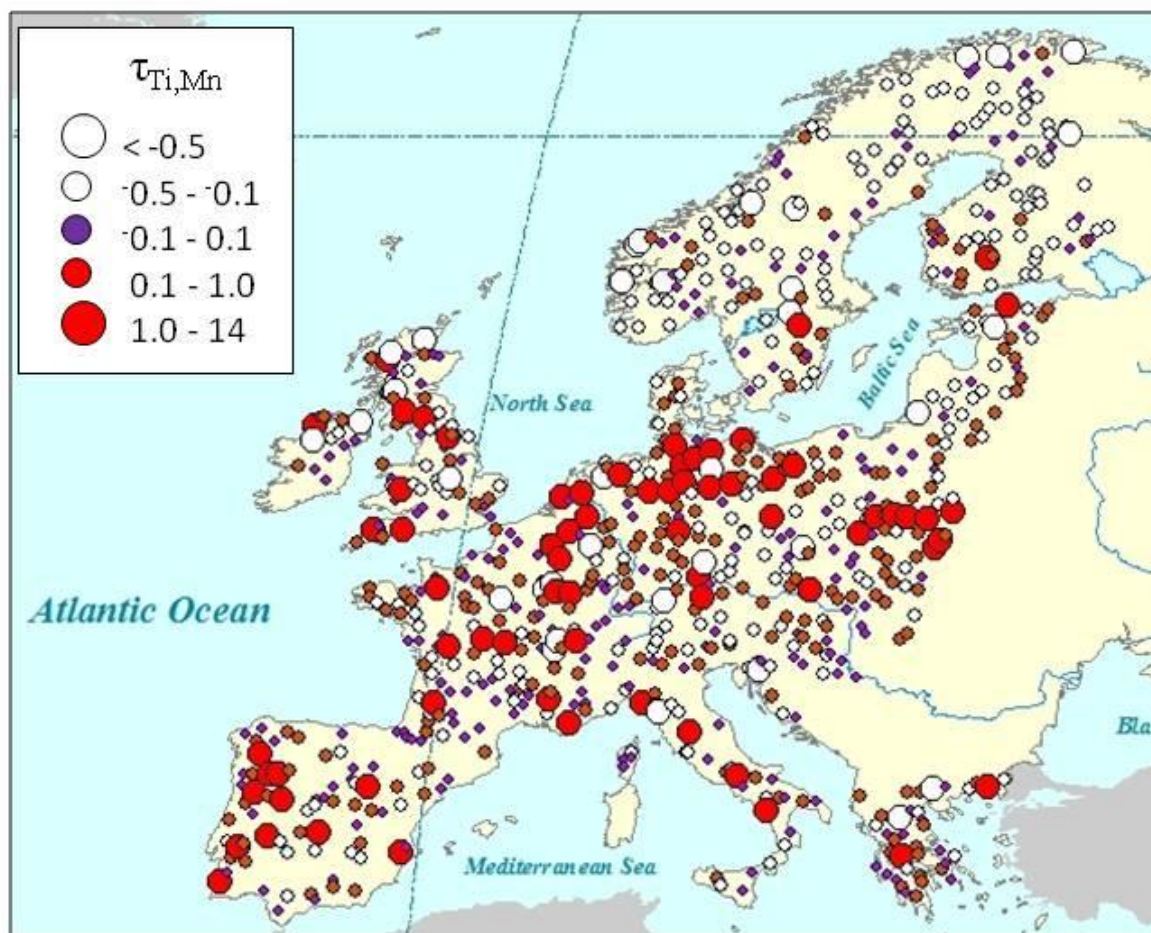


Figure A-4. Patterns of Mn enrichment in Europe topsoils. $\tau_{Ti,Mn}$ values are plotted for all soil collection sites in the FOREGS database (Foregs, 2010) and represent enrichment or depletion of Mn in the topsoil (0 - 25 cm) relative to the C horizon ($i = Ti$). These data suggest concentrations of Mn enrichment around industrialized and heavily populated regions. Red symbols are proportional to large ($\tau_{Ti,Mn} \geq 1$) or moderate ($0.1 < \tau_{Ti,Mn} < 1$) Mn enrichment, while white symbols are proportional to large ($-1 < \tau_{Ti,Mn} < -0.5$) or moderate ($-0.5 < \tau_{Ti,Mn} < -0.1$) Mn depletion, and purple symbols represent slight enrichment or depletion ($-0.1 < \tau_{Ti,Mn} < 0.1$).

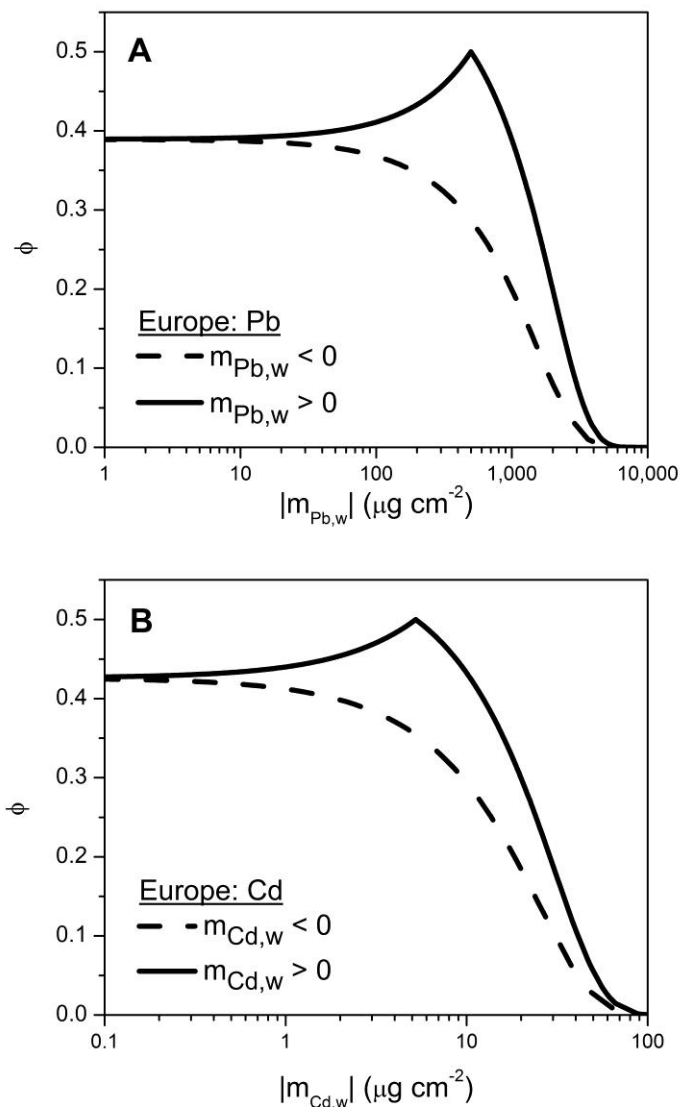


Figure A-5. Distributions of $m_{j,w}$ (Eqn.2) for $j = \text{Pb}$ (A) and $j = \text{Cd}$ (B) in European topsoils (see main text for dataset attributes). Values of $m_{j,w}$ were fit to a normal distribution to determine the fraction (ϕ) of measurements falling above or below each value of $m_{j,w}$. The absolute values of $m_{j,w}$ are plotted on a log-scale, where net enrichment ($m_{j,w} > 0$) is plotted as a solid line and net depletion ($m_{j,w} < 0$) as a dashed line. The mean of each dataset is documented by the value at the peak. A majority of soils within the dataset (73%) have $m_{j,w} > 0$ for Cd and Pb.

Table A-1.

Depth Range (cm)		Mn ($\mu\text{g g}^{-1}$)	^a Zr ($\mu\text{g g}^{-1}$)	$\tau_{\text{Zr,Mn}}$	^b $M_{\text{Mn,w}}$ (mg cm^{-2})	^b $m_{\text{Mn,w}}$ (mg cm^{-2})	$\Sigma M_{\text{Mn,w}}$ (mg cm^{-2})	^c $\Sigma m_{\text{Mn,w}}$ (mg cm^{-2})
^d A. <i>ML1</i>								
0	5.5	900	222	-0.10	4.5	-0.5		
5.5	15	5,800	243	4.33	72.9	59.2		
15	22	800	219	-0.21	8.5	-2.2		
22	27.5	1,500	207	0.58	13.2	4.8		
27.5	28	1,000	207	0.08	8.0	0.1	100	61
^d B. <i>AR1</i>								
0	2	14,400	234	12.68	16.7	15.5		
2	6	3,500	194	2.99	14.3	10.7	31	26
^d C. <i>AR2</i>								
0	2	7,400	240	5.88	8.6	7.4		
2	3.5	3,900	247	2.49	5.3	3.7		
3.5	5.5	4,600	205	3.97	9.8	7.7		
7.5	9.5	1,900	209	1.06	4.8	2.5		
16.5	22	900	217	-0.05	7.5	-0.4	36	21
^d D. <i>AR3</i>								
0	2	12,300	224	11.25	14.3	13.1		
4	6	2,100	194	1.40	4.6	2.7		
9.5	11.5	3,100	205	2.37	8.2	5.8		
15	17.5	1,500	211	0.63	5.5	2.2	33	24
<i>E. SPRT</i>								
0	10	4,600	249	3.18	50.3	38.9		
10	20	3,600	275	1.95	52.0	34.8		
20	30	1,200	246	0.15	19.3	2.7	120	76
<i>F. JBI</i>								
0	10	7,600	153	10.31	83.1	77.5		
10	20	1,200	197	0.43	17.3	5.5		
20	30	600	207	0.32	9.6	4.8		
30	40	300	180	-0.61	5.1	-8.5	120	79
<i>G. JTI</i>								
0	6.35	3,700	230	2.68	22.3	16.7		
6.35	16.51	1,800	227	0.79	24.8	11.1		
16.51	30.48	900	239	-0.19	20.0	-4.5		
30.48	40.64	700	239	-0.34	12.2	-6.4		
40.64	43.18	600	250	-0.44	2.7	-2.2		
43.18	48.26	600	215	-0.34	5.5	-3.0		
48.26	50.8	500	222	-0.44	2.3	-2.0		
50.8	55.88	400	186	-0.53	3.8	-4.2		
55.88	60.96	900	193	0.01	8.6	0.1		
60.96	66.04	600	178	-0.21	5.8	-1.6	108	3.9

Depth Range (cm)		Mn ($\mu\text{g g}^{-1}$)	^a Zr ($\mu\text{g g}^{-1}$)	$\tau_{\text{Zr,Mn}}$	^b M _{Mn,w} (mg cm^{-2})	^b m _{Mn,w} (mg cm^{-2})	^c Σ M _{Mn,w} (mg cm^{-2})	^c Σ m _{Mn,w} (mg cm^{-2})
^d H. RT08								
0	11	3,300	255	1.83	40.8	26.0		
11	16	2,600	247	1.30	18.3	10.2		
16	23	1,200	251	0.03	12.8	0.4	72	37
I. EMH1								
0	6	1,800	211	0.88	10.0	4.6		
4	12	1,800	209	0.90	17.9	8.4		
12	17	1,200	215	0.28	8.6	1.9		
17	22	1,800	211	0.88	13.8	6.4		
22	29	200	203	-0.74	2.3	-7.7		
29	36	200	205	-0.75	2.4	-8.1	55	5.5
J. EMH2								
0	5	2,000	215	1.08	8.7	4.6		
5	10	2,200	222	1.26	13.5	7.6		
10	19	1,200	224	0.23	15.5	3.0		
19	28	900	224	-0.08	12.9	-1.1		
28	36	1,900	207	1.08	25.6	13.6	76	28
K. EMH3								
0	6	2,200	217	1.22	12.3	6.7		
6	14	3,100	200	2.44	32.6	23.1		
14	20	1,200	215	0.20	10.7	1.7		
20	25	200	200	-0.74	1.6	-5.3		
25	32	400	203	-0.57	4.6	-6.0	62	20
L. 1664								
0	5	2,200	180	1.68	9.6	5.9		
5	10	2,800	215	1.88	17.1	11.1		
10	15	1,400	210	0.48	9.7	3.1	36	20
M. 1669								
0	5	11,700	200	12.00	51.0	47.0		
5	10	5,100	190	4.98	31.2	26.0		
10	15	6,000	225	4.89	41.6	34.3		
15	18	3,500	190	3.08	15.5	11.6		
18	20	2,500	185	1.98	7.6	5.0		
20	24	1,500	225	0.45	9.4	2.9	160	130
N. 1768								
0	5	1,500	220	0.57	6.5	2.4		
5	10	2,000	270	0.66	12.2	4.9		
10	15	600	290	-0.52	4.2	-4.7		
15	20	600	245	-0.44	4.5	-3.6		
20	22	800	230	-0.25	2.5	-0.8	30	-1.8

Depth Range (cm)		Mn ($\mu\text{g g}^{-1}$)	$^{\text{a}}\text{Zr}$ ($\mu\text{g g}^{-1}$)	$\tau_{\text{Zr,Mn}}$	$^{\text{b}}\text{M}_{\text{Mn,w}}$ (mg cm^{-2})	$^{\text{b}}\text{m}_{\text{Mn,w}}$ (mg cm^{-2})	$^{\text{c}}\Sigma \text{M}_{\text{Mn,w}}$ (mg cm^{-2})	$^{\text{c}}\Sigma \text{m}_{\text{Mn,w}}$ (mg cm^{-2})
<i>O. 2XX</i>								
0	5	6,600	190	6.70	28.8	25.0		
5	10	5,400	210	4.74	33.0	27.4		
10	15	3,600	210	2.77	24.9	18.1		
15	20	2,600	215	1.72	19.4	12.4		
20	30	1,300	200	0.46	20.9	6.7		
30	36	1,000	205	0.09	10.2	0.9	140	91
<i>P. 229</i>								
0	6	8,000	195	8.10	44.7	39.6		
6	10	7,000	195	6.95	34.8	30.3		
10	15	6,200	205	5.72	43.0	36.5		
15	20	4,900	210	4.17	36.6	29.4		
20	30	3,600	245	2.23	57.9	39.5		
30	40	2,900	245	1.60	49.7	30.2		
40	45	2,600	280	1.09	23.1	12.2	290	220
<i>Q. 218</i>								
0	5	4,100	250	2.65	17.9	13.0		
5	10	4,000	260	2.44	24.5	17.5		
10	15	2,900	275	1.38	20.1	11.8		
15	20	1,900	320	0.29	14.2	3.1		
20	30	800	210	-0.18	12.9	-2.7		
30	40	900	175	0.08	15.4	1.1		
40	50	800	170	0.01	14.4	0.2	120	44
<i>R. 950</i>								
0	5	2,300	195	1.65	10.0	6.3		
5	10	2,100	195	1.38	12.8	7.4		
10	15	1,300	200	0.46	9.0	2.9		
15	20	800	190	-0.09	6.0	-0.6	38	16
<i>S. 952</i>								
0	5	1,900	180	1.30	8.3	4.6		
5	10	2,100	195	1.38	12.8	7.4		
10	15	2,200	215	1.32	15.2	8.9		
15	20	2,400	200	1.67	17.9	11.2		
20	25	1,900	195	1.12	14.9	7.7		
25	30	2,200	200	1.50	18.0	11.0		
30	40	2,200	205	1.44	37.7	22.7		
40	50	1,400	185	0.68	25.1	10.1		
50	58	1,100	195	0.24	16.3	3.1		
58	70	600	180	-0.23	13.7	-4.3		
70	72	700	185	-0.16	2.7	-0.5	180	82

Depth Range (cm)		Mn ($\mu\text{g g}^{-1}$)	^a Zr ($\mu\text{g g}^{-1}$)	$\tau_{\text{Zr,Mn}}$	^b $M_{\text{Mn,w}}$ (mg cm^{-2})	^b $m_{\text{Mn,w}}$ (mg cm^{-2})	^c $\Sigma M_{\text{Mn,w}}$ (mg cm^{-2})	^c $\Sigma m_{\text{Mn,w}}$ (mg cm^{-2})
<i>T. 954</i>								
0	5	1,300	215	0.36	5.7	1.5		
5	10	1,200	185	0.40	7.3	2.0		
10	15	1,300	200	0.46	9.0	2.9		
15	20	1,200	230	0.20	9.0	1.5		
20	25	600	185	-0.26	4.7	-1.7		
25	30	700	200	-0.23	5.7	-1.7	41	4.6
^d <i>U. WRT</i>								
0	11	1,500	218	0.53	18.5	6.4		
11	15	1,400	225	0.38	7.8	2.2		
15	19	1,100	218	0.12	6.5	0.7		
19	19	400	218	-0.59	0.6	-0.9	34	8.4

a. Where Zr concentrations were not measured, they are estimated from Ti concentrations using Eqn. (1) such that $i = \text{Zr}$, $j = \text{Ti}$, and $\tau_{\text{Zr,Ti}} = -0.21$, the average depletion of Ti relative to Zr in SSHO ridge soils.

b. Mn mass ($M_{\text{Mn,w}}$) and the integrated Mn enrichment for Mn ($m_{\text{Mn,w}}$, Eqn.2) are calculated for each sample depth (Δz) using a depth-dependent bulk density value (see Table S3).

c. The summation over all sample depths gives the area-normalized mass value for each core augered to the bedrock-soil interface.

d. Zr concentrations were estimated and not measured for these soil profiles.

Table A-2. Mn addition to soils near a steel processing plant in Burnham, PA.

Distance (km)	Core Depth (cm)	Mn ($\mu\text{g g}^{-1}$) Deepest Sample	Mn ($\mu\text{g g}^{-1}$) Soil Average	$^a\text{M}_{\text{Mn,w}}$ (mg cm^{-2})	$^a\text{m}_{\text{Mn,w}} \pm \text{s.d.}$ (mg cm^{-2})
1.1	60	650	560	120	48 ± 37
1.4	58	600	1,300	52	3.7 ± 21
4.3	44	150	1,300	80	66 ± 4.8
4.8	58	390	730	64	34 ± 5.1
5.7	32	390	1,100	42	30 ± 5.1
5.7	33	230	1,100	44	31 ± 6.1
6.1	40	100	340	16	9.5 ± 7.2
6.6	65	100	180	2.5	-8.5 ± 10
14.8	49	150	180	15	2.7 ± 1.7
15.8	54	150	180	17	-5.6 ± 5.3
23.8	30	310	700	24	14 ± 2.1
23.8	27	390	960	30	20 ± 3.8

^aThe summation over all sample depths gives the area-normalized mass value for each core augered to the bedrock-soil interface.

Table A-3. Soil bulk density at SSHO.

Depth (cm)	Bulk Density (g cm^{-3})
0 - 3	0.69 ^a
0 - 7	0.96 ^b
7 - 19	1.26 ^b
17 - 20	1.83 ^a
23 - 26	1.59 ^a
41 - 44	1.73 ^a
51-54	1.76 ^a

a. Values reported in Lin (2006)

b. Values reported in Jin *et al.* (2010)

c. Bulk density (ρ_w , g cm^{-3}) changes as a function of depth (z , cm) in the soil according to the equation:

$\rho_w = 0.32 \cdot \ln(z) + 0.58$. This equation is used to estimate the bulk density of samples collected from various depths in the soil profile.

Table A-4. Literature values pertaining to atmospheric Mn deposition

Ref#	Location	Reported Value	Reported Units	Deposition Rate ($\mu\text{g cm}^{-2}\text{ yr}^{-1}$)	Year
<i>Industrial environment</i>					
3	United States	19,300	$\text{ng cm}^{-2}\text{ mo}^{-1}$	232	1964-1965
3	United States	250 - 8,300	ng m^{-3}	21 - 690	1965-1967
5	United States	5 - 10	$\mu\text{g m}^{-3}$	410 - 830	1970s
48	United States	200 - 500	ng m^{-3}	17 - 41	1979-1983
49	Brescia, Italy	0.69	$\mu\text{g m}^{-3}$	57	2001
12	Quebec, Canada	21.9	$\mu\text{g m}^{-3}$	1,820	2004
12	Quebec, Canada	0.37	$\mu\text{g m}^{-3}$	31	2004
<i>Industrial workplace</i>					
48	Chile	250	mg m^{-3}	21,000,000	1944
48	United States	5 - 8	mg m^{-3}	410,000-660,000	1980s
49	Brescia, Italy	93 - 513.71	$\mu\text{g m}^{-3}$	7,700 - 25,000	1978 - 1990
<i>Urban Environment</i>					
50	United States	23 (1.9 - 80)	$\mu\text{g L}^{-1}$		
5	United States	0.11	$\mu\text{g m}^{-3}$	9.1	1953 - 1957
5	Cincinnati, OH, U.S. ^b	9.29	$\mu\text{g m}^{-3}$	771	1955
5	United States	0.1	$\mu\text{g m}^{-3}$	8.3	1957 - 1961
5	Philadelphia, PA, U.S. ^b	9.98	$\mu\text{g m}^{-3}$	828	1961
5	Charleston, WV, U.S. ^b	9.98	$\mu\text{g m}^{-3}$	828	1961
3	United States	73	ng m^{-3}	6.05	1965-1967
3	New York City	420 - 790	$\text{ng cm}^{-2}\text{ mo}^{-1}$	5.0 - 9.48	1966-1967
8	Midwest U.S.	310	ng m^{-3}	25.71	1970-1985
8	East Chicago, U.S.	1,469	ng m^{-3}	121.8	1970-1985
48	Belgium	42 - 456	ng m^{-3}	3.5-37.8	1972-1977
48	Japan	20 - 800	ng m^{-3}	2 - 66	1973
48	Germany	3 - 16	ng m^{-3}	0.25 - 1.33	1974
12	Montreal, Canada	0.01 - 0.06	$\mu\text{g m}^{-3}$	0.83 - 4.98	1981 - 2000
3	United States	33	ng m^{-3}	2.7	1982
51	Canada	20 - 270	ng m^{-3}	1.7 - 22	1982
51	United States	5 - 390	ng m^{-3}	0.4 - 32	1982
51	Europe	23 - 850	ng m^{-3}	1.9 - 70	1982
51	Global	10 - 590	ng m^{-3}	0.8 - 49	1982
52	Chicago, U.S.	33	$\text{mg m}^{-2}\text{ y}^{-1}$	3.3	1991
53	Oporto, Portugal	14.4	ng m^{-3}	1.19	1994
10	Vancouver, Canada	350	$\mu\text{g m}^{-2}\text{ d}^{-1}$	12.78	1995

Ref#	Location	Reported Value	Reported Units	Deposition Rate ($\mu\text{g cm}^{-2}\text{ yr}^{-1}$)	Year
54	Philadelphia, PA, U.S.	0.013	ng m^{-3}	1.07	2000
55	Taichung Harbor, Taiwan	194.3	$\mu\text{g m}^{-2}\text{ d}^{-1}$	7.09	2004-2005
56	Brisbane, Australia	16.06	$\mu\text{g m}^{-2}\text{ d}^{-1}$	0.59	2007-2008
<i>Suburban, Rural and Remote Environments</i>					
48	South Pole	0.01	ng m^{-3}	0.0008	1973
57	Bermuda	0.17 - 20	ng m^{-3}	0.01-1.66	1974
48	Atlantic Ocean	0.5 - 5.4	ng m^{-3}	0.04 - 0.45	1975
48	United States avg.	20	ng m^{-3}	1.66	1979-1983
58	Adirondacks, NY, U.S.	0.6-1.7	$\mu\text{g L}^{-1}$		1981
51	Global continents	< 0.18 - 9.3	ng m^{-3}	0.01 - 0.77	1980s
51	Global Oceans	0.02 - 79	ng m^{-3}	0.002 - 6.55	1980s
51	Global polar regions	0.01 - 1.5	ng m^{-3}	0.001 - 0.12	1980s
51	Global rural regions	6.5 - 199	ng m^{-3}	0.54 - 16.5	1980s
59	Chesapeake Bay, MD, U.S.	1.4	$\text{mg m}^{-2}\text{ y}^{-1}$	0.14	1990 - 1991
52	South Haven, MI, U.S.	26	$\text{mg m}^{-2}\text{ y}^{-1}$	2.6	1991
52	Lake Michigan, U.S.	7.3	$\text{mg m}^{-2}\text{ y}^{-1}$	0.73	1991
60	Massachusetts Bay, U.S.	2.7	$\text{mg m}^{-2}\text{ y}^{-1}$	0.27	1992-1993
61	Great Lakes, U.S.	2,810 - 4,500	$\mu\text{g m}^{-2}\text{ y}^{-1}$	0.28 - 0.45	1993 - 1994
62	SW Lake Michigan, U.S.	12	$\text{mg m}^{-2}\text{ y}^{-1}$	1.2	1994 - 1995
63	Central Ontario, Canada	6.2	$\text{mg m}^{-2}\text{ y}^{-1}$	0.62	1980 - 2002
64	Osaka, Japan	29	ng m^{-3}	2.41	1999-2002
65	Midland, PA, U.S.	0.018-0.052	$\mu\text{g m}^{-3}$	1.0-4.3	2008
13	Northern Atlantic Ocean	11.6	pmol m^{-3}	0.05	2003

- a. Estimates of atmospheric deposition can be calculated as the product of Mn concentration in air multiplied by the average deposition velocity for Mn-particles ($2.63 \pm 1.17\text{ cm s}^{-1}$)^{10,47}.
- b. Locations where maximum air Mn levels were reported⁵ as indicated but may have exceeded $> 10\text{ }\mu\text{g m}^{-3}$.

References

47. Yi, S.; Totten, L.A.; Thota, S.; Yan, S.; Offenberg, J.H.; Eisenreich, S.J.; Graney, J.; Holsen, T.M. Atmospheric dry deposition of trace elements measured around the urban and industrially impacted NY-NJ harbor. *Atm. Environ.* **2006**, *40*, pp 6626-6637.
48. *Air Quality Guidelines: Manganese*. World Health Organization: Copenhagen, Denmark, 2001.
49. Lucchini, R.G.; Albini, E.; Benedetti, L.; Borghesi S.; Coccaglio, R.; Malara, E.C.; Parrinello, G.; Garattini, S.; Resola, S.; Alessio, L. High prevalence of Parkinsonian disorders associated to manganese exposure in the vicinities of ferroalloy industries. *Am. J. Ind. Med.* **2007**, *50*, pp 788-800.
50. Galloway, J.N.; Thornton, J.D.; Norton, S.A.; Volchok, H.L.; McLean, R.A.N. Trace metals in atmospheric deposition: a review and assessment. *Atm. Environ.* **1982**, *16*, pp 1677-1700.
51. *Manganese and its Compounds: Concise International Chemical Assessment Document 12*. World Health Organization: Geneva, Switzerland, 1999.
52. Holsen, T.M.; Noll, K.E.; Fang, G.; Lee, W.; Lin, J. Dry deposition and particle size distributions measured during the Lake Michigan urban air toxics study. *Environ. Sci. Technol.* **1993**, *27*, pp 1327-1333.
53. Vasconcelos, M.T.S.D.; Tavares, H.M.F. Atmospheric metal pollution (Cr, Cu, Fe, Mn, Ni, Pb and Zn) in Oporto city derived from results for low-volume aerosol samplers and for the moss *Sphagnum auriculatum* bioindicator. *Sci. Total Environ.* **1998**, *212*, pp 11-20.
54. *Southern Delaware County Air Monitoring Report*. Pennsylvania Department of Environmental Protection, Bureau of Air Quality, 2003: <http://www.state.pa.us>
55. Wu, Y.; Fang, G.; Chen, J.; Lin, C.; Huang, S.; Rau, J.; Lin, J. Ambient air particulate dry deposition, concentrations, and metallic elements at Taichung Harbor near Taiwan Strait. *Atmos. Res.* **2006**, *79*, pp 52-66.
56. Huston, R.; Chan, Y.C.; Gardner, T.; Shaw, G.; Chapman, H. Characterization of atmospheric deposition as a source of contaminants in urban rainwater tanks. *Water Res.* **2009**, *43*, pp 1630-1640.
57. Chen, L.; Duce, R.A. The sources of sulfate, vanadium and mineral matter in aerosol particles over Bermuda. *Atmos. Environ.* **1983**, *17*, pp 2055-2064.
58. Shanley, J.B. Manganese biogeochemistry in a small Adirondack forested lake watershed. *Water Resour. Res.* **1986**, *22*, pp 1647-1656.
59. Wu, Z.Y.; Han, M.; Lin, Z.C.; Ondov, J.M. Chesapeake Bay atmospheric deposition study, year 1: sources and dry deposition of selected elements in aerosol particles. *Atmos. Environ.* **1994**, *28*, pp 1471-1486.
60. Golomb, D.; Ryan, D.; Eby, N.; Underhill, J.; Zemba, S. Atmospheric deposition of toxic onto Massachusetts Bay - I. Metals. *Atmos. Environ.* **1997**, *31*, pp 1349-1359.
61. Sweet, C.W.; Weiss, A.; Vermette, S.J. Atmospheric deposition of trace metals at three sites near the Great Lakes. *Water Air Soil Pollut.* **1998**, *103*, pp 423-439.
62. Zufall, M.J.; Davidson, C.I.; Caffrey, P.F.; Ondov, J.M. Airborne concentrations and dry deposition fluxes of particulate species to surrogate surfaces deployed in southern Lake Michigan. *Environ. Sci. Technol.* **1998**, *32*, pp 1623-1628.
63. Watmough, S.A.; Eimers, M.C.; Dillon, P.J. Manganese cycling in central Ontario forests: response to soil acidification. *Appl. Geochem.* **2007**, *22*, pp 1241-1247.
64. Funasaka, K.; Sakai, M.; Shinya, M.; Miyazaki, T.; Kamiura, T.; Kaneco, S.; Ohta, K.; Fujita, T. Size distributions and characteristics of atmospheric inorganic particles by regional comparative study in Urban Osaka, Japan. *Atmos. Environ.* **2003**, *37*, pp 4597-4605.
65. PA Department of Environmental Protection, Bureau of Air Quality. DEP sampling study at USA Today report sites. EPA: 2009.

Appendix B

Supporting Figures and Tables for Chapter 3

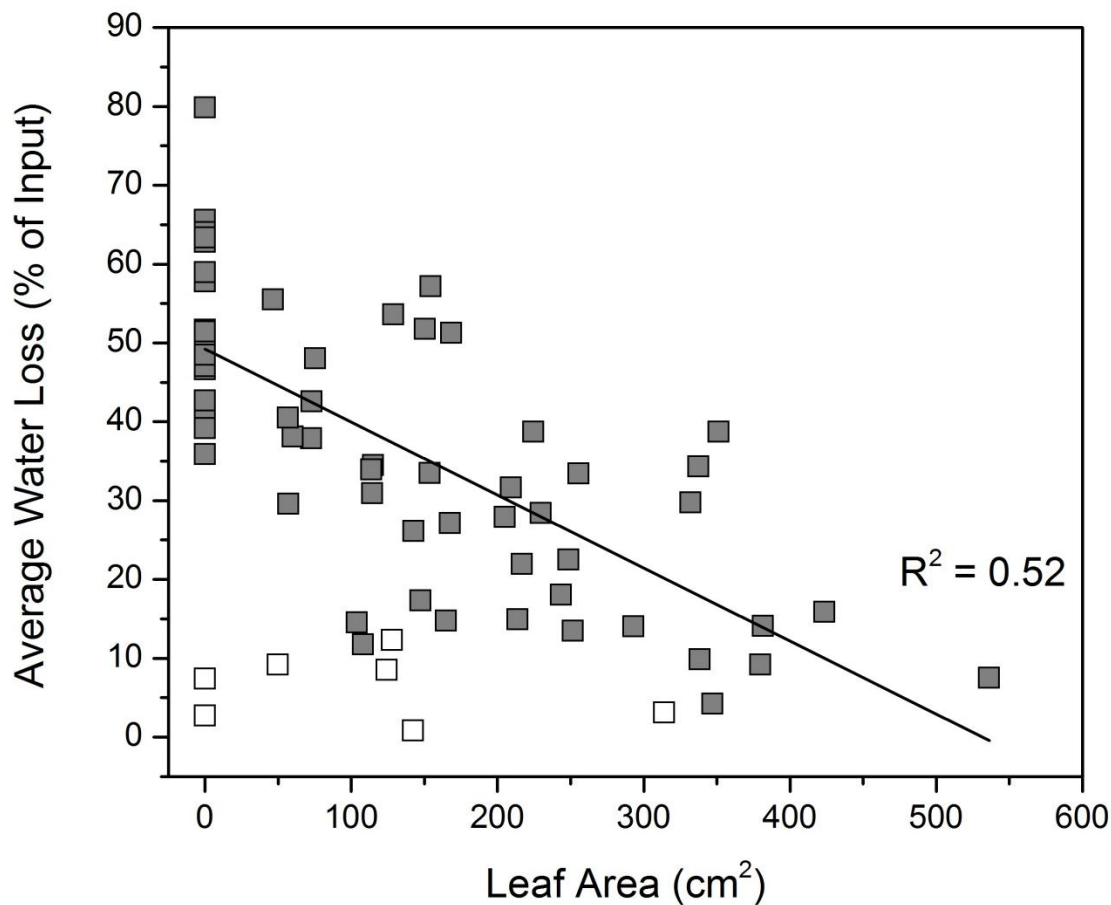


Figure B-1. The average percent of influent water that is lost as effluent from each pot decreases as a function of the leaf area measured at harvest ($p < 0.001$). Average water loss is calculated over the entire 19 weeks of the experiment. Out of 66 pots, 4 pots had values for average water loss that were > 2 standard deviations outside of the observed trend. Three additional pots had zero effluent for more than 7 out of 11 weeks after the date of Mn additions. These seven pots (open symbols) were excluded from calculations that included effluent volume.

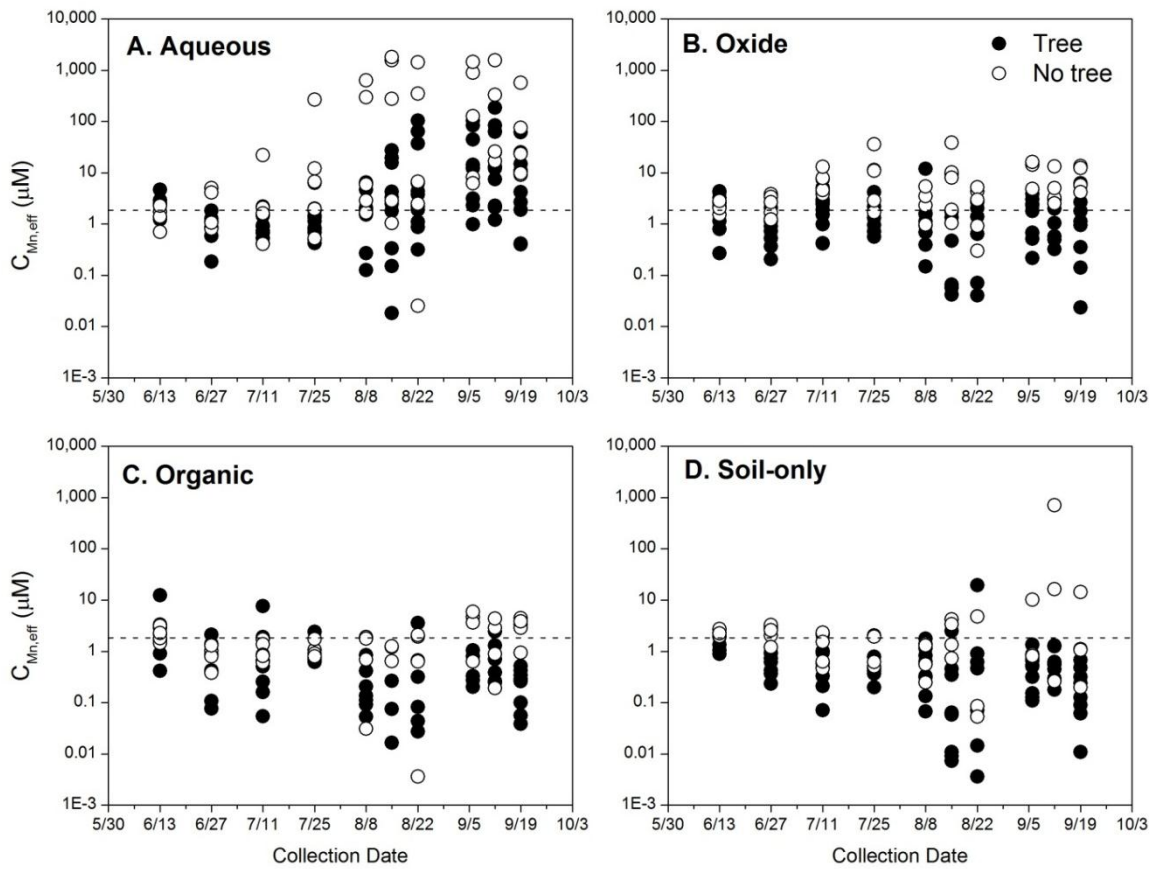


Figure B-2. Mn concentrations in effluent are plotted on a log scale for each date of effluent collection that effluent chemistry was analyzed. All replicates of each treatment are plotted. Organic and oxide additions were added on July 4 and aqueous additions were added once per week from July 4 to September 12. The dotted line indicates the average $C_{Mn,eff}$ for all pots prior to Mn additions.

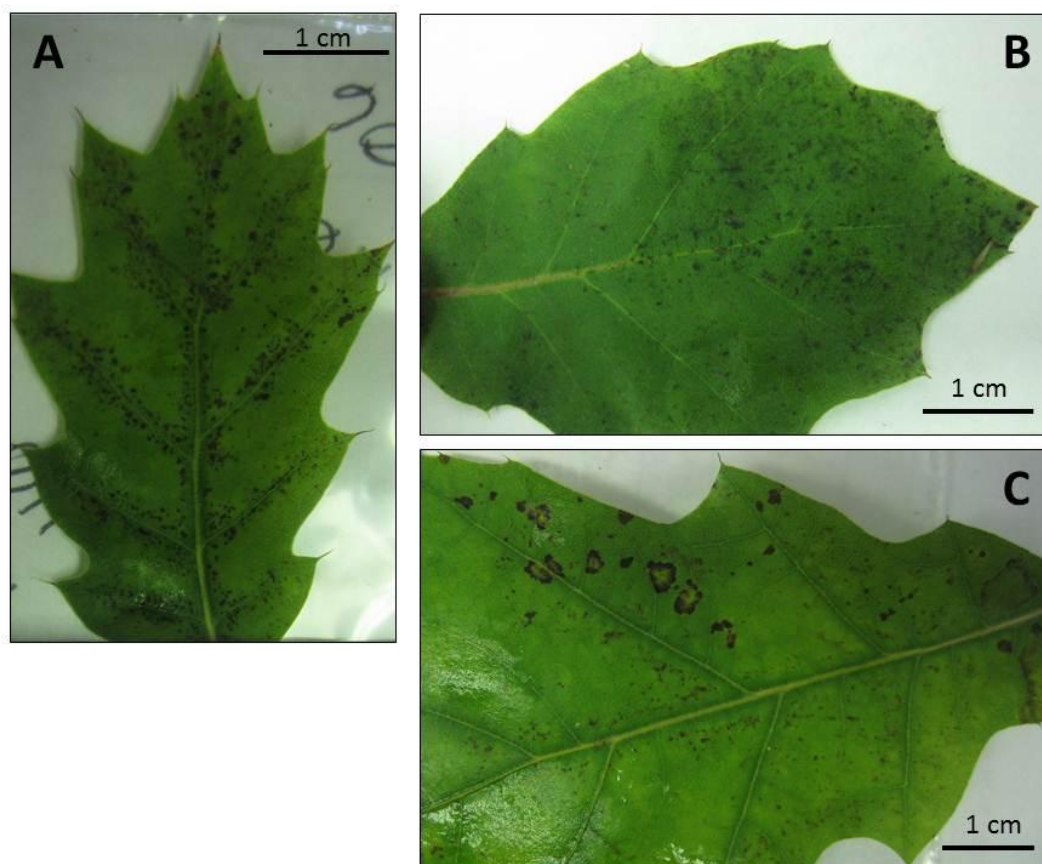


Figure B-3. Mn toxicity was observed on red oak leaves as dark spots either A) clustered around the midveins, B) dispersed across the leaf surface, or C) in rings.

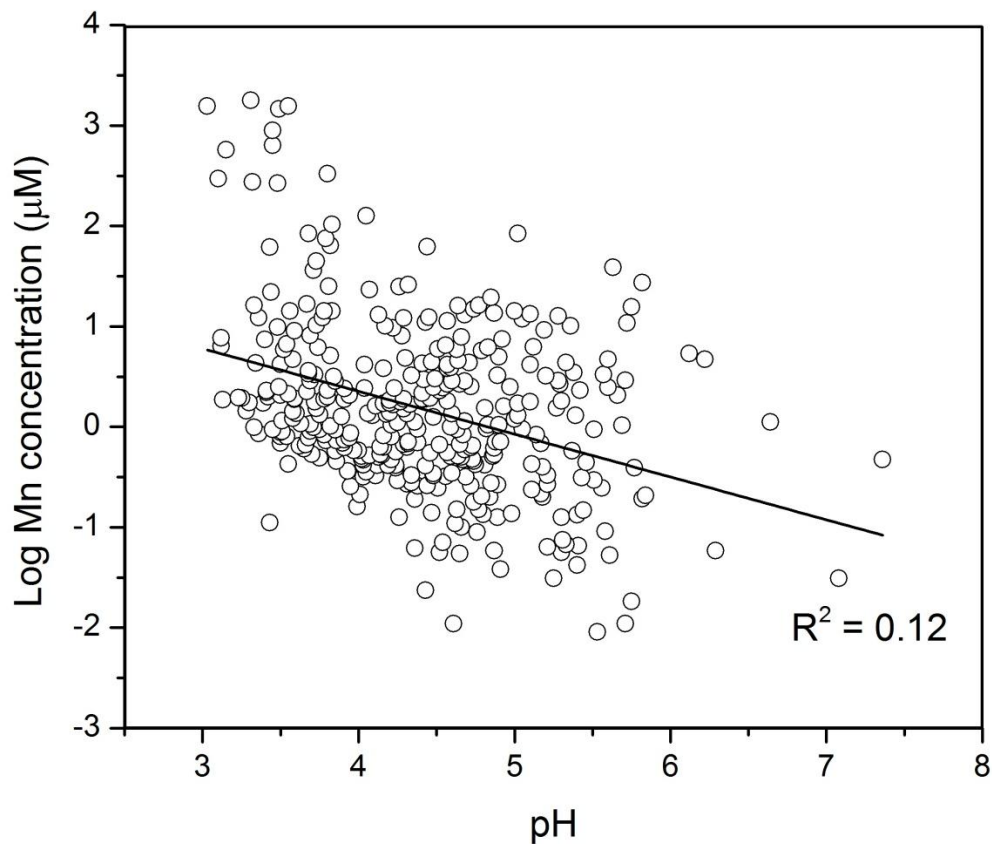


Figure B-4A) Log Mn concentration (μM) is plotted versus pH for every effluent sample for which both $C_{Mn,eff}$ and pH were measured. These data show a highly significant ($p < 0.001$) increase in Mn concentrations with decreasing pH.

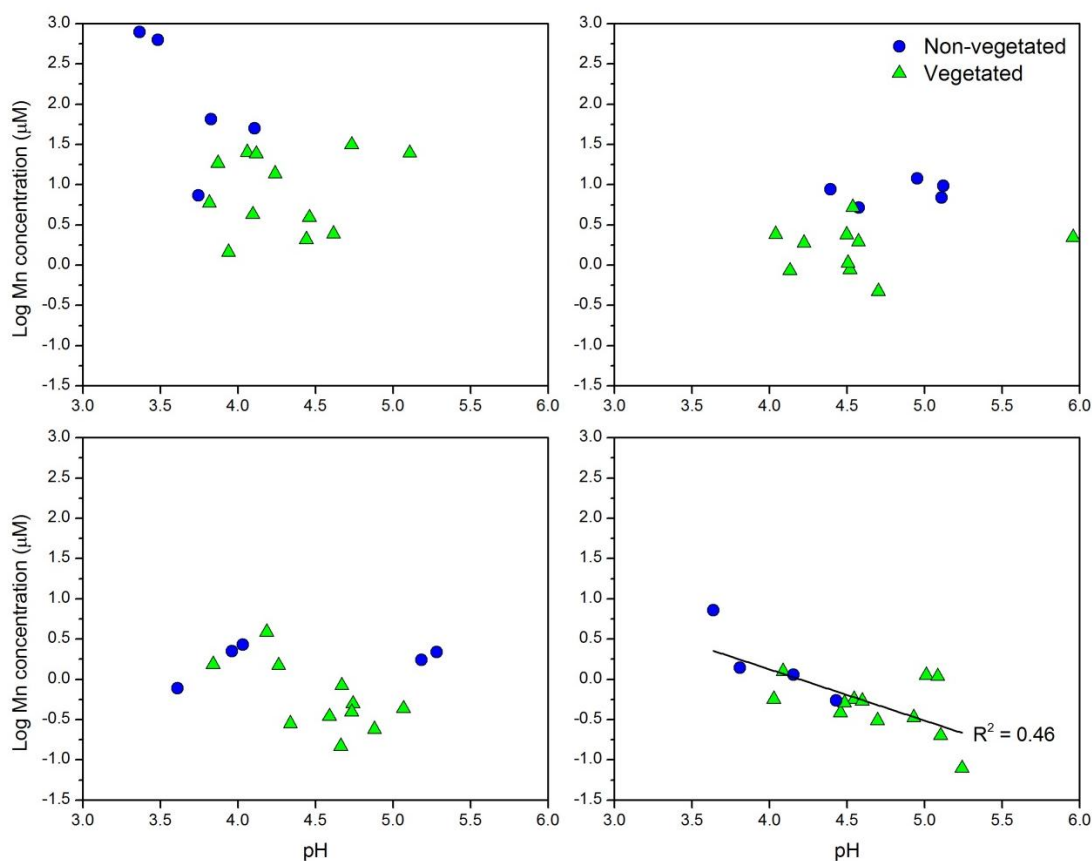


Figure B-4B) The average log Mn concentration (μM) is plotted versus average pH in effluent collected after the start of Mn additions for each replicate in vegetated (green triangles) and non-vegetated (blue circles) pots. An inverse correlation between $C_{Mn,eff}$ and pH was observed in effluent from soil-only pots ($p < 0.05$); however, no other treatments exhibited significant trends. Therefore, while pH differences may impact Mn loss from soil-only pots, they cannot explain increased Mn release from aqueous and oxide treatments or decreased Mn release from the organic treatments.

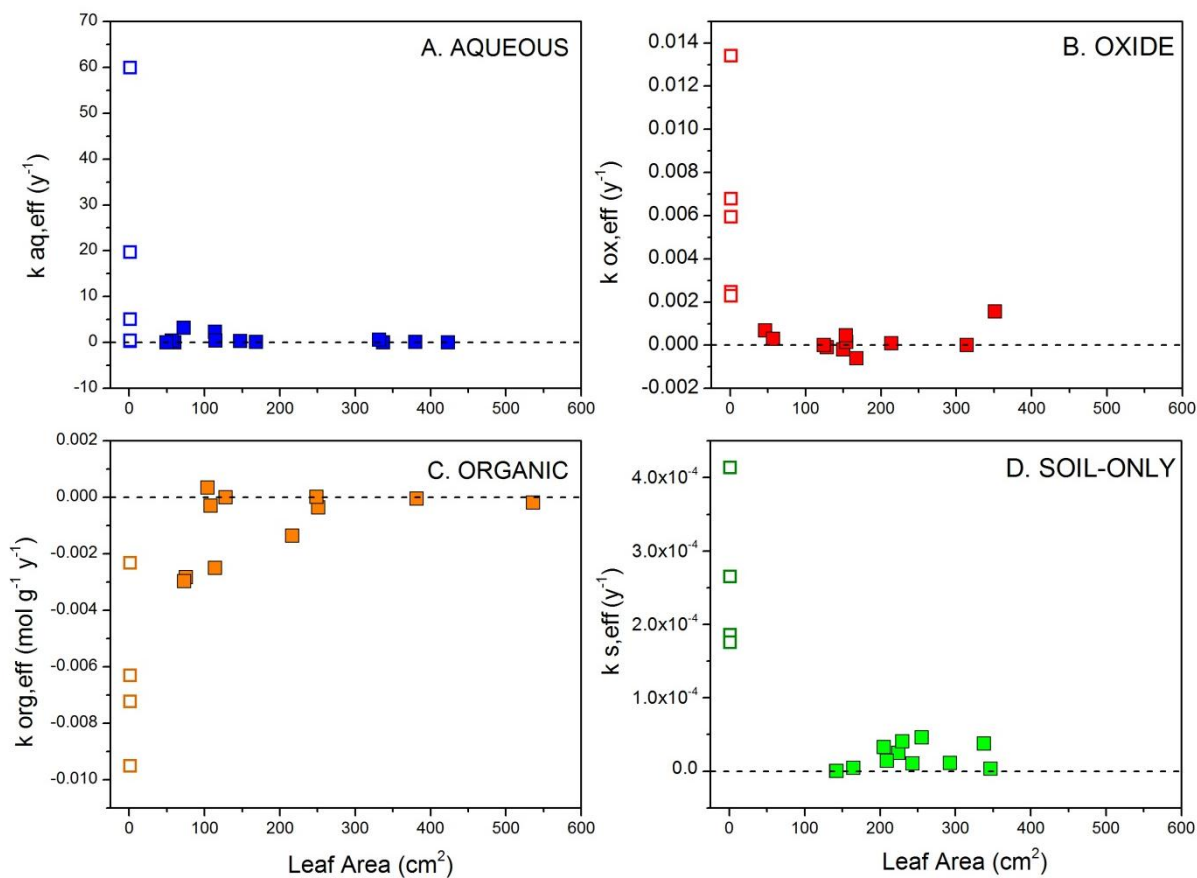


Figure B-5. First order rate constants describing the mass transfer of Mn from j to effluent ($k_{j,eff}$, y⁻¹, and $k_{org,eff}$, mol g⁻¹ y⁻¹) plotted versus leaf area for soil-only pots ($j = s$) and pots with soil plus either aqueous ($j = aq$), oxide ($j = ox$), or organic ($j = org$) Mn additions. Both vegetated (closed squares) and non-vegetated (open squares) are plotted. For soil-only, aqueous, and oxide pots, $k_{j,eff}$ in non-vegetated pots (leaf area = 0 cm²) is higher than for vegetated pots (leaf area > 0 cm²); however, no correlation between leaf area and $k_{j,eff}$ is observed in the vegetated pots alone. In pots receiving soil + organic addition, $k_{org,eff}$ is more negative in non-vegetated than vegetated pots.

Table B-1. Chemical composition of mineral soil and organic matter in mesocosms

	Al	Ca	Fe	K	Mg	Mn	Na	Si
$C_{i,S}$, mol kg ⁻¹	2.19	0.025	0.72	0.44	0.19	0.018	0.11	11.8
$M_{i,S}$, mol (Large pots)	6.99	0.081	2.31	1.41	0.61	0.057	0.34	37.7
$M_{i,S}$, mol (Small pots)	2.87	0.033	0.95	0.58	0.25	0.023	0.14	15.5
$C_{i,org}$, mol kg ⁻¹	2.68	0.081	0.58	0.58	0.23	0.10	0.08	7.47

Table B-2. Weekly effluent volumes (mL) recorded for vegetated mesocosms

Date	5/30	6/6	6/13	6/20	6/27	7/4	7/11	7/18
G02	0	0	0	0	0	20	90	43
G04	0	49	65	90	89	90	53	49
G05	88	0	9.5	58	0	101	117	98
G06	0	0	0	0	0	0	25	0
G07	35	0	51	88	107	149	125	110
G08	59	45	103	37	20	127	9.5	0
H01	117	165	181	170	184	164	175	158
H02	0	0	0	0	0	0	0	0
H03	0	0	0	0	0	36	96	56
H04	105	155	171	162	150	146	153	155
H06	75	141	141	173	166	162	147	50
H07	115	167	157	143	86	81	50	48
H08	0	0	0	0	0	63	175	164
J02	0	15	29	62	51	41	48	30
J03	0	0	0	0	0	23	123	124
J05	0	0	0	67	10.8	0	0	0
J06	75	115	131	130	165	153	107	0
J07	0	0	0	0	0	0	0	0
K01	0	0	0	14.5	29	17	0	10
K02	55	65	0	66	75	69	159	40
K03	0	0	38	23	0	0	0	0
K05	61	41	33	0	44	39	39	33
K06	51	55	31	21	48	34	23	7
K07	31	61	12.5	27	0	7.5	40	0
K08	0	0	30	54	19	21	18	0
L02	0	0	0	0	0	20	136	118
L03	49	63	141	163	164	179	175	155
L04	0	0	0	0	67	145	193	160
L05	105	149	150	166	125	102	61	37
L06	133	189	185	185	178	174	125	120
L07	0	0	0	4.5	0	0	0	0
L08	0	0	0	0	0	25	82	79
M01	96	95	165	114	127	130	139	178
M02	75	83	0	0	0	0	0	38
M04	0	0	0	0	0	169	146	130
M05	0	0	0	0	57	60	188	123
M06	0	30	36	42	54	89	166	85
M07	119	0	245	145	0	50	25	0
M08	123	181	175	172	158	151	111	79
N01	0	0	65	195	60	17	0	0
N02	117	76	170	97	123	141	109	78
N04	0	36	51	74	113	191	59	88
N05	11	122	43	94	199	205	208	189
N06	0	0	0	0	18	32	65	0
N07	105	120	162	42	145	118	7	0
N08	75	56	115	81	92	0	0	0

Date	7/25	8/1	8/8	8/15	8/22	9/6	9/12	9/19
G02	53	75	33	29	0	64	0	12
G04	0	0	69	46	0	0	20	46
G05	125	131	149	171	103	191	186	162
G06	0	0	0	0	0	0	11.5	0
G07	86	205	129	152	91	110	140	159
G08	0	0	20	60	0	0	10.5	32
H01	153	250	0	83	133	138	79	88
H02	0	0	55	87	145	147	108	120
H03	51	55	55	90	57	73	99	41
H04	155	205	153	175	165	146	176	21
H06	32	157	161	170	163	135	145	125
H07	36	113	35	126	106	107	139	144
H08	172	189	183	184	170	163	175	170
J02	31	30	120	124	137	145	160	168
J03	119	242	122	167	125	135	105	154
J05	125	61	0	0	163	0	0	0
J06	60	85	57	199	64	76	92	89
J07	0	69	25	25	42	76	112	138
K01	17	104	43	20	29	27	0	22
K02	31	57	39	55	45	37	65	68
K03	0	20	0	0	0	0	0	0
K05	28	69	87	85	72	89	92	98
K06	0	39	6	0	9	0	0	0
K07	0	130	0	0	16	0	33	24
K08	0	14.5	0	0	-	-	-	-
L02	148	144	150	167	171	166	146	180
L03	115	109	163	182	181	167	179	176
L04	168	165	60	140	89	41	155	142
L05	25	0	0	0	57	0	0	48
L06	105	147	154	175	170	171	197	198
L07	0	131	137	146	111	91	70	148
L08	92	123	111	141	125	125	153	155
M01	184	211	159	125	178	118	183	169
M02	0	83	56	0	0	0	0	0
M04	118	218	69	128	0	163	123	0
M05	75	82	81	87	93	103	125	140
M06	142	199	163	166	172	158	154	162
M07	0	83	101	127	98	59	91	49
M08	13	0	36	128	52	55	64	81
N01	0	0	43	149	64	76	125	115
N02	31	35	59	51	49	65	175	94
N04	0	14	0	0	0	0	37	29
N05	0	25	0	0	0	163	200	195
N06	85	0	0	0	0	0	0	8.5
N07	0	11	0	0	0	0	0	14
N08	0	0	65	101	78	101	114	143

Table B-3. Weekly effluent volumes (mL) recorded for non-vegetated mesocosms

Date	5/30	6/6	6/13	6/20	6/27	7/4	7/11	7/18
G01	7	0	18.5	0	0	0	31	0
G03	128	135	205	223	208	200	173	147
H05	97	129	173	141	150	180	197	153
J01	0	0	8.5	187	100	89	56	173
J04	87	157	179	170	171	165	168	141
J08	105	169	177	195	145	85	170	155
K04	39	65	37	91	90	88	90	78
L01	79	173	160	161	179	225	197	220
M03	133	203	221	223	0	296	238	219
N03	23	0	40	0	0	41	0	31
Z01	n/a	179	141	150	141	138	151	123
Z02	n/a	165	165	171	147	135	133	119
Z03	n/a	133	163	165	142	111	156	135
Z04	n/a	157	161	207	164	160	165	139
Z05	n/a	127	137	147	138	137	124	107
Z06	n/a	59	14.5	110	110	69	127	126
Z07	n/a	145	160	161	154	153	156	135
Z08	n/a	157	157	162	149	149	129	119
Z10	n/a	133	255	114	164	155	145	149
Z11	n/a	165	175	181	170	180	187	165
Date	7/25	8/1	8/8	8/15	8/22	9/6	9/12	9/19
G01	0	0	0	0	0	0	68	185
G03	158	123	209	203	197	197	212	210
H05	172	209	186	205	210	197	205	200
J01	167	219	151	73	149	151	195	146
J04	145	189	191	182	193	175	196	181
J08	142	168	165	135	125	158	193	83
K04	92	138	89	98	85	82	108	94
L01	203	94	116	206	205	133	221	60
M03	217	245	225	211	240	245	248	248
N03	0	0	0	0	0	0	0	0
Z01	120	117	122	135	124	137	149	149
Z02	114	113	124	138	103	75	49	0
Z03	131	112	123	119	118	123	142	138
Z04	137	171	165	155	150	163	174	162
Z05	85	91	76	121	83	130	166	155
Z06	120	118	129	140	122	131	65	94
Z07	138	151	103	128	0	0	0	90
Z08	111	112	109	142	119	143	162	152
Z10	135	164	167	183	175	185	195	188
Z11	165	190	183	148	171	178	165	172

Table B-4. Weekly effluent pH recorded for vegetated mesocosms

Date	5/30	6/6	6/13	6/20	6/27	7/4	7/11	7/18
G02	-	-	-	-	-	5.13	4.07	5.15
G04	-	4.63	4.76	4.44	4.57	3.77	5.29	4.98
G05	4.45	-	4.39	3.82	-	3.75	3.91	3.69
G06	-	-	-	-	-	-	4.63	-
G07	3.81	-	4.70	4.26	4.04	3.93	4.12	3.80
G08	3.55	3.35	4.01	4.30	4.41	3.68	4.52	3.97
H01	4.01	4.83	4.43	4.42	4.48	3.71	3.86	-
H02	-	-	-	-	-	-	-	-
H03	-	-	-	-	-	4.28	3.70	3.92
H04	3.30	3.42	3.49	3.55	3.73	3.60	3.71	3.65
H06	3.62	3.44	3.85	3.84	4.01	3.82	3.99	4.18
H07	4.50	3.55	4.06	4.53	4.53	4.35	4.54	4.66
H08	-	-	-	-	-	4.44	3.85	3.97
J02	-	8.34	4.18	3.84	3.64	3.71	3.82	4.11
J03	-	-	-	-	-	4.64	3.50	3.48
J05	-	-	-	4.55	4.58	-	-	-
J06	5.22	4.33	4.51	4.63	4.66	4.31	4.15	-
J07	-	-	-	-	-	-	-	-
K01	-	-	-	4.79	4.63	4.22	-	5.06
K02	4.02	3.56	-	4.04	4.27	3.96	4.01	4.59
K03	-	-	3.60	3.67	-	-	-	-
K05	3.74	3.53	3.89	-	4.54	3.58	3.66	3.62
K06	3.21	4.17	3.49	3.85	3.74	3.22	3.12	5.18
K07	3.88	3.78	3.92	3.81	-	3.73	3.59	-
K08	-	-	3.62	3.67	3.97	3.79	4.04	-
L02	-	-	-	-	-	5.51	3.95	4.34
L03	4.12	4.19	4.35	3.91	4.07	3.95	3.55	3.81
L04	-	-	-	-	4.83	3.90	4.00	3.72
L05	-	3.37	3.86	3.56	3.59	3.24	3.13	3.92
L06	3.49	3.33	3.68	3.77	3.87	3.49	3.73	3.96
L07	-	-	-	6.48	-	-	-	-
L08	-	-	-	-	-	4.49	4.24	4.41
M01	4.54	3.96	4.40	4.18	4.39	3.91	3.78	3.93
M02	3.46	3.63	-	-	-	-	-	4.05
M04	-	-	-	-	-	3.76	3.34	3.53
M05	-	-	-	-	4.62	3.98	3.33	3.57
M06	-	-	4.56	4.21	4.44	4.00	4.02	4.18
M07	3.86	-	3.92	4.25	-	3.88	4.11	-
M08	3.37	3.56	4.23	4.16	4.05	3.47	3.82	3.50
N01	-	-	4.32	4.07	4.43	4.39	-	-
N02	3.77	-	4.08	3.92	3.82	3.40	3.58	3.26
N04	-	-	4.31	4.03	4.23	3.85	3.55	3.41
N05	4.01	-	4.54	4.17	4.27	3.96	4.42	4.69
N06	-	-	-	-	4.22	3.89	4.73	-
N07	3.76	-	4.03	4.05	4.21	3.76	4.65	-
N08	4.46	-	4.61	4.98	4.61	-	-	-

Date	7/25	8/1	8/8	8/15	9/6	9/12	9/19
G02	3.78	4.56	6.22	4.85	4.83	-	4.65
G04	-	-	6.64	7.36	-	5.37	5.12
G05	3.51	4.72	5.66	4.41	3.83	3.67	3.43
G06	-	-	-	-	-	5.39	-
G07	3.75	5.11	4.46	5.75	3.80	4.92	4.29
G08	-	-	5.58	5.31	-	5.02	4.91
H01	3.90	3.34	-	5.60	3.83	5.00	4.57
H02	-	-	5.84	5.21	4.21	4.38	4.07
H03	4.03	3.84	4.31	4.34	3.84	4.26	4.19
H04	3.75	4.73	5.77	5.40	3.72	4.90	4.38
H06	4.88	4.62	3.43	5.01	4.48	4.24	4.34
H07	4.81	5.31	5.14	6.29	4.69	4.68	4.36
H08	4.31	4.40	4.41	5.30	3.56	3.82	4.43
J02	4.21	5.47	5.43	5.21	4.62	4.74	4.84
J03	3.28	3.45	4.56	3.72	3.68	3.62	4.74
J05	3.94	3.83	-	-	-	-	-
J06	4.20	5.21	4.89	4.63	4.59	4.68	5.18
J07	-	5.45	5.10	4.97	4.73	5.51	5.11
K01	4.84	5.63	5.33	5.67	5.30	-	5.06
K02	3.93	5.60	4.80	-	4.91	4.48	4.61
K03	-	4.73	-	5.50	-	-	-
K05	3.42	3.73	3.91	3.49	3.77	4.29	4.17
K06	-	5.03	5.25	-	-	-	-
K07	-	5.65	-	-	-	4.54	4.66
K08	-	6.06	-	-	-	-	-
L02	3.91	5.37	5.61	4.89	4.83	5.56	4.38
L03	3.30	5.34	5.05	4.18	4.65	4.13	4.05
L04	3.68	5.06	5.21	4.60	4.60	5.46	4.26
L05	3.91	-	-	-	-	-	4.48
L06	4.04	4.98	5.17	4.87	4.64	4.66	4.43
L07	-	5.28	5.27	5.75	5.28	5.02	4.22
L08	4.24	5.25	4.93	5.30	5.17	4.56	4.47
M01	3.75	5.43	4.81	5.41	4.49	5.20	4.57
M02	-	5.16	4.67	-	-	-	-
M04	4.32	5.25	5.44	4.20	4.23	3.80	-
M05	4.67	4.63	4.31	3.86	4.14	3.85	4.03
M06	4.29	3.44	4.75	5.25	4.85	4.72	4.25
M07	-	4.95	4.68	5.53	4.59	3.97	4.02
M08	4.41	-	5.05	5.19	4.59	4.34	4.36
N01	-	-	5.40	5.71	4.77	4.87	4.76
N02	3.12	4.52	4.33	5.82	3.73	4.44	3.81
N04	-	4.65	-	-	-	4.46	4.25
N05	-	5.89	-	-	4.52	4.48	4.57
N06	4.74	-	-	-	-	-	4.32
N07	-	6.00	-	-	-	-	5.11
N08	-	-	4.98	5.46	4.79	4.36	4.52

Table B-5. Weekly effluent pH recorded for non-vegetated mesocosms

Date	5/30	6/6	6/13	6/20	6/27	7/4	7/11	7/18
G01	5.33	-	4.72	-	-	-	4.16	-
G03	3.94	3.62	3.59	3.48	3.97	3.63	3.65	3.73
H05	4.66	4.11	4.11	4.02	3.96	4.17	3.41	3.25
J01	-	-	4.74	4.59	4.53	4.28	4.43	4.39
J04	4.11	3.77	3.87	4.32	4.33	3.80	3.60	3.34
J08	3.98	3.50	3.48	3.53	3.33	3.66	3.40	4.38
K04	3.19	3.23	4.44	3.54	3.59	3.38	3.41	3.87
L01	3.40	3.41	3.93	4.64	3.80	3.69	3.36	3.71
M03	4.31	3.84	3.78	3.62	-	4.20	3.94	3.41
N03	4.24	-	4.66	-	-	4.47	-	4.06
Z01	-	4.88	3.70	3.71	3.69	3.36	4.57	4.89
Z02	-	3.40	3.35	3.95	4.34	4.13	4.29	3.55
Z03	-	3.74	3.43	3.78	3.57	3.53	4.11	3.90
Z04	-	3.68	3.69	4.11	3.47	4.13	4.64	4.59
Z05	-	3.56	3.51	3.69	3.60	3.62	4.66	5.54
Z06	-	3.12	3.90	3.70	3.81	3.31	3.54	3.53
Z07	-	3.69	3.65	3.69	3.44	4.22	4.03	3.83
Z08	-	3.96	3.51	4.09	3.68	3.78	3.44	3.18
Z10	-	3.51	3.43	3.68	3.53	3.50	4.13	4.10
Z11	-	3.29	3.59	4.28	3.77	-	4.14	4.43
Date	7/25	8/1	8/8	8/15	8/22	9/6	9/12	9/19
G01	-	-	-	-	-	-	5.82	5.57
G03	3.63	4.86	7.08	7.83	-	5.60	4.71	4.47
H05	3.54	3.48	4.63	3.69	-	3.69	3.67	3.59
J01	4.87	5.53	4.22	4.21	-	3.74	3.80	3.48
J04	3.39	4.36	3.59	3.58	-	3.68	5.28	4.60
J08	3.71	5.77	5.42	4.42	-	3.58	5.71	4.51
K04	3.50	5.78	4.20	3.50	-	3.73	3.33	3.78
L01	3.69	6.13	4.27	3.89	-	3.52	5.33	4.16
M03	3.23	5.12	3.85	3.32	-	4.05	4.32	4.07
N03	-	-	-	-	-	-	-	-
Z01	5.02	6.16	5.51	5.69	-	5.00	5.10	4.87
Z02	3.25	4.45	4.09	4.06	-	3.95	3.21	-
Z03	3.36	3.01	3.10	3.03	-	3.45	3.55	3.79
Z04	4.57	5.21	5.38	5.63	-	4.77	4.89	4.79
Z05	5.72	6.11	6.12	5.36	-	4.64	4.90	4.45
Z06	3.50	3.79	3.50	3.62	-	4.16	3.51	3.45
Z07	4.86	4.26	4.51	3.68	-	-	-	3.69
Z08	3.48	3.53	3.45	3.31	-	3.49	3.24	3.15
Z10	4.68	4.34	4.82	4.28	-	4.30	4.72	5.10
Z11	4.72	4.57	4.57	3.79	-	4.16	4.44	5.18

Table B-6. Effluent Mn concentrations ($\mu\text{g mL}^{-1}$) in vegetated mesocosms

Date	5/30	6/13	6/27	7/11	7/25	8/8	8/15	8/22	9/6	9/12	9/19
<i>Det.Limit</i>	0.01	0.01	0.01	0.01	0.05	0.005	0.01	0.005	0.005	0.01	0.01
G02	-	-	-	< 0.01	< 0.05	0.26	1.07	-	0.34	-	0.15
G04	-	0.12	0.06	0.15	-	0.06	0.03	-	-	0.03	0.34
G05	0.33	0.13	-	0.04	0.06	0.11	0.23	2.06	5.70	10.2	3.37
G06	-	-	-	0.05	-	-	-	-	-	0.07	-
G07	0.45	0.26	0.10	0.02	< 0.05	0.11	< 0.01	0.12	0.13	0.12	0.10
G08	0.07	0.02	0.05	0.04	-	0.01	< 0.01	-	-	0.07	< 0.01
H01	0.05	0.12	0.07	0.04	< 0.05	-	0.14	0.02	0.78	0.41	0.23
H02	-	-	-	-	-	0.01	0.01	0.20	0.04	0.04	0.03
H03	-	-	-	0.03	< 0.05	0.01	0.02	0.10	0.17	0.07	0.02
H04	0.59	0.18	0.07	0.05	0.05	0.02	< 0.01	0.15	0.10	0.06	0.05
H06	0.26	0.09	0.02	< 0.01	< 0.05	0.01	< 0.01	< 0.005	0.02	0.02	0.02
H07	0.29	0.06	0.01	< 0.01	< 0.05	0.05	< 0.01	< 0.005	0.02	0.03	< 0.01
H08	-	-	-	0.05	0.07	0.10	0.10	0.24	0.78	0.92	0.61
J02	-	0.11	0.05	0.06	< 0.05	0.02	< 0.01	1.08	0.01	0.01	< 0.01
J03	-	-	< 0.01	0.05	0.08	0.36	0.18	0.21	4.61	18.3	0.82
J05	-	-	0.05	-	< 0.05	-	-	5.74	-	-	-
J06	0.13	0.07	0.01	0.03	0.10	0.01	0.01	0.05	0.05	0.12	0.02
J07	-	-	-	-	-	0.10	0.14	0.03	0.04	0.02	0.01
K01	-	-	0.02	-	< 0.05	< 0.005	< 0.01	< 0.005	0.01	-	< 0.01
K02	0.07	-	0.04	0.01	< 0.05	0.01	< 0.01	< 0.005	0.04	0.07	< 0.01
K03	-	0.23	-	-	-	-	-	-	-	-	-
K05	0.39	0.14	0.05	0.04	0.11	0.10	0.14	3.53	0.67	0.72	0.56
K06	1.08	0.68	0.12	0.42	-	< 0.005	-	< 0.005	-	-	-
K07	0.42	0.18	-	0.11	-	-	-	< 0.005	-	0.13	< 0.01
K08	-	0.24	0.11	0.13	-	-	-	-	-	-	-
L02	-	-	-	0.01	< 0.05	< 0.005	0.01	0.04	0.06	0.01	0.01
L03	0.14	0.04	0.01	0.02	0.10	0.05	0.07	0.04	0.04	0.03	0.02
L04	-	-	0.03	0.03	< 0.05	0.02	0.02	0.05	0.07	0.02	< 0.01
L05	0.65	0.12	0.08	0.10	0.13	-	-	0.02	-	-	0.02
L06	0.26	0.06	0.02	0.08	0.23	0.04	< 0.01	< 0.005	0.03	0.03	< 0.01
L07	-	-	-	-	-	0.08	0.86	0.06	0.70	0.66	0.53
L08	-	-	-	0.02	< 0.05	0.09	< 0.01	< 0.005	0.01	0.02	< 0.01
M01	0.28	0.15	0.04	0.10	0.07	0.08	< 0.01	0.08	0.17	0.18	0.15
M02	0.48	-	-	-	-	0.05	-	-	-	-	-
M04	-	-	-	0.24	< 0.05	0.01	0.09	-	0.13	0.11	-
M05	-	-	0.16	0.05	< 0.05	0.03	0.02	0.03	0.03	0.03	0.02
M06	-	< 0.01	0.02	0.03	< 0.05	0.02	< 0.01	< 0.005	0.02	0.01	0.02
M07	0.28	0.13	-	0.02	-	0.06	< 0.01	< 0.005	0.03	0.03	0.03
M08	0.61	0.15	0.05	0.28	0.12	0.65	0.50	0.11	0.21	0.18	0.06
N01	-	0.05	0.02	-	-	0.01	< 0.01	< 0.005	0.01	0.03	< 0.01
N02	0.14	0.16	0.06	0.08	0.35	0.09	1.51	0.34	2.44	1.43	1.37
N04	-	0.07	0.05	0.12	-	-	-	-	-	0.03	0.06
N05	0.04	0.01	0.03	0.16	-	-	-	-	0.13	0.14	0.10
N06	-	-	0.14	0.03	< 0.05	-	-	-	-	-	0.04
N07	0.23	0.05	< 0.01	< 0.01	-	-	-	-	-	-	0.02
N08	0.14	< 0.01	< 0.01	-	-	0.01	< 0.01	< 0.005	0.01	0.01	< 0.01

Table B-7. Effluent Al concentrations ($\mu\text{g mL}^{-1}$) in vegetated mesocosms

Date	5/30	6/13	6/27	7/11	7/25	8/8	8/15	8/22	9/6	9/12	9/19
<i>Det.Limit.</i>	0.05	0.05	0.05	0.05	0.05	0.005	0.01	0.005	0.005	0.01	0.01
G02	-	-	-	< 0.05	< 0.05	<0.005	0.01	-	0.177	-	0.01
G04	-	0.03	< 0.05	0.98	-	0.018	0.03	-	-	0.03	0.04
G05	< 0.05	0.03	-	0.03	< 0.05	0.008	0.02	0.051	0.162	0.19	0.14
G06	-	-	-	0.02	-	-	-	-	-	0.02	-
G07	< 0.05	< 0.05	0.05	0.03	< 0.05	0.035	< 0.01	0.047	0.083	0.02	0.05
G08	0.04	0.03	0.04	0.16	-	0.014	< 0.01	-	-	< 0.01	0.02
H01	< 0.05	0.03	0.03	0.03	< 0.05	-	< 0.01	0.011	0.057	< 0.01	0.02
H02	-	-	-	-	-	0.010	0.01	0.010	0.218	0.20	0.03
H03	-	-	-	0.02	< 0.05	0.026	0.01	0.020	0.263	0.01	0.02
H04	0.06	< 0.05	0.06	0.04	0.01	0.009	< 0.01	0.036	0.257	0.06	0.04
H06	< 0.05	0.33	0.04	0.03	< 0.05	0.020	0.01	0.016	0.028	0.03	0.03
H07	< 0.05	0.07	0.03	0.02	< 0.05	0.013	< 0.01	0.013	0.022	0.01	0.02
H08	-	-	-	0.03	< 0.05	0.024	< 0.01	0.014	0.085	0.09	0.08
J02	-	< 0.05	0.05	0.03	< 0.05	0.014	< 0.01	0.056	0.023	0.01	0.01
J03	-	-	0.06	0.04	< 0.05	0.028	0.07	0.094	0.200	0.37	0.03
J05	-	-	0.26	-	0.09	-	-	0.136	-	-	-
J06	0.02	0.03	0.05	0.02	< 0.05	0.013	< 0.01	0.010	0.015	0.12	0.01
J07	-	-	-	-	-	0.019	0.01	0.016	0.027	0.02	0.04
K01	-	-	0.04	-	< 0.05	0.007	< 0.01	0.019	0.027	-	< 0.01
K02	0.03	-	0.05	0.03	0.01	0.030	0.03	0.020	0.040	0.04	0.05
K03	-	< 0.05	-	-	-	-	-	-	-	-	-
K05	< 0.05	0.05	0.04	0.04	< 0.05	0.029	0.04	0.136	0.138	0.16	0.10
K06	0.09	0.05	0.05	0.11	-	0.012	-	0.027	-	-	-
K07	< 0.05	0.16	-	0.09	-	-	-	0.020	-	0.02	0.02
K08	-	< 0.05	0.06	< 0.05	-	-	-	-	-	-	-
L02	-	-	-	0.02	< 0.05	0.014	0.01	0.021	0.311	0.02	0.04
L03	< 0.05	0.03	0.04	0.15	< 0.05	0.019	0.03	0.025	0.126	0.08	0.04
L04	-	-	0.05	0.18	< 0.05	0.006	0.01	0.024	0.119	< 0.01	0.02
L05	0.06	< 0.05	0.07	0.10	< 0.05	-	-	0.032	-	-	0.03
L06	0.06	0.04	0.06	0.04	< 0.05	0.028	0.02	0.025	0.033	0.04	0.07
L07	-	-	-	-	-	0.010	< 0.01	0.011	0.017	< 0.01	0.04
L08	-	-	-	0.03	< 0.05	0.027	0.01	0.020	0.021	0.02	0.03
M01	< 0.05	0.37	0.04	0.04	< 0.05	0.007	< 0.01	0.035	0.072	0.05	0.06
M02	0.05	-	-	-	-	0.020	-	-	-	-	-
M04	-	-	-	0.06	< 0.05	0.009	0.02	-	0.060	0.05	-
M05	-	-	0.39	0.05	< 0.05	0.025	0.03	0.027	0.031	0.03	0.03
M06	-	< 0.05	0.03	0.02	< 0.05	0.014	< 0.01	0.012	0.007	0.02	0.03
M07	< 0.05	0.20	-	0.02	-	0.018	< 0.01	0.019	0.022	0.03	0.03
M08	0.06	0.04	0.06	< 0.05	< 0.05	0.020	0.26	0.024	0.035	0.54	0.04
N01	-	0.03	0.03	-	-	0.013	0.04	0.010	0.013	0.01	0.02
N02	< 0.05	0.04	0.05	0.06	0.04	0.017	< 0.01	0.041	0.330	0.07	0.27
N04	-	0.03	0.05	0.07	-	-	-	-	-	0.03	0.03
N05	0.03	0.02	0.42	< 0.05	-	-	-	-	0.019	0.02	0.02
N06	-	-	0.04	0.02	< 0.05	-	-	-	-	-	0.03
N07	< 0.05	0.03	0.04	0.22	-	-	-	-	-	-	< 0.01
N08	0.04	0.38	0.03	-	-	0.011	0.03	0.017	0.018	0.02	0.02

Table B-8. Effluent Ca concentrations ($\mu\text{g mL}^{-1}$) in vegetated mesocosms

Date	5/30	6/13	6/27	7/11	7/25	8/8	8/15	8/22	9/6	9/12	9/19
<i>Det.Limit.</i>	0.05	0.05	0.05	0.05	0.05	0.01	0.01	0.01	0.01	0.01	0.01
G02	-	-	-	1.89	1.99	10.54	10.36	-	4.16	-	2.14
G04	-	8.33	6.82	4.07	-	7.26	7.90	-	-	6.66	3.79
G05	10.58	10.24	-	4.80	4.34	5.65	11.91	21.63	34.92	41.12	28.33
G06	-	-	-	11.02	-	-	-	-	-	10.25	-
G07	6.62	9.18	5.89	6.89	7.57	12.87	16.99	15.26	19.67	21.03	19.28
G08	3.40	1.74	3.95	2.76	-	2.90	2.96	-	-	4.61	3.54
H01	5.62	2.70	3.36	2.61	2.94	-	6.94	3.34	23.82	23.15	14.07
H02	-	-	-	-	-	3.26	3.26	7.88	5.57	5.72	7.77
H03	-	-	-	1.64	1.31	2.54	2.62	2.34	6.72	2.10	1.66
H04	5.76	4.33	4.46	3.89	4.74	6.93	11.21	13.53	12.26	11.48	14.60
H06	3.60	2.25	2.30	2.78	5.28	2.55	2.56	2.35	2.17	2.29	2.54
H07	4.40	2.72	2.16	1.93	1.91	2.64	9.02	2.27	2.35	3.08	2.62
H08	-	-	-	3.60	3.95	3.51	7.69	11.30	26.47	26.60	21.37
J02	-	3.16	1.82	1.32	1.46	1.66	1.79	17.33	1.74	0.70	1.75
J03	-	-	6.36	2.55	3.28	20.85	19.93	21.06	41.12	62.56	25.85
J05	-	-	2.60	-	2.23	-	-	49.60	-	-	-
J06	3.83	3.01	2.96	1.62	1.49	1.58	4.14	6.50	1.84	6.44	2.25
J07	-	-	-	-	-	4.12	7.39	1.59	1.49	4.22	2.77
K01	-	-	6.68	-	7.29	6.44	9.75	8.51	5.61	-	4.29
K02	5.13	-	2.44	2.54	1.74	1.66	2.24	1.69	1.56	1.83	1.54
K03	-	6.37	-	-	-	-	-	-	-	-	-
K05	6.46	8.43	7.83	9.56	12.29	17.19	18.46	46.96	48.75	54.04	46.93
K06	8.00	8.38	5.58	6.24	-	9.73	-	18.82	-	-	-
K07	7.91	8.59	-	6.41	-	-	-	8.49	-	8.89	8.35
K08	-	5.50	6.80	5.96	-	-	-	-	-	-	-
L02	-	-	-	2.13	1.53	8.57	8.41	8.25	10.36	9.52	8.02
L03	2.88	2.18	2.42	2.62	2.60	3.02	7.84	5.53	6.22	5.90	5.83
L04	-	-	3.76	3.07	2.13	6.78	6.85	12.57	10.81	5.51	4.31
L05	7.08	6.22	6.06	6.40	5.60	-	-	5.13	-	-	4.81
L06	3.12	2.00	2.16	2.54	2.37	2.01	2.68	2.08	1.80	2.34	2.86
L07	-	-	-	-	-	11.42	22.74	13.93	26.46	24.18	19.08
L08	-	-	-	2.05	2.04	2.17	2.61	2.01	1.83	2.41	2.22
M01	7.39	5.04	3.99	3.95	4.40	9.14	14.87	18.25	23.56	25.34	22.57
M02	5.89	-	-	-	-	2.57	-	-	-	-	-
M04	-	-	-	5.31	5.34	8.44	7.73	-	11.69	12.05	-
M05	-	-	5.98	4.20	2.52	2.12	2.19	2.18	2.01	2.04	2.21
M06	-	2.15	1.59	1.53	1.98	2.86	2.70	2.58	3.32	4.48	5.26
M07	5.05	3.98	-	3.17	-	8.69	6.99	3.73	4.55	2.46	4.81
M08	8.22	5.54	3.69	3.84	3.96	4.98	3.85	2.43	1.80	2.94	2.33
N01	-	3.07	2.73	-	-	3.53	9.06	2.35	2.12	6.62	5.08
N02	3.40	5.49	5.36	5.27	18.76	3.59	43.11	22.06	65.28	47.44	48.71
N04	-	2.23	4.70	9.83	-	-	-	-	-	3.15	8.15
N05	5.31	1.98	1.28	1.04	-	-	-	-	4.44	3.60	3.90
N06	-	-	8.62	6.29	0.81	-	-	-	-	-	7.24
N07	3.35	2.52	1.66	4.67	-	-	-	-	-	-	6.40
N08	2.63	1.27	1.02	-	-	2.87	3.62	2.92	4.48	3.53	4.42

Table B-9. Effluent Fe concentrations ($\mu\text{g mL}^{-1}$) in vegetated mesocosms

Date	5/30	6/13	6/27	7/11	7/25	8/8	8/15	8/22	9/6	9/12	9/19
<i>Det.Limit.</i>	0.05	0.05	0.05	0.05	0.05	0.005	0.01	0.005	0.005	0.01	0.01
G02	-	-	-	0.96	< 0.05	< 0.005	< 0.01	-	0.198	-	< 0.01
G04	-	0.00	0.59	1.31	-	0.020	0.04	-	-	0.04	< 0.01
G05	< 0.05	0.01	-	0.01	< 0.05	< 0.005	< 0.01	< 0.005	0.019	< 0.01	< 0.01
G06	-	-	-	0.02	-	-	-	-	-	0.12	-
G07	< 0.05	< 0.05	0.01	0.01	< 0.05	< 0.005	< 0.01	< 0.005	0.033	< 0.01	< 0.01
G08	0.01	0.00	0.01	0.17	-	0.018	< 0.01	-	-	< 0.01	< 0.01
H01	0.01	0.00	0.01	0.08	< 0.05	-	< 0.01	< 0.005	< 0.005	< 0.01	0.04
H02	-	-	-	-	-	0.009	< 0.01	< 0.005	0.254	0.25	< 0.01
H03	-	-	-	0.01	< 0.05	< 0.005	< 0.01	< 0.005	0.308	< 0.01	< 0.01
H04	< 0.05	< 0.05	0.02	0.01	< 0.05	< 0.005	< 0.01	< 0.005	0.240	0.02	0.01
H06	< 0.05	0.48	0.01	0.01	< 0.05	0.006	< 0.01	< 0.005	< 0.005	< 0.01	< 0.01
H07	< 0.05	0.02	0.00	0.01	< 0.05	< 0.005	< 0.01	0.012	0.006	< 0.01	< 0.01
H08	-	-	-	0.01	< 0.05	< 0.005	< 0.01	< 0.005	0.005	< 0.01	< 0.01
J02	-	< 0.05	0.05	0.00	< 0.05	0.026	0.01	< 0.005	0.007	< 0.01	0.03
J03	-	-	< 0.05	0.01	0.09	< 0.005	< 0.01	< 0.005	0.008	< 0.01	0.11
J05	-	-	0.34	-	0.16	-	-	< 0.005	-	-	-
J06	0.00	0.01	0.02	0.01	< 0.05	0.022	< 0.01	< 0.005	< 0.005	0.08	< 0.01
J07	-	-	-	-	-	0.043	< 0.01	< 0.005	0.017	0.01	0.03
K01	-	-	0.01	-	< 0.05	< 0.005	< 0.01	< 0.005	0.027	-	< 0.01
K02	0.00	-	0.01	0.02	< 0.05	0.031	0.04	0.021	0.006	0.02	< 0.01
K03	-	< 0.05	-	-	-	-	-	-	-	-	-
K05	< 0.05	0.01	0.01	0.01	< 0.05	< 0.005	< 0.01	< 0.005	0.028	0.16	< 0.01
K06	< 0.05	< 0.05	< 0.05	< 0.05	-	< 0.005	-	< 0.005	-	-	-
K07	< 0.05	< 0.05	-	< 0.05	-	-	-	< 0.005	-	0.02	0.17
K08	-	< 0.05	< 0.05	< 0.05	-	-	-	-	-	-	-
L02	-	-	-	0.01	< 0.05	0.008	0.02	0.005	0.395	< 0.01	< 0.01
L03	< 0.05	0.01	0.01	0.14	< 0.05	< 0.005	< 0.01	< 0.005	0.149	0.08	< 0.01
L04	-	-	0.04	0.22	< 0.05	< 0.005	< 0.01	< 0.005	0.142	< 0.01	< 0.01
L05	< 0.05	< 0.05	0.02	0.08	0.25	-	-	< 0.005	-	-	< 0.01
L06	< 0.05	0.01	0.01	0.01	< 0.05	0.018	0.01	0.007	< 0.005	0.02	0.02
L07	-	-	-	-	-	< 0.005	< 0.01	< 0.005	< 0.005	< 0.01	< 0.01
L08	-	-	-	0.01	< 0.05	0.008	0.01	0.009	< 0.005	< 0.01	< 0.01
M01	< 0.05	0.54	0.01	0.01	< 0.05	< 0.005	< 0.01	< 0.005	0.020	0.01	0.01
M02	< 0.05	-	-	-	-	< 0.005	-	-	-	-	-
M04	-	-	-	< 0.05	< 0.05	0.014	< 0.01	-	< 0.005	< 0.01	-
M05	-	-	0.60	0.01	< 0.05	< 0.005	< 0.01	< 0.005	< 0.005	< 0.01	< 0.01
M06	-	< 0.05	0.01	0.04	< 0.05	< 0.005	< 0.01	< 0.005	< 0.005	0.01	< 0.01
M07	< 0.05	0.24	-	0.22	-	< 0.005	< 0.01	< 0.005	< 0.005	0.01	< 0.01
M08	< 0.05	0.01	0.01	< 0.05	0.07	0.024	0.36	< 0.005	< 0.005	0.81	< 0.01
N01	-	0.01	0.01	-	-	0.028	< 0.01	< 0.005	< 0.005	< 0.01	< 0.01
N02	< 0.05	0.01	0.01	0.02	< 0.05	< 0.005	< 0.01	1.029	< 0.005	< 0.01	< 0.01
N04	-	0.00	0.01	0.04	-	-	-	-	-	< 0.01	< 0.01
N05	0.00	0.01	0.68	< 0.05	-	-	-	-	< 0.005	< 0.01	< 0.01
N06	-	-	0.01	0.01	< 0.05	-	-	-	-	-	< 0.01
N07	< 0.05	0.00	0.01	0.12	-	-	-	-	-	-	< 0.01
N08	0.01	0.51	0.01	-	-	0.015	0.04	< 0.005	< 0.005	< 0.01	< 0.01

Table B-10. Effluent K concentrations ($\mu\text{g mL}^{-1}$) in vegetated mesocosms

Date	5/30	6/13	6/27	7/11	7/25	8/8	8/15	8/22	9/6	9/12	9/19
<i>Det.Limit.</i>	0.1	0.1	0.1	0.1	0.1	0.01	0.01	0.01	0.01	0.01	0.01
G02	-	-	-	1.7	1.4	2.29	1.75	-	0.74	-	0.77
G04	-	3.0	3.0	2.1	-	1.87	0.93	-	-	1.32	0.64
G05	3.2	3.7	-	2.9	3.3	3.09	4.08	5.24	6.86	6.79	5.61
G06	-	-	-	4.4	-	-	-	-	-	2.62	-
G07	2.4	3.0	2.8	3.6	3.7	4.09	3.69	3.72	3.30	3.11	3.04
G08	1.8	0.9	2.3	2.4	-	1.14	0.86	-	-	1.15	0.96
H01	2.2	1.3	1.5	1.3	2.1	-	2.70	1.06	3.68	3.74	2.68
H02	-	-	-	-	-	1.54	1.21	2.73	0.94	0.76	0.77
H03	-	-	-	1.0	1.1	0.55	0.46	0.34	0.35	0.28	0.11
H04	2.5	1.8	1.9	2.0	2.6	2.69	2.52	2.75	1.83	1.74	2.36
H06	1.8	1.1	1.1	1.5	2.2	1.14	0.83	0.81	0.66	0.77	0.74
H07	2.0	1.2	1.2	1.0	1.1	1.02	0.85	0.80	0.26	0.64	0.33
H08	-	-	-	2.1	2.8	2.38	2.82	3.58	4.79	3.72	3.26
J02	-	1.5	1.4	1.6	2.1	1.86	1.48	3.61	1.08	0.74	1.23
J03	-	-	2.3	1.8	2.1	4.36	3.54	3.48	4.46	5.93	3.81
J05	-	-	1.6	-	1.9	-	-	7.56	-	-	-
J06	1.6	1.2	1.2	1.1	1.3	1.00	0.97	0.67	0.45	0.79	0.36
J07	-	-	-	-	-	2.79	6.11	0.90	0.90	1.89	1.98
K01	-	-	3.0	-	2.0	1.54	2.38	1.25	1.13	-	1.23
K02	2.2	-	1.6	1.7	1.1	0.90	0.50	0.39	0.40	0.62	0.64
K03	-	2.3	-	-	-	-	-	-	-	-	-
K05	2.4	2.6	3.1	3.5	5.2	5.40	5.95	8.24	6.17	6.72	5.23
K06	3.0	2.6	2.0	2.6	-	3.87	-	4.64	-	-	-
K07	2.9	3.6	-	3.4	-	-	-	2.01	-	1.92	1.52
K08	-	2.0	2.7	2.1	-	-	-	-	-	-	-
L02	-	-	-	1.2	1.4	2.75	2.11	1.68	1.42	1.53	1.11
L03	1.3	0.8	1.3	1.5	2.2	1.68	5.08	2.32	1.55	1.26	1.27
L04	-	-	1.6	2.0	1.9	2.86	2.14	2.80	1.86	0.99	0.97
L05	2.6	2.3	2.6	2.8	3.0	-	-	1.87	-	-	1.50
L06	1.8	1.0	1.4	1.6	2.4	1.36	1.16	0.99	0.80	1.04	0.97
L07	-	-	-	-	-	2.45	2.62	1.48	1.88	1.81	1.59
L08	-	-	-	1.1	1.2	0.69	0.59	0.41	0.34	0.37	0.38
M01	2.4	1.8	2.1	2.2	2.9	3.28	3.90	4.32	4.28	4.33	3.85
M02	2.4	-	-	-	-	0.95	-	-	-	-	-
M04	-	-	-	2.3	3.3	3.25	2.53	-	2.65	2.63	-
M05	-	-	2.9	2.0	2.1	1.22	0.84	0.47	0.28	0.28	0.26
M06	-	1.1	0.7	0.2	1.0	0.99	0.75	0.56	0.49	0.64	0.65
M07	2.1	1.6	-	1.3	-	2.46	1.55	1.08	0.98	0.64	0.75
M08	3.0	2.0	2.0	1.5	2.3	1.57	1.45	0.83	0.60	0.91	0.73
N01	-	1.8	1.5	-	-	1.14	1.72	0.72	0.35	1.00	0.55
N02	1.7	2.1	2.5	2.7	4.9	1.64	3.59	1.83	2.49	2.59	2.63
N04	-	1.2	2.3	4.6	-	-	-	-	-	0.90	1.63
N05	1.5	0.8	0.6	0.3	-	-	-	-	0.99	0.92	0.98
N06	-	-	3.2	1.9	0.8	-	-	-	-	-	0.89
N07	1.8	1.2	1.0	3.2	-	-	-	-	-	-	0.83
N08	1.0	0.5	0.4	-	-	1.30	1.27	0.91	1.21	1.11	1.06

Table B-11. Effluent Mg concentrations ($\mu\text{g mL}^{-1}$) in vegetated mesocosms

Date	5/30	6/13	6/27	7/11	7/25	8/8	8/15	8/22	9/6	9/12	9/19
<i>Det.Limit.</i>	0.05	0.05	0.05	0.05	0.05	0.005	0.01	0.005	0.005	0.01	0.01
G02	-	-	-	0.42	0.41	3.160	2.08	-	0.795	-	0.42
G04	-	2.00	1.50	0.88	-	2.001	2.27	-	-	2.27	0.86
G05	2.79	2.55	-	1.00	0.97	1.435	2.66	4.516	7.053	8.36	5.70
G06	-	-	-	2.04	-	-	-	-	-	2.18	-
G07	1.54	2.11	1.38	1.58	1.63	2.801	4.71	3.330	4.120	4.72	4.21
G08	0.85	0.40	0.71	0.57	-	0.606	0.69	-	-	0.88	0.62
H01	1.35	0.65	0.77	0.54	0.63	-	2.00	0.756	5.158	5.83	3.08
H02	-	-	-	-	-	0.783	0.76	1.751	1.218	1.25	1.59
H03	-	-	-	0.37	0.34	0.663	0.64	0.523	1.541	0.48	0.37
H04	1.39	1.03	1.00	0.84	1.00	1.390	2.96	2.787	2.487	2.56	3.00
H06	0.85	0.52	0.53	0.64	1.14	0.549	0.57	0.500	0.439	0.47	0.49
H07	1.17	0.64	0.54	0.46	0.44	0.737	3.69	0.633	0.536	1.02	0.61
H08	-	-	-	0.86	0.95	0.807	1.94	2.519	5.678	5.69	4.53
J02	-	0.81	0.39	0.28	0.36	0.414	0.46	3.703	0.387	0.17	0.41
J03	-	-	1.27	0.56	0.77	4.297	4.05	4.287	7.958	11.68	4.95
J05	-	-	0.82	-	0.55	-	-	10.716	-	-	-
J06	0.91	0.73	0.63	0.39	0.38	0.539	1.09	1.445	0.409	1.47	0.53
J07	-	-	-	-	-	1.486	1.83	0.382	0.317	1.87	0.56
K01	-	-	1.74	-	1.92	1.653	2.77	2.006	1.532	-	1.55
K02	1.79	-	0.83	0.93	0.64	0.674	0.73	0.565	0.468	0.54	0.44
K03	-	1.37	-	-	-	-	-	-	-	-	-
K05	1.91	2.15	1.89	2.03	2.59	3.703	4.18	10.059	10.248	11.15	9.54
K06	1.81	1.79	1.07	1.30	-	1.991	-	3.493	-	-	-
K07	1.96	2.26	-	1.38	-	-	-	2.361	-	2.36	2.08
K08	-	1.45	1.61	1.06	-	-	-	-	-	-	-
L02	-	-	-	0.49	0.37	1.996	1.92	1.814	2.267	2.40	1.75
L03	0.62	0.47	0.50	0.56	0.82	0.778	1.48	1.110	1.284	1.18	1.17
L04	-	-	0.92	0.75	0.52	1.477	1.49	2.639	2.244	1.45	0.92
L05	1.64	1.40	1.33	1.37	1.25	-	-	1.124	-	-	1.00
L06	0.72	0.44	0.44	0.52	0.54	0.505	0.73	0.483	0.396	0.59	0.57
L07	-	-	-	-	-	2.475	5.40	2.912	5.447	5.32	4.01
L08	-	-	-	0.53	0.57	0.598	0.82	0.531	0.430	0.54	0.52
M01	1.87	1.10	0.90	0.84	0.98	1.816	3.53	3.718	4.796	6.04	4.64
M02	1.53	-	-	-	-	0.625	-	-	-	-	-
M04	-	-	-	1.14	1.18	1.950	1.69	-	2.412	2.53	-
M05	-	-	1.47	0.91	0.59	0.497	0.48	0.468	0.425	0.43	0.46
M06	-	0.50	0.31	0.29	0.44	0.651	0.66	0.559	0.713	0.95	1.09
M07	1.26	0.94	-	0.62	-	1.851	1.85	0.820	0.981	0.51	1.02
M08	1.97	1.26	0.80	0.71	0.89	-	1.24	0.651	0.455	0.82	0.56
N01	-	0.85	0.69	-	-	1.333	3.49	0.664	0.451	2.39	1.24
N02	0.85	1.38	1.30	1.19	4.37	0.913	10.35	5.008	13.460	10.28	10.25
N04	-	0.55	1.13	2.24	-	-	-	-	-	0.75	1.72
N05	0.74	0.27	0.25	0.16	-	-	-	-	0.786	0.69	0.76
N06	-	-	2.22	1.45	0.18	-	-	-	-	-	1.66
N07	0.72	0.53	0.30	1.05	-	-	-	-	-	-	1.29
N08	0.89	0.47	0.29	-	-	0.795	0.78	0.645	1.023	0.82	0.93

Table B-12. Effluent Na concentrations ($\mu\text{g mL}^{-1}$) in vegetated mesocosms

Date	5/30	6/13	6/27	7/11	7/25	8/8	8/15	8/22	9/6	9/12	9/19
<i>Det.Limit.</i>	0.1	0.1	0.1	0.1	0.1	0.01	0.01	0.01	0.01	0.01	0.01
G02	-	-	-	0.8	1.7	3.90	1.32	-	0.36	-	0.62
G04	-	3.4	2.8	21.0	-	10.90	9.68	-	-	10.0	7.74
G05	6.4	6.2	-	1.9	2.6	1.96	1.53	1.54	1.42	1.28	1.02
G06	-	-	-	5.6	-	-	-	-	-	3.61	-
G07	3.5	4.7	3.1	2.6	3.1	2.45	3.91	1.81	1.34	1.91	1.45
G08	2.7	0.6	2.3	3.1	-	2.27	1.22	-	-	1.97	1.06
H01	3.0	1.0	1.5	0.8	2.2	-	2.24	0.83	1.55	3.34	1.16
H02	-	-	-	-	-	2.03	0.93	1.26	0.87	0.69	0.77
H03	-	-	-	0.9	2.5	0.79	0.63	0.54	0.53	0.39	0.27
H04	3.2	1.6	2.2	1.6	2.9	2.44	3.43	2.22	1.57	1.85	2.19
H06	2.2	0.6	0.8	1.0	2.9	0.99	0.84	0.80	0.63	0.56	0.62
H07	2.5	1.1	1.0	1.4	1.7	1.98	4.78	1.31	0.84	1.42	0.96
H08	-	-	-	1.6	2.6	1.42	2.01	1.90	1.68	1.26	1.20
J02	-	1.3	0.8	0.6	1.7	1.15	0.79	3.13	0.56	0.35	0.55
J03	-	-	4.5	1.0	2.3	3.19	2.28	2.24	1.78	1.68	2.01
J05	-	-	1.4	-	2.0	-	-	3.42	-	-	-
J06	1.3	0.8	1.0	1.1	1.5	0.79	0.62	0.56	0.35	0.48	0.39
J07	-	-	-	-	-	3.24	1.94	1.13	0.79	2.72	1.07
K01	-	-	3.3	-	5.2	3.44	5.05	4.08	2.59	-	2.55
K02	2.6	-	1.6	1.6	2.0	1.16	0.75	0.61	0.66	0.59	0.60
K03	-	3.8	-	-	-	-	-	-	-	-	-
K05	3.8	4.0	3.9	4.8	5.7	4.17	3.87	4.67	3.68	3.41	2.88
K06	4.4	3.9	2.5	3.5	-	5.14	-	6.72	-	-	-
K07	4.5	4.2	-	3.6	-	-	-	5.50	-	4.58	5.01
K08	-	2.8	3.6	3.2	-	-	-	-	-	-	-
L02	-	-	-	0.7	1.4	3.50	2.65	2.68	2.40	2.68	2.01
L03	1.3	0.1	1.4	0.9	2.3	1.22	1.01	1.03	0.83	0.67	0.72
L04	-	-	2.0	1.2	2.0	2.48	1.52	1.91	1.42	1.36	0.77
L05	3.4	3.1	2.8	2.9	3.7	-	-	2.33	-	-	1.68
L06	1.8	0.5	1.1	1.8	3.3	2.38	2.21	1.84	1.41	1.67	1.83
L07	-	-	-	-	-	2.63	3.32	2.12	2.51	2.11	1.72
L08	-	-	-	1.0	2.0	1.07	1.28	1.00	0.77	0.98	0.85
M01	3.6	1.2	1.4	1.4	2.4	2.81	3.75	3.10	2.62	3.80	1.99
M02	3.1	-	-	-	-	0.86	-	-	-	-	-
M04	-	-	-	1.4	3.0	3.29	2.19	-	2.28	2.21	-
M05	-	-	2.9	0.8	1.7	0.58	0.42	0.41	0.31	0.30	0.28
M06	-	0.5	0.6	1.1	1.7	1.29	1.14	0.92	0.79	1.02	1.02
M07	2.6	1.3	-	1.1	-	2.69	2.37	1.17	0.68	0.67	0.81
M08	4.4	1.7	1.4	1.5	6.2	4.45	3.21	2.64	2.11	2.50	2.36
N01	-	1.1	0.8	-	-	1.74	4.22	0.82	0.48	2.95	1.34
N02	1.4	1.9	1.9	1.6	4.3	0.94	4.18	2.42	3.05	3.29	3.04
N04	-	0.6	2.1	3.2	-	-	-	-	-	0.77	0.59
N05	1.2	< 0.1	0.2	1.6	-	-	-	-	2.78	2.57	2.57
N06	-	-	4.8	2.3	3.4	-	-	-	-	-	2.41
N07	1.2	0.4	1.0	4.8	-	-	-	-	-	-	1.98
N08	0.9	< 0.1	0.2	-	-	1.11	0.54	0.62	0.62	0.77	0.73

Table B-13. Effluent P concentrations ($\mu\text{g mL}^{-1}$) in vegetated mesocosms

Date	5/30	6/13	6/27	7/11	7/25	8/8	8/15	8/22	9/6	9/12	9/19
<i>Det.Limit.</i>	0.10	0.10	0.10	0.10	0.10	0.01	0.01	0.01	0.01	0.01	0.01
G02	-	-	-	0.4	0.6	0.09	0.06	-	0.29	-	0.08
G04	-	0.8	0.5	0.6	-	0.09	0.10	-	-	0.14	0.17
G05	0.8	0.8	-	0.8	< 0.1	0.08	0.13	0.03	0.22	0.01	0.20
G06	-	-	-	1.0	-	-	-	-	-	0.08	-
G07	0.5	0.8	0.5	0.7	0.2	0.07	0.08	0.03	0.02	< 0.01	0.10
G08	0.6	0.6	0.7	0.3	-	0.01	0.13	-	-	0.03	0.09
H01	0.3	0.7	0.5	0.5	0.4	-	0.21	0.03	0.12	0.18	0.11
H02	-	-	-	-	-	0.11	0.47	0.08	0.10	0.05	0.27
H03	-	-	-	0.5	0.7	0.10	0.10	0.07	< 0.01	0.08	0.11
H04	0.7	0.8	0.8	0.5	< 0.1	0.04	0.10	0.10	0.04	0.06	0.06
H06	0.6	0.6	0.6	0.7	< 0.1	0.08	0.09	0.05	0.10	0.09	0.08
H07	0.5	0.7	0.5	0.7	< 0.1	0.24	0.15	0.05	0.16	0.13	0.09
H08	-	-	-	0.4	0.2	0.06	0.09	0.04	< 0.01	0.05	< 0.01
J02	-	0.6	0.7	0.7	0.3	0.10	0.56	0.04	0.76	0.10	0.78
J03	-	-	0.6	0.4	< 0.1	< 0.01	0.11	0.08	0.06	0.03	0.11
J05	-	-	0.5	-	< 0.1	-	-	0.03	-	-	-
J06	0.5	0.6	0.9	0.6	0.3	0.05	0.08	0.02	0.12	< 0.01	0.06
J07	-	-	-	-	-	0.26	7.33	0.13	0.16	0.18	0.18
K01	-	-	1.1	-	< 0.1	0.19	0.05	0.03	0.42	-	0.53
K02	0.6	-	0.6	0.5	0.3	0.11	0.08	0.05	0.12	0.34	0.08
K03	-	0.6	-	-	-	-	-	-	-	-	-
K05	0.6	0.7	0.4	0.6	0.4	0.08	0.08	0.04	0.04	0.06	0.05
K06	0.7	0.6	0.6	0.6	-	0.03	-	0.16	-	-	-
K07	0.5	0.4	-	0.4	-	-	-	0.06	-	0.28	0.07
K08	-	0.4	0.9	0.4	-	-	-	-	-	-	-
L02	-	-	-	0.4	< 0.1	0.05	0.07	< 0.01	0.15	0.06	0.13
L03	0.7	0.7	0.6	0.3	0.4	0.05	4.49	0.26	0.09	0.02	0.10
L04	-	-	0.8	0.2	0.4	0.06	0.10	0.06	< 0.01	0.09	0.26
L05	0.3	0.5	0.6	0.5	0.4	-	-	0.04	-	-	0.24
L06	0.9	0.5	0.7	0.3	0.4	0.04	0.06	< 0.01	0.12	0.05	0.10
L07	-	-	-	-	-	0.11	0.14	0.06	0.13	0.04	0.04
L08	-	-	-	0.5	< 0.1	0.06	0.09	0.09	0.09	0.09	0.08
M01	0.5	0.5	0.8	0.3	0.3	0.05	0.08	< 0.01	0.15	0.05	0.07
M02	0.6	-	-	-	-	0.05	-	-	-	-	-
M04	-	-	-	0.4	0.3	0.17	0.15	-	0.11	0.13	-
M05	-	-	0.9	0.5	0.1	0.09	0.06	0.07	0.04	0.08	0.09
M06	-	1.2	0.6	0.5	0.1	0.05	0.07	0.04	0.05	0.02	0.13
M07	0.9	0.4	-	0.4	-	0.04	0.10	0.07	0.25	0.07	0.22
M08	0.8	0.7	0.7	0.4	0.6	0.14	0.38	0.12	0.14	0.30	0.17
N01	-	0.7	0.7	-	-	0.14	0.18	0.16	0.05	0.29	0.09
N02	0.7	0.6	0.7	0.3	0.1	0.04	0.11	< 0.01	0.10	0.06	0.05
N04	-	0.6	0.6	1.2	-	-	-	-	-	0.28	1.86
N05	0.6	0.7	0.7	0.1	-	-	-	-	0.05	0.05	0.08
N06	-	-	0.6	0.3	0.5	-	-	-	-	-	0.08
N07	0.4	0.9	0.8	0.0	-	-	-	-	-	-	0.14
N08	0.8	0.4	0.6	-	-	0.30	0.76	0.11	0.39	0.17	0.26

Table B-14. Effluent Mn concentrations ($\mu\text{g mL}^{-1}$) in non-vegetated mesocosms

Date	5/30	6/13	6/27	7/11	7/25	8/8	8/15	8/22	9/6	9/12	9/19
<i>Det.Limit.</i>	0.05	0.05	0.05	0.05	0.05	0.005	0.01	0.005	0.005	0.01	0.01
G01	4.83	1.35	-	1.00	-	-	-	-	-	5.84	4.18
G03	0.78	0.64	0.59	0.73	1.50	1.560	2.41	3.781	4.971	4.72	5.02
H05	1.01	0.77	0.68	1.75	3.15	2.831	1.69	1.749	4.102	5.84	4.16
J01	-	0.73	0.63	0.69	1.30	4.229	3.66	0.185	7.252	11.46	7.01
J04	1.23	0.98	-	1.32	1.25	1.134	1.56	2.235	4.242	4.87	4.03
J08	0.96	0.68	0.53	1.14	1.34	1.470	1.48	1.169	3.773	6.29	4.03
K04	1.91	1.80	2.01	1.89	1.91	2.897	3.74	5.901	11.837	13.68	12.14
L01	1.70	0.88	0.93	1.12	1.55	2.281	2.67	3.452	5.794	6.67	4.73
M03	0.92	0.81	-	1.85	1.52	1.590	4.97	2.142	5.395	6.09	4.73
N03	1.29	0.64	-	-	-	-	-	-	-	-	-
Z01	-	0.35	0.48	0.14	0.18	0.686	0.40	0.035	0.726	0.57	0.71
Z02	-	0.18	0.38	0.25	0.38	0.405	0.70	0.085	0.665	6.44	-
Z03	-	0.19	0.65	0.19	0.76	0.396	8.87	2.386	4.444	0.49	0.80
Z04	-	0.13	0.55	0.15	0.14	4.962	0.71	0.074	0.636	0.37	0.70
Z05	-	0.16	0.55	0.33	0.70	0.149	1.36	0.145	1.095	0.48	1.40
Z06	-	0.46	0.59	0.22	0.35	0.451	0.82	0.895	1.387	1.63	1.55
Z07	-	0.19	1.01	0.16	0.16	0.651	4.21	-	-	-	2.24
Z08	-	0.17	0.68	0.90	3.28	0.152	13.11	13.927	11.148	10.46	6.09
Z10	-	0.50	1.32	0.30	0.09	10.931	0.64	0.221	0.974	0.61	1.27
Z11	-	0.16	0.42	0.28	0.15	0.624	0.55	0.175	0.967	0.43	0.92

Table B-15. Effluent Al concentrations ($\mu\text{g mL}^{-1}$) in non-vegetated mesocosms

Date	5/30	6/13	6/27	7/11	7/25	8/8	8/15	8/22	9/6	9/12	9/19
<i>Det.Limit.</i>	0.05	0.05	0.05	0.05	0.05	0.005	0.01	0.005	0.005	0.01	0.01
G01	< 0.05	< 0.05	-	0.05	-	-	-	-	-	< 0.01	0.07
G03	0.03	0.05	0.05	0.15	< 0.05	0.015	0.02	0.023	0.141	0.03	0.06
H05	< 0.05	0.41	0.04	0.17	0.01	0.060	0.04	0.037	0.097	0.11	0.08
J01	-	0.03	0.08	0.02	< 0.05	0.025	0.02	0.007	0.077	0.18	0.12
J04	< 0.05	< 0.05	0.06	0.04	< 0.05	0.058	0.04	0.069	0.085	< 0.01	0.05
J08	< 0.05	0.04	0.06	0.06	0.01	0.006	0.02	0.030	0.075	0.02	0.05
K04	0.05	< 0.05	0.09	0.09	< 0.05	0.031	0.07	0.073	0.189	0.23	0.19
L01	< 0.05	0.04	0.07	0.04	0.01	0.030	0.04	0.069	0.144	0.06	0.08
M03	< 0.05	0.04	-	< 0.05	< 0.05	0.017	0.08	0.042	0.093	0.09	0.08
N03	< 0.05	0.20	-	-	-	-	-	-	-	-	-
Z01	-	0.10	< 0.05	0.10	0.50	0.662	0.17	0.185	0.314	0.27	0.07
Z02	-	0.05	0.04	0.03	< 0.05	0.042	0.03	0.029	0.027	0.18	-
Z03	-	0.26	0.05	0.03	< 0.05	0.148	0.53	0.106	0.321	0.03	0.04
Z04	-	0.06	0.06	0.09	< 0.05	0.043	0.02	0.027	0.087	0.02	0.02
Z05	-	0.05	0.08	0.72	2.05	0.250	0.06	0.153	0.088	0.04	0.04
Z06	-	< 0.05	0.06	0.04	< 0.05	0.042	0.04	0.046	0.039	0.10	0.05
Z07	-	0.04	0.07	0.03	0.06	0.031	0.08	-	-	-	0.21
Z08	-	0.04	< 0.05	0.07	0.07	0.317	0.50	0.635	0.683	0.75	0.32
Z10	-	< 0.05	0.15	2.91	< 0.05	0.031	0.02	0.025	0.037	0.03	0.02
Z11	-	0.03	< 0.05	0.70	< 0.05	0.031	0.05	0.016	0.032	0.02	0.01

Table B-16. Effluent Ca concentrations ($\mu\text{g mL}^{-1}$) in non-vegetated mesocosms

Date	5/30	6/13	6/27	7/11	7/25	8/8	8/15	8/22	9/6	9/12	9/19
<i>Det.Limit.</i>	0.05	0.05	0.05	0.05	0.05	0.01	0.01	0.01	0.01	0.01	0.01
G01	11.80	5.20	-	4.54	-	-	-	-	-	24.70	19.99
G03	3.21	2.97	2.77	3.43	7.22	7.91	11.44	18.96	24.31	23.36	24.71
H05	4.53	3.51	3.33	7.62	13.97	13.68	8.33	8.45	19.99	28.69	20.58
J01	-	2.96	3.42	3.33	5.71	18.71	15.92	0.74	33.57	54.27	32.81
J04	5.15	4.61	-	6.47	6.05	5.46	7.22	10.90	20.86	21.77	19.25
J08	3.69	3.06	2.49	5.30	6.62	6.89	6.38	5.86	18.72	26.60	19.92
K04	7.99	8.74	8.84	8.18	9.25	13.51	18.19	27.62	54.69	63.77	57.67
L01	7.58	3.75	4.36	5.01	6.84	10.51	12.28	16.46	28.45	27.86	21.96
M03	3.60	3.24	-	7.97	6.83	7.94	25.84	10.46	27.66	29.21	23.88
N03	3.95	2.46	-	-	-	-	-	-	-	-	-
Z01	-	1.98	2.22	0.82	0.88	1.81	2.08	0.09	3.86	3.04	3.76
Z02	-	0.92	1.83	1.34	1.78	1.93	3.85	0.42	3.50	36.14	-
Z03	-	2.64	3.48	1.05	3.46	25.18	50.32	14.14	26.38	3.00	5.18
Z04	-	0.79	2.65	0.90	0.31	0.44	4.10	0.37	2.91	1.43	3.90
Z05	-	0.81	2.44	1.40	2.89	2.59	8.77	0.89	6.92	2.50	8.07
Z06	-	1.69	2.68	1.25	1.71	3.05	4.36	4.49	6.84	7.99	7.90
Z07	-	0.87	4.92	0.88	0.76	0.74	23.22	-	-	-	12.65
Z08	-	0.79	3.52	5.17	17.15	57.61	71.51	79.22	62.30	61.85	34.41
Z10	-	2.23	6.37	0.89	0.43	3.22	3.72	1.29	5.25	3.33	7.05
Z11	-	0.70	1.98	0.86	0.79	2.49	3.03	0.97	4.84	2.23	4.95

Table B-17. Effluent Fe concentrations ($\mu\text{g mL}^{-1}$) in non-vegetated mesocosms

Date	5/30	6/13	6/27	7/11	7/25	8/8	8/15	8/22	9/6	9/12	9/19
<i>Det.Limit.</i>	0.05	0.05	0.05	0.05	0.05	0.005	0.01	0.005	0.005	0.01	0.01
G01	< 0.05	< 0.05	-	0.01	-	-	-	-	-	< 0.01	< 0.01
G03	0.00	0.00	0.01	0.10	< 0.05	< 0.005	< 0.01	< 0.005	0.079	< 0.01	< 0.01
H05	< 0.05	0.60	0.01	0.09	< 0.05	< 0.005	< 0.01	< 0.005	0.040	< 0.01	< 0.01
J01	-	0.00	0.03	0.01	< 0.05	< 0.005	< 0.01	< 0.005	< 0.005	< 0.01	< 0.01
J04	< 0.05	< 0.05	0.01	0.01	< 0.05	< 0.005	< 0.01	< 0.005	< 0.005	< 0.01	< 0.01
J08	< 0.05	0.01	0.01	< 0.05	< 0.05	0.008	< 0.01	< 0.005	< 0.005	< 0.01	< 0.01
K04	< 0.05	< 0.05	< 0.05	0.04	< 0.05	< 0.005	< 0.01	< 0.005	< 0.005	< 0.01	< 0.01
L01	< 0.05	0.01	0.30	0.01	< 0.05	< 0.005	< 0.01	< 0.005	0.014	0.04	< 0.01
M03	< 0.05	0.01	-	< 0.05	< 0.05	< 0.005	< 0.01	< 0.005	< 0.005	< 0.01	< 0.01
N03	< 0.05	< 0.05	-	-	-	-	-	-	-	-	-
Z01	-	< 0.05	< 0.05	0.07	0.43	0.601	0.16	0.181	0.325	0.33	0.09
Z02	-	0.01	0.03	0.01	< 0.05	0.008	< 0.01	0.011	< 0.005	< 0.01	-
Z03	-	0.03	< 0.05	0.01	< 0.05	< 0.005	< 0.01	< 0.005	< 0.005	< 0.01	< 0.01
Z04	-	0.01	1.05	0.09	< 0.05	0.042	0.03	0.016	0.057	< 0.01	< 0.01
Z05	-	0.01	0.03	0.66	1.55	0.307	0.10	0.168	0.054	0.03	< 0.01
Z06	-	-	0.03	0.01	< 0.05	< 0.005	< 0.01	< 0.005	< 0.005	0.09	< 0.01
Z07	-	0.01	0.08	0.01	< 0.05	0.026	< 0.01	-	-	-	0.23
Z08	-	0.01	< 0.05	< 0.05	< 0.05	< 0.005	< 0.01	< 0.005	< 0.005	0.08	< 0.01
Z10	-	< 0.05	0.14	2.08	< 0.05	0.032	< 0.01	< 0.005	< 0.005	< 0.01	< 0.01
Z11	-	0.01	0.02	0.66	< 0.05	< 0.005	< 0.01	< 0.005	< 0.005	0.01	< 0.01

Table B-18. Effluent K concentrations ($\mu\text{g mL}^{-1}$) in non-vegetated mesocosms

Date	5/30	6/13	6/27	7/11	7/25	8/8	8/15	8/22	9/6	9/12	9/19
<i>Det.Limit.</i>	0.1	0.1	0.1	0.1	0.1	0.01	0.01	0.01	0.01	0.01	0.01
G01	2.8	2.3	-	2.9	-	-	-	-	-	3.38	3.02
G03	1.6	1.5	1.6	2.0	3.9	3.35	3.75	4.32	4.00	3.78	3.98
H05	1.9	1.5	1.5	2.7	4.4	4.34	2.42	2.31	3.71	3.92	3.56
J01	-	1.2	1.2	1.3	2.3	4.55	3.87	0.76	5.14	6.23	4.75
J04	2.2	1.8	-	2.7	3.5	2.44	2.50	3.01	3.06	2.98	2.81
J08	2.3	1.6	1.6	2.7	4.0	3.48	2.64	2.36	3.86	4.46	3.33
K04	3.2	3.1	3.7	3.6	4.5	4.93	5.61	6.49	8.01	8.00	6.88
L01	2.7	1.6	2.0	2.3	3.8	3.98	3.92	4.26	4.23	3.82	3.10
M03	1.7	1.3	-	2.6	3.4	3.00	6.50	3.38	5.54	4.51	4.66
N03	1.7	1.1	-	-	-	-	-	-	-	-	-
Z01	-	1.1	1.9	1.1	1.7	4.23	4.18	0.75	5.19	2.33	3.72
Z02	-	0.6	1.8	2.0	2.8	2.92	4.00	1.46	3.10	7.33	-
Z03	-	0.6	4.5	1.5	3.5	8.41	11.38	4.71	8.02	1.92	5.34
Z04	-	0.5	2.5	1.9	1.2	1.45	6.64	0.93	5.31	1.04	3.48
Z05	-	0.6	1.5	1.8	5.5	5.42	17.14	2.53	12.08	2.95	9.11
Z06	-	1.5	2.3	1.2	2.1	2.58	3.08	3.27	3.54	3.58	3.64
Z07	-	0.6	4.6	1.4	1.9	2.03	22.79	-	-	-	13.30
Z08	-	0.7	3.7	7.1	17.1	16.90	22.14	15.60	19.17	11.98	11.33
Z10	-	1.6	6.9	1.9	1.4	5.30	5.53	2.56	6.06	3.63	7.42
Z11	-	0.6	1.4	1.7	1.9	2.82	2.48	1.30	3.53	1.83	3.34

Table B-19. Effluent Mg concentrations ($\mu\text{g mL}^{-1}$) in non-vegetated mesocosms

Date	5/30	6/13	6/27	7/11	7/25	8/8	8/15	8/22	9/6	9/12	9/19
<i>Det.Limit.</i>	0.05	0.05	0.05	0.05	0.05	0.005	0.01	0.005	0.005	0.01	0.01
G01	4.83	1.35	-	1.00	-	-	-	-	-	5.84	4.18
G03	0.78	0.64	0.59	0.73	1.50	1.560	2.41	3.781	4.971	4.72	5.02
H05	1.01	0.77	0.68	1.75	3.15	2.831	1.69	1.749	4.102	5.84	4.16
J01	-	0.73	0.63	0.69	1.30	4.229	3.66	0.185	7.252	11.46	7.01
J04	1.23	0.98	-	1.32	1.25	1.134	1.56	2.235	4.242	4.87	4.03
J08	0.96	0.68	0.53	1.14	1.34	1.470	1.48	1.169	3.773	6.29	4.03
K04	1.91	1.80	2.01	1.89	1.91	2.897	3.74	5.901	11.837	13.68	12.14
L01	1.70	0.88	0.93	1.12	1.55	2.281	2.67	3.452	5.794	6.67	4.73
M03	0.92	0.81	-	1.85	1.52	1.590	4.97	2.142	5.395	6.09	4.73
N03	1.29	0.64	-	-	-	-	-	-	-	-	-
Z01	-	0.35	0.48	0.14	0.18	0.686	0.40	0.035	0.726	0.57	0.71
Z02	-	0.18	0.38	0.25	0.38	0.405	0.70	0.085	0.665	6.44	-
Z03	-	0.19	0.65	0.19	0.76	0.396	8.87	2.386	4.444	0.49	0.80
Z04	-	0.13	0.55	0.15	0.14	4.962	0.71	0.074	0.636	0.37	0.70
Z05	-	0.16	0.55	0.33	0.70	0.149	1.36	0.145	1.095	0.48	1.40
Z06	-	0.46	0.59	0.22	0.35	0.451	0.82	0.895	1.387	1.63	1.55
Z07	-	0.19	1.01	0.16	0.16	0.651	4.21	-	-	-	2.24
Z08	-	0.17	0.68	0.90	3.28	0.152	13.11	13.927	11.148	10.46	6.09
Z10	-	0.50	1.32	0.30	0.09	10.931	0.64	0.221	0.974	0.61	1.27
Z11	-	0.16	0.42	0.28	0.15	0.624	0.55	0.175	0.967	0.43	0.92

Table B-20. Effluent Na concentrations ($\mu\text{g mL}^{-1}$) in non-vegetated mesocosms

Date	5/30	6/13	6/27	7/11	7/25	8/8	8/15	8/22	9/6	9/12	9/19
<i>Det.Limit.</i>	0.1	0.1	0.1	0.1	0.1	0.01	0.01	0.01	0.01	0.01	0.01
G01	8.1	2.6	-	2.4	-	-	-	-	-	3.25	1.34
G03	1.9	1.2	1.1	1.8	4.0	2.78	2.64	2.55	1.78	1.70	1.60
H05	2.0	0.8	1.0	1.5	2.9	1.71	0.99	1.12	1.32	1.03	1.03
J01	-	2.7	1.6	1.8	3.3	5.04	3.65	0.54	3.06	3.26	2.53
J04	3.4	2.2	-	3.6	5.0	3.23	2.85	3.14	2.93	3.56	2.67
J08	2.0	1.1	1.2	3.1	5.7	5.65	3.68	2.85	4.29	6.07	3.71
K04	4.5	4.0	4.7	4.0	4.9	4.94	4.11	4.93	4.86	4.68	3.87
L01	4.0	1.9	2.0	2.0	4.0	3.00	2.37	2.22	1.81	3.03	1.44
M03	1.5	1.0	-	1.1	2.2	1.11	1.18	1.01	1.07	1.74	1.07
N03	3.2	1.4	-	-	-	-	-	-	-	-	-
Z01	-	1.4	0.7	1.2	20.8	29.6	18.3	3.80	21.1	27.4	16.7
Z02	-	<0.1	1.3	0.5	1.4	0.55	0.38	0.25	0.24	0.35	-
Z03	-	0.2	0.7	0.2	1.3	0.7	0.89	0.32	0.56	0.21	0.17
Z04	-	<0.1	0.5	2.6	7.8	3.43	4.00	1.51	13.1	3.81	6.50
Z05	-	<0.1	0.3	8.1	63.4	46.9	23.8	10.2	19.4	11.8	20.0
Z06	-	1.3	1.1	0.4	1.6	0.76	0.59	0.66	0.66	0.46	0.38
Z07	-	0.3	1.7	0.7	1.5	0.39	0.59	-	-	-	0.34
Z08	-	0.7	1.3	0.8	1.9	1.8	2.27	1.29	1.18	1.04	1.13
Z10	-	0.9	1.2	0.5	2.3	4.00	5.40	2.58	3.40	2.74	4.77
Z11	-	<0.1	0.2	0.1	1.3	0.34	0.29	0.22	0.22	0.20	0.16

Table B-21. Effluent P concentrations ($\mu\text{g mL}^{-1}$) in non-vegetated mesocosms

Date	5/30	6/13	6/27	7/11	7/25	8/8	8/15	8/22	9/6	9/12	9/19
<i>Det.Limit.</i>	0.10	0.10	0.10	0.10	0.10	0.01	0.01	0.01	0.01	0.01	0.01
G01	0.6	0.8	-	0.6	-	-	-	-	-	0.04	0.08
G03	0.6	0.6	0.7	0.2	<0.1	0.05	0.11	0.07	0.11	0.02	0.06
H05	0.6	0.3	0.9	0.4	0.2	0.08	0.07	<0.01	0.03	0.04	0.08
J01	-	0.6	0.8	0.4	<0.1	0.05	0.07	0.02	0.11	0.03	0.07
J04	0.5	0.5	-	0.8	0.1	0.05	0.08	0.03	0.06	0.07	0.05
J08	0.6	0.7	0.7	0.7	0.4	0.03	0.08	0.05	0.31	0.06	0.10
K04	0.6	0.4	0.6	0.4	0.2	0.05	0.06	0.09	0.21	0.14	0.07
L01	0.6	0.7	0.6	0.4	0.2	0.08	0.06	0.01	0.03	0.03	0.08
M03	0.6	0.6	-	0.6	0.2	0.03	2.29	0.12	1.41	0.17	1.88
N03	0.8	0.6	-	-	-	-	-	-	-	-	-
Z01	-	0.5	1.2	0.3	0.8	2.76	4.64	0.92	6.02	1.00	4.58
Z02	-	0.8	1.1	0.3	0.5	0.20	2.59	0.23	2.60	0.05	-
Z03	-	0.5	3.4	0.4	0.1	0.01	0.03	0.03	1.66	0.32	4.99
Z04	-	0.7	1.7	1.6	0.8	0.71	7.51	0.66	6.25	0.14	3.46
Z05	-	0.6	1.3	1.1	3.9	3.10	17.66	1.59	13.32	0.84	9.58
Z06	-	0.6	1.2	0.4	0.3	0.02	0.59	<0.01	0.28	0.04	0.28
Z07	-	0.5	3.9	0.5	0.2	0.17	26.02	-	-	-	14.32
Z08	-	0.6	2.5	4.8	7.0	1.58	3.46	0.02	4.83	0.36	3.66
Z10	-	0.6	4.8	0.5	0.6	3.16	5.66	0.97	4.60	0.91	6.94
Z11	-	0.6	1.3	0.5	0.6	0.49	0.98	0.16	2.22	0.29	2.42

Table B-22. Foliar characteristics at harvest

Sample	Mass (g)	Area (cm ²)	Growth (days)	Spots ^a	P wt%	K wt%	Ca w t%	Mg wt%
G02	2.50	379.74	132	+	0.11	0.46	1.26	0.18
G04	1.70	213.92	121	+	0.12	0.42	1.93	0.16
G05	0.37	72.55	132	-	0.23	0.81	0.46	0.34
G06	0.95	142.27	132	-	0.20	0.52	1.34	0.22
G07	0.43	60.21	132	+	0.19	0.59	1.44	0.07
G08	0.67	108.10	107	+	0.20	0.31	2.76	0.41
H01	0.83	168.39	121	+	0.15	0.56	1.03	0.10
H02	0.85	103.99	132	+	0.09	0.49	1.43	0.23
H03	3.36	423.62	132	+	0.10	0.45	1.75	0.22
H04	0.84	128.82	132	+	0.15	0.90	0.81	0.18
H06	0.50	75.32	132	-	0.17	0.60	1.81	0.08
H07	1.26	224.73	132	+	0.11	0.42	0.92	0.15
H08	0.33	56.66	132	-	0.16	0.63	0.50	0.27
J02	1.09	142.74	121	+	0.12	0.32	1.51	0.17
J03	0.81	114.48	132	+	0.14	0.33	2.61	0.20
J05	0.31	49.74	121	-	0.10	0.56	0.91	0.12
J06	2.69	337.41	121	-	0.11	0.32	1.93	0.22
J07	2.69	338.35	132	+	0.11	0.34	1.60	0.20
K01	0.93	164.82	114	+	0.26	0.46	1.41	0.21
K02	1.35	209.42	132	+	0.13	0.49	1.05	0.14
K03	2.34	314.00	121	+	0.11	0.39	1.72	0.30
K05	0.68	114.97	132	-	0.20	0.91	0.20	0.23
K06	0.68	127.98	132	-	0.13	0.47	1.16	0.31
K07	1.56	251.43	121	+	0.15	0.69	1.32	0.17
K08	0.83	124.37	132	+	0.19	0.52	1.07	0.12
L02	0.80	113.98	121	+	0.13	0.47	1.50	0.22
L03	0.57	150.49	121	-	0.17	0.52	1.53	0.19
L04	1.51	255.56	132	-	0.17	0.59	0.91	0.20
L05	1.84	248.62	132	-	0.17	0.60	1.46	0.26
L06	1.12	154.46	132	-	0.14	0.33	1.74	0.27
L07	1.00	147.49	121	+	0.13	0.31	2.12	0.28
L08	1.15	167.71	114	+	0.17	0.47	1.65	0.18
M01	0.25	46.50	132	-	0.17	0.28	0.57	0.21
M02	3.54	536.31	132	+	0.10	0.49	0.79	0.20
M04	0.38	57.05	114	-	0.14	0.51	1.14	0.09
M05	1.77	229.79	132	-	0.11	0.43	1.70	0.16
M06	0.46	73.07	121	+	0.11	0.39	1.92	0.17
M07	1.35	205.15	132	-	0.14	0.59	1.63	0.21
M08	2.47	351.36	132	+	0.09	0.46	1.79	0.21
N01	1.45	243.54	132	+	0.16	0.71	0.84	0.16
N02	2.24	331.97	114	+	0.12	0.61	1.23	0.09
N04	1.82	293.00	114	-	0.11	0.54	1.37	0.13
N05	0.95	153.89	121	+	0.23	0.58	1.59	0.14
N06	1.78	347.05	132	-	0.10	0.57	1.72	0.26
N07	2.87	381.51	132	+	0.09	0.57	1.49	0.18
N08	1.37	216.78	121	+	0.16	0.58	1.49	0.25

^aindicates the presence (+) or absence (-) of black spots on leaves during growth

Table B-23. Concentrations of minor elements ($\mu\text{g g}^{-1}$) in foliage at harvest

Sample	Mn	Fe	Cu	B	Al	Zn	Na
G02	5,445	50	6	43	23	23	125
G04	5,976	64	5	61	36	30	63
G05	2,019	121	7	27	38	43	318
G06	4,015	63	7	37	26	73	146
G07	6,892	64	8	29	45	38	159
G08	6,020	72	6	55	33	40	129
H01	7,335	55	7	35	20	30	53
H02	2,996	64	10	27	38	36	142
H03	4,357	46	4	37	27	24	71
H04	992	280	8	29	142	33	114
H06	4,810	81	7	32	41	37	50
H07	2,921	35	5	32	24	47	115
H08	617	149	6	43	65	24	174
J02	6,228	357	10	53	123	42	80
J03	7,500	138	7	40	33	73	207
J05	2,458	51	6	45	40	36	52
J06	4,114	53	6	41	26	33	87
J07	4,432	43	6	39	23	39	95
K01	5,132	50	8	51	22	51	79
K02	4,291	87	7	38	21	47	59
K03	4,492	41	6	39	28	40	68
K05	99	46	5	23	26	23	79
K06	3,012	98	7	22	68	35	131
K07	4,666	71	8	39	27	58	52
K08	3,398	38	5	39	30	47	59
L02	3,045	99	6	28	46	37	61
L03	4,057	81	8	51	27	23	53
L04	3,656	65	7	37	22	31	52
L05	3,905	38	7	39	18	43	48
L06	5,150	116	6	31	62	34	38
L07	7,489	88	6	40	31	42	39
L08	5,331	45	6	40	29	52	60
M01	154	78	3	15	78	15	90
M02	1,650	52	6	27	30	27	19
M04	4,713	45	6	49	33	53	68
M05	4,197	60	5	35	24	39	70
M06	6,094	80	6	50	33	25	53
M07	3,219	62	6	31	27	31	31
M08	3,574	28	4	40	23	30	30
N01	3,897	40	7	59	25	45	91
N02	7,493	56	6	60	30	25	49
N04	5,000	52	7	47	29	38	51
N05	6,640	494	8	51	102	35	39
N06	5,677	156	15	79	77	36	86
N07	2,666	32	5	41	25	20	59
N08	3,543	38	6	62	23	48	72

Table B-24. Mn additions to each vegetated mesocosm

		Mn in soil	Mass of addition	Added Mn	Total Mn
		mmol	grams	mmol	mmol
Control (soil-only)	G06	56.83	0	0	56.83
	H07	56.83	0	0	56.83
	J02	56.83	0	0	56.83
	J07	56.83	0	0	56.83
	K01	56.83	0	0	56.83
	K02	56.83	0	0	56.83
	L04	56.83	0	0	56.83
	M05	56.83	0	0	56.83
	M07	56.83	0	0	56.83
	N01	56.83	0	0	56.83
	N04	56.83	0	0	56.83
	N06	56.83	0	0	56.83
Aqueous additions	G02	56.83	50	8.00	64.83
	G05	56.83	50	8.00	64.83
	G07	56.83	50	8.00	64.83
	H01	56.83	50	8.00	64.83
	H03	56.83	50	8.00	64.83
	H08	56.83	50	8.00	64.83
	J03	56.83	50	8.00	64.83
	J05	56.83	50	8.00	64.83
	J06	56.83	50	8.00	64.83
	K05	56.83	50	8.00	64.83
	L07	56.83	50	8.00	64.83
	N02	56.83	50	8.00	64.83
Organic additions	G08	56.83	20.18	2.04	58.87
	H02	56.83	20.41	2.06	58.89
	H06	56.83	20.58	2.08	58.91
	K06	56.83	20.39	2.06	58.89
	K07	56.83	20.76	2.10	58.93
	L02	56.83	20.48	2.07	58.90
	L05	56.83	20.96	2.12	58.95
	M02	56.83	20.2	2.04	58.87
	M06	56.83	20.74	2.09	58.92
	N07	56.83	20.43	2.06	58.89
N08	56.83	20.85	2.11	58.94	
Oxide additions	G04	56.83	0.93	8.62	65.45
	H04	56.83	0.78	7.23	64.06
	K03	56.83	0.87	8.07	64.90
	K08	56.83	0.87	8.07	64.90
	L03	56.83	0.80	7.42	64.25
	L06	56.83	0.61	5.66	62.49
	L08	56.83	0.64	5.93	62.76
	M01	56.83	0.66	6.12	62.95
	M04	56.83	0.63	5.84	62.67
	M08	56.83	0.85	7.88	64.71
	N05	56.83	1.00	9.27	66.10

Table B-25. Mn additions to each non-vegetated mesocosm

		Mn in soil	Mass of addition	Added Mn	Total Mn
		mmol	grams	mmol	mmol
Control (soil-only)	K04	56.83	0	0	56.83
	N03	56.83	0	0	56.83
	Z02	23.32	0	0	23.32
	Z07	23.32	0	0	23.32
	Z11	23.32	0	0	23.32
Aqueous additions	H05	56.83	50	8.00	64.83
	J01	56.83	50	8.00	64.83
	M03	56.83	50	8.00	64.83
	Z03	23.32	50	8.00	31.32
	Z08	23.32	50	8.00	31.32
Organic additions	G01	56.83	20.79	2.10	58.93
	G03	56.83	20.97	2.12	58.95
	J04	56.83	20.45	2.07	58.90
	L01	56.83	20.74	2.09	58.92
	Z06	23.32	20.2	2.04	25.36
Oxide additions	J08	56.83	0.73	6.77	63.60
	Z01	23.32	0.87	8.07	31.39
	Z04	23.32	0.60	5.56	28.88
	Z05	23.32	0.68	6.30	29.62
	Z10	23.32	0.94	8.72	32.04

Table B-26. Summary of effluent pH values

	Average effluent pH	Standard Error
<i>Vegetated treatments</i>		
Soil-only	4.64	0.07
Aqueous	4.19	0.07
Oxide	4.53	0.09
Organic	4.54	0.08
<i>Non-vegetated treatments</i>		
Soil-only	4.05	0.11
Aqueous	3.73	0.09
Oxide	4.82	0.10
Organic	4.25	0.17

Appendix C

Section C1. Comparison of theoretical and experimental Mn K-edge values

Theoretical calculations for the energy shifts between absorption edges E_0 (*i.e.*, calculated Mn 1s orbital energies) of different Mn compounds were consistent with experimental data. Similar to previous studies (Jaszewski et al., 2011; Kuzek & Pace, 2001), we find that E_0 is strongly ligand dependent and can vary by several eV for compounds with the same Mn oxidation state (Figure C-1). All shifts are calculated relative to Mn²⁺-oxide (MnO) (Table C-1). Mn-oxides were modeled as aqueous compounds, *e.g.* Mn²⁺(OH)₄ for MnO, Mn³⁺(OH)₂ for Mn₂O₃, and Mn⁴⁺(OH)₂ for MnO₂. We infer that experimental samples contain multiple Mn species because the observed values fall between calculated values of different model compounds.

All calculations were performed by James Kubicki with the M06-2x/6-311+G(d,p) method (Zhao and Truhlar, 2008) using the program Gaussian 09 (Frisch et al., 2010). All models were energy minimized in a dielectric continuum solvent model for water (Cancès et al., 1997). No symmetry or constraints were imposed upon the structures.

References

- Cancès E., Mennucci B. and Tomasi J. (1997) A new integral equation formalism for the polarizable continuum model: Theoretical background and applications to isotropic and anisotropic dielectrics. *The Journal of Chemical Physics* **107**, 3032.
- Frisch M. (2010) Gaussian 09, Revision B 01.
- Jaszewski A. R., Petrie S., Pace Ronald J and Stranger R. (2011) Toward the assignment of the manganese oxidation pattern in the water-oxidizing complex of photosystem II: a time-dependent DFT study of XANES energies. *Chemistry (Weinheim an der Bergstrasse, Germany)* **17**, 5699–713.
- Kuzek D. and Pace R J (2001) Probing the Mn oxidation states in the OEC. Insights from spectroscopic, computational and kinetic data. *Biochimica et biophysica acta* **1503**, 123–37.
- Zhao Y. and Truhlar D. G. (2008) The M06 suite of density functionals for main group thermochemistry, thermochemical kinetics, noncovalent interactions, excited states, and transition elements: two new functionals and systematic testing of four M06-class functionals and 12 other function. *Theoretical Chemistry Accounts* **120**, 215–241.

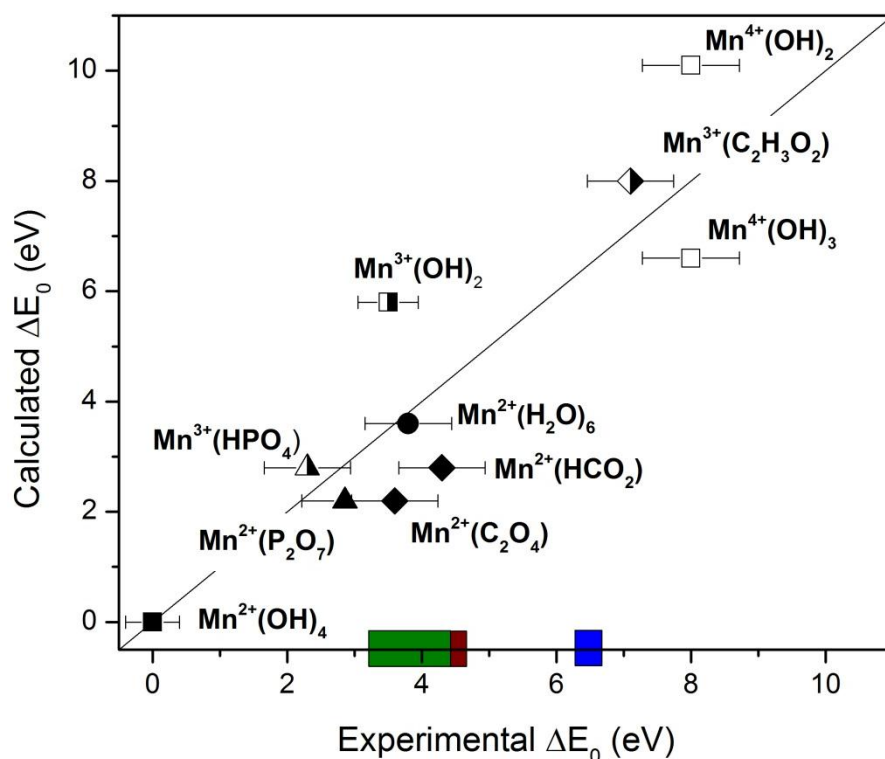


Figure C-1: Theoretical versus experimental edge energy calculations for standard compounds. E_0 energy ranges for vegetation (green), decomposing vegetation (brown), and soil (blue) samples are shown on the x-axis.

Table C-1. Theoretical and Experimental Mn K-edge E_0 (eV) values

Compound	Theoretical Structure	E_0 , Theoretical eV	E_0 , Experimental eV	ΔE_0 , Theor. ^a eV	ΔE_0 , Exper ^a eV
MnO	Mn(+2)(OH) ₄	6451.9	6544.0	0.0	0.0
Mn ₂ O ₃	Mn(+3)(OH) ₂	6457.7	6547.5	5.8	3.5
MnO ₂	Mn(+4)(OH) ₂	6462.0	6552.0	10.1	8.0
	Mn(+4)(OH) ₃	6458.5	6552.0	6.6	8.0
Mn ²⁺ (aq)	Mn ²⁺ (H ₂ O) ₆	6455.5	6547.7	3.6	3.7
Mn-formate	Mn ²⁺ (HCO ₂ ⁻)	6454.7	6548.1	2.8	4.1
Mn-oxalate	Mn ²⁺ (C ₂ O ₄ ²⁻)	6454.1	6547.6	2.2	3.6
Mn ²⁺ pyrophosphate	Mn ²⁺ (P ₂ O ₇)	6454.1	6546.9	2.2	2.9
Mn ³⁺ phosphate	Mn ³⁺ (HPO ₄)	6454.7	6546.3	2.8	2.3
Mn ³⁺ acetate	Mn ³⁺ (CH ₃ COO ⁻)	6459.9	6551.1	8.0	7.1

^a ΔE_0 is calculated as the difference between E_0 for each compound and MnO

Section C2. Analysis of buried wells

C2.1. Methods

Microporous specimen capsules (78 μm porosity, 9 mm inner diameter x 5 mm height; Electron Microscopy Sciences) were packed with crushed leaf litter and buried 10 cm deep in oxic soils of either a forest watershed (7 weeks) or in greenhouse pots containing red oak seedlings (9 weeks). The capsules (i.e. wells) were removed, embedded with resin to preserve spatial relations, and cut with a slow saw to obtain a cross-section of the well. The procedures for embedding were modified from previous procedures (Eickhorst & Tippkötter, 2008; Nunan et al., 2001; Nunan et al., 2003; Tippkötter & Ritz, 1996). In particular, once the wells were extracted from the soil, they were fixed with 3% paraformaldehyde in a Na-phosphate buffer (pH = 7.2), wrapped in parafilm, and kept in the freezer for storage. Embedding was accomplished by placing the porous wells in a glass petri dish and using transfer pipettes to exchange the embedding solutions in the dish. After fixation, the wells were rinsed three times with the Na-phosphate buffer and progressively dehydrated with cold ethanol in a series of 50% ethanol:water (15 min), 70% ethanol (15 min), 90% ethanol (10 min), and 100% ethanol (10 min). The wells were then incubated overnight in a mixture of 50% ethanol and 50% LR White embedding medium before replacing the solution with 100% LR White. After two hours, excess LR White was removed, and wells were vacuum-sealed in the petri dish using a FoodSaver vacuum sealing system. The vacuum-sealed dishes were then cured in an oven at 65°C until the resin was fully polymerized (3-5 days). Embedded wells were cut into ~2 mm thick sections with a slow saw and mounted on glass slides.

C2.2. Results

In the wells containing leaf litter, Mn is distributed more homogeneously in the greenhouse-buried wells and more discretely in the field-buried wells (Figure S2). The Mn hot spots in field-buried wells also contain ~7x higher Mn/ I_0 fluorescent counts than Mn-rich regions in greenhouse-buried wells. Given that the wells contained homogenized leaf litter prior to burial, we would expect homogenous Mn distribution if no alteration of the leaf litter occurred. Therefore, in the greenhouse-buried wells, the homogenous distribution of Mn is consistent with low alteration, while in the field-buried wells, Mn is more discretely concentrated. These observations suggest that leaf litter buried in the field was more altered (i.e. decomposed) than leaf litter buried in the greenhouse pots. Mn appears to have been mobilized and concentrated during alteration.

Additionally, μXANES spots were measured on five wells containing crushed leaf litter (Figure S3). Six spectra were taken from three different wells buried in greenhouse pots (A, B, and C in Appendix Fig. 1), while three spectra were taken from two wells buried in the field (D and E in

Appendix Fig. 1). A linear combination fit was used to compare these spots to the vegetation and soil end-members used in the previous section to investigate Mn in decomposing leaf samples. For the greenhouse-buried wells, Mn was low ($Mn/I_0 = 0.058 \pm 0.034$), homogeneously distributed, and dominated by the vegetation end-member ($98.6\% \pm 2.4\%$). In the field-buried wells, two spectra taken on Mn hot spots ($Mn/I_0 = 0.74$ and 1.09) have significant contribution from the soil end-member (64.2% and 46.9%) relative to a Mn-poor spot ($Mn/I_0 = 0.02$) which is dominated by the vegetation end-member (90.5%). These results indicate that the field-buried leaf litter experienced greater decomposition than the greenhouse-buried leaf litter, potentially due to more exposure to soil fungi, which were abundant in the field soil but only periodically observed in the greenhouse pots.

References

- Eickhorst T. and Tippkötter R. (2008) Detection of microorganisms in undisturbed soil by combining fluorescence in situ hybridization (FISH) and micropedological methods. *Soil Biology and Biochemistry* **40**, 1284–1293.
- Nunan N., Ritz Karl, Crabb D., Harris K., Wu Keijan, Crawford J. W. and Young I. M. (2001) Quantification of the in situ distribution of soil bacteria by large-scale imaging of thin sections of undisturbed soil. *FEMS Microbiology Ecology* **36**, 67–77.
- Nunan N., Wu Keijan, Young I. M., Crawford J. W. and Ritz Karl (2003) Spatial distribution of bacterial communities and their relationships with the micro-architecture of soil. *FEMS Microbiology Ecology* **44**, 203–15.
- Tippkötter R. and Ritz K (1996) Evaluation of polyester, epoxy and acrylic resins for suitability in preparation of soil thin sections for in situ biological studies. *Geoderma* **69**, 31–57.

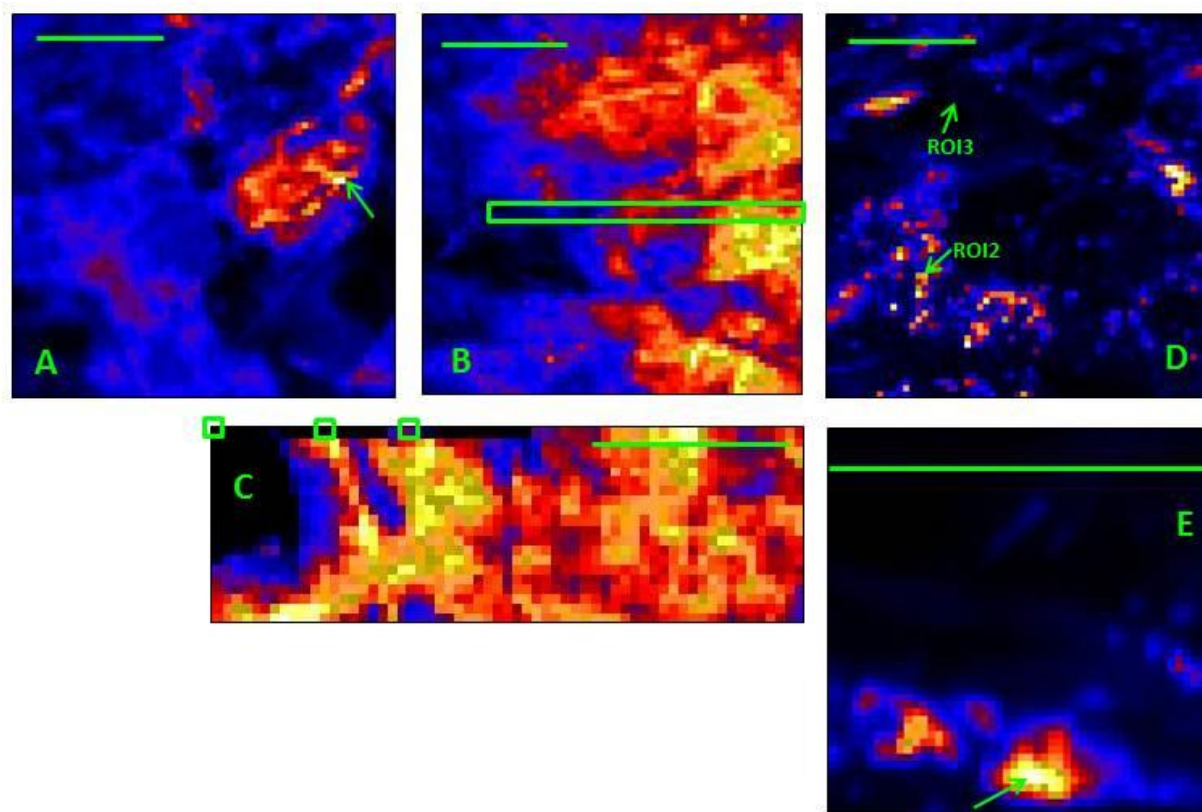


Figure C-2. Leaf litter samples buried in either greenhouse pots (A, B, C) or field soil (D and E). Arrows and boxes indicate areas targeted for μ XANES. Green scale bars are all 500 μ m.

A) Mn/I_0 values are low and range from 0.0 to 0.10. The map is 1.5 x 1.5 mm with 25 μ m step sizes. **B)** Mn is distributed diffusely ($Mn/I_0 = 0.01 - 0.14$). The map is 1.5 x 1.5 mm with 25 μ m step size. **C)** Mn is distributed diffusely across the sample ($Mn/I_0 = 0.01 - 0.16$), similar to A and B. The map is 1.5 x 0.75 mm with 25 μ m step size. **D)** Mn is distributed in distinct patches throughout the sample with a broader fluorescence range ($Mn/I_0 = 0.01 - 0.88$). The map is 1.5 x 1.5 mm with 25 μ m step size. **E)** The XRF map has a wide range of Mn fluorescence counts ($Mn/I_0 = 0.0 - 1.13$) with localized regions of high Mn that do not correlate to other elements. The map is 0.5 x 0.5 mm with 10 μ m step size.

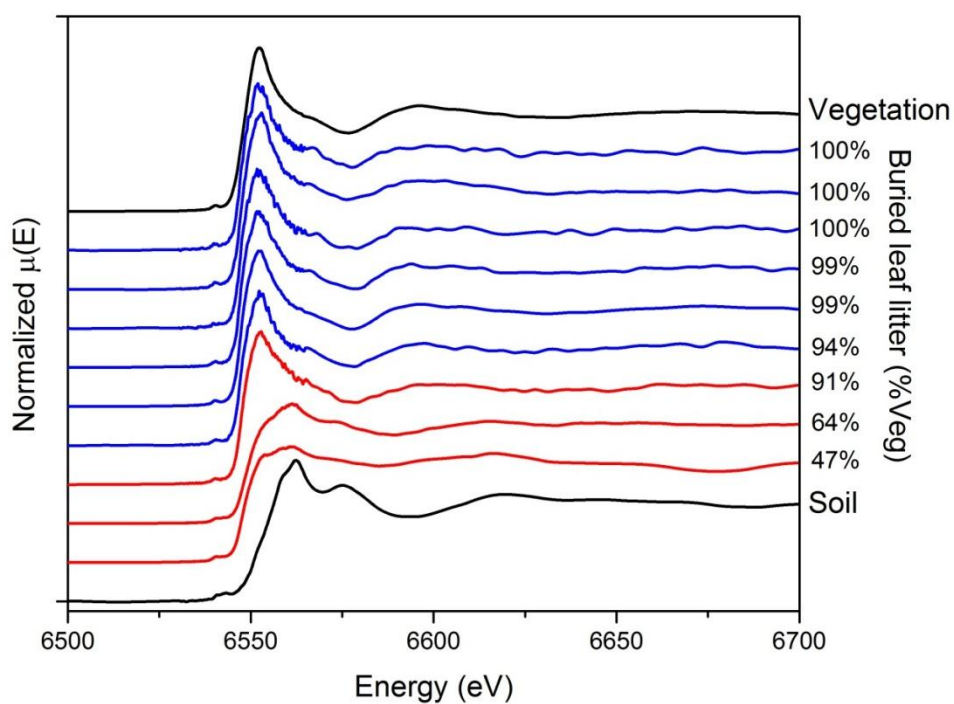


Figure C-3. XANES spectra near the Mn K-edge for leaf litter samples that were buried in soils in either greenhouse pots (blue) or a forested watershed (red) are compared to spectra for fresh vegetation and mineral soil (black). Percentages indicate the %vegetation returned in a linear combination fit with vegetation and soil end-members. These results indicate that Mn in vegetation is oxidized to the Mn-oxides present in soil during decomposition. Greenhouse wells were buried for longer (9 weeks) than field wells (7 weeks) but show less alteration.

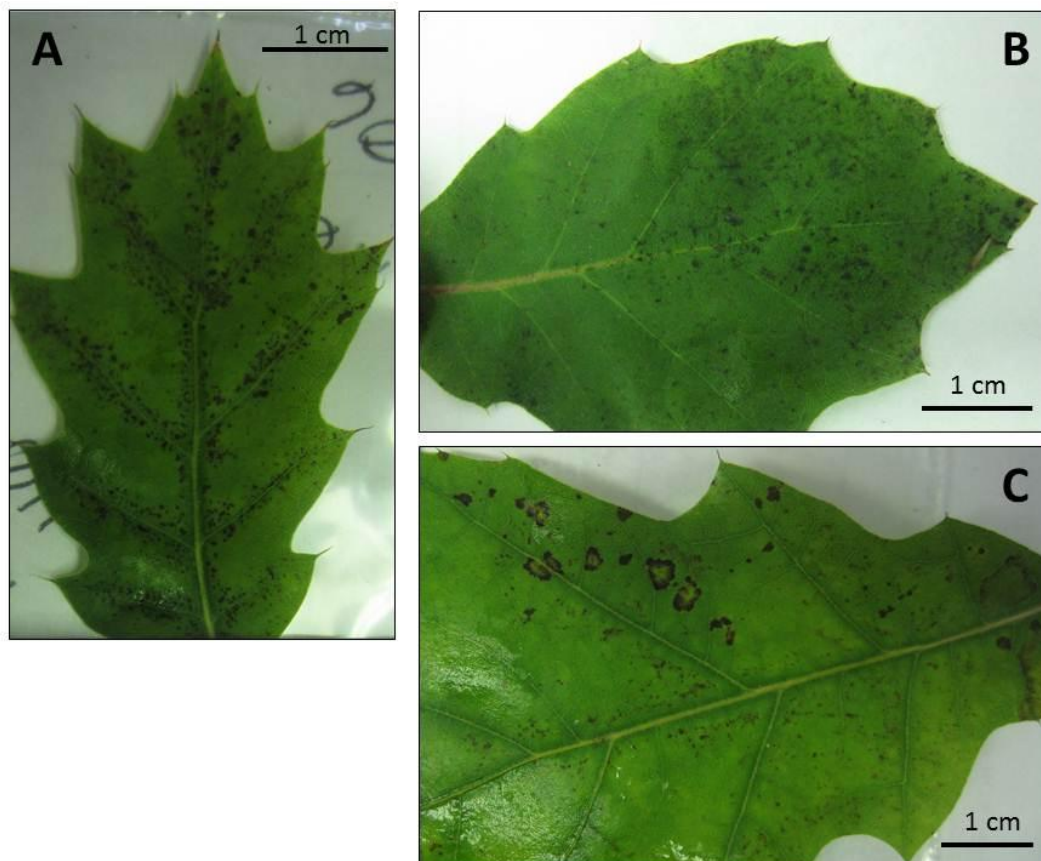
Section C3. Supplementary Figure s and Tables for Chapter 4

Figure C-4. Mn toxicity was observed on red oak leaves as dark spots either A) clustered around the midveins, B) dispersed across the leaf surface, or C) in rings.

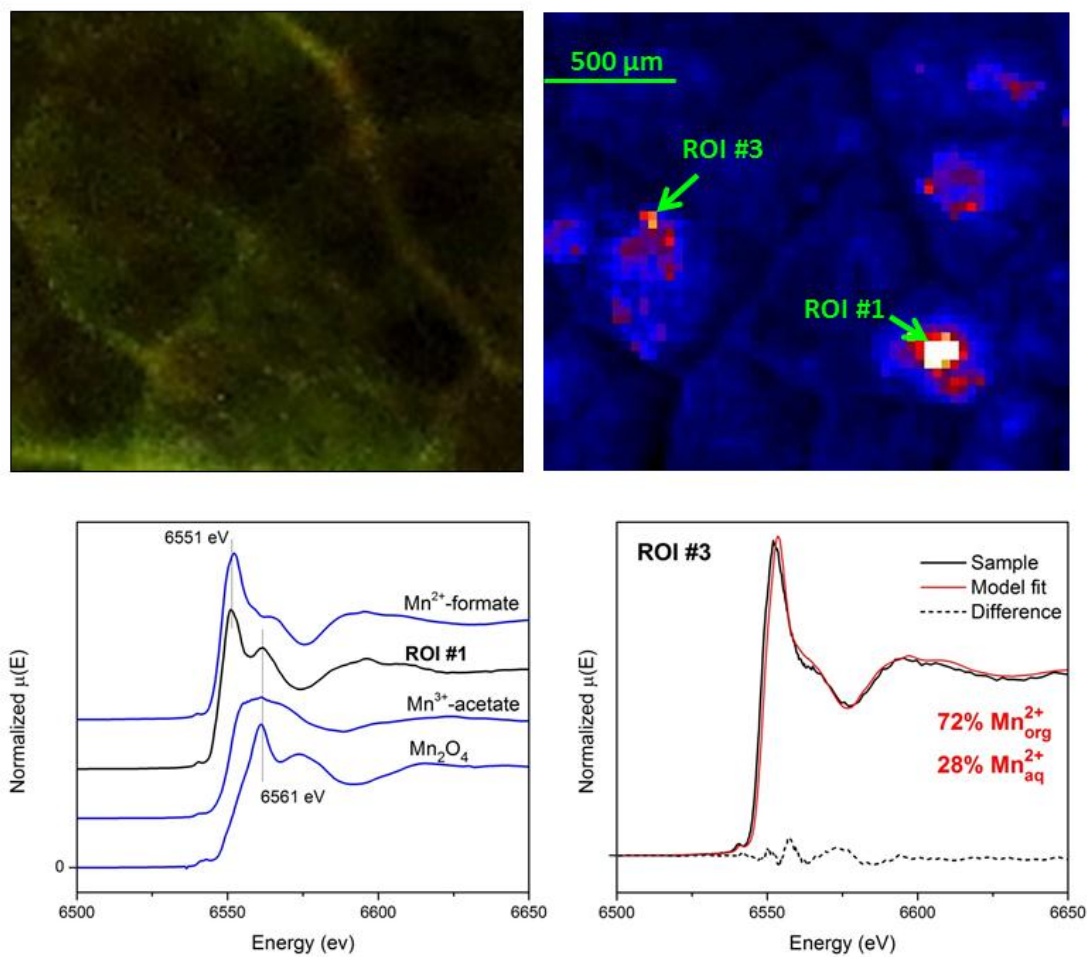


Figure C-5. Sample: F06v (3,564 ppm), leaf sample collected from the greenhouse and vacuum sealed and frozen until analysis. Two μ XANES spectra were obtained from Mn-rich regions ROI (Mn/I₀ = 1.13) and ROI3 (Mn/I₀ = 0.44).

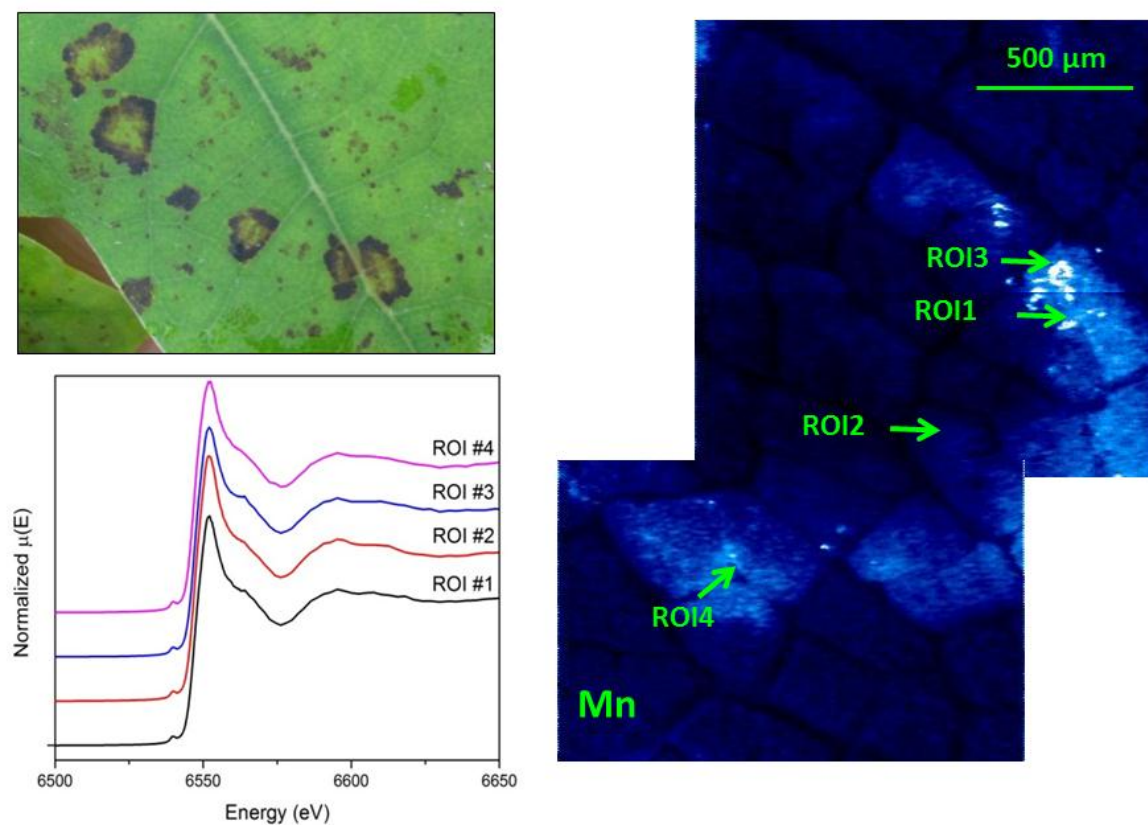


Figure C-6A: Sample H07, a leaf (2,921 ppm Mn at harvest) from a greenhouse-grown red oak seedling with visible black rings. The XRF image is a compilation of three separate but overlapping maps, each with widths of 1.5 mm and with a total height of 2.515 mm and step sizes of 5 μm. Mn-rich regions form the same ring shape observed for the black spots on the leaves.

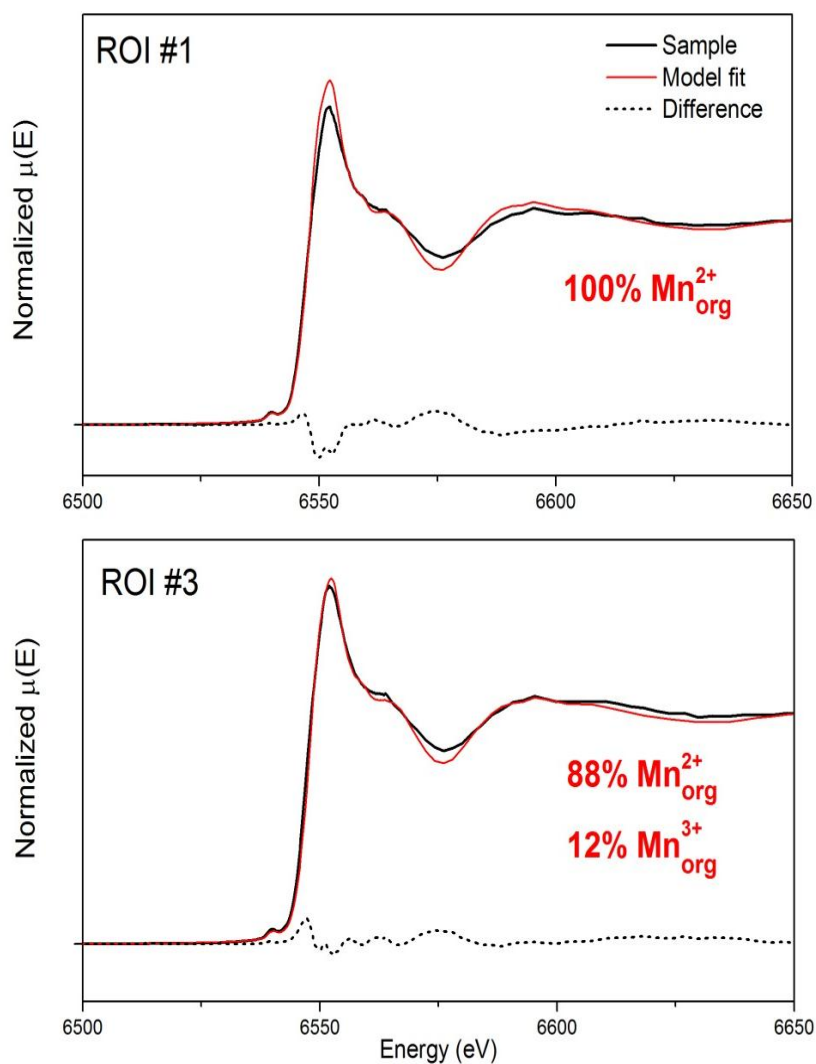


Figure C-6B: Two μ XANES spectra with similar fluorescent counts (ROI #1, $Mn/I_0 = 2.77$; ROI #3 $Mn/I_0 = 2.82$) were obtained $\sim 60 \mu\text{m}$ apart on a dark spot on leaf H07 (Figure S6-A). Linear combination fits yield 12% Mn^{3+} -acetate for ROI #3 but 0% for ROI #1, from which we infer that the dark spots contain differing amounts of Mn compounds.

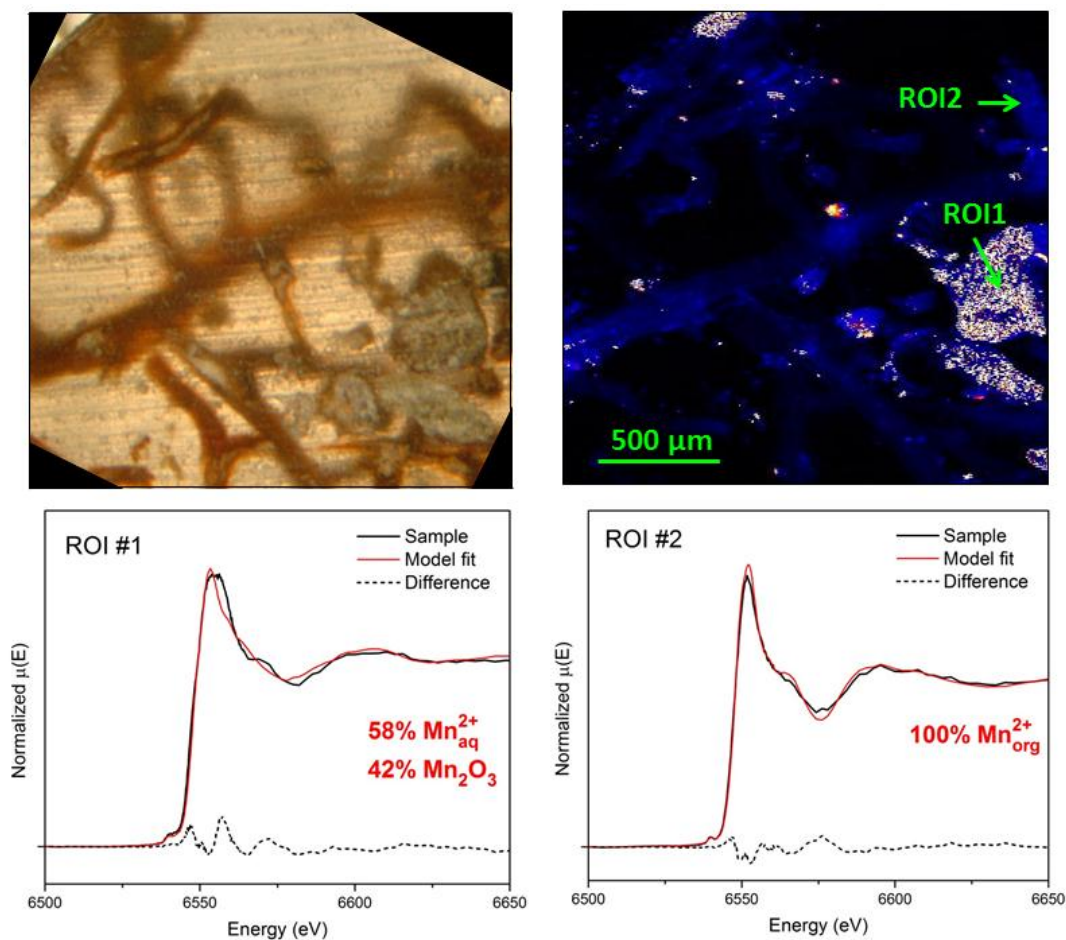


Figure C-7. Sample embedded1_2, non-woody fine roots collected from greenhouse samples, embedded in LR White resin, and cut into 1 mm thin blocks. Mn is present both in roots (ROI2) and in root-adhering soil particles (ROI1). Mn is lower in the roots ($Mn/I_0 < 0.1$) than in the soil particles ($Mn/I_0 < 1.20$).

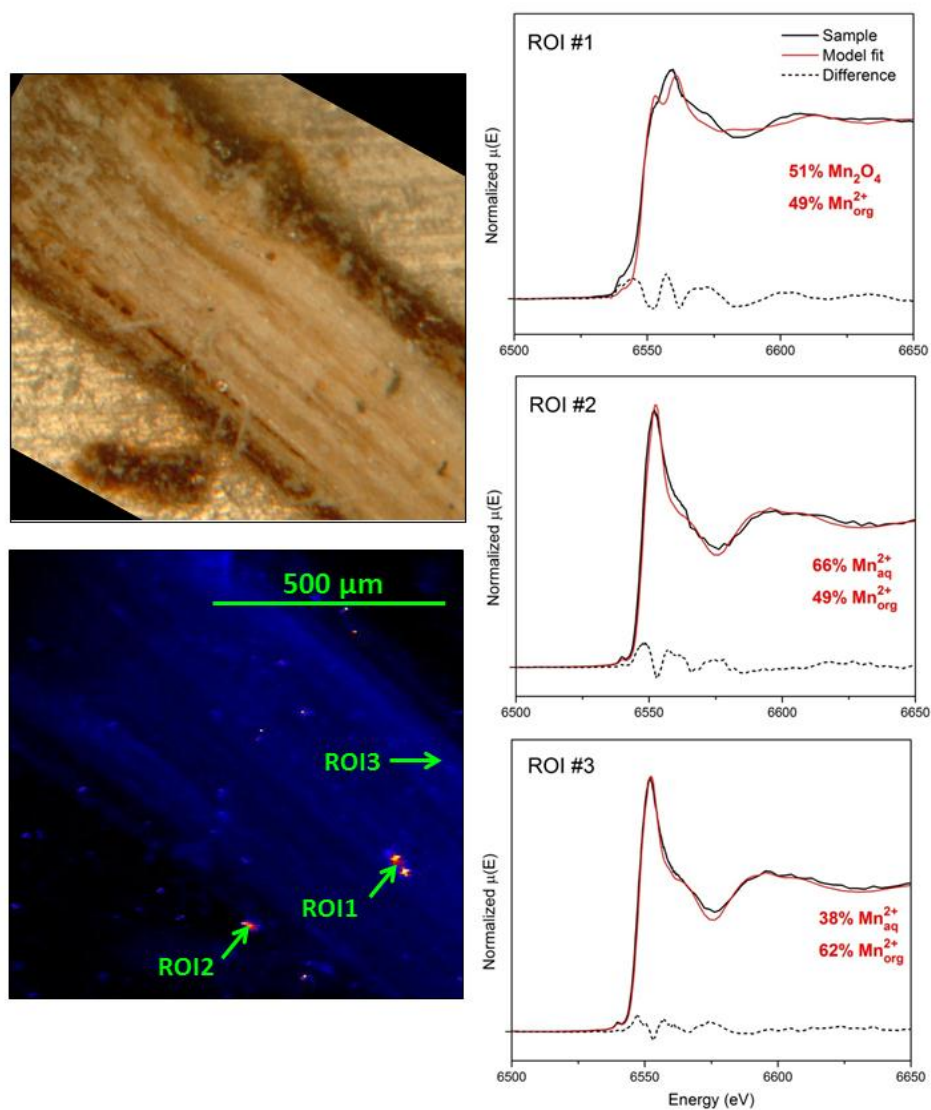


Figure C-8. Sample embedded1_1 is the longitudinal cross-section of a fine root embedded in resin. The map is 1 x 1 mm with 5 μm step sizes. Mn is low in the root tissue ($\text{Mn}/I_0 < 0.1$) but higher in the bright flecks (max 1.09). XANES spectra for three different spots reveal that ROI1 is most consistent with a combination of organic Mn^{2+} and Mn_2O_3 while ROI2 and ROI3 are most consistent with organic and aqueous Mn^{2+} , similar to vegetation samples.

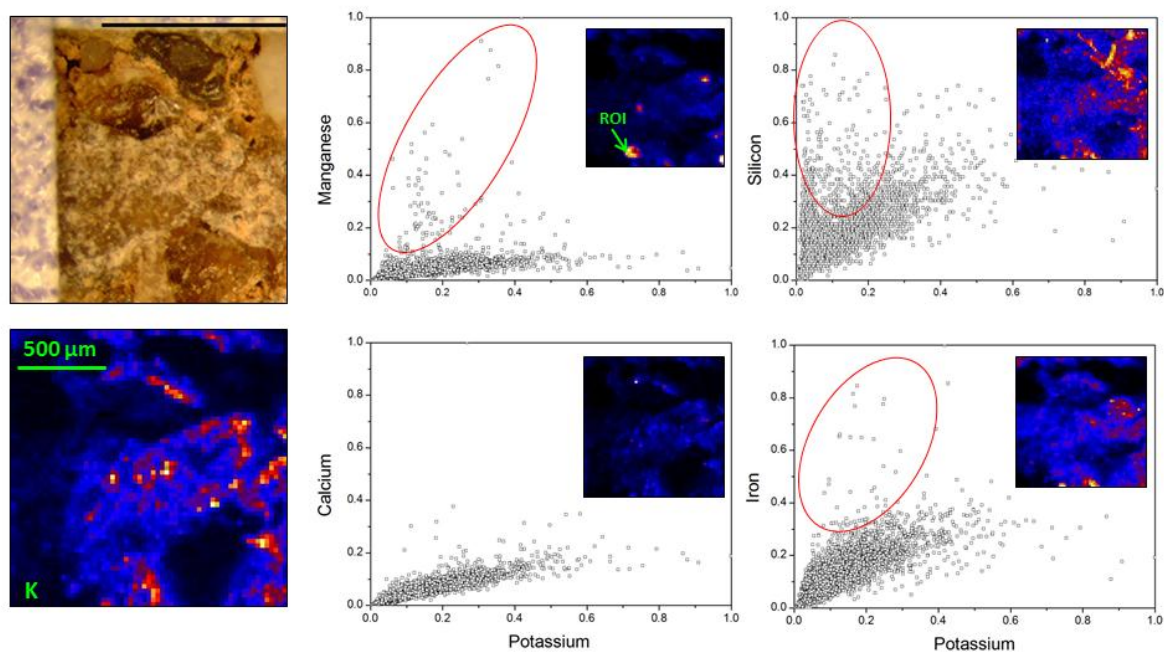


Figure C-9A. Mineral soil grains that were embedded with LR white resin and cut with a slow saw. The map is 1.5 mm x 1.5 mm with 25 μm step size. Mn/ I_0 values in the map range from 0.0 to 0.32. The Mn-rich zones in this sample are not observed to be consistently rich in any other analyzed element.

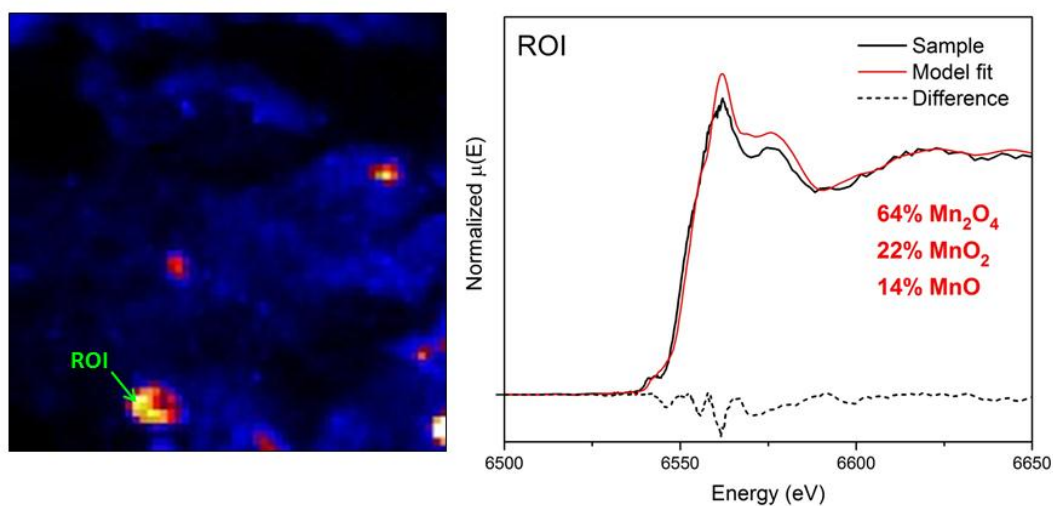


Figure C-9B. An XRF image of soil grains reveals discrete areas of high Mn concentration. A linear combination fit to the μXANES spectra from spot ROI is consistent with a combination of mixed-valence Mn-oxides, similar to the bulk soil.

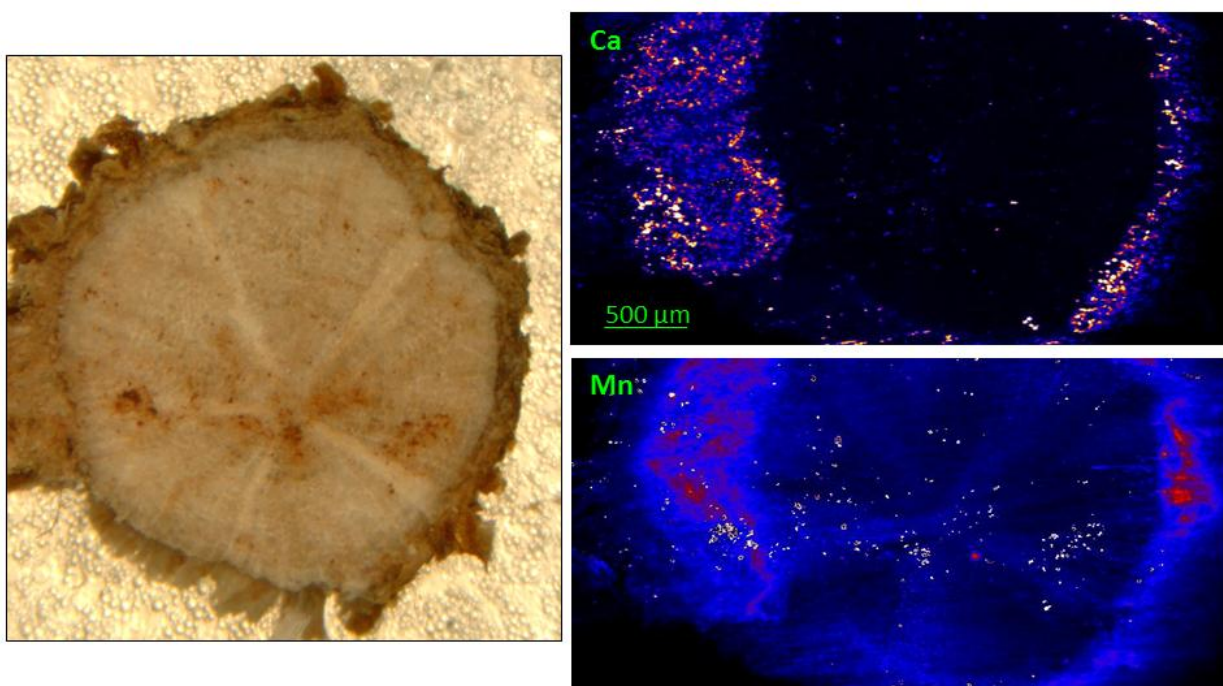


Figure C-10. Sample M02_root2. A coarse, woody root (diameter = 4 mm) from a greenhouse grown red oak seedling. The fresh root was cut into cross-section with a box cutter and vacuum sealed until analysis. Mn is concentrated in the outer portion of the root. Contamination is seen in speckles on the XRF map and red spots on the optical image.

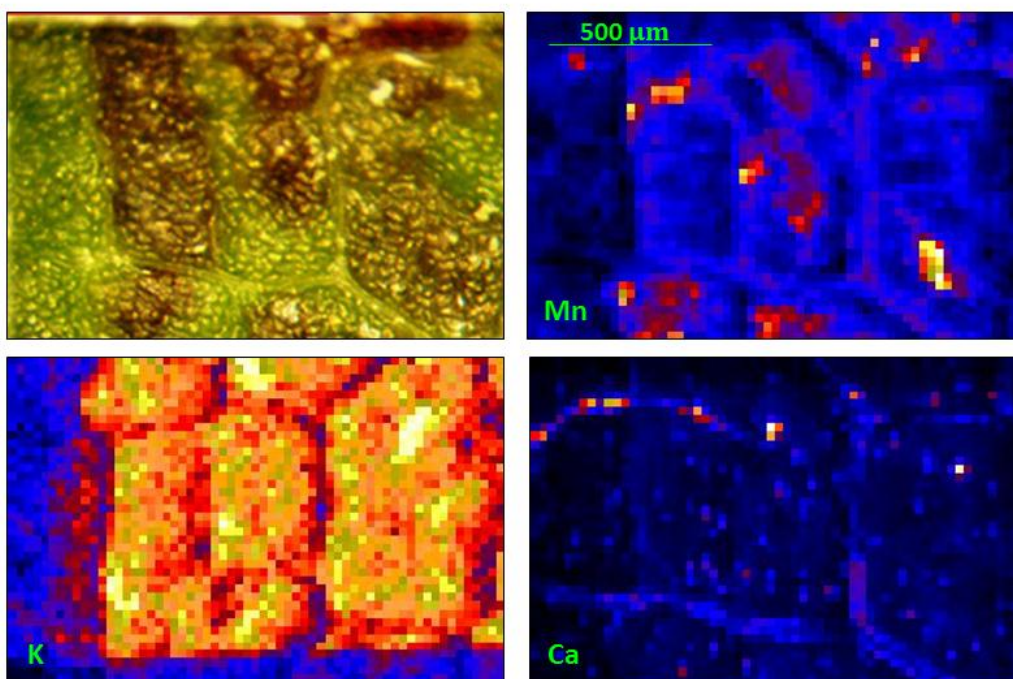


Figure C-11. Sample A01v1, a leaf collected from a greenhouse grown red oak seedling and vacuum-sealed and frozen until analysis. Mn hot-spots are observed to correlation to raised, dark spots on the leaf. In contrast, K is even dispersed inside each leaf cell and Ca is concentrated to the cell walls.

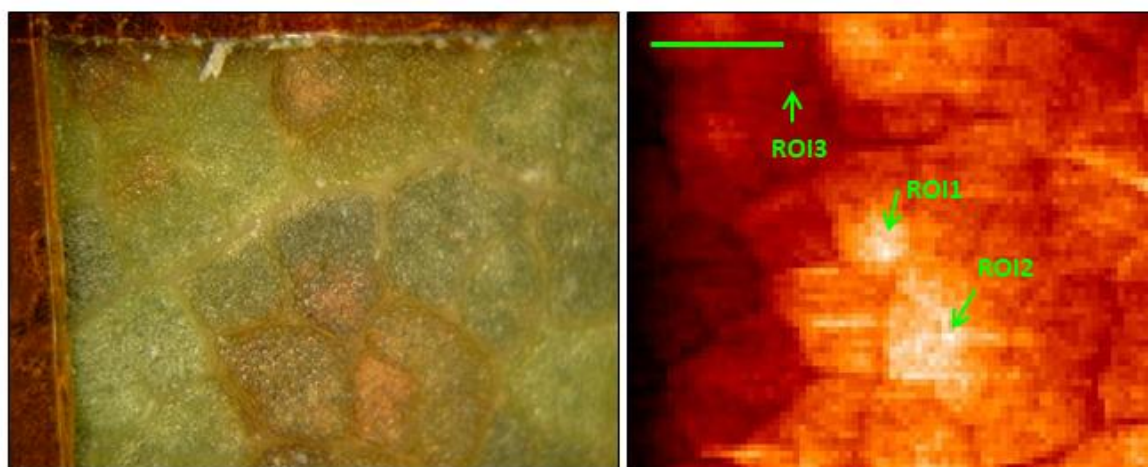


Figure C-12. Sample N05, a leaf collected from a greenhouse grown red oak seedling and vacuum-sealed and frozen until analysis. Mn rich regions correspond to dark spots on the leaf. The location of three μ XANES spectra were obtained from the leaf are indicated by green arrows.

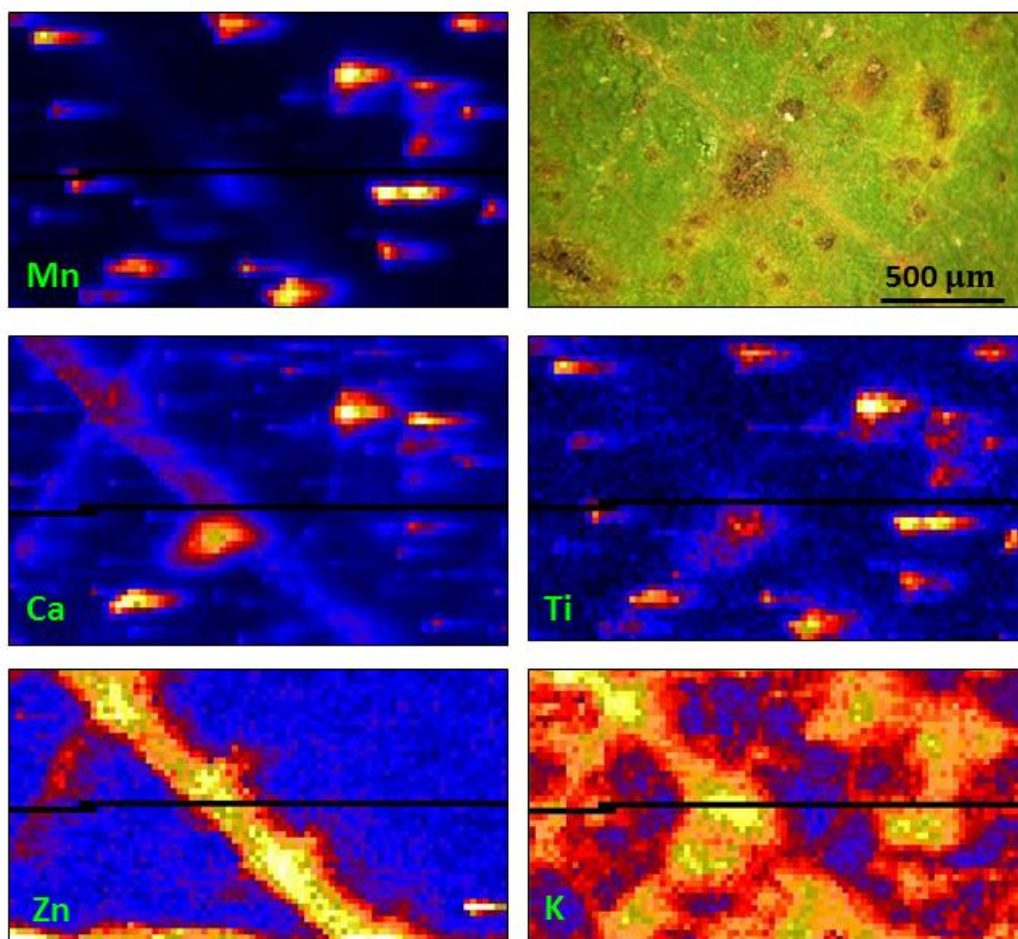


Figure C-13. Sample QUPR230_Map1, a leaf collected from a mature chestnut oak at the SSHCZO. Mn is enriched in small hot spots that correspond to dark spots on the leaf. Some of these spots are also enriched in Ca, which may indicate the presence of callose, which often precedes Mn toxicity (Wissemeier and Horst, 1987). Zn is distinctly distributed in the vein.

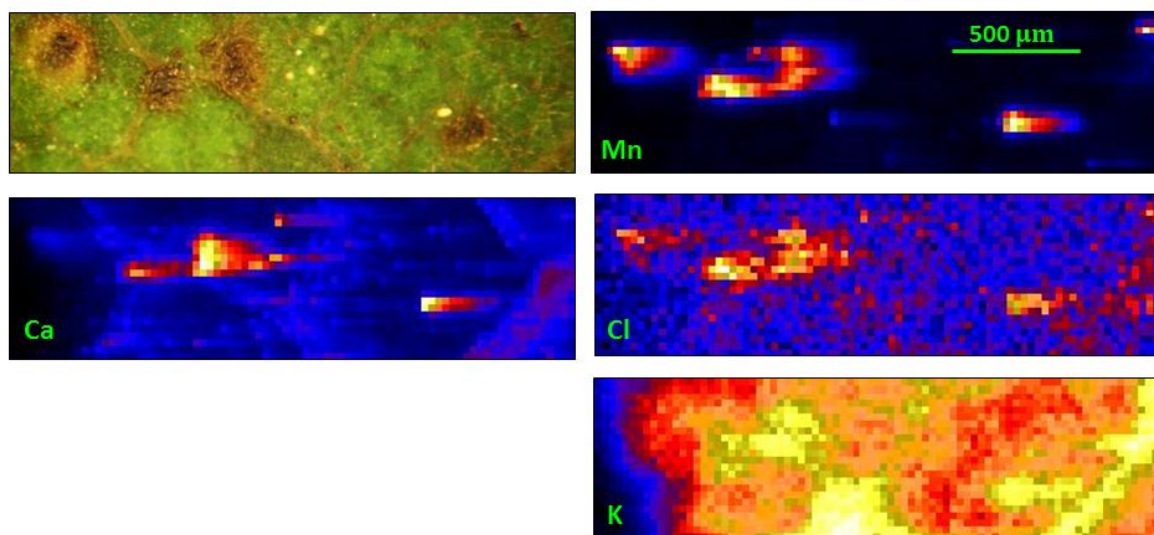


Figure C-14. Sample QUPR230_Map2, another section of the same leaf shown in Figure C-13. Again, K is diffusely distributed while Mn and Ca hotspots correspond to dark spots on the leaf.

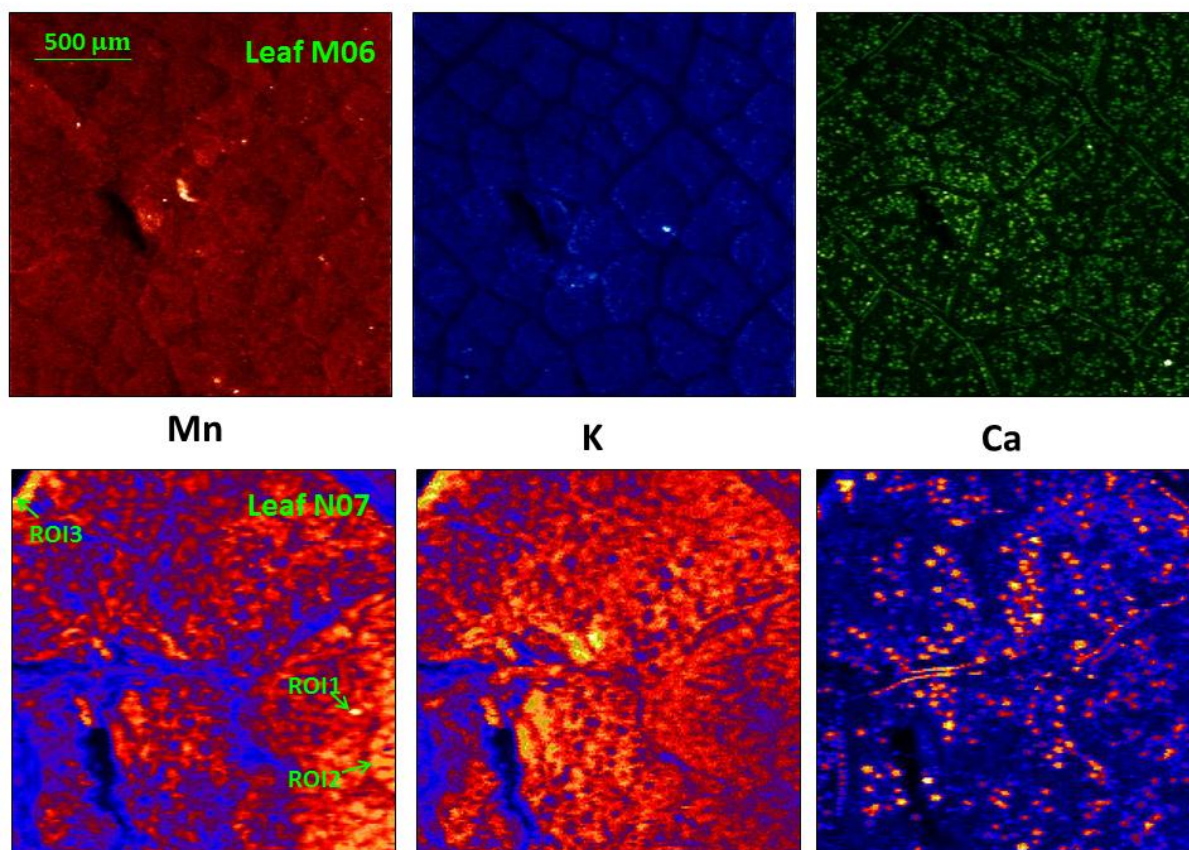


Figure C-15. *Samples M06 and N07*, leaf samples obtained from two greenhouse grown red oak seedlings, vacuum-sealed, and frozen until analysis. Each map is 2 x 2 mm with a 5 μm spot size. The images for M06 (top) are shown in three different colors for each element while the images for N07 (bottom) are all shown in the same color scheme. Here, we can observe the spotty distribution of Ca relative to the more diffuse nature of both Mn and K. Three μXANES spots were obtained from N07 and four from M06, though no optical images were available to detect the presence of dark spots on each leaf.

Appendix D

Section D1. Supporting Figures and Tables for Chapter 5

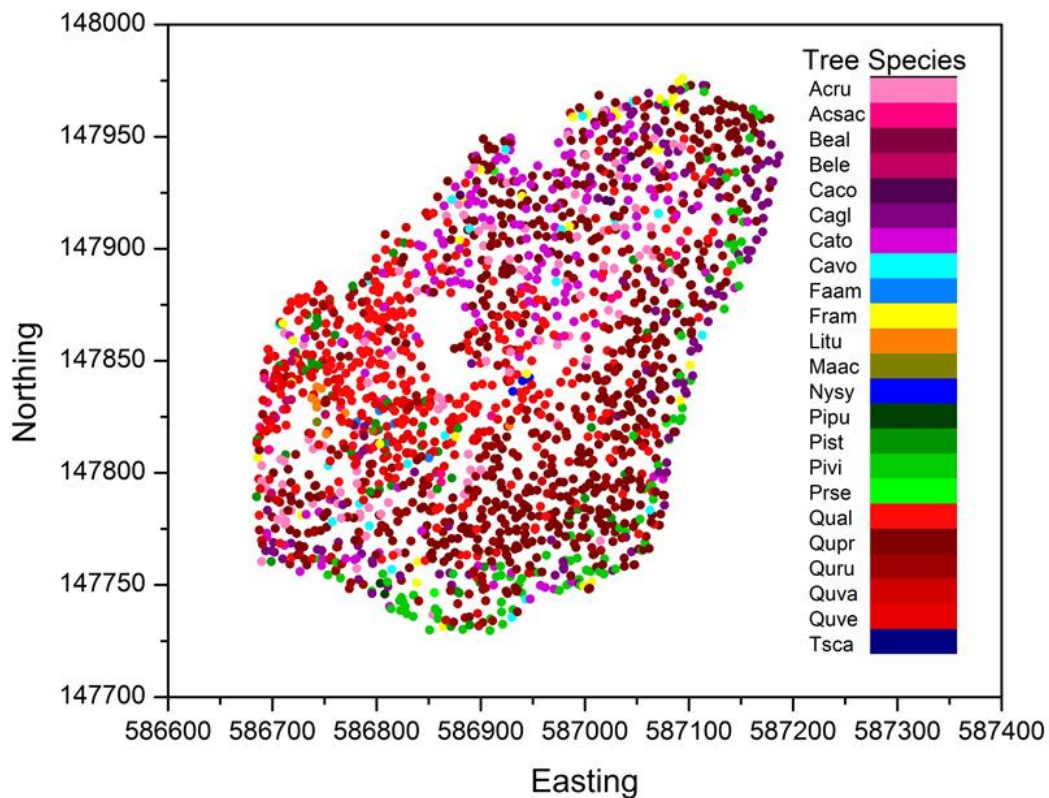


Figure D-1. Distribution of individual trees (DBH > 20 cm) surveyed in 2008 in the SSHCZO. The location of each tree is represented by a dot, and the tree species is represented by the color of the dot. Data provided by D. Eissenstat (Department of Ecosystem Science and Management, Penn State).

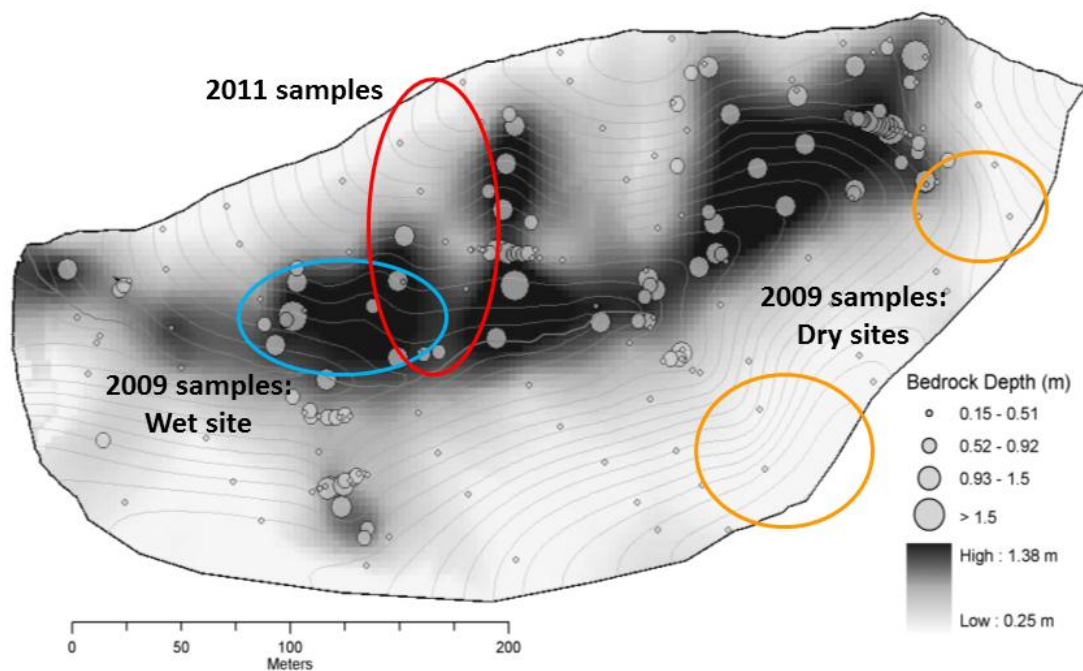


Figure D-2. Green leaf samples were collected from trees in a valley site with high soil moisture (wet site, blue circle) and two ridge sites with low soil moisture (dry sites, orange circles) in June – September 2009, and from trees along a transect (red circle) from June – September 2011. Figure adapted from Lin et al. (2006).

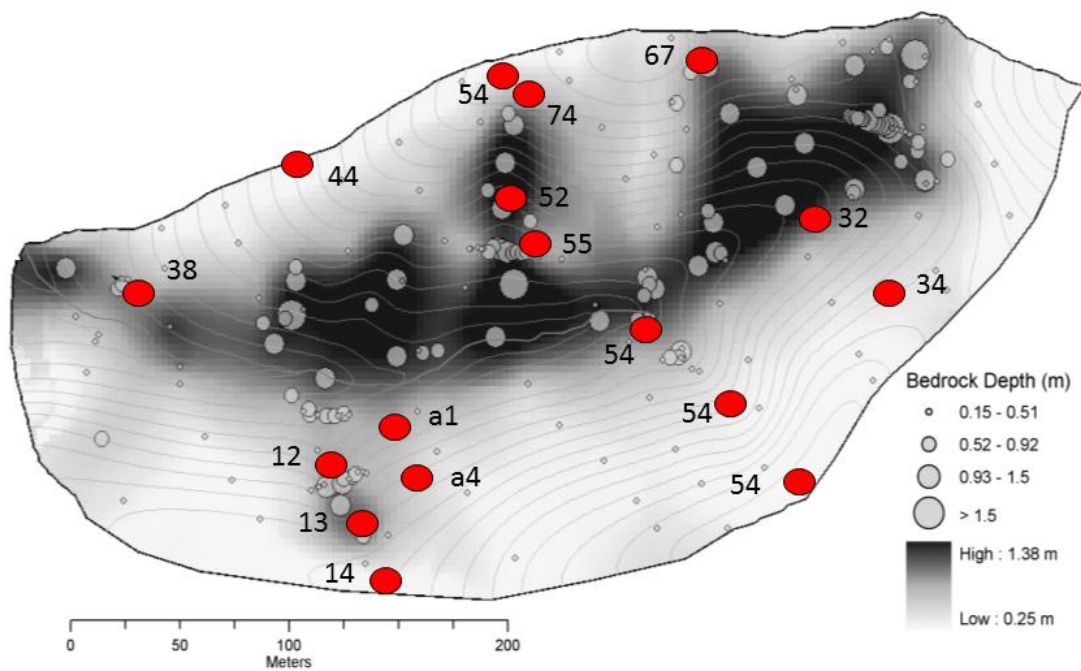


Figure D-3. Leaf litter was collected weekly from August – November 2011 from 35 litter traps placed throughout the catchment. A subset of litter samples was analyzed for bulk elemental composition, including litter collected on October 3 from 17 sites (all red symbols) and litter collected on August 31 and October 31 from 9 sites (12, 13, 14, 32, 34, 52, 54, 55, 74). Figure adapted from Lin *et al.* (2006).

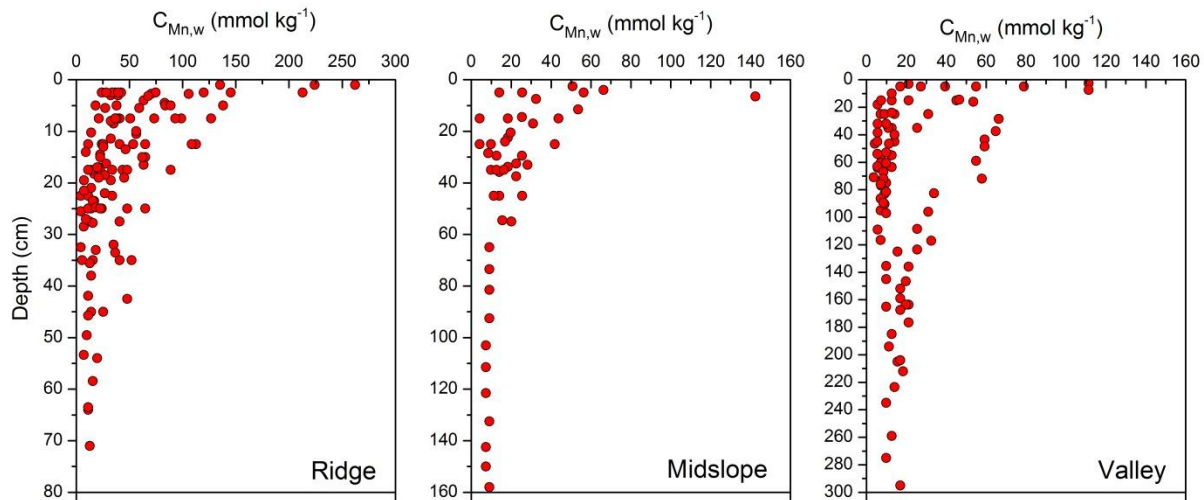


Figure D-4. Mn concentrations in bulk soil ($C_{Mn,w}$, mmol kg^{-1}) versus depth for all soil samples from cores augered at ridge ($n = 23$), slope ($n = 6$), and valley floor ($n = 7$) positions shown in Figure 5-1.

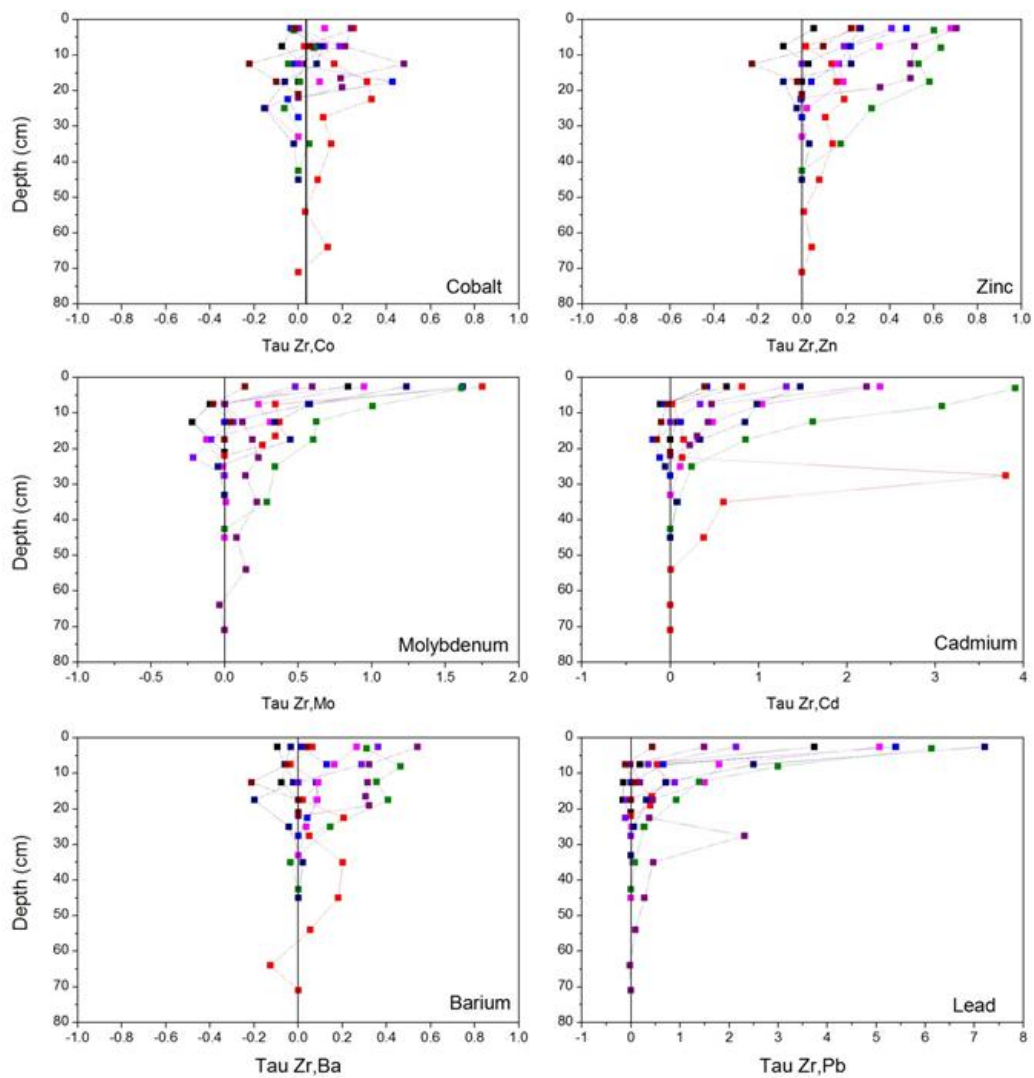


Figure D-5. $\tau_{Zr,j}$ values versus depth for a suite of elements ($j = \text{Co, Zn, Mo, Cd, Ba, Pb}$) exhibiting addition profiles in nine soil cores augered from ridge top positions at the SSHCZO.

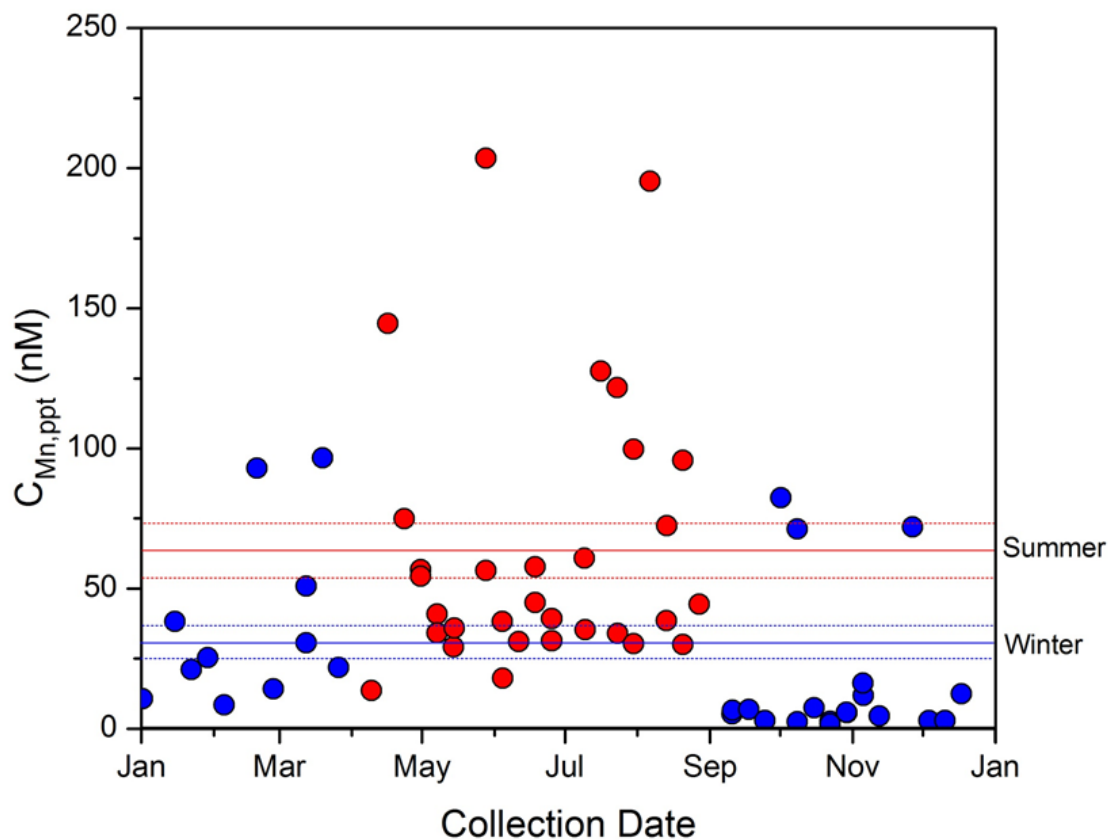


Figure D-6. Concentration of Mn in precipitation ($C_{Mn,ppt}$, nM) for samples collected in 2002 at NADP sites PA-15 and PA-42 located near SSHCZO. Each sample denotes one week of precipitation collection, and samples are grouped as summer (April – August; red symbols) or winter (September – March; blue symbols). The average and standard error of $C_{Mn,ppt}$ for summer (red lines) and winter (blue lines) are shown by solid and dotted lines, respectively.

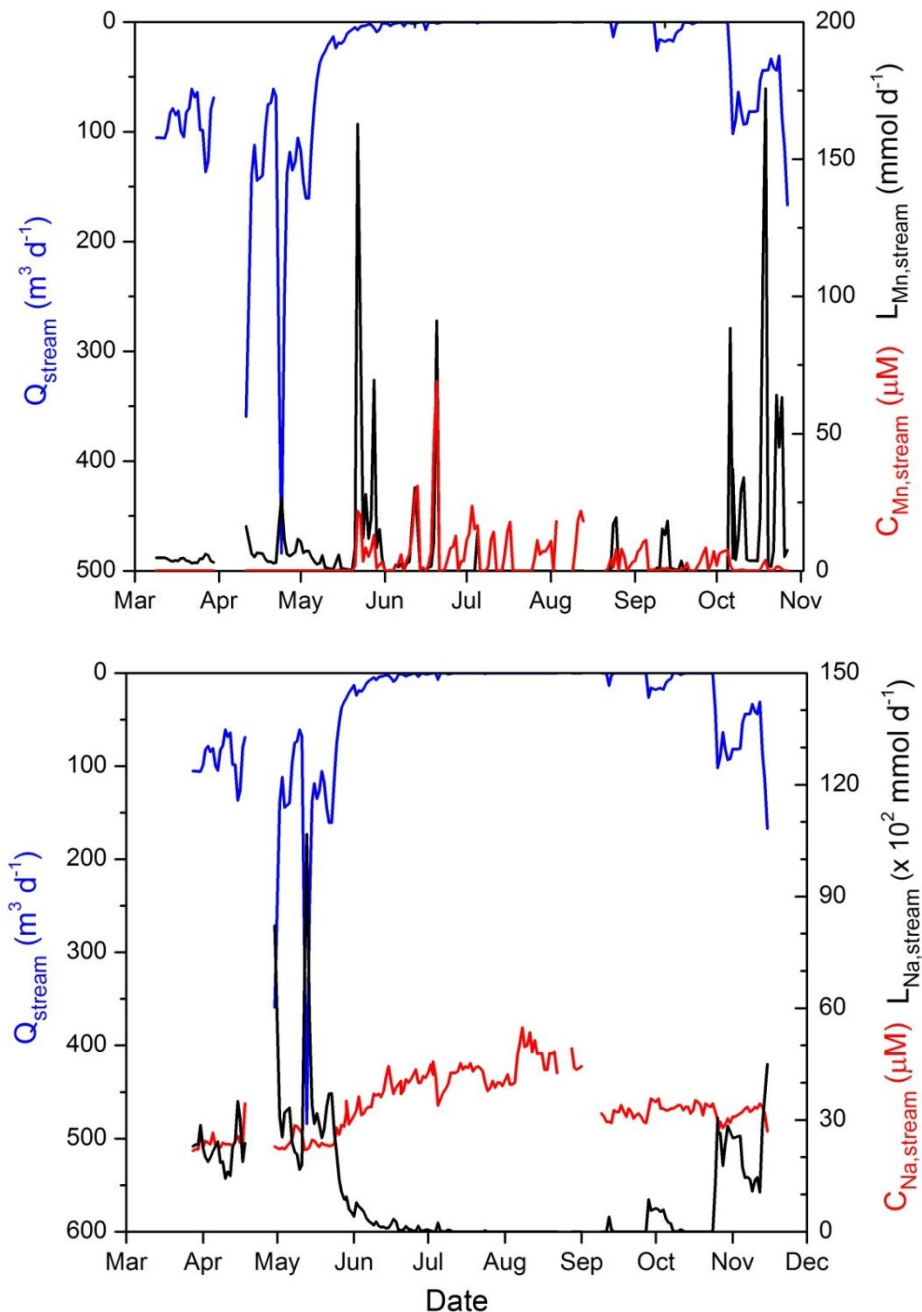


Figure D-7. Top) Values for $L_{Mn,stream}$ ($mmol d^{-1}$), the flux of dissolved Mn out of the watershed (black line, Eqn.2), reflect trends in Q_{stream} (blue line) at low discharge and $C_{Mn,stream}$ (red line) at high discharge. **Bottom)** Values for $L_{Na,stream}$ ($mmol d^{-1}$), the flux of dissolved Na out of the watershed (black line), reflect trends in Q_{stream} (blue line) at all discharge rates, and $C_{Na,stream}$ (red line) remains relatively constant.

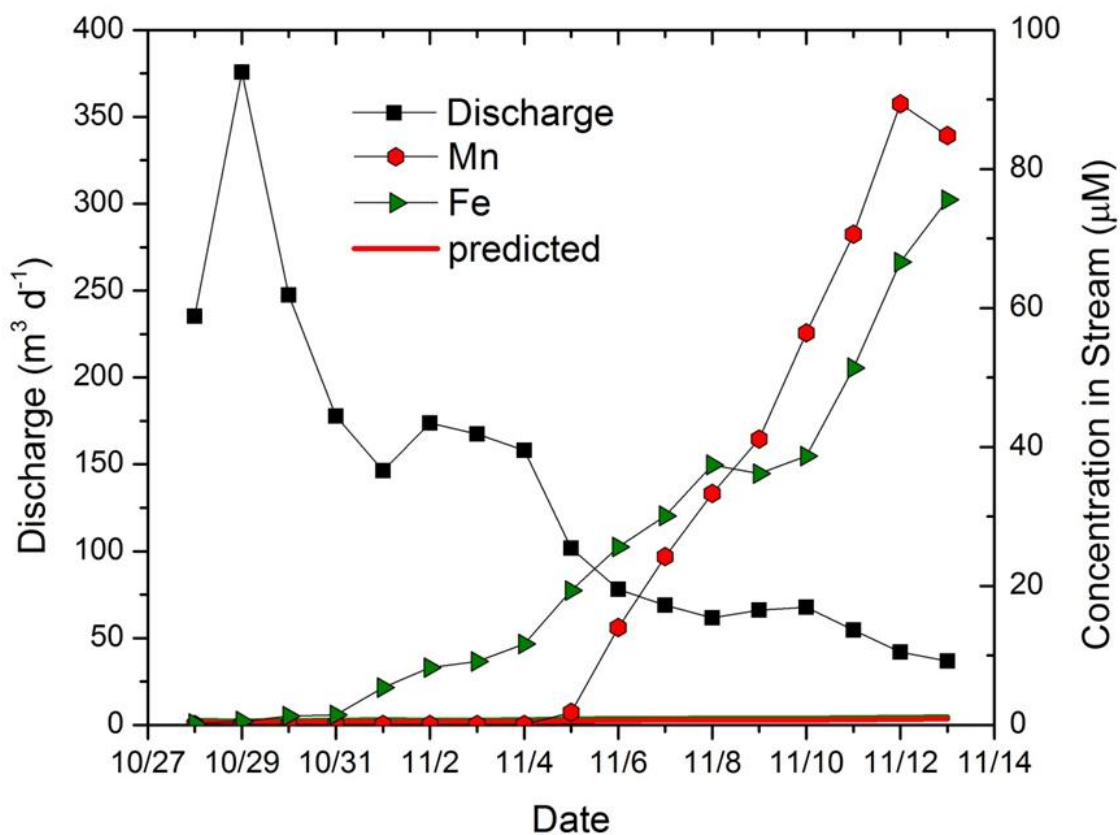


Figure D-8. Outliers for $C_{Fe,stream}$ (green right triangles) and $C_{Mn,stream}$ (red circles) occurred over a one week period in November 2009 and are plotted versus collection date with average daily discharge values (Q_{stream} , $m^3 d^{-1}$, black squares). Also plotted are the expected $C_{Mn,stream}$ (red line) and $C_{Fe,stream}$ (green line) values for calculated for Q_{stream} based on a best fit line to the values shown in Figure 5-6. Concentrations of Fe and Mn increase drastically following a period of high discharge, with Mn exhibiting a delayed response relative to Fe.

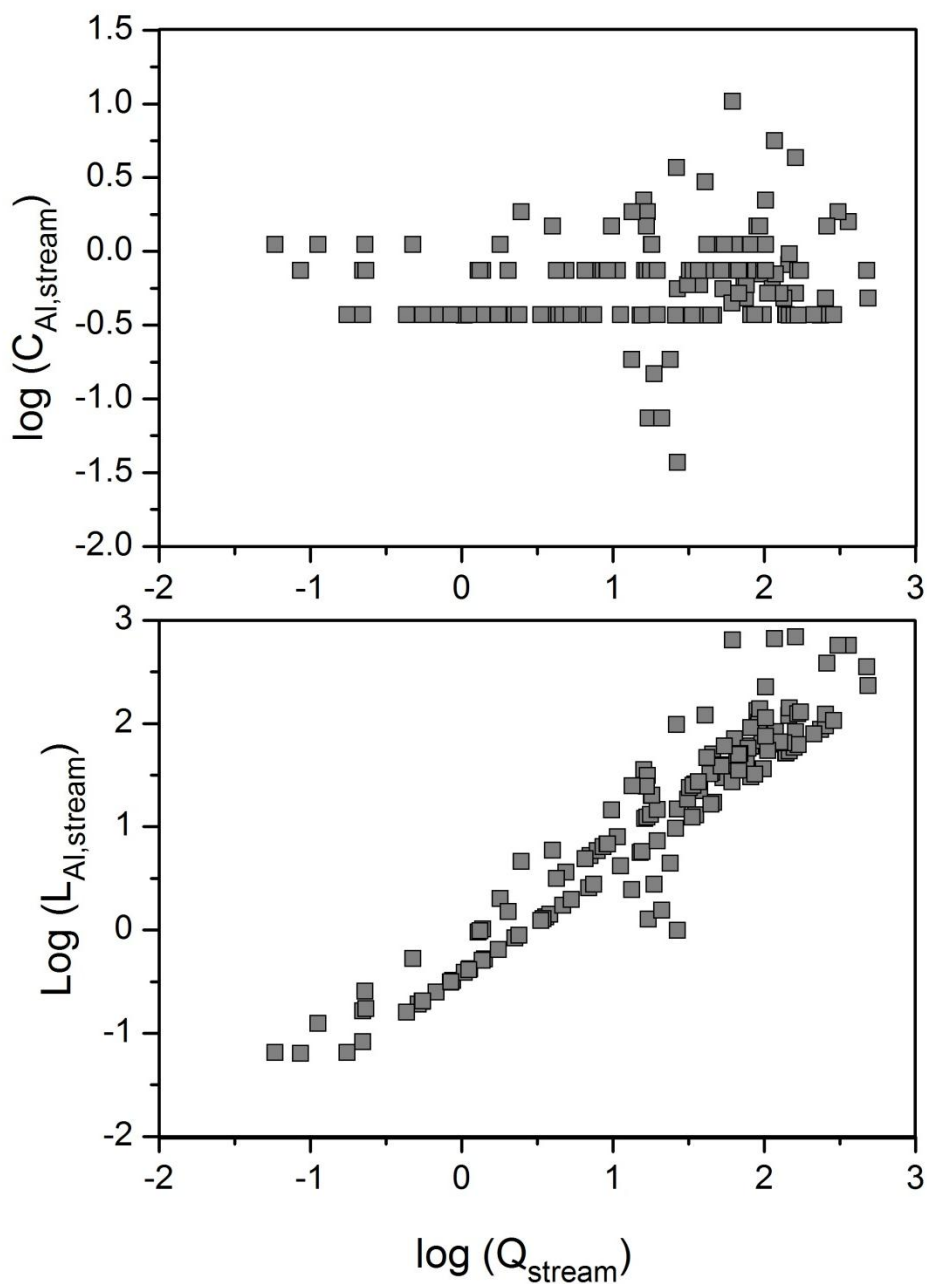


Figure D-9. Top) A log-log plot of concentrations of dissolved aluminum in stream water ($C_{Al,stream}$, μM) versus the stream discharge (Q_{stream} , $\text{m}^3 \text{d}^{-1}$). In contrast with all other measured elements (Fe, Mn, Na, Ca, Si, K, Mg), $C_{Al,stream}$ values increase at high discharge. **Bottom)** A log-log plot of the load of dissolved Al in stream water ($L_{Al,stream}$, mmol d^{-1}) plotted versus Q_{stream} . The slope of a best fit to these data points equals 1.05 (Table 5-3).

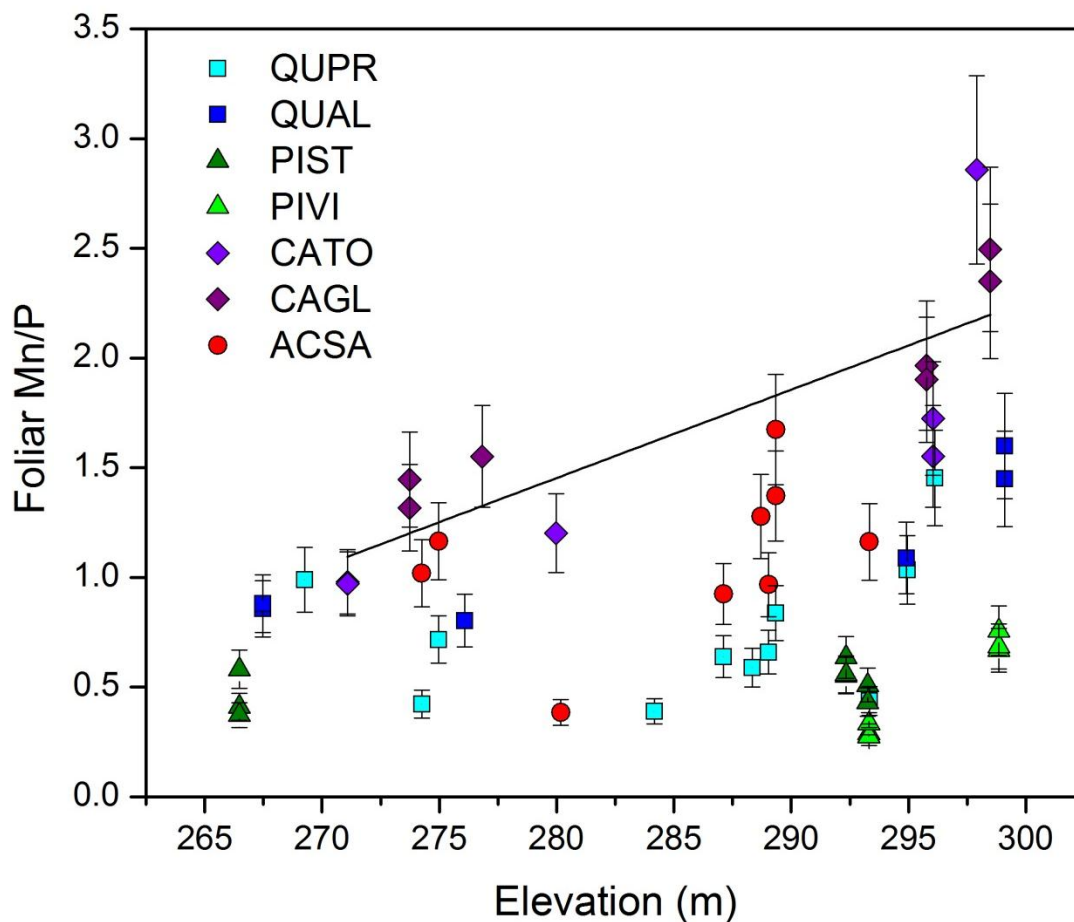


Figure D-10. Molar ratio of $C_{Mn,veg} : C_{P,veg}$ for green leaf samples plotted versus elevation, with the lowest elevations representing valley floor slope positions and the highest elevations representing ridge slope positions. $C_{Mn,veg} : C_{P,veg}$ increased with increasing elevation for hickory species only, as shown by the regression line ($R^2 = 0.65$, $p < 0.001$). Symbols are grouped by genus, including oak (QUPR/QUAL; blue squares), pine (PIST/PIVI; green triangles), hickory (CATO/CAGL; purple diamonds), and maple (ACSA; red circles). All leaf samples were collected in August and September prior to senescence.

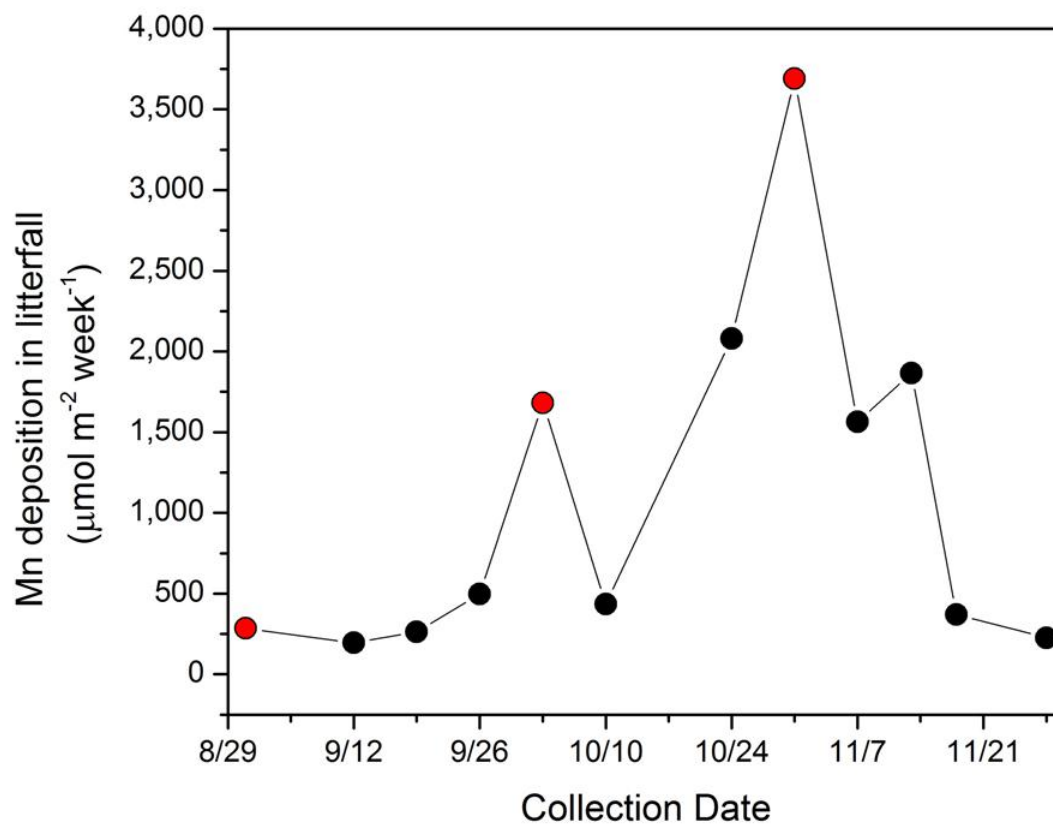


Figure D-11. Estimates for the rate of Mn delivered from trees to soils as litterfall between August – November 2011. These values are calculated as the product of litter mass measured each week (Smith, *pers. comm.*) and the concentration of Mn in leaf litter collected on three dates (red dots).

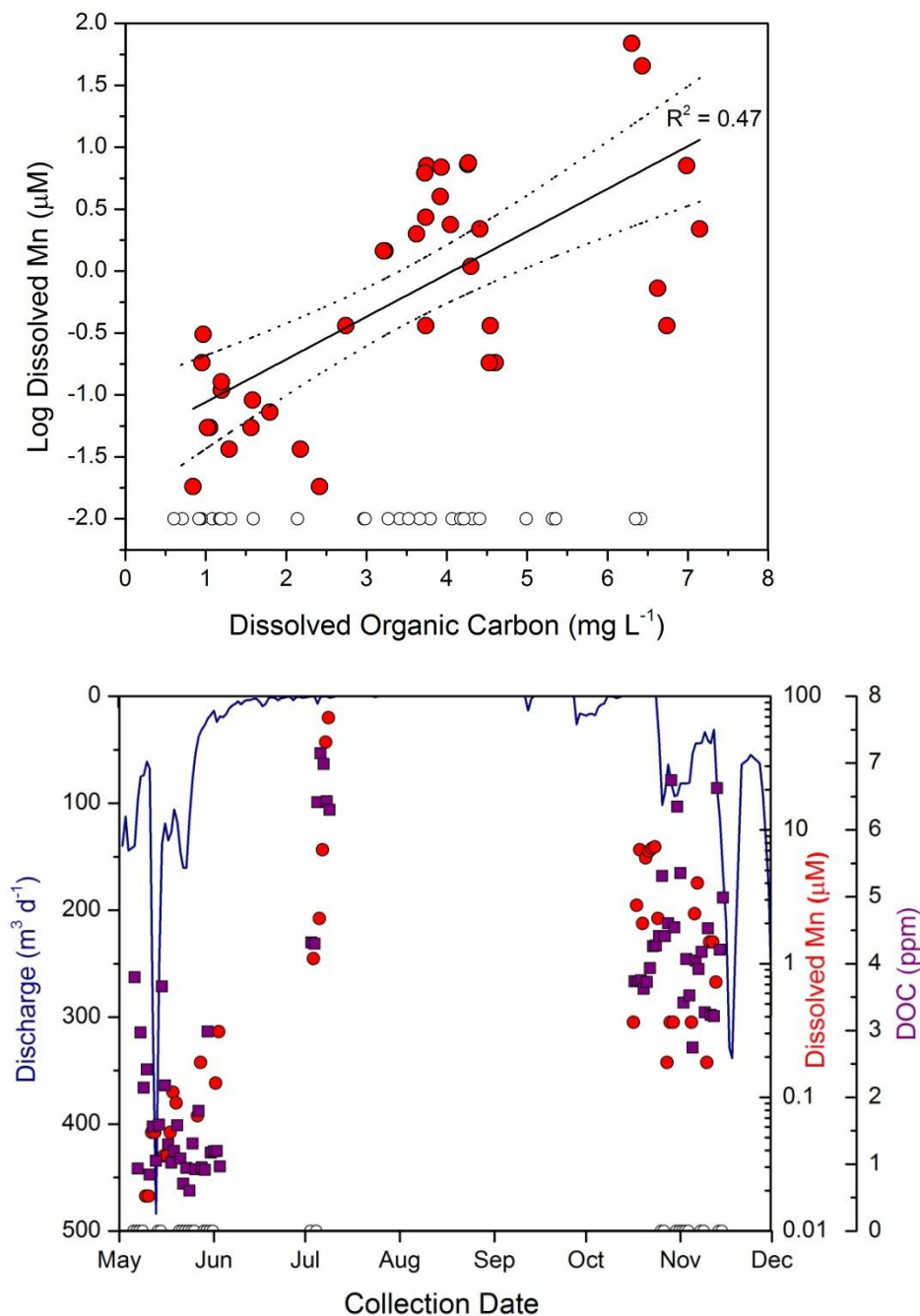


Figure D-12. Top) Concentrations of dissolved Mn in the stream ($C_{Mn,stream}$, μM) are strongly correlated with concentrations of dissolved organic carbon in the stream ($C_{DOC,stream}$, mg L^{-1}). **Bottom)** Concentrations of dissolved Mn and DOC are high in the summer and fall when discharge is low relative to the spring when discharge is high. In both graphs, $C_{Mn,stream}$ values that were below detection on ICP-AES (DL = $0.09 \mu\text{M}$) are plotted as open symbols.

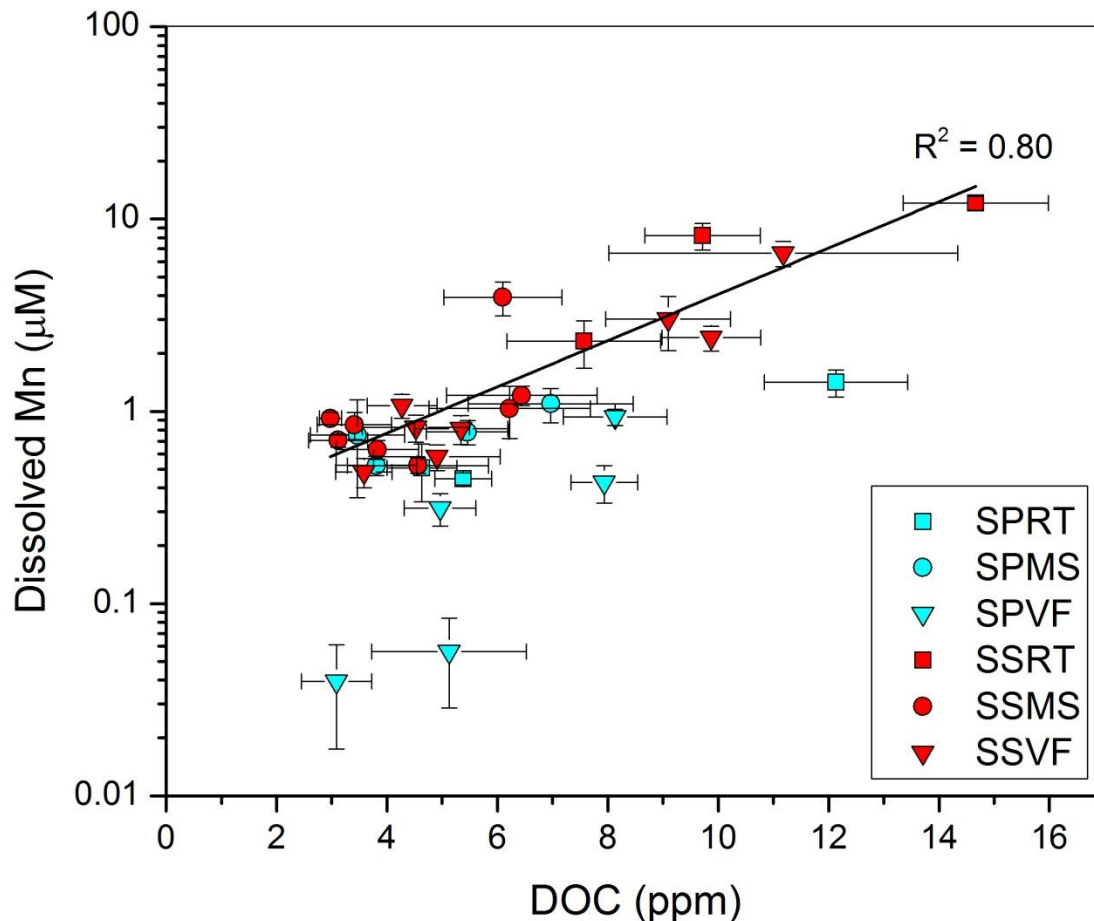


Figure D-13. Mn concentrations in pore fluids ($C_{Mn,pf}$, $\mu\text{mol L}^{-1}$) are plotted on a log-scale versus dissolved organic carbon (DOC) concentrations in pore fluids ($C_{DOC,pf}$, mg L^{-1}) for all depths in six soil profiles: soils at ridge, midslope, and valley positions on a planar transect (SPRT, SPMS, and SPVF respectively, blue symbols) and on a swale transect (SSRT, SSMS, and SSVF, red symbols). Dissolved Mn and DOC are significantly positively correlated in swale, but not planar, pore fluids ($p < 0.001$). Each symbol represents an average value for all concentrations measured at a single depth in each soil profile. Error bars indicate the standard error for Mn and DOC concentrations at each depth. Data are adapted from Andrews (2011).

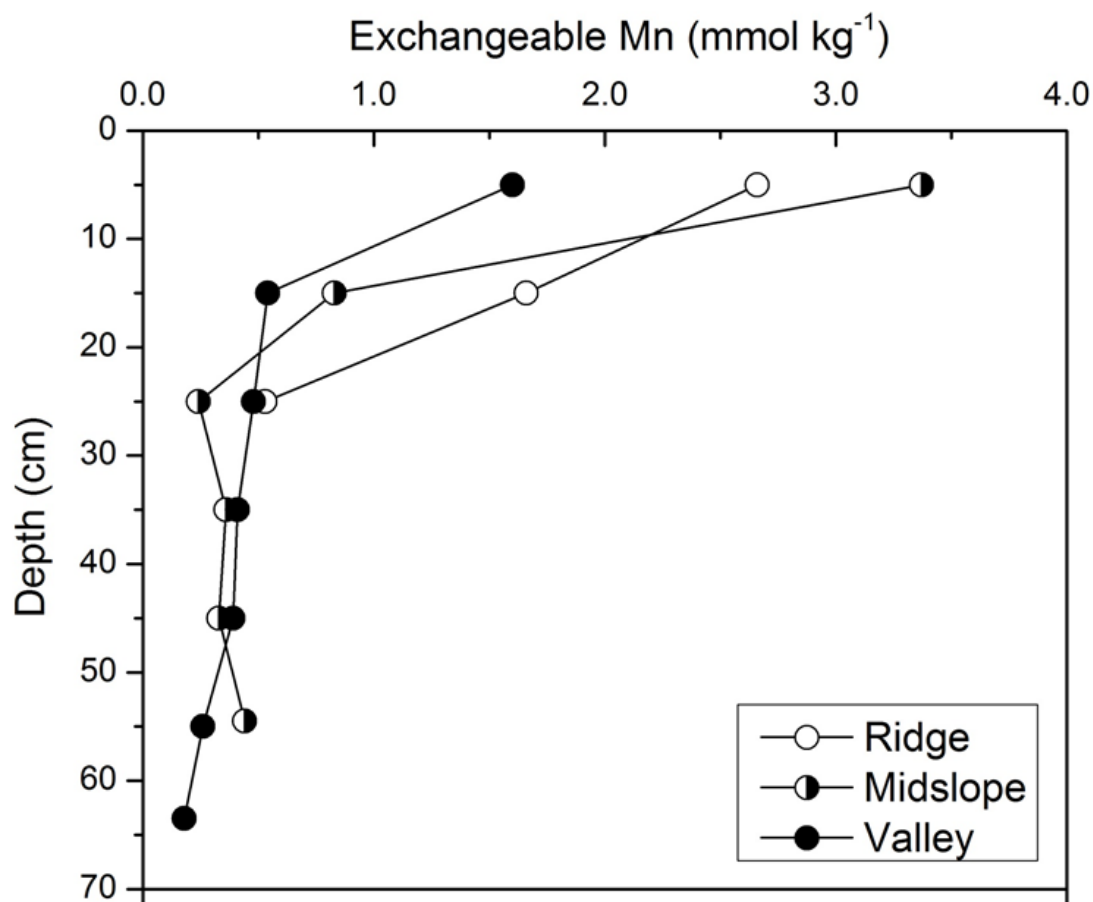


Figure D-14. Concentrations of Mn held in the cation exchange capacity ($C_{Mn,CEC}$, mmol kg⁻¹) of soils versus depth for soils augered at ridge (open symbols), midslope (half-filled symbols), and valley floor (closed symbols) positions on the south planar transect. Data were acquired from Jin et al. (2010).

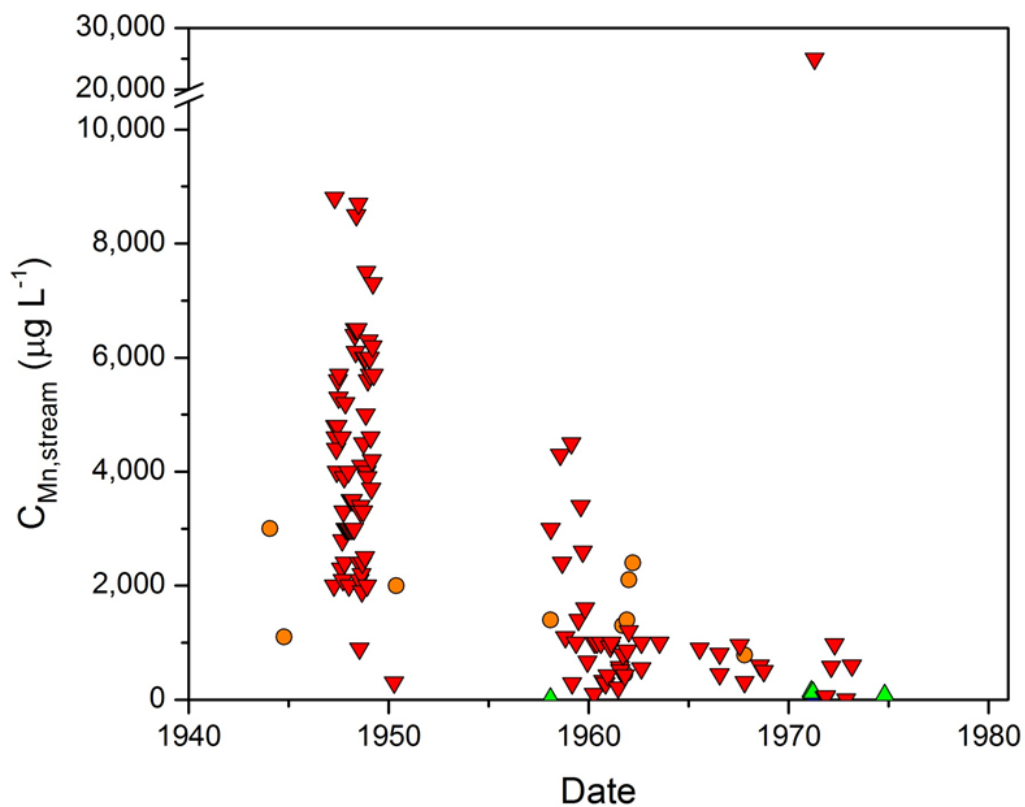


Figure D-15. Dissolved Mn concentrations ($C_{Mn,stream}$, $\mu\text{g L}^{-1}$) reported for four sites along the Lackawanna River between 1944 – 1973 (USGS). $C_{Mn,stream}$ values are high prior to 1960 and decline rapidly prior to the peak in $C_{Mn,stream}$ reported for the Susquehanna River (Figure 5-12).

Table D-1. 2002 Precipitation chemistry for NADP sites PA-15 and PA-42

SITE	Date On	Date off	pH	Mg ng g ⁻¹	Al ng g ⁻¹	K ng g ⁻¹	Ca ng g ⁻¹	Mn ng g ⁻¹	Fe ng g ⁻¹	Cu ng g ⁻¹	Zn ng g ⁻¹	Cd ng g ⁻¹	Pb ng g ⁻¹
PA15	1/1	1/8	4.78	6.391	3.355	1.058	76.17	0.588	1.088	8.021	3.495	0.025	1.684
PA15	1/15	1/22	4.31	42.14	9.491	7.446	328.3	2.100	3.953	25.86	4.643	0.028	5.252
PA42	1/22	1/29	4.40	8.701	7.165	2.901	123.6	1.155	2.887	28.71	11.29	0.019	7.014
PA15	1/29	2/5	4.15	22.08	9.991	15.78	99.33	1.391	4.497	19.88	7.788	0.026	6.375
PA15	2/5	2/12	4.29	25.13	3.823	8.073	49.21	0.463	1.948	8.499	5.339	0.011	2.814
PA15	2/19	2/26	4.63	131.7	23.06	52.51	768.8	5.107	5.351	54.45	17.71	0.037	14.56
PA15	2/26	3/5		11.67	4.582	6.774	95.71	0.779	3.249	7.848	10.44	0.015	2.318
PA15	3/12	3/19	4.39	29.22	19.34	22.08	412.6	2.796	4.026	6.129	4.932	0.014	1.701
PA42	3/12	3/19	4.48	16.74	4.144	14.04	177.5	1.682	2.029	5.976	4.528	0.014	1.504
PA15	3/19	3/26		70.10	3.597	784.4	529.8	5.312	0.784	5.033	14.27	0.044	0.873
PA15	3/26	4/2		14.38	5.158	17.19	123.8	1.196	3.385	10.92	3.790	0.018	2.571
PA15	4/9	4/16	4.65	11.76	2.434	10.94	61.18	0.746	1.545	4.066	4.330	0.023	1.305
PA15	4/16	4/23		83.22	22.31	86.4	578.4	7.944	8.084	36.30	27.50	0.098	9.869
PA15	4/23	4/30	4.43	40.66	5.671	42.74	263.4	4.119	2.216	7.970	7.849	0.025	1.755
PA42	4/30	5/7	4.36	32.03	5.368	30.77	200.9	3.117	4.410	8.728	5.674	0.017	2.309
PA15	4/30	5/7	4.20	26.41	8.063	40.43	182.4	2.991	4.749	11.84	12.58	0.019	3.416
PA42	5/7	5/14	4.29	28.02	5.498	29.15	138.2	2.244	4.381	9.166	5.683	0.016	2.750
PA15	5/7	5/14	4.36	21.12	4.987	22.54	122.1	1.879	2.135	5.967	2.500	0.011	1.470
PA15	5/14	5/21	4.79	8.180	3.004	11.48	62.12	1.600	1.475	2.901	2.477	0.010	0.843
PA42	5/14	5/21	4.77	11.65	3.11	53.55	65.53	1.971	0.535	4.882	3.618	0.008	1.324
PA42	5/28	6/4	4.41	32.34	5.645	43.6	171.4	3.099	3.639	4.582	2.488	0.023	1.755
PA15	5/28	6/4		81.62	16.97	97.25	403.8	11.18	13.99	18.95	16.15	0.040	5.132
PA42	6/4	6/11	4.34	10.42	2.869	8.845	72.90	0.988	2.595	4.765	2.887	0.006	1.239
PA15	6/4	6/11		20.03	4.855	11.08	104.2	2.104	0.966	7.390	5.673	0.017	0.453
PA42	6/11	6/18	4.24	19.56	4.935	15.03	118.2	1.708	4.563	7.518	8.517	0.022	3.925
PA15	6/18	6/25	3.99	47.24	12.56	6.463	259.0	3.175	8.759	11.18	12.06	0.047	3.804
PA42	6/18	6/25	3.94	44.26	11.03	21.16	194.1	2.472	11.01	18.57	12.17	0.051	6.592
PA42	6/25	7/2	3.96	54.39	9.658	10.23	223.3	2.160	9.756	17.29	6.811	0.007	4.876
PA15	6/25	7/2	4.14	24.75	6.572	6.629	131.7	1.723	5.527	7.192	6.453	0.005	1.907
PA42	7/9	7/16	4.07	28.84	14.26	3.806	182.8	1.938	9.993	38.52	26.67	0.045	11.51
PA15	7/9	7/16	3.84	42.66	22.25	12.66	306.6	3.345	19.93	46.08	25.20	0.049	8.570
PA42	7/16	7/23		181.7	32.78	31.54	788.9	7.005	31.20	48.13	45.53	0.090	12.20
PA42	7/23	7/30	4.14	23.15	7.332	10.87	111.4	1.868	7.284	10.05	8.415	0.006	2.005
PA15	7/23	7/30	3.96	42.48	34.98	57.43	384.4	6.686	15.53	21.58	25.27	0.027	4.124
PA42	7/30	8/6	4.07	30.67	7.332	11.98	139.8	1.668	5.441	14.27	11.14	0.019	2.572
PA15	7/30	8/6	4.16	41.11	20.95	20.14	293.3	5.477	7.836	58.17	21.81	0.049	11.04
PA15	8/6	8/13		167.3	38.51	36.2	973.7	10.73	45.00	30.87	27.26	0.088	9.260
PA42	8/13	8/20	4.00	33.72	14.85	16.63	262.3	3.979	11.91	22.29	12.42	0.030	4.564
PA15	8/13	8/20	3.85	35.89	15.73	11.53	189.5	2.120	11.65	25.50	18.76	0.015	6.440
PA42	8/20	8/27	4.08	13.90	6.783	16.09	102.4	1.652	6.155	13.42	4.157	0.020	2.185

SITE	Date On	Date off	pH	Mg ng g ⁻¹	Al ng g ⁻¹	K ng g ⁻¹	Ca ng g ⁻¹	Mn ng g ⁻¹	Fe ng g ⁻¹	Cu ng g ⁻¹	Zn ng g ⁻¹	Cd ng g ⁻¹	Pb ng g ⁻¹
PA15	8/20	8/27	3.90	31.14	18.48	16.09	297.6	5.259	11.37	13.10	10.58	0.036	2.808
PA42	8/27	9/3	4.20	18.15	28.13	7.406	272.1	2.442	7.781	45.95	25.72	0.041	9.633
PA15	9/10	9/17	4.71	3.383	2.246	0.597	21.45	0.287	1.232	26.26	49.54	0.007	4.172
PA42	9/10	9/17	4.76	5.787	1.515	0.619	22.67	0.361	0.248	13.47	10.44	0.011	1.386
PA42	9/17	9/24	4.36	10.86	2.044	2.778	24.38	0.376	1.671	11.23	2.221	0.014	1.678
PA42	9/24	10/1	4.88	3.744	0.659	< DL	18.32	0.161	0.584	6.262	1.809	< DL	0.774
PA15	10/1	10/8		63.67	21.54	174.9	355.8	4.527	10.51	61.42	18.43	0.148	11.18
PA42	10/8	10/15	4.51	1.453	0.952	< DL	12.35	3.913	467.9	13.08	3.220	0.013	2.251
PA15	10/8	10/15	4.63	2.304	1.804	< DL	18.59	0.133	5.196	5.840	2.394	0.007	1.532
PA42	10/15	10/22	4.69	15.08	0.998	< DL	47.32	0.411	0.978	7.357	5.234	0.012	2.540
PA42	10/22	10/29	4.45	1.123	0.706	< DL	11.61	0.140	0.974	14.23	5.534	0.013	2.722
PA15	10/22	10/29	4.46	1.007	0.807	< DL	9.360	0.097	0.474	8.777	3.849	0.010	2.180
PA42	10/29	11/5	4.57	8.856	1.097	< DL	33.70	0.313	1.408	9.891	2.873	0.037	1.701
PA15	10/29	11/5		3.692	1.777	0.543	47.35	0.323	1.246	6.440	3.093	0.018	1.726
PA42	11/5	11/12	4.59	5.908	1.42	4.48	47.85	0.652	0.993	7.204	1.859	0.019	1.116
PA15	11/5	11/12	4.53	10.90	1.921	2.253	79.40	0.893	1.318	12.50	4.611	0.022	2.254
PA42	11/12	11/19	4.50	2.804	1.552	< DL	31.04	0.250	1.295	14.79	5.483	0.013	2.737
PA42	11/26	12/3	4.47	51.51	8.746	12.01	371.0	3.953	2.809	23.43	6.738	0.046	2.766
PA42	12/3	12/10	5.04	2.381	1.479	< DL	27.88	0.163	1.348	10.41	3.357	0.006	1.389
PA42	12/10	12/17	4.52	1.447	1.786	< DL	22.50	0.161	1.067	7.112	3.311	0.006	0.979
PA42	12/17	12/24	4.43	17.38	3.358	11.94	78.57	0.680	3.082	28.59	11.25	0.115	5.832
	Average		4.37	30.82	8.984	38.10	192.2	2.455	13.43	17.16	10.52	0.029	3.922
	<i>Std.Dev.</i>		<i>0.04</i>	<i>4.63</i>	<i>1.19</i>	<i>14.29</i>	<i>26.01</i>	<i>0.32</i>	<i>7.70</i>	<i>1.86</i>	<i>1.30</i>	<i>0.004</i>	<i>0.43</i>

Table D-1B. Quality Control measurements

	Mg ng g ⁻¹	Al ng g ⁻¹	K ng g ⁻¹	Ca ng g ⁻¹	Mn ng g ⁻¹	Fe ng g ⁻¹	Cu ng g ⁻¹	Zn ng g ⁻¹	Cd ng g ⁻¹	Pb ng g ⁻¹
Control 1	4.202	26.880	0.465	234.9	0.041	0.804	1.843	0.914	0.013	0.066
Control 2	0.168	0.534	-0.268	5.938	0.007	0.303	2.042	0.917	0.003	0.027
Control 3	0.290	0.455	-0.495	5.259	0.007	0.242	1.262	0.683	0.001	0.023
Control 4	0.215	0.489	-0.442	4.122	0.006	0.376	2.764	0.657	0.001	0.031
Control 5	0.115	0.219	-0.454	3.210	0.000	0.115	1.597	0.366	0.001	0.022
Control 6	0.206	0.596	-0.628	5.269	0.005	0.233	1.127	0.300	0.001	0.015
Control 7	0.177	0.488	-1.138	4.810	0.004	0.200	1.317	0.240	0.001	0.016
<i>Average</i>	0.768	4.237	-0.423	37.644	0.010	0.325	1.707	0.582	0.003	0.029
<i>Std. Dev.</i>	1.515	9.985	0.478	86.986	0.014	0.226	0.570	0.283	0.004	0.017
NIST 1643e	7,415	137.4	1,970	30,140	37.01	93.62	19.39	66.24	6.097	20.62
Cert. Value	7,841	138.3	1,984	31,500	38.02	95.70	22.20	76.50	6.408	19.15
%Error	-5.43	-0.67	-0.71	-4.32	-2.66	-2.17	-12.66	-13.41	-4.853	7.68

Controls 1-7 consist of distilled water used to rinse the precipitation collection buckets. Control 1 is exceptionally high in most elements.

Table D-2. Average concentrations of elements in pore fluids on the north slope

Site		Al	Ca	K	Mg	Na	Si	Fe	Mn
		μM							
NPRT	Average	7.10	158.79	37.41	47.87	26.49	155.38	0.65	1.22
n = 51	StdError	0.34	11.20	2.30	3.36	2.23	9.42	0.21	0.22
NPMS	Average	4.04	66.61	25.98	42.79	25.92	143.00	0.76	1.29
n = 146	StdError	0.49	4.46	1.13	1.32	1.56	5.43	0.23	0.12
NPVF	Average	6.32	30.08	25.74	54.23	25.31	157.95	0.73	0.96
n = 136	StdError	0.86	1.00	2.12	1.86	1.15	4.68	0.10	0.09
Planar	Average	5.35	65.46	27.59	48.22	25.75	150.95	0.73	1.14
n = 333	StdError	0.41	3.51	1.08	1.12	0.89	3.39	0.11	0.07
NSRT	Average	3.17	55.86	43.14	18.56	36.54	124.52	0.10	0.87
n = 9	StdError	0.37	5.08	2.15	1.45	5.76	18.13	0.05	0.13
NSMS	Average	2.01	48.73	29.98	58.88	41.85	143.85	0.18	2.64
n = 28	StdError	0.39	5.20	4.42	7.26	4.68	9.88	0.05	0.44
NSVF	Average	1.50	31.45	21.66	79.23	35.03	132.71	0.12	1.20
n = 44	StdError	0.38	4.65	2.07	4.16	2.66	5.37	0.04	0.20
Swale	Average	1.86	40.14	26.92	65.46	37.56	135.65	0.14	1.66
n = 81	StdError	0.26	3.31	2.04	3.97	2.26	4.90	0.03	0.20

Table D-3. Concentrations of elements (μM) and discharge ($\text{m}^3 \text{d}^{-1}$) at the SSHCZO weir

Date	Discharge	Al	Ca	K	Mg	Na	Si	Fe	Mn
03/28/08	105.48	-	142.22	22.25	82.27	21.75	89.00	0.36	< 0.09
03/29/08	105.24	-	132.24	20.97	78.16	22.18	89.00	0.36	< 0.09
03/30/08	105.78	-	127.25	21.23	78.16	22.18	85.44	0.36	< 0.09
03/31/08	105.78	-	137.23	22.76	82.27	26.97	89.00	0.36	< 0.09
04/01/08	98.51	0.37	138.92	20.26	79.43	23.24	73.62	0.13	< 0.09
04/01/08	98.51	-	144.71	23.02	82.27	22.62	89.00	0.36	< 0.09
04/02/08	82.35	-	152.20	23.27	82.27	24.36	89.00	0.36	< 0.09
04/03/08	78.66	-	162.18	22.51	86.38	23.92	89.00	0.36	< 0.09
04/04/08	84.71	-	157.19	23.02	86.38	23.49	110.36	0.36	< 0.09
04/05/08	81.02	0.74	154.69	25.32	86.38	26.53	96.12	0.36	< 0.09
04/06/08	99.90	-	139.72	23.27	82.27	23.05	92.56	0.36	< 0.09
04/07/08	104.73	-	137.23	23.02	82.27	23.05	92.56	0.36	< 0.09
04/08/08	82.13	-	139.72	23.27	82.27	22.62	92.56	0.36	< 0.09
04/09/08	78.74	-	144.71	23.53	82.27	23.92	96.12	0.36	< 0.09
04/10/08	61.04	-	149.70	23.53	82.27	23.49	89.00	0.36	< 0.09
04/11/08	68.34	-	154.69	23.79	82.27	23.49	89.00	0.36	< 0.09
04/12/08	64.14	-	157.19	23.79	86.38	23.49	92.56	0.36	< 0.09
04/13/08	98.40	-	144.71	23.27	86.38	23.05	92.56	0.36	< 0.09
04/14/08	98.75	-	139.72	23.53	86.38	24.36	89.00	0.36	< 0.09
04/15/08	136.47	-	144.71	24.04	86.38	25.66	92.56	0.36	< 0.09
04/16/08	126.67	-	144.71	23.79	86.38	23.92	92.56	0.36	< 0.09
04/17/08	80.03	-	147.21	23.79	86.38	23.49	92.56	0.36	< 0.09
04/18/08	69.03	-	154.69	25.32	94.61	34.36	92.56	0.36	< 0.09
04/24/08	146.08	0.96	124.43	23.73	80.21	22.59	77.18	0.18	< 0.09
04/30/08	359.19	1.59	111.73	21.71	73.10	22.88	71.41	0.16	< 0.09
05/02/08	139.91	-	147.21	24.30	82.27	22.18	92.56	0.36	< 0.09
05/03/08	112.17	-	159.68	24.55	86.38	22.62	92.56	0.54	< 0.09
05/04/08	144.35	-	137.23	24.55	82.27	22.18	92.56	0.36	< 0.09
05/06/08	139.91	0.37	131.06	22.20	80.91	23.74	77.25	0.48	< 0.09
05/07/08	96.88	0.70	146.36	22.15	83.09	24.75	77.39	0.54	< 0.09
05/08/08	75.17	0.48	161.35	25.01	88.56	28.50	79.42	0.57	< 0.09
05/09/08	73.75	0.59	167.81	22.74	90.54	28.27	81.10	0.61	< 0.09
05/10/08	61.04	0.44	172.88	23.76	92.02	27.41	80.81	0.56	< 0.09
05/11/08	67.72	0.52	163.60	22.86	90.42	26.37	80.63	0.54	< 0.09
05/12/08	307.58	1.85	105.31	21.87	78.16	22.08	77.00	0.59	0.05
05/13/08	483.94	0.48	99.53	21.92	75.94	22.04	76.65	0.45	0.05
05/14/08	254.71	0.37	122.73	21.41	75.69	22.64	74.40	0.43	< 0.09
05/14/08	254.71	0.48	121.61	21.41	79.68	22.79	78.03	0.48	< 0.09
05/15/08	138.39	0.37	140.29	22.66	82.72	24.62	79.39	0.50	< 0.09

Date	Discharge	Al	Ca	K	Mg	Na	Si	Fe	Mn
05/16/08	118.67	0.70	150.97	22.43	83.34	24.47	78.18	0.70	< 0.09
05/17/08	134.98	0.48	128.99	22.30	80.34	23.49	77.61	0.54	< 0.09
05/18/08	127.02	0.52	134.28	21.69	79.64	22.72	76.75	0.54	0.05
05/19/08	105.78	0.52	135.15	21.41	81.90	23.81	77.82	0.54	0.11
05/20/08	117.16	5.63	139.82	21.89	87.37	23.41	81.17	0.70	0.09
05/21/08	145.60	0.82	127.45	22.38	79.76	23.17	76.90	0.66	< 0.09
05/22/08	160.39	0.52	126.95	21.56	82.64	23.07	79.85	0.52	< 0.09
05/23/08	160.39	4.30	134.41	21.36	85.81	23.15	80.85	0.52	< 0.09
05/24/08	113.27	0.56	151.62	21.94	86.01	23.58	80.03	0.59	< 0.09
05/25/08	76.28	0.59	171.41	27.75	90.74	27.84	79.74	0.61	< 0.09
05/26/08	53.31	0.56	187.80	22.76	91.57	26.13	79.14	0.63	< 0.09
05/27/08	37.48	0.59	206.41	26.45	98.97	28.65	83.02	0.75	0.07
05/28/08	31.07	0.59	224.98	23.35	100.00	28.22	80.70	0.81	0.18
05/29/08	26.69	0.04	219.34	24.96	104.40	31.88	82.91	0.68	< 0.09
05/29/08	26.69	0.56	238.70	24.88	104.40	35.04	81.59	0.72	0.05
05/30/08	21.06	0.07	231.84	24.81	104.32	28.83	81.49	0.73	< 0.09
05/31/08	17.10	0.07	241.87	27.29	104.52	30.10	80.46	0.79	< 0.09
06/01/08	13.28	0.19	254.82	27.67	108.60	31.13	82.81	1.00	< 0.09
06/02/08	23.90	0.19	272.43	27.52	113.45	32.69	82.06	0.54	0.13
06/03/08	18.74	0.15	282.96	28.52	118.06	36.22	84.09	0.84	0.31
06/04/08	19.68	0.74	306.89	38.36	123.41	31.32	99.68	1.07	< 0.09
06/05/08	16.75	0.74	319.36	35.81	127.52	31.75	106.80	1.25	< 0.09
06/06/08	11.24	0.37	351.80	35.81	139.86	33.06	110.36	1.07	< 0.09
06/07/08	8.62	0.74	376.75	30.69	143.97	33.49	113.92	2.15	< 0.09
06/08/08	6.93	0.37	424.15	38.36	164.54	33.49	117.48	1.25	< 0.09
06/09/08	4.67	0.37	474.05	40.92	181.00	36.97	121.04	1.79	1.82
06/10/08	7.46	0.37	531.44	43.48	197.45	36.54	131.72	1.97	21.83
06/11/08	4.25	0.74	471.56	48.59	176.88	36.97	117.48	5.01	20.01
06/12/08	3.47	0.37	439.12	35.81	156.31	36.10	110.36	1.79	3.46
06/13/08	3.34	0.37	513.97	43.48	176.88	37.84	121.04	2.69	8.37
06/14/08	2.25	0.37	561.38	46.04	189.22	41.32	124.60	2.15	5.27
06/15/08	2.39	0.37	578.84	43.48	189.22	44.37	124.60	1.97	8.00
06/16/08	5.31	0.37	551.40	43.48	185.11	40.02	121.04	2.15	13.10
06/17/08	9.19	0.74	436.63	43.48	156.31	36.97	106.80	2.86	0.91
06/18/08	6.93	0.37	466.57	38.36	164.54	38.71	106.80	2.69	2.18
06/19/08	1.38	0.74	484.03	38.36	172.77	39.58	110.36	2.69	3.27
06/20/08	1.13	0.37	439.12	35.81	160.43	40.45	103.24	0.90	< 0.09
06/20/08	1.13	0.37	461.58	33.25	160.43	36.97	103.24	2.33	< 0.09
06/21/08	1.42	0.37	503.99	35.81	176.88	37.84	110.36	3.94	< 0.09
06/22/08	3.60	0.37	546.41	43.48	189.22	40.89	113.92	3.58	< 0.09

Date	Discharge	Al	Ca	K	Mg	Na	Si	Fe	Mn
06/23/08	1.75	0.37	591.32	40.92	197.45	40.02	117.48	3.58	< 0.09
06/24/08	1.37	0.37	588.82	46.04	193.34	40.89	117.48	3.22	1.64
06/25/08	0.52	0.37	616.27	43.48	201.56	42.19	117.48	3.58	2.73
06/26/08	0.43	0.37	648.70	43.48	205.68	43.50	121.04	3.58	6.00
06/27/08	3.83	0.37	573.85	46.04	189.22	40.02	110.36	2.33	< 0.09
06/28/08	0.68	0.37	583.83	48.59	197.45	40.02	110.36	2.69	3.82
06/29/08	0.55	0.37	656.19	51.15	209.79	41.76	117.48	2.15	6.18
06/30/08	1.29	0.74	633.73	46.04	201.56	41.32	117.48	2.33	13.28
07/01/08	1.11	0.37	663.67	48.59	205.68	42.63	121.04	2.86	27.28
07/02/08	0.55	0.37	656.19	46.04	205.68	44.80	128.16	6.80	30.92
07/03/08	0.18	0.37	708.58	48.59	205.68	42.19	128.16	6.62	< 0.09
07/03/08	0.18	0.37	631.24	33.25	181.00	45.67	113.92	0.72	1.27
07/04/08	0.20	-	753.49	46.04	213.90	41.76	131.72	4.48	1.09
07/05/08	7.06	0.74	451.60	46.04	156.31	33.93	106.80	10.03	< 0.09
07/06/08	0.55	0.37	536.43	51.15	181.00	35.67	117.48	5.73	2.18
07/07/08	0.22	0.37	591.32	51.15	189.22	37.41	121.04	4.83	7.09
07/08/08	0.23	0.74	631.24	51.15	201.56	38.28	128.16	15.40	45.47
07/09/08	1.32	0.74	688.62	53.71	222.13	39.58	138.84	21.49	69.12
07/10/08	0.84	0.37	563.87	46.04	176.88	42.63	117.48	2.15	< 0.09
07/24/08	0.85	0.37	563.87	51.15	176.88	40.02	110.36	14.68	16.55
09/12/08	13.42	1.85	286.93	63.94	102.84	29.58	81.88	8.06	1.27
09/13/08	2.48	1.85	289.42	56.27	102.84	29.14	85.44	10.38	7.82
09/28/08	26.28	3.71	261.98	46.04	106.95	32.62	89.00	8.77	< 0.09
09/29/08	15.98	2.22	289.42	43.48	115.18	35.67	99.68	6.98	< 0.09
09/30/08	16.87	1.85	286.93	35.81	111.07	35.23	103.24	4.83	0.91
10/01/08	18.06	1.11	264.47	35.81	102.84	34.80	99.68	3.04	0.73
10/02/08	16.64	1.48	276.95	33.25	102.84	35.67	103.24	2.69	1.09
10/03/08	16.24	0.74	261.98	30.69	94.61	33.06	99.68	1.97	< 0.09
10/04/08	17.71	0.74	266.97	30.69	94.61	33.06	99.68	1.97	< 0.09
10/05/08	10.73	0.74	266.97	28.13	94.61	32.62	99.68	1.97	< 0.09
10/06/08	7.88	0.74	271.96	28.13	90.50	32.62	99.68	2.15	< 0.09
10/07/08	6.57	0.74	276.95	28.13	94.61	33.06	99.68	2.33	0.55
10/08/08	0.09	0.74	279.44	30.69	94.61	33.06	103.24	2.86	0.73
10/09/08	0.22	0.74	284.43	30.69	98.72	33.49	103.24	3.76	2.91
10/10/08	0.23	1.11	289.42	30.69	94.61	33.93	99.68	3.76	< 0.09
10/11/08	1.80	1.11	284.43	30.69	94.61	33.93	99.68	4.30	< 0.09
10/12/08	0.88	0.37	281.94	30.69	94.61	32.62	99.68	3.04	< 0.09
10/25/08	40.53	2.97	247.01	58.82	106.95	32.19	74.76	5.01	2.18
10/26/08	101.71	2.22	157.19	38.36	94.61	30.01	99.68	2.33	< 0.09
10/26/08	101.71	1.11	139.72	35.81	94.61	26.10	99.68	1.07	0.36

Date	Discharge	Al	Ca	K	Mg	Na	Si	Fe	Mn
10/27/08	89.32	1.48	154.69	33.25	90.50	29.58	103.24	1.79	< 0.09
10/28/08	63.61	1.11	159.68	28.13	90.50	27.84	99.68	1.43	0.18
10/29/08	81.51	1.11	172.16	30.69	90.50	28.71	99.68	1.61	0.36
10/30/08	93.38	1.48	184.63	30.69	94.61	30.45	99.68	1.79	0.36
10/31/08	92.31	1.11	192.12	28.13	94.61	29.14	99.68	1.61	< 0.09
11/01/08	81.59	0.74	207.09	28.13	94.61	30.88	99.68	1.61	< 0.09
11/02/08	81.59	0.74	209.58	28.13	94.61	30.88	103.24	2.15	< 0.09
11/03/08	81.59	0.37	219.56	28.13	94.61	31.32	103.24	2.33	< 0.09
11/04/08	80.93	0.74	229.54	28.13	94.61	31.75	106.80	2.51	< 0.09
11/05/08	53.38	0.74	239.52	28.13	98.72	32.19	106.80	3.22	0.36
11/06/08	43.92	0.74	252.00	30.69	98.72	33.06	106.80	4.48	2.36
11/07/08	43.92	0.74	256.99	28.13	98.72	33.49	110.36	4.12	4.00
11/08/08	43.76	-	249.50	30.69	98.72	32.19	106.80	2.86	< 0.09
11/09/08	33.38	-	249.50	28.13	98.72	32.62	110.36	3.58	< 0.09
11/10/08	41.30	-	249.50	28.13	98.72	33.49	106.80	3.94	0.18
11/11/08	43.99	-	274.45	28.13	98.72	33.06	106.80	4.48	1.46
11/12/08	30.96	-	249.50	30.69	98.72	34.36	106.80	4.48	1.46
11/13/08	86.80	0.37	232.04	38.36	102.84	33.49	92.56	3.22	0.73
11/14/08	114.49	-	184.63	33.25	98.72	31.75	99.68	1.07	< 0.09
11/15/08	166.74	0.74	132.24	33.25	90.50	26.97	99.68	1.25	< 0.09
03/14/09	53.09	-	144.71	22.51	90.50	26.53	89.00	0.18	0.18
03/16/09	69.68	-	149.70	23.79	90.50	27.40	92.56	0.18	0.36
03/18/09	97.51	-	132.24	23.27	86.38	26.53	92.56		0.18
04/04/09	351.54	-	104.79	23.79	74.04	23.05	89.00		0.18
04/05/09	201.75	-	114.77	25.06	78.16	25.23	89.00		0.18
04/06/09	90.03	-	129.74	24.04	82.27	24.79	89.00		0.36
04/07/09	90.74	-	132.24	24.30	86.38	26.53	92.56		0.36
04/17/09	259.22	1.48	72.36	25.58	61.70	29.58	81.88		0.73
05/05/09	213.40	0.37	99.80	30.69	78.16	31.75	96.12		0.18
05/07/09	474.56	0.74	84.83	25.58	69.93	23.05	89.00		0.91
05/08/09	287.05	0.37	102.30	25.58	78.16	25.23	92.56		0.36
06/03/09	19.61	0.37	249.50	30.69	123.41	31.32	96.12	0.90	0.55
06/29/09	32.09	0.74	249.50	28.13	123.41	33.06	106.80	0.72	0.73
08/06/09	25.97	0.37	394.21	40.41	190.46	48.28	118.19	1.43	< 0.09
08/07/09	15.53	0.37	414.17	37.85	191.28	45.24	114.28	1.61	< 0.09
08/08/09	15.16	0.37	404.19	39.13	191.69	46.98	117.12	2.51	< 0.09
08/09/09	35.28	0.37	419.16	39.13	192.51	45.67	115.34	3.04	< 0.09
08/10/09	44.52	0.37	416.67	41.94	194.98	45.67	117.12	4.66	1.64
08/11/09	52.08	0.74	439.12	40.92	197.04	45.67	119.26	4.30	6.19
08/13/09	45.55	1.11	346.81	48.34	156.31	41.32	94.34	1.79	< 0.09

Date	Discharge	Al	Ca	K	Mg	Na	Si	Fe	Mn
08/14/09	33.98	0.74	359.28	45.78	160.43	36.54	95.05	1.79	< 0.09
08/15/09	34.87	0.74	386.73	44.50	172.36	38.28	101.10	1.79	< 0.09
08/16/09	33.91	0.74	411.68	44.25	179.76	40.02	99.32	1.79	1.82
08/17/09	33.48	0.37	429.14	43.48	184.70	39.15	103.95	2.33	10.56
08/28/09	1.05	0.37	528.94	50.38	222.13	44.80	124.24	8.77	< 0.09
08/29/09	17.95	1.11	294.41	46.29	134.92	27.40	78.68	2.69	< 0.09
09/11/09	4.91	0.74	391.72	48.85	174.41	34.80	97.90	9.13	0.55
09/12/09	0.11	1.11	264.47	45.78	128.75	28.71	72.27	3.94	< 0.09
09/26/09	9.15	0.74	309.38	51.15	145.21	30.01	83.66	13.79	< 0.09
09/27/09	9.77	1.48	240.27	50.64	120.53	27.84	70.84	3.94	< 0.09
09/28/09	3.99	1.48	274.45	47.83	133.69	30.01	80.81	2.51	< 0.09
09/29/09	0.06	1.11	301.90	47.83	150.14	36.54	92.56	2.15	< 0.09
10/02/09	0.47	1.11	304.39	50.13	152.20	38.28	95.05	2.69	< 0.09
10/03/09	2.04	0.74	324.35	49.36	157.55	37.41	93.63	1.97	< 0.09
10/28/09	235.23	0.37	107.78	27.62	77.75	23.49	100.04	0.18	< 0.09
10/29/09	375.81	-	142.96	37.34	106.54	26.10	102.53	0.54	< 0.09
10/30/09	247.55	-	192.37	41.69	137.39	24.79	108.22	1.25	< 0.09
10/31/09	177.86	-	182.39	37.08	127.11	23.92	108.94	1.43	< 0.09
11/01/09	146.43	0.37	271.96	42.71	193.75	26.97	117.12	5.37	< 0.09
11/02/09	173.90	0.74	301.90	42.20	204.85	25.23	117.84	8.24	< 0.09
11/03/09	167.49	0.37	336.83	48.08	225.01	30.01	121.04	9.13	< 0.09
11/04/09	158.01	0.37	344.31	43.22	227.48	27.84	121.75	11.64	< 0.09
11/05/09	101.76	0.74	366.77	45.52	236.94	28.27	122.46	19.34	1.82
11/06/09	77.96	0.74	379.24	42.46	236.12	27.84	124.24	25.60	14.02
11/07/09	68.94	0.74	386.73	45.01	241.46	29.14	118.90	30.08	24.21
11/08/09	61.73	10.37	366.77	40.66	223.36	28.27	126.02	37.42	33.31
11/09/09	66.00	0.74	364.27	40.66	216.37	28.27	122.11	36.17	41.14
11/10/09	67.64	0.74	354.29	39.64	208.14	29.58	121.75	38.68	56.43
11/11/09	54.59	1.11	391.72	45.01	224.60	30.88	128.87	51.39	70.62
11/12/09	41.88	1.11	439.12	49.36	250.93	32.19	131.72	66.61	89.37
11/13/09	36.71	0.74	436.63	48.59	246.40	31.75	130.30	75.56	84.82
11/20/09	39.90	-	218.31	36.06	132.04	36.97	105.38	0.72	< 0.09
11/20/09	39.90	-	129.24	28.64	98.72	28.27	107.16	1.61	1.27
11/21/09	40.29	-	206.09	32.99	127.52	33.93	106.09	0.90	< 0.09
11/21/09	40.29	-	137.72	27.88	100.78	26.97	102.88	2.33	2.18
11/22/09	45.08	-	202.35	31.20	127.52	36.54	105.73	1.43	< 0.09
11/22/09	45.08	0.74	111.03	28.13	89.26	25.66	105.73	0.54	0.36
11/23/09	46.40	-	185.88	29.67	118.88	33.49	104.66	0.90	< 0.09
11/23/09	46.40	0.37	90.32	26.85	79.39	23.49	98.26	0.36	< 0.09
11/24/09	69.77	-	181.39	32.74	119.70	30.88	107.51	1.43	< 0.09
11/25/09	57.59	-	162.67	30.95	114.77	31.75	105.73	2.69	< 0.09
11/26/09	88.70	-	149.20	27.11	105.72	27.84	105.02	1.25	< 0.09
11/27/09	142.69	-	133.23	30.18	97.90	28.27	102.88	1.25	< 0.09
11/28/09	329.46	-	122.75	27.37	95.43	29.58	102.53	1.25	< 0.09
11/29/09	318.01	-	117.51	24.81	92.55	23.49	101.82	1.43	0.18
11/30/09	209.44	-	125.00	28.64	96.67	25.23	106.80	1.61	1.09
12/08/09	97.13	-	126.25	23.02	90.09	23.49	97.54	0.18	< 0.09

Note: Concentrations of Al were not reported for samples with (-)

Table D-4. Concentrations of elements in stream water at the weir when discharge = 0

Date	Al μM	Ca μM	K μM	Mg μM	Na μM	Si μM	Fe μM	Mn μM
07/11/08	0.37	578.84	38.36	176.88	42.63	117.48	1.79	< 0.09
07/12/08	0.37	596.31	46.04	181.00	42.63	121.04	3.40	0.73
07/13/08	0.37	616.27	40.92	185.11	43.06	121.04	3.94	4.37
07/14/08	0.37	638.72	43.48	189.22	45.24	124.60	4.66	8.18
07/15/08	0.37	638.72	40.92	185.11	43.50	124.60	5.01	8.91
07/16/08	0.37	658.68	40.92	193.34	44.37	124.60	6.98	12.73
07/17/08	< 0.09	661.18	46.04	193.34	43.93	128.16	5.55	< 0.09
07/18/08	0.37	663.67	46.04	197.45	45.24	124.60	8.24	3.46
07/19/08	0.37	631.24	46.04	185.11	43.06	124.60	8.95	3.64
07/20/08	0.37	666.17	51.15	197.45	43.93	128.16	13.61	11.09
07/21/08	0.37	656.19	48.59	193.34	44.37	124.60	16.47	13.46
07/22/08	0.37	668.66	48.59	197.45	43.93	131.72	14.86	23.64
07/23/08	0.37	603.79	53.71	189.22	43.06	121.04	14.68	15.28
07/25/08	0.37	491.52	48.59	160.43	37.84	103.24	11.46	< 0.09
07/26/08	0.37	503.99	48.59	164.54	38.71	103.24	10.21	< 0.09
07/27/08	0.37	516.47	48.59	168.65	40.45	106.80	12.18	< 0.09
07/28/08	0.37	513.97	56.27	168.65	38.71	106.80	12.00	1.46
07/29/08	1.11	528.94	51.15	172.77	40.02	110.36	14.86	11.64
07/30/08	0.37	526.45	53.71	172.77	40.02	110.36	15.94	14.19
07/31/08	0.37	523.95	53.71	168.65	39.15	113.92	15.40	< 0.09
08/02/08	0.37	546.41	58.82	172.77	42.19	117.48	9.49	< 0.09
08/03/08	0.74	546.41	56.27	176.88	39.58	113.92	12.89	5.46
08/04/08	0.37	533.93	56.27	168.65	39.58	113.92	23.28	14.37
08/05/08	< 0.09	526.45	53.71	168.65	40.02	124.60	9.67	17.82
08/06/08	< 0.09	558.88	61.38	172.77	47.41	121.04	1.25	< 0.09
08/07/08	0.74	588.82	61.38	185.11	50.46	117.48	19.70	< 0.09
08/08/08	0.37	591.32	61.38	189.22	54.81	117.48	21.49	< 0.09
08/09/08	0.37	598.80	63.94	189.22	49.59	124.60	19.70	< 0.09
08/10/08	0.37	596.31	63.94	185.11	50.02	128.16	26.86	< 0.09
08/11/08	0.37	601.30	63.94	189.22	53.50	128.16	34.02	< 0.09
08/12/08	0.37	598.80	63.94	189.22	48.28	124.60	32.23	< 0.09
08/13/08	0.74	606.29	63.94	193.34	51.33	128.16	30.44	< 0.09
08/14/08	0.74	586.33	63.94	193.34	47.85	121.04	57.30	4.18
08/15/08	0.37	596.31	63.94	197.45	47.85	128.16	62.67	11.09
08/16/08	0.74	588.82	63.94	197.45	47.85	128.16	59.09	6.00
08/17/08	0.74	581.34	63.94	193.34	43.50	124.60	66.25	7.09
08/18/08	0.37	568.86	61.38	189.22	43.50	121.04	66.25	7.09
08/19/08	0.74	573.85	63.94	193.34	47.85	128.16	68.04	8.55
08/20/08	0.74	581.34	66.50	193.34	47.85	131.72	82.36	10.91
08/21/08	0.37	576.35	66.50	185.11	48.28	142.40	107.43	< 0.09
08/22/08	0.37	489.02	79.28	164.54	42.63	121.04	60.88	18.01
08/28/08	0.37	563.87	69.05	185.11	49.15	142.40	84.15	< 0.09
08/29/08	0.74	518.96	86.96	176.88	43.93	135.28	94.90	8.00
08/30/08	0.74	553.89	84.40	185.11	43.50	142.40	93.11	18.19
08/31/08	0.37	566.37	81.84	185.11	43.93	145.96	98.48	21.83

Date	Al μM	Ca μM	K μM	Mg μM	Na μM	Si μM	Fe μM	Mn μM
09/01/08	0.37	561.38	84.40	185.11	44.37	153.08	100.27	18.19
09/09/08	1.11	364.27	81.84	123.41	31.75	92.56	17.91	< 0.09
09/10/08	0.74	369.26	76.73	123.41	30.88	99.68	26.86	0.55
09/11/08	0.74	376.75	74.17	123.41	29.58	99.68	25.07	4.37
09/14/08	2.59	301.90	58.82	106.95	32.62	92.56	8.42	0.36
09/15/08	3.34	326.85	56.27	115.18	32.19	96.12	11.10	8.00
09/16/08	2.97	311.88	53.71	106.95	32.19	92.56	10.56	5.46
09/17/08	1.48	311.88	53.71	111.07	33.93	96.12	10.74	< 0.09
09/18/08	1.85	319.36	56.27	106.95	32.19	96.12	11.82	1.46
09/19/08	1.85	309.38	56.27	106.95	30.88	96.12	13.07	3.09
09/20/08	1.85	324.35	56.27	111.07	33.06	96.12	14.50	3.64
09/21/08	2.22	324.35	56.27	111.07	32.19	99.68	16.47	6.91
09/22/08	1.85	314.37	51.15	106.95	30.45	96.12	16.65	8.18
09/23/08	1.85	329.34	56.27	115.18	31.32	103.24	19.70	10.37
09/24/08	1.85	334.33	58.82	119.29	31.75	106.80	21.49	11.28
09/25/08	2.22	316.87	48.59	115.18	30.88	96.12	21.49	0.18
09/26/08	2.22	316.87	51.15	115.18	29.58	96.12	21.49	0.36
09/27/08	2.22	329.34	51.15	119.29	29.14	99.68	26.86	0.55
10/13/08	1.11	286.93	33.25	98.72	33.49	103.24	5.55	1.64
10/14/08	1.11	286.93	33.25	98.72	33.49	103.24	6.98	3.46
10/15/08	0.74	294.41	30.69	94.61	31.75	99.68	8.24	6.18
10/16/08	1.11	301.90	33.25	102.84	32.62	103.24	8.77	8.37
10/17/08	1.85	304.39	35.81	102.84	35.23	106.80	8.77	0.36
10/18/08	0.74	299.40	35.81	102.84	34.80	106.80	10.38	2.73
10/19/08	0.74	301.90	38.36	106.95	33.93	106.80	12.89	7.09
10/20/08	0.74	294.41	33.25	98.72	31.32	103.24	11.82	2.00
10/21/08	1.48	291.92	38.36	102.84	34.36	103.24	13.79	6.18
10/22/08	0.37	291.92	40.92	102.84	33.93	106.80	13.61	6.91
10/23/08	1.11	294.41	40.92	102.84	33.49	106.80	14.15	7.28
10/24/08	0.37	296.91	43.48	106.95	34.36	106.80	16.47	7.46
08/27/09	< 0.09	528.94	51.41	221.72	45.67	119.26	9.13	< 0.09
08/31/09	0.74	354.29	47.31	162.90	33.93	91.85	2.69	< 0.09
09/13/09	1.11	281.94	45.52	134.51	30.01	74.05	4.12	< 0.09
09/14/09	1.11	281.94	44.25	134.10	27.40	75.12	4.48	0.18
09/15/09	0.74	289.42	48.59	139.04	31.75	76.90	4.30	3.64
09/16/09	1.11	291.92	46.04	139.45	29.14	77.25	5.01	3.46
09/17/09	1.11	301.90	46.55	143.15	30.01	78.68	6.09	5.64
09/18/09	0.74	294.41	49.10	141.92	31.32	79.03	5.91	< 0.09
09/19/09	0.74	299.40	48.59	142.33	31.75	80.10	8.06	< 0.09
09/20/09	0.74	299.40	48.59	143.56	31.75	80.46	10.74	0.55
09/21/09	0.74	306.89	48.85	145.21	30.88	81.52	11.28	0.73
09/22/09	0.74	316.87	47.83	147.26	29.14	82.24	13.43	2.91
09/23/09	0.74	311.88	47.57	146.03	28.27	81.88	13.79	6.01
09/24/09	0.74	321.86	49.87	148.91	30.45	83.66	14.50	10.19
09/25/09	0.74	334.33	52.43	155.08	30.88	85.44	14.50	19.11
09/30/09	1.11	306.89	47.83	151.38	37.84	93.98	2.15	< 0.09

Date	Al μM	Ca μM	K μM	Mg μM	Na μM	Si μM	Fe μM	Mn μM
10/01/09	1.11	304.39	47.57	150.56	36.54	94.34	2.51	< 0.09
10/04/09	0.74	334.33	50.38	161.66	39.15	95.41	1.97	< 0.09
10/05/09	0.74	331.84	50.13	160.84	37.84	95.76	2.33	0.55
10/06/09	0.74	331.84	50.38	160.84	40.02	95.76	2.51	1.09
10/07/09	0.74	334.33	52.17	162.90	40.02	96.83	2.86	2.73
10/08/09	0.74	341.82	53.20	155.08	37.84	98.61	3.04	2.91
08/30/09	0.74	339.32	48.08	155.08	32.19	88.64	2.69	< 0.09
09/01/09	0.74	369.26	47.83	167.42	35.67	93.27	3.04	0.36
09/02/09	0.74	374.25	48.08	169.89	35.23	94.34	3.22	0.55
09/03/09	0.74	376.75	47.06	169.89	34.80	94.34	4.12	3.09
09/04/09	0.74	374.25	48.59	169.89	35.67	93.98	4.12	0.36
09/05/09	0.74	379.24	49.62	174.00	37.41	95.76	4.48	0.36
09/06/09	0.74	394.21	47.57	175.65	35.23	93.63	5.91	2.00
09/07/09	0.74	396.71	53.71	181.00	43.06	97.19	7.88	6.73
09/08/09	0.74	394.21	50.38	177.29	35.67	97.54	9.67	10.37
09/09/09	0.74	401.70	47.57	177.70	34.80	99.68	10.92	13.47
09/10/09	0.74	399.20	48.85	177.70	33.93	96.12	10.38	15.47

Table D-5A. Site data for green leaf samples from 2009

Sample Name	Tree ID	Species	Northing	Easting	Site	Elevation (meters)	DBH (cm)
QUPR1w Dry 1	1755	QUPR	147799.4	587054.8	Dry 1	296.12	38.10
QUPR1w Dry 2	1895	QUPR	147883.2	587130.2	Dry 2	294.96	29.21
QUPR1w Wet 1	203	QUPR	147849.3	586820.3	Wet 1	269.27	40.13
QUPR2w Dry 1	1755	QUPR	147799.4	587054.8	Dry 1	296.12	38.10
QUPR2w Dry 2	1895	QUPR	147883.2	587130.2	Dry 2	294.96	29.21
QUPR2w Wet 1	203	QUPR	147849.3	586820.3	Wet 1	269.27	40.13
PIST1w Dry 1	1484	PIST	147799.3	587038.6	Dry 1	292.34	29.97
PIST1w Dry 2	1885	PIST	147886.8	587119.9	Dry 2	293.27	30.48
PIST1w Wet 1	267	PIST	147832.2	586847.7	Wet 1	266.48	37.85
PIST2w Dry 1	1484	PIST	147799.3	587038.6	Dry 1	292.34	29.97
PIST2w Dry 2	1885	PIST	147886.8	587119.9	Dry 2	293.27	30.48
PIST2w Wet 1	267	PIST	147832.2	586847.7	Wet 1	266.48	37.85
PIVI1w Dry 1	1689	PIVI	147814.8	587081.1	Dry 1	298.86	42.67
PIVI1w Dry 2	1901	PIVI	147902.4	587137.8	Dry 2	293.31	30.99
PIVI2w Dry 1	1689	PIVI	147814.8	587081.1	Dry 1	298.86	42.67
PIVI2w Dry 2	1901	PIVI	147902.4	587137.8	Dry 2	293.31	30.99
CAGL1w Dry 1	1788	CAGL	147800.2	587071.4	Dry 1	298.48	20.57
CAGL1w Dry 2	1905	CAGL	147897.4	587147.6	Dry 2	295.78	28.19
CAGL1w Wet 1	324	CAGL	147848.8	586891.2	Wet 1	273.73	28.70
CAGL2w Dry 1	1788	CAGL	147800.2	587071.4	Dry 1	298.48	20.57
CAGL2w Dry 2	1905	CAGL	147897.4	587147.6	Dry 2	295.78	28.19
CAGL2w Wet 1	324	CAGL	147848.8	586891.2	Wet 1	273.73	28.70
CAGL2w Wet 2	2023	CAGL	147885.7	587036.8	Wet 2	276.83	35.56
CATO1w Dry 1	1787	CATO	147798.3	587066.3	Dry 1	297.91	22.61
CATO1w Dry 2	1890	CATO	147882.5	587143.9	Dry 2	296.05	23.88
CATO1w Wet 1	158	CATO	147854.7	586810.7	Wet 1	271.10	43.94
CATO1w Wet 2	770	CATO	147909.9	587050.3	Wet 2	279.98	28.70
CATO2w Dry 1	1787	CATO	147798.3	587066.3	Dry 1	297.91	22.61
CATO2w Dry 2	1890	CATO	147882.5	587143.9	Dry 2	296.05	23.88
CATO2w Wet 1	158	CATO	147854.7	586810.7	Wet 1	271.10	43.94
QUAL1w Dry 1	1772	QUAL	147772.7	587051.7	Dry 1	299.11	32.26
QUAL1w Dry 2	1893	QUAL	147889.7	587137.0	Dry 2	294.91	28.45
QUAL1w Wet 1	197	QUAL	147839.5	586825.9	Wet 1	267.46	32.00
QUAL1 Wet 2	660	QUAL	147889.6	587017.8	Wet 2	276.08	39.62
QUAL2w Dry 1	1772	QUAL	147772.7	587051.7	Dry 1	299.11	32.26
QUAL2w Dry 2	1893	QUAL	147889.7	587137.0	Dry 2	294.91	28.45
QUAL2w Wet 1	197	QUAL	147839.5	586825.9	Wet 1	267.46	32.00

Table D-5B. Site data for green leaf samples from 2011

Tree ID	Species	Collection Date	Northing	Easting	Site	Elevation (meters)	DBH (cm)
230	QUPR	06/09/11	147930.2	586868.4	Upper	289.344	54.99
230	QUPR	09/20/11	147930.2	586868.4	Upper	289.344	54.99
330	QUPR	09/13/11	147856.2	586881.1	Lower	274.9757	33.32
332	QUPR	06/21/11	147855.4	586874.8	Lower	274.2542	31.95
332	QUPR	09/13/11	147855.4	586874.8	Lower	274.2542	31.95
333	QUPR	06/21/11	147855.4	586874.8	Lower	274.2542	38.76
340	QUPR	06/21/11	147874.4	586892.2	Lower	280.1718	33.78
351	QUPR	06/16/11	147913.0	586887.1	Middle	288.3379	43.43
351	QUPR	08/30/11	147913.0	586887.1	Middle	288.3379	43.43
352	ACSA	06/16/11	147915.1	586883.8	Middle	288.7045	30.67
352	ACSA	08/30/11	147915.1	586883.8	Middle	288.7045	30.67
356	ACSA	06/09/11	147919.8	586878.7	Middle	289.0322	27.94
356	ACSA	08/30/11	147919.8	586878.7	Middle	289.0322	27.94
358	QUPR	06/14/11	147908.4	586873.5	Middle	287.1161	55.12
358	QUPR	08/30/11	147908.4	586873.5	Middle	287.1161	55.12
390	QUPR	08/30/11	147896.1	586867.8	Middle	284.1655	28.00
396	QUPR	07/06/11	147939.9	586896.7	Upper	293.3342	29.06
437	ACSA	06/09/11	147936.1	586893.8	Upper	292.4223	28.70
2059	ACSA	06/09/11	147930.2	586868.4	Upper	289.344	25.17
2059	ACSA	09/20/11	147930.2	586868.4	Upper	289.344	25.17
2060	QUPR	08/30/11	147919.8	586878.7	Middle	289.0322	16.23
2061	ACSA	06/14/11	147908.4	586873.5	Middle	287.1161	22.38
2061	ACSA	08/30/11	147908.4	586873.5	Middle	287.1161	22.38
2062	ACSA	06/21/11	147874.4	586892.2	Lower	280.1718	21.16
2062	ACSA	09/20/11	147874.4	586892.2	Lower	280.1718	21.16
2064	ACSA	06/27/11	147856.2	586881.1	Lower	274.9757	18.10
2064	ACSA	09/13/11	147856.2	586881.1	Lower	274.9757	18.10
2065	ACSA	06/21/11	147855.4	586874.8	Lower	274.2542	10.87
2065	ACSA	09/13/11	147855.4	586874.8	Lower	274.2542	10.87
2066	ACSA	09/13/11	147939.9	586896.7	Upper	293.3342	17.61

*location values for trees with IDs > 2000 are based on measurements made for adjacent trees

Table D-6A. Element concentrations in green leaves collected in 2009

Species	Tree ID	Sample Batch	Collection Date	Mg $\mu\text{g g}^{-1}$	Al $\mu\text{g g}^{-1}$	Si $\mu\text{g g}^{-1}$	P $\mu\text{g g}^{-1}$	K $\mu\text{g g}^{-1}$	Ca $\mu\text{g g}^{-1}$
CAGL	324	1	June 2009	3,035	1,650	1,250	1,795	9,640	9,930
CAGL	324	2	07/22/09	2,392	3,727	531	1,396	8,759	11,515
CAGL	2023	2	08/03/09	3,384	6,541	480	1,195	6,669	12,988
CAGL	1788	3	08/12/09	2,228	8,058	7,541	1,160	12,367	9,081
CAGL	1788	3	08/12/09	1,270	3,357	5,659	1,073	11,701	5,211
CAGL	1905	4	08/17/09	3,116	6,084	117	1,146	11,463	10,901
CAGL	1905	3	08/17/09	2,949	6,328	531	1,157	12,262	10,053
CAGL	324	4	09/01/09	2,884	5,347	4,923	1,519	10,058	15,139
CAGL	324	3	09/01/09	636	870	5,213	1,480	10,035	10,337
CATO	158	2	07/22/09	2,738	3,814	607	1,136	8,300	9,590
CATO	777	2	08/03/09	4,047	6,190	1,077	1,316	11,706	18,589
CATO	1787	3	08/12/09	710	2,382	6,040	995	11,861	9,385
CATO	1890	3	08/17/09	1,043	3,359	5,790	1,289	11,809	6,661
CATO	1890	4	08/17/09	2,645	6,881	1,258	1,371	11,851	11,804
CATO	158	3	09/01/09	3,618	5,467	7,993	1,293	10,133	11,997
CATO	158	4	09/01/09	3,510	5,148	5,843	1,352	10,461	13,493
PIST	267	1	06/08/09	1,175	230	2,010	1,390	6,090	4,980
PIST	1484	3	08/12/09	1,087	301	6,796	1,171	5,326	2,734
PIST	1484	3	08/12/09	1,040	310	6,747	1,095	5,176	2,866
PIST	1484	4	08/12/09	866	220	3,572	952	4,815	2,279
PIST	1885	4	08/17/09	1,265	278	1,030	1,473	6,239	3,715
PIST	1885	3	08/17/09	973	327	2,852	1,179	5,122	3,037
PIST	267	3	09/01/09	1,203	218	5,507	1,141	6,392	3,500
PIST	267	3	09/01/09	634	201	6,063	1,007	5,576	1,200
PIST	267	4	09/01/09	1,334	294	5,787	1,063	5,318	4,025
PIVI	1689	3	08/12/09	193	419	5,390	1,023	3,509	2,009
PIVI	1689	4	08/12/09	783	880	465	868	3,144	2,853
PIVI	1689	3	08/12/09	947	854	1,575	892	3,399	2,837
PIVI	1901	3	08/17/09	848	506	6,680	1,027	4,899	1,493
PIVI	1901	4	08/17/09	914	472	239	1,087	5,170	1,712
PIVI	1901	3	08/17/09	954	594	8,255	1,105	4,670	1,925
QUAL	197	1	06/16/09	1,595	57	1,700	2,540	18,440	6,795
QUAL	197	2	07/22/09	1,272	122	2,675	1,878	11,326	9,113
QUAL	660	2	08/03/09	1,637	99	3,437	1,689	13,526	9,819
QUAL	1772	3	08/12/09	753	145	6,620	1,555	8,482	7,111
QUAL	1772	4	08/12/09	387	55	120	771	4,829	4,360
QUAL	1893	3	08/17/09	1,287	99	7,617	1,606	11,085	11,882
QUAL	197	3	09/01/09	1,928	95	9,691	2,060	12,155	11,706
QUAL	197	3	09/01/09	2,041	81	9,865	2,020	12,779	12,412
QUPR	203	1	June 2009	1,355	66	1,650	2,265	14,405	6,330

Species	Tree ID	Sample Batch	Collection Date	Mg $\mu\text{g g}^{-1}$	Al $\mu\text{g g}^{-1}$	Si $\mu\text{g g}^{-1}$	P $\mu\text{g g}^{-1}$	K $\mu\text{g g}^{-1}$	Ca $\mu\text{g g}^{-1}$
QUPR	1755/1895	1	06/16/09	1,510	71	1,605	1,680	13,395	6,465
QUPR	203	2	07/22/09	1,544	93	2,352	1,529	12,614	8,180
QUPR	203	2	07/22/09	1,377	68	1,072	1,483	8,858	8,205
QUPR	1755	3	08/12/09	1,076	79	7,495	1,316	8,958	5,972
QUPR	1895	3	08/17/09	1,305	112	7,651	1,155	7,019	8,442
QUPR	203	3	09/01/09	1,485	85	8,297	1,676	8,462	8,964
QURU	n/a	1	Jun.2009	1,815	41	1,140	1,945	10,015	5,975
QURU	n/a	1	06/16/09	1,940	67	1,285	1,540	10,835	6,570
QUVE	n/a	1	06/08/09	2,025	36	1,275	1,955	15,655	5,550
Species	Tree ID	Sample Batch	Collection Date	Na $\mu\text{g g}^{-1}$	Ti $\mu\text{g g}^{-1}$	Mn $\mu\text{g g}^{-1}$	Fe $\mu\text{g g}^{-1}$	Zn $\mu\text{g g}^{-1}$	Pb $\mu\text{g g}^{-1}$
CAGL	324	1	June 2009	23	3.90	1,985	79	100	0.37
CAGL	324	2	07/22/09	21	172.0	2,614	74	99	1.84
CAGL	2023	2	08/03/09	37	5.19	3,289	84	160	1.49
CAGL	1788	3	08/12/09	112	35	4,834	99	125	0.99
CAGL	1788	3	08/12/09	24	10	4,750	49	108	0.82
CAGL	1905	4	08/17/09	23	10	3,995	65	132	1.13
CAGL	1905	3	08/17/09	70	3.0	3,904	51	146	1.33
CAGL	324	4	09/01/09	19	9.3	3,898	63	141	0.97
CAGL	324	3	09/01/09	13	8.8	3,460	44	128	0.58
CATO	158	2	07/22/09	42	8.27	1,749	78	105	2.08
CATO	777	2	08/03/09	15	12.14	2,805	83	32	1.29
CATO	1787	3	08/12/09	10	8.7	5,045	54	130	1.02
CATO	1890	3	08/17/09	26	31	3,548	39	25	0.77
CATO	1890	4	08/17/09	18	13	4,193	77	32	1.13
CATO	158	3	09/01/09	98	15	2,247	65	159	0.53
CATO	158	4	09/01/09	33	7.8	2,329	63	171	0.58
PIST	267	1	06/08/09	27	4.50	1,135	84	64	bdl
PIST	1484	3	08/12/09	43	8.3	1,148	36	28	0.13
PIST	1484	3	08/12/09	17	6.9	1,235	40	38	0.21
PIST	1484	4	08/12/09	6.7	17	942	31	31	0.05
PIST	1885	4	08/17/09	4.5	4.2	1,127	45	52	0.12
PIST	1885	3	08/17/09	23	5.9	1,065	46	46	0.19
PIST	267	3	09/01/09	8.2	6.0	830	34	43	0.19
PIST	267	3	09/01/09	15	9.2	665	30	35	0.14
PIST	267	4	09/01/09	4.5	6.4	1,096	44	51	0.42
PIVI	1689	3	08/12/09	8.5	6.1	1,212	20	47	0.06
PIVI	1689	4	08/12/09	5.9	2.6	1,055	33	43	0.15
PIVI	1689	3	08/12/09	19	5.4	1,198	36	43	0.20
PIVI	1901	3	08/17/09	8.5	6.7	527	41	37	0.99

Species	Tree ID	Sample Batch	Collection Date	Na $\mu\text{g g}^{-1}$	Ti $\mu\text{g g}^{-1}$	Mn $\mu\text{g g}^{-1}$	Fe $\mu\text{g g}^{-1}$	Zn $\mu\text{g g}^{-1}$	Pb $\mu\text{g g}^{-1}$
PIVI	1901	4	08/17/09	39	4.9	528	39	43	0.09
PIVI	1901	3	08/17/09	55	11	654	40	40	0.33
QUAL	197	1	06/16/09	26	2.50	1,410	58	22	0.73
QUAL	197	2	07/22/09	42	21.95	1,847	97	44	21.59
QUAL	660	2	08/03/09	14	5.92	2,406	63	17	1.09
QUAL	1772	3	08/12/09	20	14	3,998	66	14	0.39
QUAL	1772	4	08/12/09	3.9	3.9	2,187	28	7.5	0.05
QUAL	1893	3	08/17/09	8.9	71	3,100	59	14	0.26
QUAL	197	3	09/01/09	11	10	3,133	53	22	0.15
QUAL	197	3	09/01/09	19	7.2	3,155	57	21	0.32
QUPR	203	1	June 2009	24	2.40	2,180	40	25	0.31
QUPR	1755/1895	1	06/16/09	17	4.20	3,065	92	23	0.06
QUPR	203	2	07/22/09	15	4.61	2,347	62	16	0.72
QUPR	203	2	07/22/09	15	25.36	2,525	54	15	0.65
QUPR	1755	3	08/12/09	7.6	86	3,393	63	15	0.19
QUPR	1895	3	08/17/09	7.9	7.3	2,120	65	13	0.21
QUPR	203	3	09/01/09	9.3	9.1	2,941	46	13	0.23
QURU	n/a	1	Jun.2009	12	5.40	2,705	90	24	0.04
QURU	n/a	1	06/16/09	22	4.20	2,905	175	23	0.06
QUVE	n/a	1	06/08/09	15	3.50	2,035	110	33	bdl

Table D-6B. Chemistry of duplicate washed green leaves collected in 2009

Species	Tree ID	Sample Batch	Collection Date	Mg $\mu\text{g g}^{-1}$	Al $\mu\text{g g}^{-1}$	Si $\mu\text{g g}^{-1}$	P $\mu\text{g g}^{-1}$	K $\mu\text{g g}^{-1}$	Ca $\mu\text{g g}^{-1}$
CAGL	324	1	06/16/09	2,295	1,260	1,050	1,380	7,250	7,505
CATO	158	3	09/01/09	1,568	2,549	6,503	1,266	9,160	10,074
CATO	1787	3	08/12/09	2,470	6,309	7,074	1,111	11,921	11,591
PIST	267	1	06/08/09	1,210	255	1,850	1,295	5,625	4,725
PIST	267	3	09/01/09	1,119	65	2,080	1,182	6,227	4,013
PIST	267	3	09/01/09	1,354	369	7,397	1,054	5,534	3,706
PIST	1484	3	08/12/09	991	342	379	1,128	5,400	2,715
PIST	1885	4	08/17/09	1,284	336	4,879	1,408	5,162	4,670
PIST	1885	4	08/17/09	1,229	325	4,574	1,342	4,976	4,446
PIST	1885	3	08/17/09	1,183	317	4,756	1,406	6,579	3,133
QUAL	197	1	06/16/09	1,550	69	1,590	2,535	17,725	7,175
QUAL	1893	3	08/17/09	492	22	7,586	1,439	9,031	3,557
QUPR	203	1	06/16/09	1,140	43	1,695	2,055	12,525	6,520
QUPR	203	3	09/01/09	1,117	51	6,095	1,610	8,438	6,906
QUPR	1755	3	08/12/09	1,074	80	1,239	1,197	8,384	6,154
QUPR	1895	3	08/17/09	1,140	111	453	1,211	8,936	8,368

Species	Tree ID	Sample Batch	Collection Date	Mg $\mu\text{g g}^{-1}$	Al $\mu\text{g g}^{-1}$	Si $\mu\text{g g}^{-1}$	P $\mu\text{g g}^{-1}$	K $\mu\text{g g}^{-1}$	Ca $\mu\text{g g}^{-1}$
QUPR	1755/1895	1	06/16/09	1,040	22	1,535	1,510	13,285	1,285
QURU	n/a	1	06/16/09	1,570	60	1,275	1,575	10,975	7,785
QURU	n/a	1	06/16/09	1,725	41	1,330	2,095	12,245	7,975
QUVE	n/a	1	06/08/09	2,070	145	1,255	1,790	14,145	4,770
Species	Tree ID	Sample Batch	Collection Date	Na $\mu\text{g g}^{-1}$	Ti $\mu\text{g g}^{-1}$	Mn $\mu\text{g g}^{-1}$	Fe $\mu\text{g g}^{-1}$	Zn $\mu\text{g g}^{-1}$	Pb $\mu\text{g g}^{-1}$
CAGL	324	1	06/16/09	37	4.50	1,495	36	79	0.37
CATO	158	3	09/01/09	18	8.4	2,178	54	159	0.80
CATO	1787	3	08/12/09	25	294	5,545	86	142	1.33
PIST	267	1	06/08/09	37	3.30	1,190	66	64	0.17
PIST	267	3	09/01/09	8.2	8.4	1,032	44	51	0.15
PIST	267	3	09/01/09	227	63	1,091	52	69	0.95
PIST	1484	3	08/12/09	29	5.4	1,135	37	31	0.16
PIST	1885	4	08/17/09	14	10	1,383	50	57	0.18
PIST	1885	4	08/17/09	6.3	7.6	1,347	51	55	0.11
PIST	1885	3	08/17/09	267	10	1,130	54	50	0.34
QUAL	197	1	06/16/09	30	6.70	1,250	55	26	0.25
QUAL	1893	3	08/17/09	11	7.5	2,292	17	12	0.27
QUPR	203	1	06/16/09	33	4.10	2,370	37	25	0.62
QUPR	203	3	09/01/09	14	182	2,344	47	11	0.52
QUPR	1755	3	08/12/09	35	3.8	3,693	57	20	0.38
QUPR	1895	3	08/17/09	28	4.1	2,003	54	14	0.24
QUPR	1755/1895	1	06/16/09	15	2.10	2,475	70	20	bdl
QURU	n/a	1	06/16/09	22	2.80	2,215	135	24	0.02
QURU	n/a	1	06/16/09	15	2.70	2,365	69	28	0.02
QUVE	n/a	1	06/08/09	18	4.40	2,270	71	30	0.08

Table D-6C. Quality control on foliar chemistry for green leaves collected in 2009

Sample Name	Sample Type	Mg $\mu\text{g g}^{-1}$	Al $\mu\text{g g}^{-1}$	Si $\mu\text{g g}^{-1}$	P $\mu\text{g g}^{-1}$	K $\mu\text{g g}^{-1}$	Ca $\mu\text{g g}^{-1}$
NIST 1547 certified value		4,320	249	a-----	1,370	24,300	15,600
NIST 1547-1	Method Standard	3,525	165	1,870	1,120	25,760	13,560
NIST 1547-2	Method Standard	3,215	110	2,085	1,295	21,130	11,575
NIST 1547-3	Method Standard	3,570	160	1,900	1,165	24,030	12,870
<i>Batch 1: Average % Error</i>		-20	-42		-13	-3	-19
Peach 1	Method Standard	4,147	295	1,304	1,364	23,626	14,651
Peach 2	Method Standard	4,037	245	1,190	1,291	23,027	14,120
Peach 3	Method Standard	4,170	265	1,337	1,357	23,753	14,692
<i>Batch 2: Average % Error</i>		-5	8		-2	-3	-7
P1	Method Standard	1,964	261	8,196	1,344	23,592	12,231
P2	Method Standard	1,430	292	7,619	1,272	23,293	12,026
P3	Method Standard	2,176	271	6,673	1,399	25,375	13,182
P4	Method Standard	1,168	255	1,040	1,243	22,812	11,699
<i>Batch 3: Average % Error</i>		-61	8		-4	-2	-21
PL 7	Method Standard	1,099	204	365	1,295	23,490	13,451
PL 8	Method Standard	594	196	594	1,234	22,865	13,215
PL 9	Method Standard	1,063	205	3,724	1,333	23,714	13,655
<i>Batch 4: Average % Error</i>		-79	-19		-6	-4	-14
Sample Name	Sample Type	Na $\mu\text{g g}^{-1}$	Ti $\mu\text{g g}^{-1}$	Mn $\mu\text{g g}^{-1}$	Fe $\mu\text{g g}^{-1}$	Zn $\mu\text{g g}^{-1}$	Pb $\mu\text{g g}^{-1}$
NIST 1547 certified value		24	a-----	98	218	18	0.87
NIST 1547-1	Method Standard	37	14	98	165	16	0.73
NIST 1547-2	Method Standard	31	12	80	160	20	0.82
NIST 1547-3	Method Standard	35	15	90	185	16	0.68
<i>Batch 1: Average % Error</i>		43		-9	-22	-2	-15
Peach 1	Method Standard	36	83	94	211	28	0.80
Peach 2	Method Standard	32	19	91	202	16	0.78
Peach 3	Method Standard	42	29	95	211	17	0.81
<i>Batch 2: Average % Error</i>		53		-5	-5	14	-8
P1	Method Standard	38	84	92	52	16	1.05
P2	Method Standard	31	66	92	39	16	1.04
P3	Method Standard	46	34	106	60	24	1.16
P4	Method Standard	35	27	86	60	16	0.93
<i>Batch 3: Average % Error</i>		58		-4	-76	-0.5	20
PL 7	Method Standard	36	33	91	39	20	1.15
PL 8	Method Standard	35	30	86	24	17	1.25
PL 9	Method Standard	34	31	91	35	17	1.13
<i>Batch 4: Average % Error</i>		46		-9	-85	-0.7	35

Table D-6D. Element concentrations in green leaves collected in 2011

Sample Name	Species	Tree ID	Collection date	Mg $\mu\text{g g}^{-1}$	Al $\mu\text{g g}^{-1}$	P $\mu\text{g g}^{-1}$	K $\mu\text{g g}^{-1}$	Ca $\mu\text{g g}^{-1}$	Mn $\mu\text{g g}^{-1}$
A352	ACSA	352	6/16/2011	1,593	23	1,226	5,864	9,817	2,455
A356	ACSA	356	6/9/2011	1,941	36	1,880	6,181	11,085	2,249
A437	ACSA	437	6/9/2011	1,206	34	1,335	10,348	4,786	1,839
A2059	ACSA	2059	6/9/2011	1,323	103	1,535	6,950	6,730	2,417
A2061	ACSA	2061	6/14/2011	1,038	28	1,525	4,897	6,294	1,443
A2062	ACSA	2062	6/21/2011	1,033	22	958	3,896	4,706	966
A2064	ACSA	2064	6/27/2011	1,006	37	1,289	5,262	4,361	2,156
A2065	ACSA	2065	6/21/2011	1,242	30	1,569	5,365	5,631	1,451
<i>Early summer average</i>				<i>1,298</i>	<i>39</i>	<i>1,415</i>	<i>6,095</i>	<i>6,676</i>	<i>1,872</i>
<i>Standard Deviation</i>				<i>324</i>	<i>26</i>	<i>276</i>	<i>1,941</i>	<i>2,489</i>	<i>540</i>
Q230	QUPR	230	6/9/2011	1,168	37	1,424	9,410	4,492	1,843
Q332	QUPR	332	6/21/2011	1,204	22	1,442	9,414	2,757	905
Q333	QUPR	333	6/21/2011	1,033	21	1,318	10,446	3,247	1,417
Q340	QUPR	340	6/21/2011	1,356	27	1,493	9,899	6,755	1,231
Q351	QUPR	351	6/16/2011	1,436	35	1,658	10,138	5,200	1,593
Q358	QUPR	358	6/14/2011	893	29	1,078	8,613	3,340	1,196
<i>Early summer average</i>				<i>1,181</i>	<i>28</i>	<i>1,402</i>	<i>9,653</i>	<i>4,298</i>	<i>1,364</i>
<i>Standard Deviation</i>				<i>201</i>	<i>6.5</i>	<i>194</i>	<i>651</i>	<i>1,502</i>	<i>329</i>
Oct12	ACSA	352	8/30/2011	1,635	46	1,276	6,089	11,514	2,891
Oct16	ACSA	356	8/30/2011	2,305	37	2,032	5,096	17,567	3,484
Oct2	ACSA	2059	9/20/2011	2,131	91	1,359	3,031	13,640	3,305
Oct8	ACSA	2059	9/20/2011	1,254	63	956	6,184	9,143	2,840
Oct4	ACSA	2061	8/30/2011	1,109	44	1,344	5,379	8,794	2,206
Oct5	ACSA	2062	9/20/2011	1,461	38	1,951	3,575	14,757	1,331
Oct11	ACSA	2064	9/13/2011	1,237	32	1,420	5,061	6,636	2,934
Oct6	ACSA	2065	9/13/2011	1,541	26	1,185	4,798	11,058	2,142
Oct3	ACSA	2066	9/13/2011	1,989	54	1,395	3,589	17,518	2,876
<i>Late summer average</i>				<i>1,629</i>	<i>48</i>	<i>1,435</i>	<i>4,756</i>	<i>12,292</i>	<i>2,668</i>
<i>Standard Deviation</i>				<i>424</i>	<i>20</i>	<i>345</i>	<i>1,126</i>	<i>3,862</i>	<i>666</i>
Oct7	QUPR	230	9/20/2011	1,241	57	1,939	9,756	8,923	2,881
Oct13	QUPR	330	9/13/2011	1,243	70	1,406	10,525	6,727	1,787
Oct10	QUPR	332	9/13/2011	1,802	55	2,298	10,457	5,580	1,726
Oct9	QUPR	351	8/30/2011	1,257	94	1,343	10,055	7,848	1,402
Oct17	QUPR	358	8/30/2011	1,009	33	1,227	10,844	3,648	1,390
Oct15	QUPR	390	8/30/2011	1,359	43	1,779	12,311	5,997	1,230
Oct14	QUPR	396	9/13/2011	1,172	53	1,851	11,869	5,884	1,436
Oct18	QUPR	2060	8/30/2011	1,534	56	1,418	11,181	7,026	1,659
<i>Late summer average</i>				<i>1,327</i>	<i>58</i>	<i>1,658</i>	<i>10,875</i>	<i>6,454</i>	<i>1,689</i>
<i>Standard Deviation</i>				<i>243</i>	<i>18</i>	<i>368</i>	<i>875</i>	<i>1,586</i>	<i>518</i>

Sample Name	Species	Tree ID	Collection date	Na $\mu\text{g g}^{-1}$	Fe $\mu\text{g g}^{-1}$	Zn $\mu\text{g g}^{-1}$	Mo $\mu\text{g g}^{-1}$	Pb $\mu\text{g g}^{-1}$
A352	ACSA	352	6/16/2011	29	62	23	< 0.006	< 0.07
A356	ACSA	356	6/9/2011	< 3.30	73	28	< 0.006	< 0.07
A437	ACSA	437	6/9/2011	< 3.30	39	15	< 0.006	< 0.07
A2059	ACSA	2059	6/9/2011	< 3.30	106	18	< 0.006	< 0.07
A2061	ACSA	2061	6/14/2011	< 3.30	67	17	0.036	< 0.07
A2062	ACSA	2062	6/21/2011	< 3.30	40	10	0.033	< 0.07
A2064	ACSA	2064	6/27/2011	< 3.30	95	15	< 0.006	< 0.07
A2065	ACSA	2065	6/21/2011	< 3.30	54	20	< 0.006	< 0.07
<i>Early summer average</i>				<i>5.1</i>	<i>67</i>	<i>18</i>	<i>0.035</i>	<i>bdl</i>
<i>Standard Deviation</i>				<i>9.6</i>	<i>24</i>	<i>5.5</i>	<i>0.002</i>	<i>bdl</i>
Q230	QUPR	230	6/9/2011	< 3.30	46	13	< 0.006	< 0.07
Q332	QUPR	332	6/21/2011	< 3.30	35	13	< 0.006	< 0.07
Q333	QUPR	333	6/21/2011	< 3.30	42	15	< 0.006	< 0.07
Q340	QUPR	340	6/21/2011	< 3.30	54	14	< 0.006	< 0.07
Q351	QUPR	351	6/16/2011	< 3.30	53	20	< 0.006	< 0.07
Q358	QUPR	358	6/14/2011	< 3.30	41	14	< 0.006	< 0.07
<i>Early summer average</i>				<i>bdl</i>	<i>45</i>	<i>15</i>	<i>bdl</i>	<i>bdl</i>
<i>Standard Deviation</i>				<i>bdl</i>	<i>7.7</i>	<i>2.6</i>	<i>bdl</i>	<i>bdl</i>
Oct12	ACSA	352	8/30/2011	28	80	35	< 0.006	< 0.07
Oct16	ACSA	356	8/30/2011	< 3.30	78	56	0.085	< 0.07
Oct2	ACSA	2059	9/20/2011	394	93	36	0.139	< 0.07
Oct8	ACSA	2059	9/20/2011	46	89	18	0.065	< 0.07
Oct4	ACSA	2061	8/30/2011	34	73	102	0.081	< 0.07
Oct5	ACSA	2062	9/20/2011	66	62	23	0.150	< 0.07
Oct11	ACSA	2064	9/13/2011	66	67	30	0.047	< 0.07
Oct6	ACSA	2065	9/13/2011	25	58	29	0.044	< 0.07
Oct3	ACSA	2066	9/13/2011	< 3.30	82	27	0.051	< 0.07
<i>Late summer average</i>				<i>74</i>	<i>76</i>	<i>40</i>	<i>0.083</i>	<i>bdl</i>
<i>Standard Deviation</i>				<i>122</i>	<i>12</i>	<i>26</i>	<i>0.041</i>	<i>bdl</i>
Oct7	QUPR	230	9/20/2011	29	62	27	0.046	< 0.07
Oct13	QUPR	330	9/13/2011	38	47	32	< 0.006	< 0.07
Oct10	QUPR	332	9/13/2011	< 3.30	65	20	0.085	< 0.07
Oct9	QUPR	351	8/30/2011	28	49	21	< 0.006	< 0.07
Oct17	QUPR	358	8/30/2011	26	47	22	< 0.006	< 0.07
Oct15	QUPR	390	8/30/2011	52	47	88	0.064	< 0.07
Oct14	QUPR	396	9/13/2011	< 3.30	58	26	< 0.006	< 0.07
Oct18	QUPR	2060	8/30/2011	26	57	25	0.061	< 0.07
<i>Late summer average</i>				<i>29</i>	<i>54</i>	<i>33</i>	<i>0.033</i>	<i>bdl</i>
<i>Standard Deviation</i>				<i>15</i>	<i>7.5</i>	<i>23</i>	<i>0.034</i>	<i>bdl</i>

Table D-6E. Quality control on foliar chemistry for green leaves collected in 2011

Sample Name	Sample Type	Mg µg g⁻¹	Al µg g⁻¹	P µg g⁻¹	K µg g⁻¹	Ca µg g⁻¹	Mn µg g⁻¹
NIST 1547 certified value		4,320	249	1,370	24,300	15,600	98
<i>For samples analyzed in August</i>							
B1_aug4	Method Blank	< 1.40	< 120	< 580	< 95	< 90	< 0.9
B2_aug4	Method Blank	< 1.40	< 120	< 580	< 95	< 90	< 0.9
B3_aug4	Method Blank	< 1.40	< 120	< 580	< 95	< 90	< 0.9
PL1_aug4	Method Standard	3,467	< 120	1,322	20,021	12,520	73
PL2_aug4	Method Standard	3,509	< 120	1,409	20,162	12,959	74
PL3_aug4	Method Standard	3,923	129	1,393	22,349	14,119	85
	<i>Average % Error</i>	-15.90	-48.19	0.33	-14.22	-15.39	-21.03
<i>For samples analyzed in October</i>							
B1_Oct	Method Blank	< 1.40	< 120	< 580	< 95	< 90	< 0.9
B2_Oct	Method Blank	< 1.40	< 120	< 580	< 95	< 90	< 0.9
B3_Oct	Method Blank	< 1.40	< 120	< 580	< 95	< 90	< 0.9
PL1_Oct	Method Standard	4,568	128	1,612	25,941	16,677	101
PL2_Oct	Method Standard	4,582	114	1,358	25,950	16,317	97
PL3_Oct	Method Standard	3,975	91	1,171	22,320	14,034	82
	<i>Average % Error</i>	1.27	-55.29	0.78	1.80	0.49	-4.74
Sample Name	Sample Type	Na µg g⁻¹	Fe µg g⁻¹	Zn µg g⁻¹	Mo µg g⁻¹	Pb µg g⁻¹	
NIST 1547 certified value		24	218	17.9	0.06	0.87	
<i>For samples analyzed in August</i>							
B1_aug4	Method Blank	< 3.30	< 1.48	< 0.44	< 0.006	< 0.07	
B2_aug4	Method Blank	< 3.30	< 1.48	< 0.44	< 0.006	< 0.07	
B3_aug4	Method Blank	< 3.30	< 1.48	< 0.44	< 0.006	< 0.07	
PL1_aug4	Method Standard	24.88	169.5	15.34	< 0.006	0.55	
PL2_aug4	Method Standard	23.11	164.9	14.77	< 0.006	0.56	
PL3_aug4	Method Standard	26.43	185.0	18.12	< 0.006	0.64	
	<i>Average % Error</i>	3.35	-20.58	-10.19	-	-32.78	
<i>For samples analyzed in October</i>							
B1_Oct	Method Blank	< 3.30	< 1.48	< 0.44	0.011	< 0.07	
B2_Oct	Method Blank	< 3.30	< 1.48	< 0.44	0.018	< 0.07	
B3_Oct	Method Blank	< 3.30	< 1.48	< 0.44	0.010	< 0.07	
PL1_Oct	Method Standard	32.41	254.2	24.39	0.202	0.89	
PL2_Oct	Method Standard	29.95	215.8	22.31	0.433	0.88	
PL3_Oct	Method Standard	< 3.30	192.8	16.36	0.099	0.76	
	<i>Average % Error</i>	29.93	1.35	17.43	308.16	-2.80	

**Analyzed 100x diluted (Mg, Al, P, K, Ca, Mn) and 10x diluted (Na, Al, Fe, Zn, Mo, Pb) solutions separately

Table D-7. Site data for leaf litter samples from 2011 (see Figure D-2)

Site ID	Y-coordinate	X-coordinate	Elevation (m)
12	484853.429	1925319.93	271.497928
13	484728.639	1925376.45	282.557377
14	484683.97	1925573.44	286.224178
27	485057.008	1925756.14	271.108938
29	484927.288	1925920.38	287.068051
30	484813.303	1926051.63	299.522097
32	485250.985	1926083.45	278.958361
34	485204.966	1926185.91	287.901684
38	485064.333	1925003.3	261.537332
44	485242.321	1925243.64	279.144343
52	485202.84	1925571.86	278.420771
54	485403.259	1925567.68	296.50715
55	485139.72	1925593.42	275.528763
67	485450.981	1925883.03	301.335248
74	485367.508	1925568.55	294.698679
a1	484922.896	1925504.36	271.343426
a4	484857.736	1925535.31	287.752728

Table D-8A. Element concentrations in leaf litter collected in 2011

Sample Name	Site ID	Collection Date	Mg µg g⁻¹	Al µg g⁻¹	P µg g⁻¹	K µg g⁻¹	Ca µg g⁻¹	Mn µg g⁻¹
Aug31_12	12	8/31/2011	1,173	< 8	1,213	7,448	8,095	2,849
Aug31_13	13	8/31/2011	725	141	920	721	8,269	1,304
Aug31_14	14	8/31/2011	932	383	764	1,591	5,839	1,043
Aug31_32	32	8/31/2011	1,545	219	1,104	5,828	10,804	2,138
Aug31_34	34	8/31/2011	1,421	< 8	1,330	2,649	9,230	1,804
Aug31_52	52	8/31/2011	1,286	< 8	1,135	4,908	5,035	1,822
Aug31_54	54	8/31/2011	1,543	635	1,019	2,403	8,409	1,866
Aug31_55	55	8/31/2011	989	< 8	1,428	3,050	4,485	1,809
Aug31_74	74	8/31/2011	1,429	379	1,242	5,217	7,168	1,727
<i>Average</i>			<i>1,227</i>	<i>197</i>	<i>1,128</i>	<i>3,757</i>	<i>7,481</i>	<i>1,818</i>
<i>Standard Deviation</i>			<i>292</i>	<i>227</i>	<i>206</i>	<i>2,203</i>	<i>2,053</i>	<i>168</i>
Oct3_12	12	10/3/2011	1,549	1,322	1,485	3,852	13,683	3,051
Oct3_13	13	10/3/2011	1,818	1,624	1,345	2,420	17,089	2,246
Oct3_14	14	10/3/2011	1,906	47	1,227	2,598	13,765	2,741
Oct3_27	27	10/3/2011	3,334	< 8	798	3,108	13,860	1,756
Oct3_29	29	10/3/2011	1,277	< 8	812	3,522	8,824	4,214
Oct3_30	30	10/3/2011	1,807	1,694	1,120	3,035	13,650	4,271
Oct3_32	32	10/3/2011	1,812	717	987	2,573	17,045	2,489
Oct3_34	34	10/3/2011	1,443	988	858	2,167	11,611	2,298
Sample Name	Site ID	Collection Date	Mg µg g⁻¹	Al µg g⁻¹	P µg g⁻¹	K µg g⁻¹	Ca µg g⁻¹	Mn µg g⁻¹
Oct3_38	38	10/3/2011	1,095	188	726	1,187	10,083	1,704
Oct3_44	44	10/3/2011	1,261	< 8	1,318	2,547	12,778	3,629
Oct3_52	52	10/3/2011	1,713	159	1,055	3,764	10,174	2,737
Oct3_54	54	10/3/2011	2,162	3,834	1,482	2,610	16,122	3,674
Oct3_55	55	10/3/2011	2,028	802	1,057	2,255	10,257	3,351
Oct3_67	67	10/3/2011	1,800	303	1,356	1,509	17,226	1,267
Oct3_74	74	10/3/2011	2,031	4,062	1,665	2,271	14,174	3,243
Oct3_a1	a1	10/3/2011	1,044	< 8	1,082	1,824	11,499	2,787
Oct3_a4	a4	10/3/2011	1,237	< 8	972	2,622	10,235	3,263
<i>Average</i>			<i>1,725</i>	<i>927</i>	<i>1,138</i>	<i>2,580</i>	<i>13,063</i>	<i>2,866</i>
<i>Standard Deviation</i>			<i>539</i>	<i>1,278</i>	<i>272</i>	<i>727</i>	<i>2,710</i>	<i>207</i>
Oct31_12	12	10/31/2011	1,299	< 8	651	1,993	7,877	3,591
Oct31_13	13	10/31/2011	1,380	10	703	3,098	11,215	3,977
Oct31_14	14	10/31/2011	983	< 8	490	2,348	6,176	2,777
Oct31_32	32	10/31/2011	962	< 8	509	1,574	7,967	1,986
Oct31_34	34	10/31/2011	1,419	< 8	644	2,860	11,091	3,860
Oct31_52	52	10/31/2011	1,224	< 8	701	1,397	8,783	3,192
Oct31_54	54	10/31/2011	1,005	276	706	896	10,480	4,332
Oct31_55	55	10/31/2011	892	< 8	673	1,473	6,139	2,712
Oct31_74	74	10/31/2011	914	< 8	692	927	8,761	2,759
<i>Average</i>			<i>1,120</i>	<i>35</i>	<i>641</i>	<i>1,841</i>	<i>8,721</i>	<i>3,243</i>
<i>Standard Deviation</i>			<i>210</i>	<i>90</i>	<i>83</i>	<i>793</i>	<i>1,916</i>	<i>251</i>

Table D-8B. Quality control on foliar chemistry for leaf litter collected in 2011

Sample Name	Sample Type	Mg $\mu\text{g g}^{-1}$	Al $\mu\text{g g}^{-1}$	P $\mu\text{g g}^{-1}$	K $\mu\text{g g}^{-1}$	Ca $\mu\text{g g}^{-1}$	Mn $\mu\text{g g}^{-1}$
NIST 1547 certified value		4,320	249	1,370	24,300	15,600	98
<i>For samples collected 10/03/2011</i>							
B1_Oct3	Method Blank	< 1.6	< 8	435	< 3.2	< 27	< 1.6
B2_Oct3	Method Blank	< 1.6	< 8	512	< 3.2	< 27	< 1.6
B3_Oct3	Method Blank	< 1.6	< 8	376	< 3.2	< 27	< 1.6
PL1_Oct3	Method Standard	4,765	173	1,830	27,846	17,380	95
PL2_Oct3	Method Standard	4,637	134	1,900	14,672	16,979	92
PL3_Oct3	Method Standard	3,751	74	1,529	20,199	13,605	71
<i>Average % Error</i>		1.48	-49.14	27.96	-13.97	2.49	-12.43
<i>For samples collected 08/31/2011 and 10/31/2011</i>							
B1_AugOct	Method Blank	< 1.6	< 8	< 180	< 3.2	< 27	< 1.6
B2_AugOct	Method Blank	< 1.6	< 8	< 180	< 3.2	< 27	< 1.6
B3_AugOct	Method Blank	< 1.6	< 8	< 180	< 3.2	< 27	< 1.6
PL1_AugOct	Method Standard	5,052	133	1,607	17,737	17,985	100
PL2_AugOct	Method Standard	2,812	40	1,126	16,251	9,983	50
PL3_AugOct	Method Standard	4,090	114	1,445	23,163	14,510	79
<i>Average % Error</i>		-7.77	-61.61	1.64	-21.60	-9.23	-22.16

Table D-9. Manganese concentrations in groundwater collected near the stream weir

Date	Sample ID	Dissolved Mn (μM)
9/25/2008	DC2 well	1.46
9/25/2008	DC3 well	0.73
9/25/2008	DC4 well	0.55
9/25/2008	DC4 well	4.73
10/10/2008	ISCO101008GW1	<0.09
10/11/2008	ISCO101108GW1	<0.09
10/12/2008	ISCO101208GW1	<0.09
10/13/2008	ISCO101308GW1	<0.09
10/14/2008	ISCO101408GW1	<0.09
10/15/2008	ISCO101508GW1	<0.09
10/16/2008	ISCO101608GW1	<0.09
7/14/2009	ISCO071409GW1	<0.09
7/15/2009	ISCO071509GW1	<0.09
7/16/2009	ISCO071609GW1	<0.09
7/17/2009	ISCO071709GW1	<0.09
7/18/2009	ISCO071809GW1	<0.09
7/19/2009	ISCO071909GW1	<0.09
7/20/2009	ISCO072009GW1	<0.09
7/21/2009	ISCO072109GW1	<0.09
7/22/2009	ISCO072209GW1	1.46
7/23/2009	ISCO072309GW1	2.18
7/24/2009	ISCO072409GW1	8.37
7/25/2009	ISCO072509GW1	<0.09
7/26/2009	ISCO072609GW1	<0.09
7/27/2009	ISCO072709GW1	<0.09
7/28/2009	ISCO072809GW1	<0.09
7/29/2009	ISCO072909GW1	<0.09
7/30/2009	ISCO073009GW1	<0.09
7/31/2009	ISCO073109GW1	<0.09
8/1/2009	ISCO080109GW1	<0.09
8/2/2009	ISCO080209GW1	<0.09
8/3/2009	ISCO080309GW1	3.09
8/4/2009	ISCO080409GW1	4.55
8/4/2009	ISCO080409GW	<0.09
8/5/2009	ISCO080509GW	<0.09
8/6/2009	ISCO080609GW	<0.09
8/7/2009	ISCO080709GW	<0.09
8/8/2009	ISCO080809GW	<0.09
8/9/2009	ISCO080909GW	<0.09
8/10/2009	ISCO081009GW	<0.09
8/11/2009	ISCO081109GW	<0.09

Section D2. Estimation of dissolved Mn loads at the SSHCZO weir using LOADEST

Data

The time period for this study is January 1, 2008 through December 31, 2009. Discharge data has been reported at 10 min intervals for each day in this period ($n = 144$ per day; Duffy, 2012). Here, we use an average daily discharge for the days with nonzero discharge values ($n = 575$). The discharge data are reported as H (high quality observation), L (low quality observation), M (model), or F (fitting). Most data reported for 2008-2009 is H, with some L values during winter months. Water samples ($n = 315$) were collected at the stream outlet by an ISCO sampler and subsequently hand filtered ($0.45 \mu\text{m}$) and acidified prior to analysis on an inductively coupled plasma atomic emission spectrophotometer (ICP-AES) at the Penn State Materials Characterization Laboratory. Out of the 315 days where water chemistry is available, 108 days have zero discharge and are excluded from the dataset. Of the 207 remaining days, 124 have Mn concentrations below the detection limit (DL = 5 ppb), leaving 60% of the dataset censored.

Methods

LOADEST software (Runkel et al., 2004) was used to regress concentration versus discharge in the SSHCZO dataset and approximate a total dissolved Mn load from the catchment. Three input files (CALIB, EST, and HEADER) were prepared in space-delimited text format as provided in the LOADEST example documentation. CALIB, the calibration file, was set up to provide LOADEST with date, time, flow (in ft^3/s), and concentration (in $\mu\text{g L}^{-1}$) data from the 207 days with concurrent discharge and water quality measurements. Values below the detection limit were input to the file as <5 ($5 \mu\text{g L}^{-1}$ being the detection limit) and time was arbitrarily set to 1200 hours. EST, the estimation file, contained date, time, and flow (in $\text{ft}^3 \text{s}^{-1}$) data for each day in the dataset with nonzero discharge. LOADEST uses the concentration-discharge relationship evaluated in the CALIB file to estimate Mn loads for each day reported in the EST file.

Model constraints were defined in the HEADER file. Only Mn was evaluated, so the number of constituents (NCONST) was set to 1, and the unit concentration was set to micrograms per liter ($\mu\text{g L}^{-1}$) with load output in units of kilograms per day (kg d^{-1}). We chose to include individual load estimates in the output file (PRTOPT = 1), evaluate exact standard error for the AMLE, MLE and LAD models (SEOPT = 3), and estimate load over the entire period of record (LDOPT = 0). The model number (MODNO) defines the regression model used to fit the calibration data and can be set to any of 11 built in choices. We began with model 1:

$$\ln L = a_0 + a_1 \ln(Q)$$

Here, L = calculated load, $\ln Q = \ln(\text{streamflow}) - \text{center of } \ln(\text{streamflow})$, and a_0 and a_1 are fitting parameters. Model 1 is the simplest regression as it includes only discharge as an independent variable. We compared model 1 to models that include squared discharge (model 2):

$$\ln L = a_0 + a_1 \ln(Q) + a_2 \ln(Q^2)$$

and a model that incorporates seasonality (model 6):

$$\ln L = a_0 + a_1 \ln(Q) + a_2 \ln(Q^2) + a_3 \sin(2\pi dtime) + a_4 \cos(2\pi dtime)$$

Here, additional fitting parameters (a_2 , a_3 , and a_4) and a seasonality value ($dtime = \text{decimal time} - \text{center of decimal time}$) were included and assessed for their significance.

Results

Prior to LOADEST modeling, the raw data were used to assess basic concentration-discharge trends for Mn in the stream water (Figure 5-5). Here, one half the detection limit ($DL = 0.09 \mu\text{mol L}^{-1}$) was substituted for all values of Mn concentrations in the stream ($C_{Mn,stream}$) that were $< DL$. We observed that although the non-censored data showed a clear inverse relationship between concentration and discharge, low concentrations ($< DL$) occurred at all discharge values.

Furthermore, there was a positive relationship between discharge and the observed dissolved Mn load (L_{obs}), which was calculated as the product of $C_{Mn,stream}$ and Q . For a simple estimation, we took the annual discharge averaged between 2008-2009 ($= 39,529 \text{ m}^3 \text{ y}^{-1}$) multiplied by the average Mn concentration in the stream discharge ($= 3.94 \text{ mmol m}^{-3}$) and obtained an observed load estimation of $L_{Mn,stream} = 156 \pm 38 \text{ mol Mn y}^{-1}$ (see Chapter 5). Normalized to the surface area of the catchment (7.9 hectares), the Mn flux was approximately $1.97 \text{ mmol m}^{-2} \text{ y}^{-1}$.

In the first attempt to run model 1 with this dataset, LOADEST could not converge on a residual variance value for the concentration regression model. For this reason, eight concentration values recorded in early November 2009 and visually observed to be outliers were removed from the CALIB file. Removing these values left 199 data points in the calibration for the model.

The CALIB and EST files described above were run using models 1, 2, and 6 and the statistical outputs from those runs are shown (Table D-10). Inclusion of a squared flow value (model 2) and seasonality (model 6) did not greatly improve the model fit (Table D-11), nor were these variables determined to be significant (Table D-10). Therefore, it was determined that stream flow (Q) was the only significant variable for estimation of Mn concentrations and loads, and further analysis was conducted using model 1 regression.

Although observed Mn loads varied widely ($-2 < \ln L_{obs} < -16$), model 1 predicted a much more constrained range of values ($-12 < \ln L_{pred} < -8$) for the Q values in the CALIB file (i.e. dates

for which $C_{Mn,stream}$ values are available) (Figure D-16). This indicates large discrepancy between the individual observed and predicted load values. In fact, while the observed average load calculated from the raw data equals $L_{obs} = 1.2 \times 10^{-3} \text{ kg d}^{-1}$, the predicted average load over the same dates was calculated to be $L_{pred} = 9.5 \times 10^{-5} \text{ kg d}^{-1}$, more than an order of magnitude lower. However, L_{pred} averaged for the entire 2008-2009 period ($= 5.72 \times 10^{-3} \text{ kg d}^{-1}$) is larger than L_{pred} for the dates in CALIB file (Table D-12) and equates to dissolved loads of $L_{Mn,stream} = 1.56 \text{ kg Mn y}^{-1}$ for 2008 and $L_{Mn,stream} = 1.73 \text{ kg Mn y}^{-1}$ for 2009. The difference between L_{pred} for the dates in the calibration file ($9.5 \times 10^{-5} \text{ kg d}^{-1}$) and L_{pred} for the entire period of record ($5.7 \times 10^{-3} \text{ kg d}^{-1}$) is likely explained by inadequate coverage of discharge values in the calibration file. Thirty-one stream flow values in the estimation file (max $Q = 1.7 \text{ ft}^3 \text{ s}^{-1}$) fall above the maximum stream flow in the calibration file ($Q = 0.19 \text{ ft}^3 \text{ s}^{-1}$). These values will have high dissolved Mn loads and contribute greatly to the overall dissolved load. Thus, in order to get an appropriate estimate for $L_{Mn,stream}$, the model may underpredict L_{pred} at low discharge in order to compensate for the extrapolation of $C_{Mn,stream}$ data at high discharge.

Discussion

This dataset presents challenges to evaluating a concentration-discharge relationship for manganese. A large percentage (60%) of the analyzed samples contained Mn concentrations below the detection limit. Furthermore, censored data are concentrated at, but not exclusive to, higher discharge values. This means that there is uncertainty in the concentration-discharge relationship across the whole flow range. Finally, the highest discharge events do not have associated water quality data, forcing the program to extrapolate beyond the calibration data.

In general, the model fit to the data is very poor. The regression only explains 7.7% of the load variability and 16% of the concentration variability (Table D-11). Much of the error seems to derive from the censored data. The program compensates for the abundance of censored data by calculating a model that underestimates all measured data (Figure D-17).

With these caveats in mind, we use the model results to briefly evaluate the dissolved Mn flux from Shale Hills. Between 2008-2009, the model predicts an average dissolved Mn flux of $1.65 \pm 0.09 \text{ kg y}^{-1}$ ($= 30.0 \pm 1.6 \text{ mol y}^{-1}$). If we normalize that to the surface area of the catchment (~ 7.9 hectares), the Mn flux out of the watershed is equal to $0.38 \pm 0.02 \text{ mmol m}^{-2} \text{ y}^{-1}$. This value is lower than the estimate obtained from the observed values ($L_{obs} = 1.97 \text{ mmol m}^{-2} \text{ y}^{-1}$).

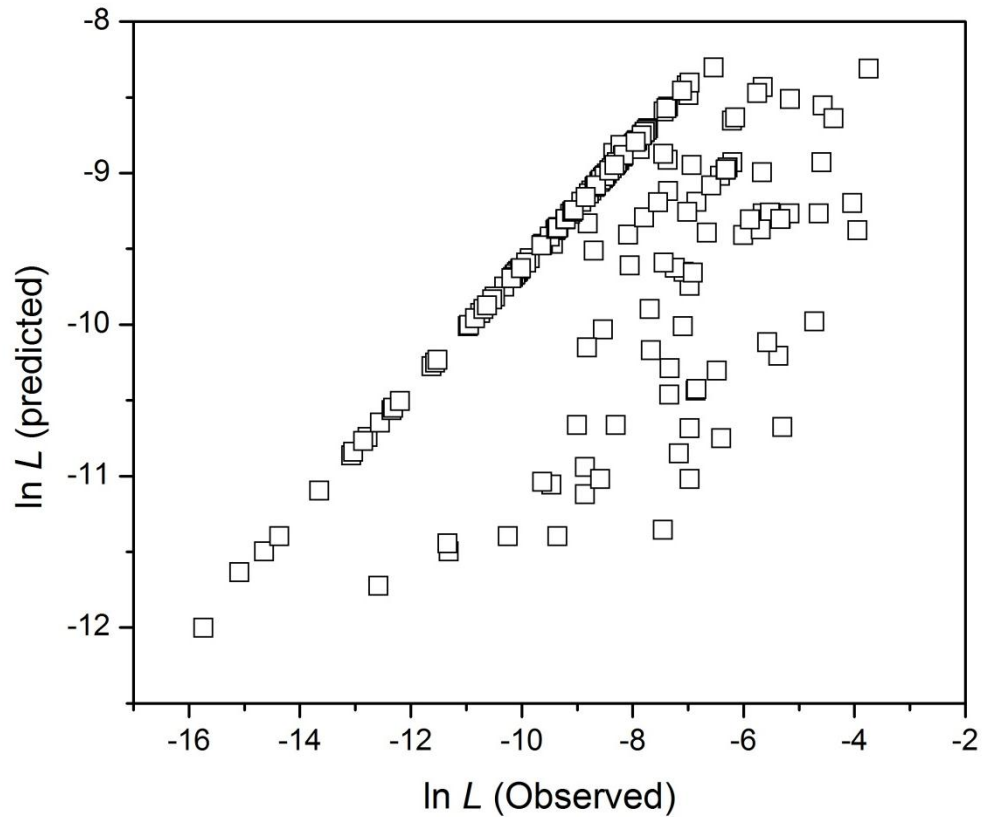


Figure D-16. Observed and predicted estimates of dissolved Mn load. Values for daily predicted loads calculated by LOADEST model 1 (L_{pred}) are plotted versus observed daily loads (L_{obs}), calculated as the product of Mn concentration in the stream ($C_{Mn,stream}$) and stream flow (Q).

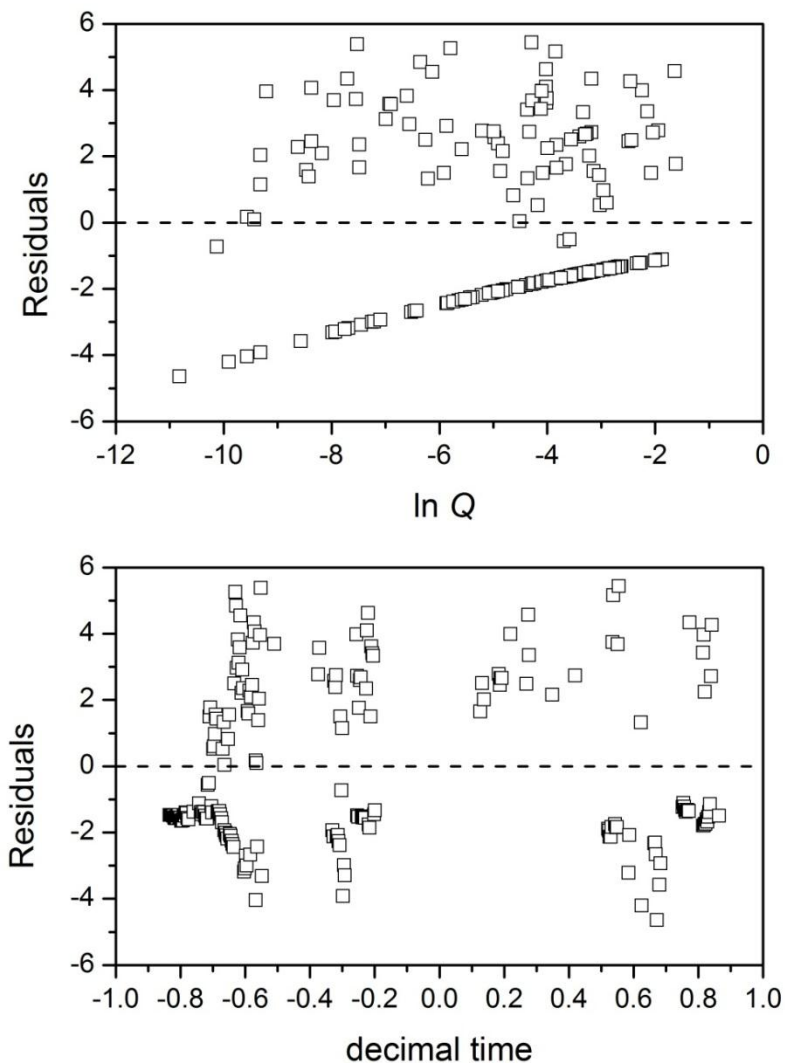


Figure D-17. Residual plots

Top) Residual values, the difference between observed and predicted loads of dissolved Mn ($= L_{obs} - L_{pred}$), are plotted versus stream flow ($\ln Q$). Residuals from non-censored data are randomly distributed, indicating that differences in Q adequately explain difference in L , but positive, indicating that L_{pred} underpredicts L_{obs} . Residuals for the censored data are plotted in negative space, indicating that the model may be underpredicting L_{obs} to compensate for the censored data. **Bottom)** Residuals show fairly random distribution as a function of adjusted decimal time (decimal time – center of decimal time), indicating a lack of seasonality in dissolved Mn loads. Non-seasonality is consistent with the non-significance of seasonality variables in the model 6 output (Table D-10).

Table D-10. LOADEST Model Parameters

	AMLE	Std.Dev.	t-ratio	P value
<i>Model 1: Ln(Load)</i>				
a0	-9.9236	0.2674	-37.11	<0.0001*
a1	0.4022	0.1103	3.65	0.0008*
<i>Model 1: Ln(Conc)</i>				
a0	1.7373	0.2674	6.5	<0.0001*
a1	-0.5978	0.1103	-5.42	<0.0001*
<i>Model 2: Ln(Load)</i>				
a0	-9.7019	0.372	-26.08	<0.0001*
a1	0.397	0.1116	3.56	0.0009*
a2	-0.0409	0.0505	-0.81	0.3999
<i>Model 2: Ln(Conc)</i>				
a0	1.9589	0.372	5.27	<0.0001*
a1	-0.603	0.1116	-5.41	<0.0001*
a2	-0.0409	0.0505	-0.81	0.3999
<i>Model 6: Ln(Load)</i>				
a0	-10.1499	0.5308	-19.12	<0.0001*
a1	0.5321	0.1532	3.47	0.0010*
a2	-0.0214	0.0533	-0.4	0.6642
a3	0.0075	0.3009	0.02	0.9736
a4	-0.8616	0.6796	-1.27	0.1979
<i>Model 6: Ln(Conc)</i>				
a0	1.5109	0.5308	2.85	0.0089*
a1	-0.4679	0.1532	-3.0500	0.0024*
a2	-0.0214	0.0533	-0.4000	0.6642
a3	0.0075	0.3009	0.0200	0.9736
a4	-0.8616	0.6796	-1.2700	0.1979

*denotes significant variable

(1) $a0 + a1*\ln Q$

(2) $a0 + a1*\ln Q + a2*\ln Q^2$

(6) $a0 + a1 \ln Q + a2 \ln Q^2 + a3*\sin(2\pi dtime) +$
 $a4*\cos(2\pi dtime)$

Table D-11. LOADEST Regression Statistics

Model	<i>AMLE Regression Statistics</i>			<i>Concentration Regression</i>	
	R-Squared %	Probability Plot Corr. Coeff.	Serial Corr. of Residuals	R-Squared %	Res. Variance
1	7.71	0.9488	0.4600	15.59	8.0736
2	7.94	0.9514	0.4620	16.22	8.0479
6	9.11	0.9510	0.4600	17.19	8.0554

Table D-12. Modeled daily load of dissolved Mn ($L_{Mn,stream}$, kg d⁻¹) in the stream at SSHCZO

	N	Mean Load	95% Confidence Intervals		Standard Error	Standard
		(kg d ⁻¹)	Lower	Upper	Prediction	Error
Est. Period	575	5.72E-03	1.03E-04	3.49E-02	1.63E-02	4.18E-03

Section D3. Discussion of m_j and W_j calculations

The integrated mass outflux or influx, $m_{j,w}$ (mmol m^{-2}), is the net loss ($m_{j,w} < 0$) or gain ($m_{j,w} > 0$) of a constituent j in the weathered soil material relative to the parent bedrock. Values of $m_{j,w}$ are calculated as the summation of $\tau_{i,j}$ (Eqn. 1 in Chapter 5) over depth, z (meters), from the mineral soil surface ($z = 0$) to the depth of auger refusal ($z = d$). This integration is corrected for volume strain (ε) following previous authors (Brimhall and Dietrich, 1987; Egli and Fitze, 2000):

$$m_{j,w} = C_{j,p} \rho_p \sum_{z=0}^{z=d} \frac{\tau_{i,j}(z) \Delta z}{\varepsilon(z) + 1}$$

Strain is a measure of soil volume change ($\varepsilon > 0$ for expansion or $\varepsilon < 0$ collapse) and is calculated for each depth interval (Δz) as $\varepsilon(z) + 1 = (C_{i,p}(z) \rho_p(z)) / (C_{i,w}(z) \rho_w(z))$ (Brimhall and Dietrich, 1987). Here, $C_{j,p}$ (mmol kg^{-1}) is the concentration of j in the parent material p , and ρ_p (kg m^{-3}) is the bulk density of the parent material.

An estimate for the long-term soil-integrated weathering rate of a constituent j in the soil (W_j , $\text{mmol m}^{-2} \text{y}^{-1}$) is calculated by dividing $m_{j,w}$ (mmol m^{-2}) by the residence time of particles in the soil profile, T_{soil} (years). In other words, we calculate W_j as the net loss of j in the soil averaged over the time that the soil has been weathering. Ma et al. (2010) determined rates of soil production (ω) in the ridge ($= 44.5 \text{ m My}^{-1}$), midslope ($= 27.5 \text{ m My}^{-1}$), and valley ($= 15.0 \text{ m My}^{-1}$) soils at Shale Hills using U-series isotope disequilibrium models. We use rates of soil production to calculate T_{soil} :

$$T_{soil} = d / \omega$$

Here, d is the thickness of the soil in meters that has been subject to weathering. In calculations of $m_{Mn,w}$ and T_{soil} to determine W_{Mn} , we exclude all soil samples for which $\tau_{Zr,Mn} > 0$ in order to eliminate the effects of atmospheric contamination. Thus, no estimate of W_{Mn} is calculated for SPRT, for which $\tau_{Zr,Mn} > 0$ at all depths.

Appendix E

Section E1. Sequential Extractions

Introduction

Students from two GEOSC 413W classes performed sequential extractions on soil samples collected from the SSHCZO in 2007 and 2009. In 2007, sequential extractions were performed on subsets of 13 soil samples collected from three ridge top soil profiles (AR1, AR2, and AR3). Soil samples included two organic horizon samples and mineral soil samples from the soil surface to the soil-bedrock interface (22 cm). Subsets of the soil included 38 – 63 μm and 63 – 2,000 μm size fractions. Sequential extractions were adapted from Kostka and Luther (1994) and Zemberyova et al. (1998) and performed using ammonium acetate to leach exchangeable Mn and Mn bound to organics (EXCH.), hydrochloric acid to leach Mn from amorphous oxides (AMOR.), and sodium dithionite to leach Mn from crystalline oxides (OXIDE). The material remaining after the three-step extraction procedure likely contained mostly silicate minerals and was analyzed for bulk chemical composition (RESIDUAL).

In 2009, sequential extractions were performed on mineral soil samples obtained from the top 5 cm of six ridge top soil profiles. In this study, the < 2 mm size fraction was analyzed. Sequential extractions were adapted from Rauret et al. (2000) and performed using acetic acid to leach water and acid-exchangeable Mn (EXCH.), hydroxylammonium chloride to leach “reducible” Mn (RED.), and ammonium acetate and hydrogen peroxide to leach “oxidizeable” Mn (OXID.). The reducible fraction should contain Mn leached from Mn-oxides while the oxidizeable fraction should contain Mn leached from organic matter. Specific details of the extractions are given below.

Methods (2007)

Size Fractionation. Soil samples were transferred to plastic weigh boats, covered with computer paper, and air dried for one week to reach constant mass. After drying, samples were homogenized using the four corners method to mix the soil. Approximately half of each sample was returned to the weigh boat for storage. The remainder was placed in a flask and disaggregated at 294rpm for 20 hours on a New Brunswick Innova 2000 Platform Shaker. Disaggregated soil was partitioned using Fisherbrand U.S. Standard Stainless Steel Test Sieves to obtain four size fractions: > 2mm, 63 μm – 2 mm, 38 – 63 μm , and < 38 μm . Each fraction was weighed and stored in a Ziploc bag. Minimal < 38 μm sample was obtained, possibly due to loss to the air during sieving.

Sequential Extraction. Exchangeable, amorphous, and oxide components were sequentially extracted from fine soil fractions into solution. Extraction protocol was modified from previous literature (Kostka and Luther, 1994; Zemberyova et al., 1998). To extract the exchangeable fraction (EXCH.), 10 mL 1M ammonium acetate (pH 7.0) was added to 0.5 g soil in a 50 mL centrifuge tube and placed in a shaker-incubator for 6 hr at 30°C and 240 rpm. The extract solution was separated through centrifugation at 4500 rpm and the supernatant was decanted into a new centrifuge tube for chemical analysis. To extract the amorphous fraction (AMOR.), 10 mL 0.5 M HCl was added to the remaining solid and shaken for 1 hr at 30°C and 240 rpm. The extract solution was separated through centrifugation at 4500 rpm and the supernatant was decanted into a new centrifuge tube for chemical analysis. To extract the oxide fraction (OXIDE), 10 mL of 50 g/L sodium dithionite solution (buffered to pH 4.8 with 0.35M acetic acid and 0.2M sodium citrate) was added to remaining solid and shaking for 4 hr at 60°C and 125 rpm. The extract solution was separated through centrifugation at 4500 rpm and the supernatant was decanted into a new centrifuge tube for chemical analysis. All sequential extraction solutions were analyzed by inductively coupled plasma atomic emission spectroscopy (ICP-AES) at the Penn State Materials Characterization Laboratory. The solid that remained after the three-step sequential extraction procedure (RESIDUAL) was fused with lithium metaborate, dissolved in 2% HNO₃, and analyzed by ICP-AES.

Methods (2009)

All soil samples were dried and sieved to collect the < 2 mm fraction for sequential extraction. A subset of the < 2 mm fraction (1 g) was added to a metal-free 50 mL centrifuge tube. To extract the exchangeable fraction (EXCH.; water- and acid-soluble elements), 40 mL 0.11 M acetic acid was added to the soil solid and shaken end over end for 16 hr at 40 rpm. The extract solution was separated through centrifugation at 3000 x g for 20 min and the supernatant was decanted into a new centrifuge tube for chemical analysis. The supernatant extract solution was dried down at 70°C. The soil was rinsed by shaking the solid with 20 mL milliQ water for 15 min at 30 rpm followed by centrifugation for 20 min at 3000 x g. The rinse supernatant was decanted and discarded.

To extract the reducible fraction (RED.; iron and manganese oxyhydroxides), 40 mL 0.5 M hydroxylammonium chloride was added to the soil solid and shaken end over end for 16 hr at 30 rpm. The extract solution was separated through centrifugation at 3000 x g for 20 min and the supernatant was decanted into a new centrifuge tube for chemical analysis. The supernatant extract solution was dried down and the solid residue was rinsed as described above.

To extract the oxidizable fraction (OXID.; organics and sulfides), 10 mL 8.8 M hydrogen peroxide was added to the soil solid and digested at room temperature for 1 hr before heating in an 85°C water bath for an additional hour. Then, 10 mL additional hydrogen peroxide was added and heated at 85°C until 1 mL of solution remained. Next, 50 mL of 1.0 M ammonium acetate was added to the solid residue and the tubes were shaken end over end for 16 hr at 30 rpm. The extract solution was separated through centrifugation at 3000 x g for 20 min and the supernatant was decanted into a new centrifuge tube for chemical analysis. The supernatant extract solution was dried down as described above. 10 mL of 2% nitric acid was added to each dried down extract solution and analyzed by inductively coupled plasma mass spectroscopy (ICP-MS).

Results and Discussion

Mineral soil samples collected from the top 5 cm of the soil profile (< 2mm size fraction) contained predominantly reducible Mn ($92 \pm 2\%$) relative to exchangeable ($5.5 \pm 1.3\%$) and oxidizable ($2.2 \pm 0.6\%$) Mn (Table E-2). The reducible Mn is likely in the form of amorphous or crystalline Mn or Fe oxyhydroxides while exchangeable Mn is sorbed onto particles and oxidizable Mn is bound to organic compounds (Zemberyova, Zwaik and Farkasovska (1998)). No analysis of the residual material was completed in the 2009 sequential extractions. The sequential extractions on the fine (38 – 63 μm) and coarse (62 – 2,000 μm) soil particles are consistent with sequential extractions on the < 2 mm fractions, with an average $86 \pm 2\%$ of the total Mn in all mineral soil samples contained in either “amorphous” (i.e. poorly-crystalline) or crystalline oxides (Table E-1). We observe that, on average at all depths, the fine particles contain a higher proportion of Mn in amorphous oxides ($55 \pm 6\%$) relative to the coarse particles ($26 \pm 4\%$). In contrast, the coarse particles contain a higher proportion of Mn in crystalline oxides ($59 \pm 3\%$) relative to the fine particles ($37 \pm 4\%$).

Total Mn in both the fine and coarse particles decreases with depth in the soil profile (Figures E-1 and E-2). In both size fractions, the proportion of Mn contained in amorphous oxides decreases with depth while the proportion of Mn contained in crystalline oxides increases with depth in the soil. This difference is more pronounced in the fine particles, which exhibit a 40% change in the amorphous and oxide proportions from the soil surface to 20 cm depth, than in the coarse particles, which exhibit a 20% change. Changes in the proportions of Mn in amorphous and crystalline oxides with depth could indicate separate pools of Mn formation. For example, initial products of Mn^{2+} oxidation are amorphous to poorly-crystalline oxides and generally exhibit a greater degree of crystallinity with aging (Tebo et al., 2004; Cui et al., 2010; Santelli et al., 2011). The high proportion of Mn in the amorphous fraction near the soil surface may indicate a more recently

precipitated source of Mn relative to the crystalline oxides that dominate the Mn fraction at depth. In other words, Mn at depth may derive from the older protolith material while Mn near the surface may derive from industrial or biogenic precipitates that are undergoing conversion to more recalcitrant oxides.

We note that no sequential extraction was completed for the > 2 mm size fraction or for soils deeper than 22 cm in the soil profile. The > 2 mm size fraction is mostly comprised of fractured bedrock and may contain a higher proportion of Mn in silicates (residual fraction) than found in the < 2mm size fractions. For XANES spectroscopy, only samples of ground bulk soil, including the > 2mm size fraction, were analyzed. Thus, XANES spectra may reflect a high concentration of Mn in residual silicate minerals that are not captured in the sequential extractions, especially for samples obtained from deep in the soil where external inputs of Mn are negligible.

References

- Cui H., Liu F., Feng X., Tan W. and Wang M. K. (2010) Aging promotes todorokite formation from layered manganese oxide at near-surface conditions. *Journal of Soils and Sediments* **10**, 1540–1547.
- Kostka J. E. and Luther G. W. (1994) Partitioning and speciation of solid phase iron in saltmarsh sediments. *Geochimica et Cosmochimica Acta* **58**, 1701–1710.
- Rauret G., López-Sánchez J.-F., Sahuquillo a., Barahona E., Lachica M., Ure a. M., Davidson C. M., Gomez a., Lück D., Bacon J., Yli-Halla M., Muntau H. and Quevauviller P. (2000) Application of a modified BCR sequential extraction (three-step) procedure for the determination of extractable trace metal contents in a sewage sludge amended soil reference material (CRM 483), complemented by a three-year stability study of acetic acid . *Journal of Environmental Monitoring* **2**, 228–233.
- Santelli C. M., Webb S. M., Dohnalkova A. C. and Hansel C. M. (2011) Diversity of Mn oxides produced by Mn(II)-oxidizing fungi. *Geochimica et Cosmochimica Acta* **75**, 2762–2776.
- Tebo B. M., Bargar J. R., Clement B. G., Dick G. J., Murray K. J., Parker D., Verity R. and Webb S. M. (2004) Biogenic manganese oxides: Properties and mechanisms of formation. *Annual Review of Earth and Planetary Sciences* **32**, 287–328.
- Zemberyova M., Zwaik A. A. H. and Farkasovska I. (1998) Sequential extraction for the speciation of some heavy metals in soils. *Journal of Radioanalytical and Nuclear Chemistry* **229**, 67–71.

Table E-1A. Mn concentrations in sequential extractions (413W 2007)

Depth (cm)		Site	Particle Size	EXCH. µg g ⁻¹	AMOR. µg g ⁻¹	OXIDE µg g ⁻¹	RESIDUAL µg g ⁻¹
O Horizon		AR3	38 – 63 µm	946	3,696	880	63
O Horizon		AR1	38 – 63 µm	233	5,797	2,774	310
0.0	2.0	AR1	38 – 63 µm	356	3,169	2,036	284
0.0	2.0	AR2	38 – 63 µm	< DL	1,936	770	108
0.0	2.0	AR3	38 – 63 µm	396	3,344	> DL	180
2.0	6.0	AR1	38 – 63 µm	123	912	799	172
4.0	6.0	AR3	38 – 63 µm	88	550	704	126
9.5	11.5	AR3	38 – 63 µm	88	396	506	49
15.0	17.5	AR3	38 – 63 µm	66	176	264	51
0.0	2.0	AR1	63 – 2,000 µm	343	2,746	3,191	423
2.0	6.0	AR1	63 – 2,000 µm	99	912	2,987	922
2.0	3.5	AR2	63 – 2,000 µm	132	572	1,892	360
3.5	5.5	AR2	63 – 2,000 µm	110	726	1,958	333
7.5	9.5	AR2	63 – 2,000 µm	66	704	1,100	234
16.5	22.0	AR2	63 – 2,000 µm	22	154	528	65

Table E-1B. %Mn in sequential extractions (413W 2007)

Depth (cm)		Site	Particle Size	EXCH. %	AMOR. %	OXIDE %	RESIDUAL %
O Horizon		AR3	38 – 63 µm	16.9	66.2	15.8	1.1
O Horizon		AR1	38 – 63 µm	2.6	63.6	30.4	3.4
0.0	2.0	AR1	38 – 63 µm	6.1	54.2	34.8	4.9
0.0	2.0	AR2	38 – 63 µm	0.0	68.8	27.4	3.8
0.0	2.0	AR3	38 – 63 µm	10.1	85.3	-	4.6
2.0	6.0	AR1	38 – 63 µm	6.1	45.5	39.8	8.6
4.0	6.0	AR3	38 – 63 µm	6.0	37.5	48.0	8.6
9.5	11.5	AR3	38 – 63 µm	8.5	38.1	48.7	4.7
15.0	17.5	AR3	38 – 63 µm	11.8	31.6	47.4	9.2
0.0	2.0	AR1	63 – 2,000 µm	5.1	41.0	47.6	6.3
2.0	6.0	AR1	63 – 2,000 µm	2.0	18.5	60.7	18.7
2.0	3.5	AR2	63 – 2,000 µm	4.5	19.3	64.0	12.2
3.5	5.5	AR2	63 – 2,000 µm	3.5	23.2	62.6	10.7
7.5	9.5	AR2	63 – 2,000 µm	3.1	33.5	52.3	11.1
16.5	22.0	AR2	63 – 2,000 µm	2.9	20.0	68.6	8.5

*Exchangeable (ammonium acetate), amorphous oxides (hydrochloric acid), crystalline oxides (sodium dithionite), and residual soil (lithium metaborate fusion)

Table E-2. Sequential extractions from 413W 2009

Depth (cm)		Sample	EXCH. $\mu\text{g g}^{-1}$	RED. $\mu\text{g g}^{-1}$	OXID. $\mu\text{g g}^{-1}$	EXCH. %	RED. %	OXID. %
0.0	5.0	G2S2 (#229)	123	8,440	96	1.4	97.5	1.1
0.0	5.0	G2S3 (#218)	109	3,660	60	2.8	95.6	1.6
0.0	5.0	G3(#1768)	200	2,589	20	7.1	92.2	0.7
0.0	5.0	G3(#1664)	192	1,937	44	8.8	89.2	2.0
0.0	5.0	G1S1(#950)	78	1,953	82	3.7	92.5	3.9
0.0	5.0	G1S3(#954)	138	1,320	61	9.1	87.0	4.0

*All samples are < 2mm size fraction

*Exchangeable (EXCH.), reducible (RED.), oxidizable (OXID.)

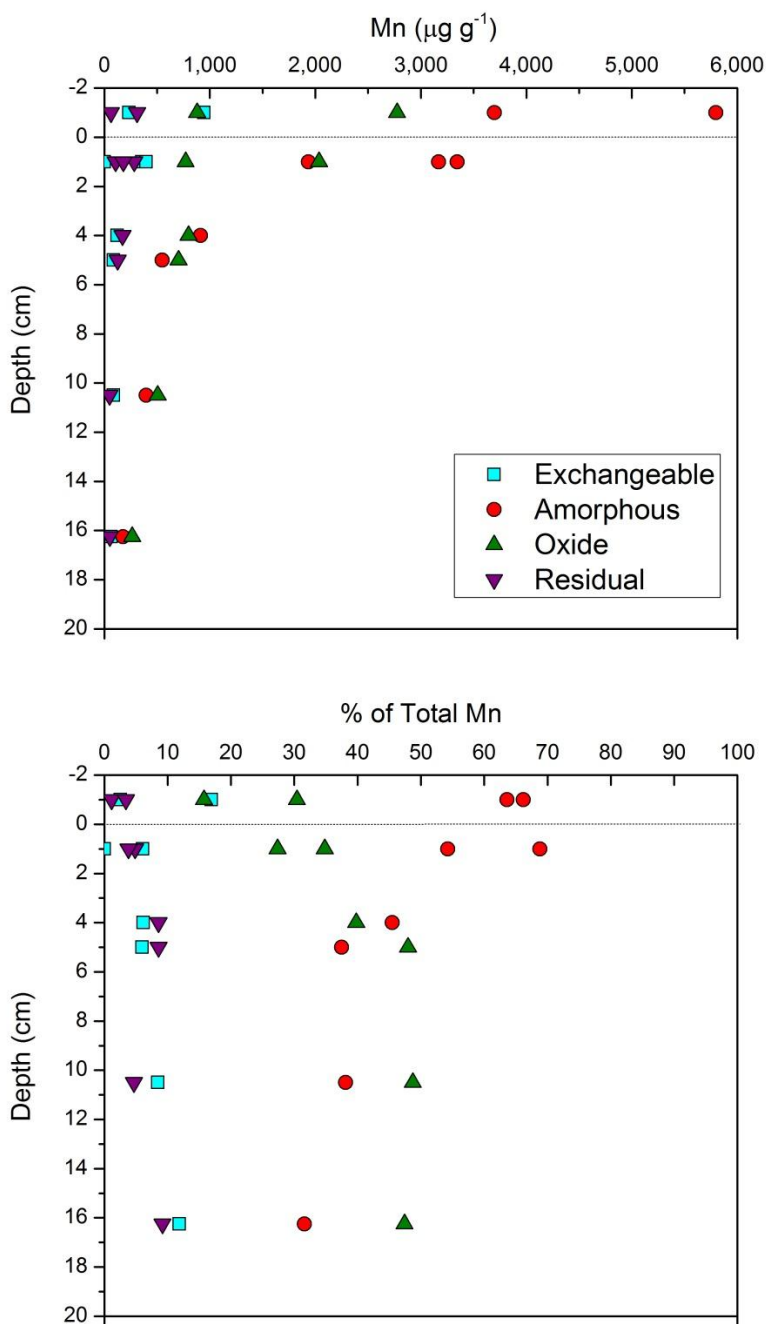


Figure E-1. Top) Mn concentrations ($\mu\text{g Mn (gram soil)}^{-1}$) present in exchangeable, amorphous, oxide, or residual fractions in fine soil particles are plotted versus depth in the soil profile. Mn was sequentially extracted from fine (38 – 63 μm diameter) soil particles in ridge top soils at SSHCZO. **Bottom)** The percent of total Mn in the fine particles that is contained in each fraction is plotted versus depth in the soil profile.

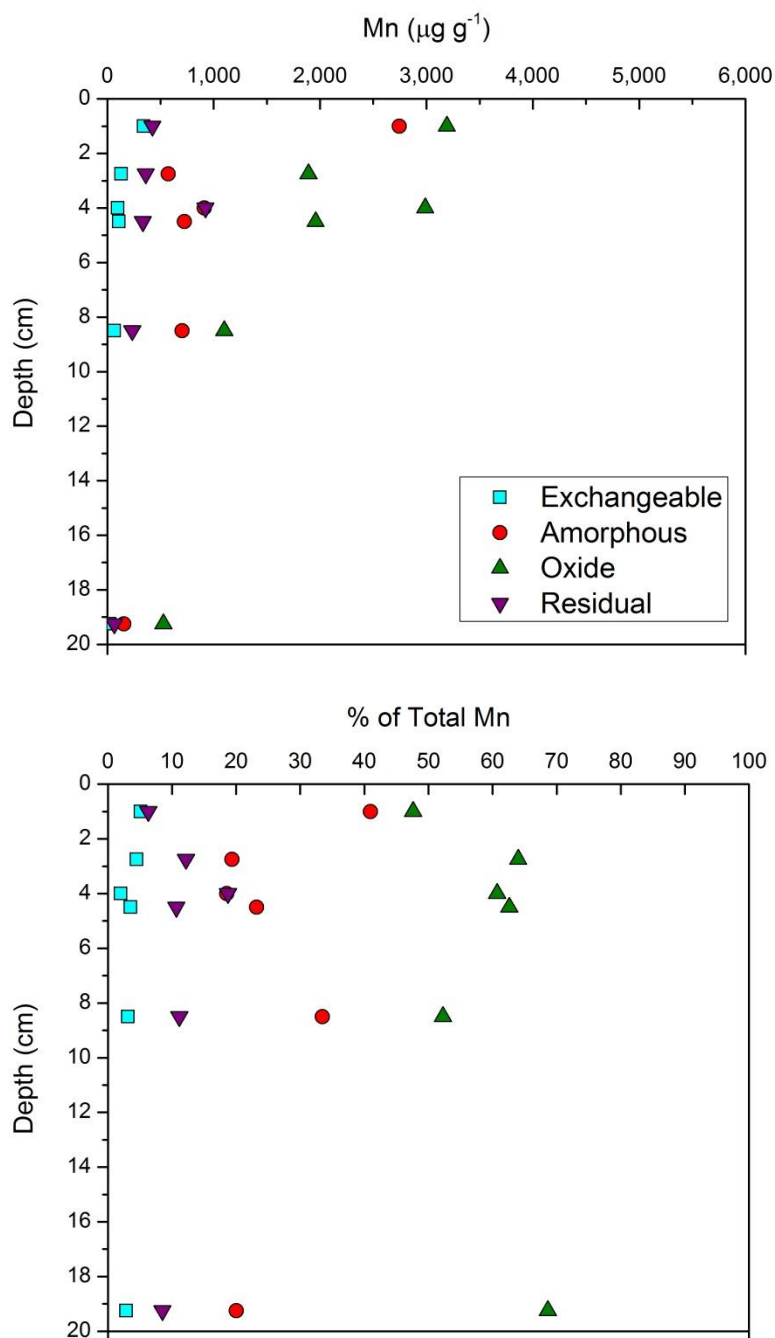


Figure E-2. Top Mn concentrations ($\mu\text{g Mn (gram soil)}^{-1}$) present in exchangeable, amorphous, oxide, or residual fractions in coarse soil particles are plotted versus depth in the soil profile. Mn was sequentially extracted from coarse ($63 - 2,000 \mu\text{m}$ diameter) soil particles in ridge top soils at SSHCZO. **Bottom**) The percent of total Mn in the coarse particles that is contained in each fraction is plotted versus depth in the soil profile.

Appendix F

Where did our rocks go? set to *Where did our love go?* (recorded by The Supremes)

Lyrics written by Elizabeth Herndon

Performed by The SUE-Premes (Sue Brantley, Elizabeth Herndon, Ashlee Dere, Heather Buss/Nichole West) in honor of Art White at his retirement

**Granite, granite
Granite don't leave me
Ooh, please don't leave me
To weather away**

**Carried by the rivers, rivers
And washed into the oceans
Ooh, please don't break down
And leave me with grus**

**You came into the crust
So intrusively
Ooh, you cooled so slowly
To an easy porphyry**

*Granite, granite
Where did our rocks go?
Granite, granite
Granite, granite, ooh granite, granite*

**Now you just surrender
So helplessly
After your orogeny
With just a little rain**

*Granite, granite
Where did our rocks go?
Granite, granite
Granite, granite, ooh granite, granite*

**Granite, granite
Where did our rocks go?
Ooh, did they weather
Did they weather away?**

*Granite, granite
Granite, granite, ooh granite, granite*

**Granite, granite
But what about limestone?
You leave me with fossils
Just dissolving away**

*Granite, granite
Where did our rocks go?
Granite, granite
Granite, granite, ooh granite, granite*

**Carried by the rivers, rivers
Washed back to the oceans
Ooh, taking my nutrients
You leave me sapro-light.**

*Granite, granite
Where did our rocks go?
Granite, granite
Granite, granite, ooh granite, granite*

**I guess I'm left with shale
Not even the gas kind
Ooh, given enough time
We're gonna frack it away**

*Granite, granite
Where did our rocks go?
Granite, granite
Granite, granite, ooh granite, granite*

**Granite, granite
Granite, don't leave me...Ooh, please don't leave me, to weather away...Ooooooh... granite**

ELIZABETH MAUREEN HERNDON – VITA

EDUCATION

- Ph.D., Geosciences and Biogeochemistry**, Pennsylvania State University (2012)
Dissertation: *Biogeochemistry of manganese contamination in a temperate forested watershed*
- B.A., Earth & Planetary Sciences** (*magna cum laude*), Washington University in Saint Louis, 2007
Honors thesis: *Microbial arsenic processes in shallow marine hydrothermal systems*
- B.A., Chemistry: Biochemistry concentration**, Washington University in Saint Louis, 2007

PUBLICATIONS

- Herndon, E.M.**, and Brantley S.L. (2011) Movement of manganese contamination through the Critical Zone. *Appl. Geochem* **26**, S40-S43.
- Herndon, E.M.**, Jin, L., and Brantley S.L. (2011) Soils reveal widespread manganese enrichment from industrial inputs. *Environ. Sci. Technol.* **45**(1), 241-247.
- Brantley S.L., ..., **Herndon E.**, ..., Yoo K. (2011) Twelve testable hypotheses on the geobiology of weathering. *Geobiology* **9**(2), 140-165.

FELLOWSHIPS

- Donald B. and Mary E. Tait Scholarship in Microbial Biogeochemistry, PSU; 2010-11
- P.D. Krynine Memorial Fund Research Grant, PSU; 2008-11
- Biogeochemistry Research Fellowship, Penn State University; 2009, 2011
- Goldschmidt Student Travel Grant, The Geochemical Society; 2008 & 2009
- Arnulf I. Muan Graduate Fellowship in Earth and Mineral Sciences, PSU; 2008-09
- Center for Environmental Kinetics Analysis Research Fellowship, Penn State; 2007-10
- University Graduate Fellowship, Penn State University; 2007-08
- Anne C. Wilson Graduate Research Award, PSU; 2007-08

AWARDS

- IAGC Faure Award for best student presentation, GES-9 conference; 2011
- Environmental Chemistry Student Symposium, 1st place Oral Presentation; 2009
- Geosciences Graduate Student Colloquium, Penn State University
- 1st place Oral Presentation by a Pre-comps student; 2009
 - 2nd place Oral Presentation by a Post-comps student; 2011
 - 1st place Oral Presentation by a Post-comps student – Peter Deines Memorial Lecture; 2012

SERVICE

- Session Chair, 22nd V.M. Goldschmidt Conference; 2012
- Chair, Geosciences annual banquet committee; 2011-12
- Elementary educational outreach, Shake Rattle and Rocks; 2010-11
- Steering committee, Environmental Chemistry Student Symposium; 2010-11
- Chair, CEKA Spring All-Hands Meeting; 2009
- Chair, Geosciences colloquium committee; 2008-09
- Chair, Geosciences graduate student welcoming committee; 2007-08

TEACHING EXPERIENCE

- Instructor: Techniques in Environmental Geochemistry, PSU; 2012
- Teaching Assistant: Earth and Life: Origin and Evolution teaching assistant, PSU; 2011
- Teaching Assistant: Techniques in Environmental Geochemistry, PSU; 2008